Continuous Hydrothermal Flow Synthesis and Characterisation of Nano-Bioceramics and their Rapid Consolidation Using Spark Plasma Sintering

Chaudhry, Aqif Anwar

Continuous Hydrothermal Flow Synthesis and Characterisation of Nano-Bioceramics and their Rapid Consolidation Using Spark Plasma Sintering

Aqif Anwar Chaudhry

A thesis submitted to the University of London for the degree of Doctor of Philosophy

Supervised by Dr. J. A. Darr

School of Engineering and Materials Science
Queen Mary, University of London

May 2008

I certify that the research in this thesis is the product of my own work and that any words and figures from the work of other people are fully acknowledged according to standard referencing.

Aqif Anwar Chaudhry

Abstract

Accidents, surgery and disease often result in the use of biomimetic materials that can replace human hard tissue and calcium phosphate bioceramics are ideally suited for this purpose. Indeed, biological apatite is a poorly crystalline, non-stoichiometric carbonated hydroxyapatite. The composition, crystallinity and particle size of synthetic calcium phosphate bioceramics directly affect their biological, mechanical and thermal performance. Hence control over these properties in synthetic bioceramics is essential in order to mimic human hard tissue in functionality. The existing methods of synthesis of calcium phosphate bioceramics are multi-step, time consuming and require strict control over synthesis conditions. Therefore, there is a requirement of a one-step, rapid synthesis technology which allows control over particle properties. The continuous hydrothermal flow synthesis (CHFS) technique addresses all such issues but it has not been used to synthesise calcium phosphate based nano-bioceramics.

The work in this thesis involves the use of CHFS technology to synthesise calcium phosphate bioceramics. It was demonstrated that the rapid crystallising environment in a CHFS system resulted in phase-pure crystalline hydroxyapatite (HA). Traditionally required long ageing times and heat-treatment were avoided. Furthermore, variations in the CHFS system parameters were correlated with properties of the synthesised nano-bioceramics.

The CHFS system was also used to substitute biologically beneficial ions (CO_3^{2-}, SiO_4^{4-}, Mg^{2+} and Zn^{2+}) into HA. Some ionic substitutions affected thermal stability and phase composition. For example, increase in magnesium contents in solution resulted in precipitation of a phase pure Mg-Whitlockite phase.

Conventional consolidation methods of HA powders require several hours of exposure to elevated temperatures which results in large grains, phase decomposition and poor mechanical properties. Spark Plasma Sintering on the other hand is capable of very high heating and cooling rates. Phase-pure and ion-substituted calcium phosphates and zirconia-hydroxyapatite phase mixtures were spark plasma sintered to high densities with these materials displaying good mechanical properties.

Acknowledgments

I would like to thank my supervisor Dr. Jawwad A. Darr for having confidence in me, facilitating my quick arrival to UK, his continuous motivation, support and career counselling. I would also like to express my gratitude to Dr. Ihtesham Rehman not only for his help and guidance regarding spectroscopy but also for his continuous patronage and inspiring discussions which extend beyond science. Dr. Fazal A. Khalid (FSME, GIKI, Pakistan) is thanked for his guidance and patronage. Dr. Mike Reece, Dr. Haixue Yan, Guiseppe Viola and Fawwad Inam are thanked for a collaboration on spark plasma sintering and mechanical testing. I would also like to thank Prof. Jonathan Knowles (EDI, UCL) for his help regarding variable temperature X-ray diffraction and his extremely useful, witty and thought provoking tips. Nicky Morden of EDI, UCL is also thanked for her help regarding elemental analysis. Dr. Monisha Phillips is thanked for her help regarding almost everything! Ranging from my frantic calls reporting a dirty STA, to the not so happy occasions where I broke BET glass tubes, I always found her smiling and have never heard her say no. Dr. Zofia Luklinska and Mick Willis of the EM unit (now Nanovision), are thanked for their help with electron microscopy. John Caulfield and Vince Ford are thanked for their help on countless occasions (equipment building, drilling, cutting, grinding etc.). Imran A. Moheet (project student) is thanked for his help on microindentation on HA which forms a part of his M.Sc. thesis. Department of Materials, QMUL and Higher Education Commission, Government of Pakistan are thanked for a partial tuition fee waiver and a scholarship, respectively.

Members and ex-members of CMTG, Yogesh, Jia, Andy, Paul, Sonia, Suela, Saba, Xiaole, Zhice, Kenan, Tian (team china), Josie and Kathryn are all thanked not only for their help regarding research but also for their friendship which has seen many biriyanis, kebabs, buffets, movies and wide-ranging discussions. I am lucky to have friends like; Saba, who helps in every possible way and tolerates my jabs, Praveen, for all those meals and Xbox sessions and Suela, for always encouraging and trusting my advice on electronics! Special thanks to Asad Sheikh for his timely help with the printing! I am also indebted to my lovely fiancé, Aisha (and family) for her relentless and unconditional support and most importantly her belief in me. Lastly but definitely not the least, I am deeply appreciative and in awe of all sorts of never ending support and encouragement from mom, dad and my amazing sisters from whom I have been away for almost last eight years.

Table of Contents

List of Figures

Chapter 1

Chapter 2

Chapter 3

Chapter 4

Chapter 5

Chapter 6

Appendix A

Appendix B

Appendix C

Appendix D

Appendix F

Appendix G

List of Tables

Chapter 1

Chapter 2

Chapter 3

Chapter 4

Chapter 5

Chapter 6

Appendix C

Appendix E

Appendix F

List of Abbreviations

BET	Brunauer, Emmett, Teller
Ca:P	Calcium to Phosphorus molar ratio
CDZ	Calcium Doped Zirconia
CMTG	Clean Materials Technology Group
CO_3-HA	Carbonate Substituted Hydroxyapatite
DSC	Differential Scanning Calorimetry
EDS	Energy Dispersive Spectroscopy
FE-SEM	Field Emission Scanning Electron Microscope
FTIR	Fourier Transform Infrared
HR-TEM	High Resolution Transmission Electron Microscope
Mg-βTCP	Magnesium stabilised tricalcium phosphate
Mg-CaP	Magnesium Substituted Calcium Phosphates
Mg-Whitlockite	Magnesium Whitlockite
nc-H_2O	Near critical water
PXRD	Powder X-ray Diffraction
sc-H_2O	Supercritical water
SEM	Scanning Electron Microscope
Si-HA	Silicate substituted Hydroxyapatite
SPS	Spark Plasma Sintering
STA	Simultaneous Thermal Analysis
TCP	Tricalcium phosphate
TEM	Transmission Electron Microscope
TGA	Thermogravimetric Analysis
VT-XRD	Variable Temperature X-ray Diffraction
Zn-CaP	Zinc Substituted Calcium Phosphates
ZrO_2-HA	Zirconia and Hydroxyapatite biphasic mixtures

Chapter 1

Literature Review on Synthesis and Consolidation of Bioceramics

In the last century, owing to improved quality of life due to discovery and development of medicines (antibiotics, vaccines), chemical treatment of water etc., there has been a major increase in human survivability (80+ years) (Hench 1998b). However, humans are faced with the challenge of outliving the 'lifetime' of human tissue as shown in Figure 1-1 (Hench & Wilson 1993).

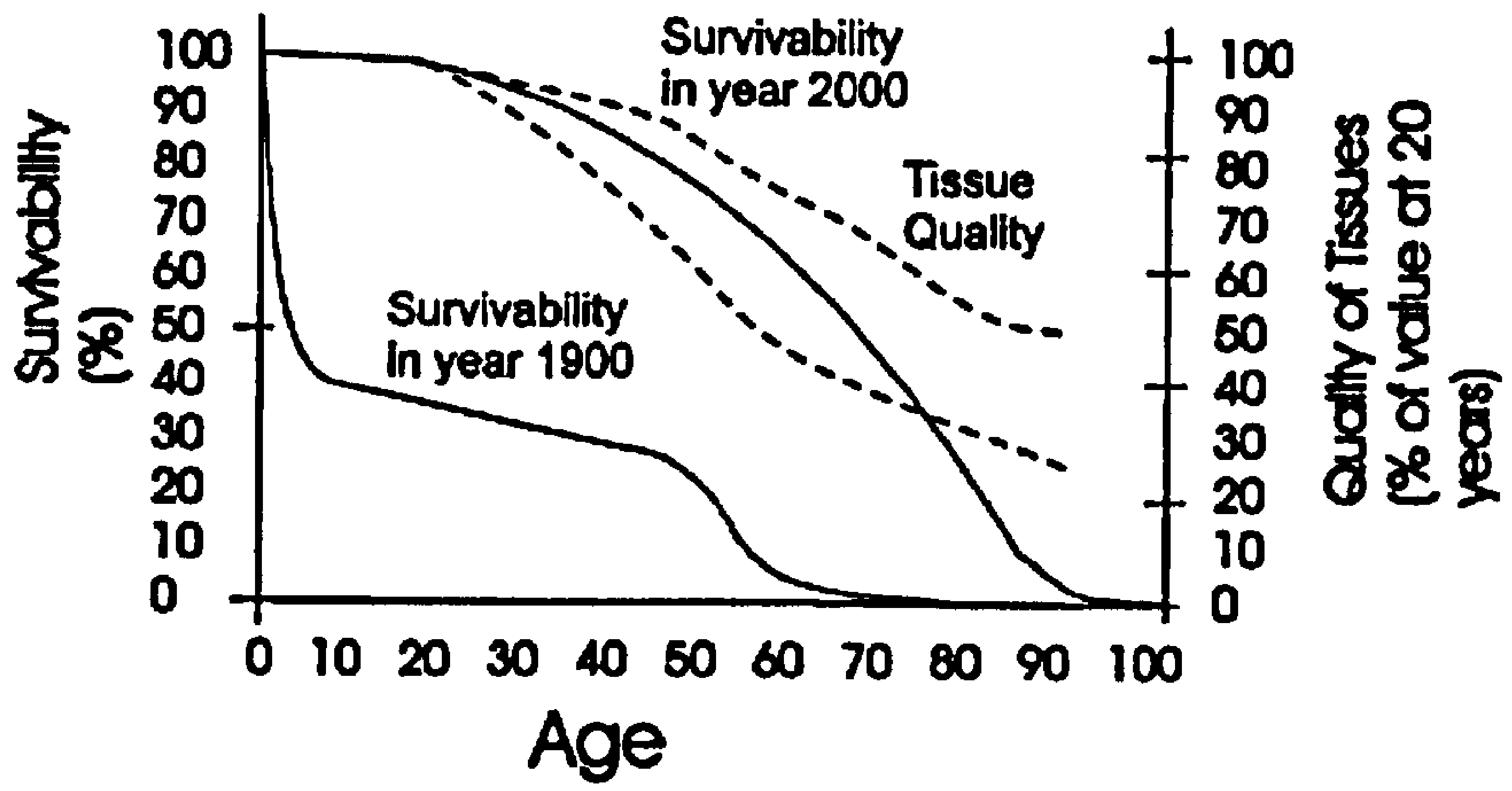

Figure 1-1 Comparison of human survivability in year 1900 vs. 2000 with effects of age on the quality of connective tissue (Hench & Wilson 1993).

In the past, diseased or damaged tissues had to be removed by the surgeon. During the last decade phenomenal attention has been directed towards research, development and utilisation of biomaterials aimed at mimicking natural tissues in chemical, mechanical and biological performance. However, before reviewing the developments in the field of biomaterials, it is important to appreciate the properties of bone and teeth as naturally occurring optimised biomaterials.

1.1 Introduction to Bone and Teeth

Bone and teeth play important functions in a human body and are referred to as hard tissues. Despite extensive research and investment, man is still far behind in designing synthetic materials which can completely replace these naturally occurring biomaterials.

1.1.1 Structure, Function and Properties of Bone

Bone is a hierarchically structured material (Fratzl et al. 2004; Rho et al. 1998). These structures work in unison to perform diverse mechanical, chemical and biological functions (Rho et al. 1998). Most bones are a sandwich structure with a dense external shell (cortical bone) and a spongy interior (only 20 volume % is bone material and the rest is bone marrow), known as cancellous bone (Fratzl et al. 2004). Bone consists of lamellae consisting of mineralised collagen fibrils. In bone, the assembly of these mineralised fibrils varies, allowing it to adapt to its mechanical function (Fratzl et al. 2004; Weiner et al. 1999; Zaffe 2005). The basic material of bone, therefore, is a nano-composite (Piekarsk 1973). This collagen-mineral composite contains nano-sized mineral platelets (biological apatite), protein and water (Fratzl et al. 2004; Wopenka & Pasteris 2005). Schematic diagram of this nano-composite is shown in Figure 1-2.

Apatite particles in bone have been reported to be between *ca.* 2 to 3 nm in thickness, 50 nm in length and 25 nm in width (the average size varies from report to report) (Rho et al. 1998; Rubin et al. 2003).

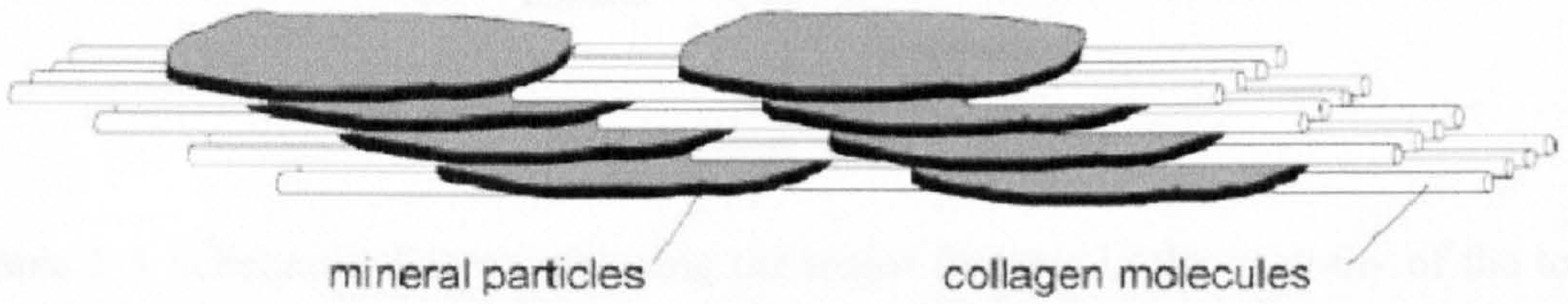

Figure 1-2 Schematic diagram of the arrangement of mineral particles in collagen fibrils (Fratzl et al. 2004).

Cortical and cancellous bones, understandably, have different mechanical properties. Bending strengths in the ranges 50 – 150 MPa and 10 – 20 MPa have been reported for cortical and cancellous bone, respectively (Hench & Wilson 1993; Thompson & Hench 1998).

An increase in age above 30 years, marks the onset of a gradual decrease in bone volume which results in reduced bone strength (both cortical and cancellous). By the age of 60-70 years, a significant decrease in bone volume takes place (Hench & Wilson 1993). This can lead to fracture. Moreover, bone diseases and trauma also result in a requirement for use of biomaterials to restore function and/or alleviate pain.

1.1.2 Structure, Function and Properties of Teeth

Tooth is a bone-like hard tissue. It comprises of an organic matrix (mostly collagen) and a reinforcement phase in the form of mineral crystals (non-stoichiometric apatite with a Ca:P molar ratio < 1.67) (Johansen 1964; Zioupos & Rogers 2006). Teeth act as hard tools for cutting and grinding and are faced with varying chemical environments on a daily basis (Jones 2001). However, teeth lack basic natural repair mechanisms because they are metabolically inactive. As protection the dentinal body of the tooth is covered with a thin (2 mm) harder enamel layer (Jones 2001; Nicholson 1998). Major features of a tooth are shown in Figure 1-3.

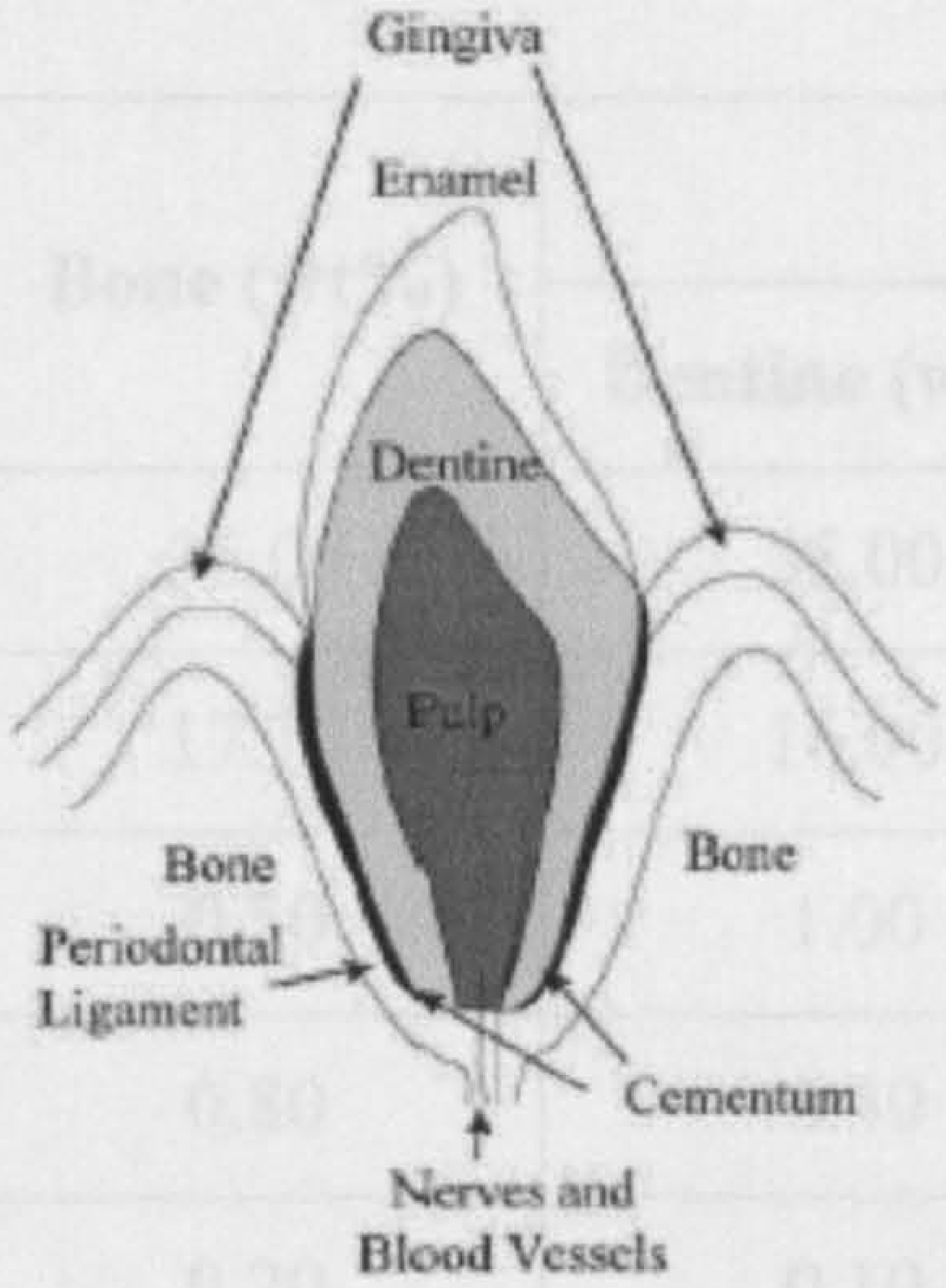

Figure 1-3 Schematic diagram showing the major features in the anatomy of the tooth (Jones 2001).

Hardness values of around 6 GPa have been reported for enamel (Cuy et al. 2002). Dentine, which is softer, has hardness values of less than 1 GPa, depending on the distance from the pulp and surrounding walls (Angker et al. 2003).

The most frequent dental surgical procedure is tooth extraction. Restoration and orthodontic procedures are also common dental treatments. These involve restoration of functionality and secondarily, good aesthetics by use of biomaterials such as wires, dentures and implants (Ratner et al. 2004).

1.1.3 Chemical Composition of Bone, Dentine and Enamel

Bone, dentine and enamel, have a water content of approximately 15 wt%, 13 wt% and 2 wt%, respectively (Aoki 1991; Nicholson 1998). The inorganic content of bone, dentine and enamel is approximately 55 wt%, 70 wt% and 96 wt%, respectively (Aoki 1991; Jones 2001; Li & Aspden 1998; Nicholson 1998). The approximate chemical composition of bone, dentine and enamel is presented in Table 1-1 in which the residuals include minor elements (e.g. Si, Zn) and oxygen. However, these contents differ by age and species (Aoki 1991). Biological apatite is a poorly crystalline hydroxyapatite (HA) represented by $Ca_{10}(PO_4)_6(OH)_2$ (Elliott 1994; Wopenka & Pasteris 2005). Biological apatite however differs from synthetic apatite as it consists of various ions such as Na^+, Mg^{2+}, Cl^-, F^-, HPO_4^{2-}, CO_3^{2-} and SiO_4^{4-} (LeGeros 2002; Wopenka & Pasteris 2005).

Table 1-1 Composition of bone, dentine and enamel (Aoki 1991).

Element	Bone (wt%)	Tooth	
		Dentine (wt%)	Enamel (wt%)
Ca	36.00	35.00	37.00
P	17.70	16.00	17.00
Mg	0.50	1.00	0.40
Na	0.80	0.40	0.60
K	0.20	0.10	0.20
C	1.60	1.10	0.80
Cl	0.20	Trace	0.30
F	0.08	0.03	0.01
Residual	47.62	46.37	43.69
Total	100	100	100

1.2 Introduction to Biomaterials

Biomaterials are required to alleviate pain and restore function to damaged part of the body (Hench & Wilson 1993; Vats et al. 2003). This need stems from the progressive deterioration of tissue with age. Loss of bone density and strength with age makes older people more susceptible to bone fracture (Hench & Wilson 1993). Biomaterials are also used in dental implants, toothpastes and dental cements. Injuries resulting from accidents or diseases also contribute to the need for biomaterials (Hench 1998a).

For any synthetic material to be implanted in the body, the following requirements must be met (Katti 2004; Ratner et al. 2004):

- It does not cause an inflammatory or toxic response beyond an acceptable level.
- It withstands chemical, mechanical and thermal loads without deterioration.
- It is manufactured economically and within permitted impurity levels according to approving bodies e.g. Food and Drug Administration, FDA.

For any material in the human body the environment is very harsh. The materials are exposed to corrosive saline solutions at 37 °C under variable mechanical loads. Furthermore, metabolic changes often occur producing various acids. All these factors have to be taken into account before a material can be declared biocompatible and suitable for implantation (Hench 1998a; Jones 2001).

Metals were the first choice biomaterials in the past due to their superior mechanical properties (Katti 2004; Staiger et al. 2006). However, it has been found that metals can release ions into the blood and surrounding tissues. Depending on the release rate, the body may develop some adaptation to this. However, metals are generally found to be toxic (Ferreira et al. 2003b). In comparison, although polymers are less toxic, when used alone they do not possess the mechanical strength to be used in load bearing applications (Katti 2004). Metals can also lead to bone deterioration as a result of elastic mismatch between growing bone and the metallic implant.

Bioceramics offer more advantages in terms of biocompatibility, therefore, their utilisation as sintered porous or block forms, reinforcements in polymeric matrices and coatings on metallic implants leads to materials with improved biocompatibility. A vast number of clinical applications of bioceramics in the human body are summarised in Figure 1-4.

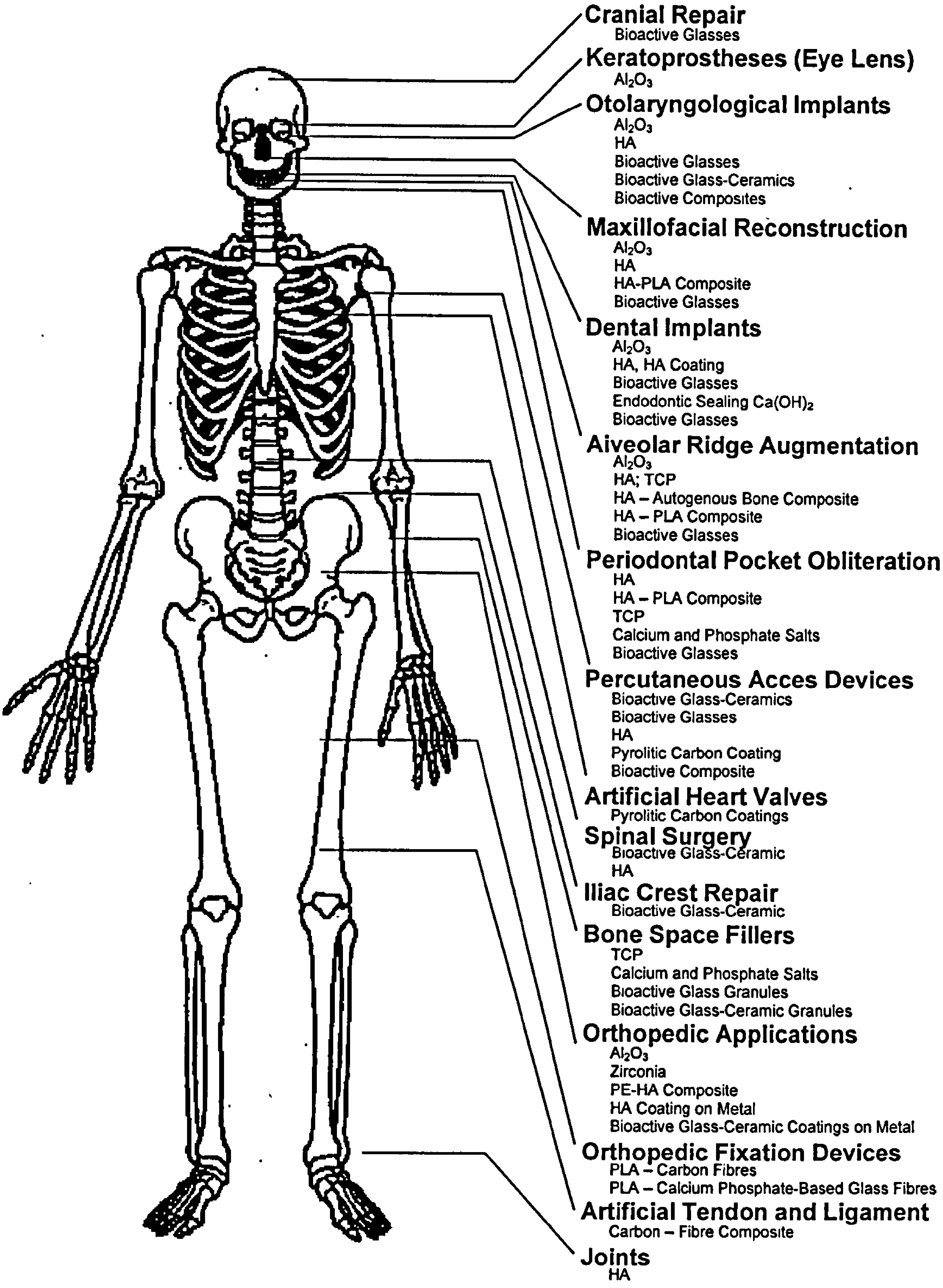

Figure 1-4 Clinical uses of bioceramics (Hench & Wilson 1993).

1.2.1 Types of Bioceramics

Bioceramics can be classified as toxic, bioinert, bioactive and resorbable based on the type of response they invoke from the surrounding tissue.

1.2.1.1 Tissue Response to Bioinert Bioceramics

Bioinert bioceramics are chemically inactive and of high strength. They attach to tissue via a mechanical interlock, also referred to as morphological fixation (Hench & Wilson 1993). The tissue response to a bioinert bioceramic is formation of a non-adherent fibrous capsule which forms to isolate the implant from the host (Hench & Wilson 1993). This is a protective mechanism and may result in complete encapsulation of an implant. If interfacial movement occurs, the fibrous capsule can become several hundred microns thick and the implant loosens as a result, which can ultimately lead to failure (Hench 1998a).

1.2.1.2 Tissue Response to Bioactive Bioceramics

Bioactive bioceramics are also referred to as surface reactive bioceramics. This is because bioactive bioceramics undergo chemical reactions at their surface in the human body. This results in bonding to tissues at the interface. Commonly, a carbonated apatite layer forms on the surface of all bioactive implants when implanted (Ducheyne & Qiu 1999; LeGeros 2002). This layer then grows and collagen fibrils become incorporated. Hence, the inorganic implant surface bonds to the surrounding tissues and this interface is similar to the naturally occurring interfaces between bone, tendons and ligaments. This type of attachment is known as bioactive fixation (Hench & Wilson 1993).

Bioactive materials are classified into two types: (Cao & Hench 1996)

- Class A, osteoproductive materials, which bond with bone and soft tissue. These facilitate a process by which a bioactive surface is colonised by osteogenic stem cells free at the implant site as a result of surgical intervention. These materials elicit both an intracellular and an extracellular response at its interface.

- Class B, osteoconductive materials. These materials only provide a biocompatible interface along which bone migrates. These materials only elicit an extracellular response at its interface.

The level of bioactivity of a specific material can be related to time for more than 50% of the interface to be bonded. The index of bioactivity, I_B, introduced by Hench is as follows,

$$I_B = \frac{100}{t_{0.5bb}} \qquad \textbf{Eq. 1-1}$$

Here $t_{0.5bb}$ is the time for more than 50% of the implant interface to be bonded to bone (Cao & Hench 1996). Bioactivity is also attributed to materials that have the ability to form a surface layer of carbonated apatite when exposed to body fluids (Ducheyne & Qiu 1999; LeGeros 2002).

1.2.1.3 Tissue Response to Resorbable Bioceramics

Resorbable bioceramics degrade gradually with time and are replaced by natural tissues. Due to this the interfacial thickness between the implant and tissue is almost non-existent. This is ideal as bone regeneration takes place; however, while the regeneration of tissue occurs, mechanical performance can be a cause of concern. It is important that the dissolution rates be matched to the body tissue repairs rates (Hench & Wilson 1993). In cases where porous ceramics are used, the attachment between tissue and the implant is called Biological fixation, which occurs due to in growth of tissues into pores (Hench & Wilson 1993).

1.2.2 Examples of Bioceramics

1.2.2.1 Alumina (Al_2O_3), Zirconia (ZrO_2) and Titania (TiO_2)

Alumina (bioinert) was the first widely used bioceramic clinically and is used even today in dental implants and total hip prostheses (Thamaraiselvi & Rajeswari 2004). It has a very high corrosion resistance, biocompatibility, low friction, high strength and high wear resistance (Marti 2000). The higher Young's modulus of Al_2O_3 however, prevents bone from being loaded – a phenomena known as stress shielding. This is responsible for loosening of the acetabular cup in patients (Hench 1998a; Katti 2004; Marti 2000).

Zirconia (bioinert) has high mechanical strength and fracture toughness due to its transformation toughening behaviour (Chevalier 2006). Zirconia ceramics exist in various crystallographic forms with varying mechanical properties. Pure zirconia ceramics cannot be used for medical applications as the sintering process leads to a phase transformation (volumetric change of the material) from tetragonal to monoclinic which occurs during cooling phase above room temperature (Manicone et al. 2007). This phase transformation is associated with a 3-4 % volume expansion generating internal material stresses and cracks. Yttria stabilised ZrO_2 has been utilised in total hip replacement (ball heads) extensively (Marti 2000). However, due to its metastability, it is prone to ageing in water. Due to this reason, recently, around 400 femoral heads failed in a very short period in 2001, despite manufacturer's claims that ageing *in vivo* was limited (Chevalier 2006). Zirconia has also been used in plasma sprayed bioceramic coatings (Kurzweg et al. 1998).

Titania is a bioinert bioceramic with good biocompatibility (Fidancevska et al. 2007). Nanostructured porous titania based devices have been used to deliver antiepileptic drugs directly to the central nervous system through the temporal lobe of the human brain (Lopez et al. 2007). Titania has also been used in plasma sprayed bioceramic coatings on Ti-6Al-4V hip endoprostheses and other metallic implants (Kurzweg et al. 1998; Marple et al. 2006). Problems with bioinert bioceramics suggest that a strong interaction between the implant and tissue is desirable (Hench 2000) which emphasises the need of a bioactive interface.

1.2.2.2 Bioactive Glasses and Glass-Ceramics

Bioactive glasses and glass-ceramics are made by traditional high temperature melting, casting and sintering. The base components in these are mostly SiO_2, Na_2O, CaO and P_2O_5. Many bioactive SiO_2 glasses are based upon a formula called "45S5" (Chen et al. 2006b). This signifies 45 wt% SiO_2. Glasses with larger amounts of P_2O_5 do not bond to bone. Figure 1-5 shows the compositional dependence of bone and soft tissue bonding of bioactive glasses and glass ceramics.

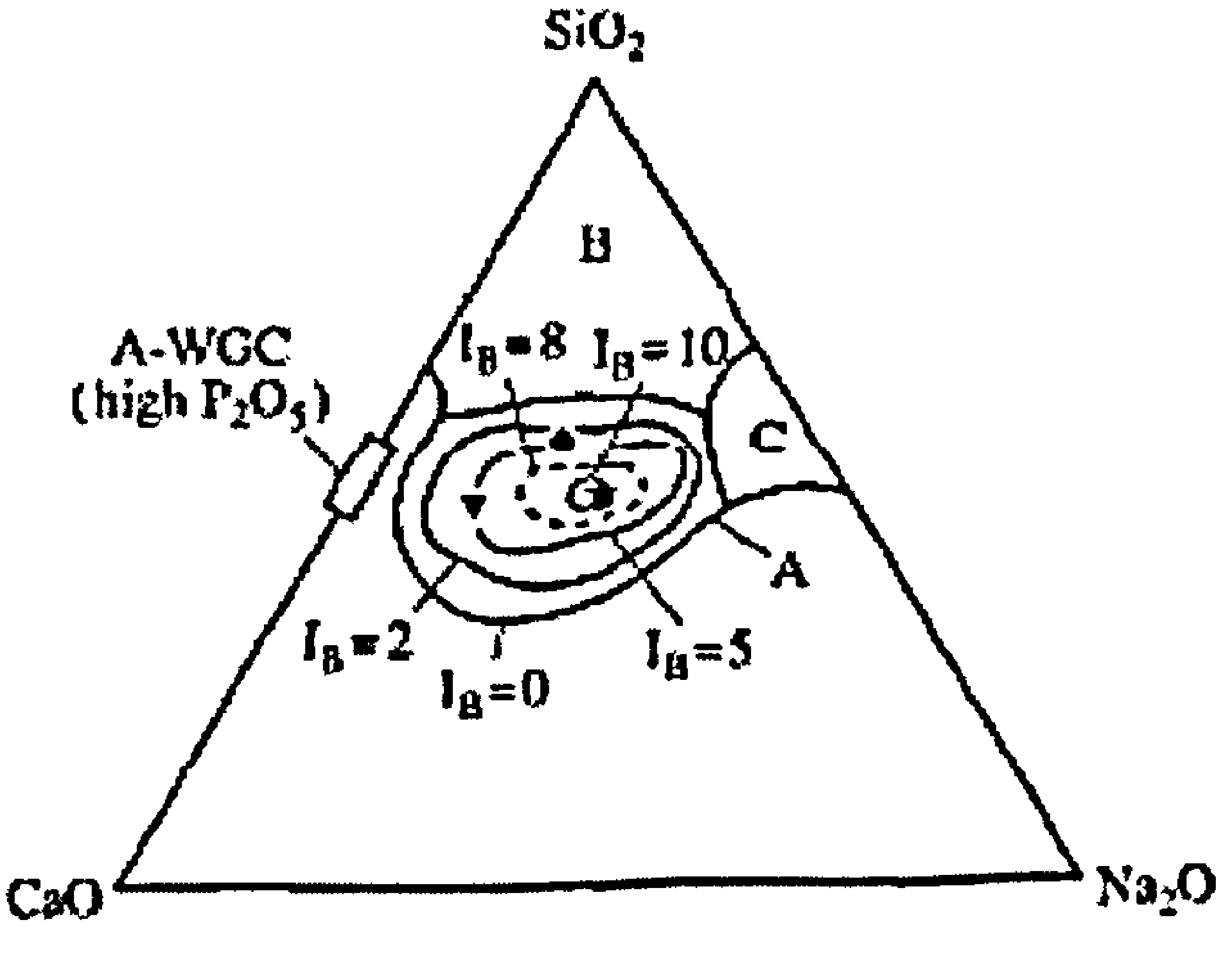

Figure 1-5 Compositional dependence of bone bonding and soft-tissue bonding of bioactive glasses and glass ceramics (Hench 1991).

In region A in Figure 1-5 glasses are bioactive and bond to bone. Glasses in region B are inert and result in the formation of a fibrous capsule at the implant-tissue interface. Region C shows glasses which are resorbed within 10-30 days in tissue. I_B lines represent the index of bioactivity. Depending on composition, therefore, certain glasses are resorbable. The region inside the dashed lines represents compositions which can even bond to soft tissue. Monophase bioglasses have restricted clinical applications due to their poor mechanical properties (Cao & Hench 1996). Crystallisation of glass results in glass-ceramics which have improved mechanical properties (composition represented by A-WGC in Figure 1-5) (Hench 1991; Kokubo et al. 1986).

Bioactive glasses and glass-ceramics have been used to replace the small bones of the middle ear damaged by chronic infection, for over a decade. 45S5 Bioglass has been used to preserve the jaw bone in patients who have had their teeth extracted prior to being fitted with dentures (Hench & Wilson 1993). Bioactive glasses have also been used as particulates which are placed around teeth that have a periodontal disease and in spinal fusion (Hench 1998a; Hench 2000).

1.2.2.3 Calcium Phosphate Ceramics

The first clinical attempt to use a calcium phosphate compound was in successful repair of a bony defect reported in 1920 (Albee 1920). It was not until the late seventies and eighties that serious efforts were made towards the development and commercialisation of calcium phosphates, particularly hydroxyapatite (Akao et al. 1981; Hench & Wilson 1993; LeGeros 2002). Today calcium phosphate ceramics are widely used and preferred materials for use in implants mainly due to the following characteristics; (Ellingsen et al. 2006)

- their similarity to bone mineral in chemical composition
- their ability to form carbonated hydroxyapatite at the surface *in vivo*
- formation of a strong biological, chemical and physical bond at the implant-tissue interface
- their ability to bind to and concentrate endogenous bone morphogenetic proteins

The calcium phosphate system represents one of the most complex families of materials due to the existence of a large number of phosphate compounds. Variations in pH, reaction conditions such as solvent, temperature, pressure, nature of precursors and compositional changes (Ca:P molar ratio) all affect the stability of the each of the calcium phosphates that may exist (Aoki 1991; Elliott 1994). Table 1-2 summarises the names, formulae and Ca:P molar ratios of various calcium phosphates.

Table 1-2 Table showing Ca:P molar ratios, formulae and names of different calcium phosphate ceramics.

Ca:P ratio	**Formula**	**Name**	**Abbreviation**
2	$Ca_4O(PO_4)_2$	Tetracalcium phosphate (Hilgenstockite)	TeCP (TTCP)
1.67	$Ca_{10}(PO_4)_6(OH)_2$	Hydroxyapatite	HA
1.50	$Ca_3(PO_4)_2$	Tricalcium phospate (α, β, γ) (Whitlockite)	TCP
1.0	$CaHPO_4.2H_2O$	Dicalcium phosphate dihydrate (Brushite)	DCPD
1.0	$CaHPO_4$	Dicalcium phosphate (Monetite)	DCP

Hydroxyapatite (HA) and tricalcium phosphate (TCP) are the amongst the most interesting calcium phosphate ceramics. Synthetic HA is bioactive and chemically similar to the mineral component of bone whereas TCP is resorbable (deAza et al. 1997; LeGeros 2002). Biphasic mixtures of TCP and HA are also promising materials as they provide stability (due to HA) and quicker bone formation and bonding (due to TCP) (Bouler et al. 2000). Calcium phosphate ceramics have been used in repair of bony defects in dental and orthopaedic applications, maxillofacial reconstruction and coatings on dental and orthopaedic implants. Their applications are shown in Figure 1-4.

1.3 Structure, Substitution, Synthesis and Consolidation of Hydroxyapatite

In this section the crystallographic structure, composition (elemental substitution into HA lattice), synthesis methods and consolidation of HA are discussed.

1.3.1 Structure of Hydroxyapatite

Hydroxyapatite is represented by the following formula; $Ca_{10}(PO_4)_6(OH)_2$. Slightly non-stoichiometric HA belongs to the hexagonal system with $P6_3/m$ space group (Hench & Wilson 1993) whereas stoichiometric hydroxyapatite is monoclinic with $P2_1/b$ space group (Elliott 1994; Morgan et al. 2000). However, most synthesis methods result in slight non-stoichiometry and hence a hexagonal structure. Figure 1-6 represents the hexagonal unit cell of hydroxyapatite showing two different calcium ion positions. The phosphorus atoms are not shown as oxygen atoms occupy most of the volume in a phosphate group. The unit cell consists of 18 ions packed closely. Each calcium ion (in hexagonal corner positions) is shared by three hexagons (12 x 1/3 = 4 Ca^{2+} ions per unit cell). At the centre of each hexagon there is a hydroxyl ion (therefore 2 OH^- per unit cell). These hydroxyl ions are surrounded by three Ca^{2+} ions per hexagon forming a ring (6 x Ca^{2+} per unit cell). These rings form a "chord" throughout the structure and many properties of HA are attributed to this. Alternating spaces in the two hexagons are filled up by three tetrahedral phosphate ions per hexagon (6 x PO_4^{3-}).

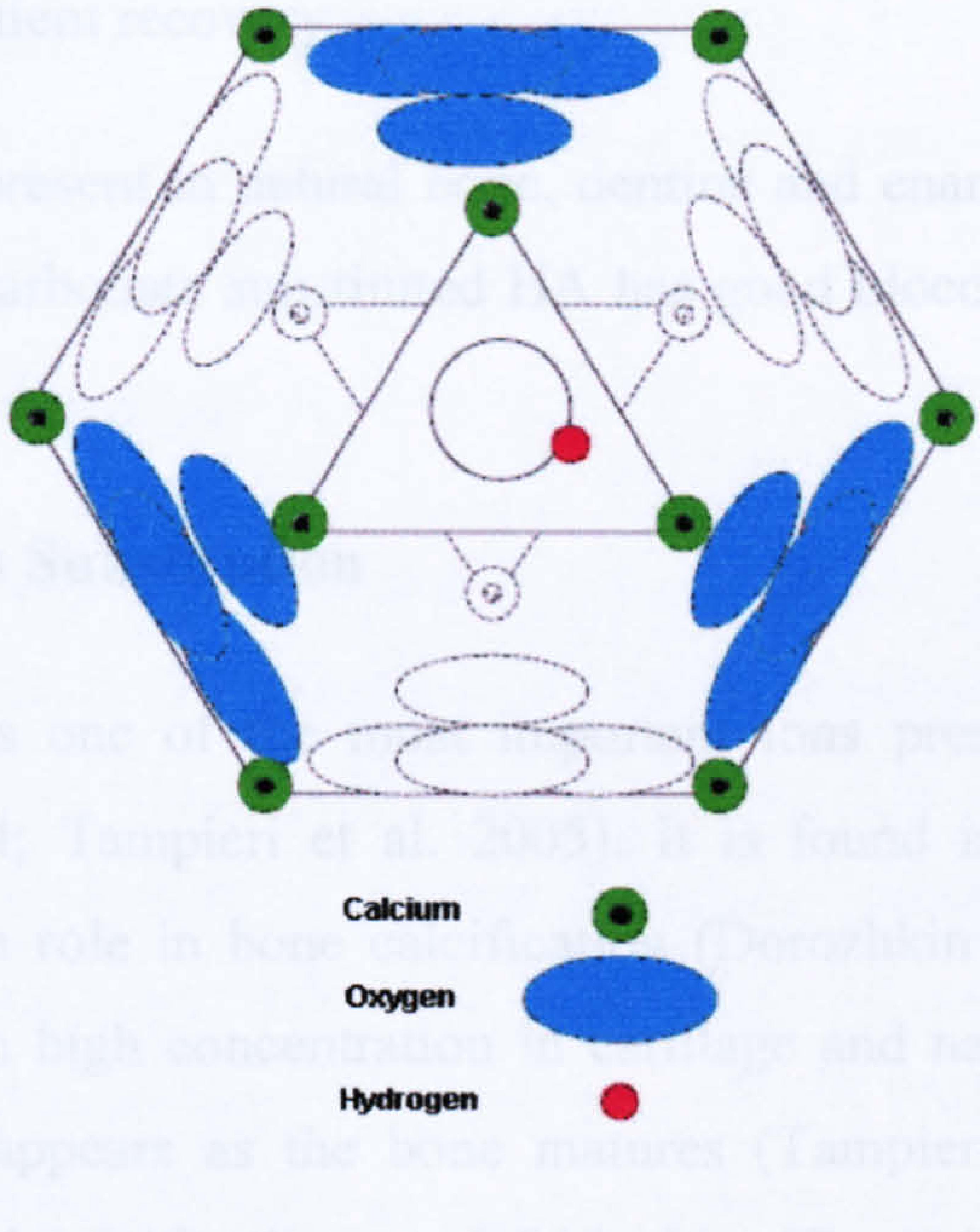

Figure 1-6 The apatite unit cell. Dashed lines represent the lower level (Sarig 2004).

1.3.2 Substitutions into Hydroxyapatite

As mentioned earlier in this chapter, synthetic hydroxyapatite differs slightly in composition from biological apatite as the latter additionally contains several substituted ions (Na^+, Mg^{2+}, Zn^{2+}, CO_3^{2-}, SiO_4^{4-}, F^-) (LeGeros 2002). It is important to understand the role of substituted ions in biological apatite. These ions play significant roles in bone formation, bone strength and their depletion in the human body is linked to several bone related illnesses. The HA lattice is very accommodative and allows various positive and negative ionic substitutions. Therefore, there is a possibility of making synthetic HA with a composition similar to biological apatite.

1.3.2.1 Carbonate Substitution

The local pH at the implant decreases immediately after implantation due to cellular activity and the enzymes produced. This initiates the partial dissolution of HA, causing the release of Ca^{2+}, HPO_4^{2-} and PO_4^{3-} and supersaturating the local environment with respect to calcium and phosphorus. The surface characteristics of HA are hence changed and a layer of carbonated hydroxyapatite forms on the surface through seeded growth on HA crystals (Cao & Hench 1996; Zhang et al. 2003). Growth of this layer is slow and is partially controlled by the crystallinity of the original synthetic HA and its dissolution kinetics. Use of synthetically produced carbonated HA which is more soluble than HA, therefore results in quicker resorption and bone formation, ultimately facilitating quicker patient recovery.

Since the HA phase present in natural bone, dentine and enamel contains up to 8 wt% carbonate, synthetic carbonate substituted HA has good biocompatibility (Krajewski et al. 2005).

1.3.2.2 Magnesium Substitution

Magnesium (Mg^{2+}) is one of the most important ions present in biological apatite (Tampieri et al. 2004; Tampieri et al. 2005). It is found in all hard tissues (up to 1.2 wt%) and plays a role in bone calcification (Dorozhkin & Epple 2002; LeGeros 1991). It is present in high concentration in cartilage and natural bone at the start of osteogenesis, but disappears as the bone matures (Tampieri et al. 2005). It is also present in pathological calcifications, as Whitlockite [$Ca_{18}(Mg,Fe)_2H_2(PO_4)_{14}$] (Kani et al. 1983; Lagier & Baud 2003; Mathew & Takagi 2001). Magnesium depletion results in decreased activity of osteoblasts and osteoclasts and leads to bone fragility (Bandyopadhyay et al. 2006). Magnesium containing hydroxyapatite coating has been shown to bond quicker to bone as compared to undoped HA coatings due to enhanced bone cell activity (Revell et al. 2004). The divalent magnesium ion (Mg^{2+}) substitutes for the calcium ion (Ca^{2+}) in HA or β-TCP (Suchanek et al. 2004). The presence of

Mg^{2+} reduces the crystallinity of HA and stabilises its thermal decomposition into β-TCP above 700 °C (Kannan et al. 2005). In the presence of excess Mg^{2+}, Whitlockite phase can be precipitated directly (LeGeros 2001).

1.3.2.3 Zinc Substitution

Zinc is an important trace element in human bone (0.012 to 0.025 wt%) (Ito et al. 2000). It has been shown that the divalent zinc ion (Zn^{2+}) promotes the activity of osteoblasts, but more than 1.2 wt% zinc content causes cytotoxicity (Ito et al. 2000). It is reported that 50 % more bone was formed when zinc substituted calcium phosphates were used on rabbit femora as compared to the phase-pure calcium phosphate (Bandyopadhyay et al. 2006). Zinc substituted HA has a favourable effect on cytokine production (a protein that controls activity of cells of the immune system) by monocytes (a type of white blood cells that destroys bacteria) (Grandjean-Laquerrier et al. 2006). Zn^{2+} replaces Ca^{2+} in HA or TCP (Tamm & Peld 2006). Partial zinc substitution of calcium in HA has been reported to decrease the thermal stability and crystallinity of HA, and increase its solubility (Li et al. 2007b). It has been reported that above 0.1 wt% content (i.e. suggested solid solubility of Zn in HA), zinc containing TCP phases appear in Zn-HA ceramics after sintering and that the presence of Zn containing TCP is necessary for osteoblast cell proliferation (Sogo et al. 2004).

1.3.2.4 Silicon Substitution

Silicon (Si) is a very important element in bone and plays a significant role in bone formation and calcification (Leventouri et al. 2003). Presence of silicon (0.5 wt%) has been detected in the basic structure of bone, an osteon, of young mice and rats (Carlisle 1970). The presence of silicon in calcium phosphates promotes both osteoblast and osteoclast activity (Hing et al. 2006; Reid et al. 2005). Silicon enters the HA lattice as silicate ions (SiO_4^{4-}) that replace phosphate ions (PO_4^{3-}) (Gibson et al. 1999). Silicon substituted HA containing 1.5 wt% silicon has been reported to be more soluble than pure HA (Porter 2006).

1.3.3 Synthesis of Hydroxyapatite

HA powders can be synthesised using dry methods (solid-state reactions) or wet-chemical methods (coprecipitation, emulsion methods, hydrothermal batch reactions). Furthermore, coatings of these powders can be deposited using deposition and plasma methods. In this section the advantages and disadvantages of some of these techniques are reviewed briefly.

1.3.3.1 Solid-State Reactions

Solid-state routes include synthesis of hydroxyapatite as a high temperature reaction product between solid calcium and phosphate precursors. Cao and co-workers reported on the synthesis of hydroxyapatite using calcium nitrate and tri-sodium phosphate ground by milling first and then heated using a microwave. For a short heating time of 0.5 minutes a spherical morphology was seen. These rounded particles elongated into nano-rods upon continuous heating for one minute as shown in Figure 1-7 (Cao et al. 2005). Carbonate containing barium hydroxyapatite has also been prepared using solid state reactions in air at 950 °C (Getman et al. 2004).

Solid-state routes also include mechanochemical methods wherein, mechanical mixing leads to chemical reactions. A mechanochemical reaction carried out in the presence of water is referred to as a mechanochemical-hydrothermal reaction (Chen et al. 2004). These methods involve reactions between solid calcium and phosphorus compounds mixed according to stoichiometry and then mixed/milled in a ball mill. Chemical reactions occur due to favourable temperatures and pressures. The contact area between the milling balls and milling container walls (and between the balls as well) is a high local temperature (up to 450 °C) and high pressure region where the reaction takes place (Cai et al. 2005). Times required to synthesise HA vary from a few hours up to 60 hours (Coreno et al. 2005; Silva et al. 2003). However, after initial mixing, these powder mixtures may require a heat treatment step to transform into phase-pure HA (Rhee 2002). This can result in lower surface areas and indeed, Chen and co-workers reported a reduction in surface area (measured using BET) from 175 $m^2 g^{-1}$ for as-prepared HA to 7.2 $m^2 g^{-1}$ after HA was heat-treated at 900 °C for one hour (Chen et al. 2004).

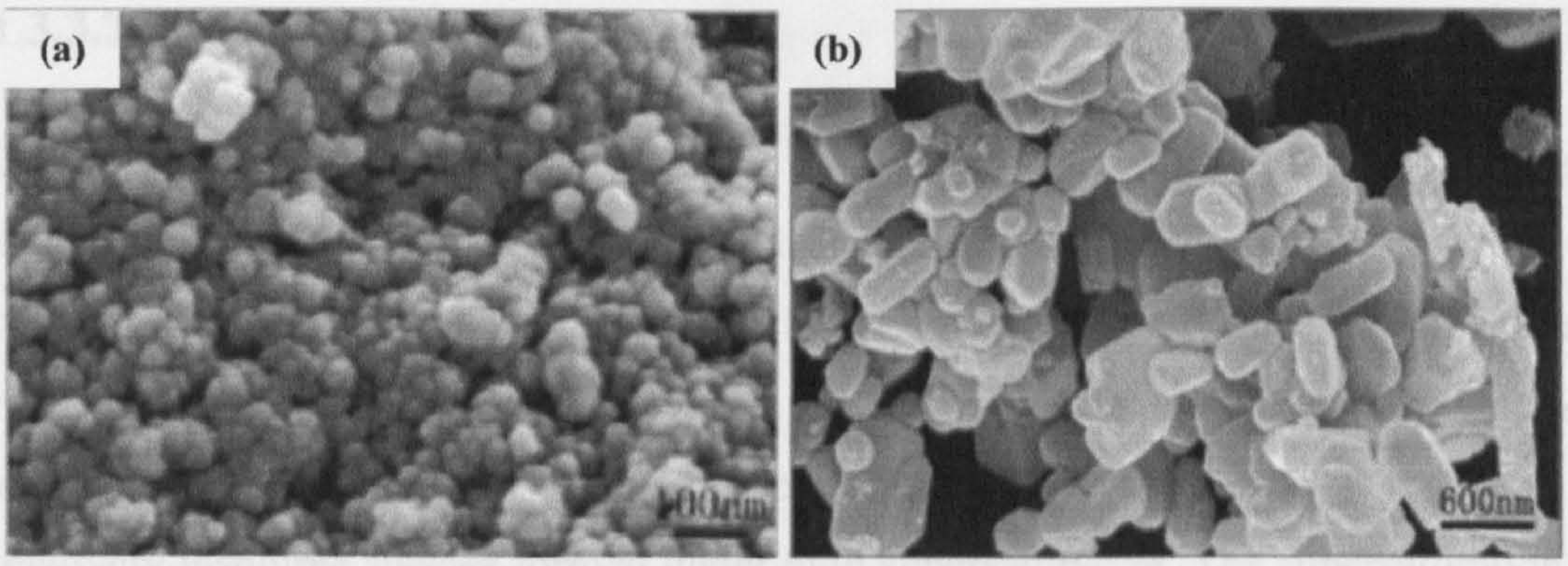

Figure 1-7 FE-SEM image of HA nanoparticles prepared by (a) microwave heating with 15 second intervals for 0.5 minutes (b) continuous microwave heating for 1 minute (Cao et al. 2005).

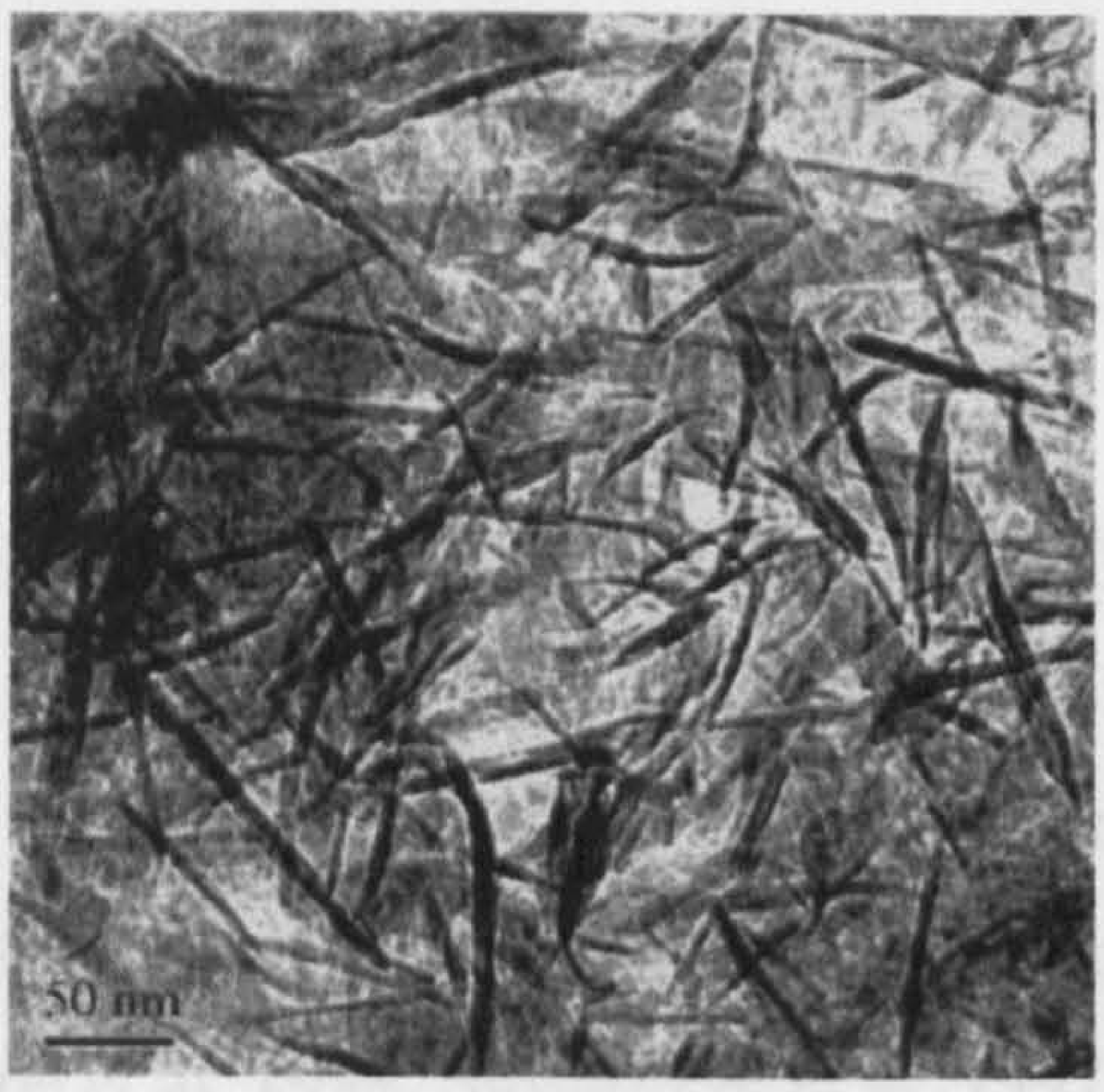

Figure 1-8 TEM micrograph of the mixture powder after grinding for 24 hours (Cai et al. 2005).

These methods have also been used to synthesise ion-substituted hydroxyapatite (Cai et al. 2005; Coreno et al. 2005; Suchanek et al. 2004; Zhang et al. 2005b). The morphology of carbonated hydroxyapatite nanofibers synthesised by grinding dicalcium phosphate dihydrate ($CaHPO_4.2H_2O$) and calcium carbonate ($CaCO_3$) for 24 hours is shown in Figure 1-8 (Cai et al. 2005).

Large quantities of crystalline powders can be synthesised using the solid-state reaction route. The processing costs and times involved are much less as compared to wet-chemical methods (Rhee 2002). However, all solid state methods are prone to presence of impurities from equipment used in ball milling (Fernandes et al. 2005).

1.3.3.2 Co-Precipitation of HA

Co-precipitation reactions usually involve a mixture of soluble calcium and phosphorus sources and the addition of base to result in precipitation of a poorly crystalline HA which has to be matured in solution to attain stoichiometry. Hence, co-precipitation refers to the simultaneous occurrence of nucleation, growth, coarsening and/or agglomeration of particles from solution. Products of precipitation reactions are relatively insoluble species formed under high supersaturation. The supersaturation is a result of a chemical reaction. The key step in co-precipitation is nucleation as a result of which large numbers of particles are formed. This is followed by secondary processes such as Ostwald ripening and aggregation which greatly affect the size, morphology and properties of the particles. Reaction conditions such as the rate of reactant addition and stirring rate are related to product size, morphology and particle size distribution. In order to achieve nanosized particles the nucleation rate must be faster than the growth rate (Cushing et al. 2004).

Typical calcium ion sources include calcium nitrate, $Ca(NO_3)_2$, calcium hydroxide, $Ca(OH)_2$ and calcium chloride, $CaCl_2$. Typical phosphate ion sources include diammonium hydrogen phosphate, $(NH_4)_2HPO_4$, phosphoric acid, H_3PO_4, potassium dihydrogen phopshate, KH_2PO_4 and di-sodium hydrogen phosphate, Na_2HPO_4 (Donadel et al. 2005; Lopez-Macipe et al. 1998; Slosarczyk et al. 1997; Tas & Aldinger 2005).

The Ca^{2+} and PO_4^{3-} sources react immediately to yield an amorphous precipitate. Initial mixing is normally carried out for two hours with the pH maintained between 10 – 11. This initial precipitate (in form of a suspension) is then aged in solution for up to a day, in order to reach the required stoichiometry (Ca:P molar ratio of *ca.* 1.67, in HA). Solution mixtures are sometimes heated up to 95 °C to speed up the process (Afshar et al. 2003; Lazic 1995; Pang & Bao 2003; Phillips et al. 2003; Saeri et al. 2003).

Slow addition of reactants and intensive stirring are employed in order to avoid local concentration inhomogeneity which can result in formation of agglomerates. However, the pH of the system plays an important role in the phase transformations of calcium phosphate phases in suspension.

Reactions carried out in basic conditions with a Ca:P molar ratio of 1.67 (at pH 10-11) result in formation of HA as shown below (Afshar et al. 2003; Aoki 1991).

$$10Ca(OH)_2 + 6H_3PO_4 \rightarrow Ca_{10}(PO_4)_6(OH)_2 + 18H_2O \qquad \textbf{Eq. 1-2}$$

$$10Ca(NO_3)_2 + 6(NH_4)_2HPO_4 + 2H_2O \rightarrow Ca_{10}(PO_4)_6(OH)_2 + 12NH_4NO_3 + 8HNO_3 \qquad \textbf{Eq. 1-3}$$

These reactions require strict control of the pH above 10 in order to yield stoichiometric HA. In addition to phase-pure HA, ion-substituted HA has also been synthesised using co-precipitation methods (Porter et al. 2005; Zou et al. 2005b). A Ca:P molar ratio of 1.5 in solution, has been reported to result in precipitation of calcium deficient hydroxyapatite (CDHA) (Siddharthan et al. 2004). Similar reagents when used under acidic conditions and even lower Ca:P molar ratios (pH 7 or below) result in the formation of brushite ($CaHPO_4.2H_2O$) or monetite ($CaHPO_4$) (Arifuzzaman & Rohani 2004; Sivakumar et al. 1998). An acidic medium favours the solubility of calcium phosphates, hence, the formation of apatite becomes difficult. In addition to strict control of reaction conditions, very long ageing times (up to 24 hours) and subsequent heat-treatment steps are required to obtain crystalline HA (Ferreira et al. 2003a; Martin & Brown 1997; Phillips et al. 2003).

Phillips and co-workers reported on the reduction in surface area from 113 m^2 g^{-1} for as-precipitated HA to 19 m^2 g^{-1} after heat-treatment at 900 °C for two hours. The corresponding particle morphologies, typical co-precipitated HA "needles" and larger rounded heat-treated HA particles are shown in Figures 1-9 (a) and (b), respectively (Phillips et al. 2003).

1.3.3.3 Sol-Gel Processing of HA

Sol-gel processing involves the hydrolysis and condensation of alkoxide-based (or similar) precursors such as tetraethyl orthosilicate (Hench 1997; Hench & West 1990; Niederberger 2007; Rajabi et al. 2007). The sol-gel process can be characterised by a series of distinct steps (Cushing et al. 2004). The first step is the formation of sol, a stable solution of the alkoxide or solvated metal precursor. The second step is gelation, wherein a gel forms. This is due to the formation of an oxide or alcohol-bridged network by a polycondensation or polyesterification reaction which causes an increase in the viscosity of the solution. The third step is the aging of the gel where it transforms into a solid mass. This is followed by drying and dehydration. Densification and decomposition of gels at temperatures (> 800 °C) is a step carried out for making dense bulk ceramics and glasses (Cushing et al. 2004).

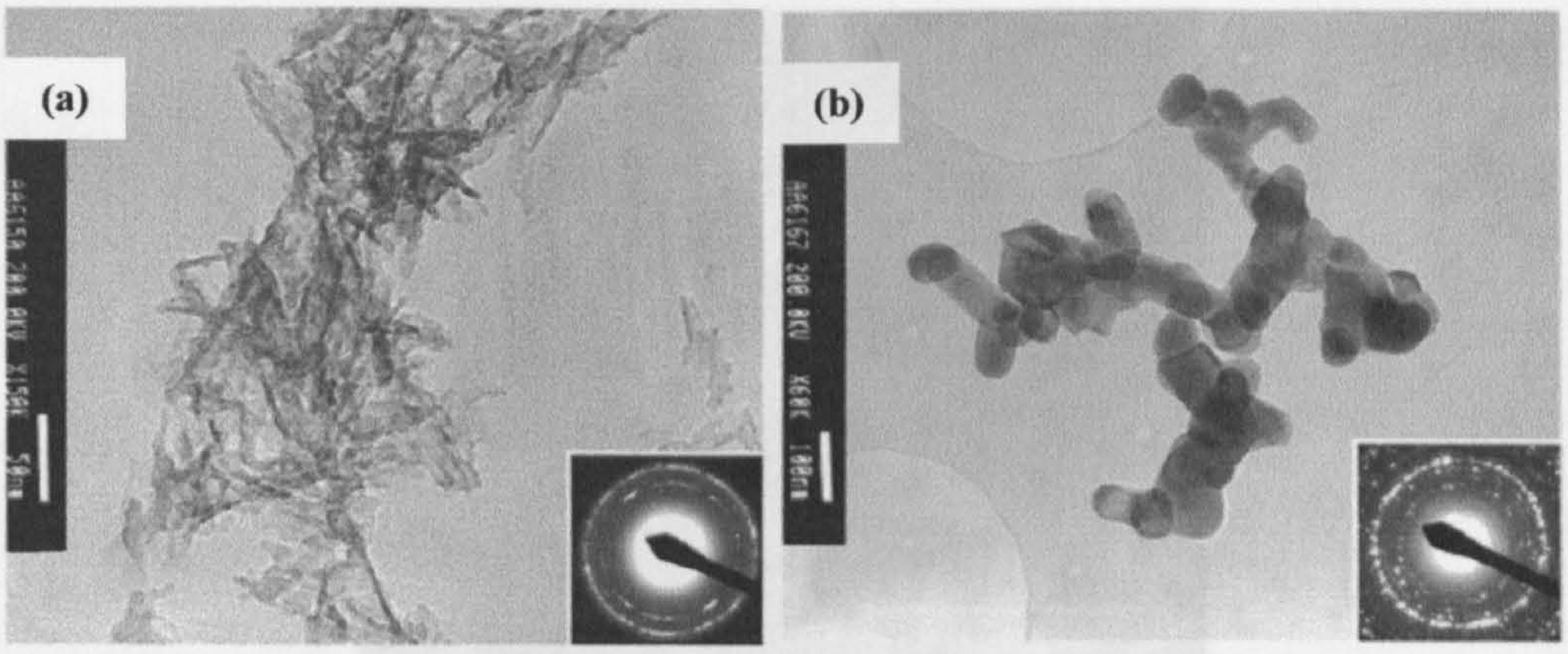

Figure 1-9 TEM images of (a) amorphous co-precipitated HA "needles" (b) heat-treated at 900 °C for two hours (Phillips et al. 2003).

The sol-gel method offers molecular level mixing of calcium and phosphate precursors improving chemical homogeneity (Hench 1997; Hench & West 1990; Niederberger 2007). It is also a convenient method to coat irregular surfaces such as sintered porous scaffolds or implants (Aksakal & Hanyaloglu 2008; Gan & Pilliar 2004; Liu et al. 2001; Phillips et al. 2003). This method is also knows as dip coating and involves repeated dipping of a substrate in a sol to build up the coating and subsequent sintering. Typical substrates include 316L stainless steel and titanium alloys (Ti-6Al-4V)(Aksakal & Hanyaloglu 2008). HA particles have been synthesised using sol-gel methods too, but require ageing up to 24 hours and subsequent heat-treatment (Liu et al. 2001; Rajabi et al. 2007; Vazquez et al. 2005) Such heat-treatments can lead to formation of sintered particles (hard agglomerates) as reported by Liu and co-workers (as shown in Figure 1-10) (Liu et al. 2001).

The sol-gel chemistry is complex. The hydrolysis, condensation and aggregation occur simultaneously making reproducibility and control over particle morphologies difficult. Additionally, as-synthesised materials are amorphous and require subsequent heat-treatment which can alter particle morphology and create agglomerates (Niederberger 2007).

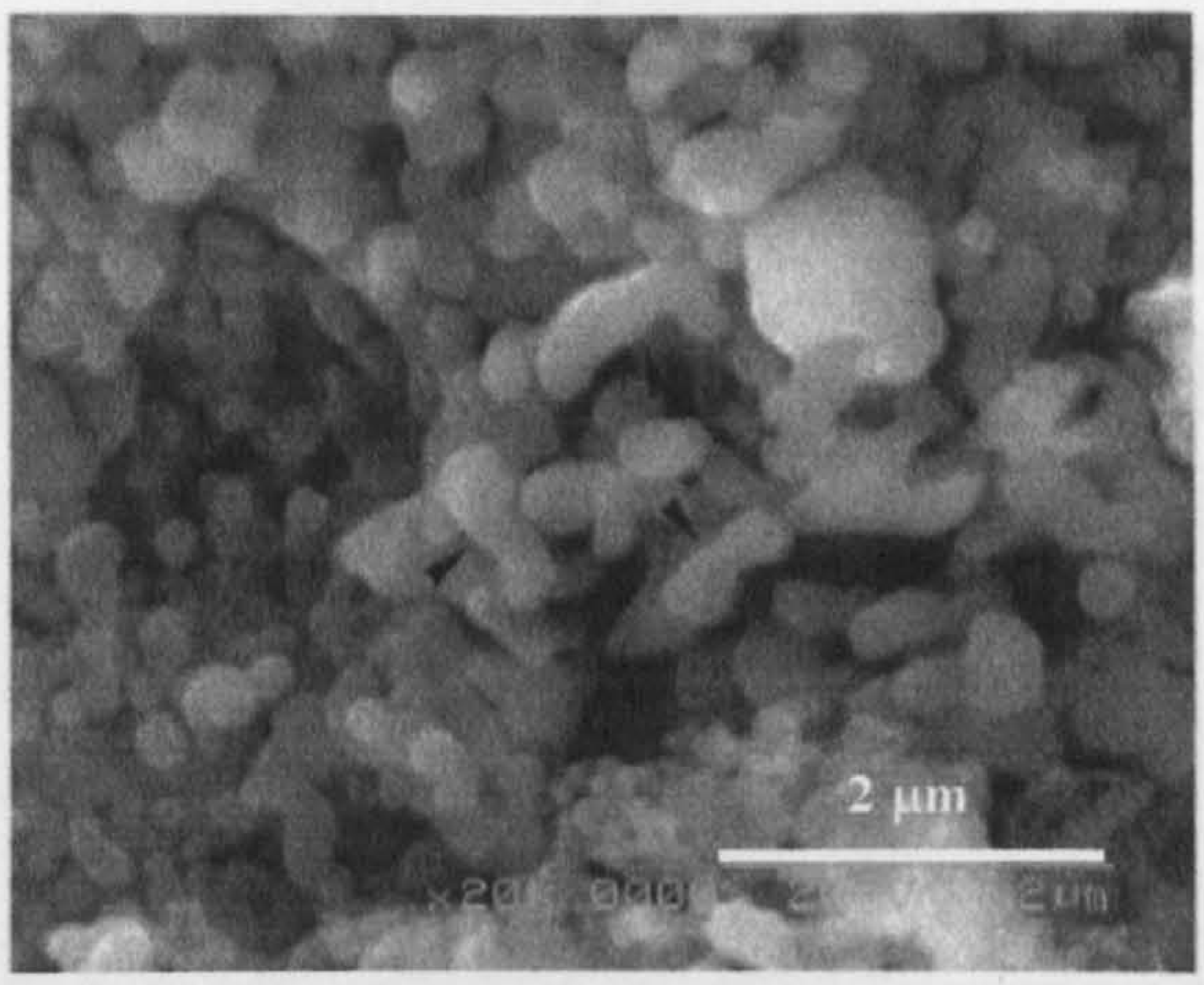

Figure 1-10 Scanning electron microscope image of HA (derived using sol-gel) heat-treated at 800 °C for 2 hours [bar = 2 µm] (Liu et al. 2001).

1.3.3.4 Emulsion Synthesis of HA

Combinations of water, oil and a surfactant can result in seemingly homogeneous and clear solutions known as emulsions. This is because the nanosized aqueous droplets or channels do not cause noticeable light scattering. Water-in-oil emulsions can be likened to extremely small water containing reactors. This leads to an increase in interfacial area of the water (Cushing et al. 2004). The terms microemulsions and macroemulsions are often used. In microemulsions, the volume of water is low enough such that the emulsion remains transparent and stable for long times. Macroemulsions have higher amounts of water in them, are opaque and are only stable when stirred continuously (Phillips et al. 2003). Reaction takes place when two different water droplets containing reagents collide and mix with each other. Such a small reaction environment results in small particle size and size homogeneity (Koumoulidis et al. 2003; Segal 1997). Emulsion techniques have been reported to result in powders with higher surface areas as compared to those produced using co-precipitation methods (Koumoulidis et al. 2003).

HA has been synthesized using emulsion routes. However, this requires use of large quantities of oil (organic solvent) and surfactants and subsequent heat-treatment is required to yield crystalline HA (Koumoulidis et al. 2003; Li et al. 2008; Lim et al. 1997; Lim et al. 1999; Phillips et al. 2003). Jarudilokkul and co-workers reported that with an increase in reaction temperature from 30 °C to 80 °C the surface area of HA decreased from 227 m^2 g^{-1} to 98 m^2 g^{-1} (Jarudilokkul et al. 2007). A TEM image showing the needle like morphology of HA with 218 m^2 g^{-1} surface area, synthesised using microemulsions (in 24 hours), (reported by Phillips and co-workers) is shown in Figure 1-11.

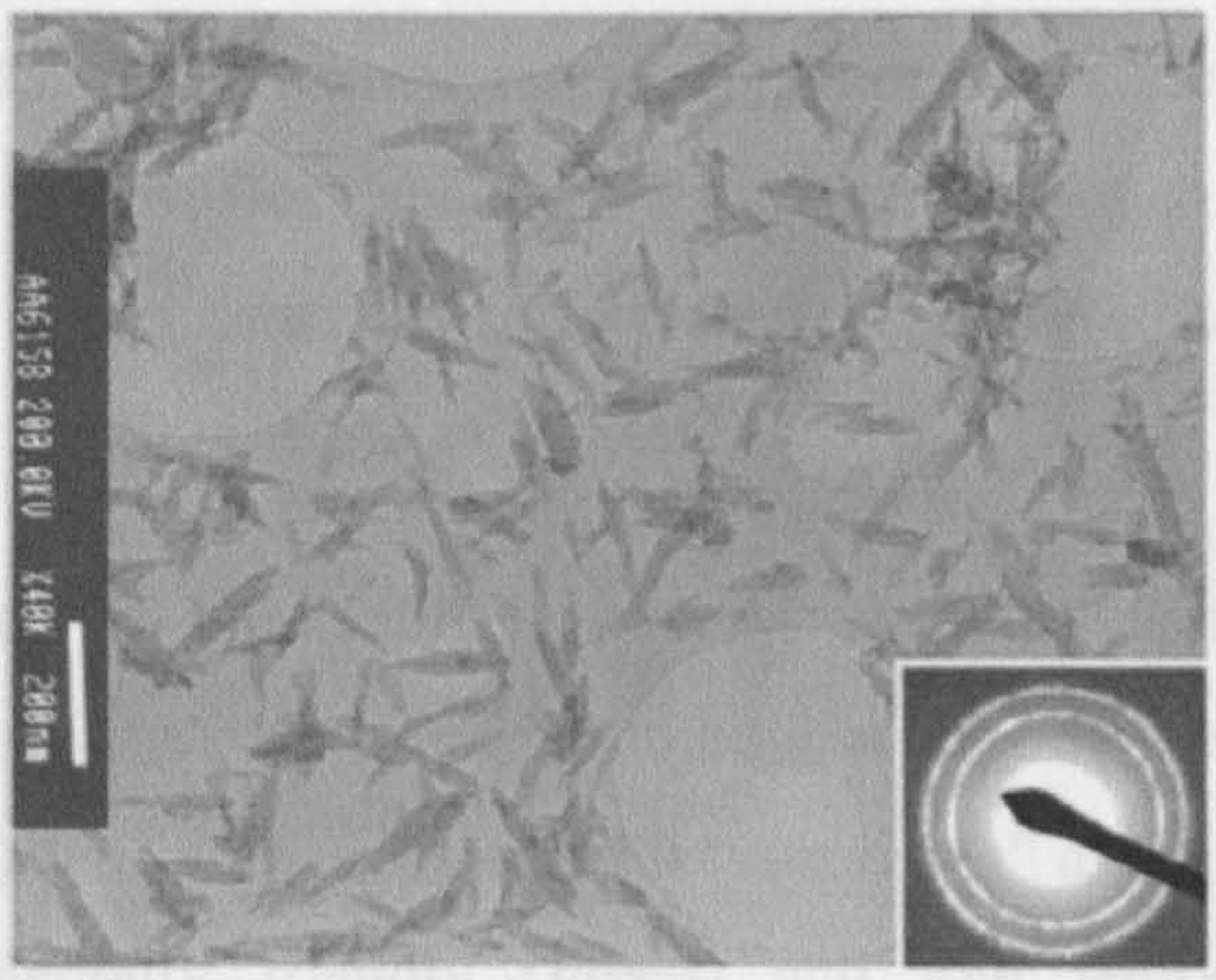

Figure 1-11 Transmission electron microscope image of HA synthesised using microemulsion technique [bar = 200 nm] (Phillips et al. 2003).

Sun and co-workers reported on the synthesis of rod-like HA using microemulsions under hydrothermal conditions (at 160 °C for 12 hours under autogenous pressure) at neutral pH (shown in Figure 1-12). With an increase in reaction pH almost spherical particles were obtained (Sun et al. 2007b).

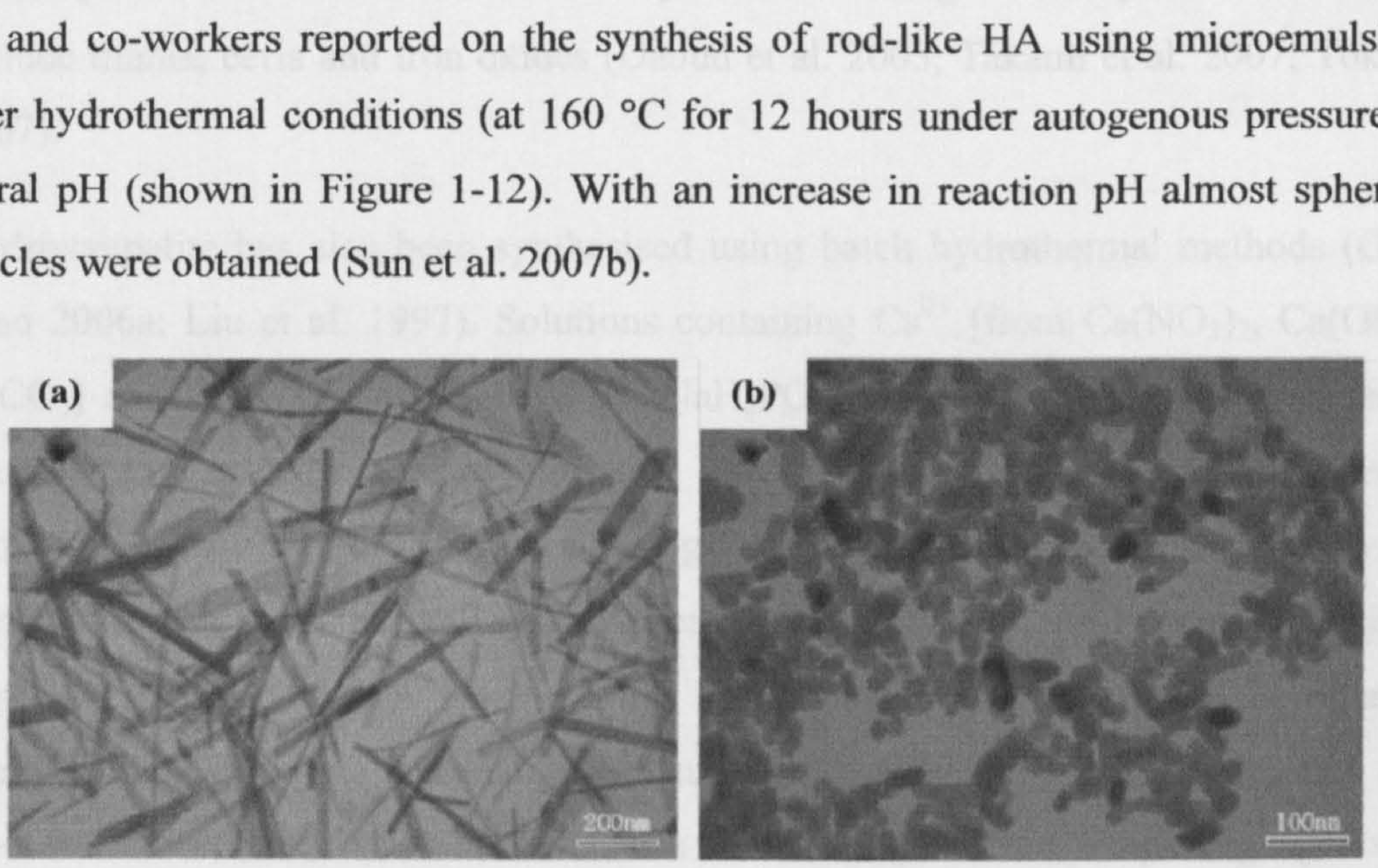

Figure 1-12 Transmission electron microscope images of HA obtained using microemulsion technique under hydrothermal conditions at (a) pH 7 [bar = 200 nm] and (b) pH 11 [bar = 100 nm] (Sun et al. 2007b).

1.3.3.5 Batch Hydrothermal Syntheses of HA

Solvents can be brought to temperatures above their boiling points by increase in autogenous pressure by heating in a sealed container (batch process). Materials which are rather insoluble under ordinary conditions can be dissolved and recrystallised using batch hydrothermal synthesis technique. When water is used as a solvent this technique is called batch hydrothermal processing. The term "hydrothermal" is of a geological origin and related the use of water (hydra) (Byrappa & Adschiri 2007; Cushing et al. 2004). During a batch hydrothermal reaction, ceramic sols are produced by chemical reactions under heat and pressure generally in the presence of an alkali or acid. Presence of an alkali or an acid has a catalytic effect on the reaction although this is not always required (Cushing et al. 2004; Kaya et al. 2002).

Based on a number of publications, interest in batch hydrothermal methods to synthesise ceramic powders, was reported to be less as compared with other techniques in 1997 (Segal 1997). The author described it "surprising" as the hydrothermal synthesis offers an environmentally friendly (green) and low temperature direct-route to submicron nanoparticles without the need of a subsequent heat-treatment step. Indeed, reports of nanoparticle synthesis using batch hydrothermal processing have increased in recent years. Some of the materials synthesised using batch hydrothermal method include titania, ceria and iron oxides (Daoud et al. 2005; Takami et al. 2007; Tok et al. 2007).

Hydroxyapatite has also been synthesised using batch hydrothermal methods (Guo & Xiao 2006a; Liu et al. 1997). Solutions containing Ca^{2+} [from $Ca(NO_3)_2$, $Ca(OH)_2$ or $CaCO_3$] and PO_4^{3-} [from $(NH_4)_2HPO_4$, NaH_2PO_4, H_3PO_4 or $CaHPO_4$] are mixed and poured into a sealed container. Pressure, temperature, pH and ageing time affect the composition, crystallinity and morphology of HA particles. As compared to other methods, batch hydrothermal synthesis produces crystalline, well-defined and phase-pure HA in a single step. Ageing times vary between a few hours to 24 hours and synthesis temperature is reported in literature between 90 and 150 °C (Arce et al. 2004; Guo & Xiao 2006b; Liu et al. 1997; Liu et al. 2003). Use of templating agents [e.g. poly(amidoamine), CTAB] in the hydrothermal batch processing of HA has also been reported (Liu et al. 2003; Riman et al. 2002; Wang et al. 2006; Yan et al. 2001; Zhang et al. 2005a). Zhou and co-workers reported on the decrease in particle size of rod-like HA from 75 x 15 nm to 65 x 26 nm (Figure 1-13) when a dendrimer (polyamidoamine, PAMAM) was used during the hydrothermal batch reaction between calcium nitrate [$Ca(NO_3)_2$] and diammonium hydrogen phosphate [$(NH_4)_2HPO_4$] at 150 °C for 10 hours (Zhou et al. 2007b). Riman and co-workers reported on the decrease in surface area of batch hydrothermal HA (made in 24 hours) from 126 m^2 g^{-1} to 50 m^2 g^{-1} when the synthesis temperature was increased from 50 °C to 200 °C (Riman et al. 2002).

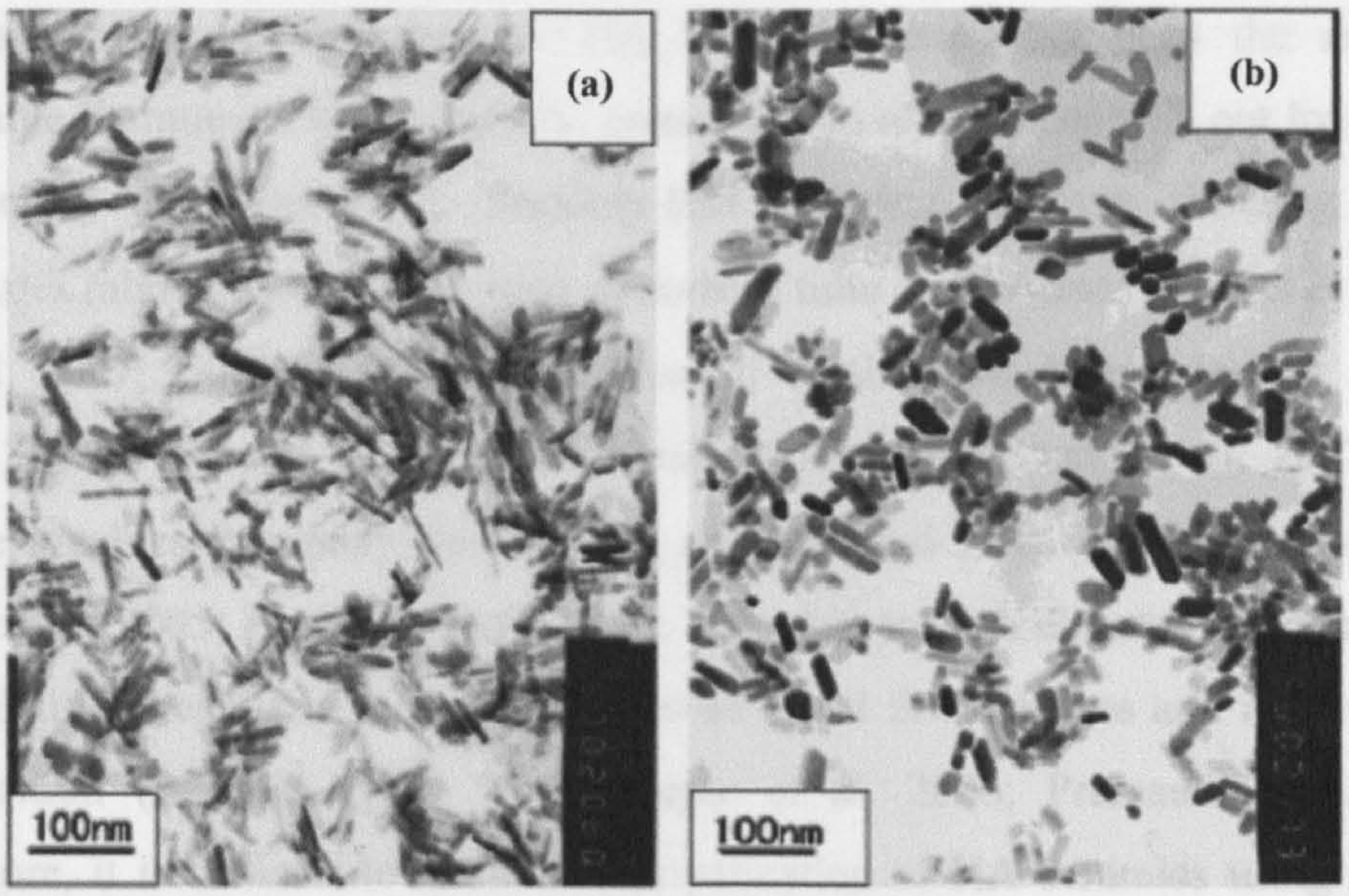

Figure 1-13 Transmission electron microscope images of HA synthesised by a batch hydrothermal reaction (a) without and (b) with a dendrimer (PAMAM) (Zhou et al. 2007b).

When reactions are carried out at pH lower than 10 and solutions have Ca:P molar ratio less than 1.67, calcium deficient HA is usually formed (Andres-Verges et al. 1998; Ivanova et al. 2001). Synthesis of various ion substituted hydroxyapatites using batch hydrothermal processing, has also been reported in literature (Jokanovic et al. 2006; Mizutani et al. 2005; Tang et al. 2005a; Tang et al. 2005b).

1.3.4 Consolidation of HA Powders

HA may be used in several physical forms which include sintered ceramics in porous or block forms (Kobayashi et al. 1993), coatings such as a bioactive coatings on metallic implants (Gross et al. 2004) and fillers for polymeric matrices (Tanner et al. 2001). The use of sintered HA in load bearing applications is limited due to its inferior mechanical properties thus it is used exclusively in low stress areas of the human body (*e.g.* ossicles in the middle ear) (Heimann & Vu 1997). In order to overcome the mechanical limitations, reinforcing agents such as zirconia (Kong et al. 2005), alumina (Kim et al. 2003; Viswanath & Ravishankar 2006), titania particles (Oktar et al. 2006), carbon (White et al. 2007) and stainless steel fibres have been used (Zou et al. 2005a). This can, however, result in increased sintering times and higher temperatures in order to obtain a fully dense sintered material.

The consolidation (or sintering) of HA based ceramics has been the subject of considerable literature. Conventionally, consolidation of HA is carried out by pressure-less sintering or hot-pressing. Pressure-less sintering involves sintering at high temperatures (above 1200 °C) for long periods of time (1-4 hours) (Barralet et al. 2003; Cai et al. 2007; Guo et al. 2003b; Kothapalli et al. 2004; Laquerriere et al. 2003; Mostafa 2005; Nayar et al. 2006; Pramanik et al. 2007; Zhang et al. 2007b). This technique involves extremely slow heating rates (around 5 °C min^{-1}) (Kothapalli et al. 2004; Mostafa 2005; Pramanik et al. 2007). Exposure to such elevated temperatures for prolonged times results in large grain sizes of about few microns and at times phase decomposition (Barralet et al. 2003; Nayar et al. 2006; Pramanik et al. 2007). Furthermore, it is difficult to attain full-densification of HA ceramics using pressure-less sintering (Kothapalli et al. 2004; Mostafa 2005). Barralet and co-workers reported on the conventional sintering of HA at 1300 °C for 2 hours to result in a sintered density of *ca.* 98% with grain sizes > 1 μm (Figure 1-14) (Barralet et al. 2003).

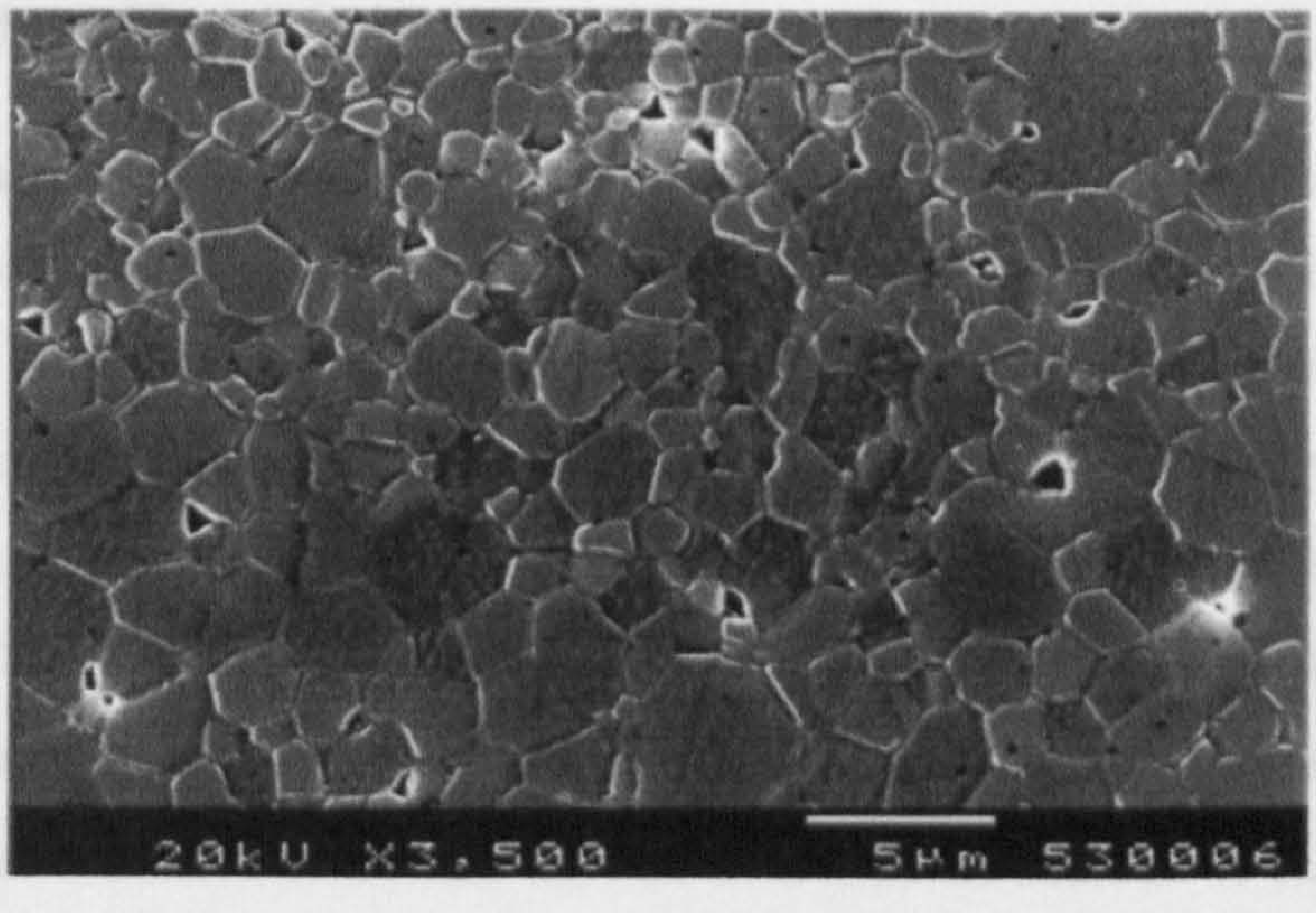

Figure 1-14 Scanning electron microscope image showing the microstructure of HA sintered in air at 1300 °C for 2 hours (Barralet et al. 2003).

In comparison to pressure-less sintering, hot-pressing has been reported to yield HA ceramics with smaller grain sizes at temperatures up to 1250 °C (10 °C min^{-1}), pressures up to 64 MPa and sintering times ranging from 1-5 hours (Bianco et al. 2007; Kobayashi et al. 2006). The application of pressure during sintering helps achieve higher sintered densities in a smaller duration as compared to conventional sintering. Indeed, Kobayashi and co-workers published their work on effect of pressure on sintering of HA in which HA was hot-pressed to a sintered density of *ca.* 92 % under

7.81 MPa. The graphite die used in this work was heated in the furnace to 800 °C at 10 °C min^{-1} and kept at this temperature for 1 hour prior to further heating to 1200 °C (at 10 °C min^{-1}) followed by immediate cooling. The sub-micron grains sizes obtained are shown in Figure 1-15 (Kobayashi et al. 2006).

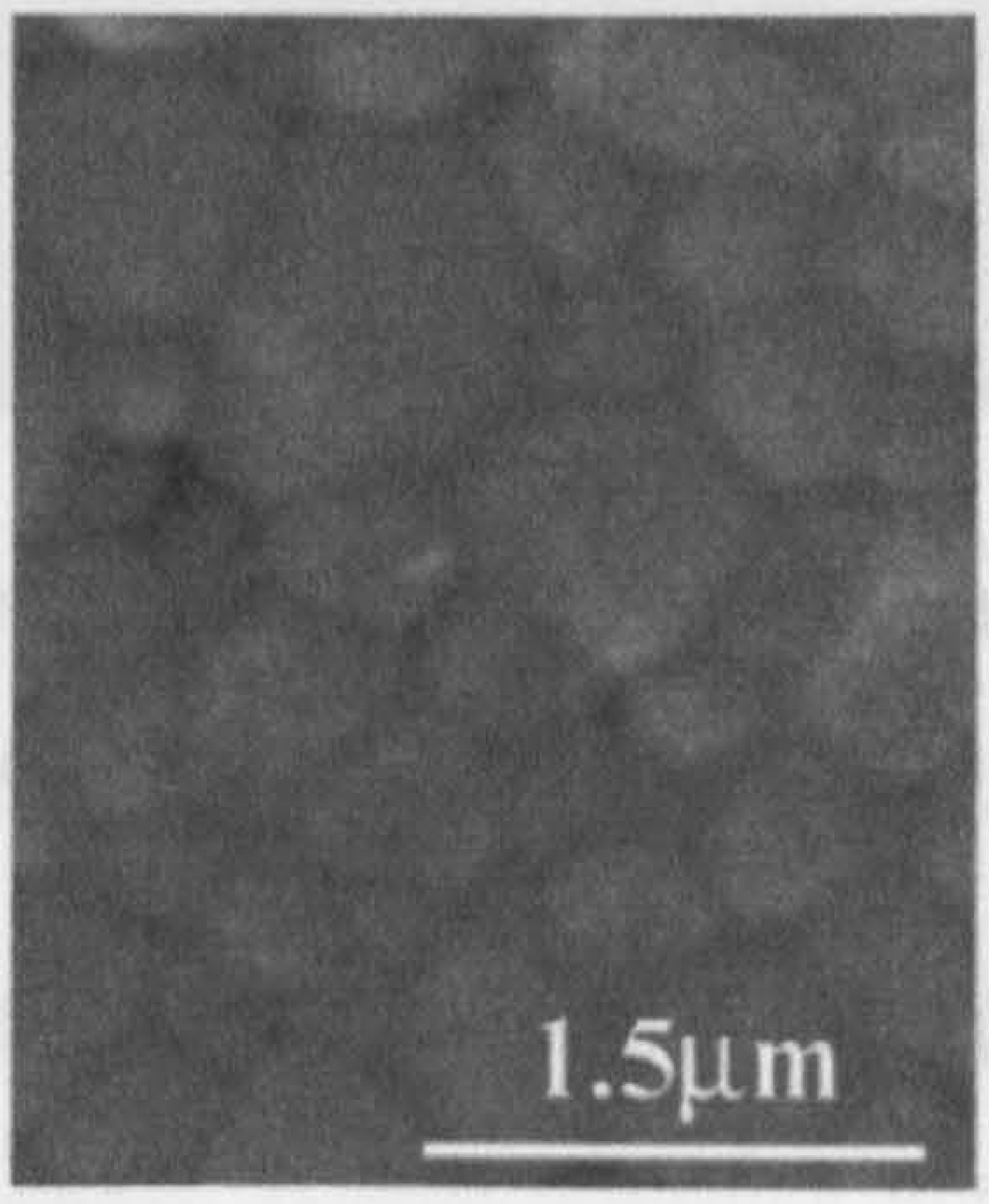

Figure 1-15 Scanning electron microscope image of HA hot-pressed at 1200 °C under 7.81 MPa (Kobayashi et al. 2006).

Gel-casting has also been used for consolidation of both, dense and porous hydroxyapatite. In gel-casting, suspensions of HA powder in a solution of organic monomer, are poured into a mold, followed by polymerisation. The casted shape can be dried and if required, cut to specifications. Prior to sintering, a low temperature heat-treatment around 300 °C is required in order to burn off the polymeric materials (Chen et al. 2008; Chen et al. 2006a; Ramay & Zhang 2003). Figure 1-16 shows the SEM images showing microstructures of gel-casted HA sintered at 1100 °C and 1300 °C for 2 hours (the latter consisted of a small amount of α-TCP in addition to HA) (Chen et al. 2008). In all these techniques (i.e. conventional sintering, hot-pressing and gel-casting) there is an inverse relationship between porosity and grain size. Therefore, a technique that allows good consolidation without considerable grain growth is extremely desirable.

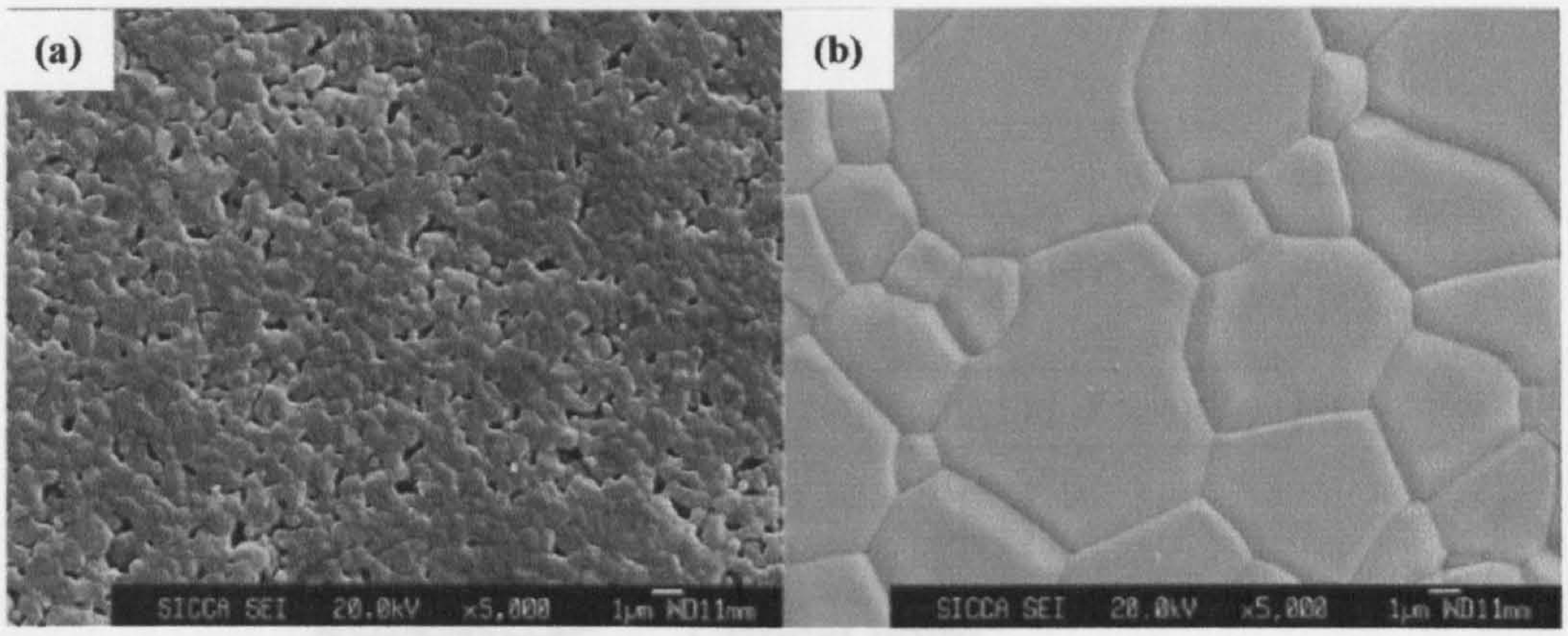

Figure 1-16 Scanning electron microscope images of gel-casted HA sintered for two hours at (a) 1100 °C [bar = 1 μm] and (b) 1300 °C [bar = 1 μm] (Chen et al. 2008).

1.4 Continuous Hydrothermal Flow Synthesis (CHFS)

Japanese researchers working in the Arai group at Tohoku University were the first ones to develop the continuous hydrothermal flow synthesis systems in the early 1990s. Since then, a few groups around the world have modified and improved the CHFS systems and expanded the range of materials that can be synthesised. However, before the basic design of CHFS systems and their numerous advantages are reviewed, it is important to understand the basic science of supercritical water used in these systems.

1.4.1 Properties of Supercritical Water

A fluid is called "supercritical" when its temperature and pressure exceed the critical temperature and pressure (which are specific for each pure substance) (Darr & Poliakoff 1999). The properties of supercritical fluids (SCFs) are totally different from those of gases and liquids. By varying temperature and pressure, the density and viscosity of the SCF can change drastically close to the critical point. The arrangements of molecules of a substance in solid, liquid, gas and supercritical state, respectively, are shown in Figure 1-17. At the critical point, the densities of liquid and gas phases become similar and the interface disappears (no meniscus) (Cansell et al. 2003; Noyori 1999). Supercritical CO_2 and H_2O are expected to replace many environmentally hazardous solvents in the near future (Hakuta et al. 2003). Water becomes supercritical above 374 °C and 22 MPa (Cushing et al. 2004) and above these limits, water exhibits variation in its dielectric constant, viscosity and ion product (Bellissent-Funel 2001).

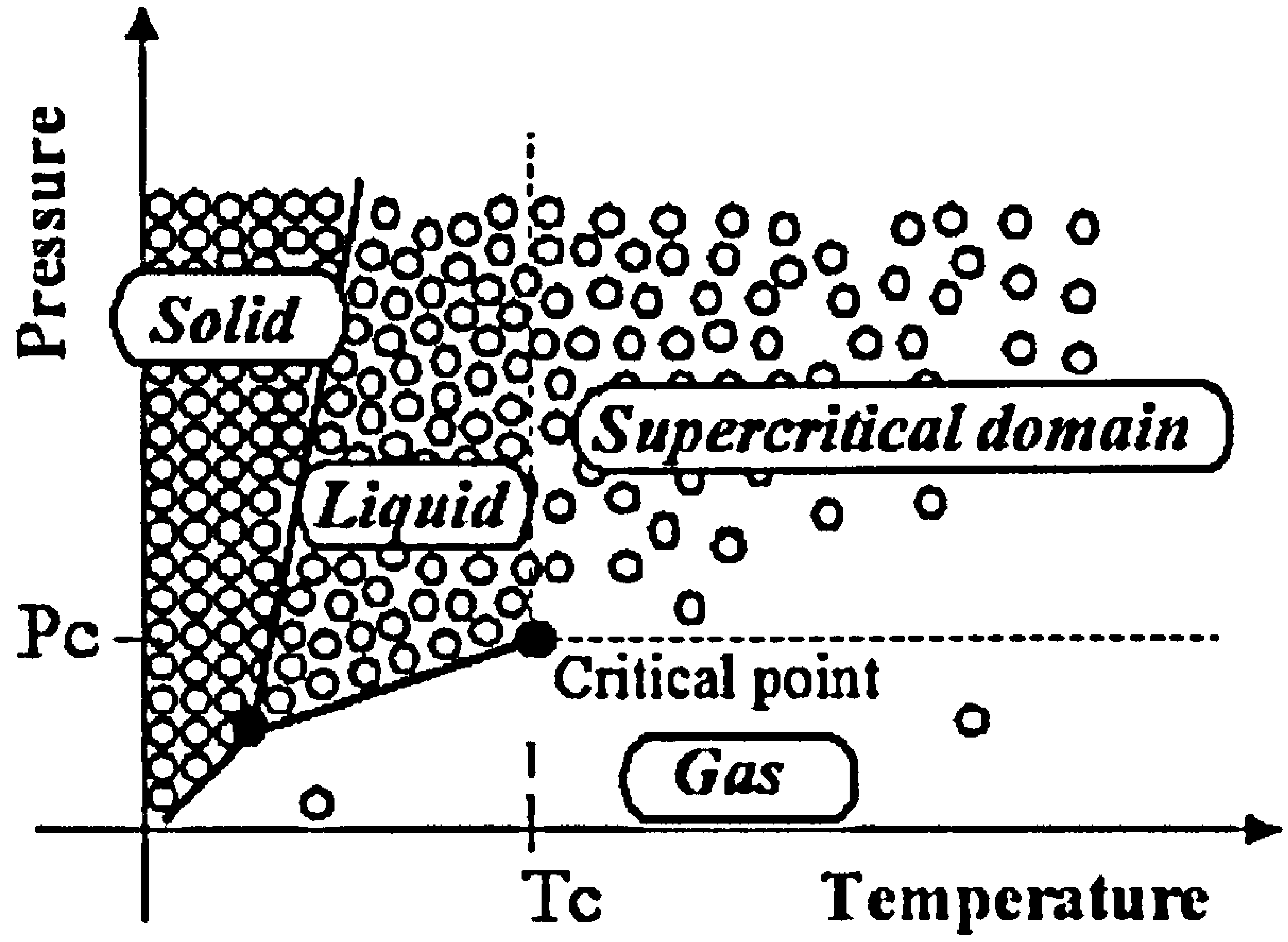

Figure 1-17 Schematic diagram of microscopic behavior of a pure substance in P-T phase diagram (Cansell et al. 2003).

Water dissolves many inorganic salts. However, the dielectric constant of water decreases with increasing temperature at constant pressure. In supercritical water, inorganic salts become insoluble and precipitate out. The key to production of nanoparticles at this point is the maximisation of supersaturation which increases the nucleation rate, leading to smaller particles (Kashchiev 1982). Hydrated metal ions can form crystalline metal oxides as a result of dehydration at high temperatures involved in supercritical water hydrothermal processing. It is believed that rapid dehydration of metal hydroxides is also a reason for the small sizes obtained, as this happens before significant growth can take place (Hakuta et al. 2003; Ziegler et al. 2001). Representative equations for hydrolysis and dehydration reactions are as follows (Lester et al. 2006).

Hydrolysis: $ML_x + xOH^- \rightarrow M(OH)_x + xL^-$ **Eq. 1-4**

Dehydration: $M(OH)_x \rightarrow MO_{x/2} + \frac{1}{2}xH_2O$ **Eq. 1-5**

For water, the ion product is a measure of its hydrolysability and the dielectric constant is a measure of its dissolving power (Figure 1-18). Above critical conditions water maintains a high ion product with variation in temperature and pressure. The dielectric constant of water however decreases remarkably near the critical point (Figure 1-19). This implies that supercritical water has a strong hydrolysing and low dissolving capability (Fukushima 2000).

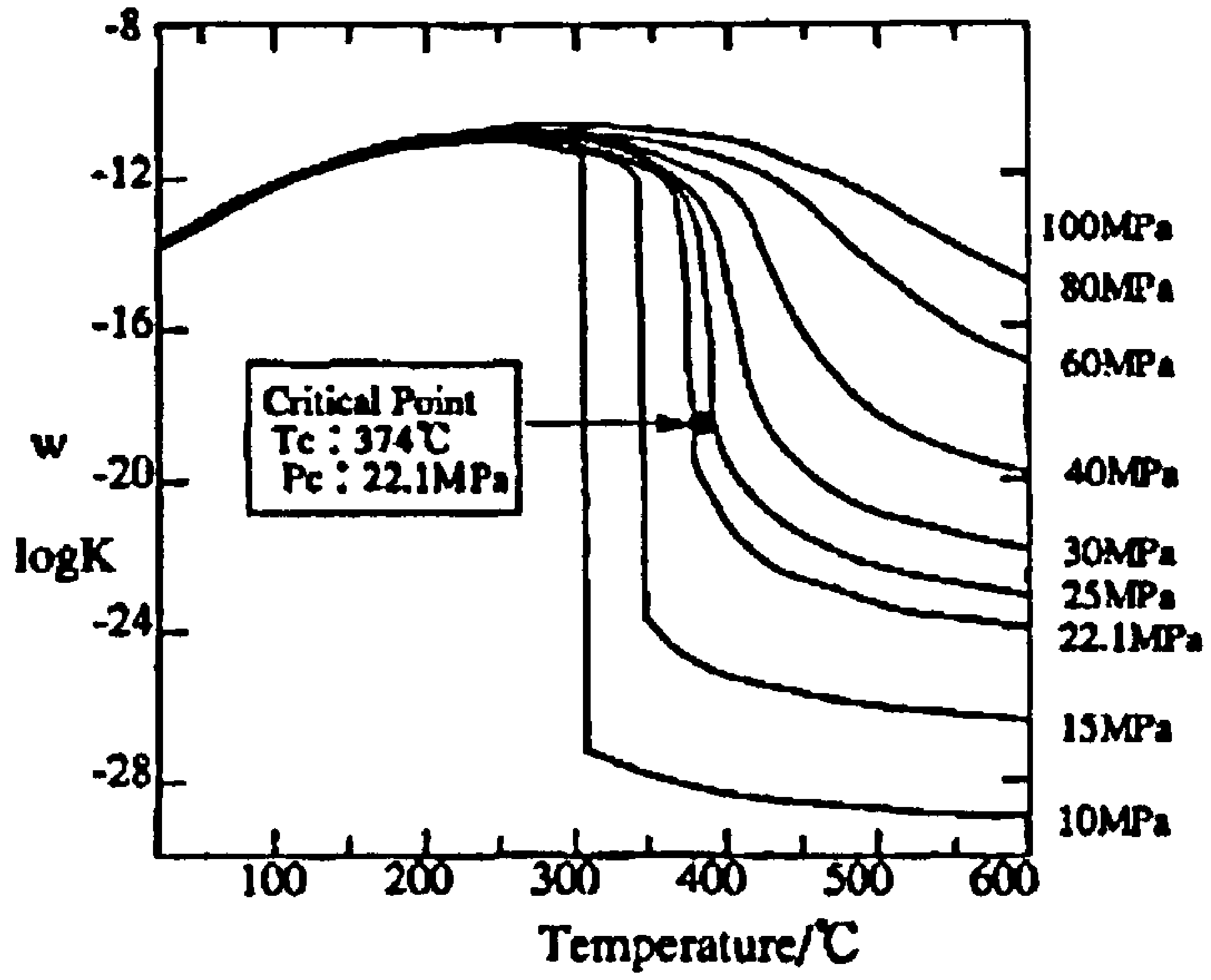

Figure 1-18 Ionic product of water as a function of temperature and pressure (Fukushima 2000).

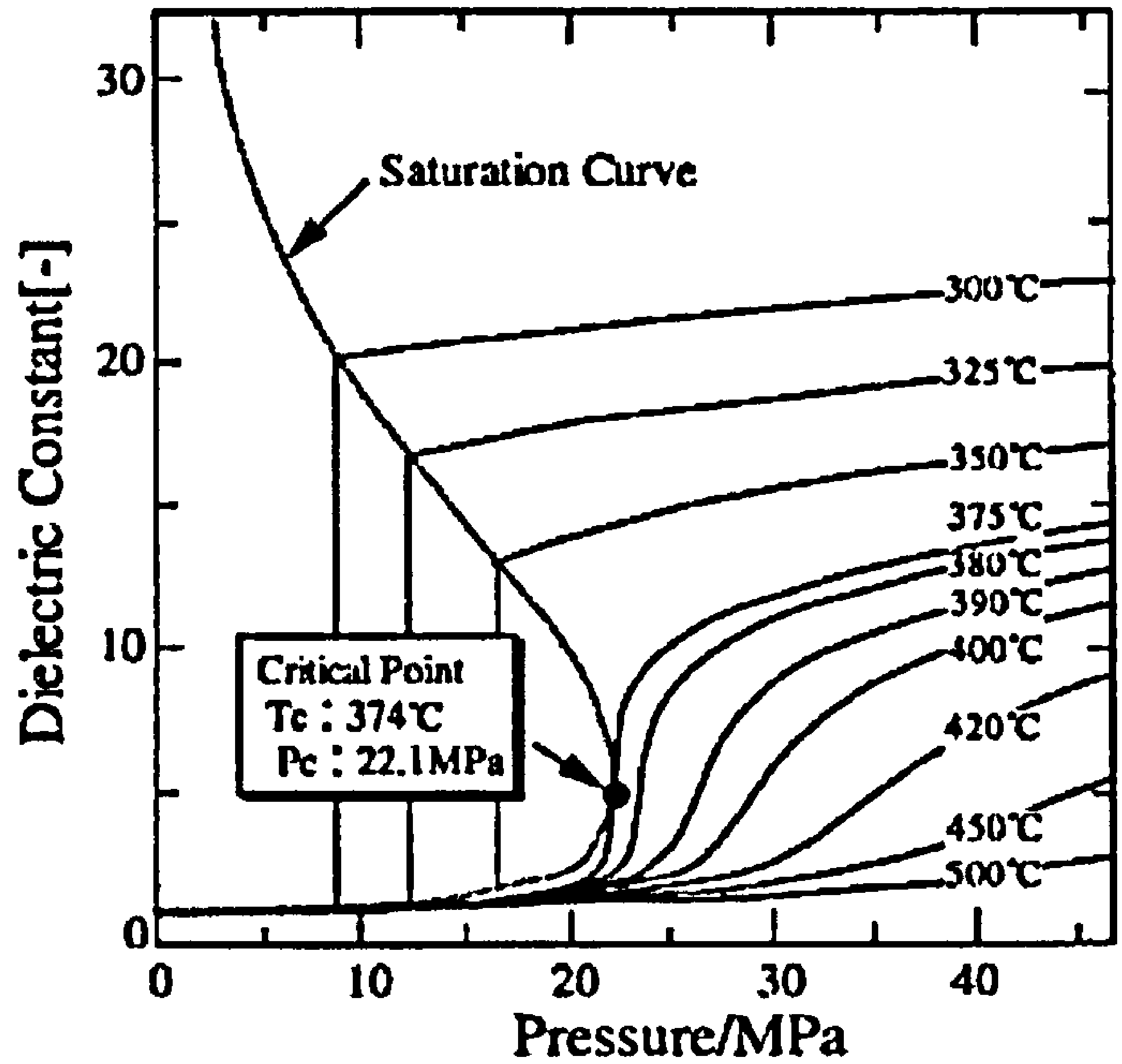

Figure 1-19 Dielectric constant of water as a function of temperature and pressure (Fukushima 2006).

1.4.2 Continous Hydrothermal Flow Synthesis: Advantages, System Design and Examples

1.4.2.1 Advantages of Flow Reactions and CHFS System Design

As mentioned earlier, the rapid change to a condition of high supersaturation increases the nucleation rate. This creates a large number of nucleation sites, which reduces the amount of material available for growth and hence results in smaller particle sizes (Kashchiev & van Rosmalen 2003). Due to slow heating, batch hydrothermal reactions generally result in micron-sized particles. In order to obtain nanosized particles using batch hydrothermal reactions, organic additives are used, which inhibit the growth of particles (Shi et al. 2007; Sun et al. 2006). Batch hydrothermal synthesis involves the use of a closed autoclave type reactor where reaction times are long (ranging from few hours up to a day) (Guo & Xiao 2006a; Li et al. 2007b; Shi et al. 2007; Sun et al. 2006).

In CHFS systems a stream of near- or supercritical water is continuously mixed with a stream of inorganic salts in solutions (Adschiri et al. 1992a; Adschiri et al. 1992b). Generally, the set-up includes two (High Performance Liquid Chromatography, HPLC) pumps, one of which pumps a metal salt solution into the CHFS system and the other pumps deionised water into a preheater [three pump systems have also been used where additional metal salt solutions or an acid or base are required (Sue et al. 2004d)]. The two streams (or feeds) meet at a mixing point (that can have different designs) and the particles are precipitated at this point. The stream (containing precipitated particles) is then cooled by passing through a cooler and large agglomerates are filtered, before it passes through a back-pressure regulator (which maintains the pressure in the system) and is collected as a suspension. In order to obtain dry powders, the suspensions are washed (to remove unreacted precursors), centrifuged and then dried (oven or freeze drying). A schematic diagram of a continuous hydrothermal flow synthesis system that was used for CHFS of ceria doped zirconia nanoparticles is shown in Figure 1-20 (Cabanas et al. 2000).

In contrast to batch hydrothermal reactions the flow process results in high diffusivity of the reactants. The faster dehydration reactions in near-critical/supercritical water result in very high hydrolysis and dehydration reaction rates. Residence times at the mixing point in continuous hydrothermal flow reactors are of the order of few seconds, being sufficient for reaction to occur. Pressure, temperature, concentration and pump flow rates can all be varied independently in a CHFS system giving the ability to affect resultant particle properties. Consequently, crystalline and nanosized particles can be produced (Darr & Poliakoff 1999).

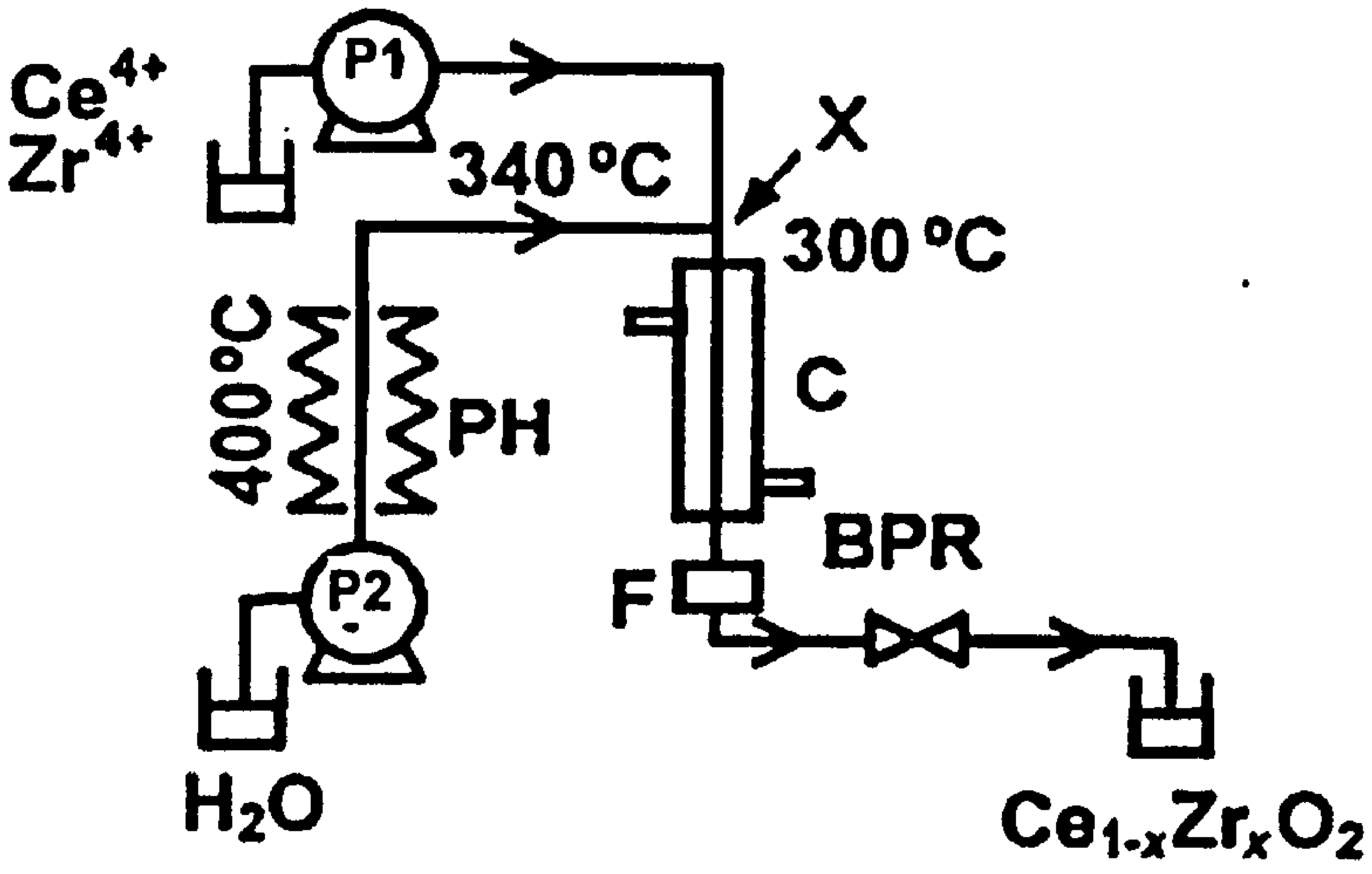

Figure 1-20 Schematic diagram of a CHFS system used for the synthesis of nanoparticles in nc-H_2O. [Pumps P, Preheater: PH, Mixing point: X, Water cooling: C, Filter: F, Back-pressure regulator (BPR)] (Cabanas et al. 2001).

One of the mixing point designs is the Swagelok™ T-piece as shown in Figure 1-21 (a) (Blood et al. 2004). However, the use of this mixing point contributes to unreliability of the CHFS technique and poor product reproducibility. This is due to accumulation and agglomeration of particles in the mixing point which reduces flow passage size and results in blockages. This requires premature system shutdowns and extensive cleaning between reactions.

In 2006, Lester and co-workers outlined the requirements of an ideal CHFS reactor. These included; homogeneous and instantaneous mixing of reactant streams, short residence times, minimal heating of the metal salt solutions prior to exposure to the supercritical water stream and rapid heating once this exposure occurred. This led to the development of a counter current reactor (mixing point) which was called the "Nozzle" reactor [shown in Figure 1-21 (b)] (Lester et al. 2006). Use of this mixing point resulted in improved reproducibility and a drastic reduction in blockages.

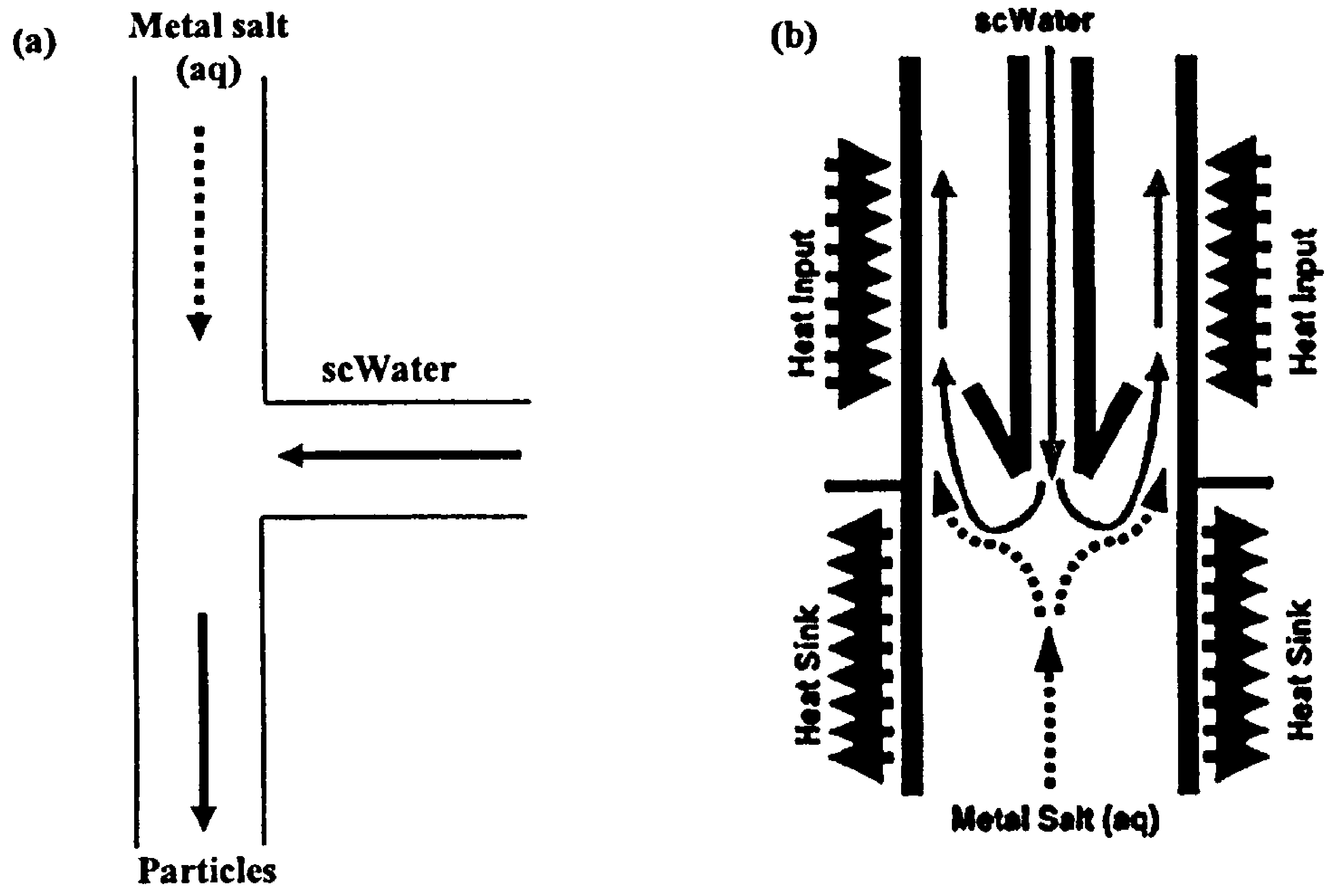

Figure 1-21 Schematic diagrams of (a) T-piece reactor and (b) Nozzle reactor showing ideal temperature profiles (Lester et al. 2006).

1.4.3 Examples of Materials Synthesised Using CHFS

Zinc oxide (ZnO) is a suitable material for varistors (Balashov et al. 1999), gas-sensors (Saha et al. 2007), catalysts (used in sunscreens) (Indarto 2008) and phosphors (Indarto 2008). Sue and co-workers from Arai's group in Japan, have reported extensively on the CHFS of zinc oxide nanoparticles (Sue et al. 2004a; Sue et al. 2004c; Sue et al. 2004b). They were able to synthesise particles [using $Zn(NO_3)_2$ salt] as small as 16 nm at 386 °C in the CHFS system (Sue et al. 2004c). The ability of CHFS systems to synthesise such small materials is of interest because the physical properties of nanosized ceramic materials (for potential electronic applications) are a function of their particle size (Millot et al. 2005).

Zirconia (ZrO_2) is a versatile ceramic which finds applications as a catalyst (Zhao et al. 2007), structural and a bioinert ceramic (Kelly & Denry 2008), refractory material (He et al. 2000) and in solid oxide fuel cells (Fischer & Blass 2006). Tetragonal zirconia nanoparticles have been synthesised using CHFS of zirconyl nitrate and zirconyl acetate under supercritical conditions (Hakuta et al. 2004). The synthesised particles were found to be *ca.* 7 nm in size and more crystalline than similar phases synthesised using conventional methods. The residence time of the particles in the reaction zone was calculated to be only 1.8 seconds. The CHFS method also allows synthesis of solid solutions such as ceria doped zirconia solid solutions (improved oxygen storage capacity) (Cabanas et al. 2000; Cabanas et al. 2001).

Titanium dioxide (TiO_2) is also a useful ceramic that finds applications as a catalyst (Zhou et al. 2007a), antibacterial material (Sunkara & Misra 2008) and a semiconductor (Liau & Lin 2008). Furthermore, in addition to ZnO, TiO_2 is widely used as a UV absorber and is the only inorganic UV absorber allowed for use in cosmetics usable by humans by the Scientific Committee on Cosmetic and Non-Food Products Intended for Consumers (Europe) and the Food and Drug Administration (FDA). There is interest in developing nanoparticles of titania (and zinc oxide) below 50 nm as they become invisible on skin (Serpone et al. 2007). Photoexcited titania is expected to inhibit malignant cell growth as suggested by work carried out on tumours in mice (Chihara et al. 2007). The CHFS method has been used to synthesise the anatase phase of titania using bis(ammonium lactacto) titanium dihydroxide precursor at 300 °C under 30 MPa. The resultant particles had a high surface area of 255 $m^2\ g^{-1}$ and crystallite size of around 3 nm (Millot et al. 2005).

In addition to these materials, barium zirconate ($BaZrO_3$ – refractory material) (Aimable et al. 2008), lithium iron phosphate ($LiFePO_4$ – cathode material in lithium ion rechargeable batteries) (Xu et al. 2008) and cobalt iron oxide ($CoFe_2O_4$ – magnetic material) (Cote et al. 2003) have also been synthesised using CHFS systems. Iron oxide nanoparticles (magnetic materials) synthesised using the CHFS technique have been the subject of considerable literature (Cabanas & Poliakoff 2001; Sato et al. 2008; Takami et al. 2007; Xu & Teja 2008).

To summarise, the continuous hydrothermal flow synthesis method offers many advantages which result in rapid, single-step synthesis of nanosized, crystalline unique particles. The rapidity of the process coupled with high temperatures and pressures involved in CHFS method may result in formation of kinetic phases and phase mixtures difficult to synthesise using conventional synthesis methods.

1.5 Spark Plasma Sintering

Use of an electric current is one of the ways of initiating sintering (Munir et al. 2006). This concept is not entirely new as patents on this topic date back to 1930s and reports on "spark sintering" were published between the 1950 – 1970 time period (Boesel 1971). Plasma Assisted Sintering (PAS), Pulsed Electric Current Sintering (PECS), Electric Pulse Assisted Consolidation (EPAC) and Spark Plasma Sintering (SPS) all refer to similar methods. Figure 1-22 shows the arrangement of a die in a SPS furnace.

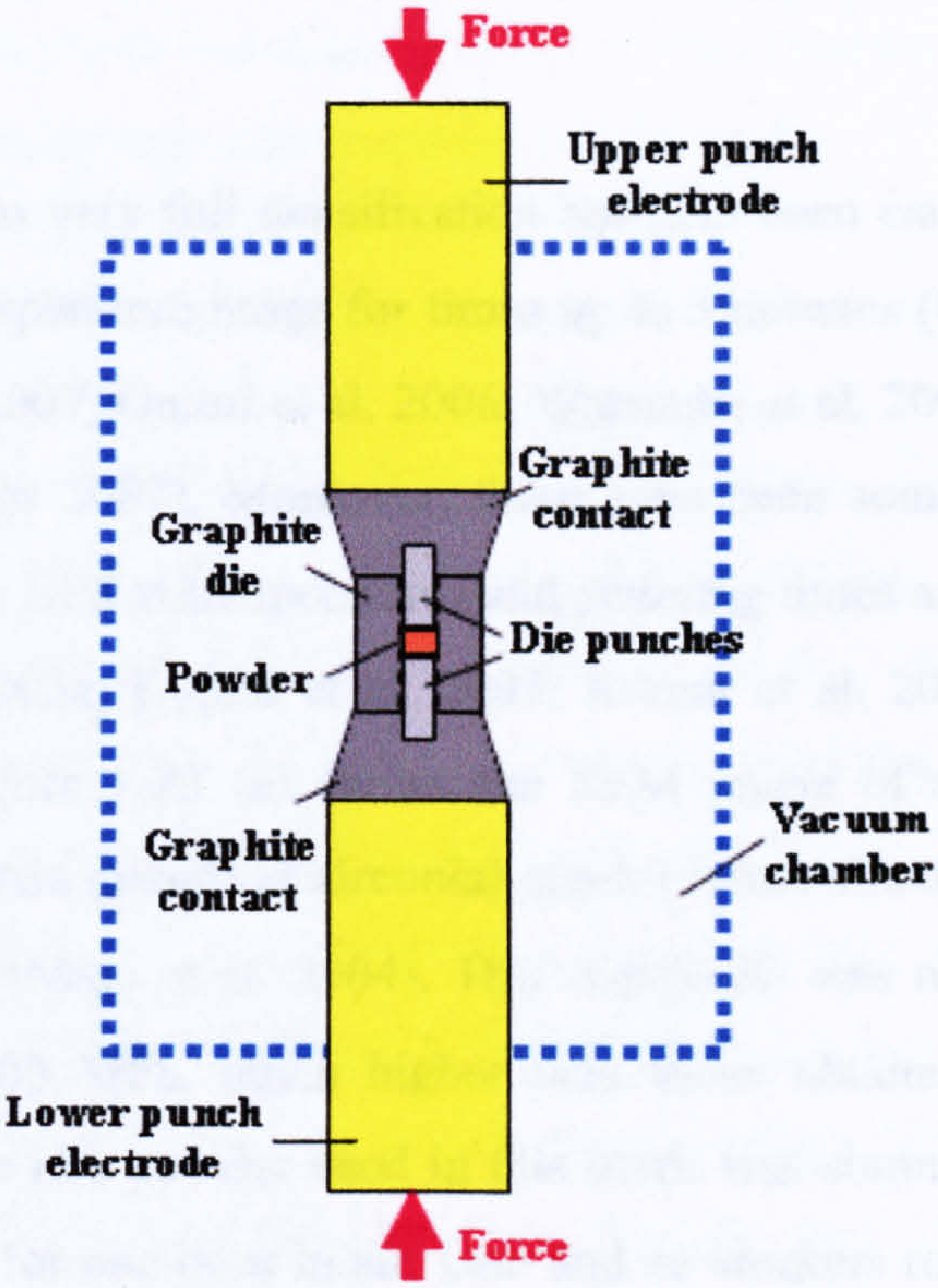

Figure 1-22 Schematic showing the die, punches and position of the powder specimen in a SPS furnace.

The SPS technique uses high direct current and uniaxial pressure to consolidate powders. Use of electric current results in very fast heating rates during spark plasma sintering. It has been shown that higher heating rates (300 °C min^{-1} as compared to 50 °C min^{-1} for alumina) result in better densification (Zhou et al. 2003). The rapid heating rates involved in SPS result in very short sintering times at lower temperatures (than conventional methods). These conditions in turn can result in nanostructured dense ceramics with higher mechanical properties. Indeed, nitrides, carbides and nano-tubes have been sintered to almost full-density in few minutes using SPS (Li et al. 2007a; Ran & Gao 2008; Sun et al. 2007a; Zhang et al. 2007a).

SPS has also been used to consolidate silver metal (Ng et al. 2008), tungsten based alloys (Mcherzynska & Matsuura 2008; Sun et al. 2008) and silicon carbide reinforced aluminium matrix composites (Zhang et al. 2008). Ng and co-workers reported the *ca.* 100 % densification of silver powder at temperature as low as 300 °C with 1000 MPa Vickers hardness (3 times higher than that obtained using conventional consolidation methods) (Ng et al. 2008). In a review published in 2006, Munir and co-workers stated that SPS of dense nanostructured ceramics increased permittivity for ferroelectrics, improved magnetic properties and reduced impurity segregation at grain boundaries (Munir et al. 2006).

Consolidation of HA to very full densification has also been carried out using SPS in the 850 – 1100 °C temperature range for times up to 5 minutes (Gu et al. 2002; Guo et al. 2005; Khalil et al. 2007; Omori et al. 2006; Watanabe et al. 2005; Xu et al. 2005; Xu et al. 2007; Xu & Khor 2007). Moreover, there have been some reports of ZrO_2-HA ceramics sintered using SPS at temperatures and sintering times as low as 1000 °C for 5 minutes (Guo et al. 2003a; Kumar et al. 2003; Kumar et al. 2005; Miao et al. 2004; Shen et al. 2001). Figure 1-23 (a) shows the SEM image of a HA-YSZ composite (containing 40 wt% yttria stabilised zirconia) spark plasma sintered to 93 % density at 1200 °C in 5 minutes (Miao et al. 2004). This composite was reported to have a 3-pt flexural strength of 200 MPa, much higher than those obtained using conventional sintering methods. The HA powder used in this work was commercially procured and heat-treated at 900 °C for one hour in air. Guo and co-workers reported the SPS of HA with even smaller grains at 825 °C for only 3 minutes under 50 MPa pressure [shown in Figure 1-23 (b)]. This HA was prepared using a batch hydrothermal reaction carried out 300 °C for 2 hours. This work however, used a 12 mm graphite die for SPS of HA (which being a small size may facilitate relatively easier consolidation).

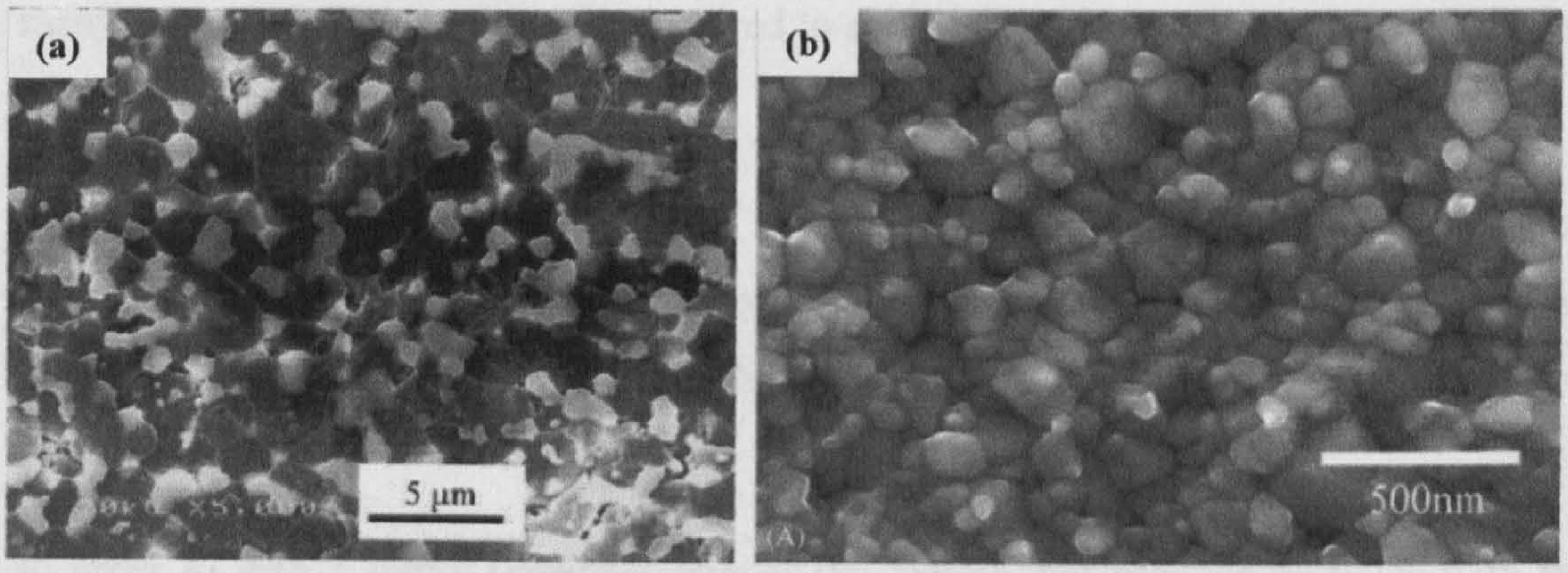

Figure 1-23 Scanning electron microscope image of (a) HA-YSZ composite spark plasma sintered at 1200 °C for 5 minutes (Miao et al. 2004) (b) phase-pure HA spark plasma sintered at 825 °C for 3 minutes (Guo et al. 2005).

Many ceramics, which are difficult to sinter using conventional methods, have been sintered to near full densification in SPS due to the higher heating and cooling rates and application of pressure during sintering. This results in reduced sintering temperatures and times which inturn result in a small grain size. Nanostructured ceramics which offer superior mechanical properties, can therefore, be obtained.

1.6 Hypothesis and Aims

The discussion in this section can now be summarised. The solid-state routes to synthesise HA are time consuming and prone to contamination. Co-precipitation of HA requires strict control and monitoring of reaction parameters such as pH, stirring rate, rate of addition of solutions etc. Moreover, it is time consuming as it requires ageing up to a day followed by a compulsory heat-treatment in order to yield crystalline HA. On the other hand, sol-gel chemistry is complex. Although sol-gel processing is suitable for bulk materials, the advantages of the process are lost when HA is required in a powder form. It is also time consuming and requires heat-treatment for burning off unwanted reagents and crystallisation of amorphous HA. Emulsion methods facilitate synthesis of powders having small particle sizes however, they are also time consuming and require a subsequent heat-treatment. Furthermore, large amounts of oil and surfactants are required making this technique environmentally unfriendly. Batch hydrothermal synthesis stands out as it offers a low-cost, low-temperature, simple and effective route to crystalline, phase-pure HA. It also facilitates ion-substitution into HA. However, in many cases, templating agents are required to achieve small sizes. Synthesis times range between a few hours up to 24 hours.

Pressure-less sintering and hot-pressing are the two most commonly used methods for consolidation of HA powders. The very long periods of time and high temperatures involved in these methods can result in very large grain sizes and at times, phase-decomposition.

In order to gain a better understanding of the factors that produce particles with the desired properties and enable their consolidation to dense nanostructured ceramics, current methods are essentially too slow and uncontrollable. Thus, there is interest in developing faster synthesis and consolidation techniques for synthetic calcium phosphates that allow a greater degree of control over particulate and bulk properties.

Continuous hydrothermal flow synthesis (CHFS) method is a rapid single step method which results in crystalline nanoparticles. CHFS systems facilitate control over particle properties through a number of controllable system parameters such as temperature, pressure, concentration and flow rates. The CHFS of several novel nanoparticles has been reported in literature however, it has not been exploited for synthesis of calcium phosphate ceramics yet. It was postulated that the rapid nucleating and crystallising environment within a hydrothermal flow reactor may facilitate accelerated synthesis of crystalline and nanosized calcium phosphates in a single step. Furthermore, the large number of variable system parameters may provide control over particle properties such as size and morphology, surface area, thermal stability, chemical composition, phase-purity and extent of ionic substitution.

Spark plasma sintering (SPS) has recently gained importance due to high heating and cooling rates involved. It has been shown to result in shortened sintering times of only a few minutes and full densification at lower temperatures, as compared to conventional consolidation techniques. It was hypothesised that the initial use of smaller nano-bioceramics synthesised using the CHFS method for consolidation via SPS will result in denser nanostructured materials. This was expected to translate into enhanced mechanical properties of these sintered materials.

Based on these inferences and hypothesis, the main aims of this project can be outlined as follows:

- To synthesise crystalline and phase-pure HA in the CHFS system in a rapid single-step manner and design a CHFS system for this purpose.
- To demonstrate control over particulate properties (with relevance to biological performance) using CHFS system parameters.
- To synthesise ion substituted calcium phosphates and explore substitution limits in the CHFS system and effects on particulate properties.
- To synthesise co-precipitates of HA and mechanically stronger phases for better mechanical properties after sintering.
- To consolidate the aforementioned bioceramic particles using SPS with the aim of improving mechanical properties of these materials.

Chapter 2

Materials and Methods

This chapter concerns experimental methods and materials used in this thesis. This includes details of chemicals used for reactions in the continuous hydrothermal flow synthesis (CHFS) system, different CHFS systems, synthesis methodology (calculations, reaction conditions), characterisation techniques (sample preparation and measurement details) and consolidation of powders via Spark Plasma Sintering (SPS).

2.1 Materials and Chemicals

The following chemicals were used for synthesis of all phase-pure calcium phosphate particles in a powdered form.

- Diammonium hydrogen phosphate, [$(NH_4)_2HPO_4$, 98.3%] supplied by Sigma-Aldrich Chemical Company (Dorset, U.K.) was used as a phosphate ion (PO_4^{3-}) source.
- Calcium nitrate tetrahydrate [$Ca(NO_3)_2.4H_2O$, 99%] supplied by Sigma-Aldrich Chemical Company (Dorset, U.K.) was used as a calcium ion (Ca^{2+}) source.

To synthesise ion-substituted calcium phosphate particles and zirconia-hydroxyapatite (ZrO_2-HA) composite powders the following chemicals were used.

- Urea [$(NH_2)_2CO$, 99.5%] supplied by VWR International (UK) was used as a carbonate ion (CO_3^{2-}) source.
- Silicon tetraacetate [$Si(OCOCH_3)_4$, 98%] supplied by Sigma-Aldrich Chemical Company (Dorset, U.K.) was used as a silicate ion (SiO_4^{4-}) source.
- Magnesium nitrate hexahydrate [$Mg(NO_3)_2.6H_2O$, 97%] supplied by Sigma-Aldrich Chemical Company (Dorset, U.K.) was used as a magnesium ion (Mg^{2+}) source.
- Zinc nitrate hexahydrate [$Zn(NO_3)_2.6H_2O$, 98%] supplied by Sigma-Aldrich Chemical Company (Dorset, U.K.) was used as a zinc ion (Zn^{2+}) source.

- Zirconyl nitrate hydrate [$ZrO(NO_3)_2.xH_2O$] supplied by Sigma-Aldrich Chemical Company (Dorset, UK) was used as a source of zirconia (ZrO_2) in ZrO_2-HA composite powders.

- Potassium hydroxide (KOH, 90%] supplied by VWR International (UK) was used in the synthesis of ZrO_2-HA composite powders in order to provide a basic reaction medium in the reactor.

All aqueous solutions for the CHFS were made using 10 MΩ deionised water. Where required, the pH of solutions was adjusted using neat ammonium hydroxide solution (NH_4OH, ≥30% w/w) supplied by VWR International (UK).

2.2 Synthesis Methods for Nanopowders

2.2.1 Continuous Hydrothermal Flow Synthesis (CHFS) Systems

CHFS systems based on a three-pump configuration (Figures 2-1 to 2-16) were used for the synthesis of all samples during the course of this work.

2.2.1.1 Continuous Hydrothermal Flow Synthesis System 1

The first continuous hydrothermal flow system was built by P. Boldrin, Dr. A. Hebb and Dr. J. A. Darr of Clean Materials Technology Group (CMTG) at Department of Materials, Queen Mary University of London in 2005. In this work it will be referred to as CHFS system 1 (Boldrin 2008).

The flow chart of CHFS system 1 in Figure 2-1 shows a three-pump configuration. The CHFS system 1 is shown in Figure 2-2. All pumps were fitted with SC-type piston pump heads (see Figure 2-3). One of these 305 Gilson HPLC pumps (with a 10SC pump head) was used to pump deionised water through the pre-heater at 10.0 mL min^{-1}. In this thesis this will be called the superheated water feed. Calcium and phosphate source solutions were pumped using two separate 305 Gilson HPLC pumps at 5.0 mL min^{-1}, respectively. These feeds will be referred to as calcium and phosphate feeds.

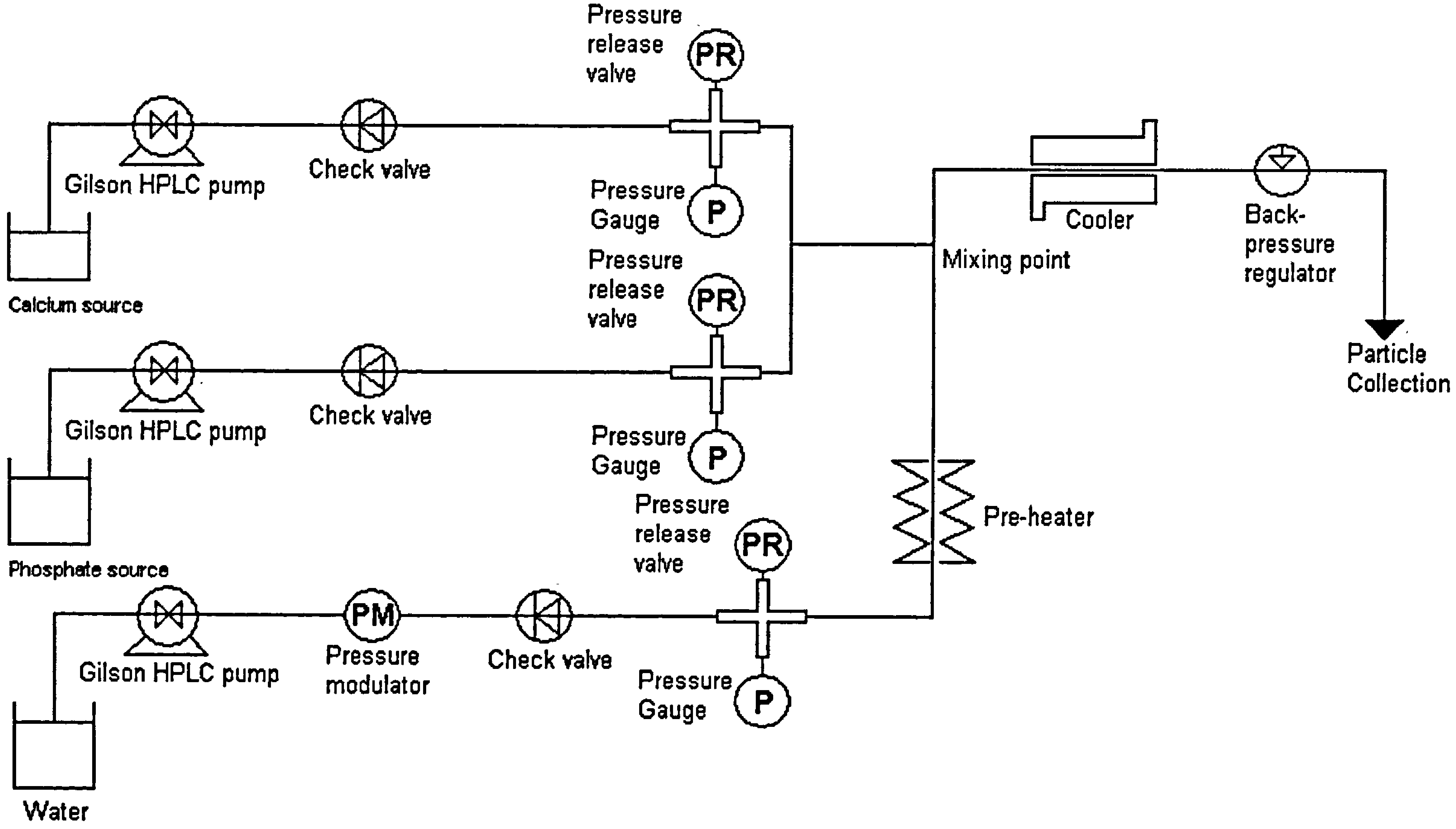

Figure 2-1 Flow Chart of the three-pump CHFS systems used during the course of this work (image taken from thesis of P. Boldrin – submitted in 2008 to Department of Materials, QMUL).

Each “feed line” consisted of a check valve, pressure release valve and a pressure gauge connected using a 1/8” (” represents inches) 316 seamless stainless steel tubing with 0.028” pipe thickness (all parts were Swagelok™). The check valve ensured one-way flow and is shown in Figure 2-4. The pressure release valve was adjusted such that it vented just before the pressure reached 4500 psi (31 MPa) (see Figure 2-5). This was a safety feature that allowed pressure to dissipate in the case of blockages in the system or any other reason which resulted in a pressure increase. An RS pressure gauge was attached in parallel to the pressure release valve in order to monitor pressures.

After passing through the valves, water in the superheated water feed then enters a custom-built electrically powered pre-heater made using Watlow components (Figure 2-6). Its schematic diagram is shown in Figure 2-7 (Kellici 2006). The heater comprised of a main cylindrical core made out of an aluminium alloy (Al 6082). A hole was drilled in the centre of this core and à 1000 W Watlow rod cartridge heater was inserted. Six metres of ¼” outer diameter 316 stainless steel seamless tubing with 0.035” wall thickness was wound around this core by hand (see Figure 2-8). Two 750 W Watlow band heaters, 4” in length and 2.5” in diameter, were then slid onto this combination. These parts were then insulated using an RS Excelflex insulating blanket. All the components were secured between two disc shaped end plates using brass studding and wing nuts. Watlow J-type thermocouples were used to monitor the temperature at the top and bottom of the pre-heater. These thermocouples and the band and cartridge heaters were connected into a Watlow heater controller. The temperature of the pre-heater was controlled and monitored using this controller.

After passing through this pre-heater the superheated water passed into a counter-current reactor. The counter-current reactor consisted of a 1/8” 316SS (SS represents stainless steel) Swagelok™ pipe swaged into a 3/8” 316SS Swagelok™ cross-piece. Schematic diagram of the counter-current reactor (this will be called the mixing point in this thesis) is shown in Figure 2-9. The mixing zone shown in the same figure approximately demarcates the highest temperature zone in which most of the nucleation and/or growth takes place.

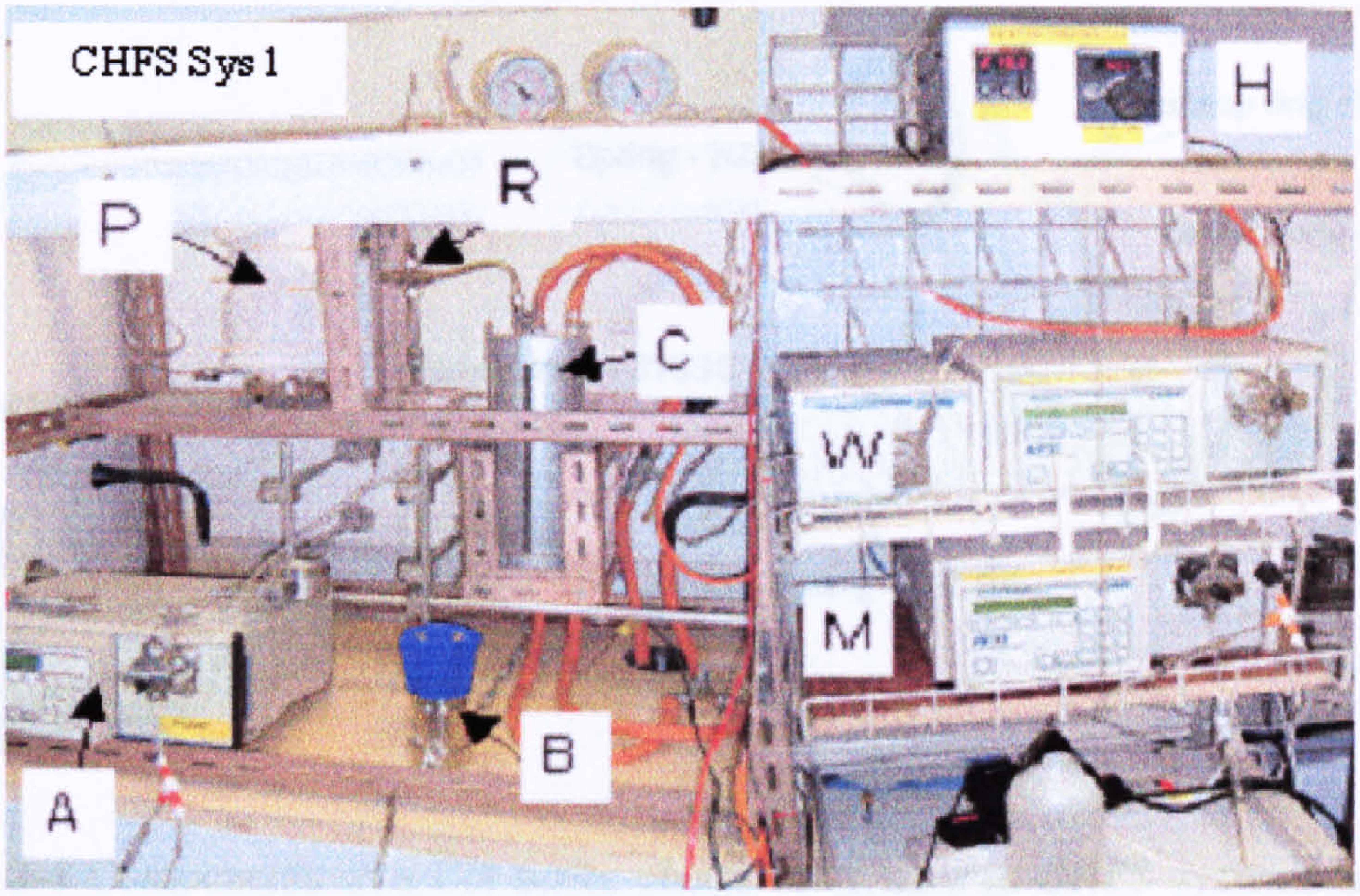

Figure 2-2 Continuous Hydrothermal Flow Synthesis System 1 [Key: A: Ca^{2+} source pump, M: PO_4^{3-} source pump, W: water pump, H: heater controller, P: water pre-heater, R: counter-current reactor (mixing point), C: cooler, B: back pressure regulator (BPR)] (Boldrin 2008).

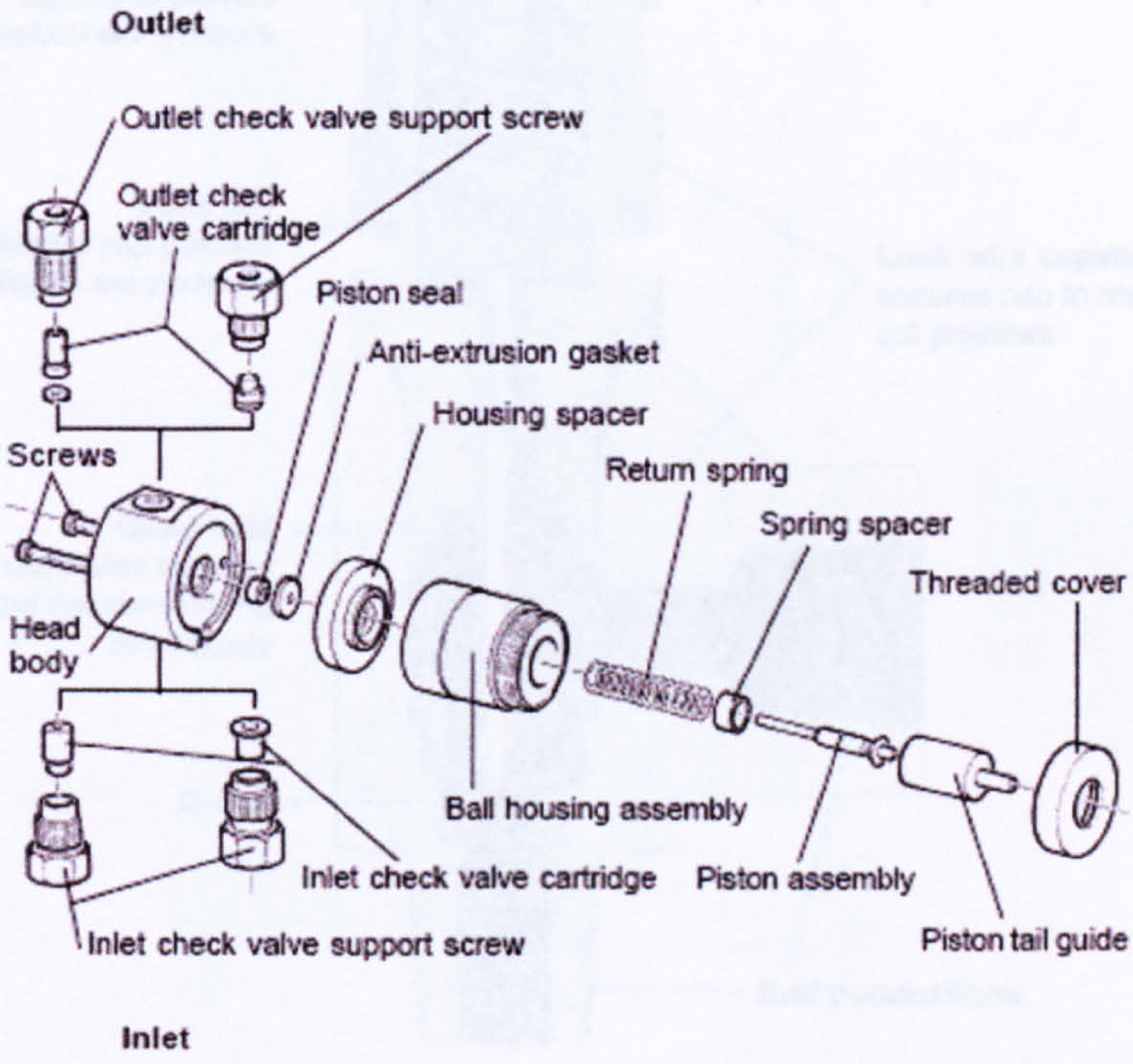

Figure 2-3 Components of a Gilson SC-type pump head (taken from Gilson web guide on "SC-type Piston Pump Heads User's Guide") (Gilson 2001).

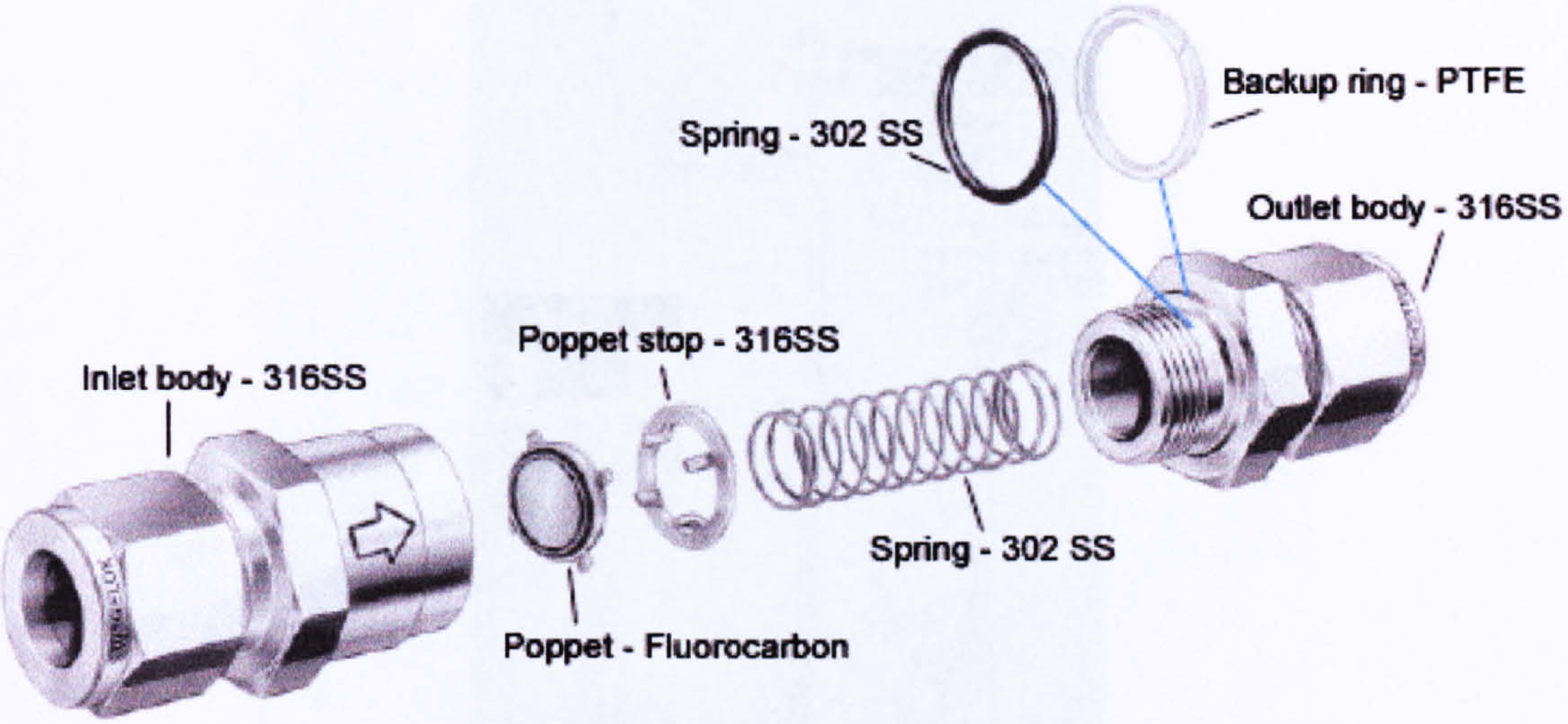

Figure 2-4 Components of a CH series check valve used in CHFS systems and their material grade (image modified from Swagelok web catalogue on "Check Valves") (Swagelok Company 2007a).

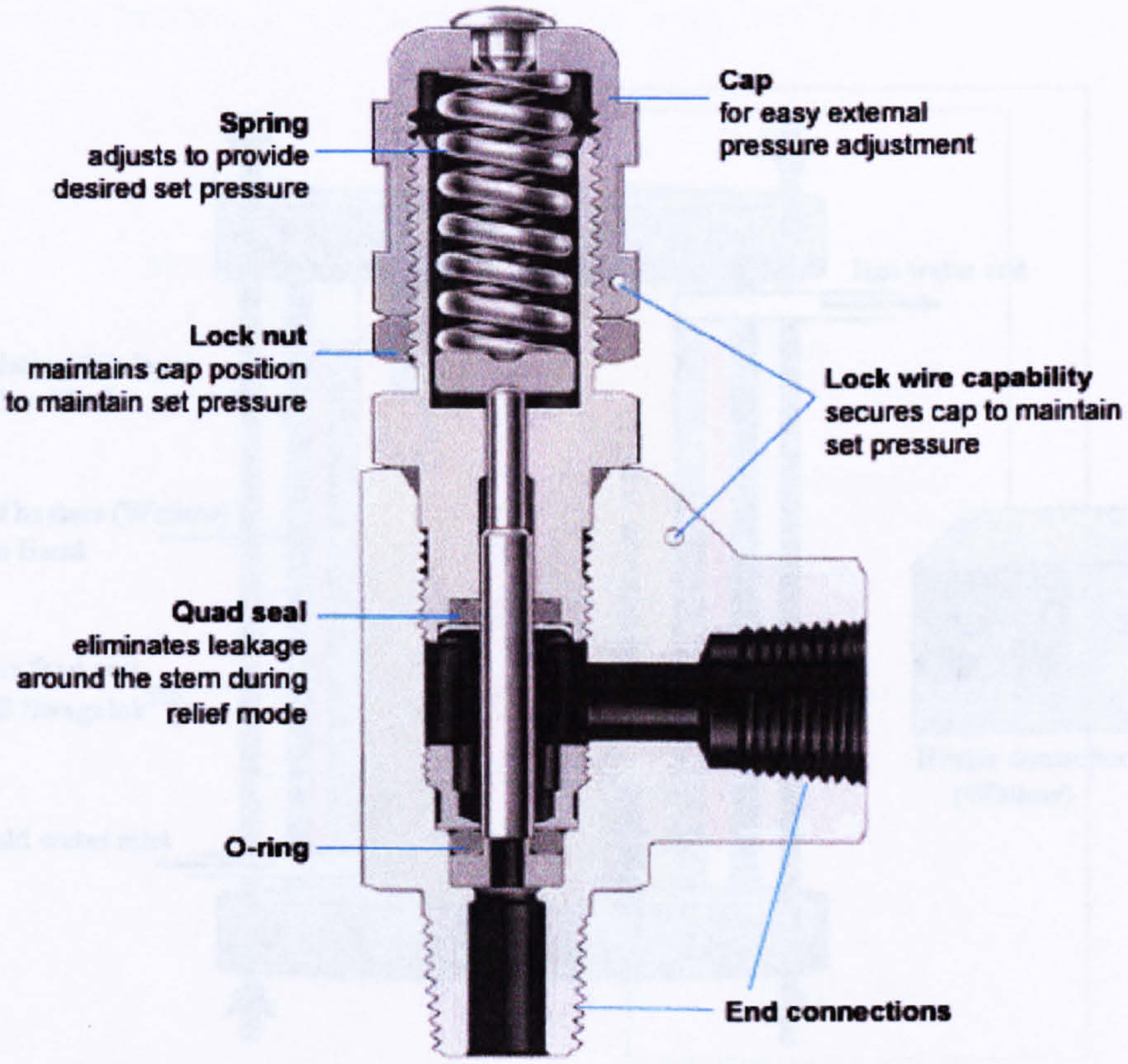

Figure 2-5 Cross-sectional view of the pressure release valve (image modified from Swagelok web catalogue on "Proportional Relief Valves") (Swagelok Company 2007b)
.

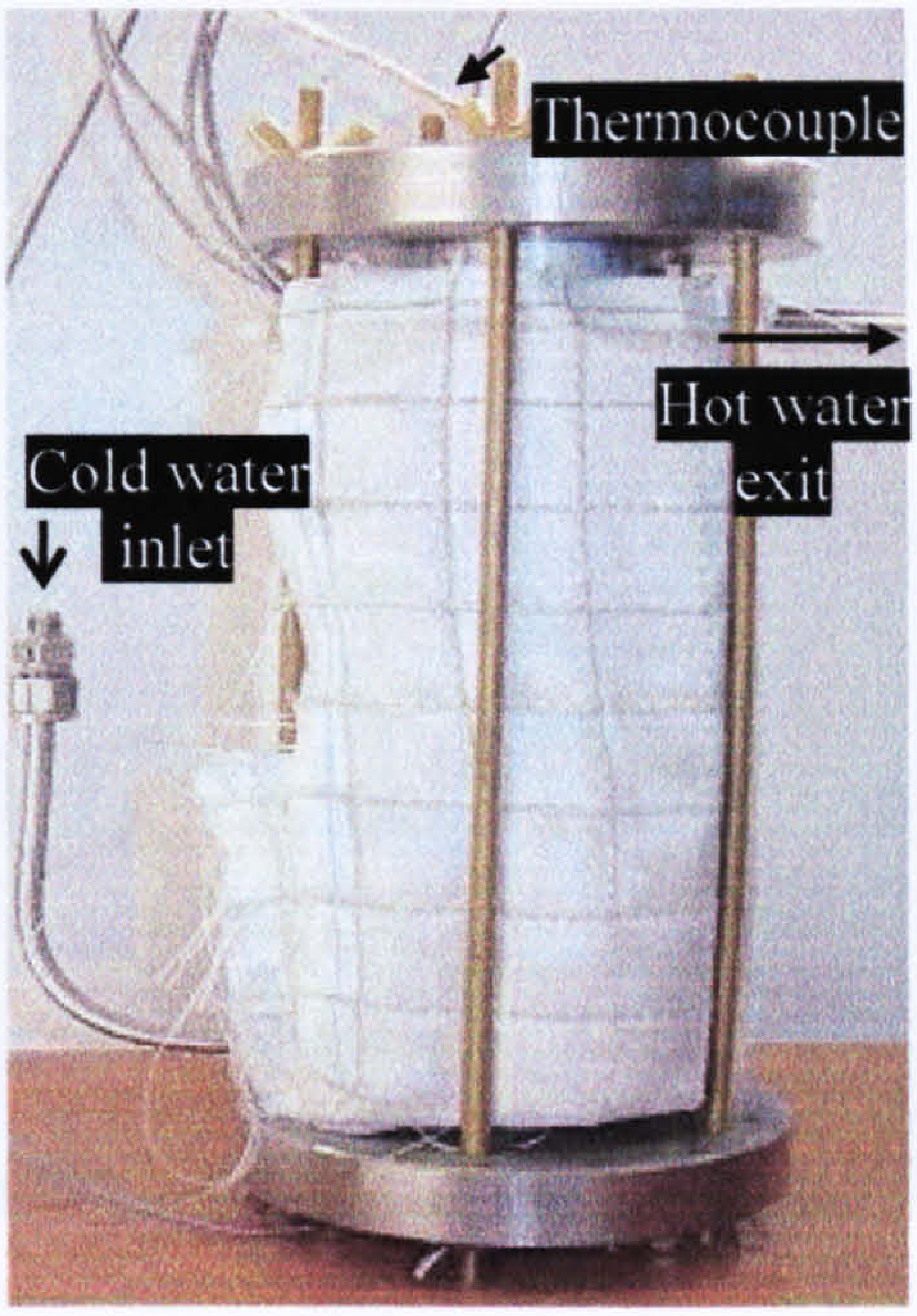

Figure 2-6 Custom-built water pre-heater (built at the Department of Materials, QMUL).

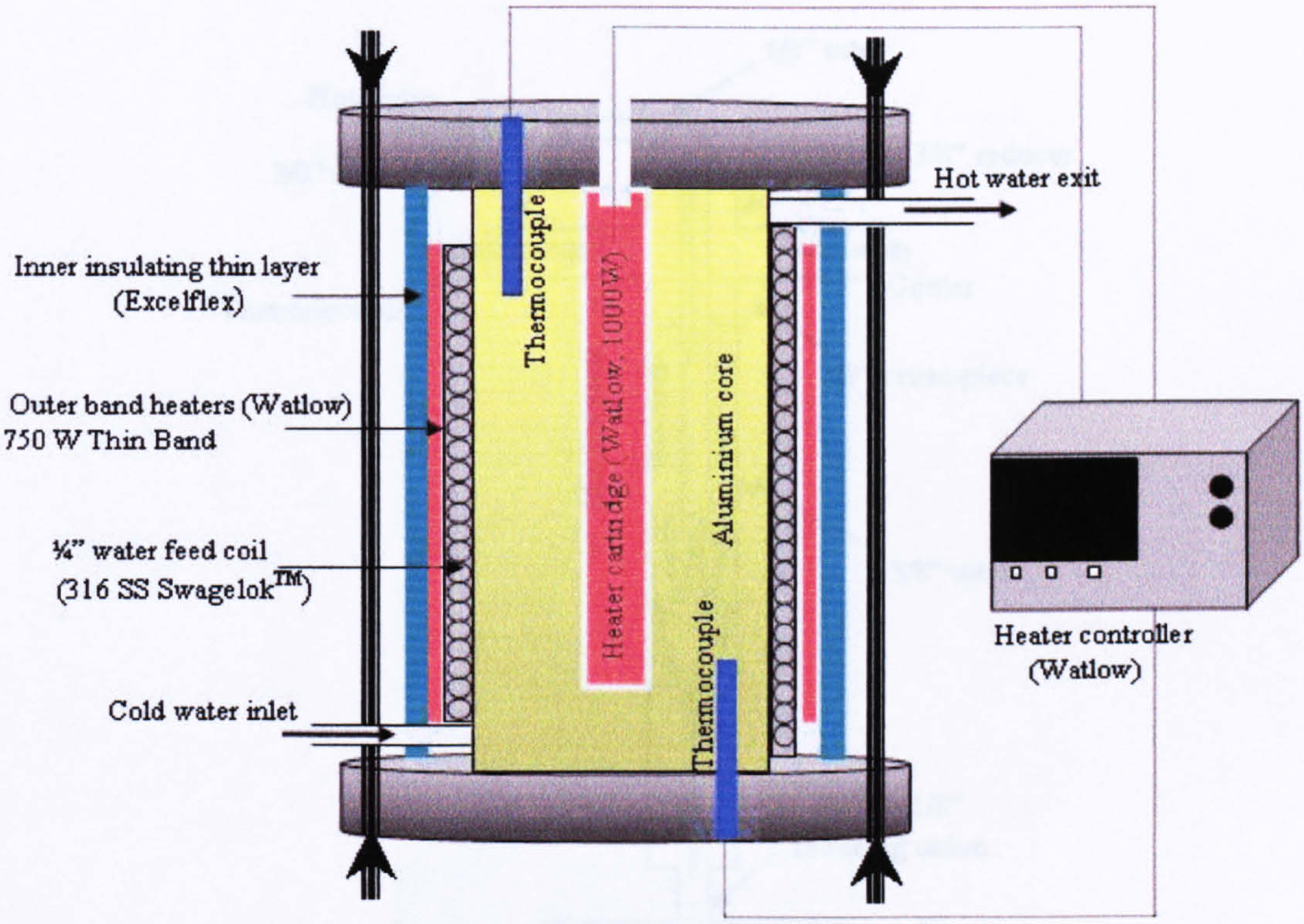

Figure 2-7 Schematic diagram of the custom built electrically powered water pre-heater (built in Department of Materials, QMUL) using ¼" 316 stainless steel Swagelok™ tubing (adapted from design of P. Hamley, University of Nottingham) (image taken from PhD thesis of S. Kellici – submitted in 2006 to Department of Materials, QMUL).

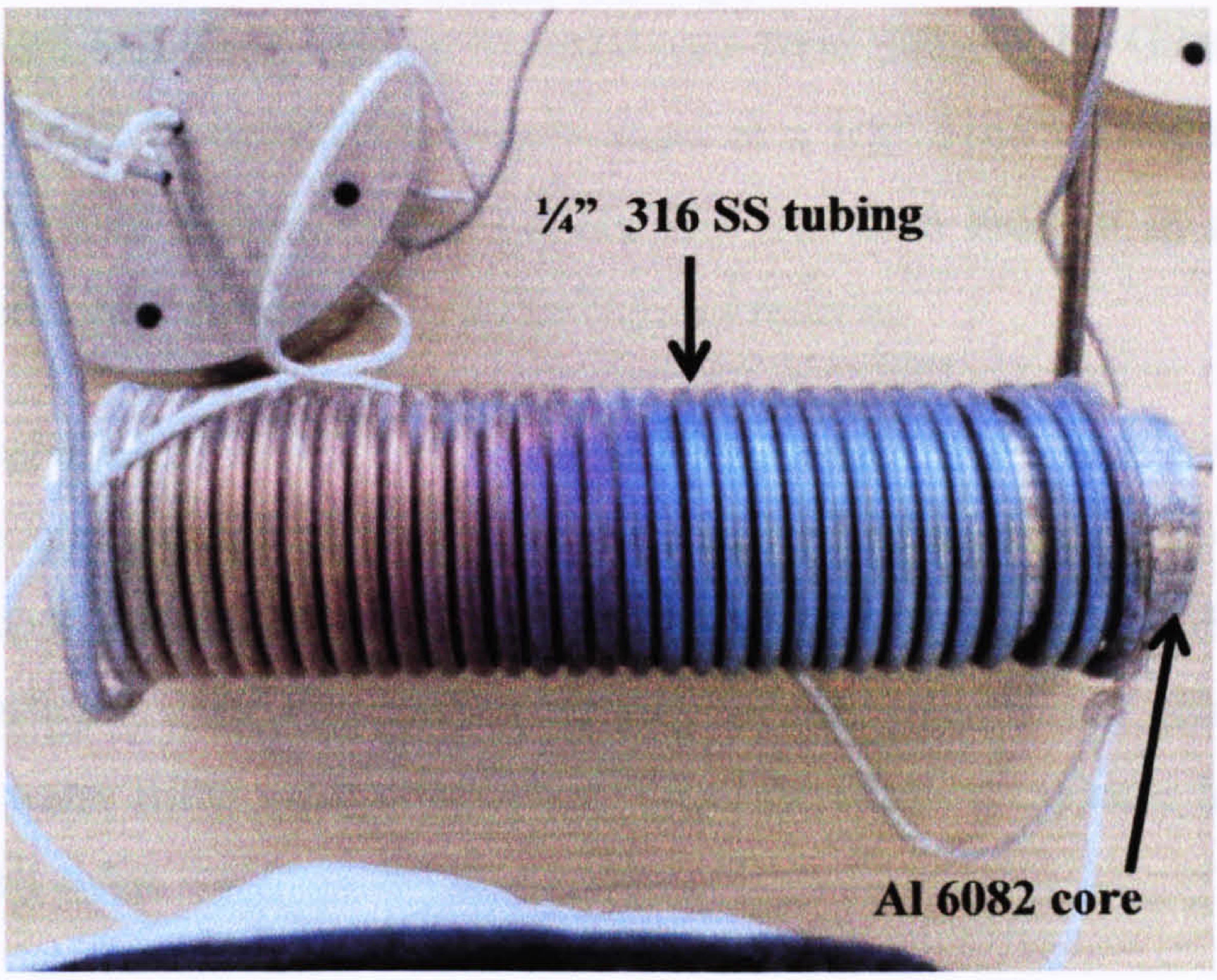

Figure 2-8 ¼" Swagelok™ tubing wound around an Al 6082 core used in the pre-heater. The tubing is coloured because it has been used and this particular image was taken after a pre-heater was retired from use in a CHFS system.

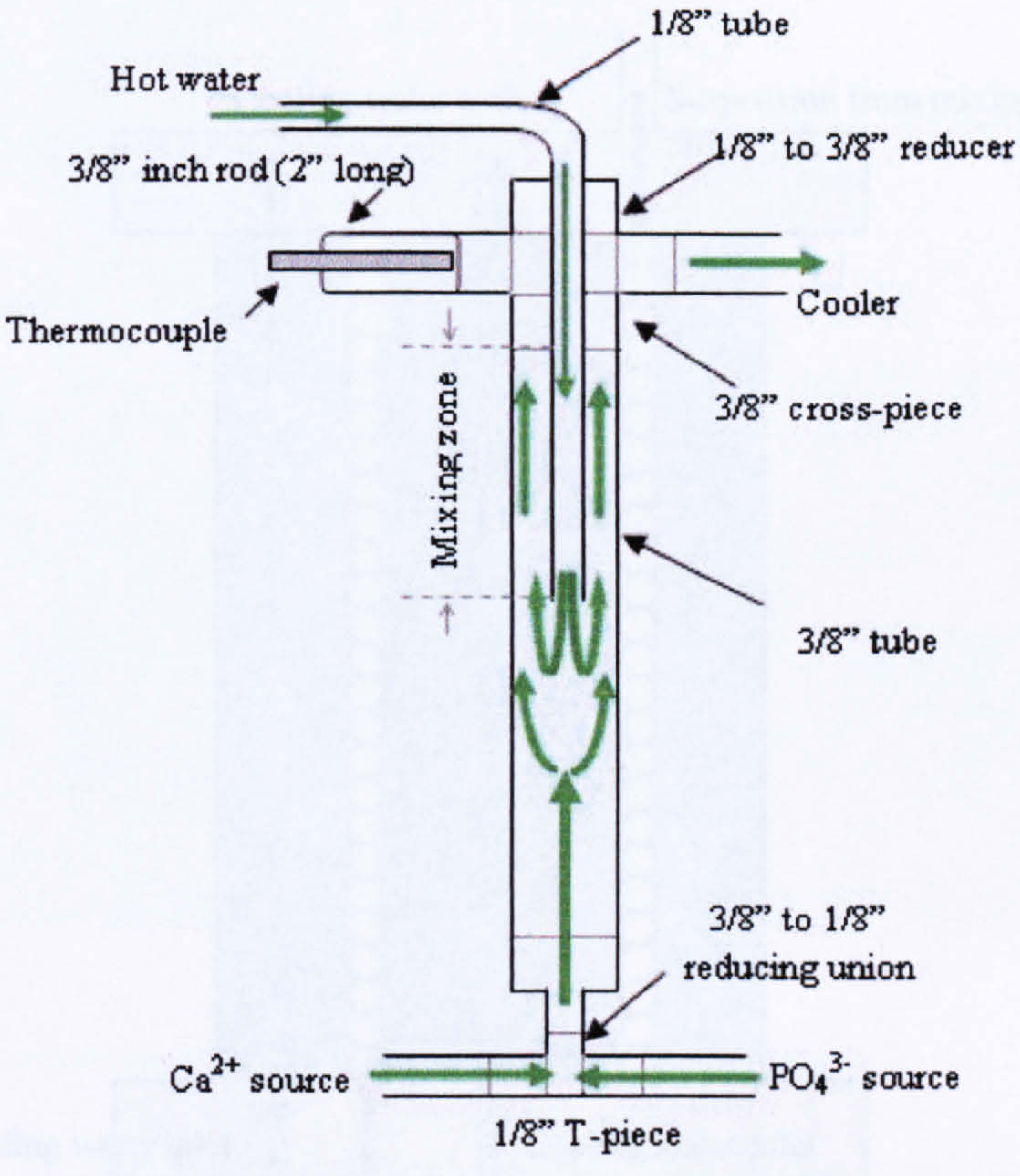

Figure 2-9 Schematic diagram of the counter-current reactor used in CHFS system 1.

Aqueous calcium and phosphate source solutions were pumped by Gilson 305 pumps through 1/8" 316SS Swagelok™ tubing to meet at a 1/8" 316SS Swagelok™ T-piece. An initial precipitate formed at the T-piece and was then brought in contact with a stream of superheated water in the counter-current reactor.

The initial precipitate, after being exposed to superheated water, then passed through a cooler. The cooler consisted of three concentric cylinders made out of aluminium continuously cooled by cooling water as shown in Figure 2-10. ¼" 316SS tubing which carries the particles from the counter current reactor was wound around the inner cylinder. The water filled inner core cylinder and the external cylinder hence provided cooling from all sides.

After cooling the particles passed through a large particle filter (15 μm) and were collected as a suspension after passing through a back-pressure regulator (BPR – Tescom). The BPR was used to maintain the pressure at 3500 psi (~24 MPa) at all times.

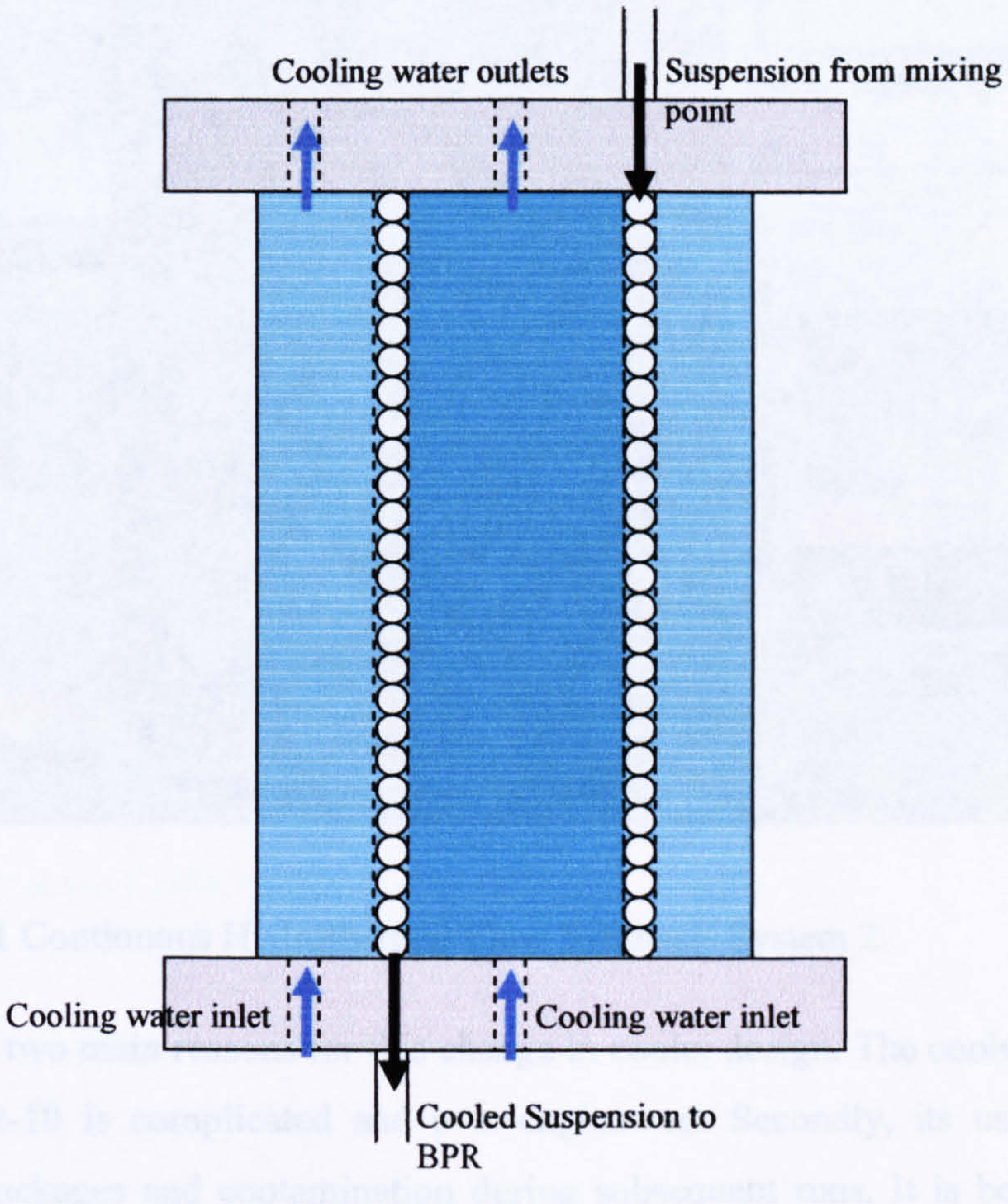

Figure 2-10 Schematic diagram of the cooler used in CHFS system 1.

2.2.1.2 Continuous Hydrothermal Flow Synthesis System 2

The second CHFS system built by CMTG is labelled as CHFS system 2 (Figure 2-11). It was designed and built by A. A. Chaudhry, S. Kellici and Dr. J. A. Darr. The design is similar to that of CHFS system 1. However, instead of using a 3/8” 316SS Swagelok™ cross-piece and tubing in the mixing point, a ¼” 316SS Swagelok™ cross-piece and tubing was used. The aim was to have faster flow through the mixing zone and hence shorter residence times. A combined flow rate of 20.0 mL min^{-1} through the system results in residence times of 28.3 and 9.9 seconds for 3/8” and ¼” cross-pieces, respectively. Additionally, the cooler design used for system 1 was replaced by a much simpler pipe-in-pipe type cooler (*ca.* 50 cm in length). The mixing point and the new cooler are shown in Figure 2-12.

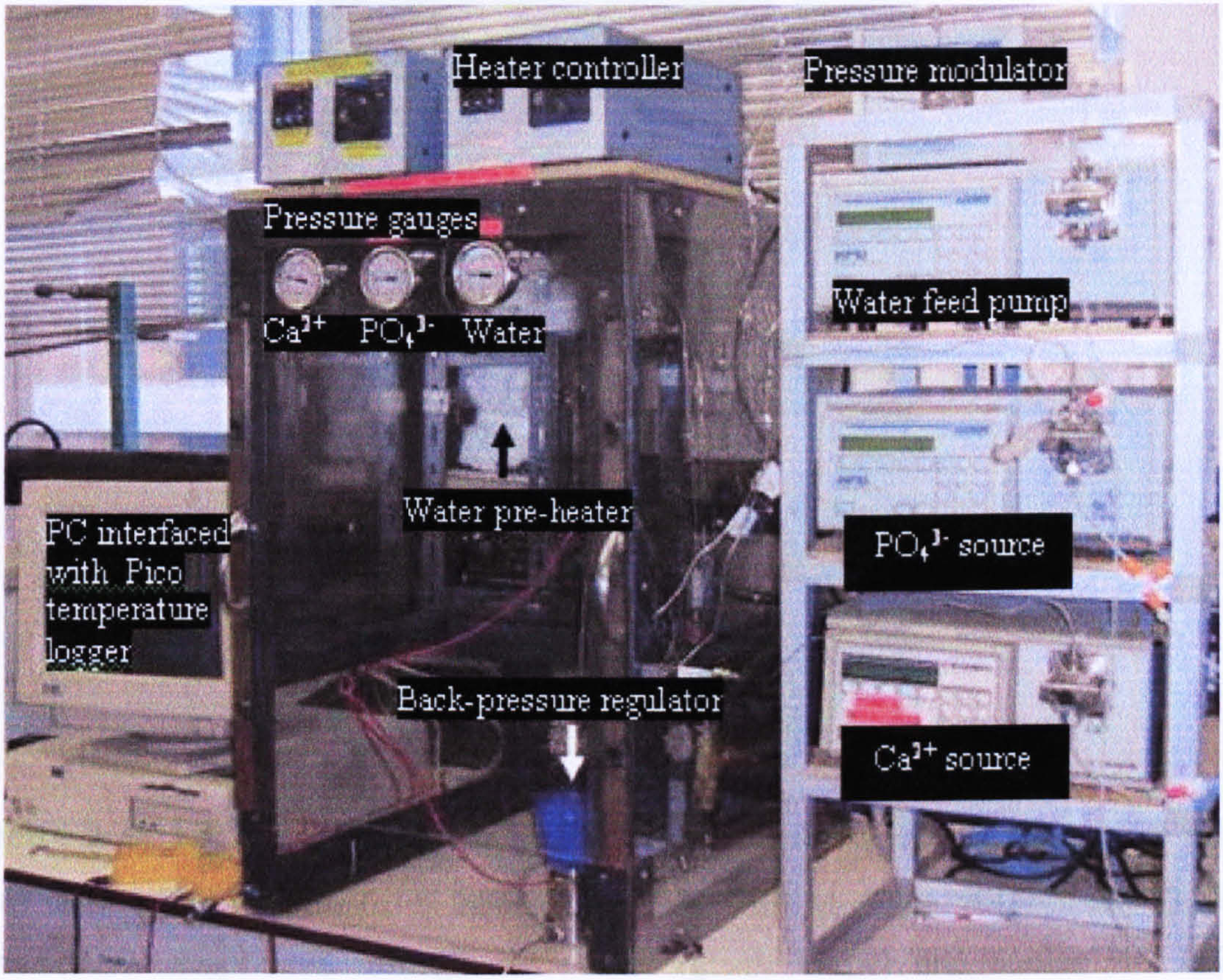

Figure 2-11 Continuous Hydrothermal Flow Synthesis System 2.

There were two main reasons for this change in cooler design. The cooler design shown in Figure 2-10 is complicated and over-engineered. Secondly, its usage resulted in constant blockages and contamination during subsequent runs. It is believed that this was due to particles settling (blocking) in the horizontal loops of the ¼” tubing around the inner core of the cooler. Therefore, the new design stemmed from the need to have a straight vertical drop for particles in suspension.

The ¼" 316SS Swagelok™ tubing carrying particle suspension from the mixing zone passes through a ¾" 316SS Swagelok™ tube connected to a continuous cooling water supply. The flow of the cooling water around the ¼" tubing was from bottom to up, ensuring that the outer tube of water was always full, which then provides cooling for the hot entry point. This arrangement is represented in Figure 2-13. As with CHFS system 1 all the parts were 316SS Swagelok™ fittings except ¾" Brass Swagelok™ T-piece used in the cooler assembly.

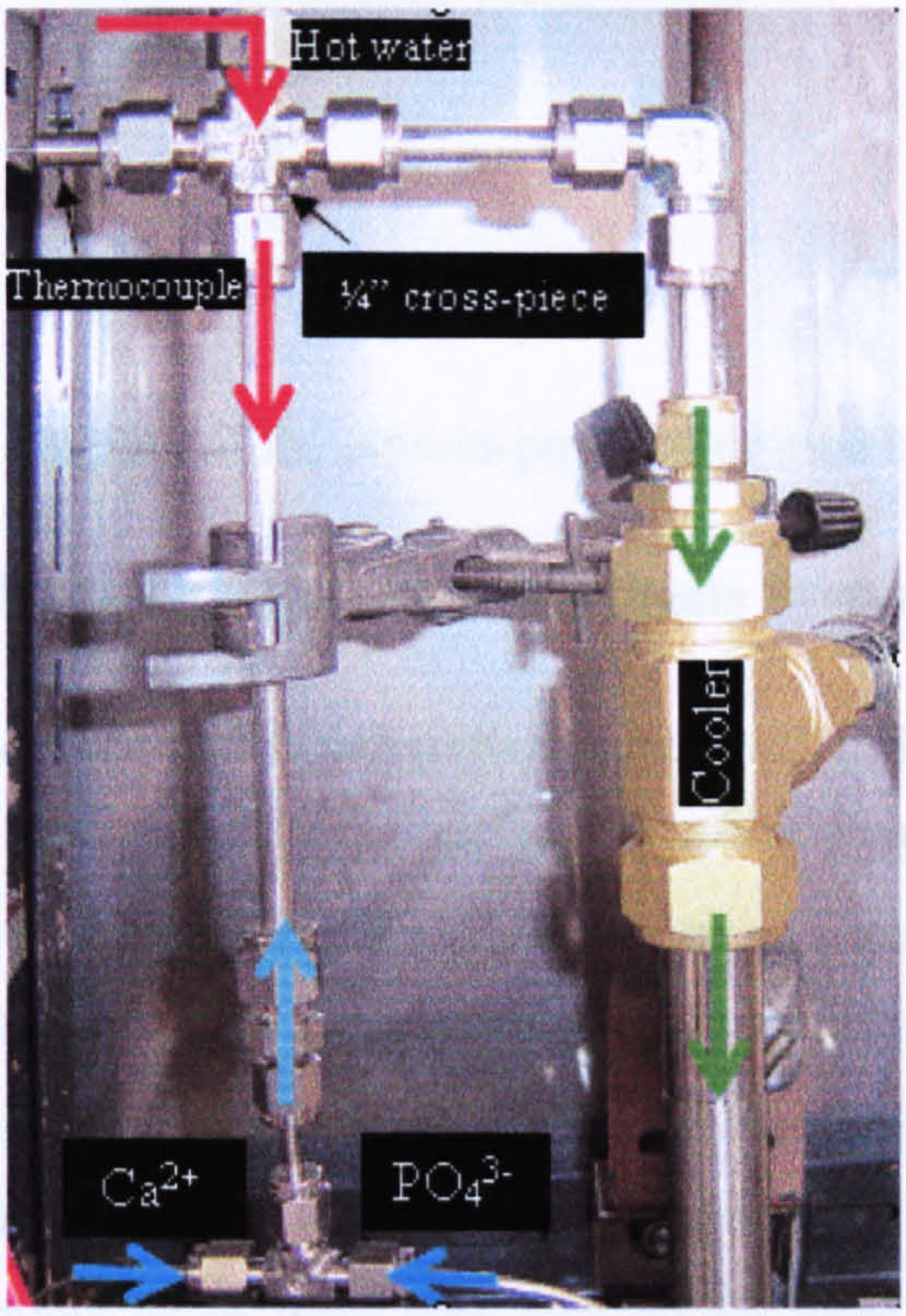

Figure 2-12 The ¼" 316SS Swagelok™ cross-piece, thermocouple connection point, flow direction of hot water (red arrows), flow direction of solutions (blue arrow), flow direction of suspension through the cooler (green arrow) and cooler ¾" 316SS Swagelok™ of the CHFS system 2.

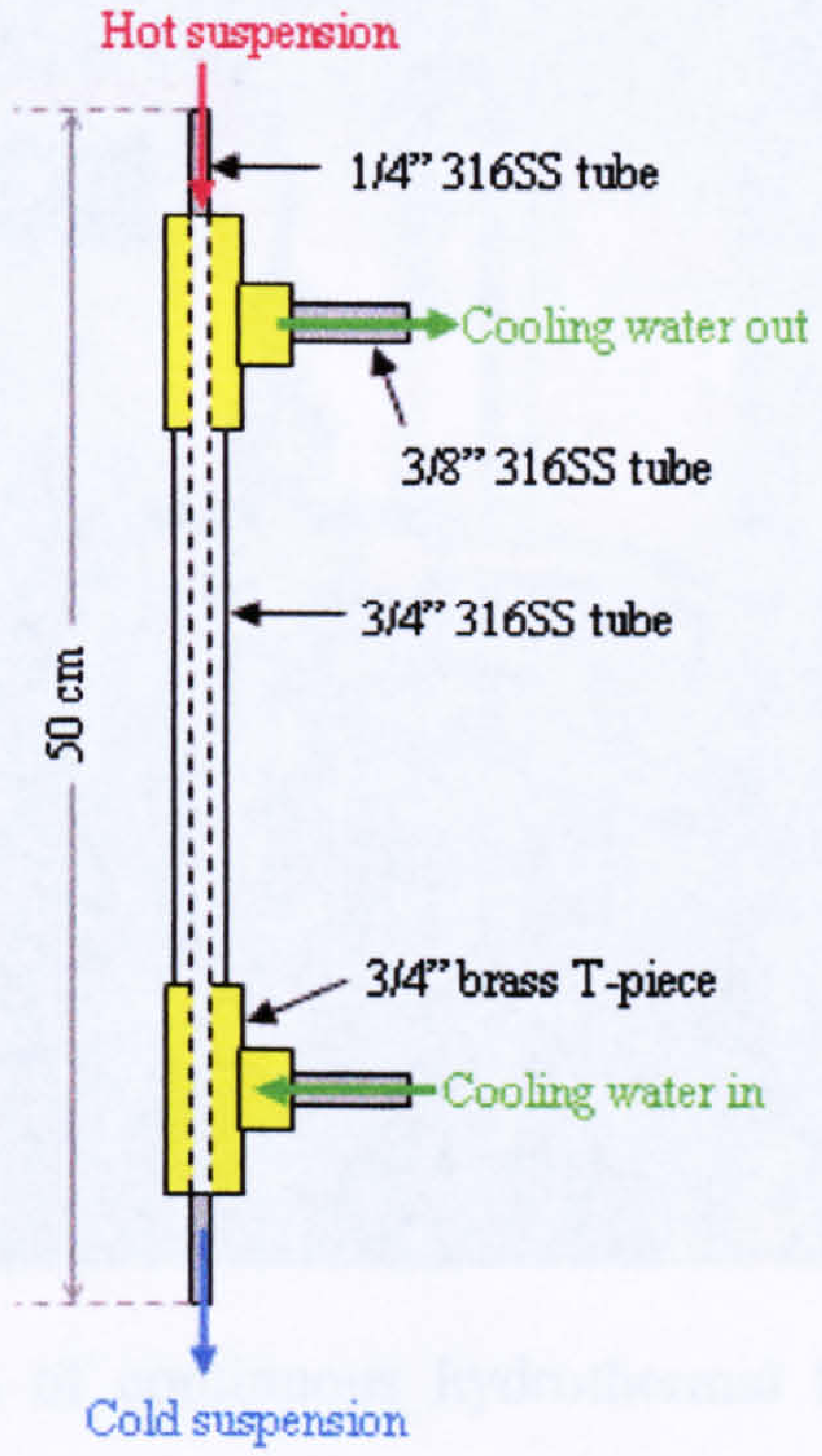

Figure 2-13 Schematic diagram of the pipe-in-pipe cooler used in CHFS system 2.

2.2.1.3 Continuous Hydrothermal Flow Synthesis System 3

The third continuous hydrothermal flow synthesis system (CHFS system 3) was built by A. A. Chaudhry and P. Boldrin of CMTG at Department of Materials, QMUL in 2006. The design of this system is very similar to CHFS systems 1 and 2. The cooler used in this system was much longer (*ca.* 1.0 m) as compared to that of system 2 (*ca.* 0.5 m). This was done to facilitate faster synthesis of particles using higher pump rates (up to combined rates of 50.0 mL min^{-1}) and higher temperatures (> 400 °C) by improving cooling. 25SC Gilson pump heads were used with all the three separate Gilson HPLC pumps. The mixing point was made using the larger 3/8" 316SS Swagelok™ parts in order to facilitate faster flow rates.

In order to maintain same temperature of the water pre-heater and the mixing point a Watlow band heater (2" diameter, 2" length, 200 W, 250 V) was introduced in the mixing zone of the system as shown in Figure 2-14. This band heater was controlled by a separate temperature controller (Eurotherm 3216e). It was hypothesised that this would result in higher yields as compared to previous systems. Technical drawings of the mixing point and its constituent pipe work are shown in Figure 2-15 and Figure 2-16. Steps of construction of the mixing point are explained in a standard operating procedure (SOP) attached as Appendix 'A'.

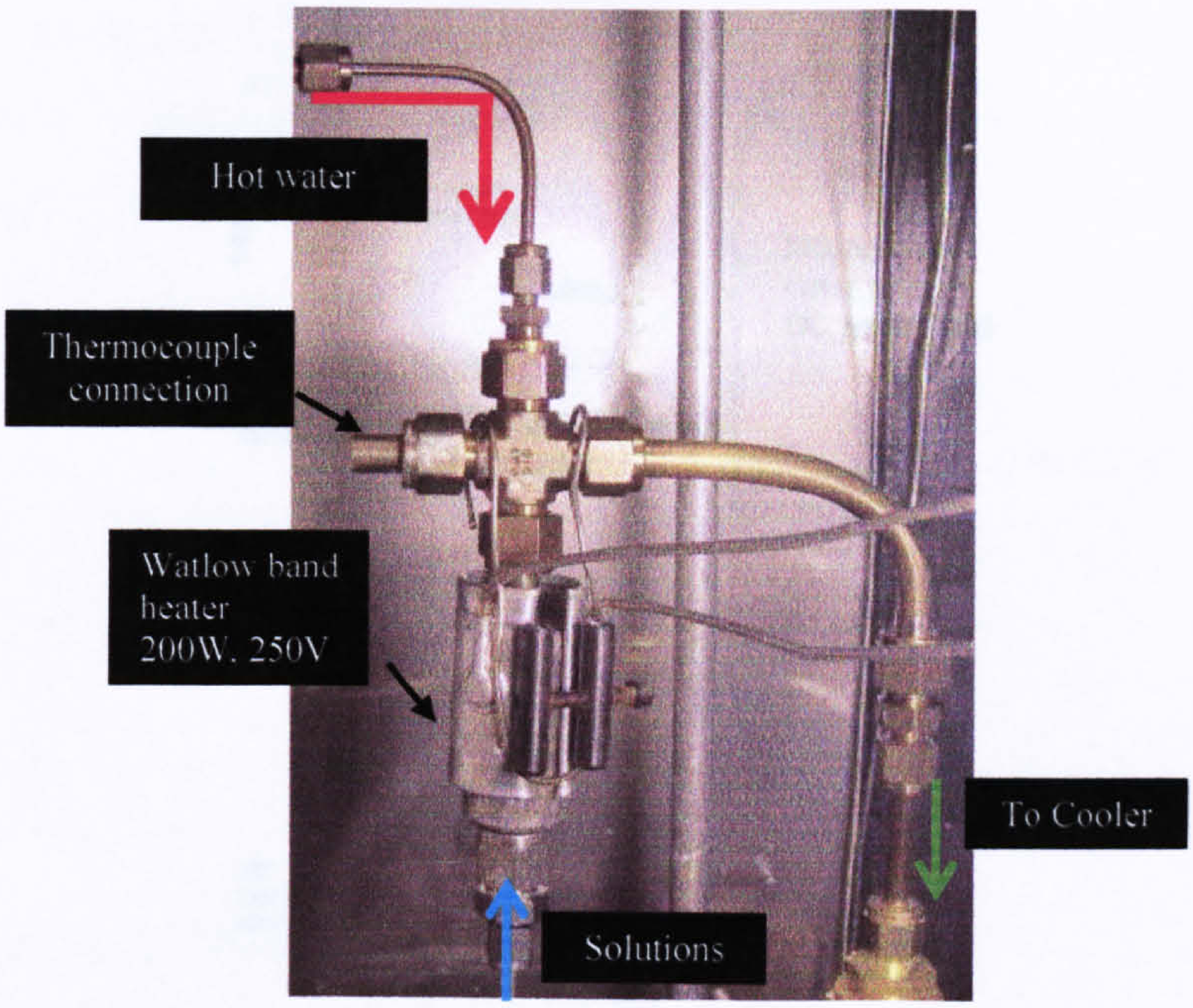

Figure 2-14 Mixing point of continuous hydrothermal flow system 3 showing the Watlow band heater.

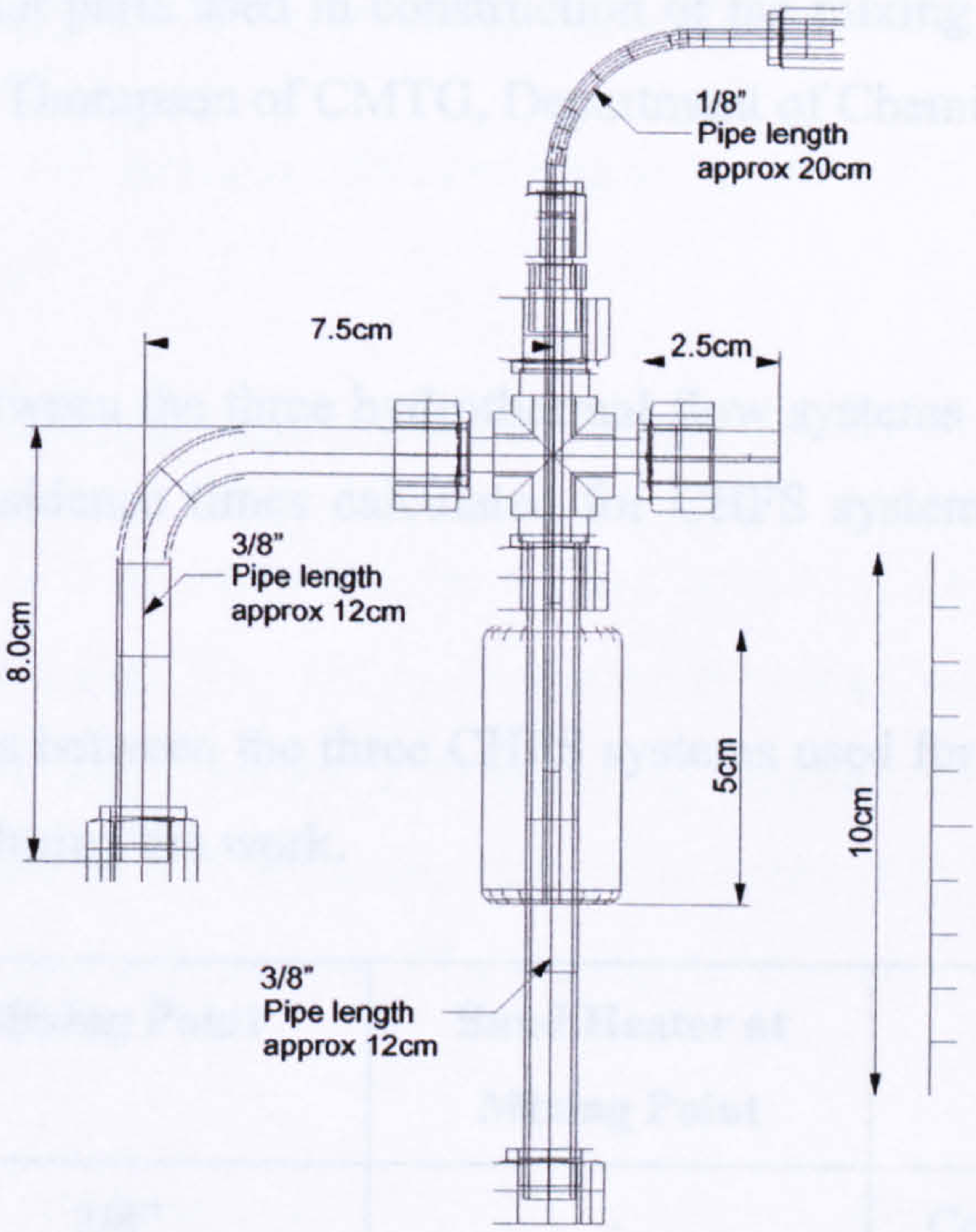

Figure 2-15 A technical drawing of the mixing point used in CHFS system 3 (prepared by K. Thompson of CMTG, Department of Chemistry, UCL) The SOP for construction of a mixing point for a CHFS system is attached as Appendix A.

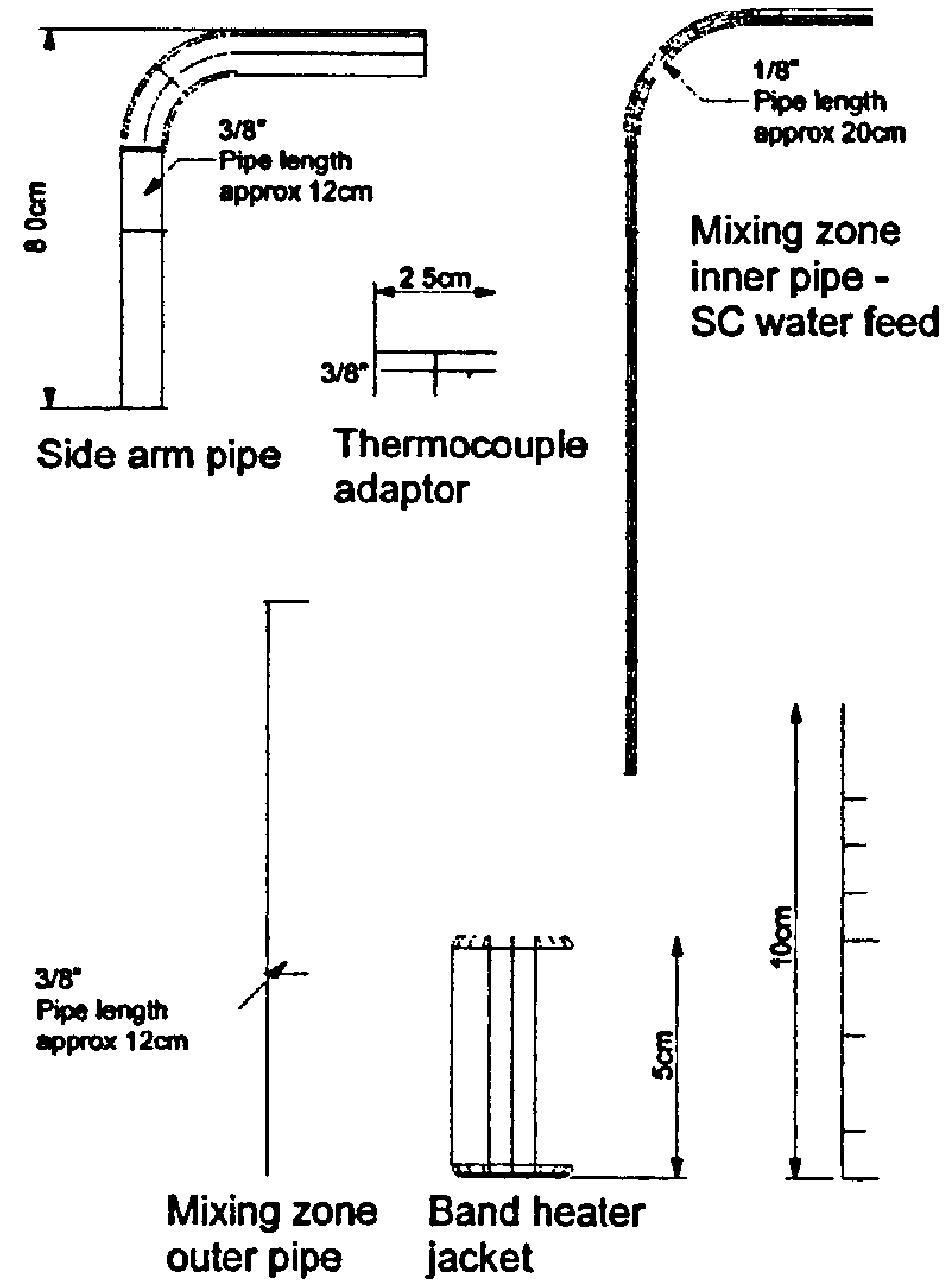

Figure 2-16 Individual parts used in construction of the mixing point shown in Figure 2-15 (prepared by K. Thompson of CMTG, Department of Chemistry, UCL).

2.2.1.4 Summary

Major differences between the three hydrothermal flow systems are summarised below in Table 2-1. The residence times calculated for CHFS system 3 are summarised in Table 2-2.

Table 2-1 Differences between the three CHFS systems used for the synthesis of nano-bioceramic powders during the work.

CHFS System	Mixing Point	Band Heater at Mixing Point	Cooler Design
1	3/8"	-	Concentric cylinders
2	1/4"	-	Pipe-in-pipe (0.5 m)
3	3/8"	Present	Pipe-in-pipe (1.0 m)

Table 2-2 Residence times calculated using a 3/8" cross-piece and tubing in CHFS system 3 [P1 = superheated water feed, P2 = calcium source feed, P3 = phosphate source feed].

Flow Rates (mL min^{-1})			Residence time (seconds)
P1	P2	P3	
10	5	5	9.9
20	10	10	4.9
25	12.5	12.5	3.9

2.2.2 Synthesis Methodology

In this section, exact amounts of chemicals used to make solutions, synthesis conditions for the CHFS systems (temperature, concentration, pH, flow rates), clean up and centrifugation parameters and freeze drying parameters are described.

2.2.2.1 Synthesis of Instant Hydroxyapatite and Effect of CHFS System Parameters

(a) Synthesis of Hydroxyapatite (Effect of Temperature)

9.86 g (41.75 mmoles) of calcium nitrate were added to 500 mL deionised water to result in 83.5 mM solution. The pH of this solution was adjusted to pH 11 using 1 mL of ammonium hydroxide solution. 3.30 g (25.00 mmoles) of diammonium hydrogen phosphate were added to 500 mL deionised water to result in a 50.0 mM solution. The pH of this solution was adjusted to pH 10 using 12 mL of neat ammonium hydroxide solution.

Experiments were conducted using CHFS system 1 described in section 2.2.1.1. Calcium nitrate and diammonium hydrogen phosphate solutions were pumped at 5.0 mL min^{-1} and deionised water was pumped through the heater at 10.0 mL min^{-1} (also known as superheated water feed). Hence a Ca:P molar ratio of *ca.* 1.67 was maintained. Samples were labelled according to the temperature of the superheated water used, thus, samples prepared at 200, 300 and 400 °C were labelled HA(200), HA(300) and HA(400), respectively. A fourth control experiment was conducted using a similar method, with the superheated water feed at 400 °C, (under acidic rather than basic conditions) and a Ca:P molar ratio of 1:1 [denoted as sample CDHA(400) where CD represents calcium deficiency]. 2.36 g (10.00 mmoles) of calcium nitrate [$Ca(NO_3)_2$] were dissolved in 200 mL deionised water to result in a 50.0 mM solution (pH 5.5). 1.32 g (10.00 mmoles) of diammonium hydrogen phosphate [$(NH_4)_2HPO_4$] were dissolved in 200 mL of deionised water to result in a 50.0 mM solution (pH 8.5). The pH of these solutions was not adjusted in order to maintain an acidic pH during reaction. All reactions were carried out under a pressure of 24 MPa.

After collection at the end of the BPR, the particles were centrifuged at 4500 rpm for 3 min in 50 mL Falcon centrifuge tubes (per 50 mL suspension). Then *ca.* 45 mL of clear liquid was removed and the centrifuge tubes were refilled with *ca.* 45 mL deionised water. The tubes were shaken vigorously in order to redisperse the precipitate and subsequently re-centrifuged at 4500 rpm for 3 min prior to freeze drying for 18 hours at 1 $\times 10^{-4}$ mbar. All samples were frozen using liquid N_2 prior to freeze drying.

(b) Synthesis of Hydroxyapatite (Effect of pH and Ca:P Molar ratio on Thermal stability)

Six separate reactions were carried out to study the effects of pH and Ca:P molar ratio on the end products. Ca:P molar ratios used in the feeds were either 1.0, 1.67 or 2.0. For each case, samples were synthesised under either acidic (pH 4.5) or basic (pH 9.5) conditions, respectively (pH measured from the suspension exiting the BPR).

1.18 g (5.00 mmoles), 1.97 g (8.40 mmoles) and 2.36 g (10.00 mmoles) of calcium nitrate were separately dissolved in 100 mL deionised water to result in three separate 100 mL solutions. All these solutions were duplicated to prepare another set of three identical solutions. The concentrations of these solutions were 50.0 mM, 83.5 mM and 100.0 mM and were intended to result in Ca:P molar ratios of 1.0, 1.67 and 2.0 respectively. The pH of all calcium nitrate solutions was 5.5. For synthesis under acidic conditions the solutions were used directly, whereas for synthesis under basic conditions, the pH was adjusted to pH 11 by adding 1 mL ammonium hydroxide solution to each solution.

0.66 g (5.00 mmoles) of diammonium hydrogen phosphate were dissolved in 100 mL deionised water to result in a 50.0 mM solution. In total six identical solutions were prepared. The pH of all diammonium hydrogen phosphate solutions was 8.5. For synthesis under acidic conditions solutions were used without pH adjustment and for synthesis under basic conditions, the pH was adjusted to pH 10 by adding 3 mL neat ammonium hydroxide solution to each solution.

The samples were labelled as 1-A, 1.67-A and 2-A for acidic and 1-B, 1.67-B and 2-B for basic conditions. The first number in the sample ID specifies the Ca:P molar ratio in solution and A and B stand for acidic (pH 4.5) or basic (pH 9.5) conditions, respectively. These pH values were measured from suspensions immediately after collection. Therefore, sample 1-A was synthesised at acidic pH (pH 4.5) with an intended Ca:P molar ratio of 1.0. Similarly, sample 1.67-A was synthesised at acidic pH (pH 4.5) with an intended Ca:P molar ratio of 1.67 and so on.

These reactions were carried out using CHFS system 3 as explained in section 2.2.1.3. Pump rates of 25.0, 12.5 and 12.5 mL min^{-1} were used for superheated water feed, calcium nitrate and diammonium hydrogen phosphate solutions, respectively. All reactions were carried out at 450 °C and 24 MPa.

(c) Synthesis of Hydroxyapatite (Effect of Different Flow rates and Temperature and Use of Heater at Mixing Point)

19.72 g (83.5 mmoles) of calcium nitrate were dissolved in 1000 mL deionised water to result in 83.5 mM stock solution. The pH of this solution was adjusted to pH 11 by adding 2.5 mL of neat ammonium hydroxide solution. 6.61 g (50.00 mmoles) of diammonium hydrogen phosphate were dissolved in 1000 mL of deionised water to result in a 50.0 mM stock solution. The pH of this solution was adjusted to pH 10 using 30 mL of neat ammonium hydroxide solution. In total, 10 different reactions were carried out using 100 mL of calcium nitrate and diammonium hydrogen phosphate solutions for each case (for reaction parameters see Table 2-3).

The flow rate regimes will be referred to as follows in this chapter; "*slow*" for 10.0, 5.0 and 5.0 mL min^{-1} (total 20.0 mL min^{-1}), "*medium*" for 20.0, 10.0 and 10.0 mL min^{-1} (total 40.0 mL min^{-1}) and "*fast*" for 25.0, 12.5 and 12.5 mL min^{-1} (total 50.0 mL min^{-1}). The three flow rates represent flow rates of superheated water, calcium nitrate and diammonium hydrogen phosphate solutions, respectively.

The temperature regime designation is explained as follows. The number represents the synthesis temperature and if this number is written with the letter "h", it indicates that a mixing zone heater regulated at the same temperature was also used. Therefore, temperature regime *400* represents a synthesis temperature of 400 °C without a mixing zone heater. Similarly, temperature regime *450h* represents a synthesis temperature of 450 °C with the mixing zone heater also set at 450 °C.

The slurries from both sets of reactions [sections 2.2.2.1 (b) and (c)] were collected from exit of the back-pressure regulator (at the end of the CHFS system) in 50 mL Falcon tubes. Between consecutive collections, the CHFS system was purged with clean water for 10 minutes. Each slurry was centrifuged at 4000 rpm for one minute (per 50 mL suspension), *ca.* 45 mL of liquid was removed from each sample and *ca.* 45 mL de-ionised water was added followed by vigorous shaking. Each sample was then re-centrifuged at 4500 rpm for 1 minute and *ca.* 45 mL liquid was removed for a final time to give concentrated slurry. The slurries were placed in a freezer at -5 °C for 60 minutes and then freeze-dried for 18 hours at 1 x10^{-4} mbar.

Table 2-3 Aims of the 10 reactions, corresponding flow rates and in-text designation codes, temperature regimes and in-text designation [P1 = superheated water flow rate, P2 = $Ca(NO_3)_2$ solution flow rate, P3 = $(NH4)_2HPO_4$].

Aim	**#**	**Flow rate**			**Designation**	**Temperature regimes (°C)**		**Designation**
		P1	**P2**	**P3**		**Heater**	**Mixing zone heater**	
Fixed flow rate, varying Temp	1	25.0	12.5	12.5	*fast*	400	0	*400*
	2	25.0	12.5	12.5		400	400	*400h*
	3	25.0	12.5	12.5		450	0	*450*
	4	25.0	12.5	12.5		450	450	*450h*
Temp. fixed at 400 °C, varying flow rates	5	10.0	5.0	5.0	*slow*	400	0	*400*
	6	20.0	10.0	10.0	*medium*	400	0	*400*
	7	25.0	12.5	12.5	*fast*	400	0	*400*
Temp. fixed at 450 °C, varying flow rates	8	10.0	5.0	5.0	*slow*	450	450	*450h*
	9	20.0	10.0	10.0	*medium*	450	450	*450h*
	10	25.0	12.5	12.5	*fast*	450	450	*450h*

2.2.2.2 Synthesis of Carbonate and Silicate Substituted Calcium Phosphates

(a) Synthesis of Carbonate Substituted Calcium Phosphates

39.44 g (167.00 mmoles) of calcium nitrate were dissolved in 2000 mL deionised water to result in 83.5 mM stock solution. The pH of this solution was adjusted to pH 11 by adding 5 mL neat ammonium hydroxide solution. All calculations were based on the formula $Ca_{10}(PO_4)_{6-x}(CO_3)_x(OH)_2$, wherein it was assumed that carbonate ions partially substitute phosphate ions in the hydroxyapatite lattice.

For a typical reagent solution, urea and diammonium hydrogen phosphate were accurately weighed and added to 300 mL deionised water so that the combined carbonate (CO_3^{2-}) and phosphate (PO_4^{3-}) ion concentration was 50.0 mM. The pH of this solution was adjusted to pH 10 by adding 9 mL of neat ammonium hydroxide solution. In all, five reactions were carried out for this study, the experimental details of which are shown in Table 2-4. The sample ID 7.5CO_3-HA represents a sample with 7.5 wt% expected carbonate content in HA. Similarly, sample ID 11.5CO_3-HA represents a sample with 11.5 wt% expected carbonate content and so on.

CHFS system 2 was used for these reactions with pump rates of 10.0, 5.0 and 5.0 mL min^{-1} for the superheated water feed, calcium nitrate and diammonium hydrogen phosphate/urea solutions, respectively. A Ca:[PO_4^{3-}+CO_3^{2-}] molar ratio of *ca.* 1.67 was hence maintained in all reagent solutions. All reactions were carried out using a superheated water feed at 400 °C and 24 MPa. All samples were centrifuged, washed and freeze-dried as explained earlier; see section 2.2.2.1 (a).

(b) Synthesis of Silicate Substituted Calcium Phosphates

For these reactions it was assumed that silicate ions partially substitute phosphate ions in HA lattice [$Ca_{10}(PO_4)_{6-x}(SiO_4)_x(OH)_{2-x}$]. In reactions for samples 1SiHA to 5SiHA (details in Table 2-5), the required amount of silicon acetate was dissolved in 100 mL of 83.5 mM calcium nitrate solution [1.97 g (8.40 mmoles) in 100 mL deionised water]. The sample ID 1SiHA represents a sample with 1.0 wt% expected silicon content and so on.

For samples 6SiHA to 10SiHA, the required amount of silicon acetate was dissolved in 100 mL of 41.8 mM calcium nitrate solution. 0.99 g (4.20 mmoles) of calcium nitrate were added to 100 mL deionised water for this solution. This was because higher concentrations of silicon acetate were not soluble in 83.5 mM calcium nitrate. For samples 1SiHA to 5SiHA, the concentration of diammonium hydrogen phosphate solutions was (50 - C) mM, where C is the concentration of silicon acetate (in mM). Similarly, the concentration of diammonium hydrogen phosphate solutions for samples 6SiHA to 10SiHA was (25 – concentration of silicon acetate) mM. All these details are summarised in Table 2-5. The pH of these 100 mL diammonium hydrogen phosphate solutions was adjusted to pH 10 by adding 3 mL of neat ammonium hydroxide solution.

Table 2-4 Sample IDs, expected wt% of carbonate, x values [according to $Ca_{10}(PO_4)_{6-x}(CO_3)_x(OH)_2$] and corresponding amounts of reagents used.

Sample ID	Carbonate Wt%	x	$(NH_4)_2HPO_4$ (300 mL deionised water)		$(NH_2)_2CO$ added to 300 mL $(NH_4)_2HPO_4$ solution	
			mmoles	Wt (g)	mmoles	Wt (g)
7.5CO_3-HA	7.5	1.2	12.00	1.59	3.00	0.18
11.5CO_3-HA	11.5	1.8	10.50	1.39	4.50	0.27
15.7CO_3-HA	15.7	2.4	9.00	1.19	6.00	0.36
20CO_3-HA	20.0	3.0	7.50	0.99	7.50	0.45
24.6CO_3-HA	24.6	3.6	6.00	0.79	9.00	0.54

CHFS system 3 was used for these reactions and pump rates of 10.0, 5.0 and 5.0 mL min^{-1} were used for superheated water feed, calcium nitrate/silicon acetate and diammonium hydrogen phosphate solutions, respectively. A Ca:[PO_4^{3-}+SiO_4^{4-}] molar ratio of *ca.* 1.67 was hence maintained in all reactions. All reactions were carried out using a superheated water feed at 400 °C and 24 MPa. All samples were centrifuged, washed and freeze-dried as explained earlier; see section 2.2.2.1 (a).

Table 2-5 Sample IDs, expected wt% of silicon, x values [according to $Ca_{10}(PO_4)_{6-x}(SiO_4)_x(OH)_{2-x}$] and corresponding amounts of reagents used. *These reactions were run at half concentration due to the inability to dissolve silicon acetate in 83.5 mM calcium nitrate solution.

Sample ID	Silicon Wt%	x	$(NH_4)_2HPO_4$ (in 100 mL deionised water)		$Si(OCOCH_3)_4$ (added to 100 mL $(NH_4)_2HPO_4$ solution)	
			mmoles	Wt (g)	mmoles	Wt (g)
1SiHA	1	0.4	4.70	0.62	0.30	0.08
2SiHA	2	0.7	4.40	0.58	0.60	0.15
3SiHA	3	1.0	4.10	0.55	0.90	0.23
4SiHA	4	1.4	3.90	0.51	1.10	0.30
5SiHA	5	1.7	3.60	0.47	1.40	0.37
6SiHA*	6	2.0	1.70	0.22	0.80	0.22
8SiHA*	8	2.6	1.40	0.19	1.10	0.29
10SiHA*	10	3.2	1.20	0.16	1.30	0.35

2.2.2.3 Synthesis of Magnesium and Zinc Substituted Calcium Phosphates

(a) Synthesis of Magnesium Substituted Calcium Phosphates

For these reactions it was assumed that magnesium ions partially substitute the calcium ions in HA. Hence all calculations were based on the formula for Mg-substituted HA, $Ca_{10-x}Mg_x(PO_4)_6(OH)_2$. For a typical reagent solution, magnesium nitrate and calcium nitrate were accurately weighed and added to 100 mL deionised water so that the total metal ion concentration was 83.5 mM (see Table 2-6).

13.21 g (100.00 mmoles) of diammonium hydrogen phosphate were dissolved in 2000 mL deionised water to result in a 50.0 mM stock solution. The pH of this solution was adjusted to pH 10 by adding 60 mL of neat ammonium hydroxide solution. Sample ID 0.5Mg-CaP represents a sample with 0.5 wt% magnesium in the solution based on the aforementioned formula. Similarly 1Mg-CaP represents a sample with 1.0 wt% magnesium and so on.

Table 2-6 Sample IDs, expected wt% of magnesium, x values [according to $Ca_{10}Mg_{10-x}(PO_4)_6(OH)_2$] and corresponding amounts of reagents used.

Sample ID	Mg Wt%	x	$Ca(NO_3)_2.4H_2O$ (in 100 mL deionised water)		$Mg(NO_3)_2.6H_2O$ (added to 100 mL $Ca(NO_3)_2$ solution)	
			mmoles	Wt (g)	mmoles	Wt (g)
0.5Mg-CaP	0.5	0.2	8.20	1.93	0.20	0.04
1Mg-CaP	1	0.4	8.00	1.89	0.40	0.09
1.5Mg-CaP	1.5	0.6	7.80	1.85	0.50	0.13
2Mg-CaP	2	0.8	7.70	1.81	0.70	0.18
4Mg-CaP	4	1.6	7.00	1.65	1.40	0.35
6Mg-CaP	6	2.4	6.40	1.50	2.00	0.51
8Mg-CaP	8	3.1	5.70	1.35	2.60	0.67
10Mg-CaP	10	3.9	5.10	1.21	3.20	0.83
12Mg-CaP	12	4.6	4.50	1.07	3.90	0.99
14Mg-CaP	14	5.3	3.90	0.93	4.40	1.14
MgP	28.7	10	0	0	8.4	2.14

CHFS system 3 was used to carry out these reactions and pump rates of 20.0, 10.0 and 10.0 mL min^{-1} were used for superheated water feed, calcium/magnesium nitrate and diammonium hydrogen phosphate solutions, respectively. A (Ca + Mg):P molar ratio of *ca.* 1.67 was hence maintained. All reactions were carried out using a superheated water feed at 400 °C and 24 MPa (mixing zone heater was also set to 450 °C). All samples were centrifuged, washed and freeze-dried as explained earlier; see section 2.2.2.1 (c).

(b) Synthesis of Zinc Substituted Calcium Phosphates

For these reactions it was assumed that zinc ions partially substitute calcium ions in HA according to the following formula; $Ca_{10-x}Zn_x(PO_4)_6(OH)_2$. For a typical reagent solution in the reactor, zinc nitrate and calcium nitrate were accurately weighed and added to 100 mL deionised water so that the total metal ion concentration was 83.5 mM (see Table 2-7).

Table 2-7 Sample IDs, expected wt% of zinc, x values [according to $Ca_{10-x}Zn_x(PO_4)_6(OH)_2$] and corresponding amounts of reagents used.

Sample ID	Zn Wt%	x	$Ca(NO_3)_2.4H_2O$ (in 100 mL deionised water)		$Zn(NO_3)_2.6H_2O$ (added to 100 mL $Ca(NO_3)_2$ solution)	
			mmoles	**Wt (g)**	**mmoles**	**Wt (g)**
1.3Zn-CaP	1.3	0.2	8.20	1.93	0.20	0.05
5.1Zn-CaP	5.1	0.8	7.70	1.81	0.70	0.20
10Zn-CaP	10.0	1.6	7.00	1.66	1.30	0.40
14.7Zn-CaP	14.7	2.4	6.40	1.50	2.00	0.60
19.3Zn-CaP	19.3	3.2	5.70	1.34	2.70	0.80
23.7Zn-CaP	23.7	4.0	5.00	1.18	3.30	0.99
28Zn-CaP	28	4.8	4.40	1.03	4.00	1.19
32Zn-CaP	32	5.6	3.70	0.87	4.70	1.39

6.61 g (50.00 mmoles) of diammonium hydrogen phosphate were dissolved in 1000 mL deionised water to result in a 50.0 mM stock solution. The pH of this solution was adjusted to pH 10 by adding 30 mL of neat ammonium hydroxide solution. Sample ID 1.3Zn-CaP represents a sample with expected 1.3 wt% zinc based on the aforementioned formula. Similarly 5.1Zn-CaP represents a sample with expected 5.1 wt% zinc and so on.

CHFS system 3 was used for syntheses and pump rates of 25.0, 12.5 and 12.5 mL min^{-1} were used for superheated water feed, calcium/zinc nitrate and diammonium hydrogen phosphate solutions, respectively. A (Ca + Zn):P molar ratio of *ca.* 1.67 was hence maintained in all the reactions. All reactions were carried out using a superheated water feed at 450 °C and 24 MPa (mixing zone heater was also set to 450 °C). All samples were centrifuged, washed and freeze-dried as explained earlier; see section 2.2.2.1 (c).

2.2.2.4 Synthesis of Hydroxyapatite, Calcium Doped Zirconia-Hydroxyapatite (CDZ-HA) Mixtures and Ion-Substituted Calcium Phosphate Powders for Spark Plasma Sintering

(a) Synthesis of Hydroxyapatite

HA for spark plasma sintering was synthesised using two different Ca:P molar ratios in solution (1.67 and 2.0).

(i) Ca:P molar ratio of 1.67

19.72 g (83.50 mmoles) of calcium nitrate were dissolved in 1000 mL deionised water to result in a 83.5 mM concentration. The pH of this solution was adjusted to pH 11 using 2.5 mL of neat ammonium hydroxide solution. 6.61 g (50.00 mmoles) of diammonium hydrogen phosphate were dissolved in 1000 mL deionised water to result in 50.0 mM concentration. The pH of this solution was adjusted to pH 10 by adding 30 mL of neat ammonium hydroxide solution. This sample was labelled *ℓ*-HA(450)* where *ℓ* represents the 1.67 (low) ratio, 450 °C is the synthesis temperature and the * denotes the use of a band heater.

(ii) Ca:P molar ratio of 2.0

23.62 g (100.00 mmoles) of calcium nitrate were dissolved in 1000 mL deionised water to result in a 100.0 mM concentration. The pH of this solution was adjusted to pH 11 using 2.5 mL of neat ammonium hydroxide solution. 6.61 g (50.00 mmoles) of diammonium hydrogen phosphate were dissolved in 1000 mL deionised water to result in a 50.0 mM concentration. The pH of this solution was adjusted to pH 10 by adding 30 mL of neat ammonium hydroxide solution. This sample was labelled *m*-HA(450)* where *m* represents the 2.0 (medium) ratio, 450 °C is the synthesis temperature and the * denotes the use of a band heater.

(b) Synthesis of CDZ-HA mixtures

CDZ-HA mixtures were synthesised using two different Ca:P molar ratios in solution (1.67 and 2.5). In total, seven reactions were carried out for this study.

(i) Ca:P molar ratio of 1.67

Two identical solutions of calcium nitrate were prepared by adding 19.72 g (83.50 mmole) in 1000 mL deionised water to result in 83.5 mM concentration. 6.04 g (26.00 mmole) of zirconyl nitrate were added to the first 1000 mL of 83.5 mM calcium nitrate solution (pH 2). Assuming 100% yields of HA and ZrO_2 this composition will yield 25 wt% ZrO_2 in HA (theoretically calculated). 18.12 g (78.40 mmoles) of zirconyl nitrate were added to the second 1000 mL of 83.5 mM calcium nitrate solution (pH 2). Assuming 100% yields this composition will yield 50 wt% ZrO_2 in HA (theoretically calculated). 13.20 g (100.00 mmole) of diammonium hydrogen phosphate were dissolved in 2000 mL deionised water to prepare a stock solution with 50.0 mM concentration. These samples are labelled as L-25 and L-50 (where L represents a lower Ca:P molar ratio of 1.67 and the number represents the theoretically calculated weight percentage of zirconia in the mixture).

(ii) Ca:P molar ratio of 2.5

Four identical solutions of calcium nitrate were prepared by adding 29.52 g (125.00 mmole) in 1000 mL deionised water to result in a 125.0 mM concentration (pH 2). 0.95 g (4.00 mmole), 2.01 g (9.00 mmole), 6.04 g (26.00 mmole) and 18.13 g (78.00 mmole) of zirconyl nitrate were added to each of these four calcium nitrate solutions separately (pH 2 for all four solutions). These corresponded to expected 5 wt%, 10 wt%, 25 wt% and 75 wt% ZrO_2 in HA, respectively (amounts were theoretically calculated).

26.42 g (200.00 mmole) of diammonium hydrogen phosphate were added to 4000 mL of deionised water to result in a stock solution of 50.0 mM concentration. The pH of this solution was adjusted to pH 10 by adding 120 mL of neat ammonium hydroxide solution. These samples are labelled as H-5, H-10, H-25 and H-50 (where H represents a higher Ca:P molar ratio of 2.5 and the number represents the theoretically calculated weight percentage of zirconia in the mixture).

Another sample was prepared by dissolving 16.53 g (70.00 mmole) of calcium nitrate and 30.06 g (130.00 mmole) of zirconyl nitrate in 500 mL deionised water to result in an overall 400.0 mM concentration. 1000 mM KOH solution (pH 14) was prepared by dissolving 23.06 g (411.00 mmole) in 1000 mL deionised water. This sample is labelled as H-100 (H in this case represents excess calcium).

(c) Synthesis of Ion-Substituted Calcium Phosphate Powders

In total eight reactions were carried out for this study which included six ion-substituted and two HA samples (with 1.67 and 2.0 in-solution Ca:P molar ratio). The samples are labelled as 7.5CO_3-HA$^{\phi}$ [solution preparation explained in section 2.2.2.2 (a)], 5Si-HA$^{\phi}$ [see section 2.2.2.2 (b)], 0.5Mg-CaP$^{\phi}$, 1.5Mg-CaP$^{\phi}$, 6Mg-CaP$^{\phi}$ [see 2.2.2.3 (a)] and 1.3Zn-CaP$^{\phi}$ [see section 2.2.2.3 (b)]. The two HA samples were prepared as described earlier in section 0 (a). The reagent concentrations and method of solution preparation was identical to that for samples with identical sample IDs. However, in this case, the $^{\phi}$ suffix represents different CHFS parameters (faster flow rates and use of a mixing zone heater).

All these samples [in section 2.2.2.4 (a) to (c)] were synthesised using flow rates of 25.0, 12.5 and 12.5 mL min^{-1} for superheated water feed, calcium nitrate (mixed with corresponding substituting ion source or zirconyl nitrate) and diammonium hydrogen phosphate (mixed with corresponding substituting ion source) solutions, respectively. For sample H-100, the third flow rate of 12.5 mL min^{-1} represents the pumping rate of KOH solution. The synthesis temperature was set at 450 °C while the small 200 W band heater in the mixing zone was also adjusted to 450 °C. All samples were centrifuged, washed and freeze-dried as explained earlier; see section 2.2.2.1(c). However, sample *m*-HA(450)* [mentioned in 2.2.2.4 (a)] required centrifugation at 5000 rpm for 20 minutes.

The sintering parameters for spark plasma sintering for all these nano-bioceramics are discussed in section 6.3 of Chapter 6.

2.3 Characterisation and Sintering

In this section, techniques used to characterise as-crystallised powders from the CHFS systems and sintered disks and are explained. Equipment and methodology for Spark Plasma Sintering (SPS) is also explained.

2.3.1 Centrifugation

A Sigma 4K15 Centrifuge with a rotor housing four buckets, having a capacity of seven 50 mL Falcon tubes each, was used to centrifuge the suspensions after collection from CHFS systems.

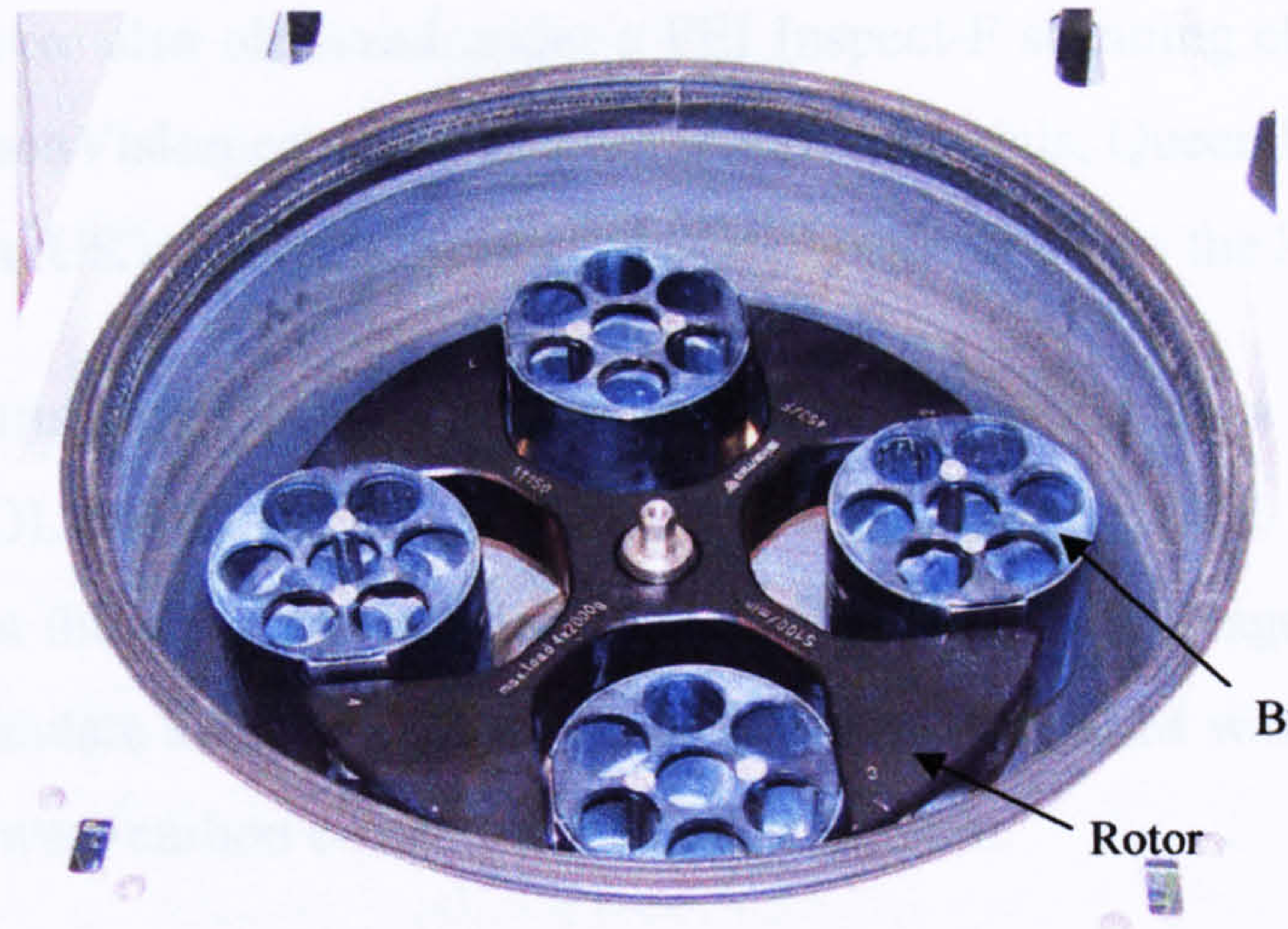

Figure 2-17 Close up inside the centrifuge showing the rotor with a capacity of four buckets.

2.3.2 Freeze Drying

After centrifugation all samples were freeze-dried using a Virtis Advantage Freeze Dryer, Model 2.0 ES, supplied by BioPharma. Samples were frozen prior to freeze drying. With exception of samples mentioned in section 2.2.2.1 (a) which were frozen by adding liquid nitrogen to the centrifuge tubes, all other samples in this thesis were frozen by placing them in a freezer at -5 °C for at least 1 hour prior to freeze drying. Freeze drying was carried out for 18 hours under a *ca.* 1 x 10^{-4} mbar vacuum.

2.3.3 Microscopy

2.3.3.1 Optical Microscopy

An Olympus BX-60 Optical Microscope located at the NanoVision Centre of Department of Materials at Queen Mary University of London was used to capture images of indents on sintered samples. Olympus Imaging software was used to capture the images in JPEG format on a PC and to measure the indent size.

2.3.3.2 Scanning Electron Microscopy

A JEOL JSM-6300F scanning field emission electron microscope located at Department of Materials of Queen Mary University of London (London, UK) was used to analyse the microstructure of fractured surfaces of sintered disks. Disks were gold coated prior to use in the FESEM.

Sintered disks were also observed under a FEI Inspect-F scanning electron microscope located at the NanoVision centre of Department of Materials, Queen Mary University of London (London, UK). Samples were gold coated prior to use in the SEM.

An Oxford Instruments Inca 400 EDS detector connected to a scanning electron microscope (JEOL 5410 LZSEM) at Eastman Dental Institute, UCL (London, UK) was used to carry out the elemental analysis for all the samples. Averages of 10 area scans were used to calculate average elemental composition. The SEM was operated at 25 kV and all samples were carbon coated prior to measurement.

2.3.3.3 Transmission Electron Microscopy

A Jeol 2010 Transmission Electron Microscope (TEM) located at Department of Materials of Queen Mary University of London (London, UK) was used for generating images of particles. A 200 kV accelerating voltage was used. Powdered samples were suspended in ethanol and ultrasonicated for two minutes to yield a very dilute suspension. 3 mm diameter copper grids (procured from Agar Scientific) were dipped in the suspension and were extracted and dried prior to use in a single tilt holder of the TEM. Image Tool UTHSCSA version 3.0 software was used for estimating particle size. Furthermore, the EDS detector attached to this TEM was also used for elemental analysis.

The high resolution TEM image of sample HA(400) in Chapter 3 was captured on an FEI Tecnai F20 Supertwin at Johnson Matthey (London, UK). A JEOL 4000HR TEM located at Department of Materials, University of Oxford (Oxford, UK) was used for generating images on selected samples mentioned in Chapter 5. All HR-TEM images were analysed using the Digital Micrograph software developed by Gatan.

2.3.4 X-ray Diffraction (XRD)

2.3.4.1 Siemens D5000 X-ray Diffractometer

Purity and phase composition of the samples were determined by powder x-ray diffraction (XRD) using a Siemens/Bruker D5000 Diffractometer with monochromatic Cu-K_α radiation ($\lambda = 0.15418$ nm). This diffractometer is located at the Department of Materials, Queen Mary University of London. The generator power settings were 40 mA and 40 kV. Short scans were collected over the 2θ range 5-70° with a step size of 0.02° and a count time of 1 second. Long scans were collected over the 2θ range 5-110°

with a step size of 0.02° and a count time of 10 seconds. Phases were identified using the Joint Committee on Powder Diffraction Standards (JCPDS) database, in the XRD evaluation program Diffracplus EVA^{TM} Version 5.0 (Bruker-AXS, Germany).

2.3.4.2 X-pert Pro PW3064/60 Diffractometer

An X-pert Pro PW3064/60 diffractometer with a high-throughput stage was also used for collection of x-ray diffraction patterns. This diffractometer is located the Department of Materials of Queen Mary University of London and the samples were run by Dr. R. M. Wilson. Continuous scans were collected over the 2θ range 5-120° with a step size of 0.033423° for 200 s per step.

2.3.4.3 Stoe StadiP Transmission Capillary Powder Diffractometer

Rietveld refinement was carried out for representative magnesium substituted samples. Data was collected on a Stoe StadiP transmission capillary powder diffractometer situated in the Department of Chemistry of UCL. This work was carried out as collaboration between CMTG, UCL and Dr. J. Cockcroft and Dr. M. Vickers. The equipment was operated by Dr. M. Vickers. The X-ray tube was run at 40 mA and 30 kV onto a copper target monochromated by a Ge 111 crystal to select the Kα1 wavelength at 1.54056 Å. Diffracted X-rays were collected with a Linear Position Sensitive Detector covering a nominal 6° 2θ. Samples were prepared by sieving at 75 microns and mounting in a 0.3 mm borosilicate glass capillary. The detector was scanned from 2 to 95 ° 2θ stepping at 0.1° 2θ with a count time of 30 seconds per step and repeated 8 times. The 8 scans were compared and checked for consistency and then added together to created a summed data set. The long scan time was necessary to provide statistically viable data from weaker peaks.

Analysis of the data was done with the PROFIL Rietveld refinement program (Cockcroft 2005). The unit cell of the hydroxyapatite model was being studied, not the atomic positions or occupancies, so these were fixed from the published models. If present, the Whitlockite model was included and its unit cell refined to improve the Rwp fit values. The models used for the refinement were taken from the ICSD (International Centre for Diffraction Studies) with HA from Sudarsanan and Young and co-workers and Whitlockite from Schroeder et. al (Schroeder et al. 1977; Sudarsanan & Young 1982).

2.3.4.4 Brüker D8 Advance Diffractometer

A Brüker D8 Advance diffractometer with a Ni filtered Cu-Kα radiation and a Lynx Eye detector was used to study in-situ phase behavior of HA-ZrO_2 samples as a function of temperature. This work was carried out at Eastman Dental Institute (EDI), UCL, London and the equipment was operated by Prof. J. Knowles. To perform the high temperature experiments, an Anton Paar HTK16 heating stage with an Anton Paar TCU 2000 control unit was used, integrated with the Brüker control software. The as-precipitated powders were placed on a platinum heater stage. Heating temperature was observed using a R-type thermocouple welded to the bottom of the platinum heater strip (temperature accuracy ± 1K). After sealing, the platinum heater enclosure was purged with air at a 2 mL min^{-1} flow rate. The sample was heated at 10 °C min^{-1} up to 1200 °C. Data was collected over 2θ ranges of 21 - 36° and 48-52° with a step size of 0.02 and a count time of 1 s after 50° intervals. During collection, the sample temperature was kept constant.

The scan parameters and types of diffractometers used for all the samples in this thesis are summarised in Table 2-8. The crystallite size was calculated using the Scherrer equation shown below.

$$t = \frac{0.9\lambda}{B\cos\theta} \qquad \textbf{Eq. 2-1}$$

Where t = crystallite size in nm, λ = wavelength of X-rays, B = full-width at half-maximum in radians, θ = angle corresponding to the peak.

2.3.5 Brunauer, Emmet, Teller Surface Area Analysis

Brunauer, Emmet, Teller (BET) surface area measurements (using N_2 gas adsorption method), were performed on a Micromeritics Gemini analyser located at the Department of Materials of Queen Mary University of London. BET tubes were washed and dried overnight in an oven at 100 °C. The tubes were allowed to equilibrate with the system for an hour at 80 °C while being purged with nitrogen. Then the powders were weighed, and degassed at 80 °C for 2 hours. After the drying they were weighed again and then analysed.

Table 2-8 Scan parameters [2θ (°) range, step size (°) and count time per step (seconds)] and types of diffractometers used for all samples.

Sample Series [corresponding section]	**Scan Parameters**			**Diffractometer**
	2θ range (°)	**Step size (°)**	**Count time (seconds)**	
Instant Hydroxyapatite [2.2.2.1 (a)]	5 – 110	0.02	1.0	Siemens D5000
CO_3^{2-} substituted calcium phosphates [2.2.2.2 (a)]				
SiO_4^{4-} substituted calcium phosphates [2.2.2.2 (b)]	5 – 120	0.033423	200	X-pert Pro PW3064/60
Mg^{2+} substituted calcium phosphates [2.2.2.3 (a)]	5 – 70	0.02	10	Siemens D5000
XRD patterns for Rietveld Refinement on selected compositions [2.2.2.3 (b)]	2 – 95	0.1	30	Stoe StadiP Transmission Capillary
Zn^{2+} substituted calcium phosphates [2.2.2.3 (b)]	5 – 120	0.033423	200	X-pert Pro PW3064/60
HA and ZrO_2-HA powders for SPS [2.2.2.4]				
VT-XRD on selected ZrO_2-HA compositions	21 – 36	0.02	1.0	Brüker D8 Advance
Ion-substituted calcium phosphate powders for SPS [2.2.2.4 (c)]	5 – 120	0.033423	200	X-pert Pro PW3064/60
All SPS Discs	5 – 120	0.033423	200	X-pert Pro PW3064/60

2.3.6 Fourier Transform Infrared and Raman Spectroscopy

Raman and Fourier Transform Infra Red (FTIR) spectroscopy were carried out in order to detect phases and determine phase composition (and hence supplement XRD data).

2.3.6.1 Raman Spectroscopy

A Nicolet Almega Dispersive Raman Spectrometer (785 nm laser) was used. The data was collected in different wavenumber ranges for different series of samples and the number and time of scans were optimised for reliable data (minimum fluorescence) in shortest period of time without any compromise in data quality (details in Table 2-9).

Table 2-9 Sample series and corresponding sections of the chapter, type of sample compartment, number of scans and average scan time.

Sample Series [corresponding section]	**Sample Compartment**		**No. of scans**	**Scan time (seconds)**
	XYZ-stage	**Microscope**		
Instant Hydroxyapatite [2.2.2.1 (a)]	√	-	128	10
CO_3^{2-} substituted calcium phosphates [2.2.2.2 (a)]	√	-	20	2
SiO_4^{4-} substituted calcium phosphates [2.2.2.2 (b)]	√	-	20	2
Mg^{2+} substituted calcium phosphates [2.2.2.3 (a)]	√	-	20	2
Zn^{2+} substituted calcium phosphates [2.2.2.3 (b)]	-	√	20	2
ZrO_2-HA [2.2.2.4 (b)]	-	√	64	1
Sintered Discs	-	√	64	1

Figures 2-18 and 2-19 show the XYZ stage and microscope compartment of the Nicolet Almega Dispersive Raman Spectrometer. The XYZ stage required a sample holder. These sample holders were made of either brass or aluminium and powered samples were packed in a cavity on their surface. The microscope compartment was easier to use, because samples (both powdered and bulk) were placed on a quartz slide under the microscope.

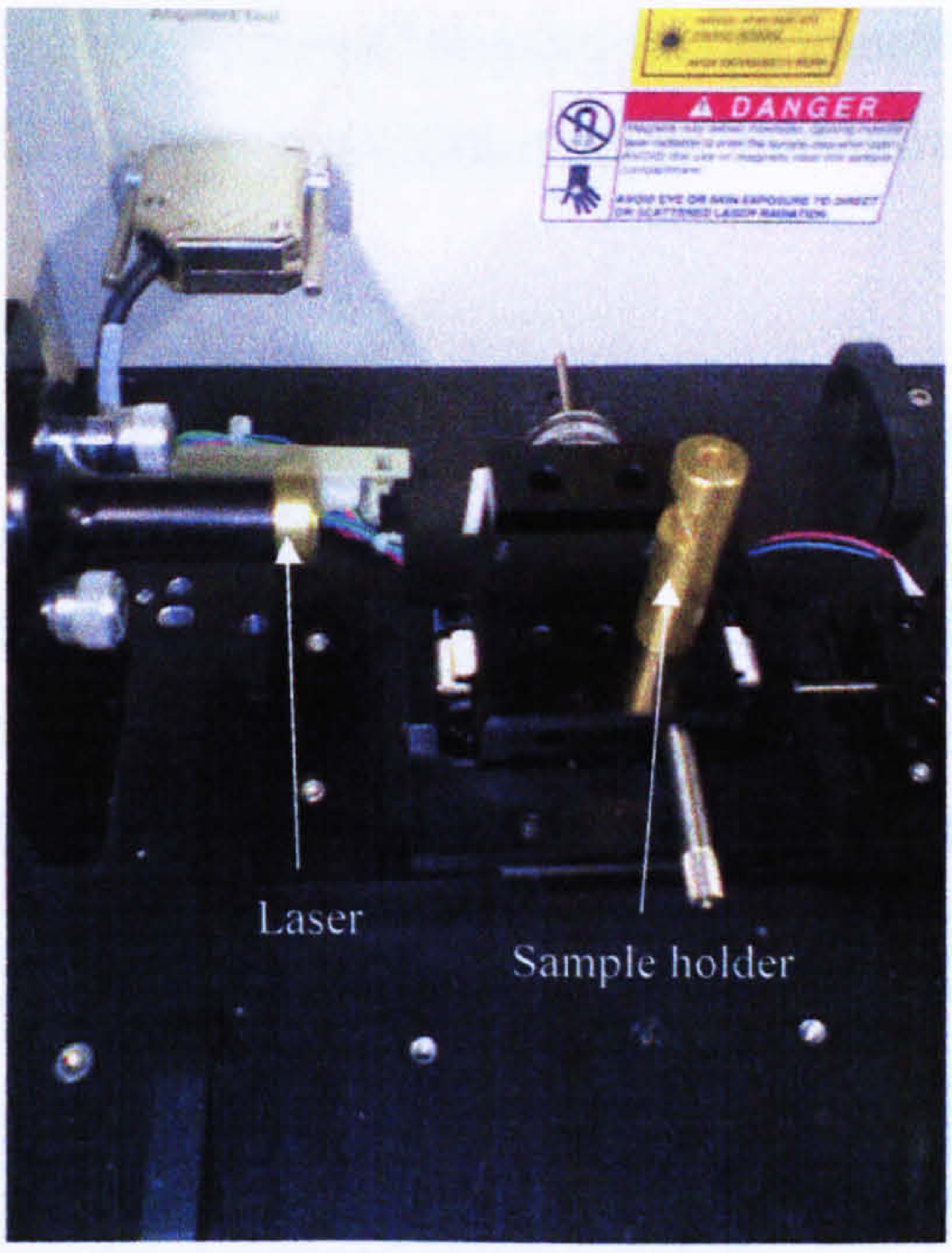

Figure 2-18 The XYZ stage of the Nicolet Almega Dispersive Raman Spectrometer.

Figure 2-19 The microscope compartment of Nicolet Almega Dispersive Raman Spectrometer.

2.3.6.2 Fourier Transform Infra Red (FTIR) Spectroscopy

Fourier-Transform Infrared (FTIR) spectra of the samples were collected using a Nicolet FTIR 800 spectrometer, fitted with a helium purged photoacoustic sampler

(MTec PAS cell) or a diffuse reflectance infra-red fourier transform sampling (DRIFTS) cell, controlled by a 680D Spectral Workstation (in the mid-infrared region).

(a) PAS Cell

Using the PAS cell spectra were obtained in the wave number range 4000 - 400 cm^{-1}, at 8 cm^{-1} spectral resolution, averaging 256 scans. In order to get rid of atmospheric CO_2, the sample chamber was purged with pre-dried helium gas (passed over magnesium perchlorate). The background spectrum was collected using carbon black and all spectra were adjusted accordingly (see Table 2-10). Figure 2-20 shows the PAS cell.

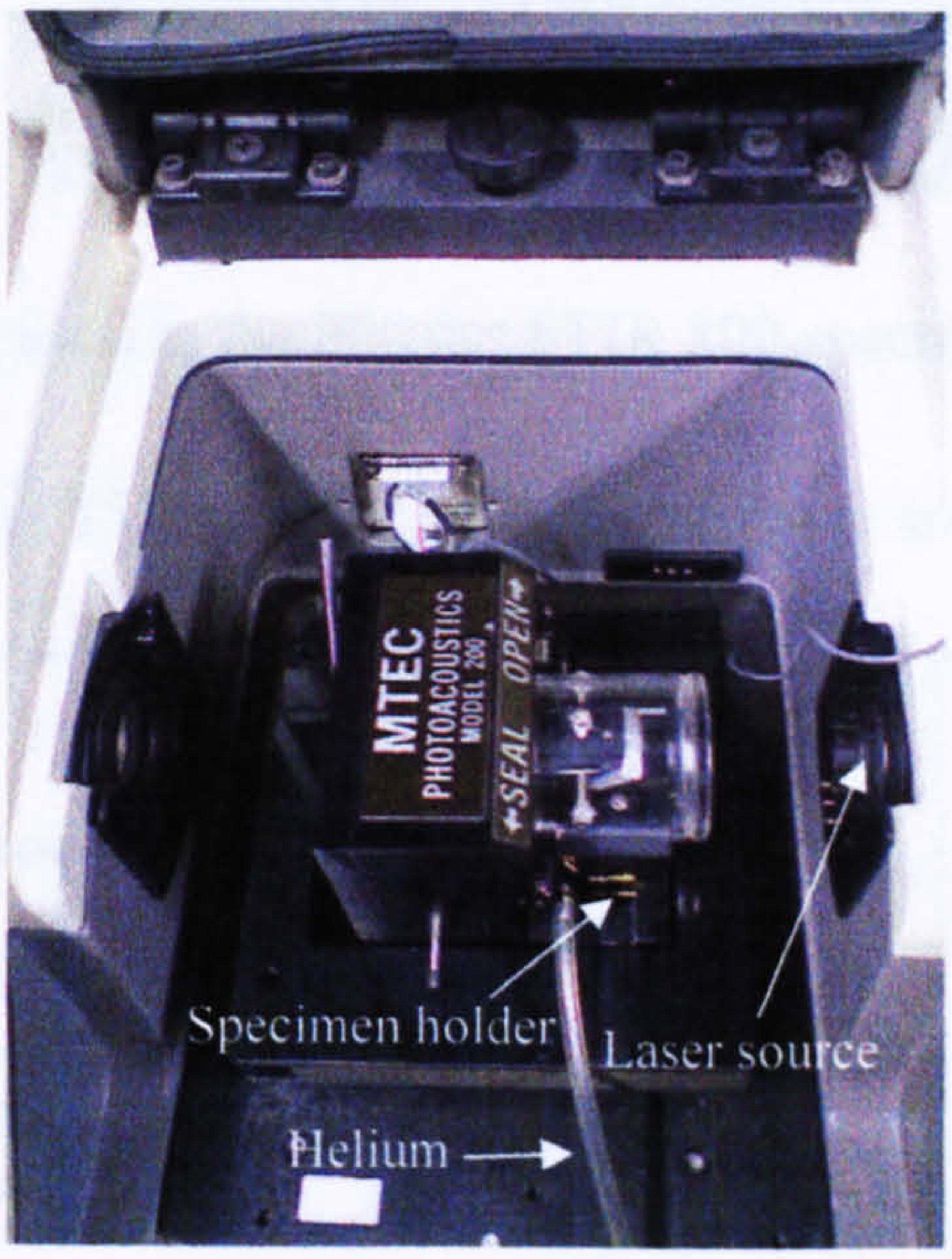

Figure 2-20 MTec PAS cell used in the Nicolet FTIR 800 spectrometer.

(b) DRIFTS Cell

Prior to use in the DRIFTS cell samples were ground into a fine powder and diluted with approximately 90 % potassium bromide powder. Spectra were obtained in the wave number range 4000 - 400 cm^{-1} with 64 scans and a spectral resolution of 8 cm^{-1}. Backgrounds were collected using a polished mirror and all spectra were adjusted accordingly (see Table 2-10).

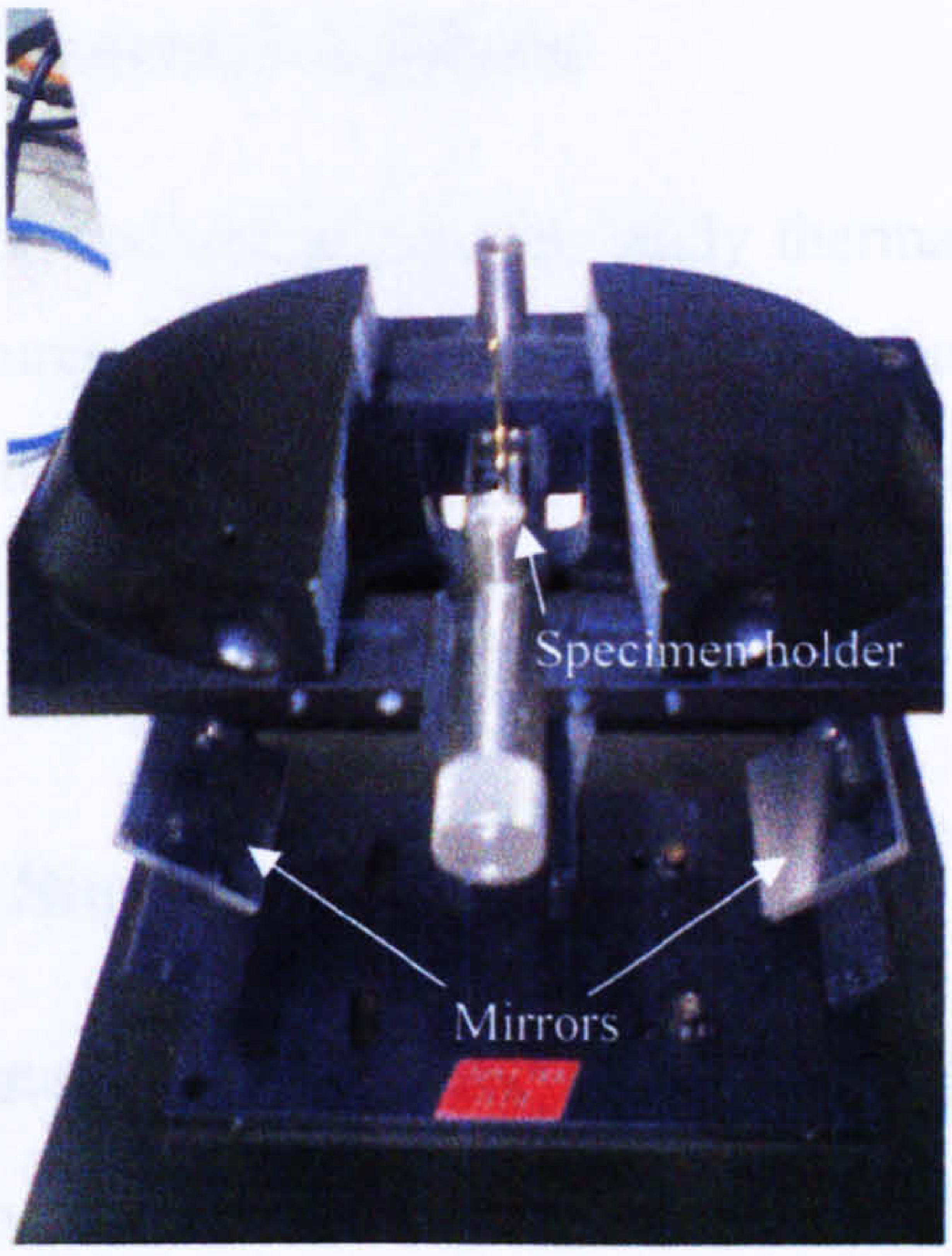

Figure 2-21 DRIFTS cell used in the Nicolet FTIR 800 spectrometer.

Table 2-10 Sample series, FTIR cell type, number of scans and spectral resolution.

Sample Series [corresponding section]	**Cell Type**		**No. of scans**	**Spectral resolution (cm^{-1})**
	PAS	**DRIFTS**		
Instant Hydroxyapatite [2.2.2.1 (a)]	√	-	256	4
CO_3^{2-} substituted calcium phosphates [2.2.2.2 (a)]	√	-	256	8
SiO_4^{4-} substituted calcium phosphates [2.2.2.2 (b)]	√	-	256	8
Mg^{2+} substituted calcium phosphates [2.2.2.3 (a)]	√	-	256	8
Zn^{2+} substituted calcium phosphates [2.2.2.3 (b)]	-	√	64	8

2.3.7 ^{29}Si Magic Angle Spinning Nuclear Magnetic Resonance

^{29}Si magic angle spinning nuclear magnetic resonance (MAS-NMR) was carried out for sample 5-SiHA using the solid-state NMR research service at Department of Chemistry, Durham University (Durham, UK). The data was collected by Dr. David Apperley.

2.3.8 Simultaneous Thermal Analysis

Thermal analyses were carried out in order to study thermal behavior of phases, their decomposition temperatures and weight loss. Simultaneous differential scanning calorimetry (DSC) and thermogravimetric analyses (TGA) were carried out using a Polymer Labs STA 1500 using a heating rate of 10 °C min^{-1} in the 30 – 1200 °C temperature range under nitrogen.

2.3.9 Spark Plasma Sintering

Powders were consolidated using a spark plasma sintering furnace (FCT System HPD 25/1) at Nanoforce, Department of Materials, Queen Mary University of London (London, UK). Samples were accurately weighed and poured into a 20 mm diameter graphite die (30 mm and 40 mm diameters were also used). The graphite die was then press-sealed using a PerkinElmer hydraulic press. The die was placed in the heating chamber of the SPS sintering furnace and heated up to the desired temperature at 200 °C min^{-1}. Force was applied on all the samples during sintering such that it always resulted in 100 MPa pressure. The schematic diagram of the SPS furnace and die arrangement is shown in Figure 2-22.

Cooling rates were varied (along with pressure during cooling) as discussed in section 6.3 of Chapter 6. After sintering, the graphite die was allowed to cool down in the furnace to room temperature prior to extraction. The sample was extracted from the die using a PerkinElmer hydraulic press.

The graphite residue on the samples' surfaces was removed by grinding on a 500 grit size grinding paper on a horizontally rotating grinding wheel. It was ensured that grinding was carried out at the radially most distant region of the grinding wheel in order to result in straight unidirectional scratches on the surface.

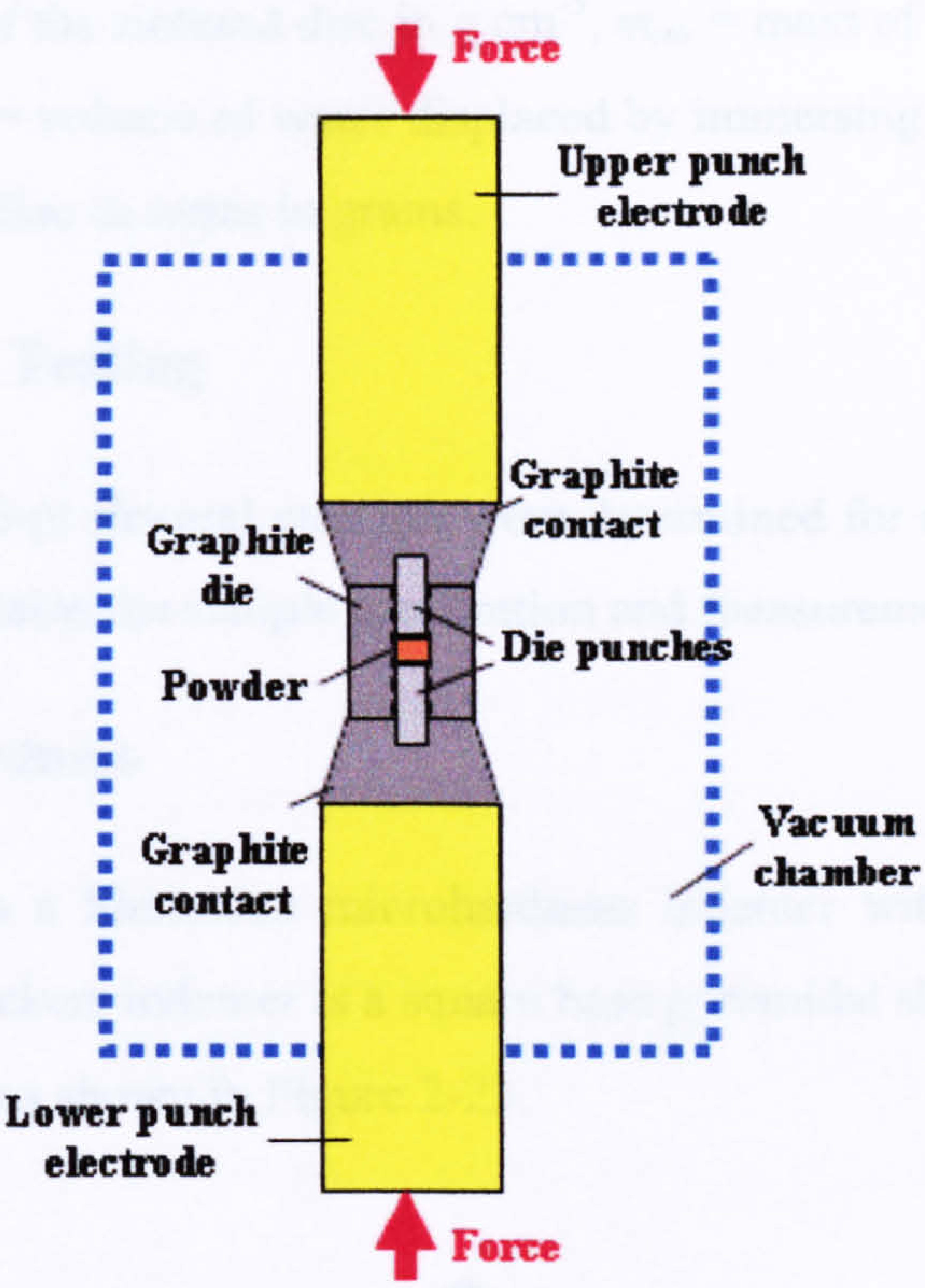

Figure 2-22 Schematic diagram of the SPS furnace showing important parts and die arrangement.

2.3.10 Density Calculation and Measurement

Theoretical densities of co-crystallised phase-mixtures were calculated using the following formula;

$$\rho_{mixture} = \frac{m_{HA} + m_{ZrO_2}}{V_{HA} + V_{ZrO_2}} \qquad \textbf{Eq. 2-2}$$

Where $\rho_{mixture}$ = density of the biphasic mixture, m_{HA} = wt% of HA in the mixture, m_{ZrO2} = wt% of ZrO_2 in the mixture, $V_{HA} = m_{HA} / \rho_{HA}$ *and* $V_{ZrO2} = m_{ZrO2} / \rho_{ZrO2}$. ρ_{HA} and ρ_{ZrO2} were assigned values of 3.16 g cm^{3-} and 6.05 g cm^{3-}.

Actual densities of the sintered discs were measured using Archimedes' principle. It assumes a density of 1 g cm^{-3} for water.

$$\rho_{disc} = \frac{m_{air}}{(m_{air} - m_{water})} \qquad \textbf{Eq. 2-3}$$

Where ρ_{disc} = density of the sintered disc in g cm^{-3}, m_{air} = mass of the sintered disc in air in grams, $m_{air} - m_{water}$ = volume of water displaced by immersing the disc in cm^3, m_{water} = mass of the sintered disc in water in grams.

2.3.11 Mechanical Testing

Vickers hardness and 3-pt flexural strength were determined for representative sintered discs. This section explains the sample preparation and measurement methods.

2.3.11.1 Vickers Hardness

Indents were made on a Shimadzu microhardness indenter with a Vickers hardness indentation tip. The Vickers indenter is a square base pyramidal shape diamond indenter with 136 ° face angles as shown in Figure 2-23.

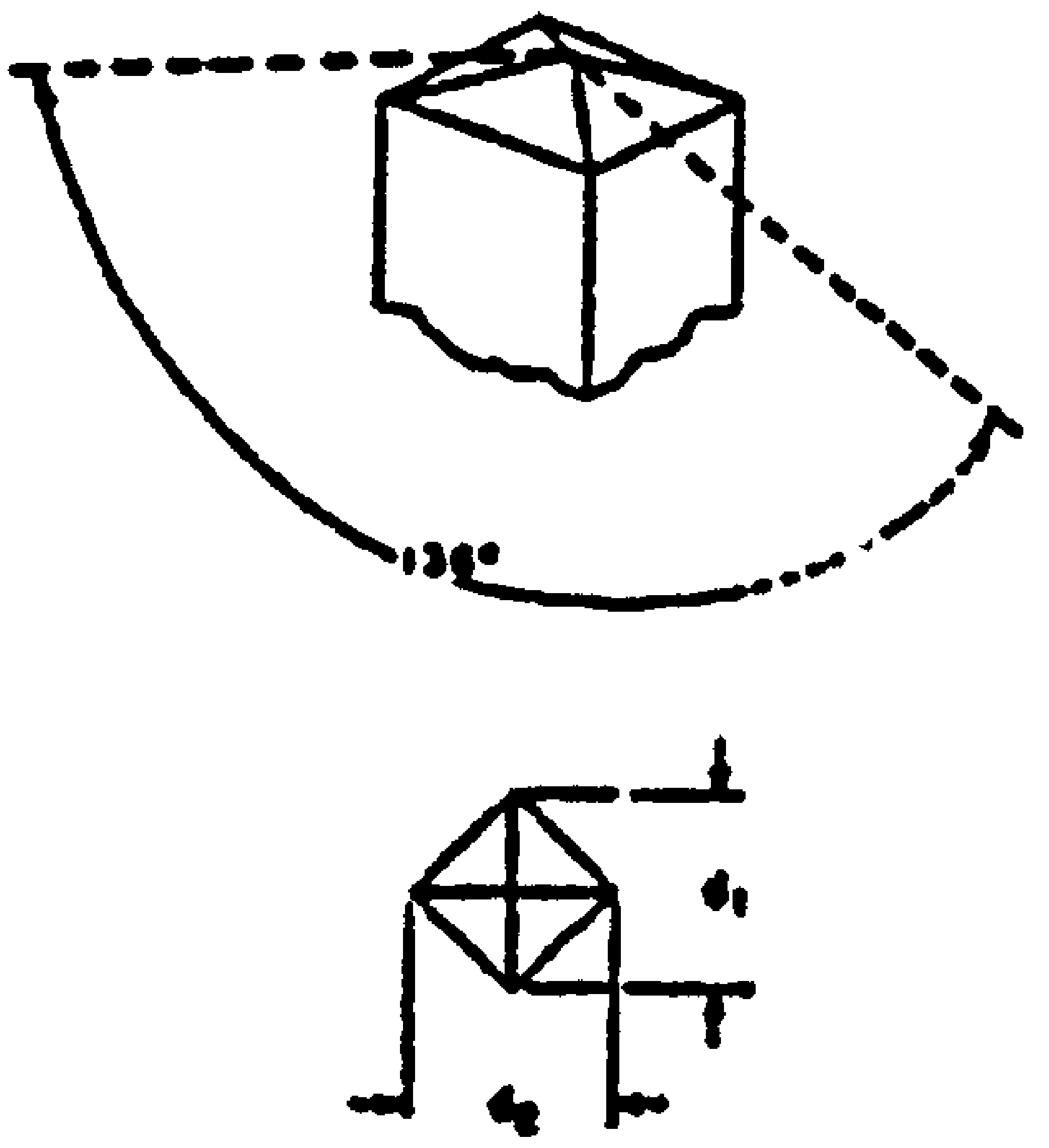

Figure 2-23 Geometry of the Vickers indenter and the indent (Hetzner 2003).

Prior to indentation all samples were ground using 800, 1000, 2000 and 4000 grit sized grinding papers to result in a relatively scratch free surface. This grinding routine resulted in an almost mirror-like finish on the sintered discs. A loading force of 300 g and holding time of 15 seconds were used for indents. In total 8 indents were made and 16 diagonals were measured. The indents were then observed using an Olympus BX-60 Optical Microscope as mentioned in section 2.3.3.1. Vickers hardness (HV) was measured using the following equation,

$$HV = 1854.4 \times \frac{L}{d^2} \quad \textbf{Eq. 2-4}$$

where L is the load in grams-force and d is the average of two diagonal lengths of an indent in μm as mentioned in the ASTM standard E384. 1854.4 is a geometrical constant. In order to convert the HV hardness value to GPa the values were multiplied by 0.009807.

2.3.11.2 Three-point (3-pt) Flexural Strength

40 mm diameter spark plasma sintered discs were cut using a diamond cutter (Model 660, South Bay Technology Inc.) at Eastman Dental Institute, UCL (London, UK) into 5 or 6 specimens (per disc) with rectangular cross-sections. The top and bottom faces of the specimens (with respect to sintering position in the SPS furnace) were ground on 800, 1000 and 2000 grit size SiC grinding papers. After each grinding step it was ensured that the surface consisted of straight scratches on the surface along the length of the specimen. These scratches decreased with increasing grit size of the grinding papers eventually leading to an almost mirror-like finish. The final average dimensions were 25 x 3 x 2 mm for these specimens [Figure 2-24 (a)]. All edges and corners on these specimens were rounded on 2000 grit size grinding paper to get rid of high stress concentration points which may lead to lower flexural strength values. Prior to loading in the jig, after a visual inspection, the relatively better polished surface was placed facing downwards. This was to ensure that under tension, scratches or kinks did not lead to a lower flexural strength value. The specimens are shown in Figure 2-25.

Figure 2-24 (b) shows the schematic representation of the 3-pt flexural strength test. Figure 2-26 shows an actual photograph of the arrangement of a specimen in the flexural test jig. The numbers 1, 2 and 3 show the three points of contact. The span length of 20 mm is also shown. The test was carried out using a 20kN Instron 8511.20 load cell with a loading rate of 500 N min^{-1}. This corresponded to *ca.* 0.2 mm min^{-1} strain rate. Prior to testing, all samples were pre-loaded at 2 N force. The 3-pt flexural strength was determined using the following equation from ASTM standard C1161;

$$S = \frac{3PL}{2bd^2} \qquad \textbf{Eq. 2-5}$$

Where P = break force in newtons, L = outer support span, b = specimen width, d = specimen thickness.

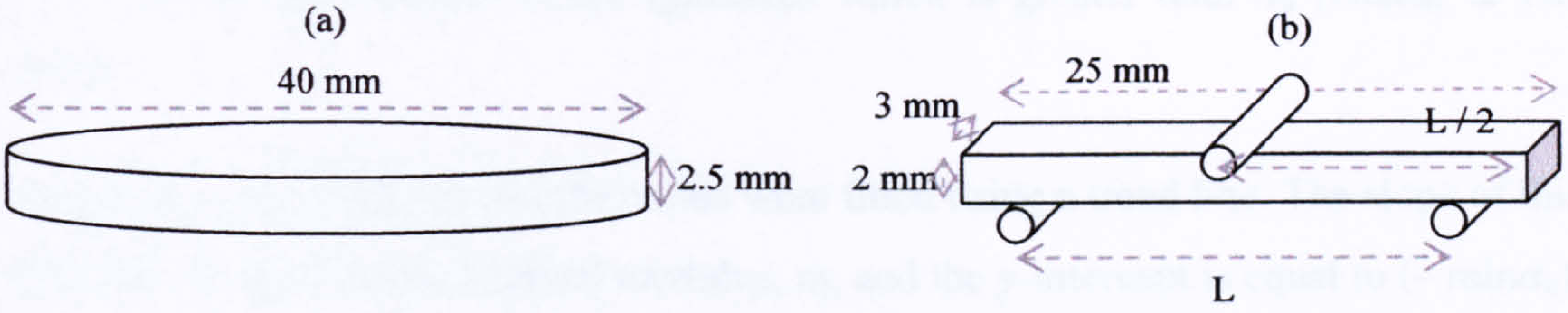

Figure 2-24 Schematic diagrams showing (a) the dimensions assumed for the 40 mm disc to calculate mass required (b) 3-pt flexural test configuration according to ASTM standard 1161.

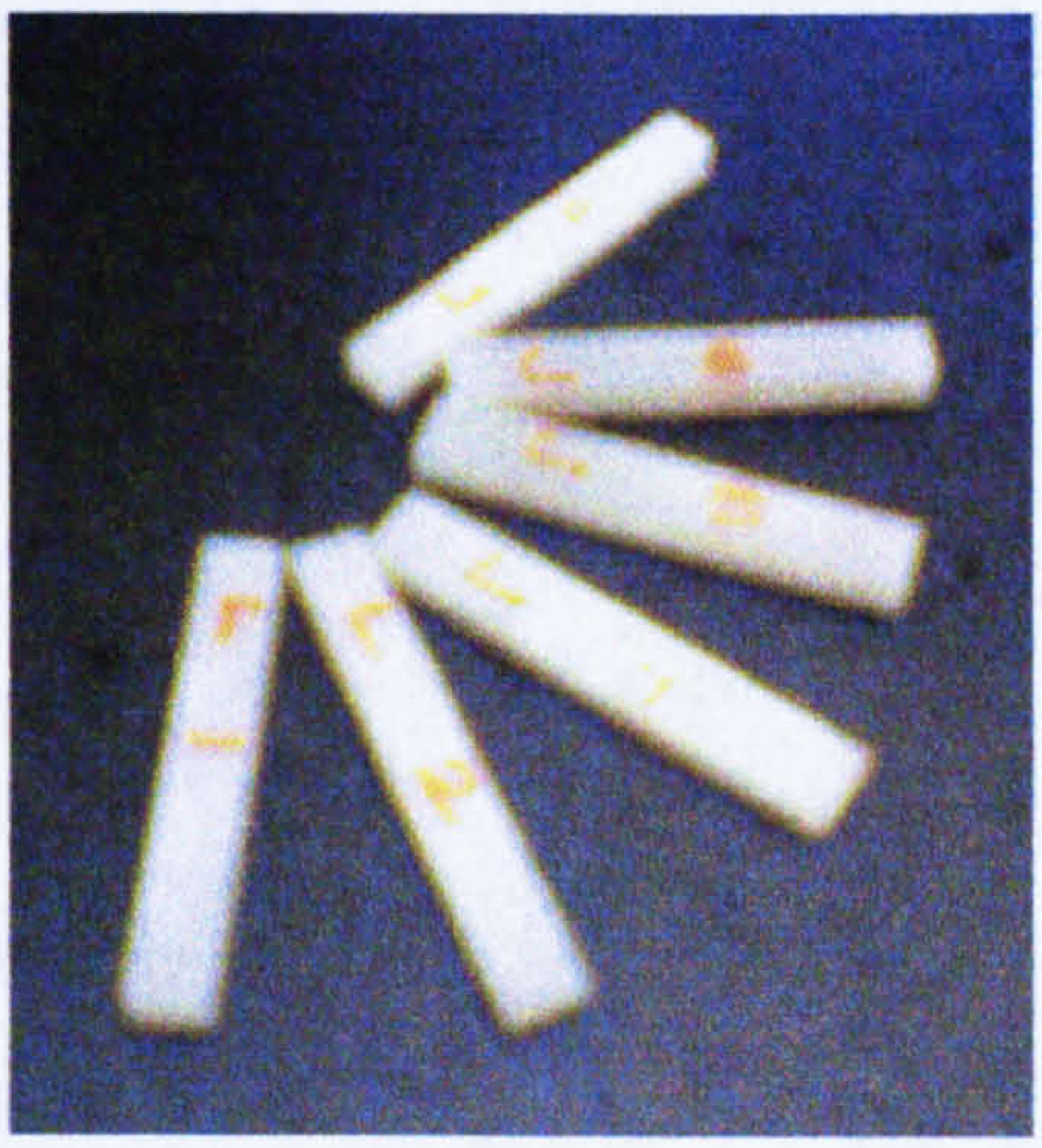

Figure 2-25 Specimens with rectangular cross-sections for 3-pt flexural strength determination.

2.3.11.3 Weibull Statistical Analysis

Due to the dependence of crack initiation (and fracture) on microstructure, the strength of ceramics can vary significantly for similar samples. Weibull statistical analysis should therefore be used to quantify this dispersion. It is a mathematical distribution which presents the probability of failure as a function of stress. The linearisation method was adopted for determination of the Weibull modulus, as represented by the following equation;

$$\ln\ln(\frac{1}{1-P_f}) = m\ln\sigma - m\ln\sigma_0 \qquad \textbf{Eq. 2-6}$$

Where P_f = probability of fracture which is equal to j/(n+1) [n = number of specimens and j is the rank number when the flexural strength values are ranked from the least (j = 1) to the maximum (j = 10, if 10 tests were carried out)], m = Weibull modulus,

σ = 3-pt flexural strength of the specimen which is greater than σ_0 (Huang & Hing 2002).

Equation 2-5 was plotted and the points were fitted using a trend line. The slope of this trend line is equal to the Weibull modulus, m, and the y-intercept is equal to ($-\, m\ln\sigma_0$).

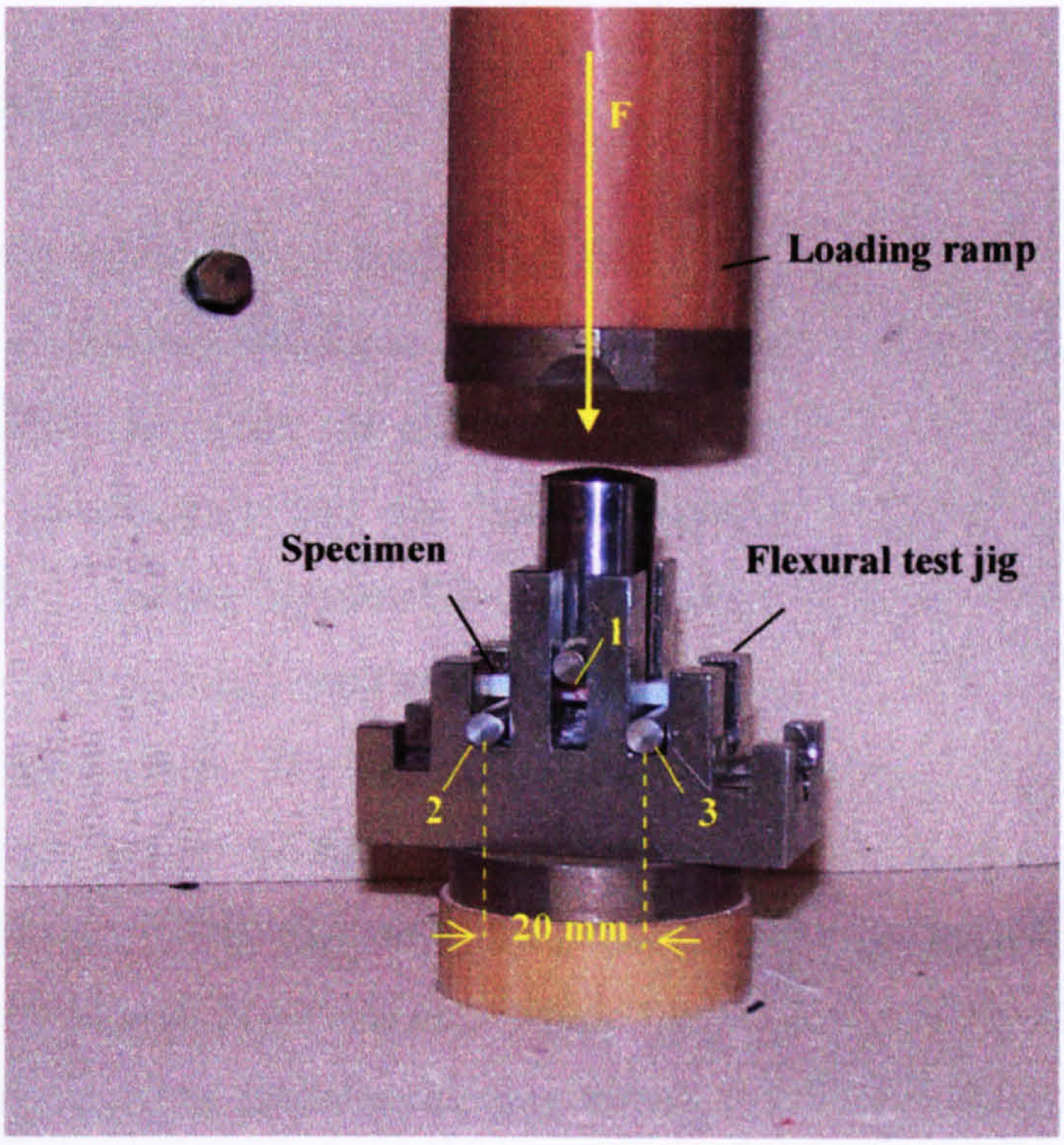

Figure 2-26 Arrangement of the jig under the loading ramp and the arrangement of the specimen in a 3-pt lay out. The numbers 1, 2 and 3 in the figure show the three contact points.

Chapter 3

Instant Nano-Hydroxyapatite and Effect of CHFS System Parameters

3.1 Introduction

Synthetic hydroxyapatite [HA, $Ca_{10}(PO_4)_6(OH)_2$, Ca:P molar ratio 1.67], is a bioactive material that is chemically similar to biological apatite, the mineral component of bone (Porter et al. 2004). However, as explained in Chapter 1, biological apatites contain multiple ionic substitutions and are non-stoichiometric (Ca:P molar ratio < 1.67) (Leventouri 2006). Indeed, human bone is a natural composite comprising of nano-apatite rods ($<$ 100 nm long) arranged in lamellae and bound to collagen (Fratzl et al. 2004). Thus, synthetic nano-HA is of interest as a biocompatible phase reinforcement in biomedical composites, for filling bulk bone defects and for coatings on metal implants (Hench 1991; Hench 1998). HA and other calcium phosphates are also of interest as components in injectable bone cements where controlling particle properties (e.g. size and shape) is often used to modulate cement setting behaviour (Ginebra et al. 2004).

HA powders and coatings can be synthesised using a number of methods including sol-gel processing (Bigi et al. 2004), co-precipitation (Pang & Bao 2003; Phillips et al. 2003), emulsion techniques (Lim et al. 1997; Phillips et al. 2003), batch hydrothermal processes (Kothapalli et al. 2005; Liu et al. 2003; Riman et al. 2002; Wang et al. 2006; Zhang et al. 2005), mechano-chemical methods (Rhee 2002) and chemical vapour deposition (Darr et al. 2004). The disadvantages of these methods include the following; they often require very precise control over reaction conditions (Bigi et al. 2004; Darr et al. 2004; Kothapalli et al. 2005; Lim et al. 1997; Liu et al. 2003; Pang & Bao 2003; Phillips et al. 2003; Rhee 2002; Riman et al. 2002; Wang et al. 2006; Zhang et al. 2005), require expensive starting materials (Bigi et al. 2004; Darr et al. 2004) or large amounts of toxic organic solvents (Lim et al. 1997; Phillips et al. 2003) or they are usually time consuming (Bigi et al. 2004; Kothapalli et al. 2005; Lim et al. 1997; Pang & Bao 2003; Phillips et al. 2003; Wang et al. 2006). For example, in wet chemical syntheses of HA, a maturation step (>18 hours), followed by a heat treatment of 650 °C, is required (Kim et al. 2005; Pang & Bao 2003; Phillips et al. 2003). Failure to allow sufficient maturation, gives a phase separated product upon heat treatment, which can adversely affect biological properties in vivo. Furthermore, the aforementioned synthesis approaches give little or no control over HA particle characteristics (i.e. particle size, agglomeration, surface area, shape, etc.) (Arce et al. 2004; Cao et al. 2005).

Calcium phosphates that can be precipitated directly from solution include hydroxyapatite, calcium deficient hydroxyapatite, brushite [$CaHPO_4.2H_2O$, Ca:P molar ratio 1.0] and its dehydrated form, monetite [$CaHPO_4$, Ca:P molar ratio 1.0] (Elliott 1994). Typically, these materials are produced from co-precipitation reactions at pH 10 – 11, pH < 10 and pH < 4 – 6, respectively (Kumta et al. 2005). Hence, there is a strong influence of pH on phase precipitation and subsequent phase solubilities (Kumta et al. 2005; Tang et al. 2003).

Batch hydrothermal syntheses of HA as reported in the literature are normally conducted in the range 60 – 150 °C for up to 24 hours to yield crystalline HA rods (Kothapalli et al. 2005; Liu et al. 2003; Riman et al. 2002; Wang et al. 2006; Zhang et al. 2005). Such batch reactions can include organic templating agents (Wang et al. 2006; Zhang et al. 2005), which are surface bound and therefore potentially unsuitable for biomedical applications as they may elicit an adverse response in vivo. In batch processes there is essentially little or no control over particle growth to affect size and shape. Hence there is interest to develop processes that allow a great degree of control.

To gain a better understanding of the factors that produce particles with the desired properties, current synthesis methods are essentially too slow and unpredictable. Thus, there is interest in developing faster synthesis techniques for synthetic apatites that allow a greater degree of control over particle properties.

Continuous hydrothermal syntheses have recently gained interest as a fast and controllable method for producing inorganic nano-materials (particles < 500 nm) (Cabanas et al. 2000; Cabanas et al. 2001; Hakuta et al. 2005; Sue et al. 2004). Previous examples include the rapid synthesis of nano-materials (<100 nm diameter) that normally require long synthesis times or that are difficult to manufacture using more conventional methods (Cabanas et al. 2000; Cabanas et al. 2001; Hakuta et al. 2005; Sue et al. 2004). The rapid nucleating and crystallising environment within a continuous hydrothermal flow synthesis reactor facilitates accelerated synthesis of crystalline nano-apatites in a single step. This is because there is a sudden change in dielectric constant, hence the metal salts are no longer soluble. The high ion product also results in a very hydrolysing environment. Hence, the process gives maximum supersaturation and rapid nucleation. This may result in small particles.

In this chapter, the rapid, single step synthesis of crystalline nano-particle hydroxyapatite rods in a continuous hydrothermal flow synthesis (CHFS) system is described. The effect of changing pH and Ca:P molar ratio in solution on apatitic thermal stability is also addressed. Furthermore, the effect of different flow rates and temperature regimes on surface area and yield of crystallising apatitic nanoparticles is also investigated.

3.2 Experimental

3.2.1 Synthesis of Hydroxyapatite (Effect of Temperature)

Initially three different reactions were carried out. 500 mL of 83.5 mM calcium nitrate solution (pH 11) was pumped through CHFS system 1 to react with 50.0 mM diammonium hydrogen phosphate solution (pH 10). The CHFS system 1 is described in section 2.2.1.1. Calcium nitrate and diammonium hydrogen phosphate solutions were both pumped at 5.0 mL min^{-1} and deionised water was pumped through the heater at 10.0 mL min^{-1}, respectively. The pH of the exiting suspension was measured to be 10.

Samples were labelled according to the temperature of the superheated water used, thus, samples prepared at 200, 300 and 400 °C were labelled HA(200), HA(300) and HA(400), respectively. A fourth control experiment was conducted using a similar method, with the superheated water feed at 400 °C, (under acidic rather than basic conditions) and a Ca:P molar ratio of 1:1 [denoted as sample CDHA(400) where CD represents calcium deficiency]. 50.0 mM calcium nitrate solution (pH 5.5) was pumped to react with 50.0 mM diammonium hydrogen phosphate solution (pH 8.5). The pH of these solutions was not adjusted in order to maintain an acidic pH during reaction. The pH of the exiting suspension was measured to be 6. All reactions were carried out under a pressure of 24 MPa.

After collection at the end of the back pressure regulator (BPR), the particles were washed, centrifuged, frozen and then freeze dried. Details are given in section 2.2.2.1 (a).

3.2.2 Synthesis of Hydroxyapatite (Effect of pH and Ca:P Molar Ratio on Thermal stability)

In total six different reactions were carried out. 50.0 M, 83.5 M and 100.0 mM calcium nitrate solutions were reacted with 50.0 mM diammonium hydrogen phosphate solution for such that the Ca:P molar ratios were *ca.* 1.0, 1.67 and 2.0, respectively.

The samples were labelled as 1-A, 1.67-A and 2-A for acidic and 1-B, 1.67-B and 2-B for basic conditions. The first number in the sample ID specifies the Ca:P molar ratio and A and B stand for acidic (pH 4.5) or basic (pH 9.5) conditions, respectively. These pH values were measured from suspensions immediately after collection. Therefore, sample 1-A was synthesised at acidic pH (pH 4.5) with Ca:P molar ratio of 1.0. Similarly, sample 1.67-A was synthesised at acidic pH (pH 4.5) with a Ca:P molar ratio of 1.67 and so on. These details are explained in section 2.2.2.1 (b).

Reactions were carried out using CHFS system 3 (described in section 2.2.1.3). The superheated water feed, calcium nitrate and diammonium hydrogen phosphate solutions were pumped at 25.0, 12.5 and 12.5 mL min^{-1}, respectively. All reactions were carried out at 450 °C and 24 MPa. Additionally, a small 5.0 cm long, 200 W Watlow band heater set to 450 °C was also used. After collection at the end of the BPR, the particles were washed, centrifuged, frozen and then freeze dried.

3.2.2.1 Effect of Different Flow Rates and Temperature Regimes on Surface Area and Yield

In total, 10 different reactions were carried out by reacting 100 mL of 83.5 mM calcium nitrate and 50.0 mM diammonium hydrogen phosphate solutions for each reaction. The flow rate regimes will be referred to as follows in this chapter; "*slow*" for 10, 5 and 5 mL min^{-1} (total 20 mL min^{-1}), "*medium*" for 20, 10 and 10 mL min^{-1} (total 40 mL min^{-1}) and "*fast*" for 25, 12.5 and 12.5 mL min^{-1} (total 50 mL min^{-1}). The three flow rates represent flow rates of superheated water, calcium nitrate and diammonium hydrogen phosphate solutions, respectively.

The temperature regime designation is explained as follows. The number represents the synthesis temperature and if this number is written with the letter "h", it suggests that a mixing zone heater regulated at the same temperature was also used. Therefore, temperature regime *400* represents a synthesis temperature of 400 °C without a mixing zone heater. Similarly, temperature regime *450h* represents a synthesis temperature of 450 °C with the mixing zone heater also set at 450 °C.

Solution preparation, labelling, corresponding flow rates and temperature regimes are also explained in section 2.2.2.1 (c) (summarised in Table 2-3). Reactions were carried out using CHFS system 3 (described in section 2.2.1.3). Additionally, where required, a small 5.0 cm long, 200 W Watlow band heater set to 450 °C was also used. After collection at the end of the BPR, the particles were washed, centrifuged, frozen and then freeze dried.

3.3 Results and Discussion

3.3.1 Synthesis of Hydroxyapatite (Effect of Temperature)

This section explains the effect of different temperatures of the superheated water feed on the synthesis of hydroxyapatite in the continuous hydrothermal flow system by means of several characterisation techniques.

3.3.1.1 Transmission Electron Microscopy

TEM was used to study the particle size and morphology. TEM images of the powders synthesised with superheated water at 200 °C, HA(200), revealed small agglomerates as seen in Figure 3-1 (a). TEM images for HA(300) showed well defined rods of *ca.* 65 (± 33) x 15 (± 3) nm (aspect ratio *ca.* 4.3, 50 particles sampled) as seen in Figure 3-1 (b). Figure 3-1 (c) and (d) showed well defined crystalline rods of *ca.* 140 (± 58) x 40 (± 12) nm (aspect ratio *ca.* 3.5, 50 particles sampled) for HA(400). TEM analyses suggested that particles increase in size with increasing synthesis temperature. Moreover, a high temperature during synthesis tended to give a better defined shape and they appear to agglomerate less.

HRTEM studies on sample HA(400) provided further insight into growth of rods shown in Figures 3-1 (c) and (d) [later determined to be phase-pure HA]. The lattice fringes shown in Figure 3-2 correspond to the (100) plane and suggest growth along the [001] direction. The lattice fringes run parallel to the length (longer dimension) of the HA rods suggesting that the particles are single crystals.

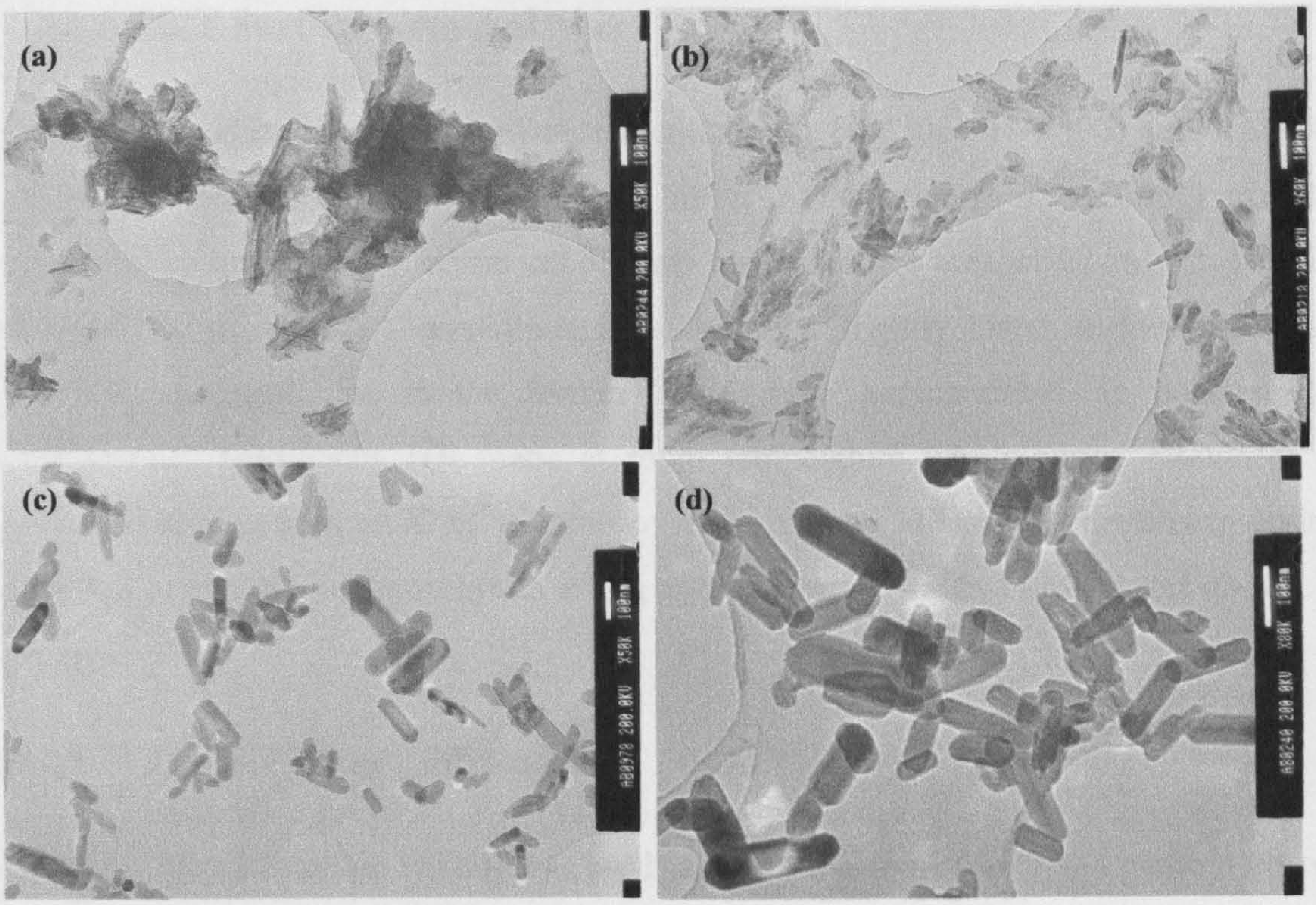

Figure 3-1 Transmission Electron Microscope images of samples (a) HA(200) at x50k magnification [bar = 100 nm] (b) HA(300) at x50k magnification [bar = 100 nm] (c) HA(400) at x50k magnification [bar = 100 nm] and (d) HA(400) at x80k magnification [bar = 100 nm].

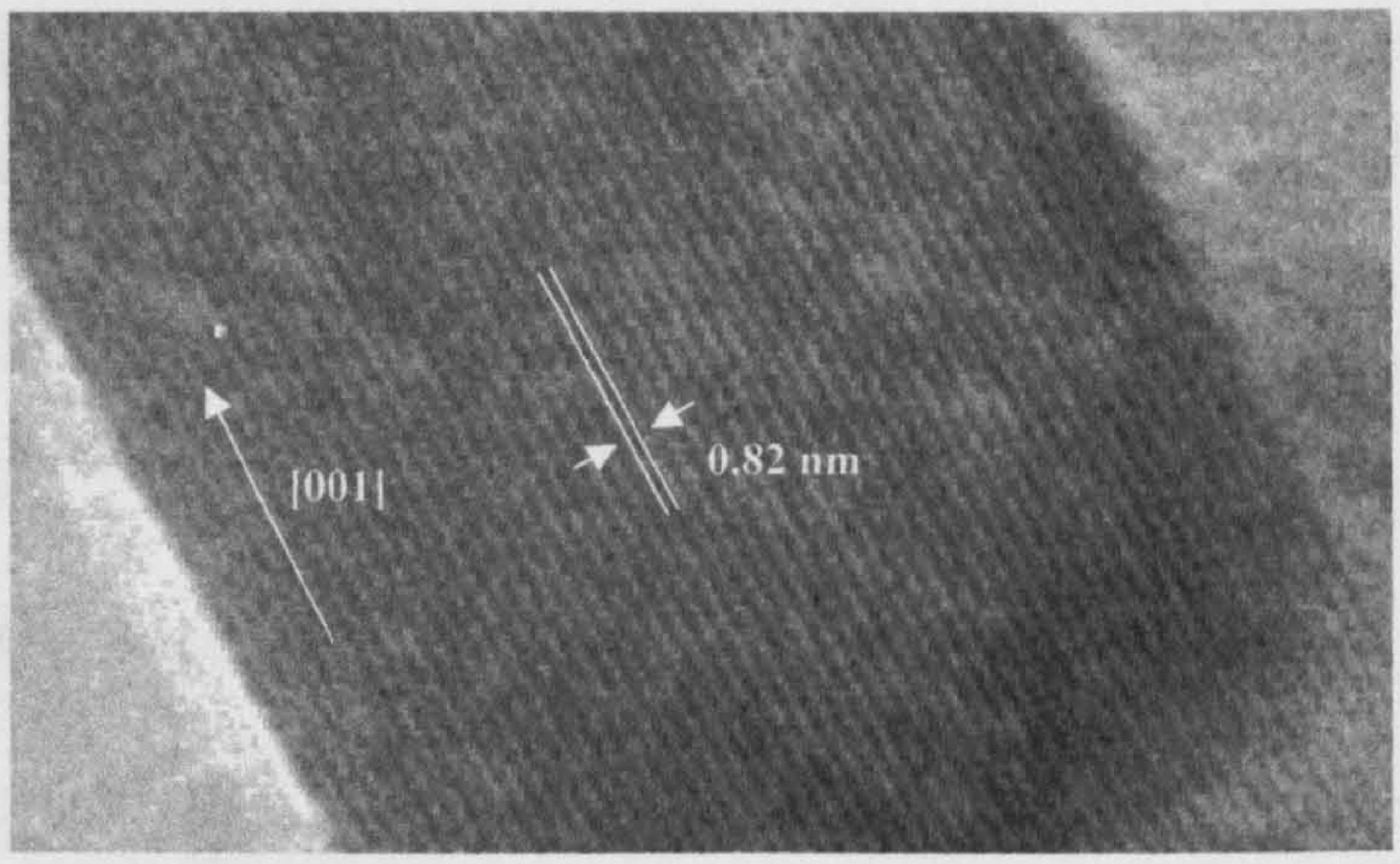

Figure 3-2 Transmission electron microscope image of sample HA(400) showing lattice fringes corresponding to the (100) plane suggesting growth along the [001] direction.

3.3.1.2 BET Surface Area Anlaysis

BET surface area (N_2 adsorption) measurements for HA(200), HA(300) and HA(400) were measured at *ca.* 88, 100 and 39 $m^2\ g^{-1}$, respectively. The control sample, CDHA(400) (made under acidic conditions) had a surface area of 67 $m^2\ g^{-1}$. Despite HA(200) being the least crystalline, it possesses a slightly lower surface area than HA(300), possibly due to the former being more agglomerated. In contrast "as precipitated" amorphous HA made at room temperature was reported elsewhere to possess a surface area of 90 $m^2\ g^{-1}$ after oven drying and 113 $m^2\ g^{-1}$ after freeze drying (Phillips et al. 2003). These results are in good agreement with TEM images shown in Figure 3-1.

3.3.1.3 Powder X-ray Diffraction

Powder X-ray diffraction (XRD) was used to assess the crystallinity and phase purity of samples. A Siemens D500 diffractometer was used for all samples (explained in section 2.3.4.1). A broad XRD pattern for HA(200) suggested an apatite-like structure [Figure 3-3 (d)]. XRD patterns of HA(300), CDHA(400) and HA(400) showed a good match to phase pure HA [all patterns compared to JCPDS pattern 09-0432] (Koutsopoulos 2002). The XRD peaks became increasingly sharper and well resolved, with increasing synthesis temperature, the pattern for CDHA(400) being noticeably less sharp than the HA(400) sample. This was possibly due to CDHA(400) being a disordered, highly non-stoichiometric structure (Ca:P molar ratio of 1.0 in solution at pH 4.5). In comparison, it was expected that HA(400), with a Ca:P molar ratio of 1.67 in solution at pH 10, will have higher stoichiometry.

3.3.1.4 Raman Spectroscopy

Raman spectroscopy was carried out in order to supplement crystallographic data and detect substitutions in the apatite lattice. Peaks in Raman spectra shown in Figure 3-4 all corresponded to those normally observed for HA (Penel et al. 1998). It was seen that peaks became narrower and more intense with increasing synthesis temperature. In Figure 3-4 for sample HA(400), the peaks at 1078, 1049 and 1030 cm^{-1} corresponded to asymmetric stretching mode (ν_3) of the P-O bond in phosphate. The peak at 1078 cm^{-1} also corresponded to the symmetric stretching mode (ν_1) of the C-O bond in B-type carbonate (where carbonate ions partially substitute phosphate ions in the HA lattice). Presence of carbonate in HA is unsurprising as deionised water was not degassed prior to use in the CHFS system and may have contained small amounts of dissolved carbonate ions. The peak at 965 cm^{-1} corresponded to the symmetric stretching mode (ν_1) of the P-O bond in phosphate. Peaks at 610, 593 and 583 cm^{-1} corresponded to the bending mode (ν_4) of the O-P-O linkage in phosphate. Bending mode (ν_2) of the O-P-O linkage in phosphate resulted in peaks at 450 and 433 cm^{-1}. In Figure 3-4 (b) [for sample CDHA(400)] the peak corresponding to symmetric stretching mode (ν_1) of the P-O bond in phosphate appeared at 961 cm^{-1}. This was possibly due to a defect structure, also observed in X-ray diffraction data in Figure 3-3 (b). In Figures 3-4 (b) and (d) peaks at 692 cm^{-1} possibly corresponded to the bending mode (ν_4) of B-type substituted carbonate in samples CDHA(400) and HA(200), respectively (Nishino et al. 1981). This peak was not seen for HA(300) and HA(400), which indicates that carbonate ions are more easily accommodated in the poorly crystalline lattice [for sample HA(200)] or a highly defect structure [for sample CDHA(400)].

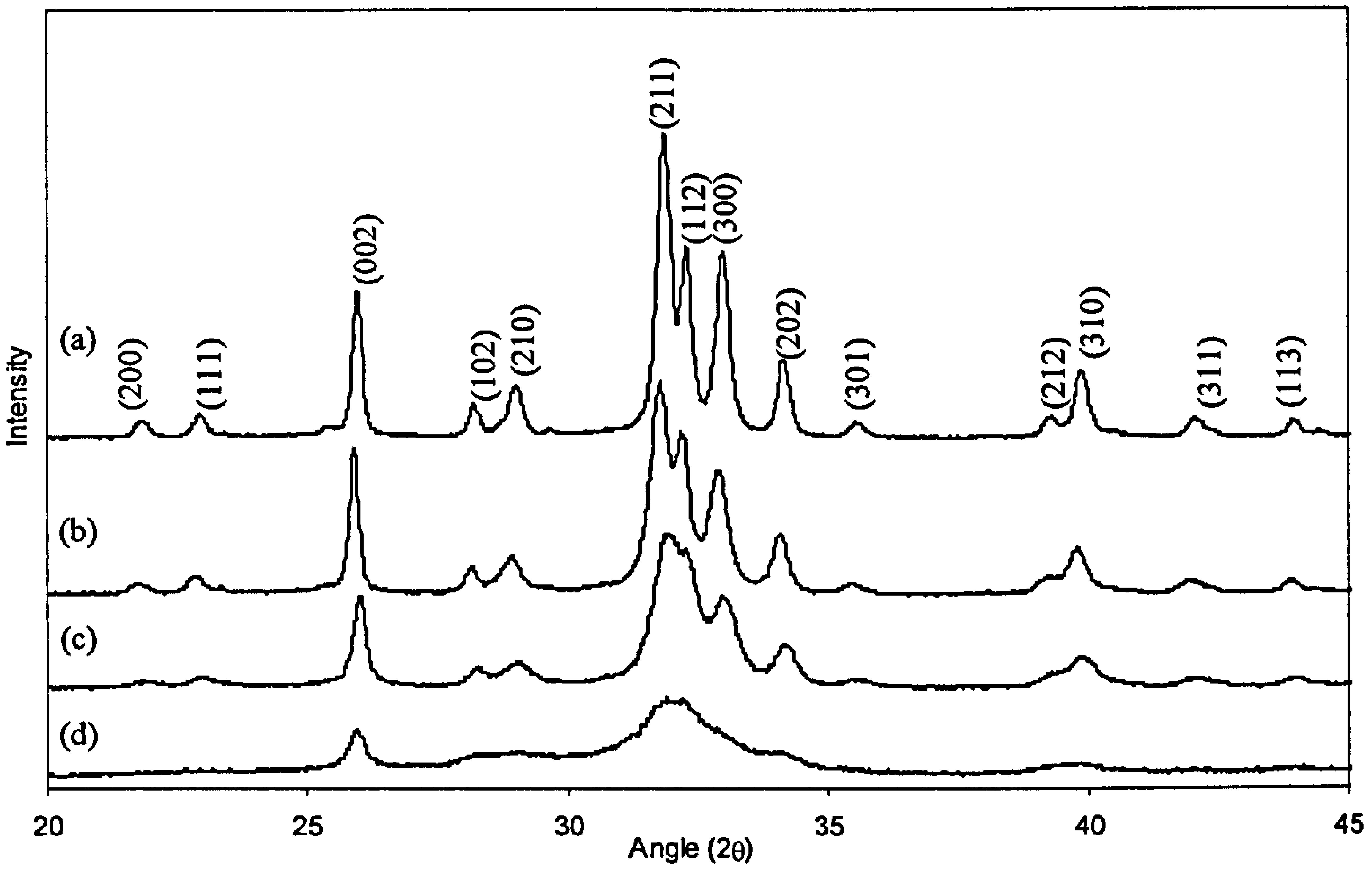

Figure 3-3 Powder X-ray diffraction patterns of samples (a) HA(400) (b) CDHA(400) (c) HA(300) and (d) HA(200).

3.3.1.5 Fourier Transform Infrared Spectroscopy

FTIR spectra of HA(400) [Figure 3-5 (a)] revealed peaks at 3570 and 633 cm^{-1} corresponding to stretching (ν_s) and librational mode (ν_L) of the hydroxyl group (OH$^-$) in HA. These peaks grew stronger and sharper with increasing synthesis temperature.

Both these peaks are present for CDHA(400) in Figure 3-5 (b) and HA(300) in Figure 3-5 (c), but the peak at 633 cm^{-1} is absent from the spectrum of HA(200) as seen in Figure 3-5 (d). The intensity of the peak at 1639 cm^{-1} corresponding to the bending mode (ν_2) for adsorbed water was observed to decrease with increasing synthesis temperature. This suggested that loosely incorporated OH^- groups became more incorporated into the lattice with an increase in synthesis temperature. This was also seen by the decrease in intensity of the broad band in the range 3700-2800 cm^{-1} (due to adsorbed water molecules) and the appearance of a peak at 633 cm^{-1} (librational mode of OH^-), with increasing synthesis temperature. Peaks at 1453 and 1414 cm^{-1} corresponded to stretching mode (ν_3) of the C-O bond in carbonate (CO_3^{2-}) substituted in HA. Peaks at 1096 and 1031 cm^{-1} corresponded to the asymmetric stretching mode (ν_3) of the P-O bond in phosphate, whilst the peak at 961 cm^{-1} corresponds to the symmetric stretching (ν_1) of the same bond. The peak at 872 cm^{-1} corresponding to bending mode (ν_2) of the O-C-O linkage in carbonate also became sharper with an increase in synthesis temperature. The sharpness and intensity of peaks at 603, 567 and 466 cm^{-1}, corresponding to bending modes of the O-P-O linkage in phosphate, increased with increasing synthesis temperature. The FTIR spectrum in Figure 3-5 (b) revealed similar peaks for CDHA(400) except the carbonate band that was observed around 1400 cm^{-1} in other samples. This is possibly due to acidic conditions of the reaction (pH 6) and subsequent presence of HPO_4^{2-} in the lattice as suggested by the peak at 881 cm^{-1} which is a characteristic peak of hydrogen phosphate group. This suggests that the phase composition is governed predominantly by pH and not Ca:P molar ratio in the CHFS system, as Ca:P molar ratio in this case was 1.0 not 1.67 [sample CDHA(400)] as in the case for samples HA(200), HA(300) and HA(400), respectively.

3.3.1.6 Simultaneous Thermal Analysis

Thermal behaviour of samples was assessed using Simultaneous Thermal Analysis (STA) [includes Simultaneous Themogravimetric Analysis (TGA) and Differential Scanning Calorimetry (DSC)] from 30 °C to 1200 °C. The TGA weight loss plot for sample HA(400) in Figure 3-6 (a) showed three overlapping regions of weight loss at 30-170 °C (1.20 wt% loss), 170-595 °C (1.85 wt% loss) and 595-1014 °C (1.11 wt%), respectively. Thereafter, there was a sudden weight loss (5.65 wt%) up to 1200 °C to give a final weight loss of 9.80 wt% possibly due to decompostition of the remaining material.

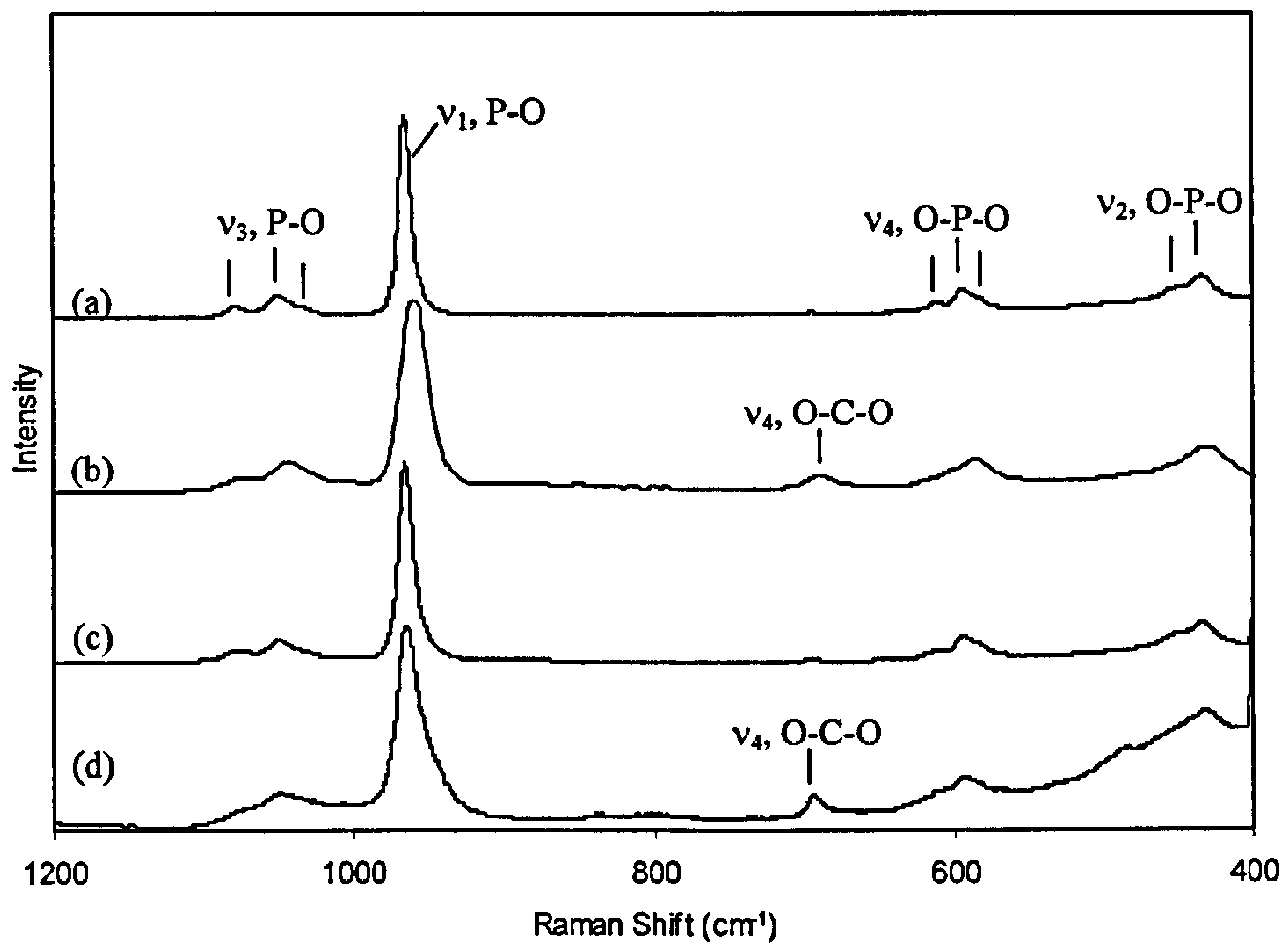

Figure 3-4 Raman spectra in the range 1200 – 400 cm^{-1} for samples (a) HA(400) (b) CDHA(400) (c) HA(300) and (d) HA(200).

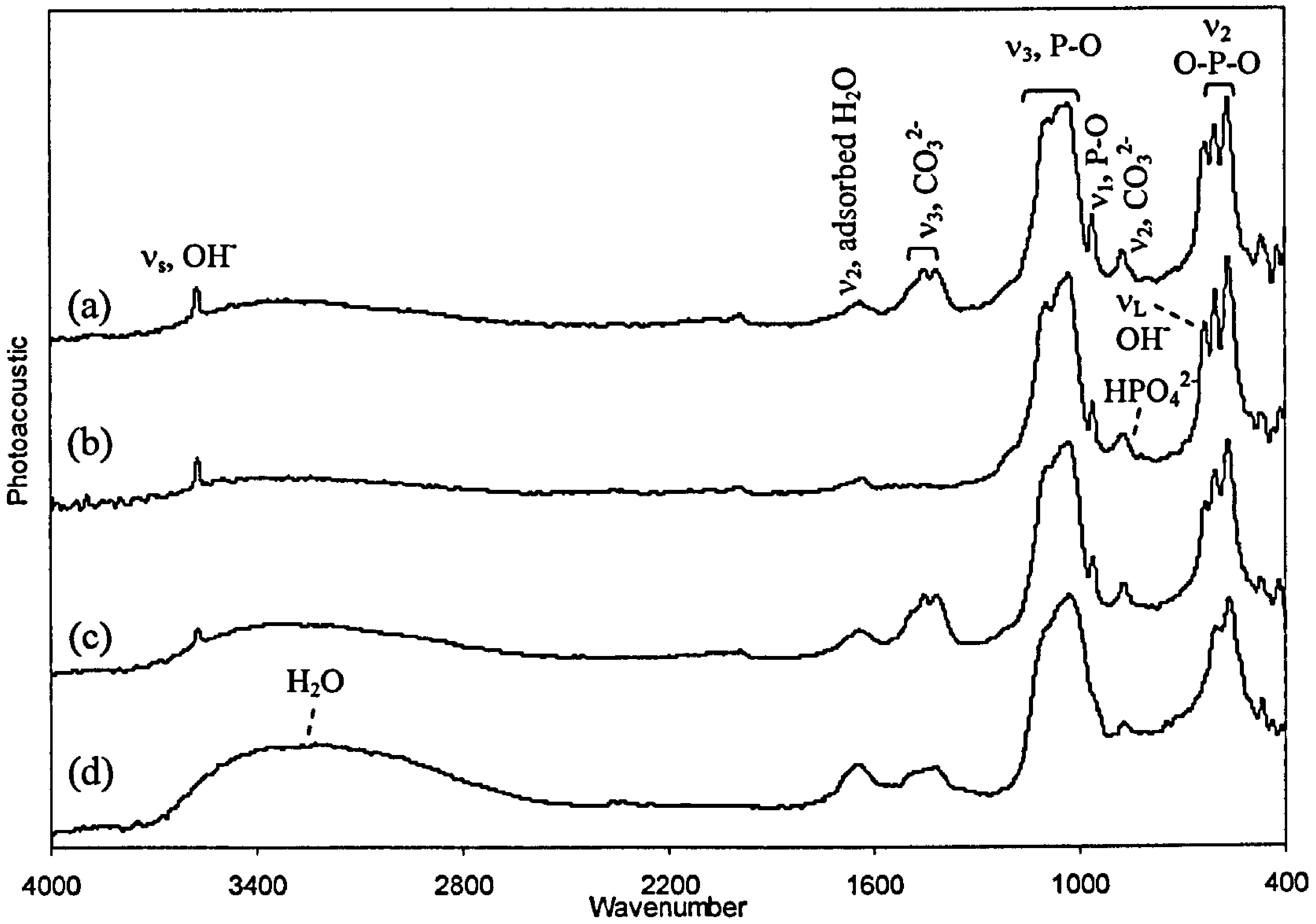

Figure 3-5 FTIR spectra in the range 4000 – 400 cm^{-1} for samples (a) HA(400) (b) CDHA(400) (c) HA(300) and (d) HA(200).

The first weight loss was presumably due to loss of weakly associated water, whilst the loss of lattice water and CO_2 occured for the second and third weight losses up to 1014°C, respectively. Differential scanning calorimetry (DSC) data for HA(400) in the range was rather featureless revealing only a broad endotherm centred at *ca.* 70 °C. Presumably this was because the material is already crysatlline as prepared.

For similar temperature regions, the TGA for sample CDHA(400) shown in Figure 3-6 (b) revealed a total weight loss of 11.9 wt%. This was more than that observed for sample HA(400) in Figure 3-6 (a), possibly due to the loss of HPO_4^{2-} groups for the latter during heating. Moreover, a sudden weight loss was noticeable, centred at 775 °C in the TGA plot shown in Figure 3-6 (b) (a corresponding endotherm was seen in the DSC plot). In contrast, the STA data for HA(300) showed a very smooth weight loss up to 1011 °C with only 8.18 wt% total loss at this temperature (only one endotherm in the DSC plot at *ca.* 70 °C). As expected, HA(200) showed the largest TGA weight loss by 1008 °C (total loss = 16.03 wt%) as shown in Figure 3-6 (d). HA(200) lost most of its weight early on (due to loss of weakly associated water). This was analogous to the presence of a distinct broad band (due to water) in the FTIR data for sample HA(200) between 3700-2800 cm^{-1} [Figure 3-5 (d)]. Similar to sample CDHA(400), sample HA(200) also showed an additonal endotherm centered at 750 °C (the corresponding weight loss is visible in the TGA plot) as compared to that of HA(300) and HA(400) which we attributed to the phase transformation of calcium deficient HA (CDHA) into beta-tricalcium phosphate, (β-TCP) and stoichiometric HA. In his book on "Structure and Chemistry of the Apatites and Other Calcium Orthophospates" published in 1996, Elliot represented the decompositon of a calcium deficient and carbonate substituted hydroxyapatite as follows;

$$BCaP \rightarrow xCa_{10}(PO_4)_6(OH_2) + y\beta - Ca_3(PO_4)_2 + H_2O + CO_2 \qquad \textbf{3-1}$$

3.3.1.7 Heat Treatment

Figure 3-7 shows powder XRD pattern of sample HA(200) heat-treated in air at 800 °C for 2 hours. It clearly shows a biphasic mixture of β-TCP and HA. HA peaks were compared to JCPDS pattern 09-432 and β-TCP peaks were compared to JCPDS pattern 09-169. This confirmed that the sudden weight loss in the TGA plot shown in Figure 3-6 (d) around 750 °C for sample HA(200) corresponded to the decomposition of a calcium deficient HA into β-TCP and stoichiometric HA.

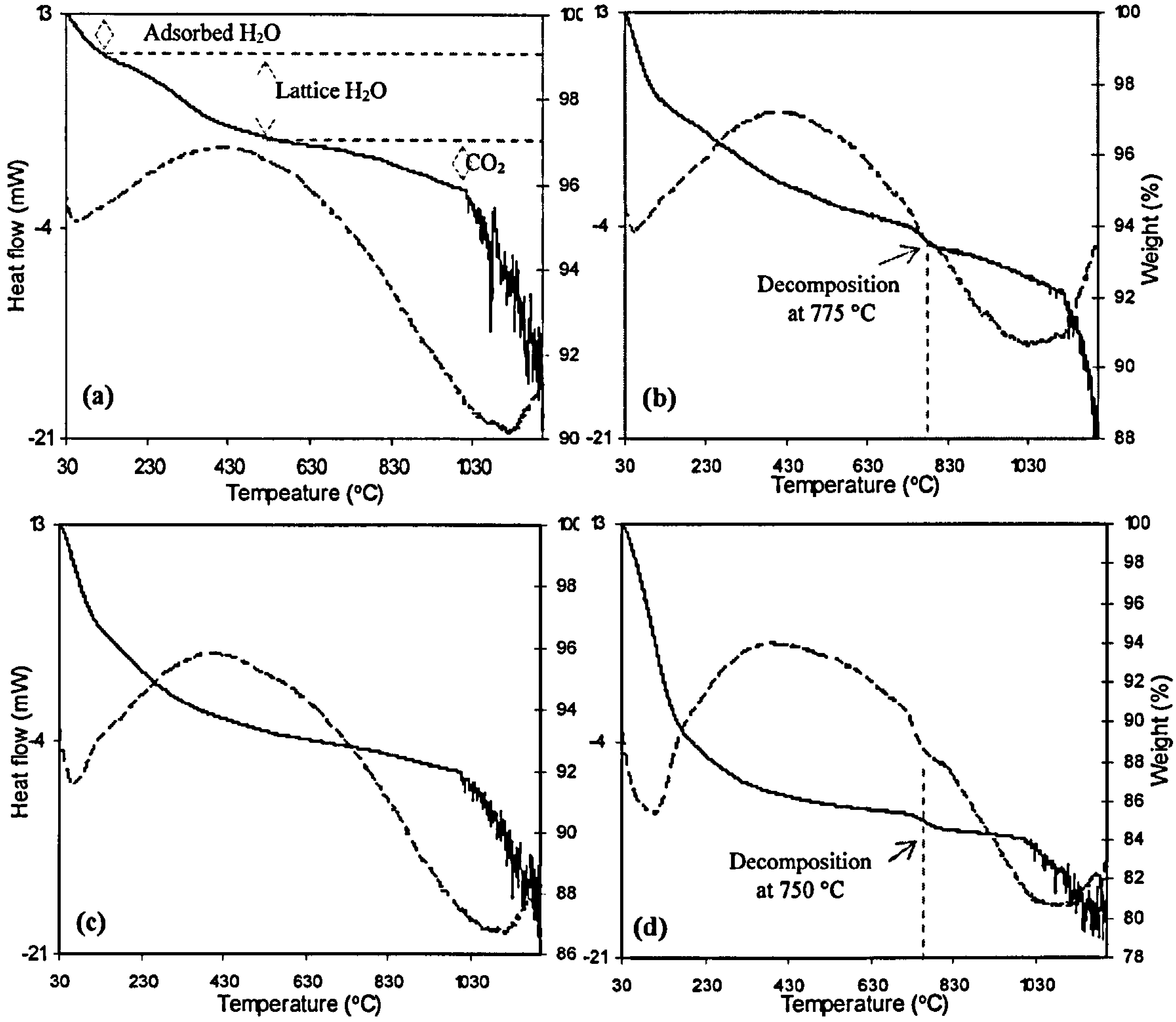

Figure 3-6 Simultaneous Thermal Analysis (STA) data showing TGA (solid line) and DSC (dotted line) plots for (a) HA(400) (b) CDHA(400) (c) HA(300) and (d) HA(200).

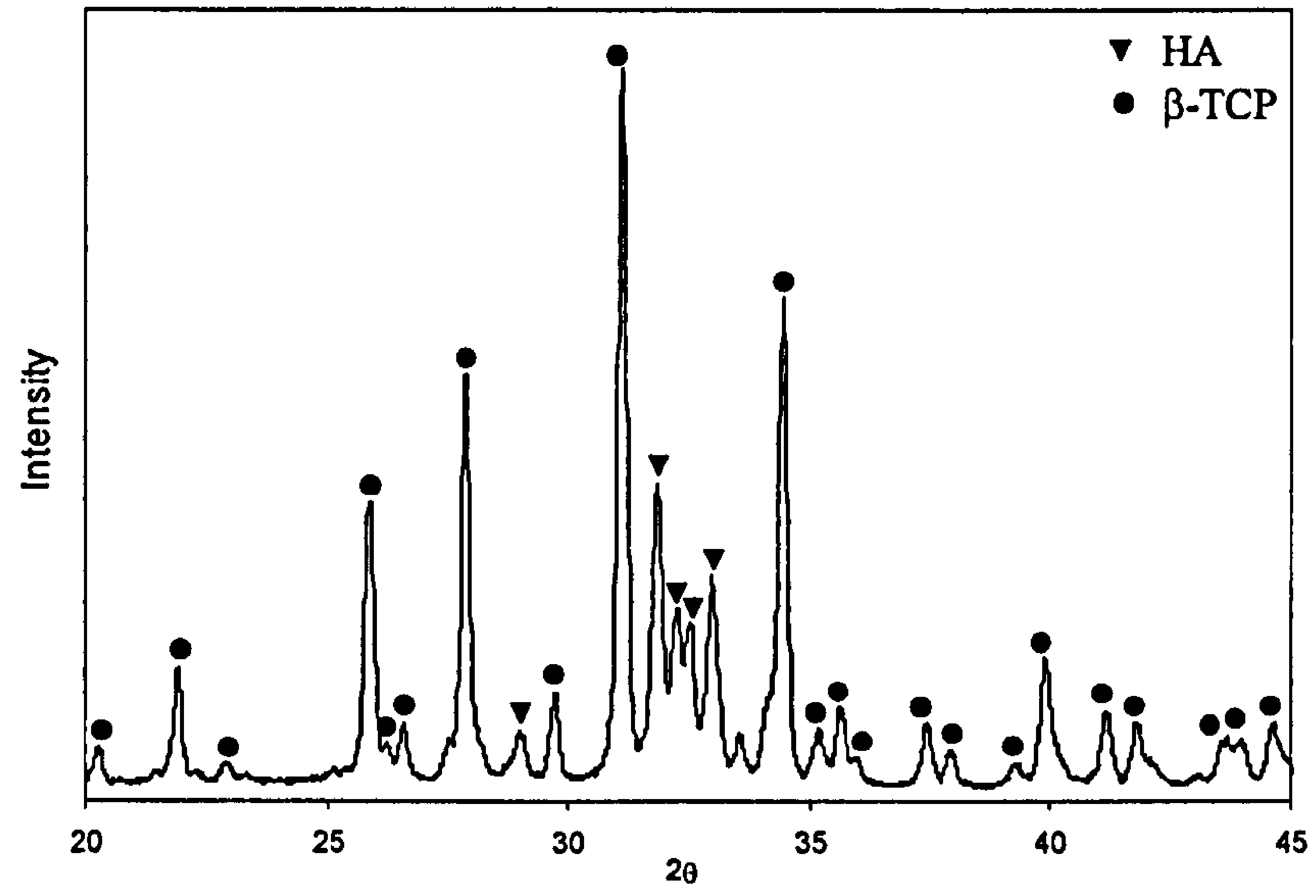

Figure 3-7 Powder X-ray powder diffraction pattern for sample HA(200) heat treated at 800 °C for 2 hours.

3.3.1.8 Elemental Analyses

Elemental analyses were performed on samples HA(400) and HA(200), respectively, using an EDS detector attached to a scanning electron microscope (compositions shown in Table 3-1). The details of the technique and equipment are mentioned in section 2.3.3.2. Results suggest that sample HA(400) is calcium deficient (Ca:P ratio 1.57), however, it is thermally stable up to *ca.* 1014 °C as revealed by simultaneous thermal analysis. The Ca:P molar ratio for sample HA(200) was measured to be 1.52. This suggested that HA(200) was more non-stoichiometric. Indeed, the phase decomposition at 750 °C in air suggests a lower stoichiometry of HA(200) in comparison to HA(400). Calcium deficient HA has been observed to decompose into β-TCP at 650 °C when Ca:P molar ratio was 1.5 (Siddharthan et al. 2004).

Table 3-1 Samples IDs, elemental composition (atomic %) as average values of 10 area scans and corresponding Ca:P molar ratios. SD represents standard deviation.

Sample ID	Atomic %			Ca:P (± SD)
	Ca	P	O	
HA(400)	15.48	9.85	74.66	1.57 (±0.06)
HA(200)	15.87	10.47	73.66	1.52 (±0.06)

3.3.2 Effect of CHFS System Parameters

3.3.2.1 Effect of pH and Ca:P Molar Ratio on Thermal Stability

Six reactions were carried out for this study as explained in section 2.2.2.1 (b) (i). The XRD patterns are shown in Appendix B, wherein, all samples gave a good match to JCPDS pattern 09-432 (phase-pure hydroxyapatite). The corresponding TGA and DSC plots are shown in Figure 3-8. It can be seen that samples 1-A, 1.67-A and 2-A [Figures 3-8 (a), (c) and (e)] all showed a sudden weight loss of *ca.* 0.62 wt%, 0.59 wt% and 0.50 wt%, respectively, in corresponding TGA plots. The corresponding endotherm was also observed in DSC plots centred at *ca.* 750 °C. As mentioned earlier, this was due to the phase transformation of calcium deficient hydroxyapatite into β-TCP and stoichiometric hydroxyapatite. These results suggest that the pH, not Ca:P molar ratio, is the dominating factor for determining stoichiometry (and subsequent thermal stability) of the resulting apatite. For sample 1-B the Ca:P molar ratio of 1.0 in solution was apparently too low to yield a thermally stable apatite (0.58 wt% loss in TGA plots at *ca.* 750 °C). Under similar basic conditions it was observed that a starting molar ratio of 1.67 [sample 1.67-B in Figure 3-8 (d)] resulted in minimal phase transformation at *ca.* 750 °C (only 0.25 wt% loss at *ca.* 750 °C in TGA plot). A weak endotherm in the corresponding DSC plot was also visible. In Figure 3-8 (e) it was observed that sample 2-B was thermally stable up to 1050 °C because it was synthesised using excess calcium in solution at a high pH (pH 9.5). All these results are summarised in Table 3-2.

It is interesting to note that in comparison to sample 1.67-B, sample HA(400) [Figure 3-6 (a)] showed no endotherm around 750 °C in the DSC plot and no weight loss in the range 700 – 800 °C in the corresponding TGA plot. This suggested that use of a faster flow rate (12.5 mL min^{-1} for sample 1.67-B as compared to 5 mL min^{-1} for sample HA(400)] for calcium nitrate and diammonium hydrogen phosphate solutions lowered the stoichiometry of the apatite more as to make the material slightly thermally unstable. This is understandable because *fast* flow rates in this case resulted in a lower residence time (3.9 seconds as compared to 9.9 seconds for *slow* flow rates) for precipitated particles; i.e. the time the particles spent in the mixing zone exposed to maximum temperature was lowered. The residence times are shown in Table 2-2 in section 2.2.1.4 in Chapter 2. Elemental analysis of sample 1.67-B carried out using an EDS detector attached to a SEM revealed a Ca:P molar ratio of 1.50 (standard deviation: ± 0.06).

Table 3-2 Samples IDs, Ca:P molar ratio, pH of exiting suspension and their thermal behavior based on TGA.

Sample ID	**Ca:P ratio**	**pH of exiting suspension**	**Sudden weight loss in TGA plot at *ca.* 750 °C**
1-A	1.0	4.5	Yes
1-B	1.0	9.5	Yes
1.67-A	1.67	4.5	Yes
1.67-B	1.67	9.5	Minimal
2-A	2.0	4.5	Yes
2-B	2.0	9.5	No

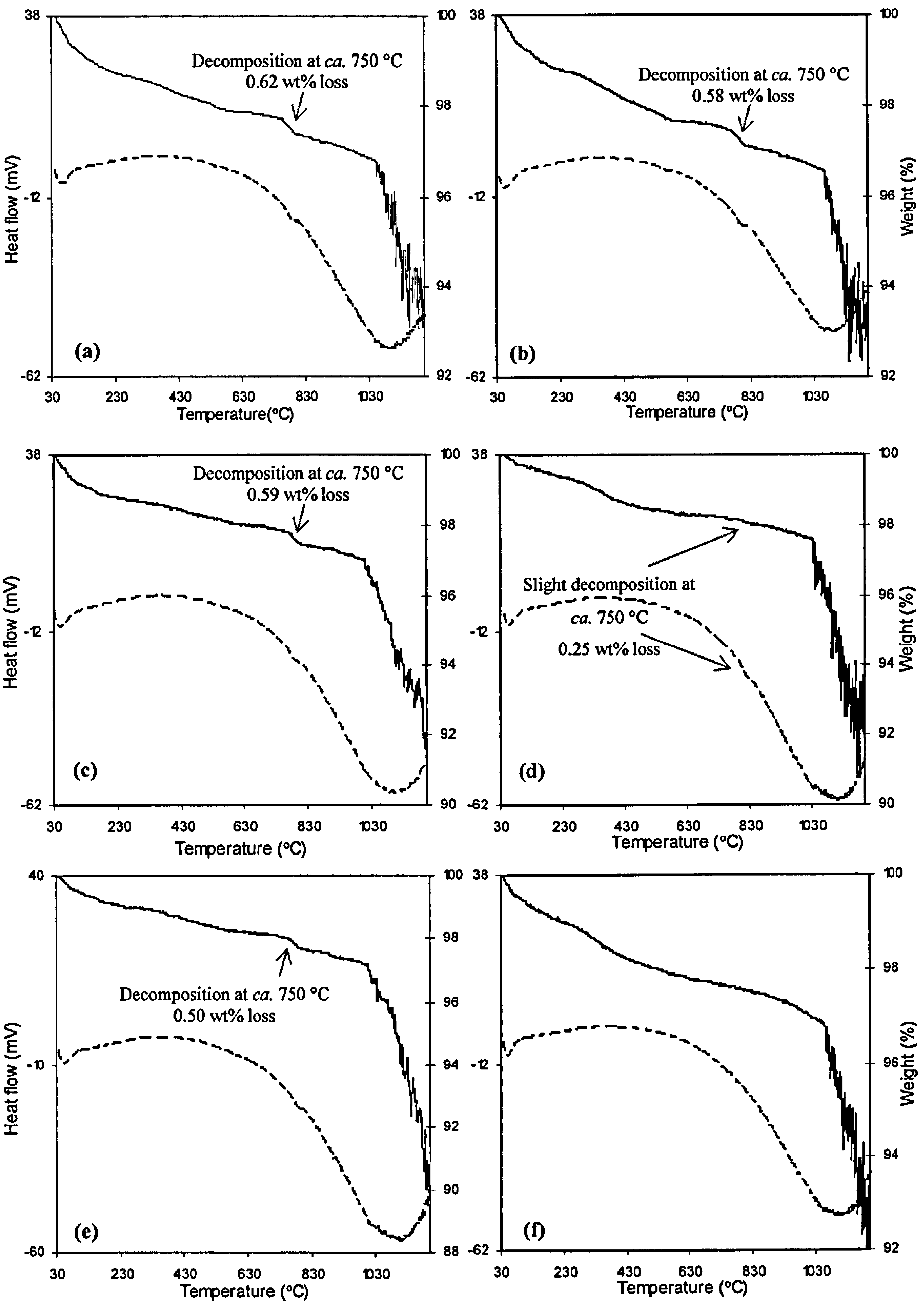

Figure 3-8 Simultaneous Thermal Analysis (STA) data showing TGA (solid line) and DSC (dotted line) plots for samples (a) 1-A (b) 1-B (c) 1.67-A (d) 1.67-B (e) 2-A and (f) 2-B.

3.3.2.2 Effect of Different Flow Rates and Temperature Regimes on Surface Area and Yield

For this study, 10 different reactions were carried out using CHFS system 3. Figure 3-9 shows the effect of different flow rates for two different temperature regimes. Increase in flow rates shows no significant effect on yield (%). However, the yield for a *slow* flow rate at *450h* temperature regime is lower (76 %) than that at *400* temperature regime. It is possible the increased yields using a *slow* flow rate for the *450h* temperature regime resulted in partial blockage of the mixing point and large particle filter in the CHFS system 3, resulting in an overall lower yield. Figure 3-10 suggests that there is minimal effect of increase in flow rates on the surface area of crystallising particles.

Figure 3-11 shows the effect of different temperature regimes on surface areas and yield (%) for a fixed *fast* flow rate. It was seen that there was minimal or no effect on the surface area of crystallising particles with an increase in heating in the CHFS system. However, the *450h* temperature regime gave a maximum yield of 90 % as compared to a minimum of 75 % for *400* temperature regime. Indeed, the use of a band heater in the mixing zone of CMTG CHFS systems has been reported to allow a reaction to reach completion (Boldrin et al. 2007).

The measured mixing point temperatures for various temperature regimes and flow rates are summarised in Table 3-3. For a given temperature regime it was observed that an increase in flow rates increase the temperature at the mixing point. This was due to the less heat loss for the superheated water feed due to increased velocity in the CHFS system.

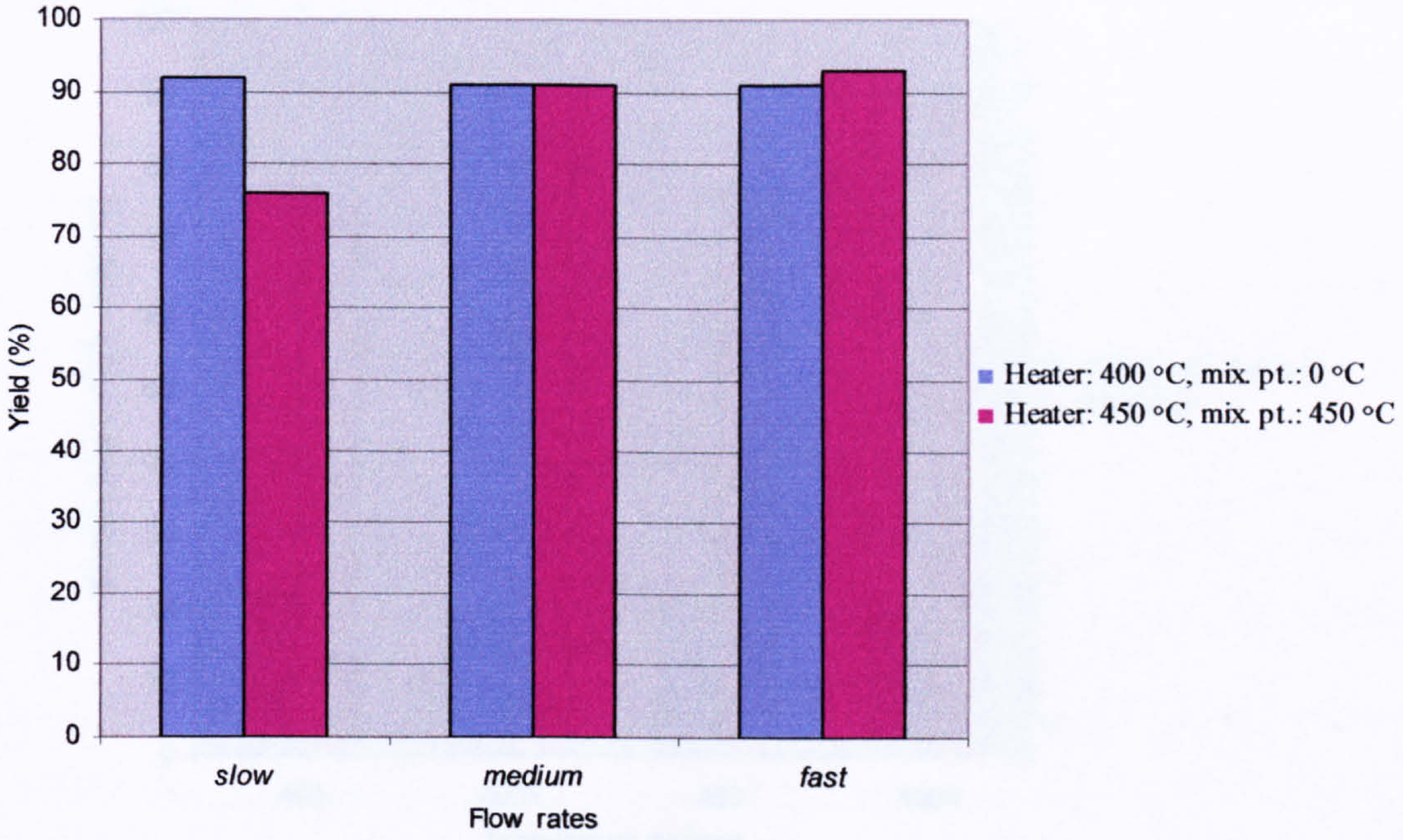

Figure 3-9 Effect of different flow rates on yield (%) for the heater set at 🟦 400 °C (mixing point heater was not used), 🟪 450 °C with the mixing point heater set at 450 °C. [Key: *slow* = combined flow rate of 20 mL min^{-1}, *medium* = combined flow rate of 40 mL min^{-1}, *fast* = combined flow rate of 50 mL min^{-1}].

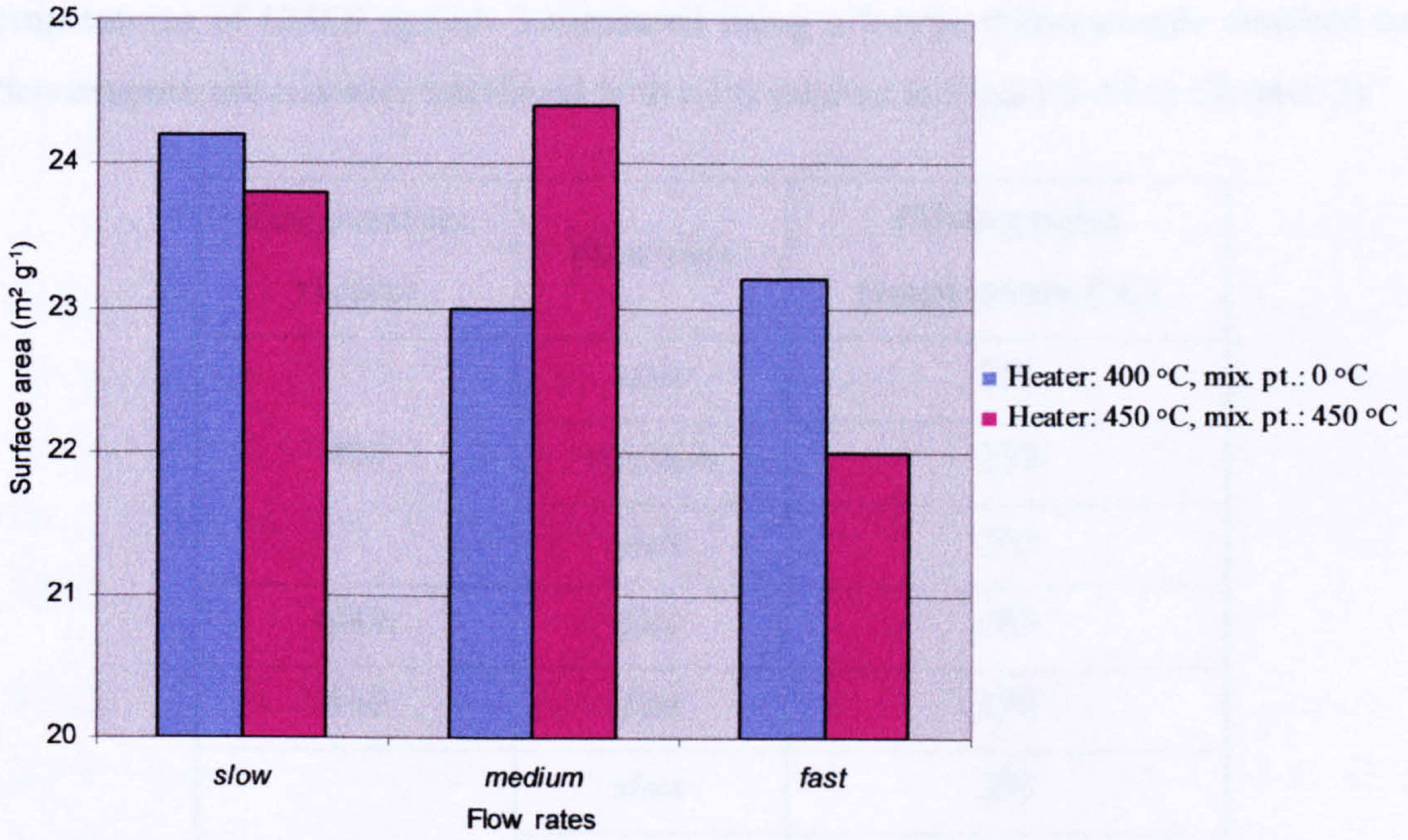

Figure 3-10 Effect of different flow rates on surface area (m^2 g^{-1}) for heater set at 🟦 400 °C (mixing point heater was not used), 🟪 450 °C with the mixing point heater set at 450 °C [Key: *slow* = combined flow rate of 20 mL min^{-1}, *medium* = combined flow rate of 40 mL min^{-1}, *fast* = combined flow rate of 50 mL min^{-1}].

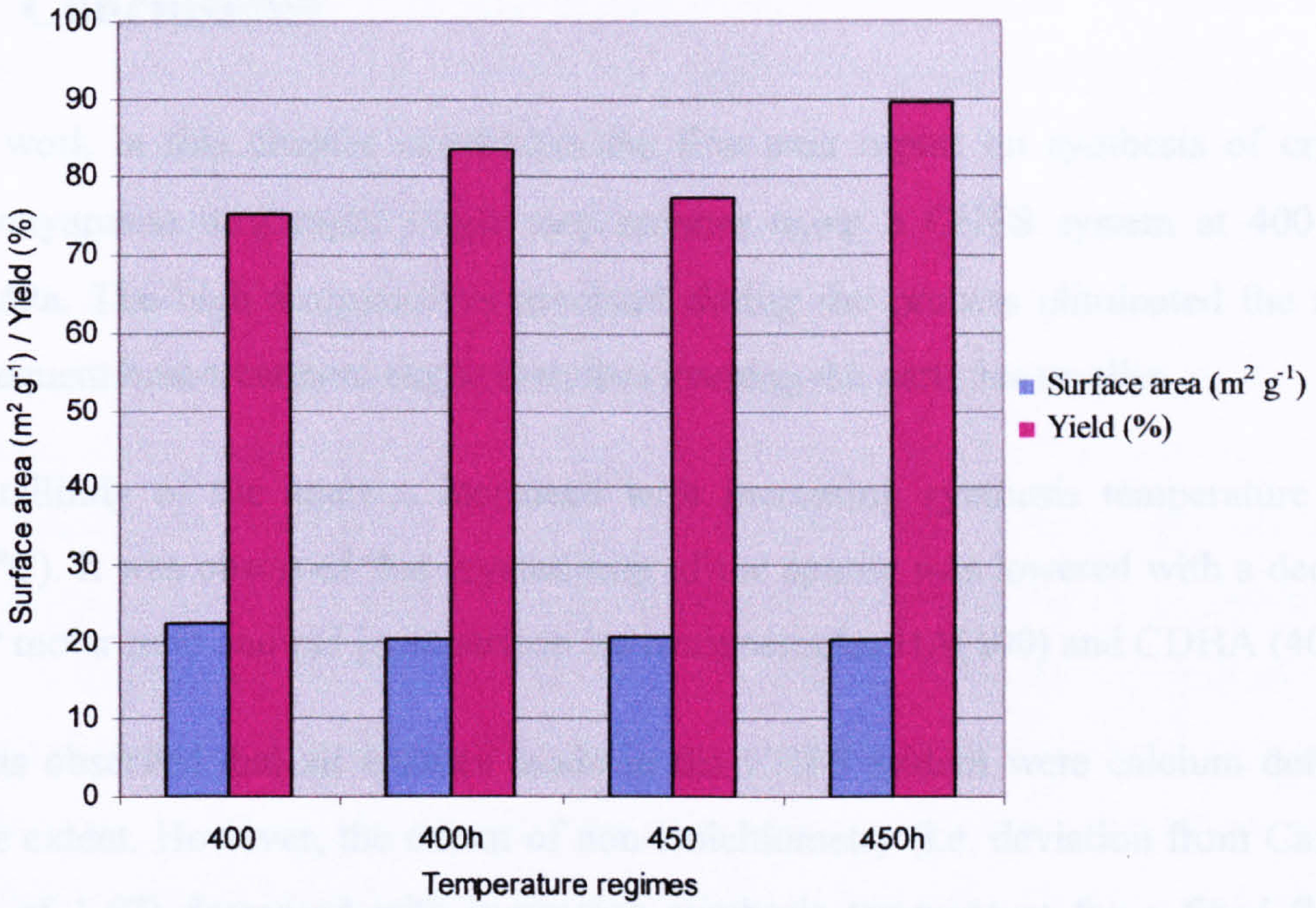

Figure 3-11 Effect of different temperature regimes on ■ surface area (m^2 g^{-1}) and ■ Yield (%) for a fixed *fast* flow rate. The letter "h" represents the use of a mixing point heater set at the same temperature the heater was set at.

Table 3-3 Different temperature regimes, flow rates and corresponding mixing point temperatures of CHFS system 3 measured using a k-type thermocouple attached to a Pico temperature recorder interfaced with a PC (shown in Figure 2-14 in Chapter 2).

Temperature regime	**Flow rate**	**Mixing point temperature (°C)**
400	*slow*	251
	medium	257
	fast	261
400h	*fast*	285
450	*fast*	290
450h	*slow*	293
	medium	303
	fast	308

3.4 Conclusions

The work in this chapter constitutes the first ever report on synthesis of crystalline hydroxyapatite in a rapid single step manner using a CHFS system at 400 °C and 24 MPa. The high temperatures involved during the process eliminated the need for subsequent heat-treatment steps; therefore keeping the particles smaller.

Crystallinity of the apatites increased with increasing synthesis temperature (200 to 400 °C). It was observed that crystallinity of the apatite was lowered with a decrease in Ca:P molar ratio and pH [comparison between samples HA(400) and CDHA (400)].

It was observed that all apatites made in the CHFS system were calcium deficient to some extent. However, the extent of non-stoichiometry (i.e. deviation from Ca:P molar ratio of 1.67) decreased with increasing synthesis temperature for a fixed flow rate. Sample HA(200) had an average Ca:P molar ratio of *ca.* 1.52 as compared to *ca.* 1.57 for sample HA(400). This increase made the corresponding apatite more thermally stable; the phase transformation of calcium deficient hydroxyapatite into β-TCP and stoichiometric HA could not be observed in corresponding TGA and DSC plots.

For similar concentrations and pH (Ca:P molar ratio of *ca.* 1.67, pH 10) sample 1.67-B synthesised at *450h* temperature regime at a *fast* flow rate was more calcium deficient (Ca:P molar ratio of *ca.* 1.51) as compared to sample HA(400) (Ca:P molar ratio of *ca.* 1.57) which was made at *400* temperature regime at a *slow* flow rate. It was initially thought that the Ca:P molar ratio would increase due to more intense heating, as seen for samples HA(200) and HA(400). However, this result suggested that increase in flow rate results in a lower Ca:P molar ratio possibly due to a small residence time; the time the precipitating suspension spends in the mixing zone prior to passing through the cooler.

It was observed that samples synthesised at pH 10 with Ca:P molar ratios of *ca.* 1.67 and 2.0 resulted in minimal or no phase transformation at *ca.* 750 °C. All other samples whether made at acidic or basic pH, resulted in this phase transformation. It is concluded that in the CHFS system, pH was the dominating factor for attaining more thermally stable apatites (up to *ca.* 1050 °C).

Variation in flow rates and temperature regimes gave minimal or no variation in surface areas of the crystallising apatites and their yields (%).

The CHFS system has been reported previously for synthesis of various materials. However, this report work was the first report of exploitation of this technique to synthesise calcium phosphate based bioceramics. The results show that CHFS technology is very promising for calcium phosphates as it can allow rapid and effective control of synthesis temperature, variation in flow rates and synthesis pH; all factors which effect resulting composition, particle size, stoichiometry and thermal stability. Based on these encouraging results, it was evident that the CHFS systems may be of use synthesising ion-substituted calcium phosphates and calcium phosphate based composite powders. Biological apatite differs from synthetic HA as it contains various ionic substitutions and there have been reports in literature on improvement of biocompatibility of HA after ionic substitutions. Furthermore, use of HA in load bearing applications is limited due to its poor mechanical properties. A method which can facilitate synthesis of intimately mixed composite mixtures for enhanced mechanical performance is very desirable. These endeavours are reported in following chapters. Part of this work was published in Chemical Communications, Issue 21, 2006, titled "Instant Nano-Hydroxyapatite: A Continuous and Rapid Hydrothermal Synthesis".

3.5 Future Work

Since the solution pH was determined to be the dominating factor in the resultant apatitic stoichiometry it would be interesting to use different bases (NaOH, KOH) for pH adjustment of solutions while being careful about sodium or potassium substitutions in the HA lattice.

Different residences times (due to varying flow rates) affected the thermal stability of the resulting HA phases. It would be interesting to modify the mixing zone of the CHFS systems to consist of a longer mixing zone. The length of this zone could then be correlated to the resultant stoichiometry in HA. This may result in a larger particle size which may be count acted by carrying out reactions at lower temperatures.

Chapter 4

Synthesis and Characterisation of Carbonate and Silicate Substituted Calcium Phosphates

4.1 Introduction

As mentioned in Chapter 1, synthetic hydroxyapatite [HA, $Ca_{10}(PO_4)_6(OH)_2$, Ca:P molar ratio 1.67], is a bioactive material that is chemically similar to biological apatite, the mineral component of bone (Porter et al. 2004). However, biological apatite is a poorly crystalline, non-stoichiometric material (Ca:P molar ratio < 1.67) that contains additional ions in the structure (Na^+, SiO_4^{4-}, CO_3^{2-}, Zn^{2+}, Mg^{2+} etc.) (Barralet et al. 2003; LeGeros 2002; Leventouri 2006; Webster et al. 2004; Wopenka & Pasteris 2005).

Human bone contains up to 8 wt% carbonate ions that occupy phosphate and hydroxide positions in the apatite lattice (Barralet et al. 1998). It has been shown that the presence of carbonate in synthetic HA leads to structural disorder and a higher solubility (Barralet et al. 1998; Barralet et al. 2000). This is useful because although HA can bond to surrounding tissue, this process is very slow (Ito et al. 1997; Landi et al. 2003). Carbonate substituted hydroxyapatite is therefore, considered as an optimised biomaterial, which leads to faster bonding between an inserted implant and human bone (Ito et al. 1997; Landi et al. 2003; Murugan & Ramakrishna 2006; Porter et al. 2005; Tang et al. 2003).

Substitution of carbonate ions in the HA lattice can be of two types, A-type, where carbonate ion substitutes the hydroxyl ion and B-type, where the carbonate ion substitutes the phosphate ion (Barralet et al. 1998; Barralet et al. 2000; Elliott 1994; Gibson & Bonfield 2002; Landi et al. 2003). A-type carbonated hydroxyapatite can be formed when carbon dioxide gas is passed over HA at high temperature in the range 500 – 1100 °C (Barralet et al. 1998; Barralet et al. 2000). This substitution reaction can be represented as follows (Elliott 1994);

$$Ca_{10}(PO_4)_6(OH)_2 + xCO_2 \rightarrow Ca_{10}(PO_4)_6(OH)_{2-2x}(CO_3)_x + xH_2O \qquad \textbf{Eq. 4-1}$$

B-type carbonated HA can be formed by precipitation from solution and can result in a material with lower particle crystallinity and smaller crystal size (Barralet et al. 1998; Barralet et al. 2000). B-type carbonate substitution is more complicated than A-type carbonate substitution into HA. Carbonate ions (CO_3^{2-}) substituting for phosphate ions (PO_4^{3-}) require a reduction in the number of calcium ions to maintain charge balance. Kühl and Nebergall in 1963 proposed the following formula for B-type carbonate substituted HA (Kuhl & Nebergall 1963);

$$Ca_{10-x+y}(CO_3)_x(PO_4)_{6-x}(OH)_{2-x+2y} \qquad \textbf{Eq. 4-2}$$

Sodium ions (Na^+) can partially substitute calcium ions (Ca^{2+}) in HA leading to stabilisation of a B-type carbonate substituted HA (Gibson & Bonfield 2002; Nelson & Featherstone 1982). This substitution leads to $Ca_{10-x}Na_x(PO_4)_{6-x}(CO_3)_x(OH)_2$. The charge balance can be represented as follows;

$$Na^+ + CO_3^{2-} \leftrightarrow Ca^{2+} + PO_4^{3-} \qquad \textbf{Eq. 4-3}$$

In reports by Vignoles et. al. and Doie et. al. ammonium carbonate was used as a carbonate source, in order to avoid using a sodium based source (Doi et al. 1982; Vignoles et al. 1987). However, this resulted in incorporation of ammonium ions (NH_4^+) in the HA lattice. Absorption bands corresponding to the ammonium ion (NH_4^+) have been reported to appear at 3200 and 1400 cm^{-1} in FTIR spectra (Okada et al. 2003). Gibson et. al. later reported synthesis of carbonate substituted hydroxyapatite using carbonated water which avoided incorporation of unwanted ions in the HA lattice (Gibson & Bonfield 2002).

Carbonate substituted hydroxyapatite has also been synthesised at 140 °C in 24 hours under autogenous pressure using a batch hydrothermal process with urea as a carbonate source (Mizutani et al. 2005). Hydrothermal treatment has also been used to form carbonate substituted hydroxyapatite coatings using plasma spray coated brushite as a precursor material (Han et al. 2002).

In addition to calcium phosphates, calcium carbonate is also a known biocompatible material (Redey et al. 1999; Vuola et al. 1996; Vuola et al. 1998). Indeed, calcium carbonate implants have been studied, due to their relatively faster resorption, and therefore, quicker onset of neo bone formation. Three weeks after implantation 10.8 % bone formation was observed under microscope as compared to 4.8 % for HA implants inserted in muscular cavities of rats (Vuola et al. 1996; Vuola et al. 1998). Bone regeneration, around dental implants used in alveolar ridge treatment, has been reported after use of compositions which included calcium carbonate (Corrente et al. 1997). Stephen Mann's research group based at University of Bristol has reported extensively on morphological and phase control of calcium carbonate particles synthesised using microemulsions and its biological uses (Green et al. 2004; Thachepan et al. 2006). However, complete resorption of a porous bone substitute (before bone has filled the pores), is disadvantageous as a controlled replacement is preferred (Vuola et al. 1996). Hence, calcium carbonate and calcium phosphate mixtures are of interest as they may offer tailorable dissolution and regrowth rates. This way the defect is able to function or take a load whilst the repair process is underway.

Although HA is known to be bioactive and osteoconductive, it has a relatively slow rate of dissolution and osseointegration (Hench 1991). One of the methods to improve the osseointegration of HA is to substitute traces of elements such as silicon, in the HA lattice (Porter 2006). One of the earliest works on role of silicon in bone was reported in the 1970s by Carlisle, wherein the presence of 0.5 wt% silicon was reported in mineralising osteoid regions in young mice and rats (Carlisle 1970). Silicon has also been reported to play an important role in the formation of collagen (Carlisle 1982). Silicon substituted HA (Si-HA) has been reported to promote rapid bone mineralisation, however, it also leads to a smaller crystallite size and faster dissolution (Botelho et al. 2006; Patel et al. 2002; Porter et al. 2003; Thian et al. 2006b). Use of silicon substituted HA as sintered granules in femoral condyles of rabbits resulted in significantly greater bone formation (37.5 %) when compared (after 23 days of implantation) to the case where phase-pure HA (22.0 %) was used (Patel et al. 2002). Due to the importance attached to presence of silicon in calcifying regions of bone, attempts have been made to incorporate silicon in the HA lattice. Silicon substituted hydroxyapatite has been synthesised using wet-precipitation and batch hydrothermal techniques (Gibson et al. 1999; Hing et al. 2006; Kim et al. 2003; Leventouri et al. 2003; Tang et al. 2005a; Tang et al. 2005b). There have also been many reports on the development of silicon substituted HA coatings on metallic substrates for enhanced osseointegration (Thian et al. 2005a; Thian et al. 2005b; Thian et al. 2006a; Thian et al. 2006c; Thian et al. 2007). Silicon enters the HA lattice in the form of silicate ions (SiO_4^{4-}) which substitute for phosphate ions (PO_4^{3-}). Silicon levels of up to 4 wt% in HA have been reported using a batch hydrothermal process (Gibson et al. 2002; Tang et al. 2005b). This substitution can be represented as follows;

$$Ca_{10}(PO_4)_6(OH)_2 + xSiO_4^{4-} \rightarrow Ca_{10}(PO_4)_{6-x}(SiO_4)_x(OH)_{2-x} + xPO_4^{3-} + xOH^- \quad \textbf{Eq. 4-4}$$

As mentioned in the previous chapters, current methods for the synthesis of calcium phosphates (and ion substituted calcium phosphates) are rather slow and unpredictable. In my research, it postulated that the rapid crystallizing continuous environment in a CHFS system would result in one-step rapid formation of hydroxyapatite as explained in Chapter 3. In this chapter this processing method was used to incorporate carbonate and silicate ions into the HA lattice. The materials were characterised them using various analytical techniques (TEM, BET, XRD, Raman, FTIR, STA, NMR) to assess the effects of substitution.

4.2 Experimental

4.2.1 Carbonate Substituted Calcium Phosphates

In total five separate reactions were carried out for this study. Urea (carbonate ion source) was added to diammonium hydrogen phosphate to result in overall 50.0 mM concentration (adjusted pH 10). This solution was reacted with 83.5 mM calcium nitrate solution (adjusted pH 11). The pH of both the solutions was adjusted using neat ammonium hydroxide solution. It was assumed that carbonate enters the HA lattice according to; $Ca_{10}(PO_4)_{6-x}(CO_3)_x(OH)_2$, where in it was assumed that B-type carbonate substitution takes place. Samples are labelled as 7.5CO_3-HA, 11.5CO_3-HA, 15.7CO_3-HA, 20CO_3-HA and 24.6CO_3-HA. The numbers in the sample IDs represent the theoretically expected carbonate content (wt %). The preparation of solutions and other details are explained in section 2.2.2.2 (a) and Table 2-4.

CHFS system 2 (described in section 2.2.1.2) was used for these reactions with pump rates of 10.0, 5.0 and 5.0 mL min^{-1} for the superheated water feed, calcium nitrate and diammonium hydrogen phosphate/urea solutions, respectively. A Ca:[PO_4^{3-}+CO_3^{2-}] molar ratio of *ca.* 1.67 was hence maintained in all reagent solutions. All reactions were carried out using a superheated water feed at 400 °C and 24 MPa. All samples were centrifuged, washed and freeze-dried as explained earlier; see section 2.2.2.1 (b).

4.2.2 Silicate Substituted Calcium Phosphates

In total eight reactions were carried out for this study. Silicon acetate was used as a silicate ion source and was dissolved in 83.5 mM calcium nitrate (pH 3.5). The diammonium hydrogen phosphate solutions were prepared such that the combined concentration of silicate and phosphate ions was 50.0 mM. The pH of diammonium hydrogen phosphate solution was adjusted to pH 10 using neat ammonium hydroxide solution. The pH of the calcium nitrate solution (which contained dissolved silicon acetate) was not adjusted as it was observed that it reacted with ammonium hydroxide to result in a dilute suspension. It was assumed that silicate replaces phosphate in the HA lattice according to; $Ca_{10}(PO_4)_{6-x}(SiO_4)_x(OH)_{2-x}$. Samples are labelled as 1SiHA, 2SiHA, 3SiHA, 4SiHA, 5SiHA, 6SiHA, 8SiHA and 10SiHA. The numbers in the samples IDs represent the theoretically expected amount of silicon content (wt %). Solution preparation and other details are explained in section 2.2.2.2 (b) and Table 2-5.

CHFS system 3 (described in section 2.2.1.3) was used for these reactions and pump rates of 10.0, 5.0 and 5.0 mL min^{-1} were used for superheated water feed, calcium nitrate/silicon acetate and diammonium hydrogen phosphate solutions, respectively. A $Ca:[PO_4^{3-}+SiO_4^{4-}]$ molar ratio of *ca.* 1.67 was hence maintained in all reactions. All reactions were carried out using a superheated water feed at 400 °C and 24 MPa. All samples were centrifuged, washed and freeze-dried as explained earlier in section 2.2.2.1 (b).

4.3 Results and Discussion

4.3.1 Transmission Electron Microscopy

Transmission electron microscopy was carried out to determine particle size and morphology. Figure 4-1 (a) for sample 7.5CO_3-HA shows rods of size *ca.* 146 (± 77) x 50 (± 18) nm (aspect ratio *ca.* 2.92, 50 particles sampled). Deviation from strict rod-like shape of particles of HA as reported in the previous Chapter 3, was evident (Chaudhry et al. 2006). The particle size was further reduced with increasing carbonate content, from *ca.* 109 (± 34) x 41 (± 10) nm in Figure 4-1 (b) for sample 15.7CO_3-HA (aspect ratio *ca.* 2.7, 50 particles sampled) to *ca.* 64 (± 34) x 27 (± 8) nm in Figure 4-1 (c) for sample 24.6CO_3-HA (aspect ratio *ca.* 2.4, 50 particles sampled). The cube-like morphology of some particles in Figure 4-1 (c) was similar to that of calcium carbonate (calcite) as reported in a previous TEM investigation (Wang et al. 2006).

Transmission electron microscopy was also carried out to assess the effect of silicon substitution in HA on particle morphology and size. Figures 4-2 (a) and (b) show TEM images of HA (reported in section 3.3.1.1 in Chapter 3, *ca.* 140 (± 58) x 40 (± 12), aspect ratio 3.5) and sample 5SiHA (*ca.* 184 (± 28) x 41 (± 7) nm, aspect ratio 4.4, 50 particles sampled), respectively. It was observed that the presence of silicon slightly increased the particle size (aspect ratio changes from *ca.* 3.5 to 4.4), narrows the size distribution (lower standard deviations) as compared to HA and makes the nanorods less defined on its growing edges. The TEM investigation suggested opposite effects of presence of carbonate ions as compared to that of silicate ions in solution on particle size and morphology.

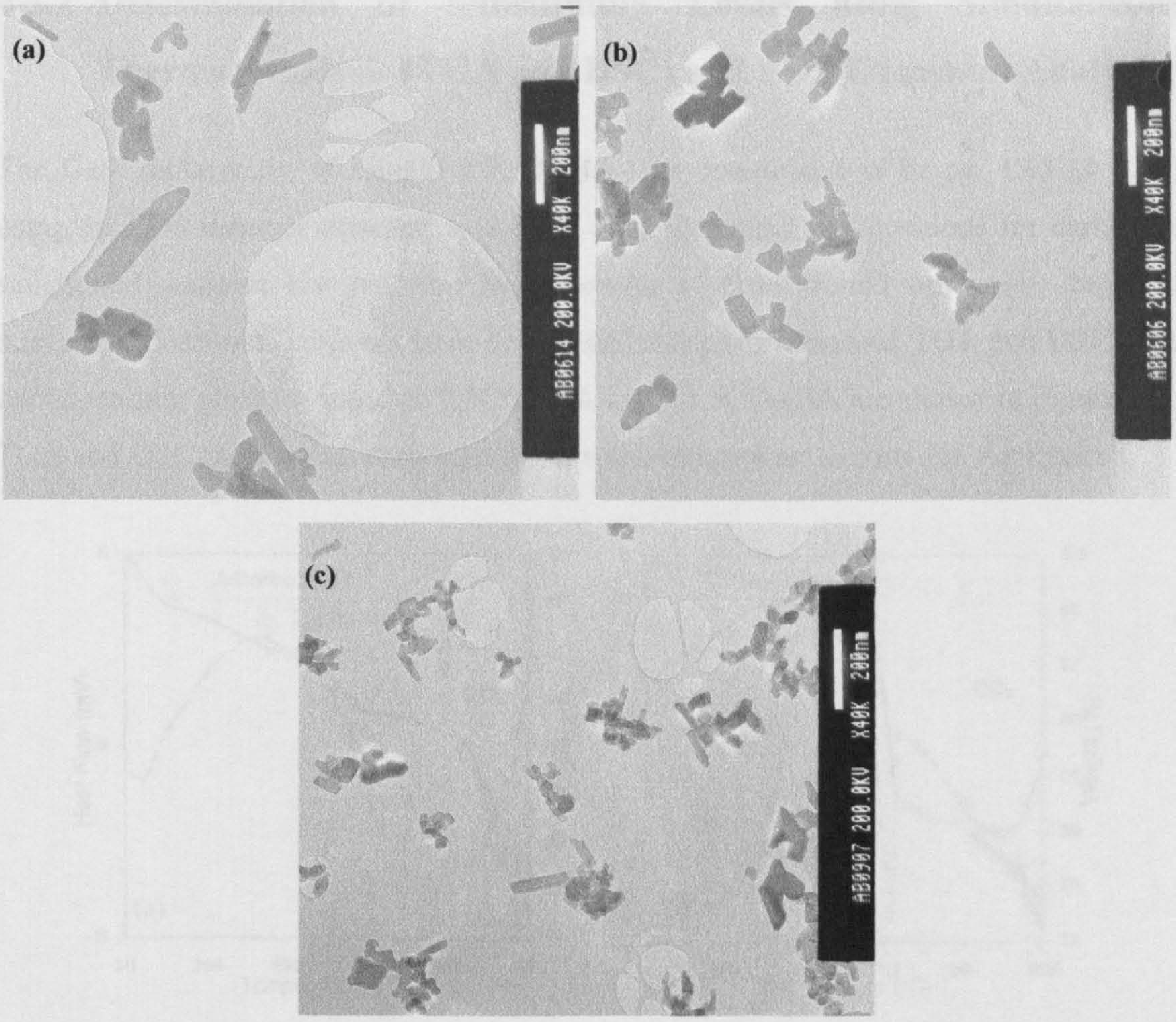

Figure 4-1 Transmission electron microscope images of (a) sample 7.5CO_3-HA at x40k magnification [bar = 200 nm] (b) sample 15.7CO_3-HA at x40k magnification [bar = 200 nm] and (c) sample 24.6CO_3-HA at x40k magnification [bar = 200 nm].

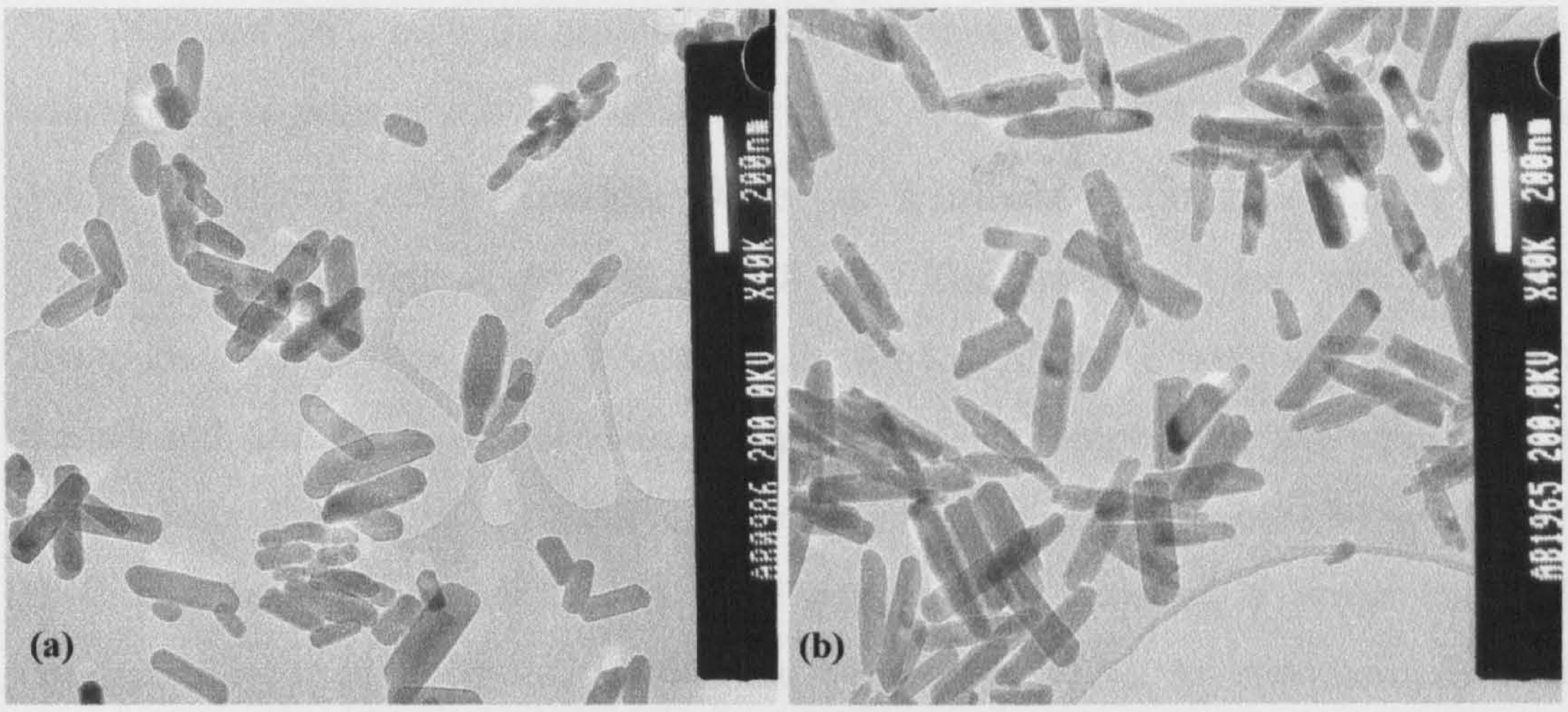

Figure 4-2 Transmission electron microscope images of (a) HA at x40k magnification [bar = 200 nm] and (b) 5SiHA at x40k magnification [bar = 200 nm].

4.3.2 Determination of Substitution Levels using Simultaneous Thermal Analysis (TGA and DSC) and EDS Elemental Analysis

The Ca:P molar ratio of sample 7.5CO_3-HA was determined to be *ca.* 1.45 (± 0.04) using an EDS detector attached to a SEM. The elemental compositions for carbonate substituted samples are reported in Appendix C (later found out to be biphasic mixtures). Carbonate contents were determined using simultaneous TGA and DSC. The corresponding plots for samples 7.5CO_3-HA and 24.6CO_3-HA are shown in Figure 4-3. TGA and DSC plots for all carbonate substituted samples are reported in Appendix C.

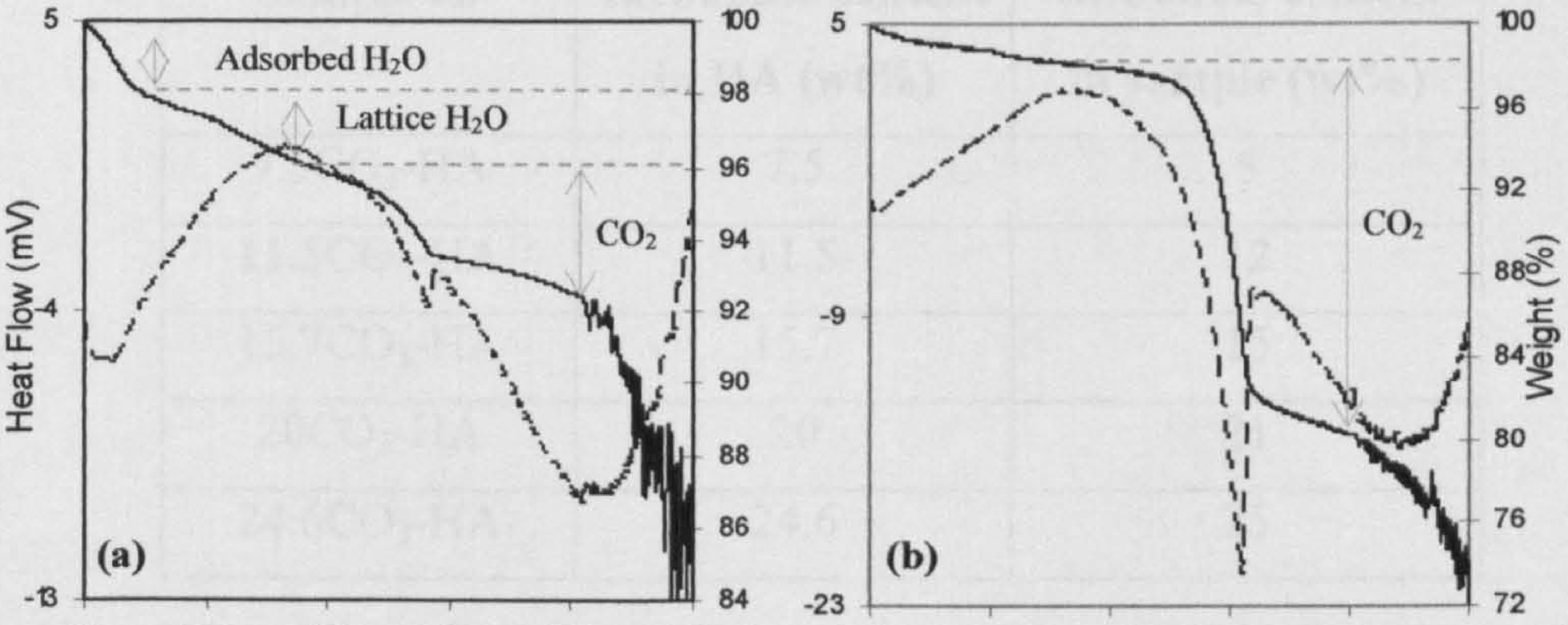

Figure 4-3 Simultaneous Thermal Analysis (STA) data showing DSC (dotted line) and TGA (solid line) plots for samples (a) 7.5CO_3-HA and (b) 24.6CO_3-HA.

The TGA and DSC plots for sample 7.5CO_3-HA shown in Figure 4-3 (a) showed three overlapping regions of weight loss at 30 - 200°C (2.2 wt%), 200 - 460°C (1.7 wt%) and 460 – 990°C (3.7 wt%). Thereafter there was a sudden weight loss (8.2 wt%) up to 1200°C to give a final weight loss of 15.8 wt%. The first weight loss was presumably due to loss of weakly associated water, whilst the loss of lattice water and CO_2 occur for the second and third weight losses respectively. Decomposition accounted for the weight loss after 990°C. The carbonate content was calculated to be around 5 wt%. DSC plot for sample 7.5CO_3-HA in Figure 4-3 (a) revealed a broad endotherm corresponding to loss of weakly associated water at *ca.* 70 °C. An endotherm centred at *ca.* 700 °C corresponded to the weight loss due to loss of CO_2 from sample 7.5CO_3-HA.

Figure 4-3 (b) shows TGA and DSC plots for sample 24.6CO_3-HA, which were similar to those for sample 7.5CO_3-HA [Figure 4-3 (a)]. However, the weight loss in the range 470 and 983 °C was 18 wt% (loss of CO_2). The carbonate content was calculated to be around 24.5 wt%. This CO_2 loss corresponds to carbonate loss from the apatite lattice and $CaCO_3$ (as determined using XRD, explained in the following sections). The expected carbonate contents in HA and measured carbonate contents are summarised in Table 4-1.

Table 4-1 Expected and measured carbonate content (determined using TGA) of carbonate substituted samples.

Sample ID	**Expected carbonate content in HA (wt%)**	**Measured carbonate content in sample (wt%)**
7.5CO_3-HA	7.5	5
11.5CO_3-HA	11.5	12
15.7CO_3-HA	15.7	15
20CO_3-HA	20	21
24.6CO_3-HA	24.6	25

An EDS detector (attached to a SEM) was also used to determine the elemental compositions of silicate substituted samples as mentioned in Appendix C. It was noticed that the obtained silicon contents (see Table 4-2) were markedly less compared to expected content unlike for carbonate substitution. Moreover, the percentage theoretical yield in the CHFS system decreased with increasing silicon content in the solution. This suggested that there was a threshold for silicon substitution into HA using CHFS technique (using current parameters) with silicon acetate as a silicate ion source.

Table 4-2 Silicon content (as an average of 10 area scans on EDS) and corresponding yields.

Sample ID	Expected silicon content in HA (wt%)	Silicon content in sample (wt%)	Yield (%)
1SiHA	1	0.26	77
2SiHA	2	0.39	76
3SiHA	3	0.56	75
4SiHA	4	0.53	56
5SiHA	5	0.81	48
6SiHA	6	0.63	50
8SiHA	8	0.93	41
10SiHA	10	1.05	30

4.3.3 BET Surface Area Analysis

BET surface areas were measured for samples in this study using multipoint BET surface area analysis. Figure 4-4 shows the variation in surface areas with increasing carbonate content (determined using TGA) for carbonate substituted samples. There was little or no change in surface area with increase in urea content with all the surface areas falling in the range 20.8 – 27.5 m^2 g^{-1}. Although the TEM images in Figures 4-1 (a) to (c) revealed decreasing crystallite size with increase in urea in solution, it was also observed that the particles appeared to be more agglomerated and less distinct [Figure 4-1 (c)]. This might account for the slight decrease in surface area witnessed for samples 20CO_3-HA and 24.6CO_3-HA.

Figure 4-4 also shows the variation in surface areas with silicon content in silicate substituted samples. It was observed that the surface area increases slightly for sample 2SiHA (41 m^2 g^{-1}) but overall remains relatively unchanged in the range 31.1 – 35.4 m^2 g^{-1}. This result suggested that the amount of silicon substituting into hydroxyapatite was not too different for all samples. Indeed, this was confirmed by elemental analysis shown in Table 4-2.

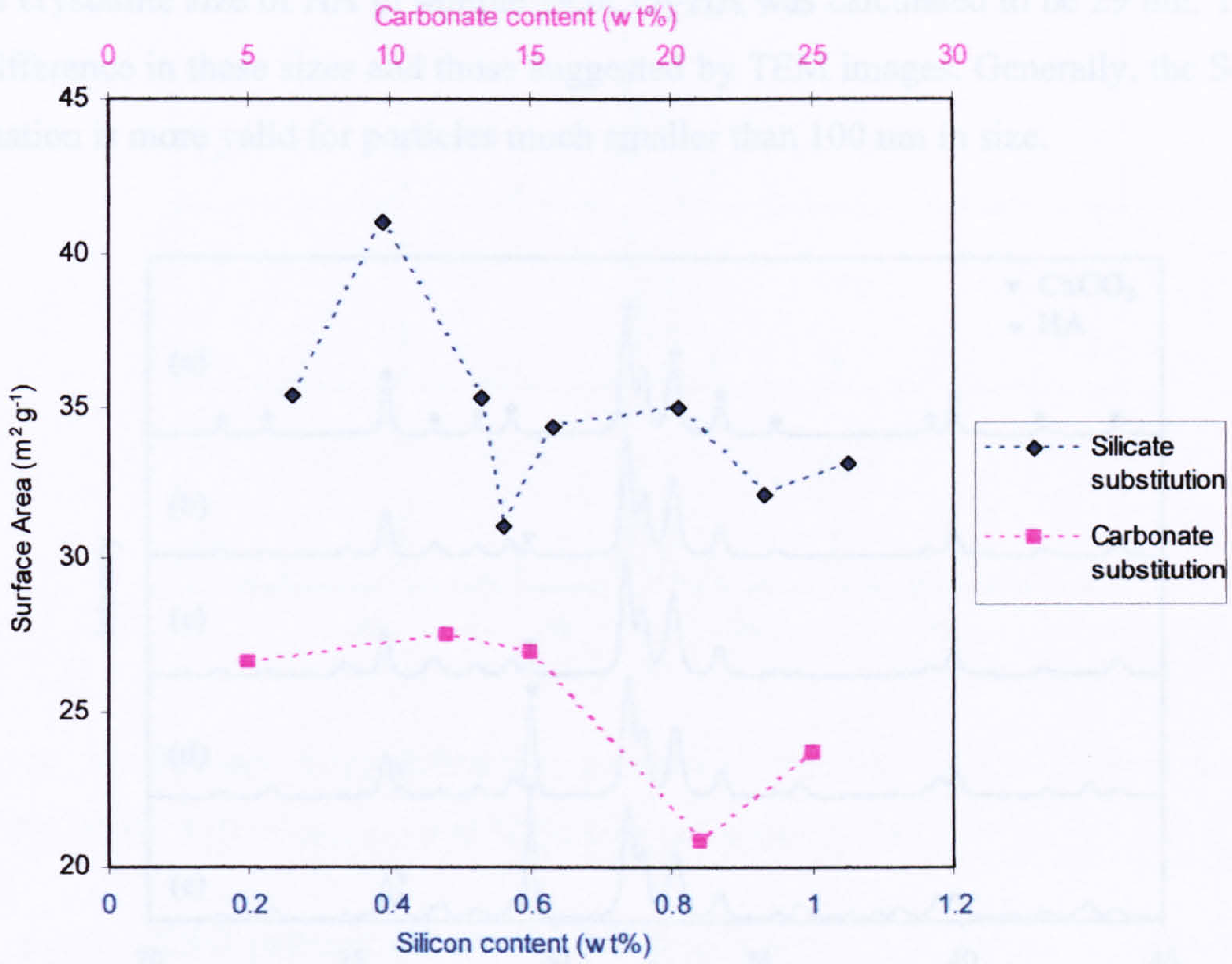

Figure 4-4 BET surface area of carbonate and silicate substituted samples as function of substitution levels.

4.3.4 Powder X-ray Diffraction

Powder X-ray diffraction data was collected for all samples in order to analyse the effect of carbonate and silicate substitution on crystallinity and phase-purity. XRD pattern for sample 7.5CO_3-HA in Figure 4-5 (a) gave a good match to line pattern for phase-pure hydroxyapatite [JCPDS pattern 09-0432]. XRD pattern in Figure 4-5 (b) shows the on-set of formation of calcium carbonate [compared to JCPDS pattern 47-1473, calcite] in sample 11.5CO_3-HA. With increasing carbonate content, it was seen in Figure 4-5 (c) (for sample 15.7CO_3-HA) and Figure 4-5 (d) (for sample 20CO_3-HA) that the peaks corresponding to calcium carbonate (calcite) increased in intensity. Peaks at 31.8° and 32.2°, corresponding to HA, became broader with increasing carbonate content, the peaks in Figure 4-5 (e) for sample 24.6CO_3-HA being clearly less distinct as compared to Figure 4-5 (a) for sample 7.5CO_3-HA. This was possibly due to decrease in particle size (as seen in TEM images) and crystallinity. Application of the Scherrer equation to the (002) peak in the corresponding XRD patterns suggested a crystallite size of 33 nm for sample 7.5CO_3-HA. A crystallite size of 32 nm was calculated for HA in the biphasic samples 11.5CO_3-HA, 15.7CO_3-HA and 20CO_3-HA.

The crystallite size of HA in sample 24.6CO_3-HA was calculated to be 29 nm. There is a difference in these sizes and those suggested by TEM images. Generally, the Scherrer equation is more valid for particles much smaller than 100 nm in size.

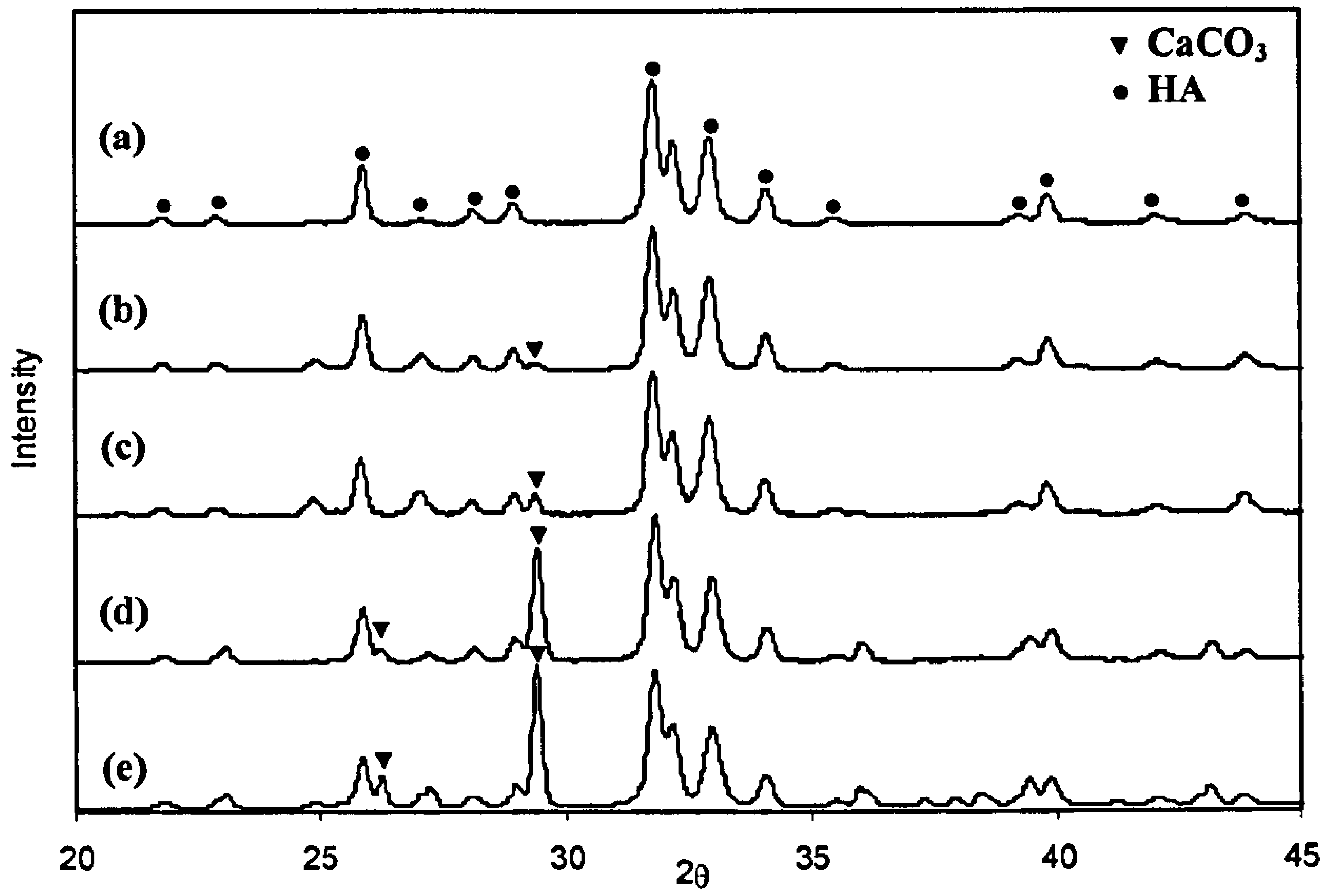

Figure 4-5 Powder X-ray diffraction patterns of samples (a) 7.5CO_3-HA (b) 11.5CO_3-HA (c) 15.7CO_3-HA (d) 20CO_3-HA and (e) 24.6CO_3-HA.

Figure 4-6 shows the powder XRD patterns of sample 7.5CO_3-HA heat treated at 730 °C, 850 °C and 990 °C. These temperatures were chosen from the corresponding TGA plot of the same sample. As compared to Figure 4-5 (a) peaks corresponding to HA in Figure 4-6 were understandably sharper (due to crystallisation upon heating). Heat treatment at 730 °C resulted in phase-pure crystalline HA [Figure 4-6 (a)]. This confirmed that the corresponding weight loss in the TGA plot shown in Figure 4-3 (a) was not due to any thermal decomposition and correctly represented CO_2 loss. However, heat treatment at 850 °C and 990 °C resulted in appearance of a small peak of calcium oxide (compared to JCPDS pattern 37-1497). This was due to thermal decomposition of calcium deficient HA lattice for sample 7.5CO_3-HA.

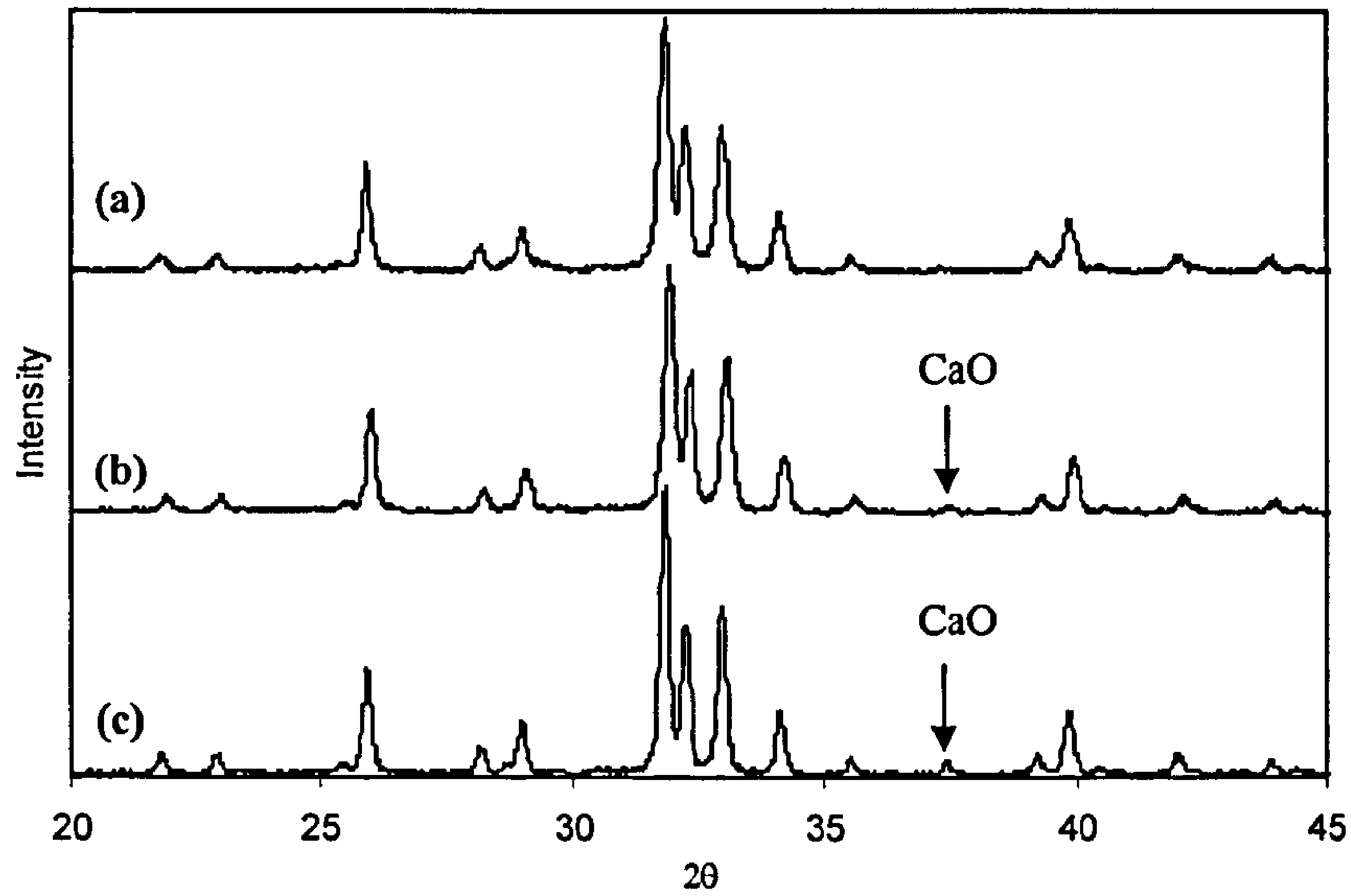

Figure 4-6 Powder X-ray diffraction patterns of sample 7.5CO_3-HA heat treated at (a) 730 °C (b) 850 °C and (c) 990 °C [unmarked peaks = HA].

All powder XRD patterns for silicate substituted samples in Figure 4-7 gave a good match to JCPDS pattern 09-432, corresponding to crystalline hydroxyapatite. Figures 4-7 (a) to (h) revealed no visible effect of increasing silicon content on phase-purity or crystallinity of the HA phase. This result and the decrease in percentage yield from 77% (for sample 1SiHA) to 33% (for sample 10SiHA) suggested that the progressive addition of the silicate precursor gave increasingly lower yields and reached a maximum substitution level under such CHFS conditions used herein. The main crystallographic planes (hkl) are also marked on the corresponding peaks in Figure 4-7.

Seemingly sample 7.5CO_3-HA and 1SiHA are very similar as they both gave a good match to JCPDS patter 09-432 which corresponds to phase-pure crystalline HA. However, there are some differences in peak intensities. In the XRD pattern for sample 7.5CO_3-HA the peaks corresponding to (002), (211) and (300) planes appeared at 25.8°, 31.8° and 32.9° respectively. The ratio of the intensities of peaks corresponding to (211) and (002) planes (I_{211} / I_{002}) was calculated to be 2.7. Similarly I_{300} / I_{002} for sample 7.5CO_3-HA was calculated to be 1.6. For sample 1SiHA I_{211} / I_{002} and I_{300} / I_{002} were calculated to be 1.2 and 0.8, considerably smaller than those observed for the carbonate substituted sample. Decrease in these ratios suggested an increase in the aspect ratio of the particles. This hypothesis is supported by the TEM images in Figures 4-1 and 4-2. The (002) and (300) peaks in XRD patterns are good representatives of the aspect ratio of rod-like HA particles (Guo et al. 2005).

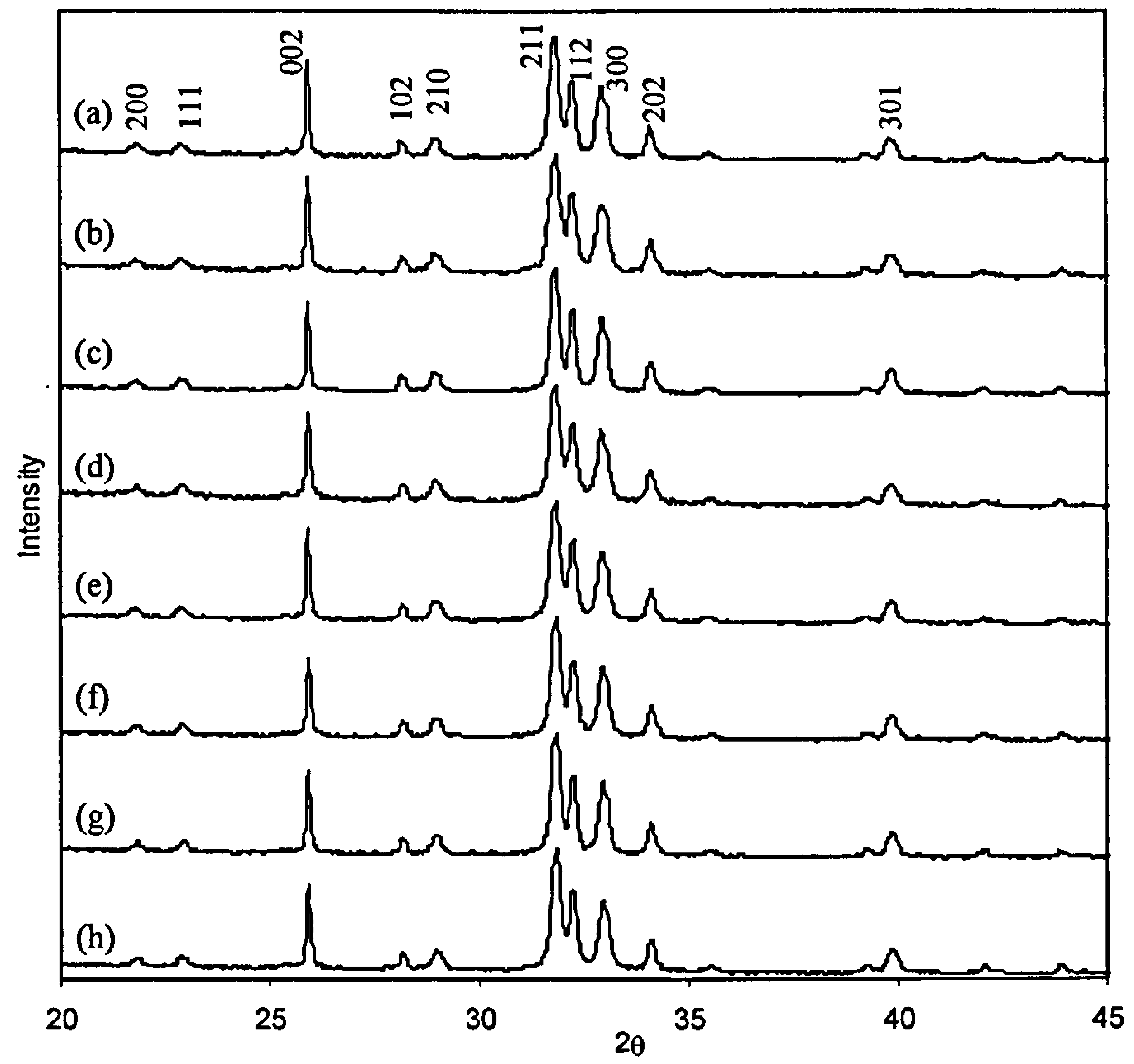

Figure 4-7 Powder X-ray diffraction patterns for samples (a) 1SiHA (b) 2SiHA (c) 3SiHA (d) 4SiHA (e) 5SiHA (f) 6SiHA (g) 7SiHA and (h) 8SiHA.

4.3.5 Raman Spectroscopy

Raman spectroscopy was carried out in order to reinforce crystallographic observations and assess phase purity. Figure 4-8 shows Raman spectra for all the carbonate substituted samples. In Figure 4-8 (a) for sample 7.5CO$_3$-HA the very weak peak at 1090 cm^{-1} corresponded to asymmetric stretching (ν_1) of the C-O bond in carbonate from calcium carbonate (calcite) (Gunasekaran et al. 2006). However, this was not observed in the corresponding XRD pattern, shown in Figure 4-5 (a). This suggested that this peak might be due to asymmetric stretching (ν_3) of the P-O bond in phosphate. The increase in the intensity of peak at 1090 cm^{-1} in Figures 4-8 (a) to (e) was due to an increase in calcium carbonate content, as confirmed by analogous XRD data. Peaks at 1072 cm^{-1} and 1048 cm^{-1} corresponded to asymmetric stretching (υ_3) of the P-O bond in phosphate. The peak at 1072 cm^{-1} may also represent symmetric stretching (υ_1) of the C-O bond in carbonate (Awonusi et al. 2007; Penel et al. 1998). With an increase in carbonate content it was observed that the peak at 1072 cm^{-1} increased in intensity (for samples 7.5CO$_3$-HA, 11.5CO$_3$-HA and 15.7CO$_3$-HA in Figures 4-8 (a) to (c), respectively). This peak was partially obscured by the peak at 1090 cm^{-1} for samples 20CO$_3$-HA and 24.6CO$_3$-HA as shown in Figures 4-8 (d) and (e), respectively. In Figure 4-8 (a), peak at 961 cm^{-1} was due to the symmetric stretching mode (υ_1) of the P-O bond in phosphate, whilst peaks at 606 cm^{-1}, 593 cm^{-1} and 581 cm^{-1} corresponded to v_4 bending modes of the O-P-O linkage in phosphate. The peaks at 444 cm^{-1} and 435 cm^{-1} corresponded to v_2 bending modes of the O-P-O linkage in phosphate. The appearance of a weak peak at 712 cm^{-1} in Figures 4-8 (d) and (e) was possibly due to bending mode (υ_4) of the O-C-O linkage in carbonate from larger amounts of calcite present in samples 20CO$_3$-HA and 24.6CO$_3$-HA (Gunasekaran et al. 2006).

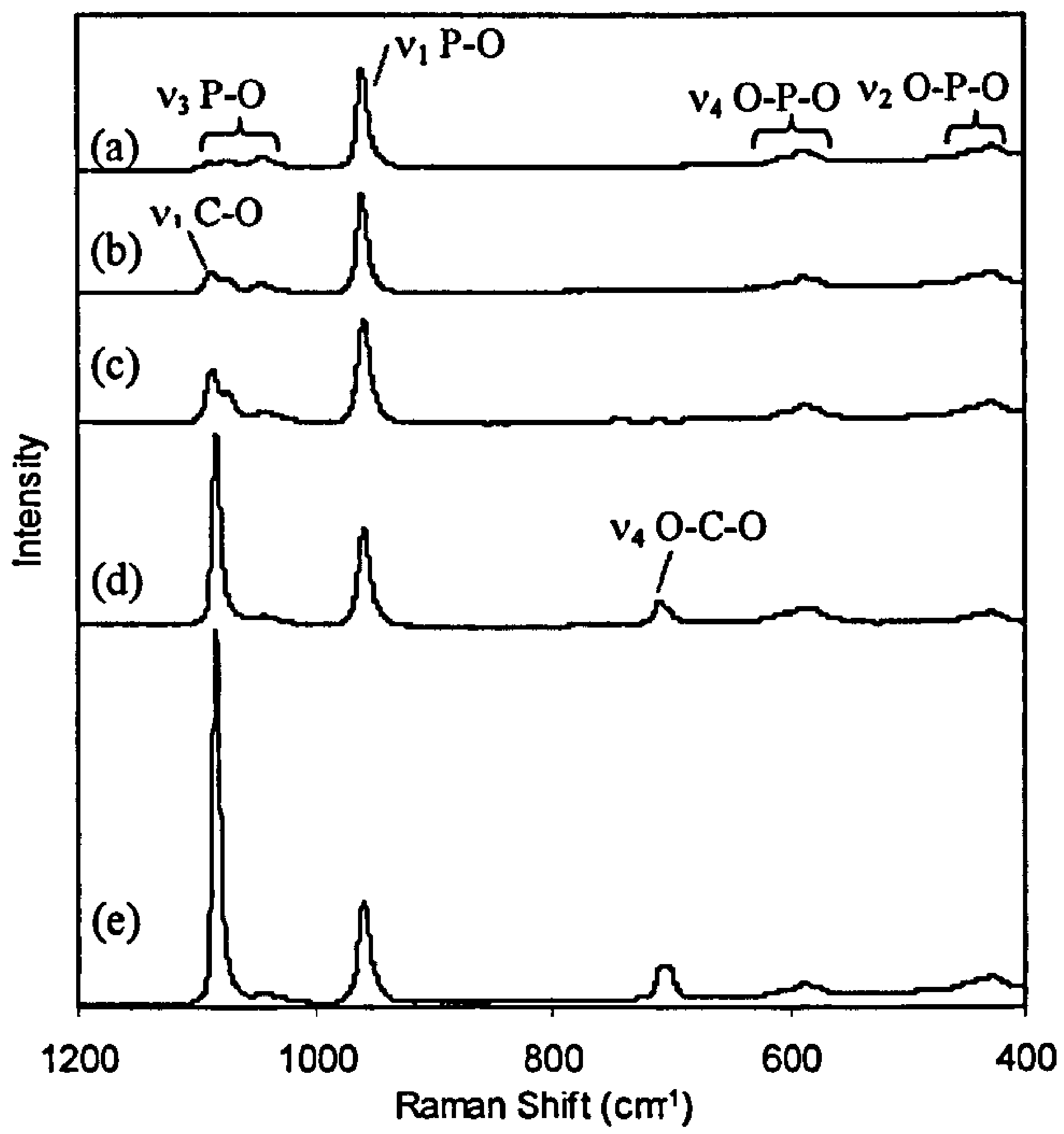

Figure 4-8 Raman spectroscopy data for the range 1200 – 400 cm^{-1} for samples (a) 7.5CO$_3$-HA (b) 11.5CO$_3$-HA (c) 15.7CO$_3$-HA (d) 20CO$_3$-HA and (e) 24.6CO$_3$-HA.

Raman spectra for all silicon substituted samples are shown in Figure 4-9. Figure 4-9 (a) showing the Raman spectrum for sample 1SiHA revealed peaks at 1080 cm^{-1} and 1049 cm^{-1} corresponding to asymmetric stretching (υ_3) of the P-O bond in phosphate. The peak around 960 cm^{-1} corresponded to the symmetric stretching mode (υ_1) of the P-O bond in phosphate. Peaks at 595 and 438 cm^{-1} corresponded to the υ_4 and υ_2 bending, respectively, of the O-P-O linkage in phosphate. No change was observed in Figures 4-9 (a) to (h) with increasing silicon content in solution.

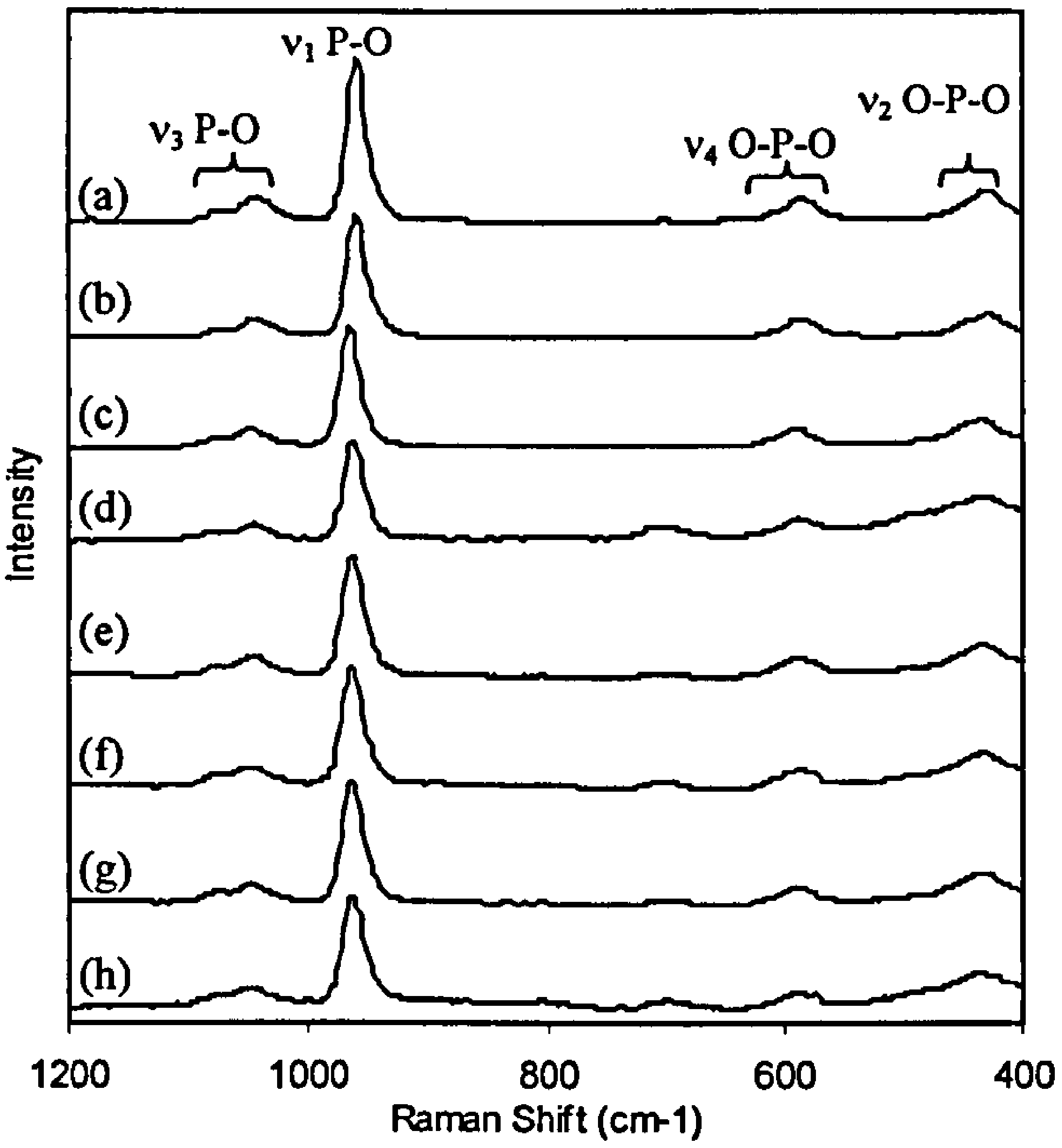

Figure 4-9 Raman spectroscopy data in the range 1200 – 400 cm^{-1} for samples (a) 1SiHA (b) 2SiHA (c) 3SiHA (d) 4SiHA (e) 5SiHA (f) 6SiHA (g) 8SiHA and (h) 10SiHA.

4.3.6 Fourier Transform Infrared Spectroscopy

FTIR spectroscopy was carried out on all carbonate and silicate substituted samples in order to compliment observations made using XRD and Raman spectroscopy. Figure 4-10 shows the FTIR spectra of the carbonate substituted samples. In Figure 4-10 (a) for sample 7.5CO$_3$-HA, peaks at 3570 and 633 cm^{-1} corresponded to stretching mode (v_s) and librational mode (υ_L) of the hydroxyl group in a hydroxyapatite lattice. The bands in the range 1590-1300 cm^{-1} corresponded to asymmetric stretching (v_3) of the C-O bond of carbonate in both A- and B-type carbonate substitutions in HA. However given the fact that CHFS is a wet chemical method, B-type carbonate substitution was expected (where carbonate ions are substituted for phosphate ions in the HA lattice). This is also supported by the observation that the peak at 3570 cm^{-1} did not diminish with an increase in urea concentration in the reagent solution suggesting that carbonate substitution for hydroxyl groups in the HA lattice does not take place. Comparison of the hydroxyl peak at 3570 cm^{-1} in Figure 4-10 (a) with the same peak in Figure 3-5 (a) for sample HA(400) revealed similar intensities suggesting that A-type substitution did not take place. With an increase in urea concentration there was an increase in the intensity of the bands in the range 1590-1300 cm^{-1}, corresponding to carbonate asymmetric stretching [Figures 4-10 (a) and (b)] corresponding to samples 7.5CO_3-HA and 11.5CO_3-HA, respectively. This may be due to increased carbonate substitution into the HA lattice and/or appearance of calcite. The band 1090-1030 cm^{-1} corresponded to asymmetric stretching modes (υ_3) of the P-O bond in phosphate. Peak at 961 cm^{-1} corresponded to the symmetric stretching mode (υ_1) of the P-O bonds of phosphate. In Figure 4-10 (a) the peak at 876 cm^{-1} corresponded to the bending mode (ν_2) of the O-C-O linkage in carbonate. This peak showed a marked increase in intensity with an increase in amount of urea concentration in solution as witnessed in Figures 4-10 (b) to (e). Peaks at 603 cm^{-1}, 568 cm^{-1} and 472 cm^{-1} in Figure 4-10 (a) corresponded to bending modes of O-P-O linkages in phosphate. From the FTIR data it was observed that the carbonate peaks (1590-1300 cm^{-1} and 876 cm^{-1}) reached their maximum intensity for 11.5CO_3-HA in Figure 4-10 (b). Any further increase in amount of urea concentration in reagent solutions contributed to more formation of calcium carbonate as seen in analogous XRD and Raman data. In Figure 4-10 (d), for sample 20CO_3-HA, a peak appeared at 1793 cm^{-1} which has been reported to be due to presence of calcite (Jackson 1998). Gunasekaran et. al. reported a peak at 1798 cm^{-1} for calcite and attributed it to a combination of asymmetric stretching (ν_1) and bending (ν_4) of bonds related to carbonate (Gunasekaran et al. 2006). Also, in the same spectrum, a shoulder appeared at 865 cm^{-1} which resolved into a peak for sample 24.6CO_3-HA in Figure 4-10 (e). This peak was attributed to the bending mode (ν_2) of the O-C-O linkage in carbonate from calcite (Gunasekaran et al. 2006). Peak at 713 cm^{-1} for samples 20CO_3-HA and 24.6CO_3-HA in Figures 4-10 (d) and (e) corresponded to bending mode (υ_4) of the O-C-O linkage in carbonate from calcite.

The FTIR spectrum for sample 1SiHA in Figure 4-11 (a) revealed peaks similar to those generally seen for hydroxyapatite; these include peaks at 3571 cm^{-1} and 633 cm^{-1} due to the stretching mode (υ_s) and the liberational mode (υ_L), respectively, of hydroxyl groups in HA. The weak band in the range 1565-1380 cm^{-1} corresponded to asymmetric stretching (ν_3) of the C-O bond of carbonate in both A- and B-type carbonate substitutions in HA. A band in the range 1180-980 cm^{-1}, corresponded to asymmetric P-O stretching (υ_3) of the phosphate group, whilst a peak at 964 cm^{-1} corresponded to symmetric P-O stretching (ν_1) of phosphate. The peaks at 602 and 563 cm^{-1} corresponded to the υ_4 bending mode, whilst the peak at 489 cm^{-1} corresponded to the υ_2 bending mode of the O-P-O linkage in phosphate. The weak peak centered at ca. 872 cm^{-1} was due to the bending mode (υ_2) of the O-C-O linkage in a small amount of carbonate which is present in HA. The OH$^-$ stretching peak at 3571 cm^{-1} decreased in intensity with increasing silicon substitution [Figures 4-11 (a) to (h)]. This confirmed that silicon was being substituted in the HA lattice in the form of silicate, SiO_4^{4-} substituting phosphate, PO_4^{3-}. In order to maintain the charge balance, OH^{-1} is lost, causing a decrease in intensity of the OH^{-1} peak at 3571 cm^{-1}. Furthermore, it was noticed that increasing silicon content increased the intensity of the carbonate band in the range 1560-1380 cm^{-1}. This was possibly due to easier incorporation of CO_3^{2-} in the already distorted lattice (due to SiO_4^{4-} incorporation and OH^{-1} loss). As we have reported earlier, the presence of carbonate peaks was unsurprising, as deionised water used in preparation of solutions and synthesis in the CHFS reactor was not degassed prior to use and may contain dissolved carbonate (Chaudhry et al. 2006).

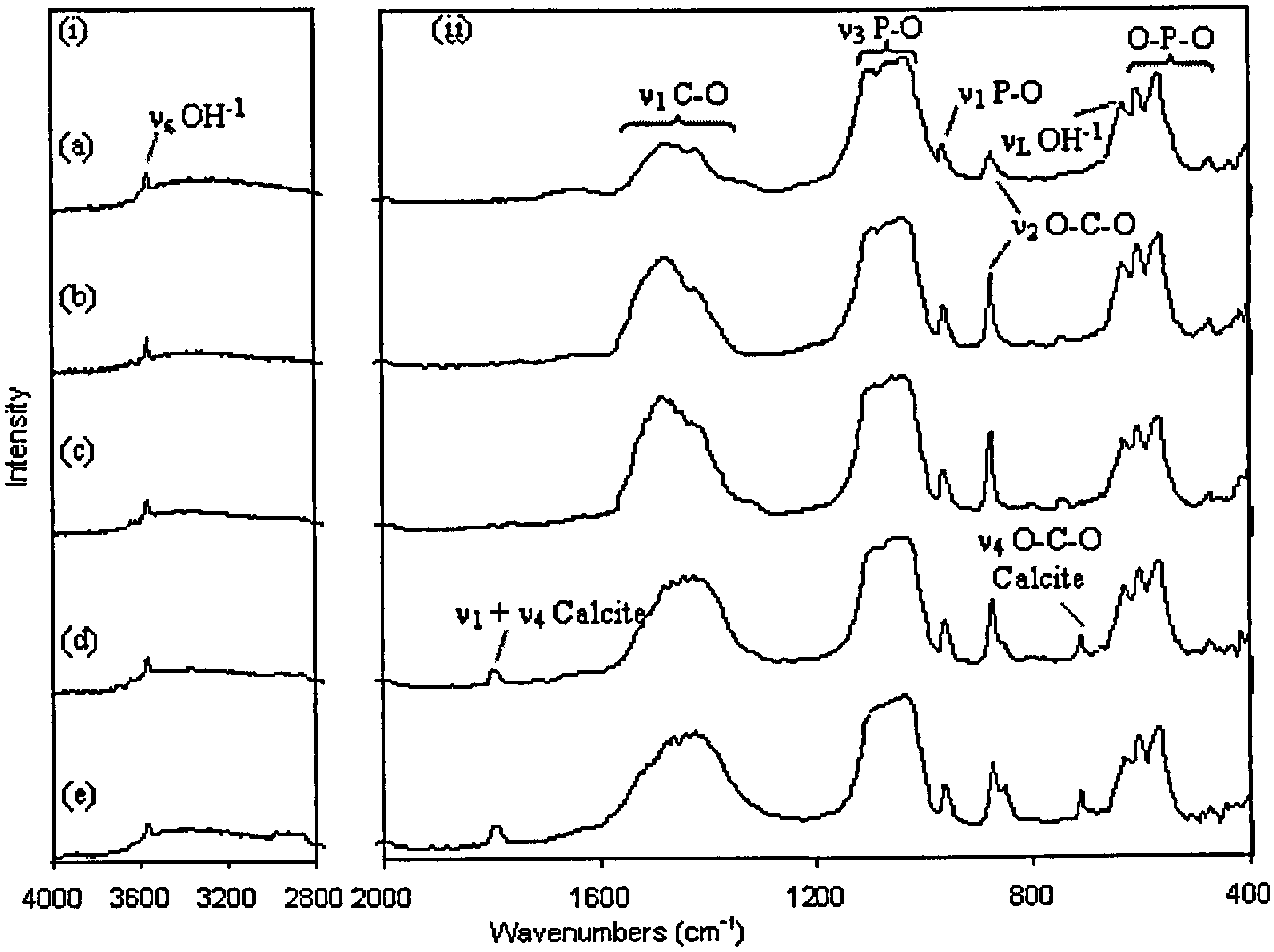

Figure 4-10 FTIR spectroscopy data for ranges (i) 4000 – 2800 cm^{-1} and (ii) 2000 – 400 cm^{-1} for samples (a) 7.5CO_3-HA (b) 11.5CO_3-HA (c) 15.7CO_3-HA (d) 20CO_3-HA and (e) 24.6CO_3-HA.

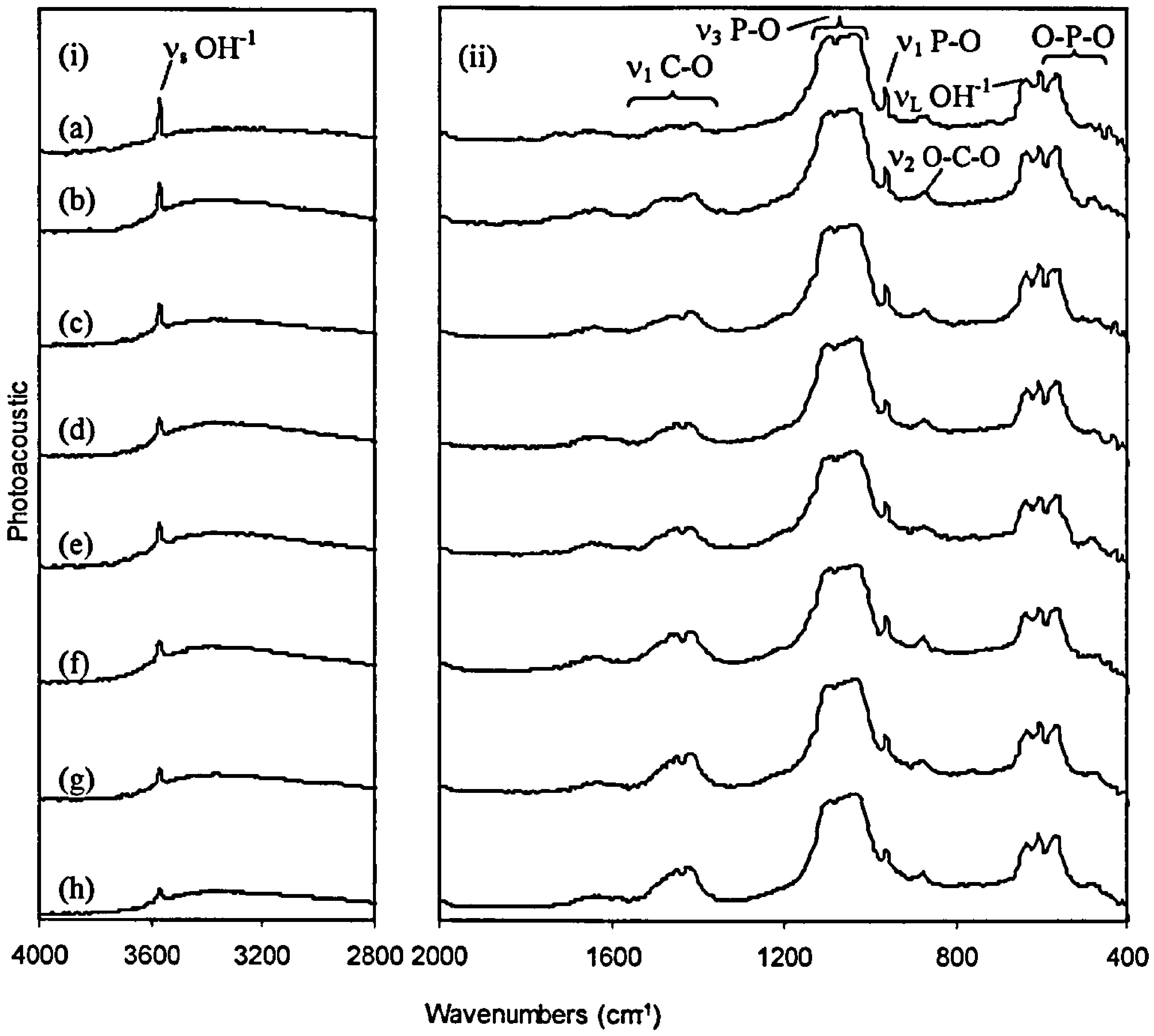

Figure 4-11 FTIR spectroscopy data for ranges (i) 4000 – 2800 cm^{-1} and (ii) 2000 – 400 cm^{-1} for samples (a) 1SiHA (b) 2SiHA (c) 3SiHA (d) 4SiHA (e) 5SiHA (f) 6SiHA (g) 8SiHA and (h) 10SiHA.

4.3.7 ^{29}Si MAS-NMR

^{29}Si MAS-NMR result for sample 5SiHA is shown in Figure 4-12. A range of environments were seen for silicon (-72.5, -91.1 and -99.2 ppm). The most intense peak at – 72.5 comes from the silicate, $Si(O^-)_4$ environment (Q^0) which corresponded to SiO_4^{4-} substituting PO_4^{3-} in the HA lattice wherein the silicon is not bonded to any other silicon. The peaks at -91.1 and 99.2 are possibly due to the Q^2 and Q^3 environments (Diaz et al. 2006). This suggested that silicon substituted in the HA synthesised in CHFS systems may be bonded in more ways than initially thought, i.e. the Q^0 environment (possibly due to non-stoichiometry).

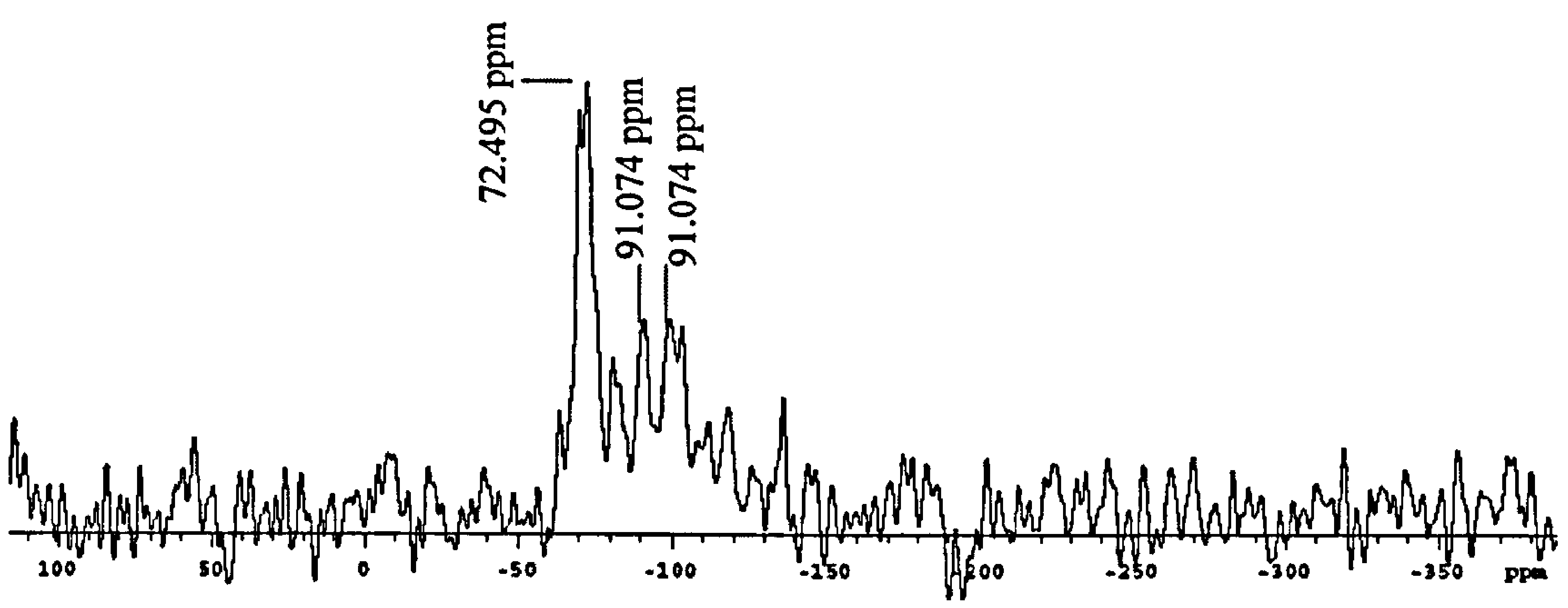

Figure 4-12 ^{29}Si magic angle spinning nuclear magnetic resonance data for sample 5SiHA.

4.4 Conclusions

Phase pure, crystalline and nano-sized carbonate substituted hydroxyapatite with *ca.* 5 wt% substituted carbonate content (sample 7.5CO$_3$-HA) was synthesised using the CHFS system using urea as a carbonate source. It was noticed that a further increase in urea concentration in solution resulted in biphasic mixtures of carbonate substituted hydroxyapatite and calcium carbonate (calcite). Increase in urea concentration in solution also decreased the particle size of HA. Sample 7.5CO$_3$-HA was found to be calcium deficient with a Ca:P molar ratio of 1.45 (± 0.04). Indeed, biological apatite is a calcium deficient carbonate substituted hydroxyapatite.

Phase-pure crystalline and nano-sized silicate substituted hydroxyapatite was also synthesised using a CHFS system with silicon acetate as silicate ion source. The silicon content in samples increased with increasing silicon acetate concentration in the solution and a maximum of *ca.* 1.1 wt% substituted silicon content was obtained. However, it is suggested that a substitution threshold of *ca.* 1.1 wt% exists for synthesis of silicate substituted hydroxyapatite in the CHFS system using silicon acetate as a silicate ion source. This is supported by the progressive decrease in yields of Si-HA with increasing silicon content in solution.

This work on substitution of carbonate and silicate ions in HA follows our initial work on CHFS of hydroxyapatite as reported in Chapter 2. In this chapter, the capability of the CHFS to synthesise ion substituted HA nanoparticles with tailorable properties in a rapid single step manner was highlighted. Having successfully synthesised anion substituted HA nanoparticles it was hypothesised that the CHFS environment would also be ideal for cationic substitutions into HA (such as Mg^{2+} and Zn^{2+}) which are also biologically beneficial ions. The results of these endeavours are reported in following chapters.

4.5 Future Work

Use of precursors other than silicon acetate (for silicon substitution) may address the difficulty faced in the dissolution of silicon acetate in water. Furthermore, it would be interesting to correlate system parameters such as flow rates (and hence residence times), temperature and pressure with the substitution levels in HA. This could further strengthen the capability of the CHFS systems to synthesise particles with tailorable properties with higher precision. Coupled carbonate and silicate substitutions in HA can be attempted aiming at materials with good potential biocompatibility.

Chapter 5

Synthesis and Characterisation of Magnesium and Zinc Substituted Calcium Phosphates

5.1 Introduction

As mentioned in earlier chapters, biological apatites differ from synthetic HA in that the former additionally contain carbonate, silicate, magnesium, zinc, sodium and fluoride ions, to name a few (LeGeros 2002; Terpstra & Driessens 1986; Webster et al. 2004; Wopenka & Pasteris 2005). These ions strongly influence physical properties and biological behaviors of biological apatites (Gibson & Bonfield 2002).

In magnesium containing biological apatites (Mayer et al. 1997) such as those found in pathological calcifications, human dental calculus or carious lesions, a magnesium stabilized β-TCP (Mg-βTCP) or magnesium Whitlockite [Mg-Whitlockite, $Ca_{18}Mg_2H_2(PO_4)_{14}$] is often formed (Kim et al. 2003; Lagier & Baud 2003; Tang et al. 2001). The terms β-TCP and Whitlockite have been used interchangeably. However, there are small differences between the two. Elliot suggested that the term Whitlockite should be used for the mineral or similar synthetic materials in which HPO_4^{2-} and Mg^{2+} ions are present as part of the structure and β-TCP should be used for the low temperature polymorph of $Ca_3(PO_4)_2$ (Calvo & Gopal 1975; Elliott 1994). This nomenclature is used in this thesis. Mg-βTCP refers to a material in which calcium is partially replaced by magnesium and no HPO_4^{2-} ions are present.

Dentine, enamel and bone typically contain up to 1.1, 0.4 and 1.0 wt% magnesium ions, respectively (Bertoni et al. 1998; Zyman et al. 2006). In calcified tissues, the magnesium ion content is higher at the beginning of the calcification process and decreases with increasing calcification (Mayer et al. 1997; Suchanek et al. 2004a; Zyman et al. 2006). Magnesium depletion in humans can result in decreased osteoblastic and osteoclastic activities and bone fragility (Kannan et al. 2006; Mayer et al. 1997). It was reported by Katsumata and co-workers that a magnesium restricted diet in rats, induced an increase in bone resorption and decrease in bone formation (Katsumata et al. 2006). In addition to this, it was shown that rats fed on magnesium supplemented diets, had increased dynamic strength in their bones (Toba et al. 2000).

Magnesium substitution for calcium in HA reduces crystallinity, increases solubility, and lowers the temperature at which thermal conversion of HA into β-TCP occurs (Bertoni et al. 1998; Bigi et al. 1993; Correia et al. 1996; Gibson & Bonfield 2002; Suchanek et al. 2004a). Fadeev and co-workers showed that with increasing magnesium substitution into HA, the temperature at which HA to TCP thermal conversion occurred, was lowered from 700 °C to 300 °C (Fadeev et al. 2003). Magnesium substitution can also affect thermal phase stability of the TCP phase and sintering behaviour (Yoshida et al. 2005). For example, the β-TCP to α-TCP phase transformation temperature normally occurs at *ca.* 1180°C, however, magnesium substitution for calcium can increase the transformation temperature to *ca.* 1500°C (Blumenthal 1989b; Yoshida et al. 2005). This enables improved sintering of pure Mg-βTCP at elevated temperatures without deleterious formation of α-TCP (a less bioactive polymorph). Interestingly, when carbonate and magnesium ions are simultaneously substituted into HA at basic pH 9, the resulting apatite is much more thermally stable (up to *ca.* 1200°C or so) (Blumenthal 1989b; Gibson & Bonfield 2002; Zyman et al. 2006).

Magnesium substituted HA (Mg-HA) can be made via precipitation reactions from solution (Ergun et al. 2002; Gibson & Bonfield 2002; Kannan et al. 2005; Kannan & Ferreira 2006; Legeros et al. 2004; Yamasaki et al. 2002) or by solid-state reactions (Kannan et al. 2006; Pan et al. 2003). Magnesium substitution levels of up to 1.57 wt% have been reported using precipitation reactions (Mayer et al. 1997). Surprisingly, as much as 28.4 wt% substitution of magnesium in HA (with no secondary phase formation) has also been claimed in the literature using mechanochemical synthesis techniques (Suchanek et al. 2004b). It should however be noted that an excess of magnesium ions can also be undesirable, as it is known to reduce bioactivity in certain biomaterials (Serre et al. 1998).

As well as Mg-HA, other related phases such as Mg-Whitlockite (or Mg-βTCP), can also be made from precipitation reactions at relatively low temperatures (range 37 to 95°C) and acidic or neutral pH (Bigi et al. 1993; LeGeros et al. 2004; Legeros et al. 2004). It was suggested that in Whitlockite *ca.* 5% of the cations should be substituted by magnesium ions in order for it to be directly precipitated in aqueous systems (Rowles 1968). Crystalline Whitlockite or Mg-βTCP is usually made from a wet precipitated amorphous phase that requires a further heat treatment step (Bigi et al. 1993; Correia et al. 1996; Elliott 1994). Fadeev and co-workers reported on the co-precipitation of an amorphous phase which they identified as $Ca_{2.7}Mg_{0.3}(PO_4)_2.H_2O$ using elemental analysis (Fadeev et al. 2003). Abdelkader and co-workers reported on the synthesis of crystalline Whitlockite [$Ca_{18}Mg_2H_2(PO_4)_{14}$] by a reaction of diammonium hydrogen phosphate, calcium nitrate and magnesium nitrate in distilled water (pH 5.6) at 100 °C (Ben Abdelkader et al. 2004). Phase-pure β-TCP on the other hand, is routinely obtained via solid-state reactions or via thermal decomposition of calcium-deficient hydroxyapatite (CDHA) near or above 750°C (Enderle et al. 2005; Kannan et al. 2005; Kannan & Ferreira 2006; Legeros et al. 2004).

Zinc contents in human bone are typically around 0.0217 wt% (Li et al. 2007). Moreover, zinc in the human body also plays a vital role in many biological functions including mineralisation of tissues (Brandaoneto et al. 1995). Zinc is a co-factor for many enzymes, is essential for DNA replication and promotes osteoblastic cell activity (Ito et al. 2002; Ito et al. 2005; Li et al. 2007; Sogo et al. 2004). It has been reported that osteoblastic cells cultured on coatings of zinc containing organoapatite formed mineralised bone nodules within twelve days of culture compared to a full month required to do the same in the absence of zinc (Storrie & Stupp 2005). Another study revealed that when rats were fed a zinc deficient diet they had lower body weights and an average 45 % reduction in cancellous bone mass and fewer and thinner trabeculae in the trabecular bone architecture (Eberle et al. 1999). To promote bone formation, the optimum zinc content for calcium phosphate ceramics used in rabbit femora was reported to be 0.316 wt% (Kawamura et al. 2000).

It is known that use of HA based prostheses often leads to release of debris in the surroundings (Grandjean-Laquerrier et al. 2006). These particles are phagocyted by monocytes in the body and these activated monocytes produce cytokines, which are inflammatory mediators, causing osteoclastic activity. It has been reported that zinc in the HA increases the production of anti-inflammatory cytokines and decreases the production of inflammatory cytokines (Grandjean-Laquerrier et al. 2006). HA has also been investigated as an adsorbent for removing pathogenic proteins during blood purification (Takemoto et al. 2004) Indeed, zinc containing HA has been reported to have higher protein selective adsorption activity (Fujii et al. 2006; Hayakawa et al. 2007).

During syntheses, the presence of zinc in the reagents effects the growth of HA and results in a smaller crystallite size (Kanzaki et al. 2000; Kanzaki et al. 2001). Moreover, zinc substituted HA dissolves more rapidly compared to pure HA (Jallot et al. 2005). Zinc has also been reported to decrease the thermal stability of hydroxyapatite (Sogo et al. 2004). Zinc substituted hydroxyapatite has been synthesised using wet-precipitation (Miyaji et al. 2005), the sol-gel technique (Kalita & Bhatt 2007) and batch hydrothermal methods (Li et al. 2007). In addition to zinc substituted hydroxyapatite, depending on reaction pH and temperature, direct precipitation of Zn-substituted tricalcium phosphate has been reported at certain zinc concentrations (0.5 – 2 mM L^{-1})(LeGeros et al. 1999; Miao et al. 2006).

Hydroxyapatite is generally formed in the hexagonal $P6_3/m$ space group whereas β-TCP crystallises in the rhombohedral space R3c group (Tamm & Peld 2006; Yashima et al. 2003). Cationic substitutions for calcium severely strain the hydroxyapatite lattice and at higher levels, can cause the lattice to collapse (Bigi et al. 1996). Magnesium and zinc ions have been reported to substitute Ca(2) sites in the hydroxyapatite lattice possibly due to the shorter calcium-oxygen distance in Ca(2) site (Bigi et al. 1996; Tamm & Peld 2006).

It is not always desirable to produce simply phase pure HA. Biphasic calcium phosphate (BCP) mixtures are of interest for use in repair of periodontal and bone defects, (Bouler et al. 2000; Gouin et al. 1995) as bone graft substitutes in mastoid cavity obliteration (Daculsi et al. 1992) and scoliosis surgery (Delecrin et al. 2000). Within these applications, the ability to control crystallinity strongly affects the resorbability. Thus, the ability to prepare biphasic mixtures with controlled crystallinity and phase composition is of great interest.

In the chapters 2 and 3 we demonstrated the ability of the CHFS system to synthesise carbonate and silicate substituted calcium phosphates with tailorable properties in a rapid single step. It was also mentioned that the current methods for synthesis of calcium phosphates are too slow, multistep and often require subsequent heat-treatment steps. Moreover, stabilised tricalcium phosphates have not been precipitated in a crystalline form in a rapid single step process previously to our knowledge. It was postulated that in addition to synthesis of biologically beneficial ion substituted HA, presence of substituting cations in solution at higher concentration levels may stabilise crystalline Mg-Whitlockite or Mg-βTCP phases rather than HA with exposure to superheated water. This is desirable as the TCP based phases have higher solubility than HA. In this chapter, synthesis using CHFS route and characterisation of cation substituted (Mg^{2+} and Zn^{2+}) calcium phosphates is presented.

5.2 Experimental

5.2.1 Synthesis of Magnesium Substituted Calcium Phosphates

For these reactions it was assumed that magnesium ions partially substitute the calcium ions in HA. Hence all calculations were based on the formula for Mg-substituted HA, $Ca_{10-x}Mg_x(PO_4)_6(OH)_2$. For a typical reagent solution in the reactor, magnesium nitrate and calcium nitrate were accurately weighed and added to 100 mL deionised water so that the total metal ion concentration was 83.5 mM (see Table 2-6 in Chapter 2).

A pH adjusted (pH 10, using neat ammonium hydroxide solution) 50.0 mM diammonium hydrogen phosphate stock solution was used. Sample ID 0.5Mg-CaP represents a sample with 0.5 wt% magnesium in the solution based on the aforementioned formula. Similarly 1Mg-CaP represents a sample with 1.0 wt% magnesium and so on.

CHFS system 3 was used to carry out these reactions and pump rates of 20.0, 10.0 and 10.0 mL min^{-1} were used for superheated water feed, calcium/magnesium nitrate and diammonium hydrogen phosphate solutions, respectively. A (Ca + Mg):P molar ratio of *ca.* 1.67 was hence maintained. All reactions were carried out using a superheated water feed at 400 °C and 24 MPa. Additionally, a small 5 cm long, 200 W band heater set to 400 °C was used to maintain the temperature at the mixing point. All samples were centrifuged, washed and freeze-dried as explained earlier; see section 2.2.2.1 (b).

5.2.2 Synthesis of Zinc Substituted Calcium Phosphates

For these reactions it was assumed that the zinc ions partially substitute calcium ions in HA according to the following formula; $Ca_{10-x}Zn_x(OH)_2(PO_4)_6$. For a typical reagent solution in the reactor, zinc nitrate and calcium nitrate were accurately weighed and added to 100 mL deionised water so that the total metal ion concentration was 83.5 mM (see Table 2-7 in Chapter 2).

A pH adjusted (pH 10, using ammonium hydroxide solution) 50.0 mM diammonium hydrogen phosphate stock solution was used. Sample ID 1.3Zn-CaP represents a sample with expected 1.3 wt% zinc based on the aforementioned formula. Similarly 5.1Zn-CaP represents a sample with expected 5.1 wt% zinc and so on.

CHFS system 3 was used for syntheses and pump rates of 25.0, 12.5 and 12.5 mL min^{-1} were used for superheated water feed, calcium/zinc nitrate and diammonium hydrogen phosphate solutions, respectively. A (Ca + Zn):P molar ratio of *ca.* 1.67 was hence maintained in all the reactions. All reactions were carried out using a superheated water feed at 450 °C and 24 MPa. Additionally, a small 5 cm long, 200 W band heater set to 450 °C was used to maintain the temperature at the mixing point. All samples were centrifuged, washed and freeze-dried as explained earlier; see section 2.2.2.1 (b).

5.3 Results and Discussion

5.3.1 Transmission Electron Microscopy

For selected samples, transmission electron microscopy (TEM) was used to investigate the particle morphology with ever increasing magnesium and zinc content in the reagents. TEM images for magnesium substituted samples are shown in Figures 5-1 (a) to (h).

Figures 5-1 (a) and (b) revealed distinct nano-rods of *ca.* 234 (± 93) x 57 (± 16) nm (50 particles sampled) for sample 0.5Mg-CaP. TEM images of sample 4Mg-CaP are shown in Figures 5-1 (c) and (d). A mixture of both lozenge shaped particles and semi-spherical agglomerates of *ca.* 30 – 60 nm (average particle size is 43 nm ± 12 nm; 50 particles sampled) sized particles were observed. Figures 5-1 (e) and (f) show TEM images of sample 6Mg-CaP in which agglomerates as large as *ca.* 600 nm in diameter comprise of particles *ca.* 50 - 100 nm in diameter (average particle size is 47 nm ± 17 nm; 50 particles sampled). The TEM image in Figure 5-1 (f) suggested that the spherical particles are possibly hollow (however this can not be definitely stated). TEM images of sample 10Mg-CaP in Figures 5-1 (g) and (h) showed very small poorly defined particles *ca.* 37 nm ± 13 nm in diameter (range: 20 – 60 nm; 50 particles sampled) which also appear to be hollow.

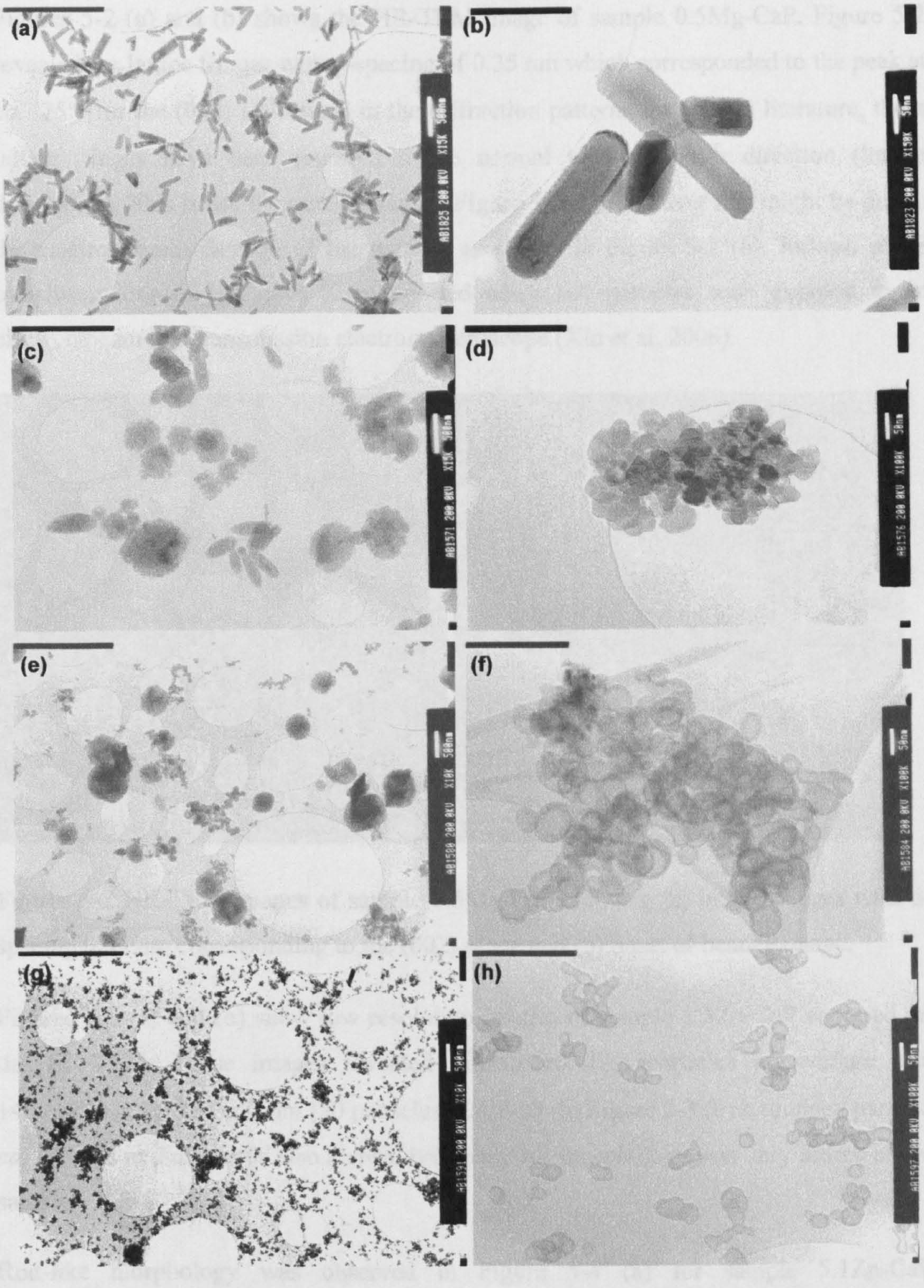

Figure 5-1 Transmission electron microscope images of sample 0.5Mg-CaP at (a) x15k magnification [bar = 500 nm] and (b) x150k magnification [bar = 50 nm], of sample 4Mg-CaP at (c) x15k magnification [bar = 500 nm] and (d) x100k magnification [bar = 50 nm], of sample 6Mg-CaP at (e) x10k magnification [bar = 500 nm] and (f) x100k magnification [bar = 50 nm] and of sample 10Mg-CaP at (g) x10k magnification [bar = 500 nm] and (h) x100k magnification [bar = 50 nm].

Figures 5-2 (a) and (b) shows the HR-TEM image of sample 0.5Mg-CaP. Figure 5-2 revealed the lattice fringes with d-spacing of 0.35 nm which corresponded to the peak at *ca.* 25° [for the (002) reflection] in the diffraction patterns for HA. In literature, these lattice fringes have been reported to be normal to the growth direction (longer dimension). This is not the case as seen in Figure 5-2 (a), however this might be due to the electron beam damage of the particle as shown in Figure 5-2 (b). Indeed, phase transformations of HA have been reported when HA particles were exposed to an electron beam in a transmission electron microscope (Xin et al. 2006).

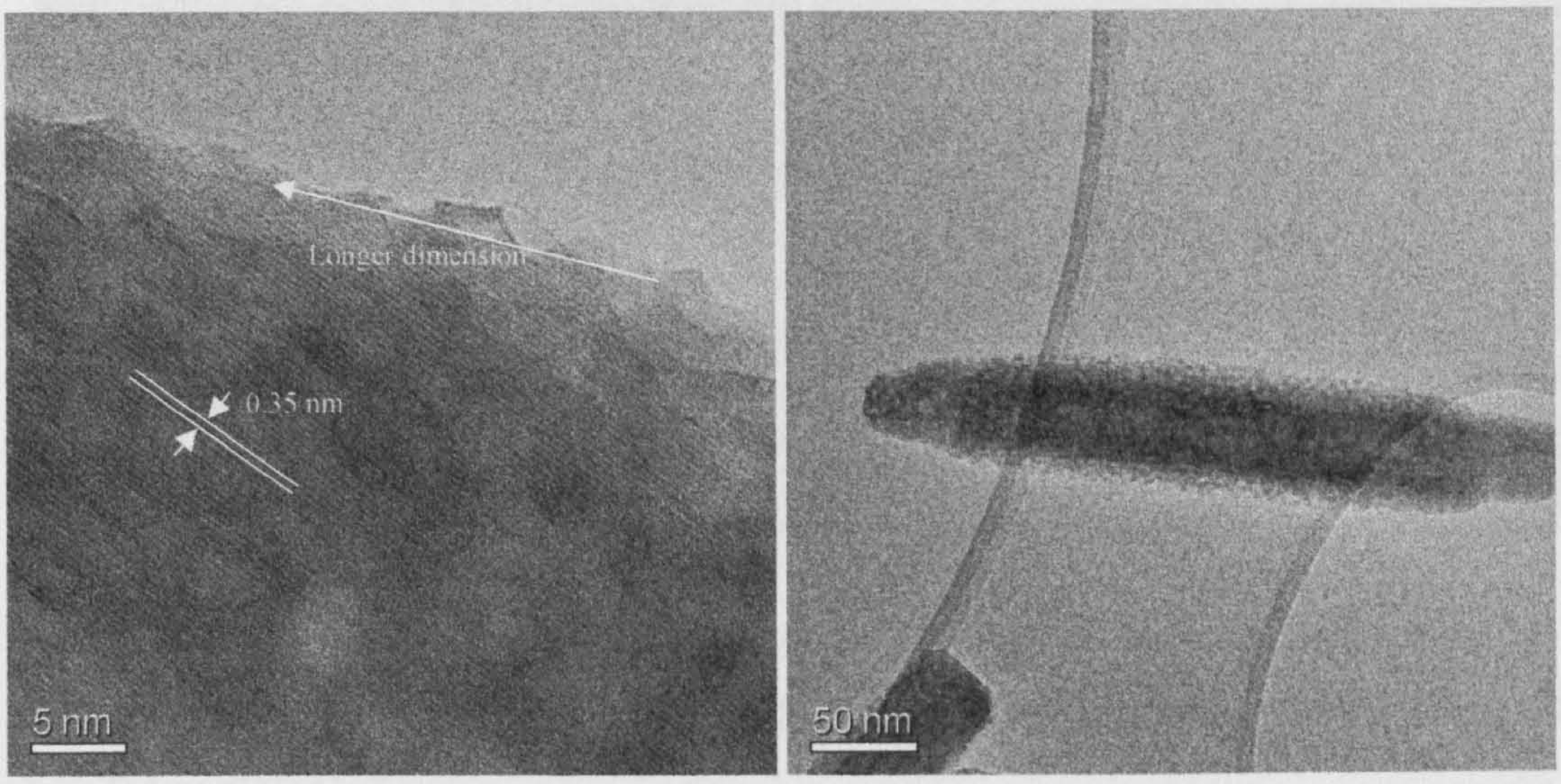

Figure 5-2 HR-TEM images of sample 0.5Mg-CaP showing (a) lattice fringes with d-spacing 0.35 nm corresponding to the (002) plane and (b) onset of beam damage.

Figures 5-3 (a) and (b) show low resolution images of sample 1.3Zn-CaP captured on the HR-TEM. These images revealed distinct rod-like particles of average size 146 (± 42) nm x 41 (± 7) nm [50 particles sampled]. In Figure 5-3 (b) a rounded particle *ca.* 245 nm in diameter is also shown, however, this morphology was very scarce in the sample.

Rod-like morphology was observed in Figure 5-4 (a) for sample 5.1Zn-CaP [294 (± 108) x 85 (± 13) nm, 50 particles sampled], similar to that reported in chapter 2 for non-substituted HA (Chaudhry et al. 2006). However large oval shaped particles > 1 x 0.5 μm [20 particles sampled] were also noticed in the same sample as shown in Figure 5-4 (b). Further addition of zinc in reagents lead to wide ranging particle sizes and different morphologies as observed in Figures 5-4 (c) to (f) for samples 10Zn-CaP to 32Zn-CaP, respectively. It was observed that increase in zinc concentration in reagents lead to acicular features on particles with rod-like and oval morphologies. In a study carried out by Kanzaki and co-workers it was shown that the presence of zinc in a crystallising environment did not effect the nucleation but inhibited the growth of hydroxyapatite by adsorbing on the growing interface (Kanzaki et al. 2000; Kanzaki et al. 2001).

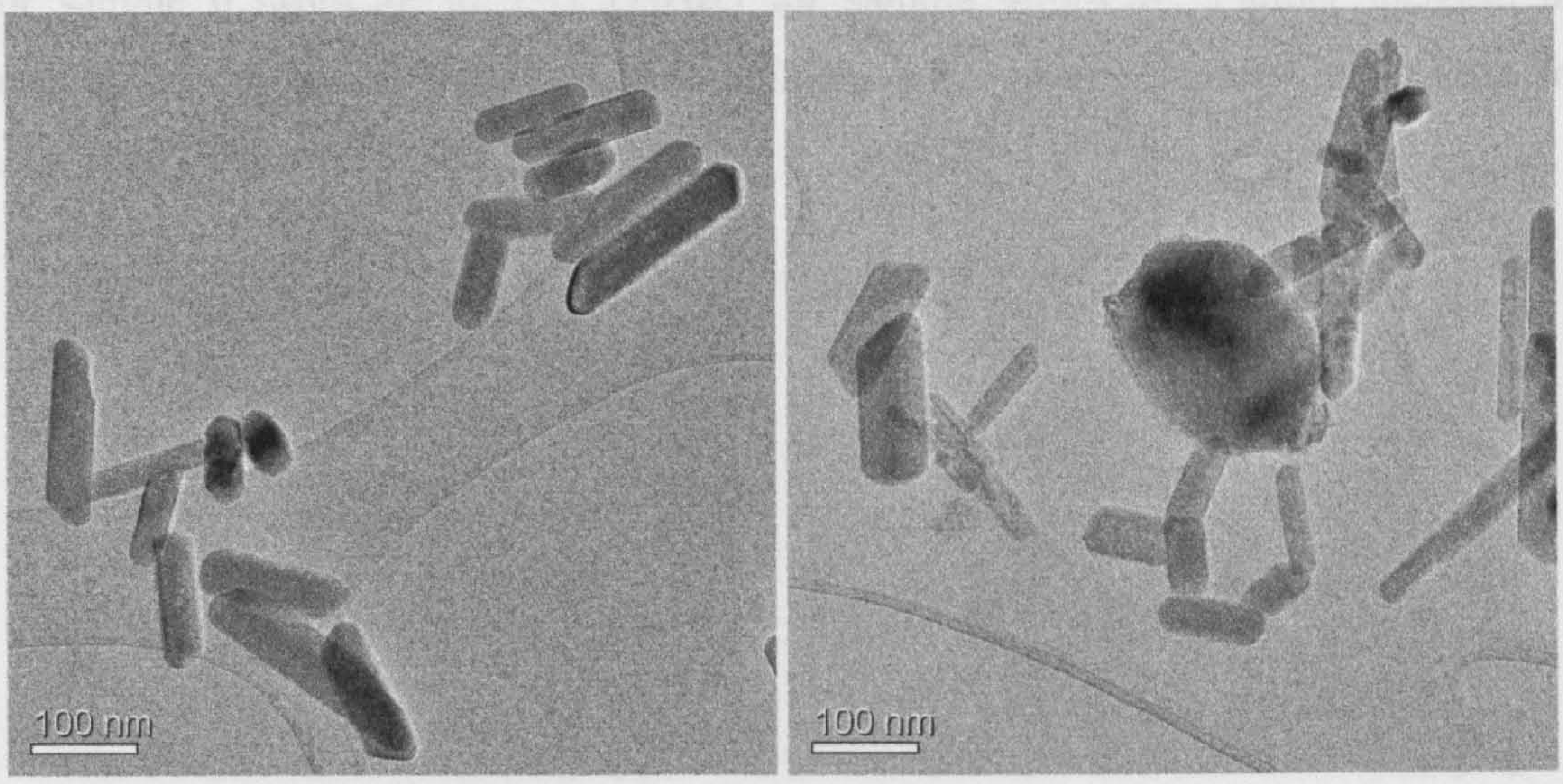

Figure 5-3 HR-TEM images of sample 1.3Zn-CaP at magnification x40k [bar = 100 nm] showing (a) typical CHFS HA rod-like morphology and (b) very few rounded particles.

5.3.2 Elemental Analyses

Elemental analyses (by EDS attached to TEM) for selected samples (three areas selected per sample) suggested the magnesium substitution levels in powders were 0.49 ± 0.24 wt% for the rods in sample 1Mg-CaP, 4.06 ± 0.6 wt% for the agglomerates in sample 4Mg-CaP, 6.78 ± 0.31 wt% for sample 6Mg-CaP and 8.33 ± 0.87 wt% for sample 10Mg-CaP. In sample 4Mg-CaP the EDS was focused on three lozenge shaped particles which form a slightly different shape to the majority of the sample (the vast majority are rounded agglomerates) and suggested a Mg wt % of 2.67± 0.83 wt%. This suggested that the lozenge shaped particles in sample 4Mg-CaP may be slightly lower in Mg compared to the more rounded agglomerates. The lozenge shape can essentially be viewed as a rounded rod like shape (such as the rods observed at lower magnesium substitution levels for Mg-HA). Elemental analyses were also carried out on all magnesium substituted samples to determine the magnesium content using an EDS detector attached to a SEM for more accurate average values (shown in Table 5-1). The detailed elemental analyses for magnesium substituted samples are presented in Table E-1 of Appendix E. It was noticed that the measured magnesium content was very close to the expected amount in the samples. This suggested that the CHFS is a reasonably efficient method wherein the subsequent yields are high. With increasing magnesium content in the reagent solutions, the (Ca+Mg):P molar ratio decreased from 1.46 (±0.04) for sample 0.5Mg-CaP to 1.31 (±0.02) for sample 4Mg-CaP. Further increase in magnesium content in reagents solutions increase the aforementioned molar ratio to 1.59 (±0.07) for sample 14Mg-CaP.

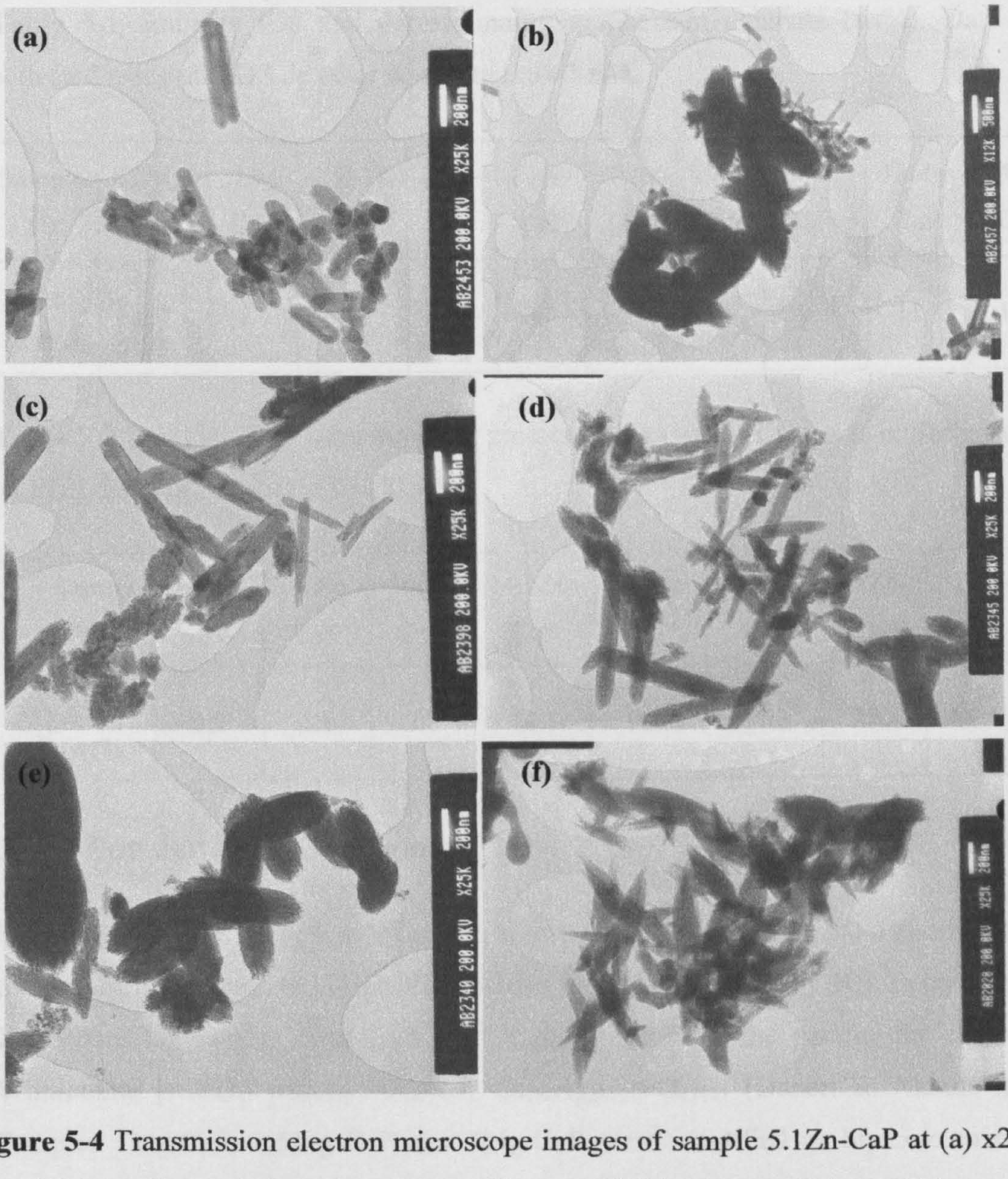

Figure 5-4 Transmission electron microscope images of sample 5.1Zn-CaP at (a) x25k magnification [bar = 200 nm] and (b) x12k magnification [bar = 500 nm] (c) sample 10Zn-CaP at x25k magnification [bar = 200 nm] (d) sample 14.7Zn-CaP at x25k magnification [bar = 200 nm] (e) sample 19.3Zn-CaP at x25k magnification [bar = 200 nm] and (f) 32Zn-CaP at x25k magnification [bar = 200 nm].

Table 5-2 shows the average zinc content (wt%) in all zinc substituted samples. The detailed elemental analyses for zinc substituted samples are presented in Table 2, Appendix D. Sample 1.3Zn-CaP was determined to have a (Ca+Zn):P molar ratio of 1.49 (± 0.12), the sample being calcium deficient similar to sample 0.5Mg-CaP. It was observed that the difference, between the expected weight percent of zinc in the sample and the actual content measured using EDS, was low. For sample 32Zn-CaP the much lower zinc content measured was nearly half of that expected (see Table E-2 in Appendix E for detailed elemental analysis of all samples).

Table 5-1 Samples IDs and corresponding magnesium contents (wt%). Data was collected using an EDS detector connected to a SEM.

Sample ID	0.5Mg-CaP	1Mg-CaP	1.5Mg-CaP	2Mg-CaP	4Mg-CaP	6Mg-CaP	8Mg-CaP	10Mg-CaP	12Mg-CaP	14Mg-CaP
Mg (wt%)	0.7	1.0	1.6	2.1	3.9	5.8	8.0	9.1	11.4	13.1

Table 5-2 Samples IDs, corresponding zinc contents (wt%). Data was collected using an EDS detector connected to a SEM.

Sample ID	1.3Zn-CaP	5.1Zn-CaP	10Zn-CaP	14.7Zn-CaP	19.3Zn-CaP	23.7Zn-CaP	28Zn-CaP	32Zn-CaP
Zn (wt%)	0.9	6.1	7.8	10.5	11.7	17.8	21.2	16.4

5.3.3 Powder X-ray Diffraction

The PXRD data for sample 0.5Mg-CaP, shown in Figure 5-5 (a), gave a good match to the pattern for crystalline HA [JCPDS pattern 09-0432, $Ca_5(PO_4)_3(OH)$]. In contrast, the XRD data for sample 6Mg-CaP gave a good match to the pattern for crystalline Whitlockite [JCPDS pattern 70-2064, $Ca_{18}Mg_2H_2(PO_4)_{14}$] (Guneri & Akkurt 2005). Samples 1Mg-CaP, 1.5Mg-CaP and 2Mg-CaP were identified as biphasic mixtures. Samples 1Mg-CaP and 1.5Mg-CaP gave a good match to the aforementioned pattern for HA and magnesium stabilised β-tricalcium phosphate (Mg-βTCP, compared to JCPDS pattern 70-0681) [Figures 5-5 (b) to (c)]. However, for sample 2Mg-CaP the second phase gave a better match to JCPDS pattern 70-2064 as shown in Figure 5-5 (d). This suggested that increase in magnesium leads to Whitlockite phase instead of Mg-βTCP (different composition but similar structure). Increasing the magnesium content further [Figures 5-5 (f) to (j)] resulted in significantly broader XRD peaks closely matching the pattern 70-2064 for $Ca_{18}Mg_2H_2(PO_4)_{14}$ (Guneri & Akkurt 2005). This was not surprising given that magnesium is known to retard the crystallisation and growth of calcium phosphates in solution and to stabilise Whitlockite (Blumenthal 1989). It was observed in Table E-1 in Appendix E that the (Ca+Mg):P molar ratio increased with increasing magnesium in solutions and levelled off for samples 10Mg-CaP [1.56 ± 0.04], 12Mg-CaP [1.53 ± 0.05] and 14Mg-CaP [1.59 ± 0.07]. It may represent a stoichiometric Whitlockite phase. It may also be possible that a calcium rich phase exists but is hard to detect given the amorphous nature. The XRD data for sample MgP in Figure 5-5 (k) showed broad peaks, suggesting the material is amorphous. The broad peak positions approximated to several standard patterns, particularly JCPDS patterns 11-0041 and 08-0038 for magnesium phosphates $Mg(PO_4)_3$ and $Mg_2P_2O_7$, respectively.

Rietveld refinements using the high-resolution PXRD transmission data were used to obtain accurate unit-cell dimensions for Mg-substituted materials and weight percent proportion of HA to Mg-Whitlockite present. A fit for sample 0.5Mg-CaP is shown in Figure 5-6 (space group = $P6_3/m$, c = 9.419 Å, a = 6.869 Å). Rietveld refinement revealed anisotropic peak broadening for HA with the width of all 001 reflections being significantly narrower. This suggested preferential crystalline growth along the c direction, which is consistent with the rod-like forms as seen in Figure 5-1 (b). Mixed phase refinements with both HA and Mg-Whitlockite present produced similar quality fits as indicated by the Rwp. Rietveld refinements revealed that *ca.* 70 wt% HA and *ca.* 30% Mg-βTCP (or Mg-Whitlockite) were present in the sample 1.5Mg-CaP (see Figure 5-7) (Whitlockite: space group = R3c, c = 37.226 Å, a = 10.389 Å, Hydroxyapatite: space group = $P6_3/m$, c = 9.413, a = 6.851). Sample 4Mg-CaP was found to contain *ca.* 95 wt% HA and *ca.* 5 wt% Whitlockite by refinement (see Figure 5-8) (Whitlockite: space group = R3c, c = 37.038 Å, a = 10.336 Å, Hydroxyapatite: space group = $P6_3/m$, c = 9.408 Å, a = 6.818 Å). It was observed that both the c and a parameters for both HA and Whitlockite decreased with increasing magnesium concentration in the samples. This is understandable, as magnesium substitutes for calcium in these calcium phosphates and being a smaller ion resulted in shrinkage of the lattice. Refinement of the unit cell of HA showed that a systematic volume decrease occured with increased levels of magnesium in solution (Figure 5-9). Although there is a slight deviation from the line for sample

4Mg-CaP cell volume, this could be a real effect indicating that the structure is approaching magnesium saturation and that magnesium take-up is no longer proportional to magnesium in solution. Nevertheless, the overall decrease in unit cell volume of 5 Å^3 was clearly observed, and this reflects the reduction in average cation size in exchanging Ca^{2+} with Mg^{2+}. The small magnitude of the value stemed from the small number of Mg^{2+} ions being substituted into the overall structure (which is less than one Mg per unit cell). A similar effect was obtained from the refinement of the Whitlockite cell parameters, where the unit cell volume for sample 1.5Mg-CaP is *ca.* 3480 Å^3. Increasing the magnesium content in solution (samples 1.5Mg-CaP to 4Mg-CaP) resulted in a decrease in unit cell volume of about 52 Å^3.

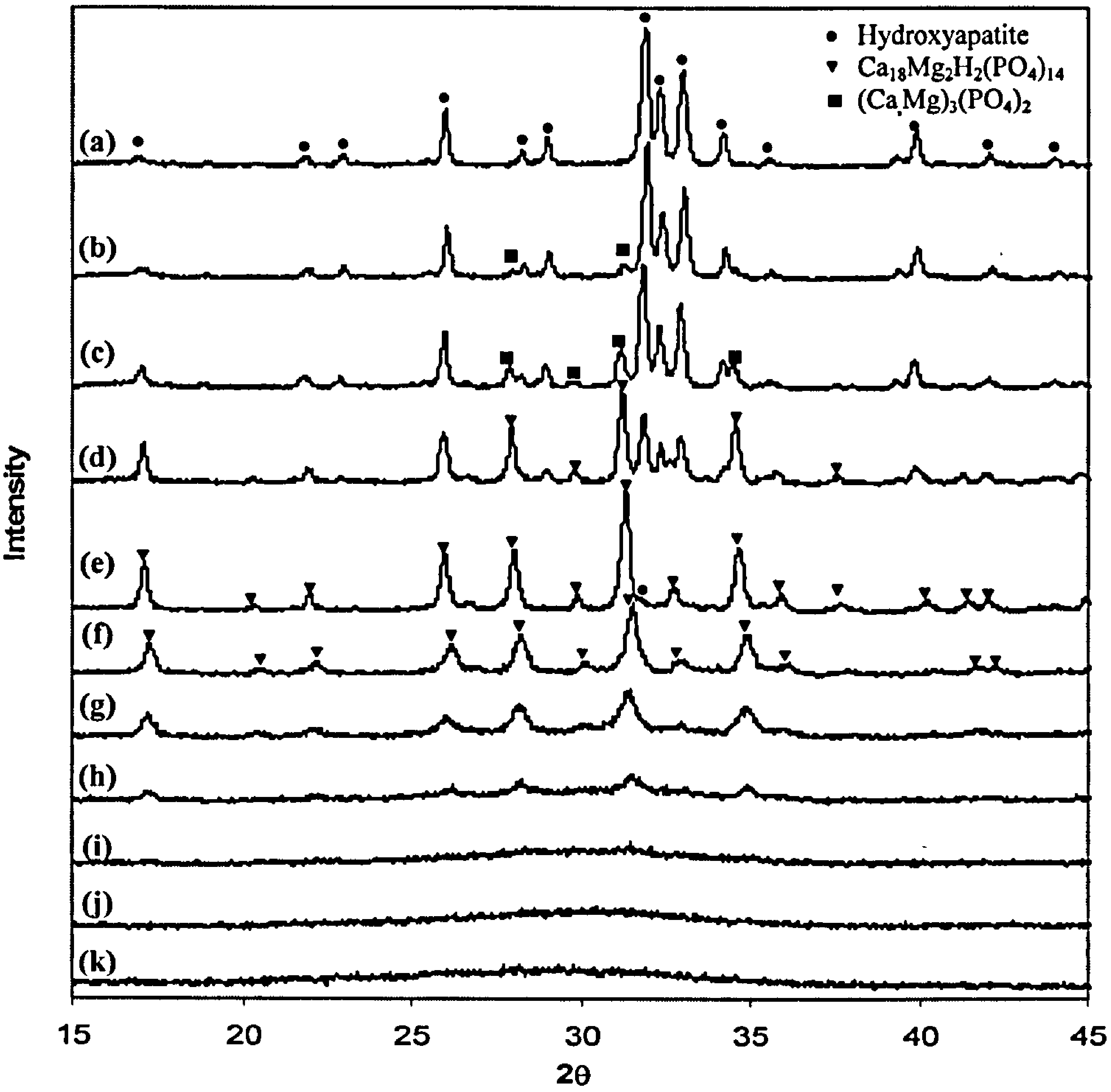

Figure 5-5 X-ray powder diffraction patterns of as-precipitated Mg-substituted calcium phosphate powders for samples (a) 0.5Mg-CaP (b) 1Mg-CaP (c) 1.5Mg-CaP (d) 2Mg-CaP (e) 4Mg-CaP (f) 6Mg-CaP (g) 8Mg-CaP (h) 10Mg-CaP (i) 12Mg-CaP (j) 14Mg-CaP and (k) MgP. Note: phase separation from pure Mg-substituted HA (Mg-HA) into a mixture of Mg-HA and Mg-Whitlockite (or Mg-βTCP) occurs from XRD pattern (b) and for several higher Mg loadings.

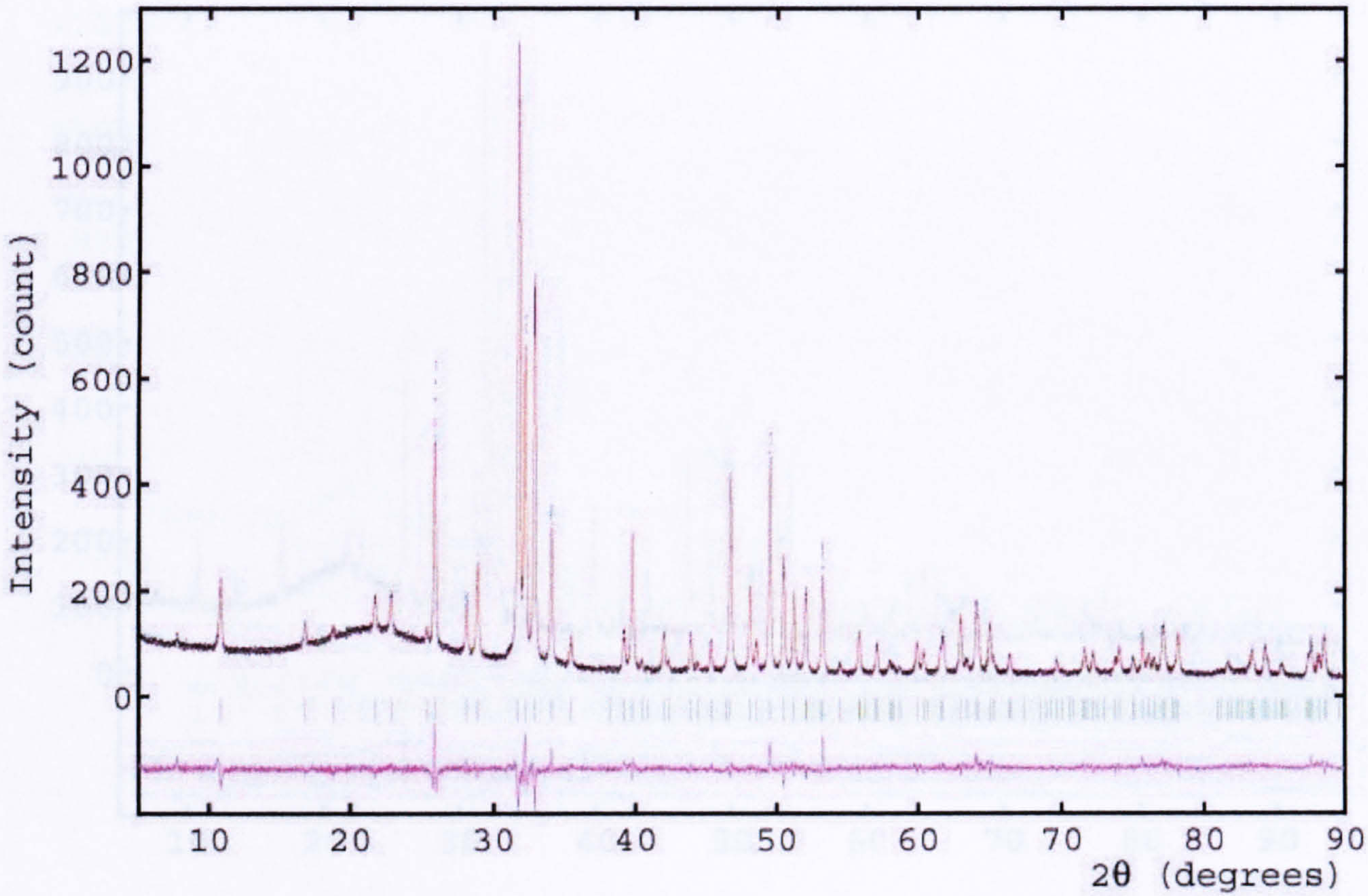

Figure 5-6 Rietveld refinement analysis of samples 0.5Mg-CaP showing the collected XRD data (black dots), calculated profile (brown line) and difference (red line).

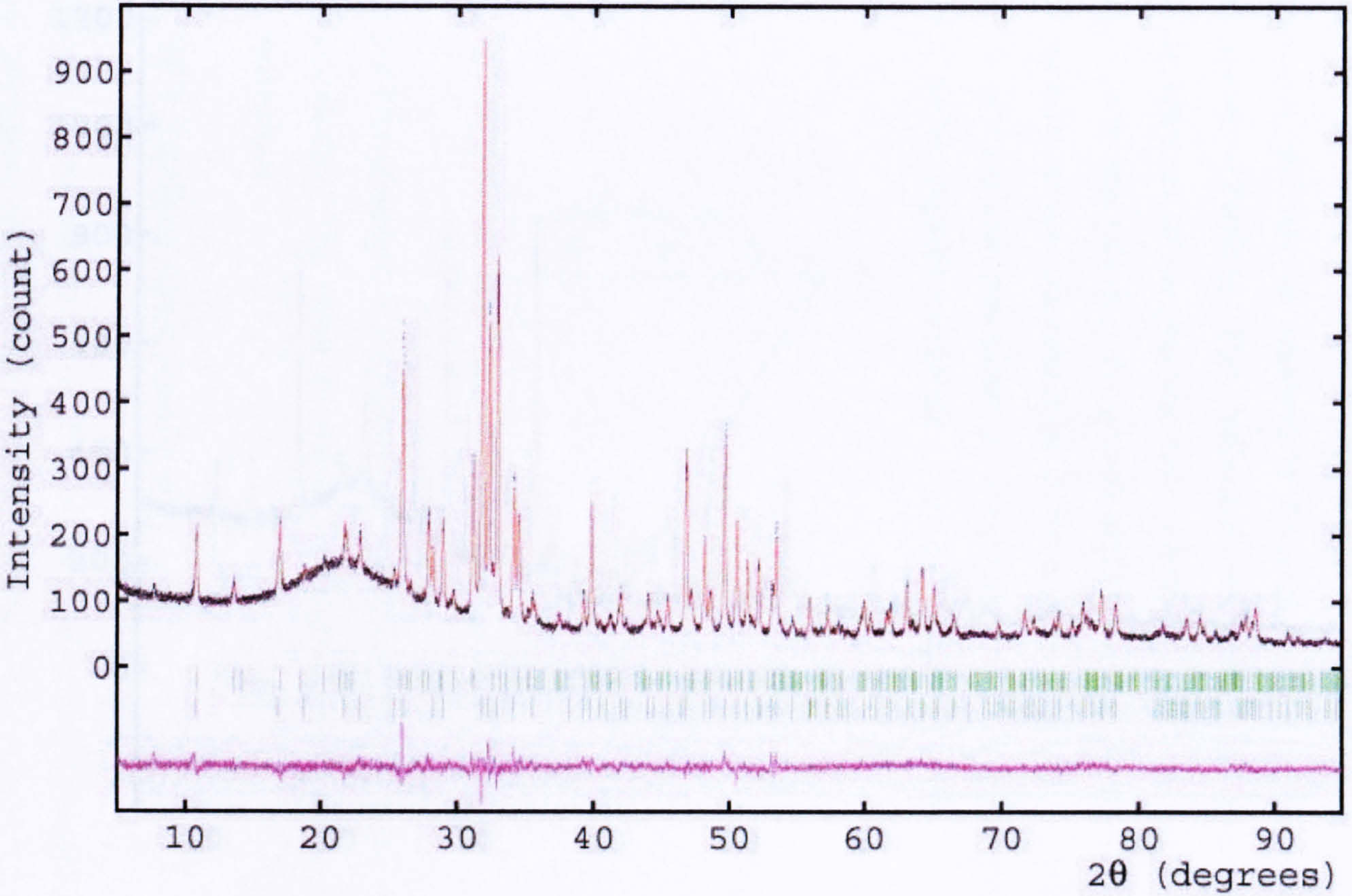

Figure 5-7 Rietveld refinement analysis of samples 1.5Mg-CaP showing the collected XRD data (black dots), calculated profile (brown line) and difference (red line).

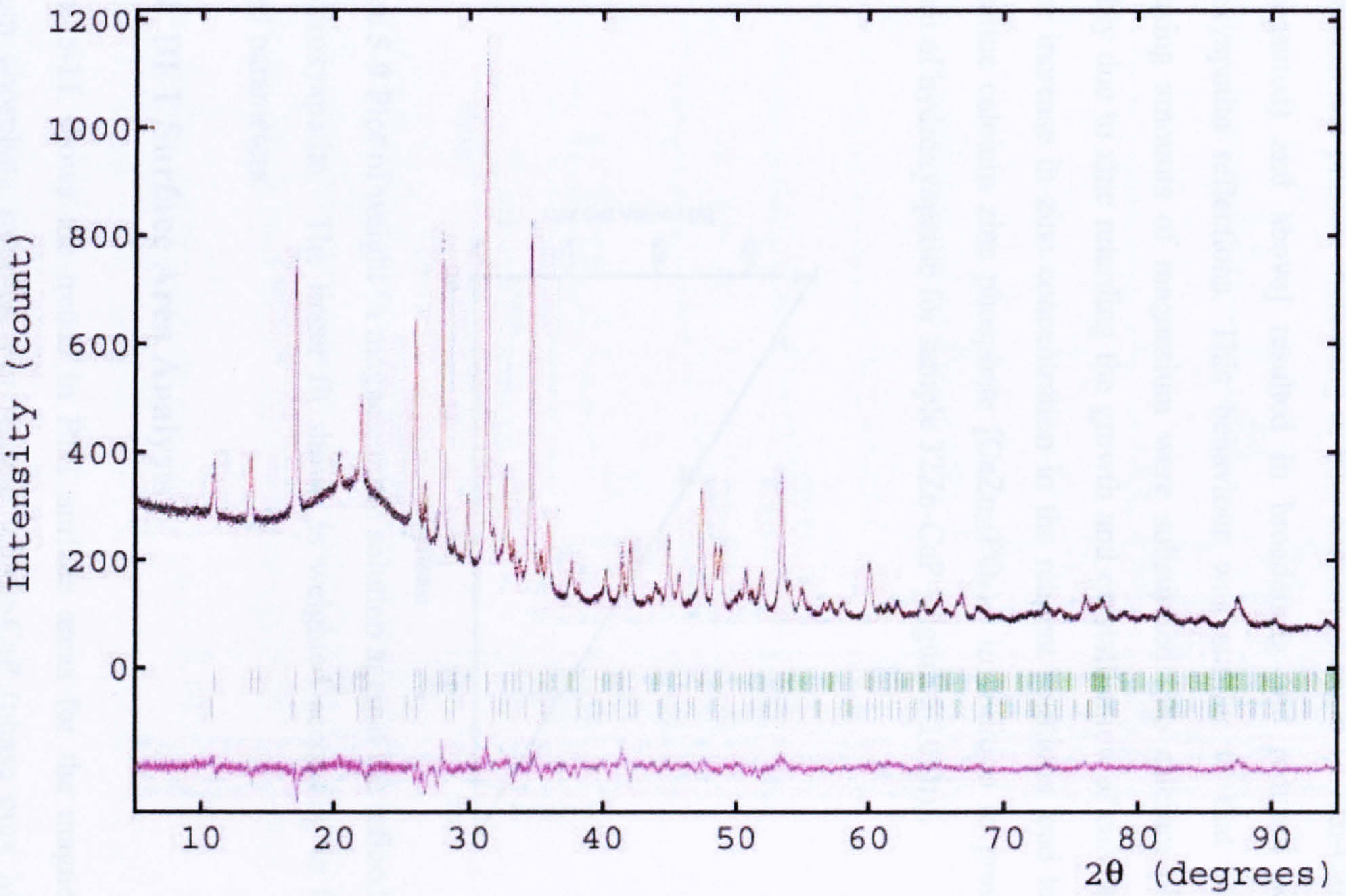

Figure 5-8 Rietveld refinement analysis of samples 4Mg-CaP showing the collected XRD data (black dots), calculated profile (brown line) and difference (red line).

The powder XRD patterns for zinc substituted samples are shown in Figure 5-10. Sample 1.3Zn-CaP gave a good match to the pattern for crystalline hydroxyapatite (JCPDS pattern 09-432) as shown in Figure 5-10 (a). However, for sample 5.1Zn-CaP very weak peaks corresponding to calcium zinc phosphate [$CaZn_2(PO_4)_2$] appeared as shown in Figure 5-10 (b) (compared to JCPDS pattern 020-248). Samples 5.1Zn-CaP to 28Zn-CaP shown in Figures 5-10 (b) to (g) were biphasic mixtures of the aforementioned phases. Increasing in zinc content [sample 14.7Zn-CaP (10.5 wt% zinc as measured) and above] resulted in broadening and reduced peak intensity of hydroxyapatite reflections. This behaviour was similar to that seen earlier when increasing amounts of magnesium were substituted into calcium phosphates and is possibly due to zinc retarding the growth and crystallisation of calcium phosphates. A further increase in zinc concentration in the reagent solutions lead to precipitation of crystalline calcium zinc phosphate [$CaZn_2(PO_4)_2$] in addition to presence of a minor amount of hydroxyapatite for sample 32Zn-CaP [Figure 5-10 (h)].

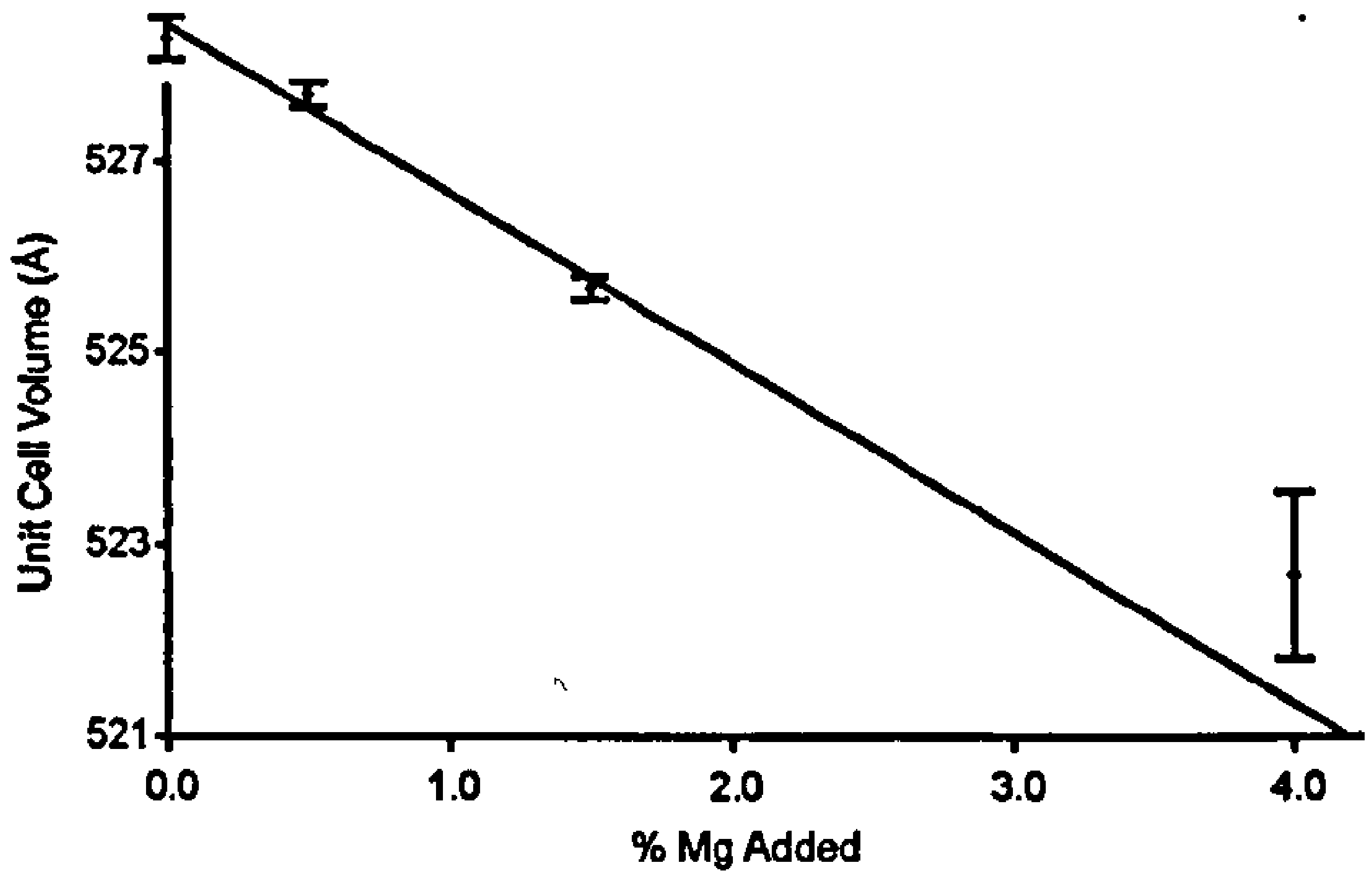

Figure 5-9 Plot of weight % magnesium in solution against the refined unit cell volume of hydroxyapatite. The linear fit shown is weighted according to the errors on the refined parameters.

5.3.4 BET Surface Area Analysis

Figure 5-11 shows the trends in BET surface areas for the magnesium substituted calcium phosphate samples. For sample 0.5Mg-CaP (phase pure Mg-HA) the BET surface area was 20.7 $m^2 g^{-1}$. Samples 1Mg-CaP, 1.5Mg-CaP, 2Mg-CaP and 4Mg-CaP had lower surface areas of 19.4, 16.2, 12.1 and 10.6 $m^2 g^{-1}$. Moreover, phase-pure Mg-Whitlockite samples 6Mg-CaP and 8Mg-CaP (phase-pure Whitlockite) also had relatively low surface areas of 10.3 and 11.7 $m^2 g^{-1}$, respectively. This is unsurprising given the extent of agglomeration observed in TEM Figures 5-1 (c) to (f). The surface area showed a *ca.* five fold increase for samples 10Mg-CaP (50.2 $m^2 g^{-1}$), 12Mg-CaP (54.3 $m^2 g^{-1}$) and 14Mg-CaP (62.3 $m^2 g^{-1}$), respectively. This suggested that there was possibly a threshold above which Mg-substitution severely retarded crystallisation and growth of particles in solution under these conditions. This argument is supported by TEM images shown in Figures 5-1 (a) to (h).

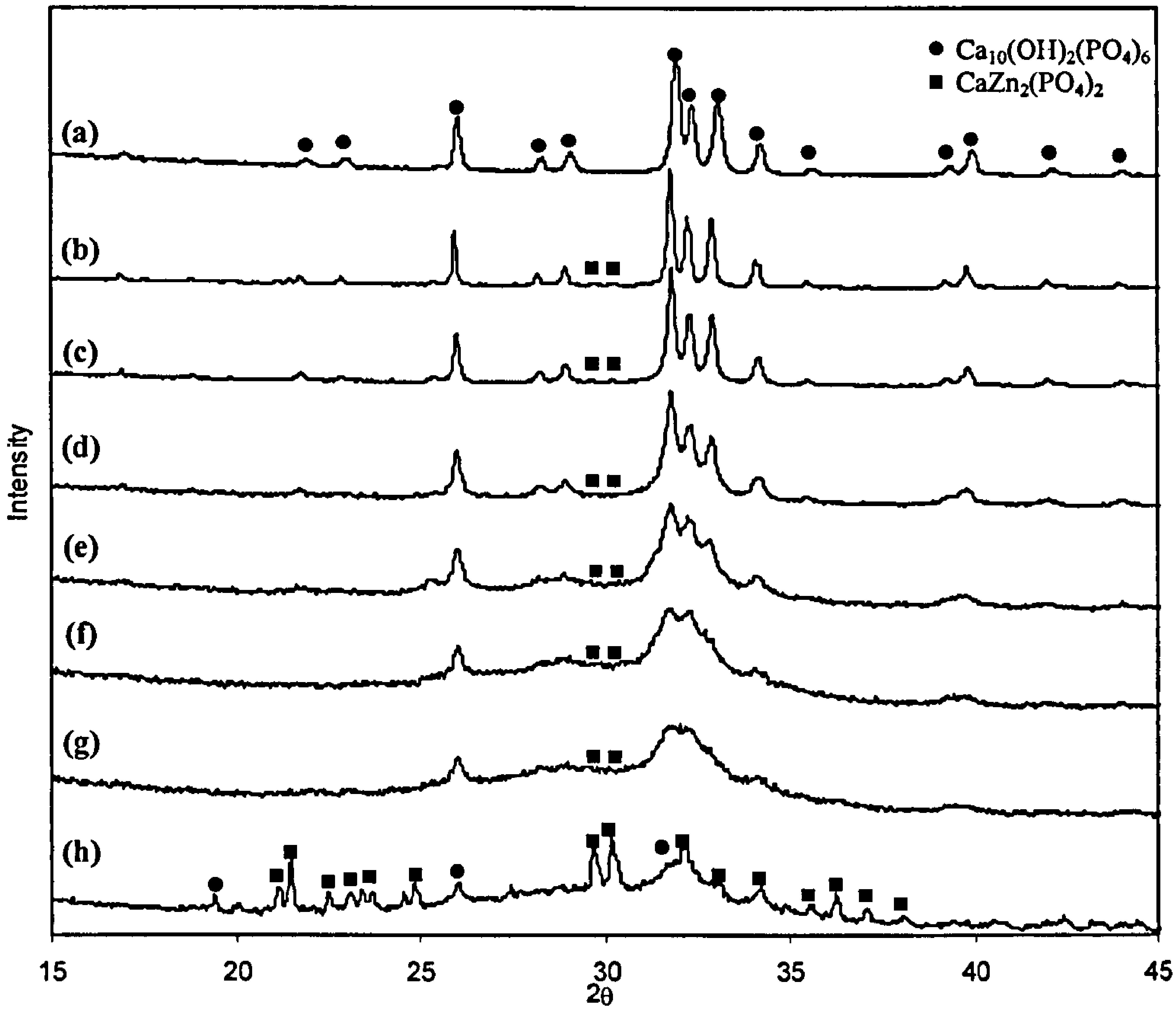

Figure 5-10 Powder X-ray diffraction patterns of as-precipitated Zn-substituted calcium phosphate powders for samples (a) 1.3Zn-CaP (b) 5.1Zn-CaP (c) 10Zn-CaP (d) 14.7Zn-CaP (e) 19.3Zn-CaP (f) 23.7Zn-CaP (g) 28Zn-CaP and (h) 32Zn-CaP.

Increase in zinc content did not result in a particular trend for BET surface areas as shown in Figure 5-10. Samples 1.3Zn-CaP, 5.1Zn-CaP, 10Zn-CaP, 14.7Zn-CaP, 19.3Zn-CaP, 23.7Zn-CaP, 28Zn-CaP and 32Zn-CaP had surface areas of 14.8, 14.3, 16.2, 15.4, 13.9, 13.0, 13.1 and 6.6 m^2g^{-1}, respectively. Overall, the surface area decreased slightly with increasing zinc content and all zinc doped calcium phosphate samples possessed a lower surface area compared to HA made under similar conditions (22 $m^2 g^{-1}$ mentioned in Chapter 3).

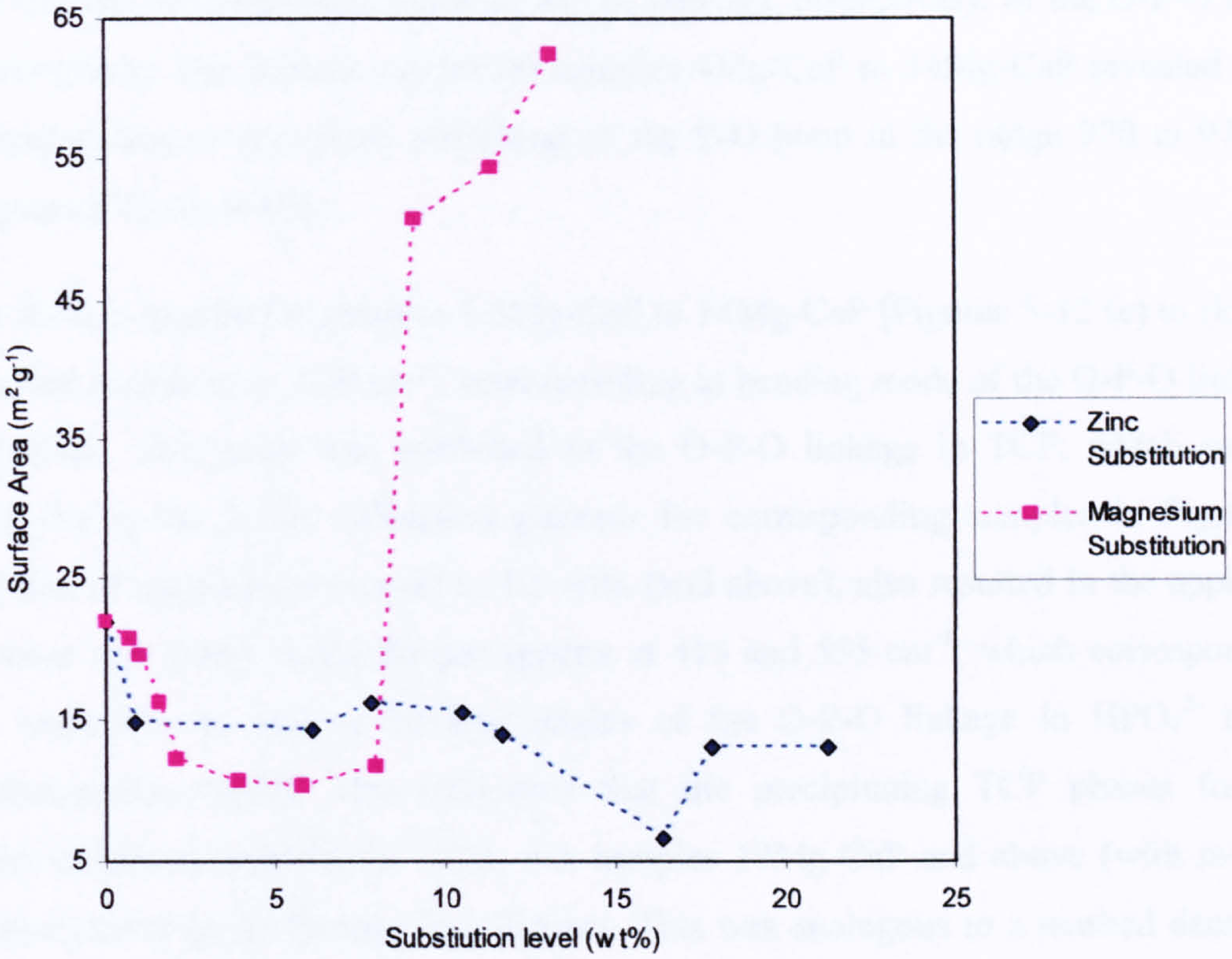

Figure 5-11 Variation in surface area of Mg-substituted calcium phosphates (and biphasic mixtures) with increasing magnesium and zinc content (wt%, measured by EDS) in the samples.

5.3.5 Raman Spectroscopy

Raman spectroscopy and FTIR spectroscopy were used to analyze the samples and aid identification of the different calcium phosphates present (Gibson et al. 2000; Gibson & Bonfield 2002; Rehman et al. 2000).

Figure 5-12 shows Raman spectra for magnesium substituted samples. Peaks in Figures 5-12 (a) to (d) for samples 0.5Mg-CaP to 2Mg-CaP were very similar to those observed for phase pure HA. Peaks at ca. 1083 and 1054 cm^{-1} in the Raman spectra, for these samples, correspond to asymmetric stretching (υ_3) of the P-O bond in phosphate. The peak around 970 cm^{-1} corresponded to the symmetric stretching mode (υ_1) of the P-O bond of the phosphate group. This peak is generally observed around 963 cm^{-1} in HA (Penel et al. 1997). The shift could be due to magnesium incorporation into the HA lattice which in turn may influence the vibrational characteristics of this bond. Indeed, Rietveld refinements revealed reduction in both c and a lattice parameters of HA with increase in magnesium substitution as discussed in section 5.3.1.2. Peaks at 615 cm^{-1}

and 437 cm^{-1} corresponded to the υ_4 and υ_2 bending, respectively, of the O-P-O linkage in phosphate. The Raman spectra for samples 4Mg-CaP to 14Mg-CaP revealed a peak corresponding to symmetric stretching of the P-O bond in the range 970 to 976 cm^{-1} [Figures 5-12 (e) to (i)].

The Raman spectra for samples 1.5Mg-CaP to 14Mg-CaP [Figures 5-12 (c) to (k)] each revealed a peak at *ca.* 630 cm^{-1}, corresponding to bending mode of the O-P-O linkage in phosphate. This peak was attributed to the O-P-O linkage in TCP, which was also observed in the X-ray diffraction patterns for corresponding samples in Figure 5-5. Increase of magnesium content to 1.5 wt% (and above), also resulted in the appearance of more new peaks in the Raman spectra at 415 and 555 cm^{-1}, which corresponded to the respective υ_2 and υ_4 bending modes of the O-P-O linkage in HPO_4^{2-} in TCP (Koutsopoulos 2002). This suggested that the precipitating TCP phases for these compositions contain HPO_4^{2-} ions. For samples 10Mg-CaP and above (with more Mg content) these peaks became less distinct. This was analogous to a marked decrease in crystallinity as seen in corresponding diffraction patterns in Figure 5-5 and a large increase in surface area as seen in Figure 5-11.

Figure 5-13 shows the Raman spectra for all zinc substituted calcium phosphate samples. All samples showed the following peaks; at *ca.* 1077 and 1049 cm^{-1} for asymmetric stretching (ν_3) and at *ca.* 964 cm^{-1} for symmetric stretching (ν_1) of the P-O bond in phosphate in HA (zinc substituted HA), at *ca.* 606 and 589 cm^{-1} for ν_4 bending and at *ca.* 487 and 431 cm^{-1} for ν_2 bending of the O-P-O linkage in phosphate in HA. For samples 1.3Zn-CaP to 28Zn-CaP it was observed that all the peaks became broader and less intense as shown in Figures 5-13 (a) to (g). This corresponded to decreasing crystallinity of the corresponding samples as observed from their X-ray diffraction patterns shown in Figure 5-10.

In Figure 5-13 (b) the Raman spectrum for sample 5.1Zn-CaP shows a small peak/shoulder at *ca.* 999 cm^{-1} which persists for higher zinc loading samples. This corresponded to the appearance of $CaZn_2(PO_4)_2$ phase peaks in Figure 5-10 (b) for the same sample. The ν_1 vibration of this phase has been reported to occur at *ca.* 997 cm^{-1} for α and β-Hopeite (polymorphs of zinc phosphate tetrahydrates) (Herschke et al. 2006). Additionally, a Raman peak appeared at *ca.* 976 cm^{-1} in the corresponding spectrum for sample 32Zn-CaP in Figure 5-13 (h). This was possibly due to formation of zinc stabilised TCP (Zn-TCP) as the literature shows a very strong peak corresponding to the symmetric stretching (ν_1) of the P-O bond in TCP at *ca.* 970 cm^{-1}. The Raman spectrum of sample 32Zn-CaP shows extra peaks which were not observed for any other sample at 1795, 1608, 1424, 1292 and 1138 cm^{-1}. These are assigned to the presence of crystalline calcium zinc phosphate ($CaZn_2(PO_4)_2$) in the sample [as seen in Figure 5-10 (h)].

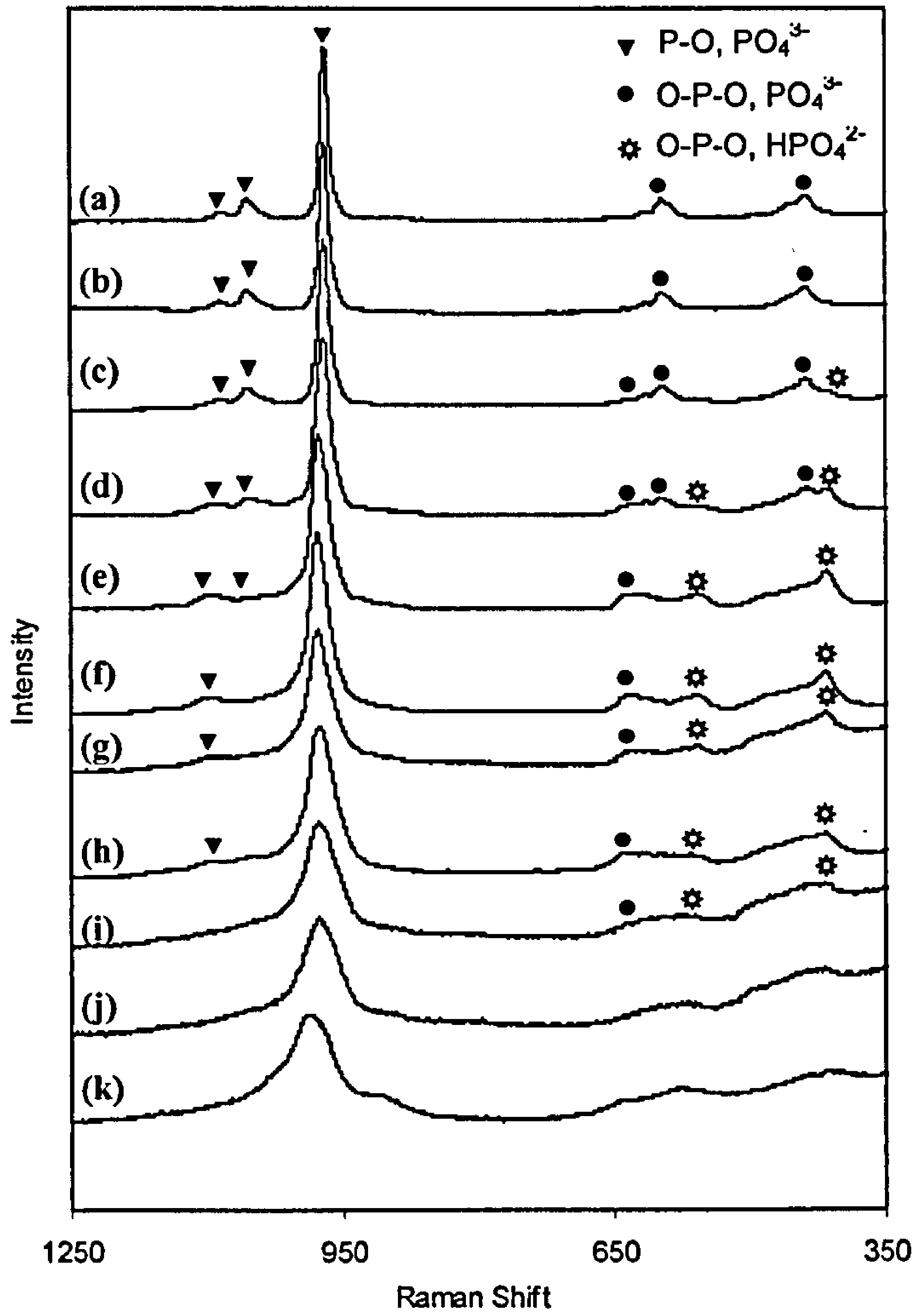

Figure 5-12 Raman spectra in the range 1250 – 350 cm^{-1} for samples (a) 0.5Mg-CaP (b) 1Mg-CaP (c) 1.5Mg-CaP (d) 2Mg-CaP (e) 4Mg-CaP (f) 6Mg-CaP (g) 8Mg-CaP (h) 10Mg-CaP (i) 12Mg-CaP (j) 14Mg-CaP and (k) MgP. **Note:** the peak corresponding to O-P-O bending of the HPO_4^{2-} group can be seen in Figure 5-12 (c) and increases for samples with higher magnesium substitution.

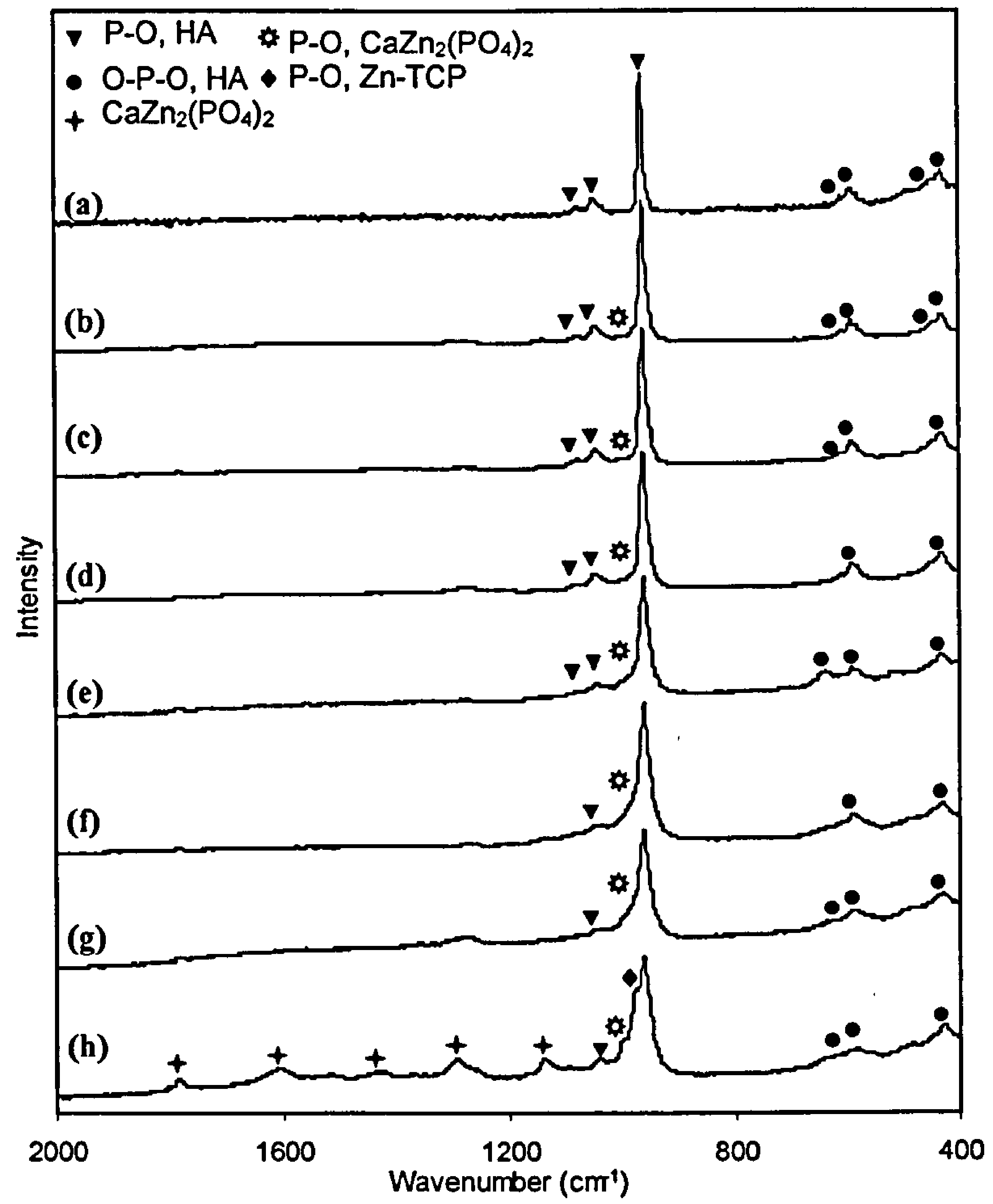

Figure 5-13 Raman spectra in the range 2000 – 400 cm^{-1} for samples (a) 1.3Zn-CaP (b) 5.1Zn-CaP (c) 10Zn-CaP (d) 14.7Zn-CaP (e) 19.3Zn-CaP (f) 23.7Zn-CaP (g) 28Zn-CaP and (h) 32Zn-CaP.

5.3.6 Fourier Transform Infrared Spectroscopy

The FTIR spectrum for sample 0.5Mg-CaP in Figure 5-14 (a) revealed peaks similar to those normally seen for hydroxyapatite; these include peaks at 3570 cm^{-1} (strong) and 636 cm^{-1} due to the stretching mode (υ_S) and the liberational mode (υ_L), respectively, of hydroxyl groups (Koutsopoulos 2002; Rehman & Bonfield 1997). In Figure 5-14 (A) the OH^{-1} peaks at *ca.* 3570 cm^{-1} were normalised with respect to the intensity obtained for this peak in first spectrum, i.e. for sample 0.5Mg-CaP. A band in the range 1150-990 cm^{-1} corresponded to asymmetric P-O stretching (υ_3) of the phosphate group, whilst a peak at 964 cm^{-1} corresponded to symmetric P-O stretching (v_1) of phosphate. The peaks at 605 and 567 cm^{-1} both corresponded to the υ_4 bending mode of the O-P-O linkage in phosphate, whilst the peak at 478 cm^{-1}, was due to the υ_2 bending mode of the O-P-O linkage in phosphate. The weak peak centered at ca. 872 cm^{-1} may be due to the bending mode (υ_2) of the O-C-O linkage of a minute amount of carbonate which may be present.

With an increase in magnesium content, for samples 0.5Mg-CaP to 2Mg-CaP there was a decrease in the intensity of hydroxyl peaks at 3570 and 633 cm^{-1} in the corresponding FTIR spectra. This was due to the onset of progessive Whitlockite formation (as suggested from the PXRD data) for samples 1Mg-CaP, 1.5Mg-CaP, 2Mg-CaP and 4Mg-CaP. The FTIR spectra for sample 6Mg-CaP and higher magnesium contents [as seen in Figures 5-14 (f) to (j)], revealed the phosphate band (range 1150 – 990 cm^{-1}) that became broader with increasing magnesium substitution. This coincided with a decrease in crystallinity of Mg-Whitlockite (as suggested from powder XRD data). There was also a decrease in the intensity of the phosphate peak at 964 cm^{-1} with increasing magnesium content (accompanying a decreasing amount of HA). For biphasic samples and phase pure Whitlockite [i.e. samples 1Mg-CaP to 14Mg-CaP, Figures 5-14 (b) to (j)], this peak may also be due to the presence of HPO_4^{2-}. Figure 5-14 (k) shows the FTIR spectrum for sample MgP. Bands centered at 3000 and 1650 cm^{-1} were observed due to the presence of adsorbed water molecules in the sample. The weak bands centered at 1450 and 870 cm^{-1} were assigned as the C-O stretching vibrations of a small amount of carbonate that may be present. Sample MgP showed phosphate group vibrations similar to those seen for other samples.

Figure 5-15 shows the FTIR spectra for all zinc substituted samples. All spectra showed peaks normally observed for HA. In Figure 5-13 (a) the FTIR spectrum for sample 1.3Zn-CaP revealed peaks at 3753 cm^{-1} and 3570 cm^{-1} corresponding to the asymmetric (ν_3) O-H stretching in water and stretching mode (υ_s) of the hydroxyl group in HA. Another peak at 633 cm^{-1} corresponded to the liberational mode (υ_L) of hydroxyl groups in HA (Koutsopoulos 2002; Rehman & Bonfield 1997). In the same spectrum a large broad band centered at *ca.* 3400 cm^{-1} and a weak broad peak centered at *ca.* 1650 cm^{-1} correspond to adsorbed water molecules and bending (ν_2) of water, respectively. Peaks in the range 1450-1380 cm^{-1} corresponded to asymmetric C-O stretching (ν_3) of carbonate which suggested that a small amount of carbonate may be present. The band in the range 1250-1000 cm^{-1} corresponded to the asymmetric P-O stretching (υ_3) in phosphate whilst a peak at 963 cm^{-1}, corresponded to symmetric P-O stretching (ν_1) of phosphate. The weak peak centered at *ca.* 875 cm^{-1} may be due to the bending mode (υ_2) of the O-C-O linkage in carbonate a small amount of which may be present. The peaks at 604 and 598 cm^{-1} correspond to the υ_4 bending mode of the O-P-O linkage in phosphate.

It was observed that increasing zinc content in samples resulted in a decrease in the intensity of the OH^{-1} peaks at *ca.* 3570 and 633 cm^{-1}. Furthermore, carbonate bands were only observed in the FTIR spectrum for sample 1.3Zn-CaP shown in Figure 5-15 (a). This suggested that with higher amount of zinc in the samples, carbonate uptake by the lattice was decreased. This trend is similar to that observed for magnesium substituted calcium phosphate samples mentioned earlier. The main band in the range 1250-1000 cm^{-1} (υ_3, P-O) was observed to become less distinct and broader. This corresponded to a decrease in crystallinity of the zinc substituted calcium phosphate samples as seen in Figure 5-10. This may also be due to appearance of additional HPO_4^{2-} peaks which are partially obscured (at *ca.* 1215 cm^{-1} and 961 cm^{-1} respectively).

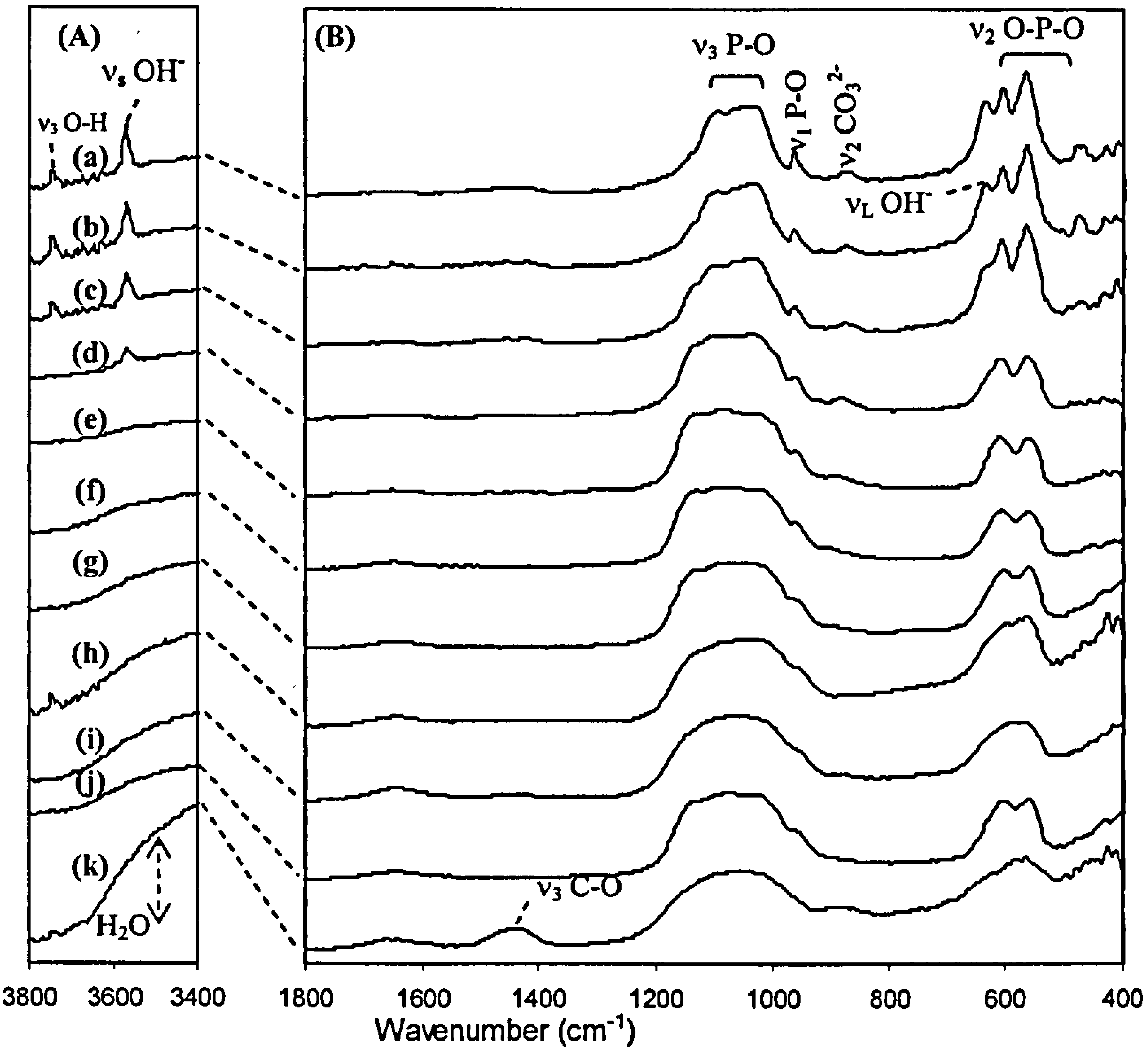

Figure 5-14 FTIR spectra in ranges (A) 3800 – 3400 cm^{-1} and (B) 1800 – 400 cm^{-1}, respectively, for samples (a) 0.5Mg-CaP (b) 1Mg-CaP (c) 1.5Mg-CaP (d) 2Mg-CaP (e) 4Mg-CaP (f) 6Mg-CaP (g) 8Mg-CaP (h) 10Mg-CaP (i) 12Mg-CaP (j) 14Mg-CaP and (k) MgP.

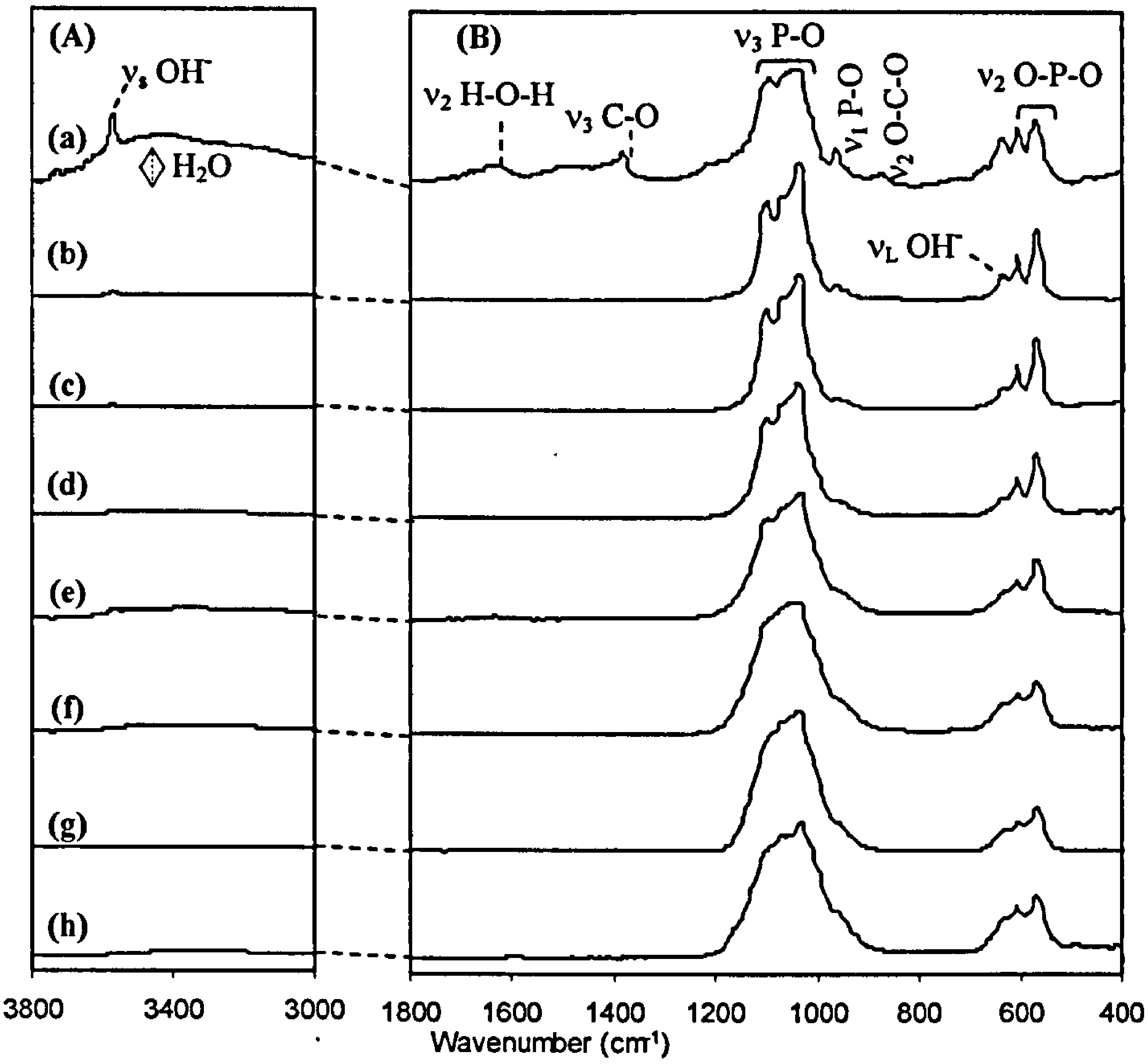

Figure 5-15 FTIR spectra in ranges (A) 3800 – 3000 cm^{-1} and (B) 1800 – 400 cm^{-1}, respectively, for samples (a) 1.3Zn-CaP (b) 5.1Zn-CaP (c) 10Zn-CaP (d) 14.7Zn-CaP (e) 19.3Zn-CaP (f) 23.7Zn-CaP (g) 28Zn-CaP and (h) 32Zn-CaP.

5.4 Conclusions

Phase-pure magnesium (0.7 wt% for sample 0.5 Mg-CaP) and zinc substituted hydroxyapatite (0.9 wt% for sample 1.3Zn-CaP) were synthesised using the CHFS technique. Conventionally required long ageing times and subsequent heat treatments were avoided and the apatites were obtained crystalline and phase-pure in a rapid single step method.

Increase in magnesium content significantly above 0.7 wt% (as measured) in our experiments led to precipitation of biphasic mixtures of Mg-βTCP/Whitlockite and magnesium substituted hydroxyapatite (starting from sample 1Mg-CaP). For a measured magnesium content of 5.8 wt% magnesium in sample 6Mg-CaP, phase-pure, crystalline magnesium Whitlockite [$Ca_{18}Mg_2H_2(PO_4)_{14}$] was obtained. Elemental analysis suggested that the calcium phosphates synthesised were non-stoichiometric. Further increases in magnesium content resulted in a decrease in crystallinity of magnesium substituted calcium phosphates and a *ca.* five fold increase in surface area. Increasing magnesium content affected the morphology of precipitating particles, beginning from roundening of HA-rods till the precipitation of very small nano-sized (<50 nm) seemingly hollow spherical particles which were amorphous magnesium Whitlockite. Rietveld refinement confirmed the presence of magnesium ions in the HA lattice and the both the lattice parameters (c and a) decreased with increasing substitution of magnesium into HA.

Above a measured zinc content of 0.9 wt% in zinc substituted calcium phosphate samples from our experiments, biphasic mixtures of a calcium zinc phosphate phase [$CaZn_2(PO_4)_2$] and zinc substituted hydroxyapatite were precipitated. Although a biphasic mixture was still observed for sample 32Zn-CaP (16.4 wt% zinc), the relative amount and crystallinity of calcium zinc phosphate phase appeared to increase.

A wide range of phase-pure cation substituted apatites and their biphasic mixtures were synthesised using the CHFS system in a rapid, single step manner. Coupled with the synthesis of anion doped calcium phosphates, this work elaborates the versatility of the CHFS system. Wherein, pure and ion substituted calcium phosphates can be synthesised with tailorable properties, such as crystallinity, composition, surface area, particle size, thermal stability and varying levels of non-stoichiometry. Therefore, the CHFS system is a versatile and useful tool for the syntheses of nano-bioceramics. To further exploit the CHFS technique syntheses of HA based ceramic composite mixtures were planned. It was hypothesised that the CHFS system will enable synthesis of intimately mixed composite mixtures which may ultimately lead to enhanced mechanical properties. The results of these endeavours are reported in the following sections.

5.5 Future Work

Coupled carbonate and magnesium substitutions in HA synthesised in the CHFS system would be interesting. Such coupled substitutions have been reported to enhance the thermal stability of HA. As mentioned in the previous chapter, it would be interesting to correlate system parameters such as flow rates (and hence residence times), temperature and pressure with the substitution levels in HA. Dissolution/SBF related work is also suggested for these materials in order to show enhanced dissolution of biphasic mixtures of HA and TCP related phases co-precipitated in the CHFS systems.

Chapter 6

Spark Plasma Sintering of Nano-Bioceramics using Continuous Hydrothermal Flow Synthesis Technique

6.1 Introduction

Hydroxyapatite [HA, $Ca_{10}(OH)_2(PO_4)_6$] is a synthetic ceramic chemically similar to biological apatite, the mineral component of bone (Hench 1998a; Hench 1998b; Hench 2000). It has been utilised, as reinforcement in biomedical polymers, as a coating on metallic implants and as a scaffold material for bone growth (Hench 1998a; Hench 1998b; Hench 2000; Katti 2004). Indeed, HA has found success in hard tissue surgery as it is bioactive whilst being relatively insoluble and able to bond to surrounding natural tissue (Caria et al. 2007; Storck et al. 2007). Due to its inferior mechanical properties (wear resistance, strength etc.), use of HA in load bearing applications is limited and has been used exclusively in low stress areas of the human body (e.g. ossicles in the middle ear) (Heimann & Vu 1997). In order to overcome the mechanical limitations of HA, reinforcing agents such as zirconia, alumina and titania particles, and carbon and stainless steel fibres, have been used (Kim et al. 2003a; Kong et al. 2005; Oktar et al. 2006; Roeder et al. 2003; Viswanath & Ravishankar 2006; White et al. 2007). Mostly large additions of these reinforcements are required to yield significant increase in mechanical performance (e.g. high flexural strength) (Ahn et al. 2005). In most cases, this also requires high sintering temperatures and long treatment times. In particular small amounts of ZrO_2 additions (*ca.* 1.5 wt%) to HA powders have been shown to improve bending strength (3-pt) of dense discs drastically (183 to 243 MPa) (Ahn et al. 2005). ZrO_2-HA formulations have therefore, been exploited as robust coatings for biomedical applications (Balamurugan et al. 2007; Suzuki et al. 2006).

HA-ZrO_2 ceramics are normally sintered from mixtures of separately synthesised HA and ZrO_2 powders (Adolfsson et al. 2000; Chiu et al. 2007; Evis et al. 2006; Guo et al. 2003a; Kim et al. 2002b; Kim et al. 2002a; Kim et al. 2003b; Kumar et al. 2005; Li et al. 1996; Mansur et al. 1998; Matsuno et al. 2003; Miao et al. 2004; Rao & Kannan 2002; Zhang et al. 2006) or from co-precipitated powders (Rapacz-Kmita et al. 2004;

Silva et al. 2001a; Silva et al. 2001b; Silva et al. 2002; Silva & Lameiras 2000; Sung et al. 2007; Sung & Kim 2003; Whited et al. 2006). A room temperature co-precipitation method has been reported to result in homogeneously mixed particles of ZrO_2 and HA, which are easily compacted and sintered (Silva & Domingues 1997). Traditionally, hydroxyapatite requires up to 18 hours of maturation time (to obtain the correct 1.67 stoichiometry) after precipitation and is followed by a subsequent heat-treatment at temperatures above 600 °C for crystallisation (Phillips et al. 2003). Indeed, co-precipitation of HA-ZrO_2 nanoparticles also requires long ageing periods (up to 17 hours) and a subsequent heat-treatment is required (up to 1000 °C) (Rapacz-Kmita et al. 2004; Sung et al. 2007). Hence, there is considerable interest in faster and homogeneous routes to ZrO_2-HA co-precipitates.

The sintering or densification of these powders has also been the subject of considerable literature. Conventionally, consolidation of HA based ceramics is carried out using pressure-less sintering or hot-pressing. Pressure-less sintering involves sintering at high temperatures (above 1200°C) for long periods of time (1-4 hours) (Barralet et al. 2003; Cai et al. 2007; Guo et al. 2003b; Kothapalli et al. 2004; Laquerriere et al. 2003; Mostafa 2005; Nayar et al. 2006; Pramanik et al. 2007; Zhang et al. 2007). This technique involves extremely slow heating rates (around 5 °C/min) (Kothapalli et al. 2004; Mostafa 2005; Pramanik et al. 2007). Exposure to such elevated temperatures for prolonged times results in large grain sizes of a few microns and sometimes phase decomposition can occur (Barralet et al. 2003; Nayar et al. 2006; Pramanik et al. 2007). It is difficult to attain full-densification of HA ceramics using pressure-less sintering (Kothapalli et al. 2004; Mostafa 2005). For this reason, glass (31 mol% Na_2O, 24 mol% CaO, 45 mol% P_2O_5) has been used as a sintering aid in HA (Knowles et al. 1996). However, in contrast to pressure-less sintering, hot-pressing has been reported to yield denser HA ceramics (~ 95% theoretical sintered density) at temperatures up to 1250 °C (10 °C/min), pressures up to 64 MPa and sintering times ranging from 1-4 hours (Bianco et al. 2007; Kobayashi et al. 2006).

As well as pure HA there is a great deal of interest in sintering HA based composites with other reinforcing ceramics such as ZrO_2 and this has been the subject of substantial literature as well. Conventional methods of consolidation of HA-ZrO_2 powders also include pressure-less sintering (up to 1500°C and 4 hours) (Chiu et al. 2007; Delgado et al. 1999; Evis et al. 2006; Heimann & Vu 1997; Kim et al. 2002b; Mansur et al. 1998;

Rao & Kannan 2002; Silva et al. 2001a; Towler et al. 2000; Zhang et al. 2006) and hot-pressing (up to 1225°C, 160 MPa and 1 hour) (Adolfsson et al. 2000; Evis & Doremus 2007; Inuzuka et al. 2004; Li et al. 1996; Matsumoto et al. 2002; Matsuno et al. 2000; Sung et al. 2007). The high temperatures and long sintering periods required for these methods, result in grain sizes up to a several microns (HA up to 5 µm, ZrO_2 up to 3 µm) (Silva et al. 2001a). If smaller grain sizes could be obtained for HA and HA-ZrO_2 composites they would be expected to show superior mechanical performance (flexural strength, hardness, wear resistance etc.) as also predicted by Hall-Petch law (which states that yield strength of a material is indirectly proportional to grain size).

Recently, consolidation of ceramics using spark plasma sintering (SPS) has gained importance due to the speed of this method and ability to control grain growth. Samples can be sintered at lower temperatures under pressure using rapid heating and cooling rates for extremely small sintering times (few minutes); resulting in nanostructured ceramics (Munir et al. 2006). Indeed, consolidation of HA to very high densification has been carried out using SPS (Gu et al. 2002; Guo et al. 2005; Khalil et al. 2007; Omori et al. 2006; Watanabe et al. 2005; Xu et al. 2005; Xu et al. 2007; Xu & Khor 2007). Vickers hardness up to 6 GPa have been reported for HA sintered using SPS (Gu et al. 2002; Xu et al. 2005; Xu & Khor 2007). The flexural strength (3-pt) of hydroxyapatite sintered in a spark plasma furnace has been reported to be *ca.* 85 MPa (Shi et al. 2006) which compares to 55 MPa for HA sintered conventionally at 1250 °C for two hours (Pramanik et al. 2007). However, in an earlier publication in 2004, Miao and co-workers reported a higher 3-pt flexural strength of 110 MPa for HA spark plasma sintered at 1000 °C for 5 minutes (Miao et al. 2004). Pramanik and co-workers had used HA synthesised using co-precipitation which was heat-treated before sintering (Pramanik et al. 2007). Miao and co-workers on the other hand used commercially available HA. Slightly higher values of conventionally sintered HA were reported by Chen and co-workers. In their work, HA was sintered at 1250 °C for 2 hours to result in a *ca.* 2 µm grain size, 85% sintered density and 85 MPa 3-pt flexural strength (Chen et al. 2008).

Moreover, there have been some reports of ZrO_2-HA ceramics sintered using SPS at temperatures and sintering times as low as 1000°C and 5 minutes (Guo et al. 2003a; Kumar et al. 2003; Kumar et al. 2005; Miao et al. 2004; Shen et al. 2001). In a report on spark plasma sintering of zirconia-hydroxyapatite composite powders, the Vickers hardness and flexural strength varied between 5.4 GPa and 94 MPa, respectively, for pure sintered HA, to 14.2 GPa and 929 MPa, respectively, for pure sintered zirconia (Shen et al. 2001). Miao and co-workers were able to obtain a 3-pt flexural strength of 200 MPa for 40 wt% YSZ (yttria stabilised zirconia) in HA. The composite was sintered to 93% theoretical density in 5 minutes at 1200 °C and the HA grain size exceed 1 μm (Miao et al. 2004).

Most low temperature methods for the synthesis of phase-pure hydroxyapatite or composite mixtures of hydroxyapatite and a second reinforcing phase, are multi-step, time consuming methods. Moreover, the powders synthesised are amorphous as made and they require ageing and heat-treatment to attain stoichiometry and crystallinity as explained in previous chapters. In chapters 3, 4 and 5 the CHFS of phase-pure and ion doped calcium phosphates and co-precipitates was reported. As the CHFS method can give access to very small size for intimately mixed HA and other phases, the rapid consolidation to retain a small grain size via SPS should offer access to dense nanostructured ceramics.

This chapter addresses the synthesis of phase-pure hydroxyapatite in large quantities (to sustain powder consuming sintering studies) and its consolidation using a SPS furnace. Effect of reagent solution concentration on thermal stability of resulting apatites was also discussed. Furthermore, the sintering cycle was optimised to yield fully dense, phase-pure, non-cracked disc shaped samples. The co-precipitation of HA and calcium doped zirconia (CDZ) mixtures (with varying contents of ZrO_2) in the CHFS system and their subsequent consolidation using a SPS furnace is also discussed. The thermal stability of these composite powders was assessed using in-situ variable temperature X-ray diffraction up to 1200 °C. The sinterability of selected compositions (from previous chapters) for ion-substituted calcium phosphates is also discussed in this chapter. Selected discs were also tested for Vickers hardness and 3-pt bending strength.

6.2 Experimental Data

6.2.1 Synthesis of Hydroxyapatite for SPS

HA for spark plasma sintering was synthesised using two different Ca:P molar ratios in solution (1.67 and 2.0). For a 1.67 ratio, 83.50 mM calcium nitrate solution (adjusted to pH 11 using neat ammonium hydroxide) was reacted with 50 mM diammonium hydrogen phosphate solution (adjusted to pH 10 using ammonium hydroxide) in the CHFS system. This sample was labelled ℓ-HA(450)* where ℓ represents the 1.67 (low) ratio, 450 °C is the synthesis temperature and * denotes the use of a band heater.

For a 2.0 ratio, 100.0 mM calcium nitrate solution (adjusted to pH 11 using ammonium hydroxide) was reacted with 50.0 mM diammonium hydrogen phosphate solution (adjusted to pH 10 by adding ammonium hydroxide) in the CHFS. This sample was labelled *m*-HA(450)* where *m* represents the 2.0 (medium) ratio, 450 °C is the synthesis temperature and * denotes the use of a band heater.

Details of amounts of reagents used and solution preparation for all these reactions are mentioned in section 2.2.2.4 (a).

6.2.2 Synthesis of CDZ-HA Mixtures

CDZ-HA mixtures were synthesised using two different Ca:P molar ratios in solution (1.67 and 2.5). In total, seven reactions were carried out for this study.

For a ratio of 1.67, two identical 83.5 mM calcium nitrate solutions were prepared. Different amounts of zirconyl nitrate were added to both these solutions such that they would result in 25 wt% and 50 wt% ZrO_2 in HA (calculated theoretically). A 50.0 mM stock solution of diammonium hydrogen phosphate (adjusted to pH 10 using ammonium hydroxide) was used. These samples are labelled as L-25 and L-50 (where L represents a lower Ca:P molar ratio of 1.67 and the number represents the theoretically calculated weight percentage of zirconia in the mixture).

For a ratio of 2.5, four identical solutions of 125.0 mM calcium nitrate were prepared. Zirconyl nitrate was added to each of these four calcium nitrate solutions separately (pH 2 for all four solutions). These corresponded to expected 5 wt%, 10 wt%, 25 wt% and 75 wt% ZrO_2 in HA, respectively (amounts were theoretically calculated). A stock solution of 50.0 mM diammonium hydrogen phosphate solution (adjusted to pH 10 using ammonium hydroxide) was used. These samples are labelled as H-5, H-10, H-25 and H-50 (where H represents a higher Ca:P molar ratio of 2.5 and the number represents the theoretically calculated weight percentage of zirconia in the mixture). Another sample was prepared by dissolving calcium nitrate and zirconyl nitrate together to result in an overall 400.0 mM concentration (pH 2). 1.0 M KOH solution (pH 14) was also used. This sample is labelled as H-100 (H in this case represents excess calcium).

Details of amounts of reagents used and solution preparation for all these reactions are mentioned in section 2.2.2.4 (b).

6.2.3 Synthesis of Ion-Substituted Calcium Phosphate Powders

In total eight reactions were carried out for this study which included six ion-substituted and two HA samples (with 1.67 and 2.0 in-solution Ca:P molar ratio). The samples are labelled as $7.5CO_3$-HA$^{\phi}$ [solution preparation explained in section 2.2.2.2 (a)], 5Si-HA$^{\phi}$ [see section 2.2.2.2 (b)], 0.5Mg-CaP$^{\phi}$, 1.5Mg-CaP$^{\phi}$, 6Mg-CaP$^{\phi}$ [see 2.2.2.3 (a)] and 1.3Zn-CaP$^{\phi}$ [see section 2.2.2.3 (b)]. The two HA samples were prepared as described earlier in section 2.2.2.4 (a). The reagent concentrations and method of solution preparation was exactly similar to that for samples with identical sample IDs. However, in this case, the $^{\phi}$ suffix represents different CHFS parameters (faster flow rates and use of a mixing zone heater).

All the samples mentioned in the current chapter [details in section 2.2.2.4] were synthesised using flow rates of 25, 12.5 and 12.5 ml min^{-1} for superheated water feed, calcium nitrate (mixed with corresponding substituting ion source or zirconyl nitrate) and diammonium hydrogen phosphate (mixed with corresponding substituting ion source) solutions, respectively. For sample H-100, the third flow rate of 12.5 mL min^{-1} represents the pumping rate of KOH solution. The synthesis temperature was set at 450 °C while the small 200 W band heater in the mixing zone was also adjusted to 450 °C. All samples were centrifuged, washed and freeze-dried as explained earlier; see section 2.2.2.1 (b). However, sample *m*-HA(450)* [mentioned in 2.2.2.4 (a)] required centrifugation at 5000 rpm for 20 minutes. The heating rate and pressure during sintering were 200 C min^{-1} and 100 MPa respectively, in all the cases. Other SPS parameters (time, temperature, cooling rate, point of application and/or removal of force) are discussed within the results and discussion section of this chapter.

6.2.4 Spark Plasma Sintering of HA and 10 wt% CDZ-HA Ceramics for 3-pt Flexural Strength Determination

Large discs (40 mm diameter) of samples *m*-HA(450)* and H-10 were spark plasma sintered for this study. 10.0 g of HA and 10.5 g of H-10 were used for each disc.

Typical yields for 1000 mL of reagents pumped to react in the CHFS were *ca.* 7.7 g. This required 80 minutes of pumping time to obtain a suspension from the CHFS system which was then washed, centrifuged and freeze dried prior to spark plasma sintering. From sample *m*-HA(450)* two discs each, were sintered at 950 and 1000 °C. Additionally, two discs of sample H-10 were sintered at 1000 °C. All samples were sintered for 5 minutes 15 seconds using a 40 mm graphite die. The discs were then cut into 25 x 3 x 2 mm rectangular strips using a diamond cutter for 3-pt flexural strength determination according to ASTM standard 1161. Prior to testing, all flexural test samples were polished as described in section 2.3.10.2.

6.3 Results and Discussion

6.3.1 Synthesis, Characterisation and SPS of Hydroxyapatite

6.3.1.1 Electron Microscopy

Transmission electron microscopy was used to assess the particle size and morphology of HA prior to sintering. Distinct crystalline nano-rods *ca.* 166 (± 62) x 39 (± 14) nm in size [50 particles sampled] can be seen in Figure 6-1 for sample *ℓ*-HA(450)*. In chapter 3, the particles size of similar rods for sample HA(400) was reported to be *ca.* 140 (± 58) x 40 (± 12) nm (aspect ratio *ca.* 3.5, 50 particles sampled). This difference was due to higher pre-heater temperature (450 °C instead of 400 °C) and also due to the presence of a band heater in the mixing zone which maintained a high temperature and possibly affected the growth and crystallisation of these rods. This reasoning was supported by BET surface area measurements. The surface areas were measured to be 22 m^2 g^{-1} and 24 m^2 g^{-1} for samples *ℓ*-HA(450)* and *m*-HA(450)* respectively, which are lower compared to 39 m^2g^{-1} for sample HA(400). The change in Ca:P molar ratio from 1.67 to 2.0 (in solution) caused no measurable change in the surface area of the particles.

The Ca:P molar ratios for powder samples *ℓ*-HA(450)* and *m*-HA(450)* measured using an EDS detector attached to a SEM were 1.39 (± 0.04) and 1.42 (± 0.03), respectively (see Table 6-1). In comparison, HA(400) as discussed in chapter 3, had a Ca:P molar ratio of 1.57 (± 0.06). This difference was due to a shortened residence time of 3.9 seconds (due to faster flow rates) for samples *ℓ*-HA(450)* and *m*-HA(450)* as compared to 9.9 seconds (due to slower flow rates) for sample HA(400), respectively.

Table 6-1 Samples IDs, elemental composition (atomic %) as average values of 10 area scans and corresponding Ca:P molar ratios. SD represents standard deviation.

Sample ID	**Atomic %**			**Ca:P (± SD)**
	Ca	**P**	**O**	
ℓ-HA(450)*	11.92	7.78	79.49	1.39 (±0.04)
m-HA(450)*	13.08	8.26	77.73	1.42 (±0.03)

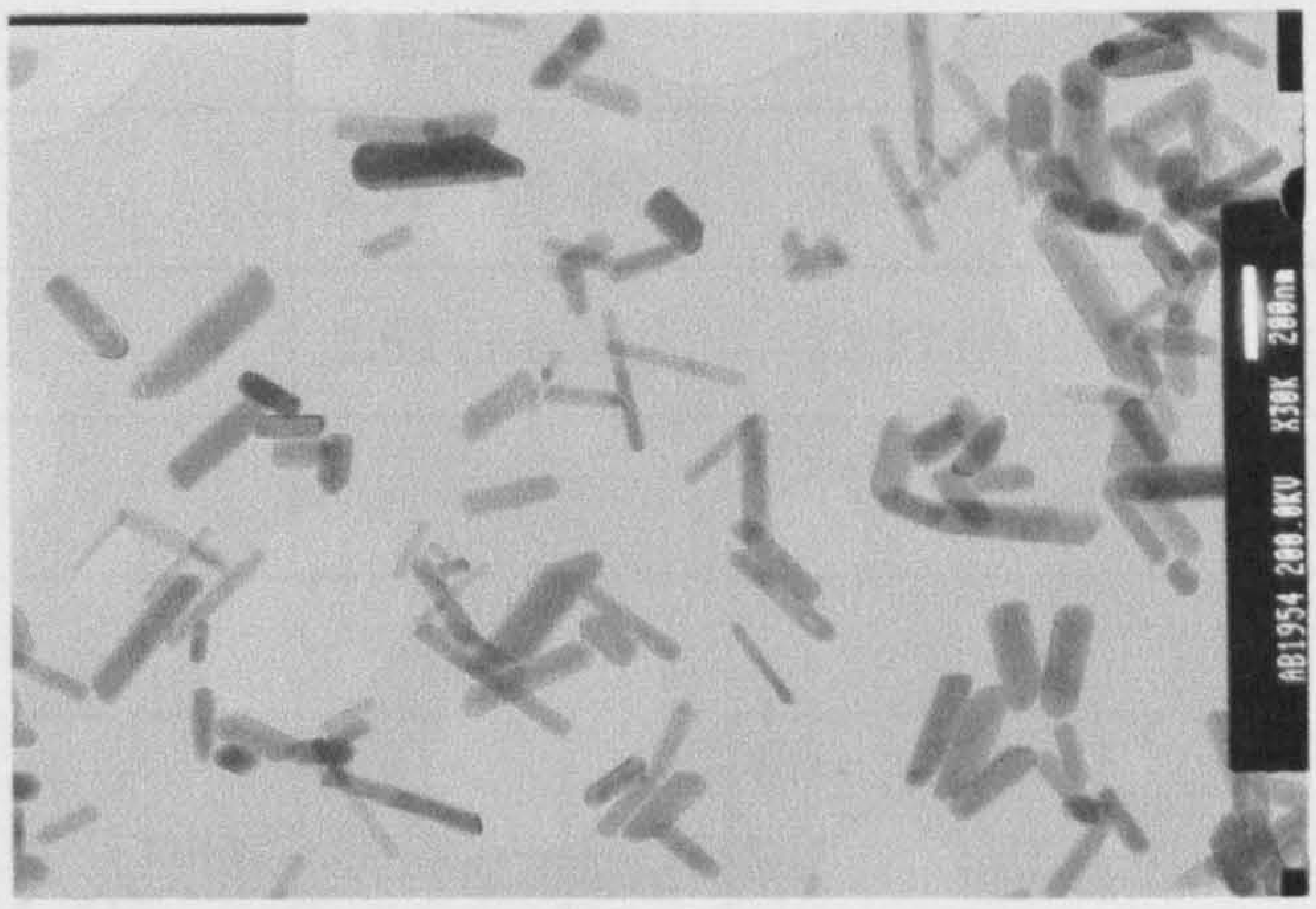

Figure 6-1 Transmission Electron Microscope (TEM) image of sample *ℓ*-HA(450)* at x30k magnification [bar = 200 nm].

Initially, five discs using sample *ℓ*-HA(450)*, 20 mm in diameter (2.0 g powder per disc), were consolidated in the spark plasma sintering furnace at 750 °C, 850 °C, 950 °C, 1000 °C and 1050 °C. The sintered densities are shown in Table 6-2. The heating rate and pressure during sintering were 200 °C min^{-1} and 100 MPa (31.4 kN force), respectively, for all discs. The cooling rate was 225 °C min^{-1} for all discs (sintering regime 1) except the one sample sintered at 1000 °C where the cooling rate was 50 °C min^{-1} (see Figure 6-2 for sintering regimes 1 and 2). It was observed that some samples with a cooling rate of 225 °C min^{-1} cracked and a cooling rate of 50 °C min^{-1} resulted in an un-cracked sample. The sample sintered at 750 °C underwent little or no consolidation and hence crumbled when handled.

Table 6-2 Sintering temperatures of the SPS furnace, corresponding densities and % theoretical densities of discs sintered from sample ℓ-HA(450)*. ξ "Cracked" refers to when sintered discs were found to be cracked into two or three pieces. Ψ "crumbled" refers to when sintered discs cracked into many pieces, as if crushed.

Sintering temperature	**Density (g/cm^3)**	**% theoretical density**	**Comments**
1050	3.16 (± 0.07)	100.00 (± 2.14)	Cracked$^{\xi}$
1000	3.02 (± 0.04)	95.68 (± 1.26)	Intact
950	2.98 (± 0.05)	94.27 (± 1.67)	Cracked$^{\xi}$
850	2.62 (± 0.04)	82.87 (± 1.19)	Intact
750	-	-	Crumbled$^{\Psi}$

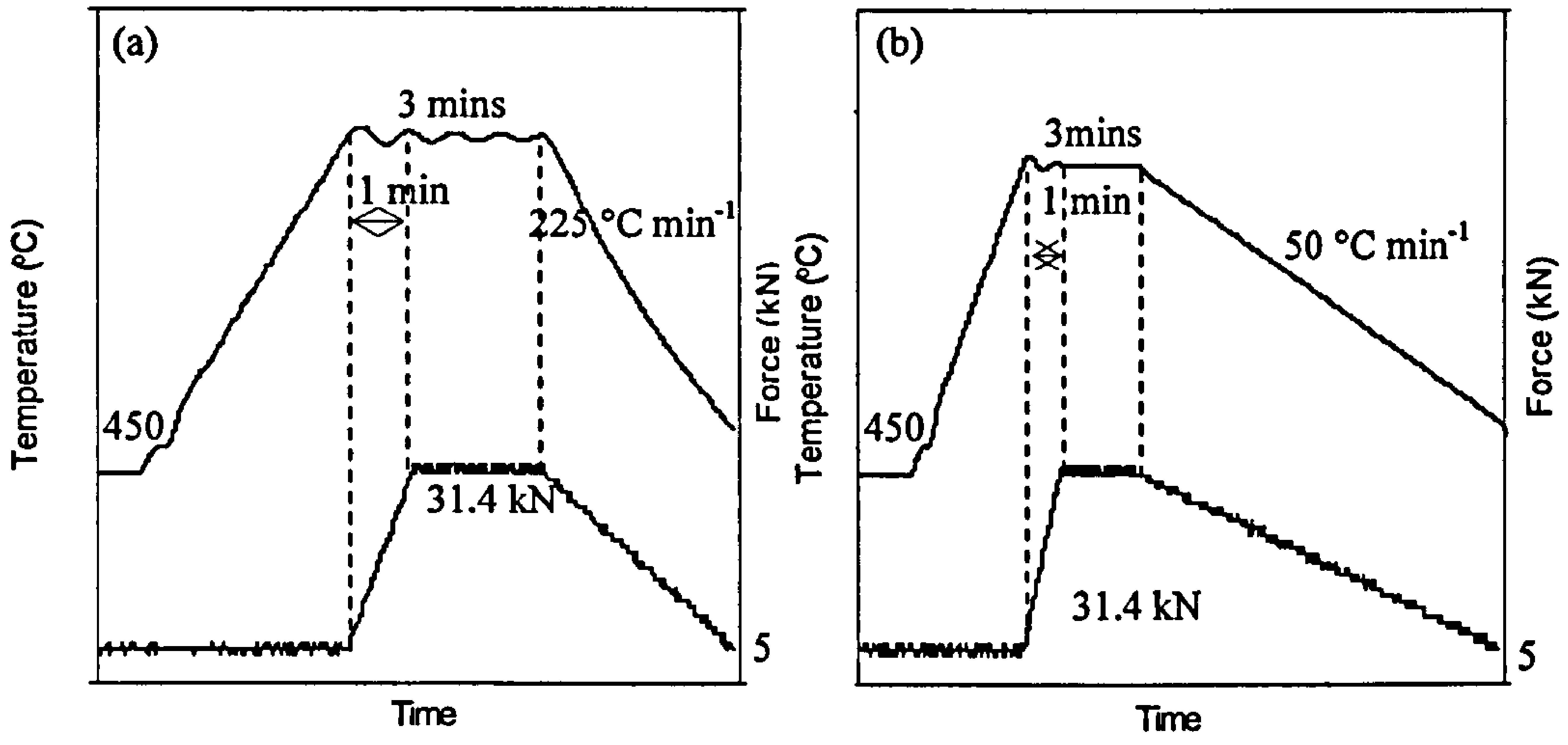

Figure 6-2 Temperature and load variation with time for spark plasma sintering cycles (a) 1 and (b) 2.

HA synthesised in CHFS system 3 was sintered conventionally in a box furnace for 2 hours at 800, 900 and 1000 °C (details in Appendix F). The heating and cooling rates were 2.5 °C min^{-1}. This resulted in sintered densities of 48%, 51% and 60%, respectively. Thus, conventional sintering of CHFS HA resulted in inferior ceramics as compared to spark plasma sintered HA.

Microstructures of fractured surfaces of spark plasma sintered discs were observed under a scanning electron microscope as shown in Figures 6-3 (a) to (f). Figures 6-3 (a) and (b) showed sub-micron features [range 150-400 nm; avg. 232 nm (± 60 nm); 20 grains sampled] on the disc sintered at 1050 °C. The SEM images reveal minimal porosity, in agreement with the measured *ca.* 100% theoretical density. Figures 6-3 (c) and (d) revealed HA sintered at 1000°C to have a grain size in the range *ca.* 150 – 400 nm [avg. 285 nm (± 82 nm); 20 grains sampled]. However, more porosity was observed in the disc sintered at 1000°C as compared to the one sintered at 1050°C as visible in Figure 6-3 (b). Figures 6-3 (e) and (f) revealed the sample sintered at 950°C to be more porous with an average grain size of *ca.* 188 nm [± 22 nm; 20 grains sampled]. This grain size was small as, at this temperature, full densification and grain growth had not taken place. The SEM images were therefore, in rough agreement with the densities measured using the Archimedes' principle as shown in Table 6-2.

6.3.1.2 Powder X-ray Diffraction

Powder X-ray powder diffraction studies were carried out to identify phases and assess the phase-purity and crystallinity of HA powders and sintered discs. Figures 6-4 (a) to (f) show XRD patterns of discs sintered at 1050 °C, 1000 °C, 950 °C and 850 °C and powder samples ℓ-HA(450)* and HA(400). The patterns shown in Figures 6-4 (e) and (f) gave a good match to phase-pure crystalline HA [compared to JCPDS pattern 09-432]. However, it was observed that sample ℓ-HA(450)* showed sharper peaks in comparison to those for HA(400), due to the higher crystallinity of the former.

In Figures 6-4 (a) to (d) the XRD patterns for discs sintered at 1050 °C, 1000 °C, 950 °C and 850 °C, respectively, using powder sample ℓ-HA(450)* are shown. The major phase in samples sintered in the temperature range 950 – 1050 °C was HA except a very small amount of α-tricalcium phosphate (compared to JCPDS pattern 09-348) as shown in Figures 6-4 (a) to (c). This was possibly due to non-stoichiometry in the precipitated sample [Ca:P molar ratio of 1.39 for powder sample ℓ-HA(450)*]. Indeed calcium deficient apatites have been reported to decompose into tricalcium phosphates above 750 °C (this temperature increases with higher stoichiometry) (Kannan & Ferreira 2006). The disc sintered at 850 °C revealed phase-pure HA as shown in Figure 6-4 (d). Evidently, the calcium deficient HA, despite the calcium deficiency, is stable at this temperature.

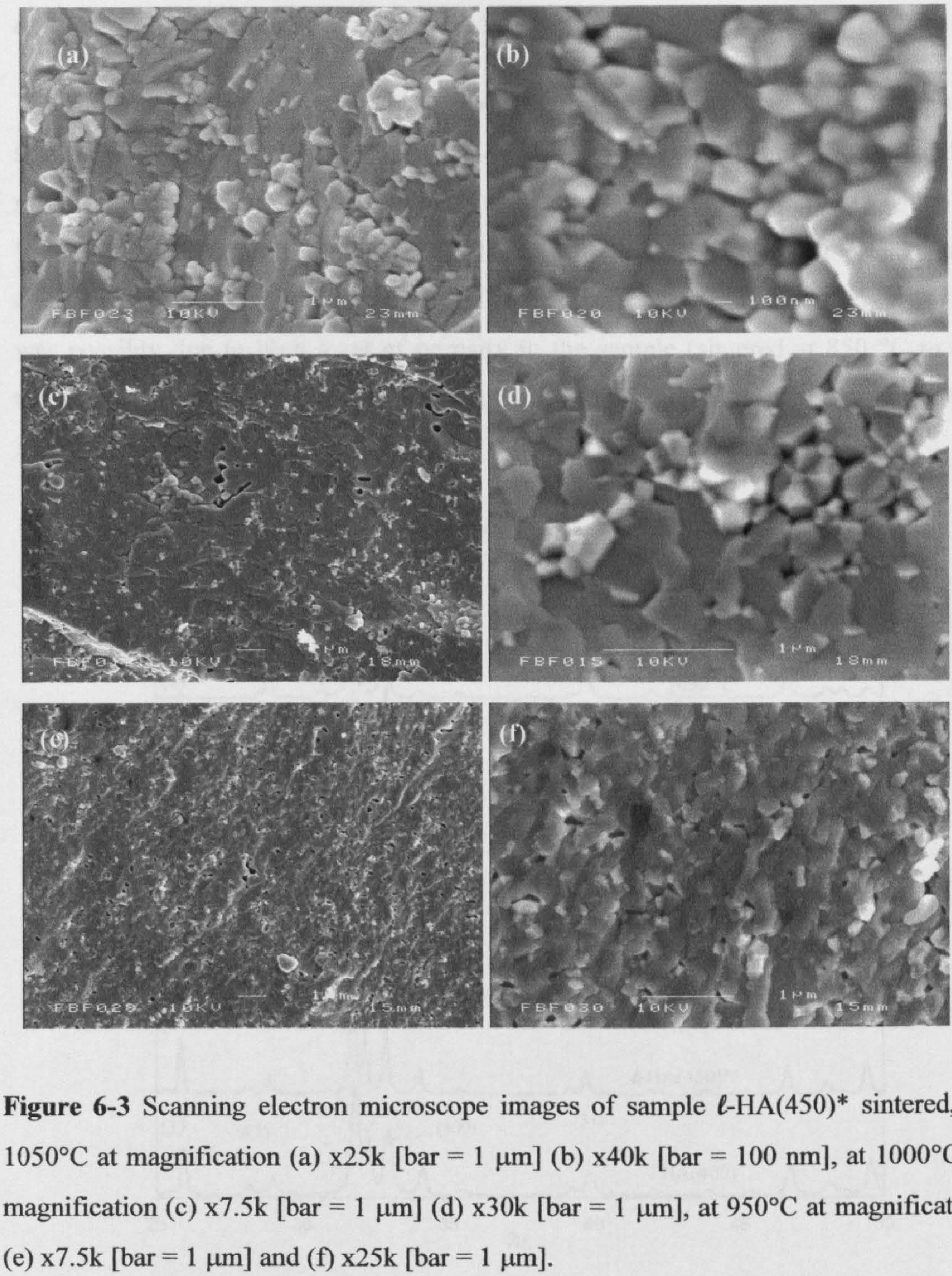

Figure 6-3 Scanning electron microscope images of sample ℓ-HA(450)* sintered, at 1050°C at magnification (a) x25k [bar = 1 μm] (b) x40k [bar = 100 nm], at 1000°C at magnification (c) x7.5k [bar = 1 μm] (d) x30k [bar = 1 μm], at 950°C at magnification (e) x7.5k [bar = 1 μm] and (f) x25k [bar = 1 μm].

It was also observed that after sintering (SPS) the peaks corresponding to (002) and (112) planes decreased in intensity and peaks corresponding to (300) and (310) planes increased in intensity. This was due to the decrease in the aspect ratio of HA rods, as seen in Figure 6-1, upon sintering which symbolises particle growth and coalescence.

6.3.1.3 Microhardness

The hardness of sintered samples was analysed using micro indentation with a diamond shaped Vickers indentation tip. Figure 6-5 (a) to (d) revealed diamond shaped indents made on discs sintered (SPS) at 1050 °C, 1000 °C, 950 °C and 850 °C which had Vickers hardness values of 5.7, 5.5, 5.4 and 1.8 GPa, respectively (measured using equation 2-3 shown in section 2.3.10.1). The elongated shape of indent in Figure 6-5 (d) was possibly due to high level of porosity in the sample (sintered at 850 °C to 83% theoretical density). Overall, it was observed that the hardness of the sintered discs increased with sintered density.

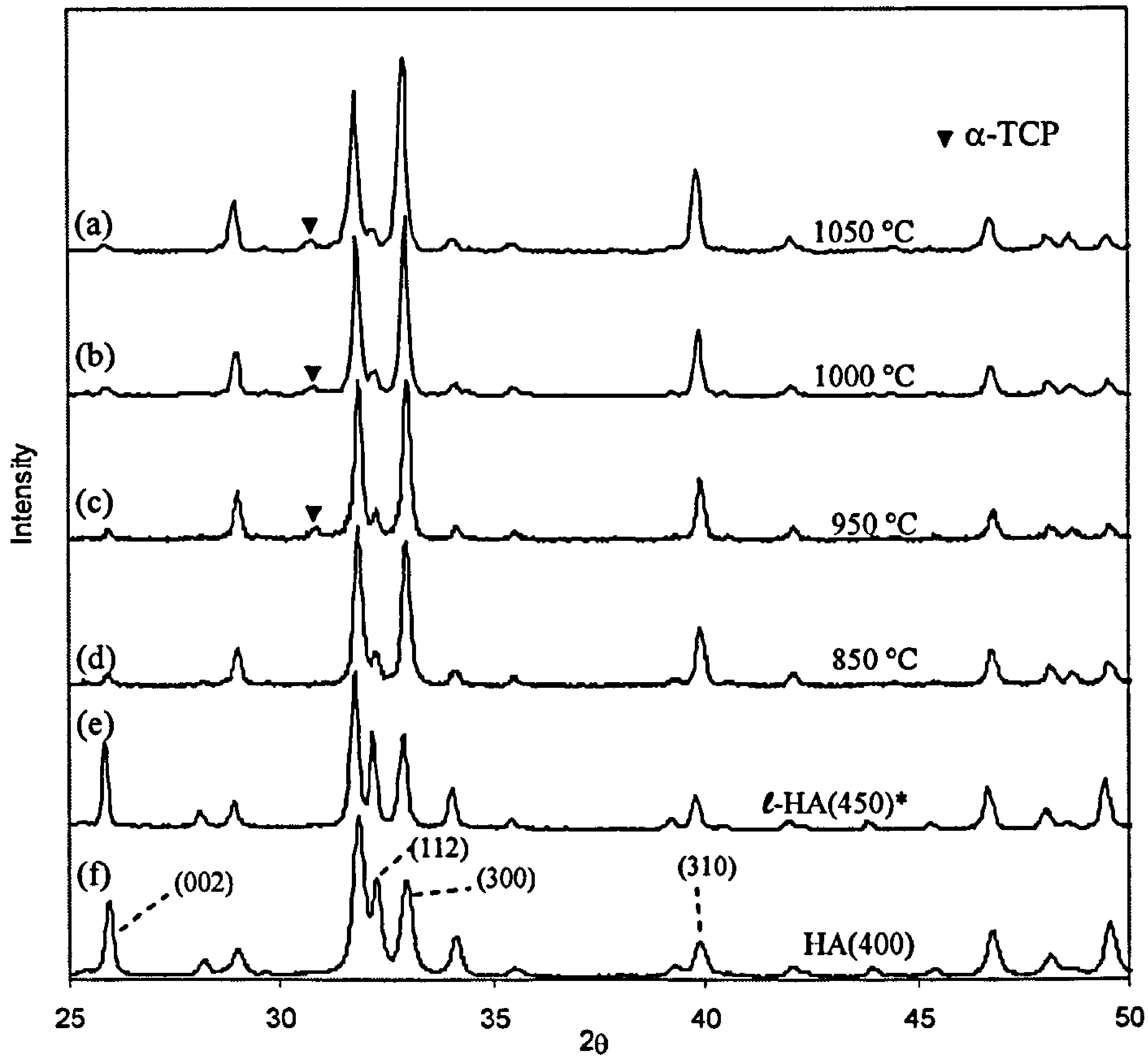

Figure 6-4 Powder X-ray powder diffraction patterns of, discs spark plasma sintered at (a) 1050 °C (b) 1000 °C (c) 950 °C and (d) 850 °C and HA powder samples (e) ℓ-HA(450)* and (f) HA(400).

Figure 6-2 shows sintering regimes 1 and 2 for sample ℓ-HA(450)* sintered at 1050, 950, 850 and 750 °C. As almost all these discs were found to be cracked when extracted from the graphite die, a similar sintering regime, with a slower cooling rate of 50 °C min^{-1} was used in an attempt to reduce the "thermal shock" and hence avoid brittle failure of the sintered discs. The figures show the temperature variation with time above 450 °C as the pyrometer attached to the SPS furnace was not able to read temperatures lower than this value. Moreover, a slight oscillation (*ca.* ±10 °C) in temperature was observed as the set sintering temperature was achieved in the furnace. This oscillation decreased with increasing time. This was attributed to variation in conduction due to movement of upper and lower punches of the graphite die with the application of pressure and also relative motion caused by shrinkage of the discs during sintering. A minimum load of 5 kN was always maintained on the die containing the HA powder and this load was increased, as the temperature reached the required sintering temperature, to 31.4 kN in one minute and then maintained for two minutes. The load applied was gradually decreased to 5 kN, the minimum load possible in the SPS furnace, matching the time taken to reduce the temperature to 450 °C. Beyond this point graphite die was rapidly water cooled using an in-built cooling system and extracted from the furnace when the temperature was low enough for handling (~ 70 °C).

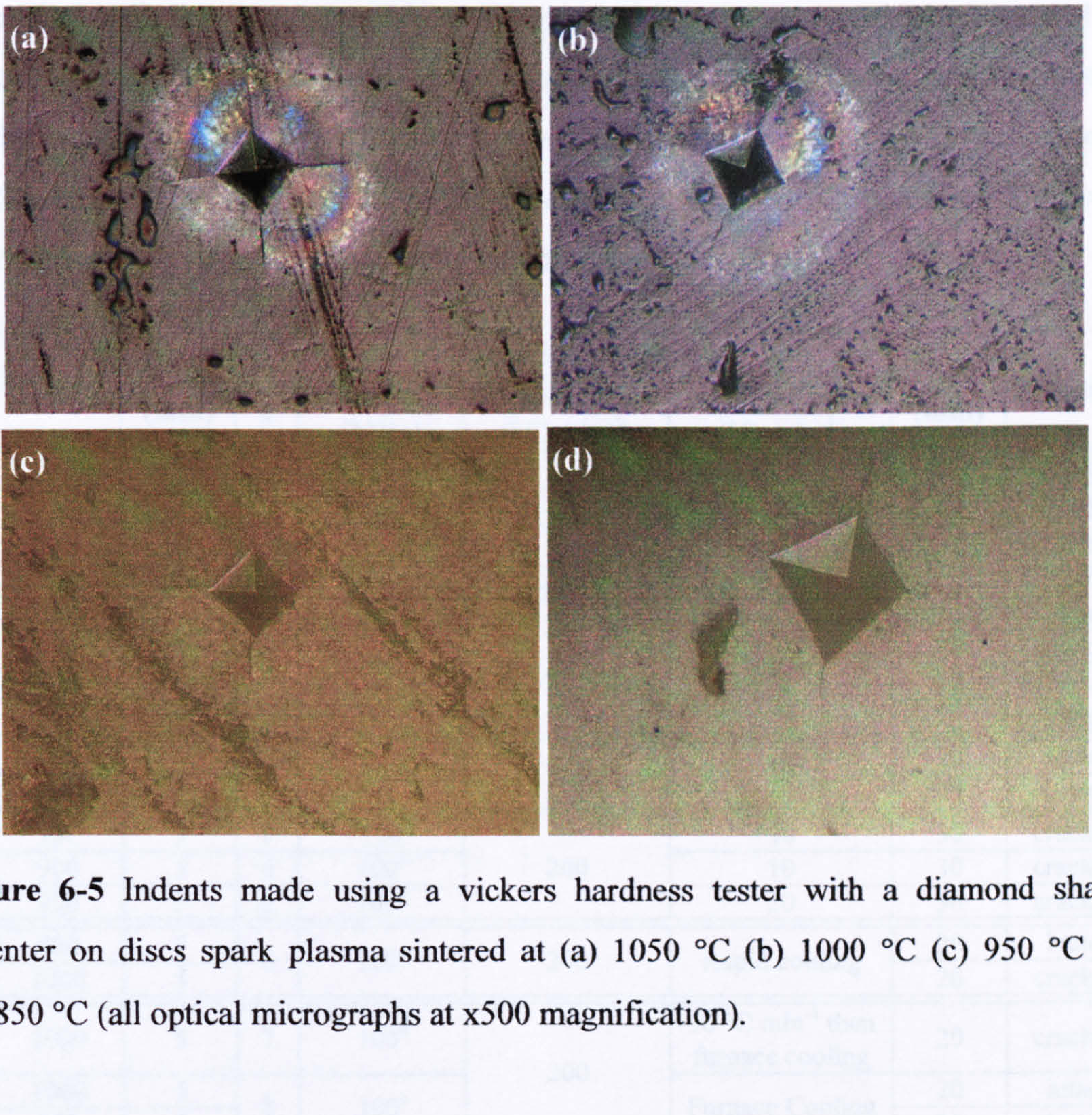

Figure 6-5 Indents made using a vickers hardness tester with a diamond shaped indenter on discs spark plasma sintered at (a) 1050 °C (b) 1000 °C (c) 950 °C and (d) 850 °C (all optical micrographs at x500 magnification).

6.3.1.4 Optimisation of the Sintering Cycle

As discussed earlier, sintering carried out using sintering cycle 1 [shown in Figure 6-2 (a)] resulted in dense but cracked discs (using 20 mm graphite die). All the discs cracked in a similar brittle fashion; into two or three pieces. The sintering cycle 2 [shown in Figure 6-2 (b)], at 1000 °C, resulted in an intact disc. Therefore, discs were sintered at 950, 900 and 850 °C using sintering cycle 2, for 5 minutes (using 20 mm die). The sintering time was increased in order to obtain denser sintered discs at lower temperature. However, the discs sintered at 950 and 900 °C cracked. The disc sintered at 850 °C remained intact (similar to the previous case where sintering cycle 1 was used). This temperature is apparently low enough not to cause thermal cracking. During optimisation of the sintering cycle, certain parameters remained unchanged; 1) the heating rate was always 200 °C min^{-1} 2) the force was applied when the temperature reached the set sintering temperature and 3) it took 1 minute for the force to increase from 5 kN to 31.4 kN for a 20 mm die and 70.7 kN for a 30 mm die.

Table 6-3 Sintering temperature and time, corresponding sintering cycles and their details, die diameter and status of the extracted discs after sintering [Force reduced to 5kN, ^{a} = by 650 °C, ^{b} = by 800 °C, ^{c} = in 30 seconds during 50 °C min^{-1} cooling followed by rapid cooling, ^{d} = in 20 seconds during 50 °C min^{-1} cooling followed by furnace cooling, ^{e} = in 15 seconds followed by furnace cooling].

T (°C)	Time (min)	Sintering Cycle				Die ϕ (mm)	Status
		#	Pressure (MPa)	Heating rate (°C min^{-1})	Cooling rate (°C min^{-1})		
1050	3	1	100	200	225	20	Cracked
950	3					20	Cracked
850	3					20	intact
750	3					20	crumbled
1000	5	2	100	200	50	20	intact
950	5					20	cracked
900	5					20	cracked
850	5					20	intact
950	5	3	100	200	20	20	intact
900	5					20	intact
900	5	3	100	200	20	30	cracked
900	5	4	100^{a}		10	30	cracked
900	5	5	100^{b}		20	30	cracked
900	5	6	100^{c}	200	Rapid cooling	20	intact
1000	5					20	cracked
1000	5	7	100^{d}	200	50 °C min^{-1} then furnace cooling	20	cracked
1000	5	8	100^{e}		Furnace Cooling	20	intact
950	5					20	intact

The sintering cycle was further modified to have a cooling rate of 20°C min^{-1} and HA was sintered at 950 and 900 °C for 5 mins (using 20 mm die) [sintering cycle 3 shown in Figure 6-6 (a)]. Both these discs remained intact however, when the same cycle was used to sinter a 30 mm sample at 900 °C for 5 minutes, the sample cracked. It was hypothesised that the cooling rate was too fast and the difference in thermal expansion coefficients of graphite and hydroxyapatite resulted in cracking. It was also considered that in addition to the cooling rate, the release of force on the die may be a contributing factor to cracking as well. Therefore, the sintering cycle was further modified to have a cooling rate of 10 °C min^{-1} and HA was sintered at 900 °C for 5 minutes (using 30 mm die). The force was maintained at 70.7 kN (100 MPa) and while cooling, it was decreased to 5 kN as the temperature dropped to 650 °C [sintering cycle 4 as shown in Figure 6-6 (b)]. Below this temperature the die cooled down with minimum force applied to it. However, this sample was found to be cracked after extraction as well.

The sintering cycle was modified again to sinter HA at 900 °C for 5 minutes under 70.7 kN force (100 MPa pressure on a 30 mm die) with a cooling rate of 20 °C min^{-1}. However, this time the force on the die was brought to a minimum as the die cooled down to 800 °C [sintering cycle 5 shown in Figure 6-6 (c)]. Below this temperature the die cooled down with minimum force applied to it. This sample too, was found to be cracked.

Another HA disc was sintered at 900 °C for 5 minutes under 31.4 kN force (100 MPa load on a 20 mm die). After completion of 5 minutes the die was first cooled at a relatively slow cooling rate, 50 °C min^{-1} for 15 seconds, during which the force was decreased to 5 kN. After this point the die was rapidly cooled down to room temperature within a few minutes [sintering cycle 6 shown in Figure 6-6 (d)]. It was thought that a slow cooling rate coupled with a gradual decrease in force followed by "compaction free" cooling might result in an intact sample. After extraction the dense sintered disc was found to be intact and totally crack free. However, use of a similar sintering cycle for sintering at 1000 °C for 5 minutes resulted in a cracked disc. Nonetheless, these results showed that the key to obtaining crack free samples was the early removal of force.

Another HA disc was sintered at 1000 °C for 5 minutes under 31.4 kN force (100 MPa on 20 mm die) with a further modified force cycle during cooling. After the completion of 5 minutes sintering time, the force was decreased to 5 kN while maintaining a cooling rate of 50 °C min^{-1}. Once the force was down to 5 kN the die was allowed to cool down in the furnace without interference. This is referred to as furnace cooling (takes approximately 20 minutes to cool down to below 100 °C) [sintering cycle 7 as shown in Figure 6-6 (e)]. This disc was found to be cracked.

It was decided that the die would be unloaded while it was at the sintering temperature and then furnace cooled. Two additional HA discs were sintered at 1000 and 900 °C, respectively, for 5 minutes under 31.4 kN (100 MPa pressure for a 20 mm die). After the 5 minutes were complete, the temperature was maintained for 15 more seconds as the die was unloaded to 5 kN. Therefore, the net sintering time was 5 minutes 15 seconds. Once under minimum force (5 kN) the die was furnace cooled (sintering cycle 8, shown in Figure 6-6 (f)]. On extraction both discs were found to be intact. More discs were sintered using the same sintering cycle at 950 and 900 °C for 5 minutes and 15 seconds using a 30 mm die. They too, were found to be intact and completely crack free. For all the sintering cycles, discs sintered at 1000 °C or above, were transparent, as shown in Figure 6-7. This confirms that the grain size is smaller than the wavelength of light (i.e. 400 – 700 nm) as a result of which light can travel through the sintered disc (Fang et al. 1995). The transparency also suggests that the sintered densities are almost 100% theoretical density (because pores scatter light).

Sintering of sample ℓ-HA(450)* at 1050, 1000 and 950 °C lead to slight decomposition of HA into α-TCP, as shown in corresponding XRD patterns in Figure 6-4. Therefore, sample *m*-HA(450)* (Ca:P molar ratio of 1.42) was then sintered at 1000 and 900 °C for 5 minutes 15 seconds using sintering cycle shown in Figure 6-6 (f). The sintered densities were *ca.* 100, and 99 % respectively, and the discs were intact and completely crack free. X-ray diffraction was used to assess the phase purity of these samples and corresponding XRD patterns in Figures 6-8 (a) and (b) revealed phase-pure HA with no signs of any other decomposition product. Figure 6-8 (c) shows the XRD pattern of sample *m*-HA(450)* revealing phase-pure HA. This proved that although the Ca:P molar ratios of samples ℓ-HA(450)* and *m*-HA(450)* were slightly different (1.39 and 1.42 respectively), the difference was sufficient to make *m*-HA(450)* thermally stable up to 1000 °C in the SPS furnace. The Ca:P molar ratios of samples ℓ-HA(450)* and *m*-HA(450)* sintered at 900 °C were both found to *ca.* 1.58 (±0.01). This suggested that evaporation of HPO$_4$ groups during sintering might have occurred which resulted in an increase in Ca:P molar ratio. The peaks corresponding to (002), (112), (300) and (310) planes in the HA lattice showed similar trends as observed in Figure 6-4.

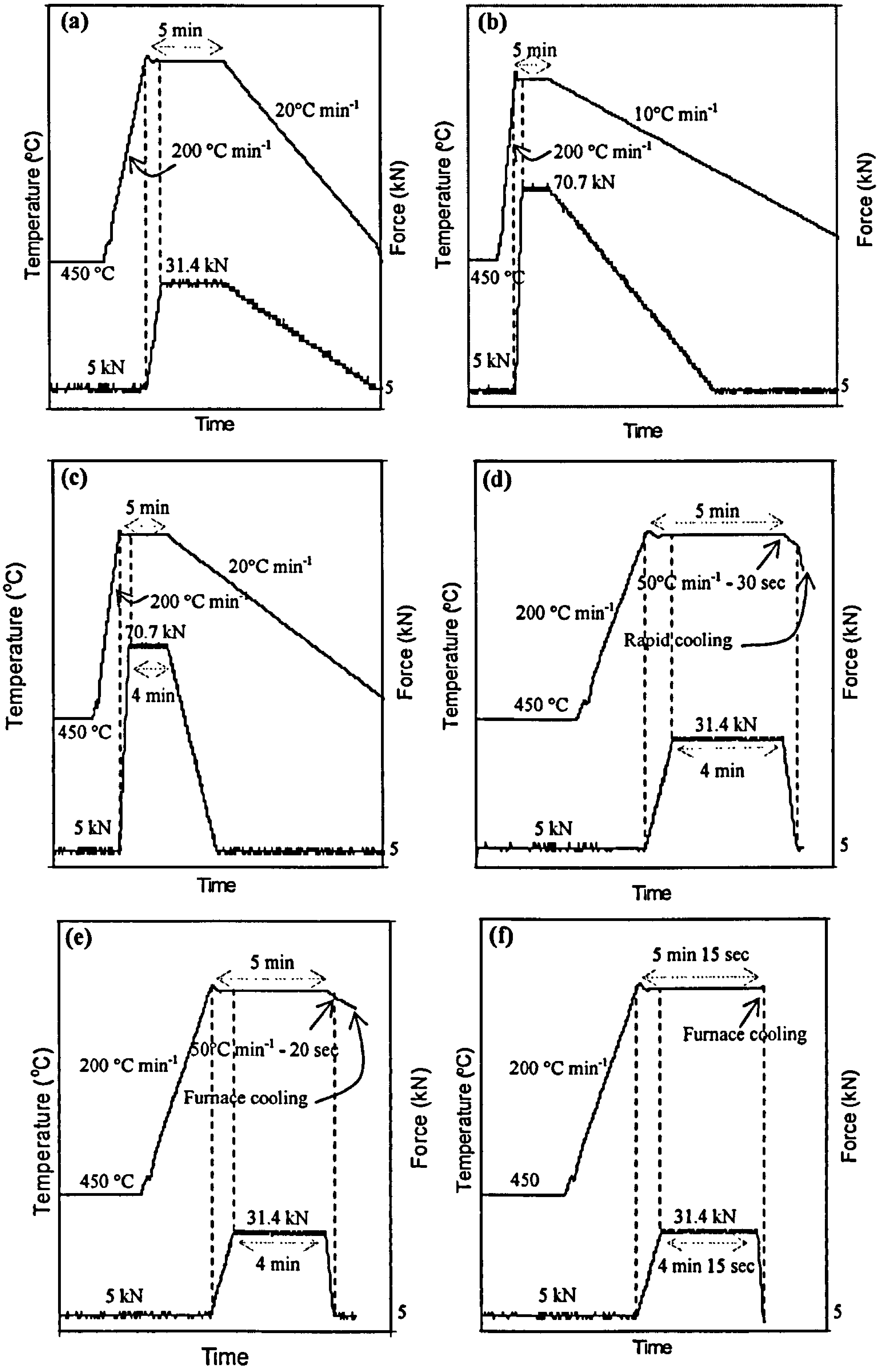

Figure 6-6 Temperature and load variation for spark plasma sintering cycles (a) 3 (b) 4 (c) 5 (d) 6 (e) 7 and (f) 8.

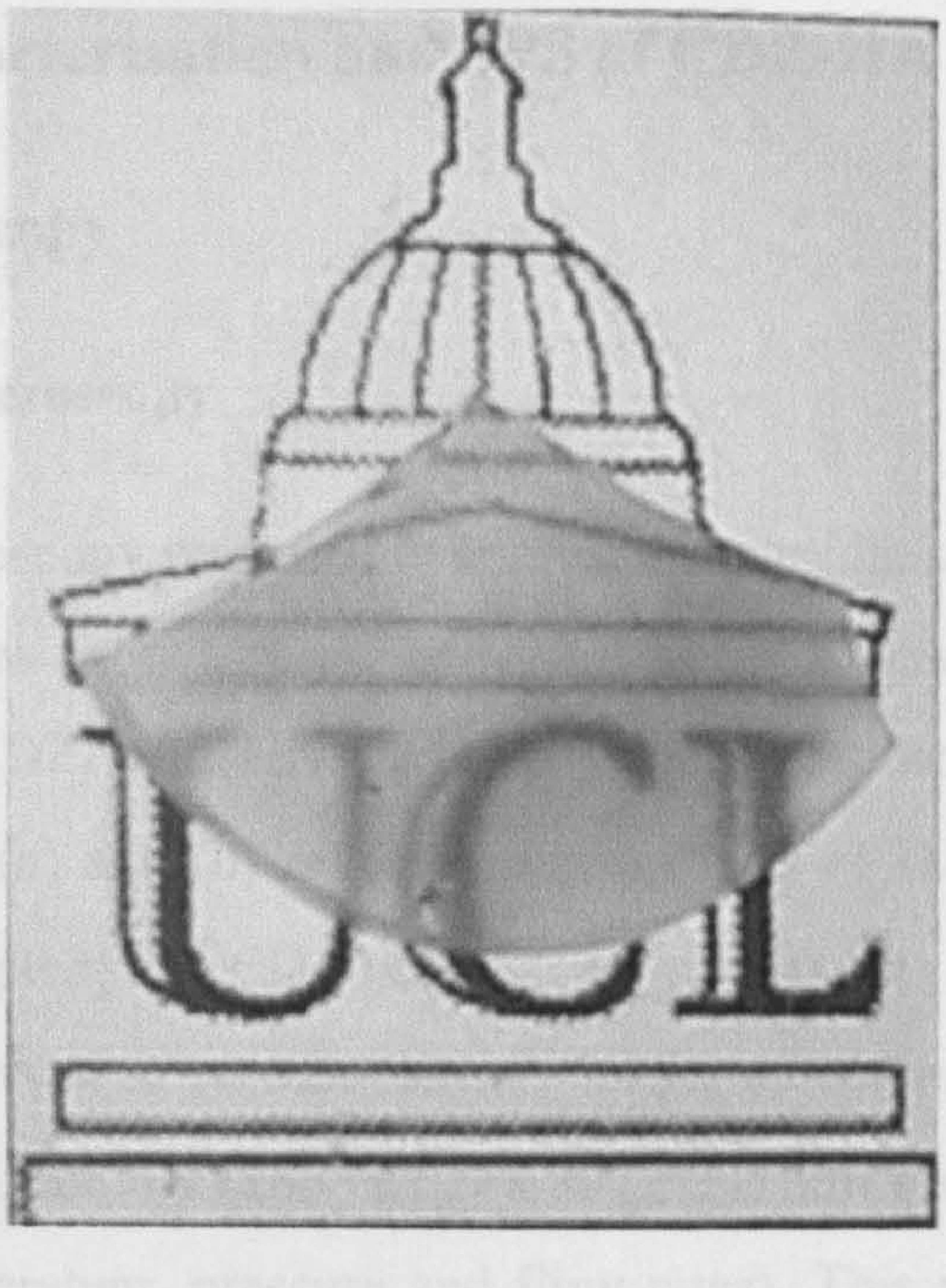

Figure 6-7 Transparent HA disc portion spark plasma sintered at 1000 °C for 5 minutes.

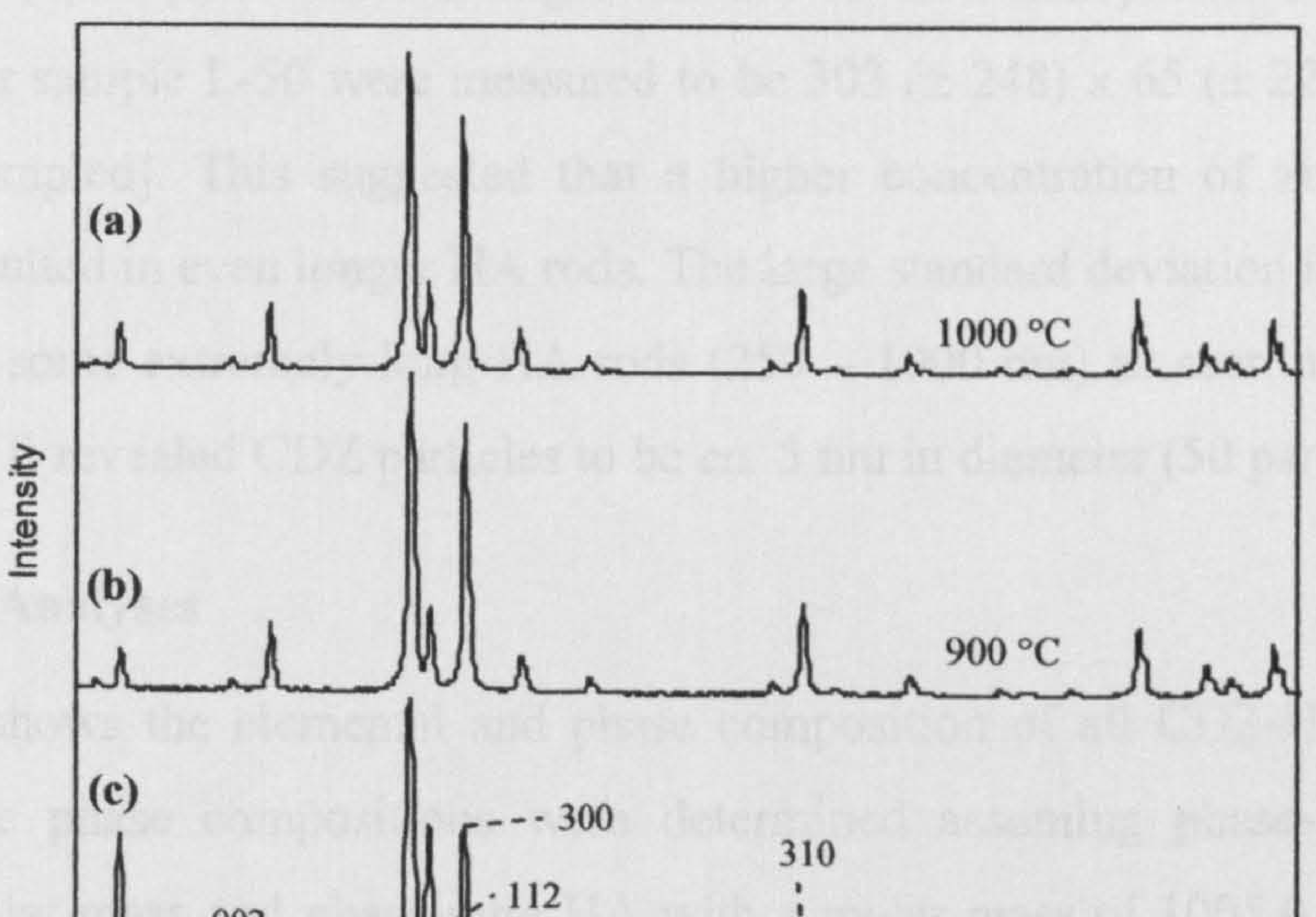

Figure 6-8 Powder X-ray diffraction patterns of discs sintered (a) 1000 °C and (b) 900 °C from (c) sample ***m***-HA(450)*.

6.3.2 Synthesis, Characterisation and SPS of CDZ-HA Mixtures

6.3.2.1 Electron Microscopy

Transmission Electron Microscopy

Transmission electron microscopy was used to analyse the particle size and morphology of samples L-25 and L-50 as show in Figures 6-9 (a) to (f). It was observed that both calcium doped zirconia (CDZ) and HA particles largely retained their independent morphologies. Figures 6-9 (a) and (b) revealed distinct rods of HA [270 (± 75) x 58 (± 19) nm: 50 particles sampled] and CDZ nanoparticles (< 10 nm). The HA rods in the presence of CDZ were observed to be considerably longer as compared to those shown for sample *ℓ*-HA(450)* in Figure 6-1 [166 (± 62) x 39 (± 14) nm] for otherwise identical synthesis parameters (temperature, pressure and flow rates). This was possibly due to preferential growth of HA in the [001] direction in the presence of zirconium ions. Figures 6-9 (c) to (f) revealed a larger amount of CDZ nanoparticles in sample L-50. HA rods for sample L-50 were measured to be 303 (± 248) x 65 (± 22) nm in size [50 particles sampled]. This suggested that a higher concentration of zirconium ions in solution resulted in even longer HA rods. The large standard deviation in average length was due to some extremely long HA rods (250 – 1000 nm) as seen in Figure 6-9 (c). Figure 6-9 (f) revealed CDZ particles to be *ca.* 5 nm in diameter (50 particles sampled).

Elemental Analyses

Table 6-4 shows the elemental and phase composition of all CDZ-HA samples. The approximate phase compositions were determined assuming phase-pure ZrO_2 with 123.2 g molar mass and phase-pure HA with a molar mass of 1005.0 g. This exercise revealed the observed phase compositions to be quite similar to the theoretically expected values. For sample H-100 the empirical formula was calculated to be $Ca_{0.26}Zr_{0.74}O_y$.

6.3.2.2 BET Surface Area Analysis

The BET technique (N_2 adsorption) was used to measure the surface area of all powders in this study (as shown in Figure 6-10). Samples L-25 and L-50 had surface areas of 81.8 m^2 g^{-1} and 165.3 m^2 g^{-1}, respectively. Samples H-5, H-10, H-25 and H-50 had surface areas of 41.3 m^2 g^{-1}, 54.1 m^2 g^{-1}, 94.8 m^2 g^{-1} and 177 m^2 g^{-1}, respectively. It was noticed that the increase in surface area with amount of CDZ in the as-precipitated mixture was nearly linear. This is understandable because CDZ has a higher surface area. Several TEM images of the mixtures can be seen in Figure 6-10. It was also observed that a higher in-solution Ca:P molar ratio, resulted in higher surface area of the as-precipitated mixtures as represented by the difference in the solid and dotted line in Figure 6-10.

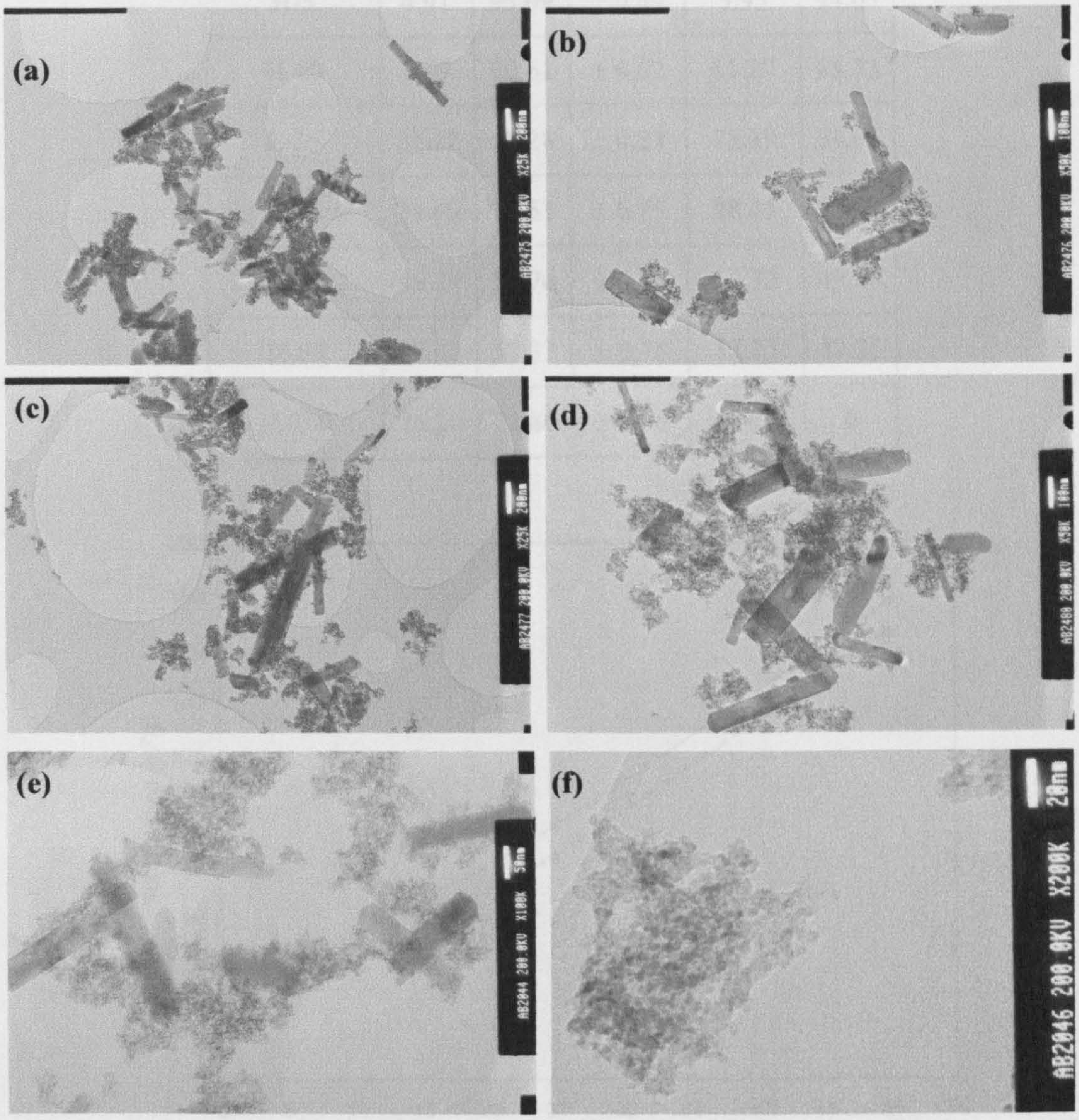

Figure 6-9 Transmission electron microscope images of, sample L-25 at (a) x25k magnification [bar = 200 nm] (b) x50k magnification [bar = 100 nm] and sample L-50 at (c) x25k magnification [bar = 200 nm] (d) x50k magnification [bar = 100 nm] (e) x100k magnification [bar = 50 nm] and (f) x200k magnification [bar = 20 nm].

Table 6-4 Samples IDs, corresponding measured elemental (atomic %) and phase (weight %) composition as average values of 10 different area scans using an EDS detector attached to a SEM. SD represents standard deviation.

Sample ID	Atomic %			Wt%	
	Zr	Ca	SD	ZrO2	HA
H-5	4.91	95.09	± 0.40	5.95	94.05
H-10	9.39	90.61	± 0.62	11.27	88.73
L-25	21.72	78.28	± 0.23	25.39	74.61
H-25	24.49	75.51	± 0.75	28.45	71.55
L-50	45.24	54.76	± 0.39	50.32	49.68
H-50	47.67	52.33	± 0.76	52.75	47.25
H-100	26.20	73.80	± 1.06	100	0

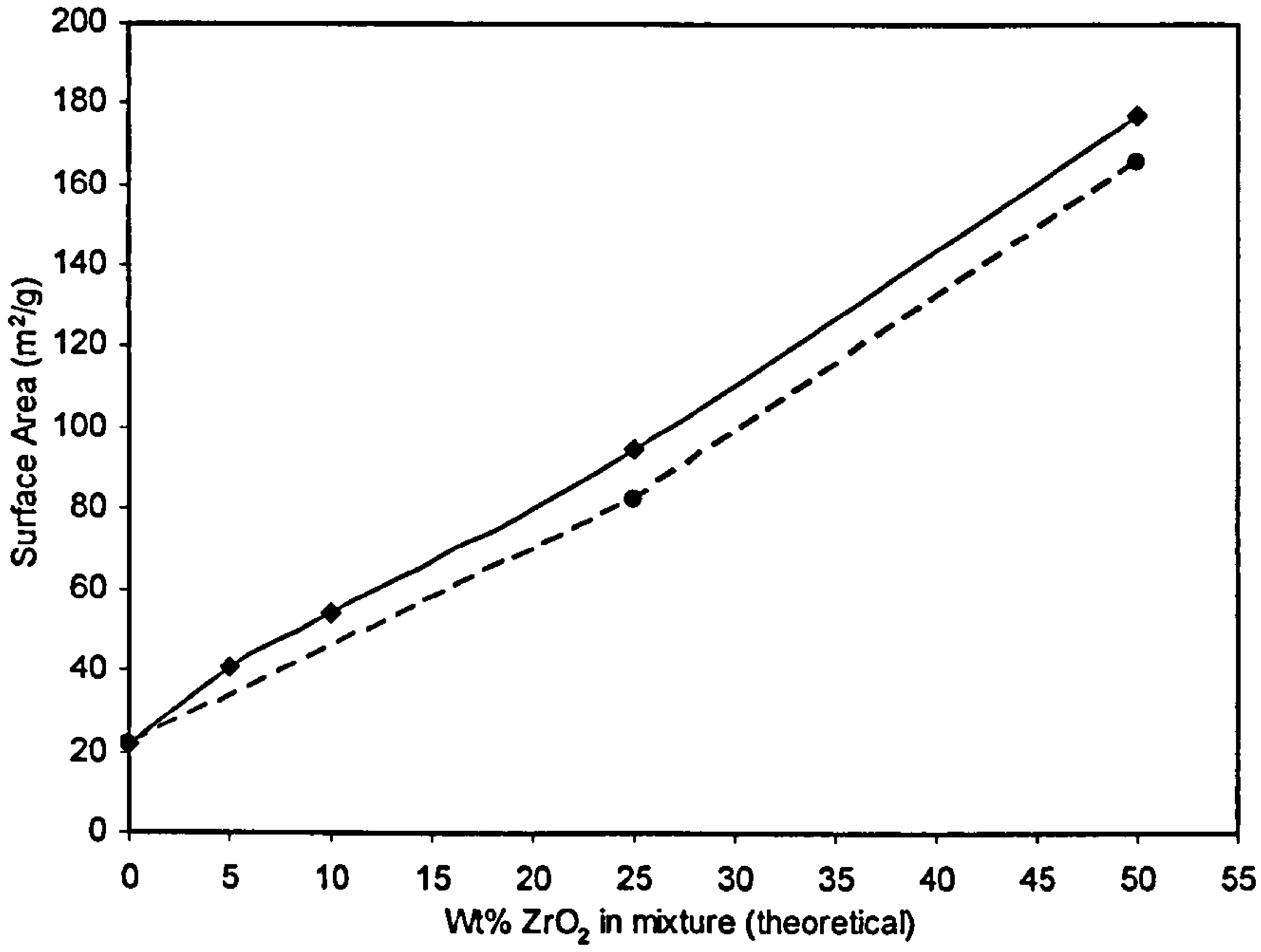

Figure 6-10 Increase in surface area of composite powders with weight percent of ZrO_2 in as-precipitated samples for in-solution Ca:P molar ratio of (♦) 2.5 [solid line] and (•) 1.67 [dotted line].

6.3.2.3 X-ray Diffraction

Powder X-ray powder diffraction patterns of all as-precipitated samples are shown in Figures 6-11 (a) to (f). The unmarked peaks correspond to crystalline HA (JCPDS pattern 09-432) and the marked peaks gave good match to both tetragonal zirconia and cubic calcium stabilised zirconia, $Ca_{0.15}Zr_{0.85}O_{1.85}$ (JCPDS patterns 42-1164 and 26-341, respectively). It has been reported that differentiation between cubic and tetragonal phases of zirconia is difficult based only on X-ray diffraction. However, Raman spectroscopy is an effective method to determine the presence of these polymorphs (Ghosh et al. 2006). Figure 6-11 (g) shows the diffraction pattern for sample H-100 which corresponded to phase pure (cubic or tetragonal) CDZ. It was observed that the CDZ peaks were broad and had low intensity in Figures 6-11 (b) to (g). This was attributed to low crystallinity and the small size of zirconia nanoparticles [5 nm, as shown in Figure 6-9 (f)]. It was observed that the main CDZ peak centred at *ca.* 30.5° did not appear for sample H-5 as seen in Figure 6-11 (a). This was possibly due to a low amount of CDZ in the mixture, which remained undetected using current scan parameters. However, the surface area of sample H-5 (41.3 $m^2 g^{-1}$) was higher than that of phase-pure HA (22 $m^2 g^{-1}$) made under similar conditions (see Figure 6-10). This confirmed the presence of CDZ (also supported by elemental analyses data shown in Table 6-4).

Although differentiation between the cubic and tetragonal polymorphs of zirconia is difficult, evidence in literature suggests that particle sizes below 15-20 nm stabilise the tetragonal phase (Siu et al. 1999). Several images in Figure 6-9 revealed CDZ to be *ca.* 5 nm in diameter.

These powder samples were then spark plasma sintered at 900 and 1000 °C, except sample H-100 which was sintered only at 1000 °C. Samples H-5 and H-10 were sintered at 900 and 1000 °C, respectively, for 5 minutes 15 seconds using sintering cycle 8 shown in Figure 6-6 (f). This sintering cycle was chosen in order to avoid cracking which may arise due to high content of HA in these samples and indeed, intact crack free discs were obtained. The densities (in g cm^{-3}) were measured using the Archimedes principle. The % theoretical density was calculated using densities of powders calculated using equation 2-1 in section 2.3.9 of chapter 2 based on the assumption that only two phases are present (HA and ZrO_2). All this data is summarised in Table 6-5.

Sample H-5 sintered at 900 and 1000 °C resulted in discs with densities of 3.10 (*ca.* 95%) and 3.08 (*ca.* 95%) g cm^{-3}, respectively. Sample H-10 sintered at 900 and 1000 °C resulted in discs with densities of 2.98 (*ca.* 89%) and 3.30 (*ca.* 99 %) g cm^{-3}, respectively. Samples L-25 and L-50 sintered at 900 and 1000 °C for 5 minutes using sintering cycle 2 shown in Figure 6-2 (b), also resulted in intact crack free discs. Sample L-25 sintered at 900°C and 1000 °C resulted in densities of 2.78 (*ca.* 77%) and 3.42 (*ca.* 96%) g cm^{-3}, respectively, whereas sample L-50 sintered at 900 and 1000 °C resulted in densities of 3.08 (*ca.* 74%) and 3.79 (*ca.* 91%) g cm^{-3}, respectively. However, when samples H-25 and H-50 were sintered at the same temperatures, using the same sintering cycle 2, the discs cracked. This might be attributed to different phase thermal behavior (contraction/expansion) as compared to that for samples L-25 and L-50 (due to higher amount of calcium in the former samples). Use of sintering cycle 6 on the other hand, resulted in intact crack free samples with densities of 3.02 (*ca.* 82%) and 3.48 (*ca.* 95%) g cm^{-3} for sample H-25 sintered at 900 and 1000 °C, respectively. Densities of 3.12 (*ca.* 74%) and 3.80 (*ca.* 90%) g cm^{-3} were obtained for sample H-50 sintered at 900 and 1000 °C, respectively.

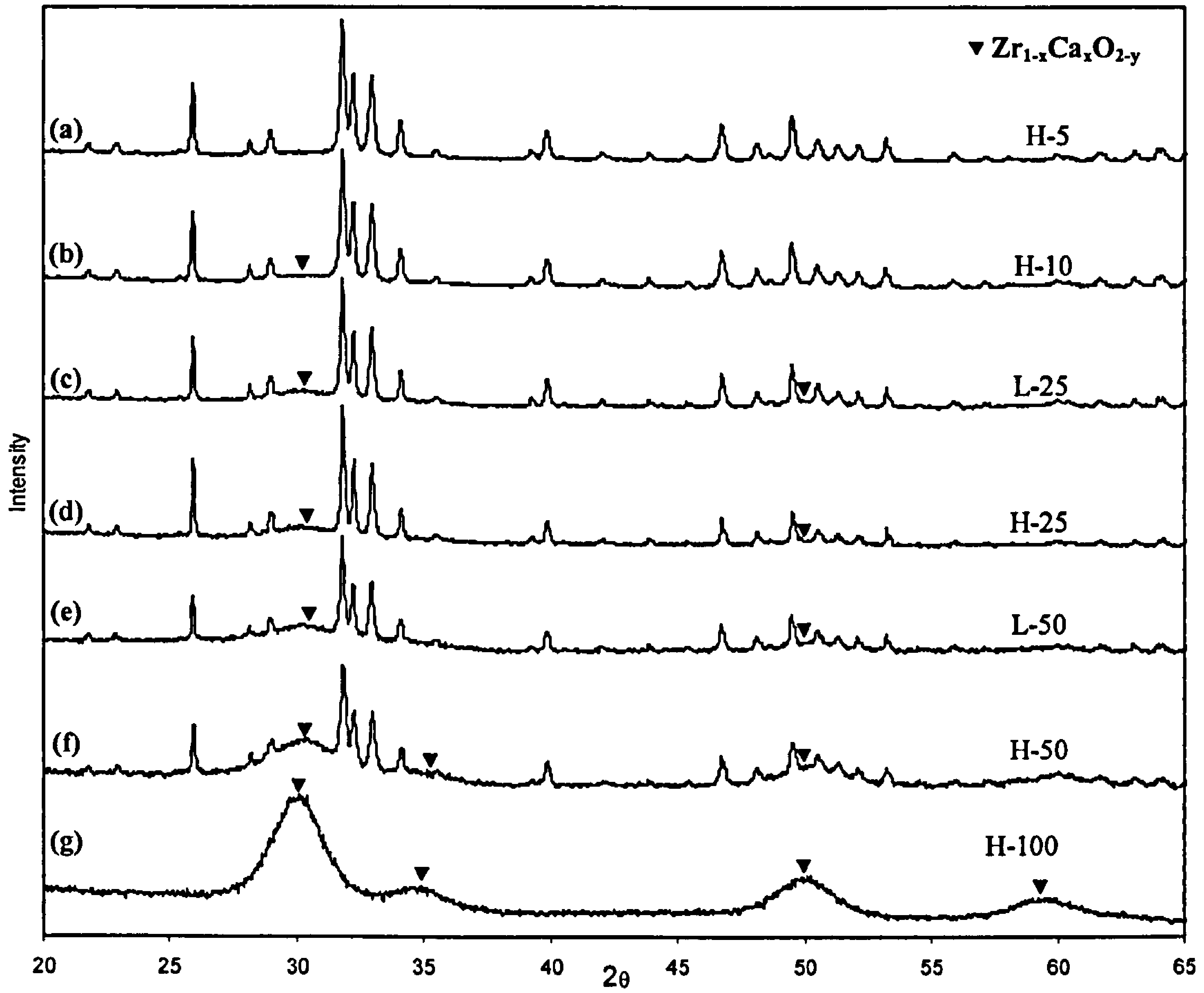

Figure 6-11 Powder X-ray diffraction patterns for as-precipitated samples (a) H-5 (b) H-10 (c) L-25 (d) H-25 (e) L-50 (f) H-50 and (g) H-100. Unmarked peaks correspond to HA.

Figures 6-12 (a) to (m) show the XRD patterns of discs spark plasma sintered from powders (the corresponding powder XRD patterns are shown in Figure 6-11). X-ray diffraction patterns of sample H-5 sintered at 900 and 1000 °C (shown in Figures 6-12 (a) and (b)] revealed only two phases, phase-pure HA and calcium doped zirconia, CDZ (compared to JCPDS patterns 26-341 for cubic $Ca_{0.15}O_{1.85}Zr_{0.85}$ and 42-1164 for tetragonal ZrO_2), respectively. Similarly, XRD patterns in Figures 6-12 (c) and (d) for sample H-10 sintered at 900 and 1000 °C, respectively, revealed phase-pure HA and CDZ. The intensity of the main CDZ peak at 30.5° was observed to increase with increasing CDZ content and sintering temperature. Sintering sample L-25 at 900 °C also resulted in phase pure CDZ and HA as shown in Figure 6-12 (e).

When sintered at 1000 °C it resulted in formation of small amount of a third phase, β-TCP (compared to JCPDS pattern 9-169) as shown in Figure 6-12 (f). It is already known that HA discs sintered in section 6.3.1 from samples with in-solution Ca:P molar ratio of *ca.* 1.67, resulted in slight decomposition and formation of TCP phases. This was due to a final Ca:P molar ratio lower than 1.67 (phase-pure HA was subsequently obtained using a 2.0 in-solution Ca:P molar ratio). Similarly, sample L-25 was also synthesised with an in-solution Ca:P molar ratio of *ca.* 1.67 and this ultimately resulted in appearance of TCP peaks after sintering. X-ray diffraction patterns of discs sintered from samples H-5 and H-10 in the 900 – 1000 °C range [Figures 6-12 (a) to (d)] did not reveal any TCP phase, due to a higher in-solution Ca:P molar ratio of *ca.* 2.5.

Sample H-25 (similar CDZ content to L-25 but with an in-solution Ca:P molar ratio of *ca.* 2.5) sintered at 900 and 1000 °C yielded phase-pure CDZ and HA only, as shown in Figures 6-12 (g) and (h), respectively. This suggested that for a composition of 28.45 wt% CDZ and 71.55 wt% HA, an in-solution Ca:P molar ratio of 2.5, results in a thermally stable HA phase up to 1000 °C after SPS.

Sample L-50 sintered at 900 °C consisted mainly of CDZ and HA as shown in Figure 6-12 (i) (a small peak corresponding to β-TCP was also observed). Additionally, a very small peak, partially obscured by the main HA peak at 31.8° corresponding to calcium zirconate, $CaZrO_3$, was also observed (compared to JCPDS pattern 35-079). When sintered at 1000 °C, the β-TCP and $CaZrO_3$ peaks increased in intensity as the HA peaks diminished or were obscured by the $CaZrO_3$ peak at 31.6° as shown in Figure

6-12 (j). This suggested that the higher amount of CDZ in these samples (*ca.* 50 wt%) resulted in a solid state reaction of HA and CDZ to form $CaZrO_3$.

Table 6-5 Sample IDs, calculated densities, sintering temperatures and times and measured densities of HA-CDZ and CDZ sintered discs. * Sample HA-100s density of 5.50 g cm^{-3} was taken from unit cell details of the JCPDS pattern 26-341. The calculated densities assume mixtures of HA and ZrO_2 only.

Sample ID	Theoretical density (g cm^{-3})	Sintering Conditions		Measured density	
		Temp. (°C)	Time (min:sec)	(g cm^{-3})	(%)
H-5	3.25	900	5:15	3.10 (± 0.07)	95.28 (± 2.17)
		1000	5:15	3.08 (± 0.08)	94.74 (± 2.36)
H-10	3.34	900	5:15	2.98 (± 0.04)	89.31 (± 2.98)
		1000	5:15	3.30 (± 0.03)	98.75 (± 0.93)
L-25	3.59	900	5:00	2.78 (± 0.04)	77.39 (± 1.22)
		1000	5:00	3.42 (± 0.04)	95.13 (± 1.11)
H-25	3.65	900	5:00	3.02 (± 0.08)	82.62 (± 2.19)
		1000	5:00	3.48 (± 0.10)	95.42 (± 2.74)
L-50	4.16	900	5:00	3.08 (± 0.11)	74.00 (± 2.64)
		1000	5:00	3.79 (± 0.07)	91.10 (± 1.58)
H-50	4.22	900	5:00	3.12 (± 0.09)	74.04 (± 2.20)
		1000	5:00	3.80 (± 0.05)	90.05 (± 1.28)
H-100*	5.55	1000	5:00	3.19 (± 0.17)	57.56 (± 3.06)

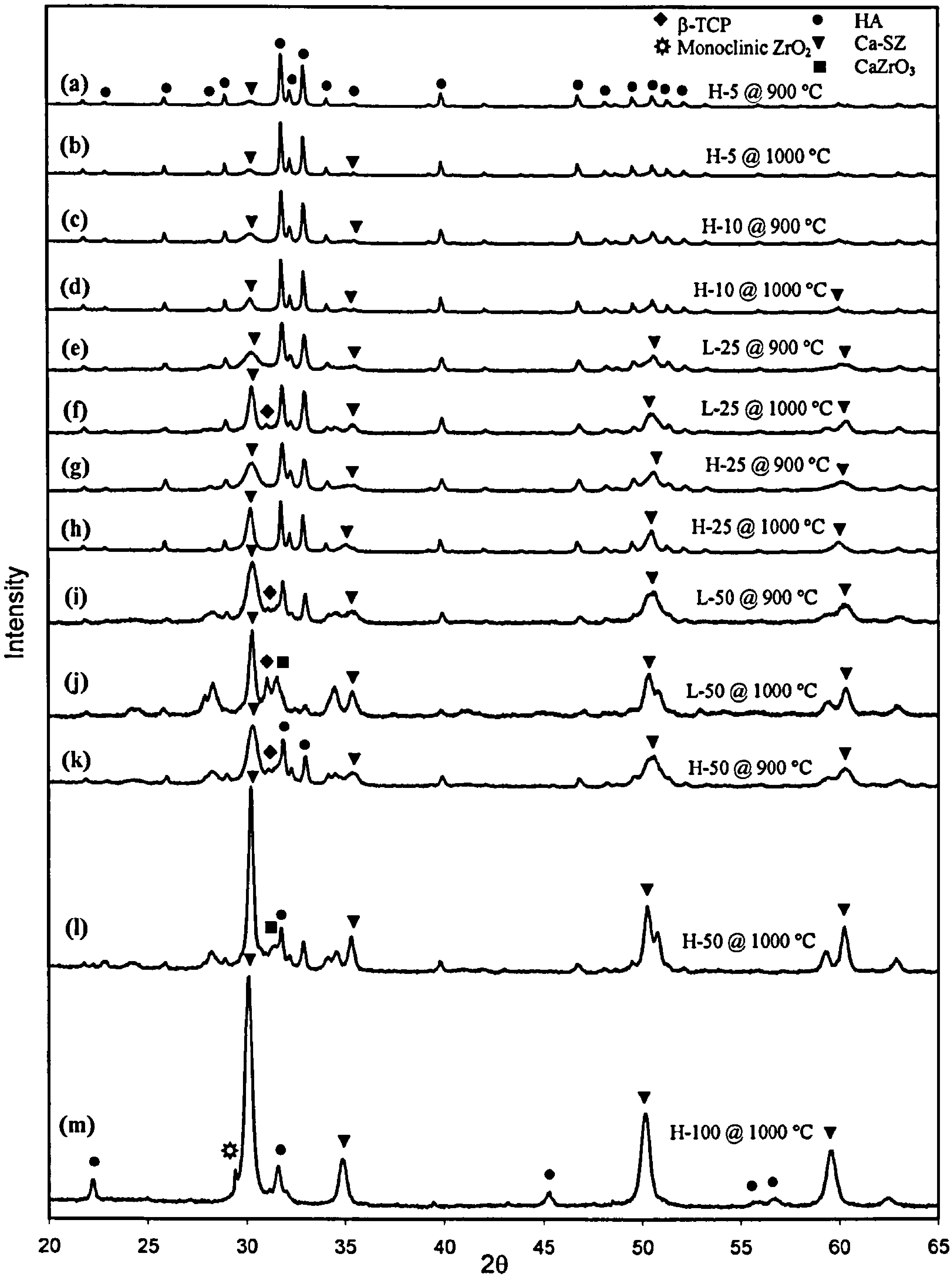

Figure 6-12 X-ray diffraction patterns of sample, H-5 spark plasma sintered at (a) 900 and (b) 1000 °C, H-10 sintered (SPS) at (c) 900 and (d) 1000 °C, L-25 sintered (SPS) at (e) 900 and (f) 1000 °C, H-25 sintered (SPS) at (g) 900 and (h) 1000 °C, L-50 sintered (SPS) at (i) 900 and (j) 1000 °C, H-50 sintered (SPS) at (k) 900 and (l) 1000 °C and (m) H-100 sintered (SPS) at 1000 °C.

Sample H-50 sintered (SPS) at 900 °C revealed mainly HA and CDZ peaks as shown in Figure 6-12 (k). Very small peaks corresponding to β-TCP and $CaZrO_3$ were also noticed (similar behavior was noticed in discs sintered from L-50 at 900 °C). However, H-50 sintered at 1000 °C had a composition of mainly HA and CDZ as compared to L-50 sintered at the same temperature [Figure 6-12 (l)]. Peaks corresponding to β-TCP and $CaZrO_3$ were also observed. In comparison to L-50 sintered at 1000 °C, H-50 sintered at the same temperature showed two differences. Firstly, HA was present in H-50 sintered at 1000 °C due to the higher in-solution Ca:P molar ratio of 2.5 (instead of 1.67). Secondly, the intensity of the $CaZrO_3$ peak was much lower. This suggested that a higher Ca:P molar ratio during CHFS synthesis of powders made HA more thermally stable and decreased the amount of $CaZrO_3$ formed at 1000 °C.

Figure 6-12 (m) shows the XRD pattern for sample H-100 sintered at 1000 °C in which peaks corresponding to CDZ (either cubic or tetragonal) and $CaZrO_3$ were observed. A small peak for monoclinic CDZ (compared to JCPDS pattern 37-1484) was also observed. Figure 6-13 shows an equilibrium phase diagram for calcia (CaO) and zirconia (ZrO_2) mixtures. In sample H-100 the calcium content was determined using an EDS detector attached to a SEM, to be 26 mol. % with respect to zirconium. For similar compositions, the region marked by the vertical dashed line and arrows in Figure 6-13 is relevant. Therefore, the appearance of calcium zirconate is understandable.

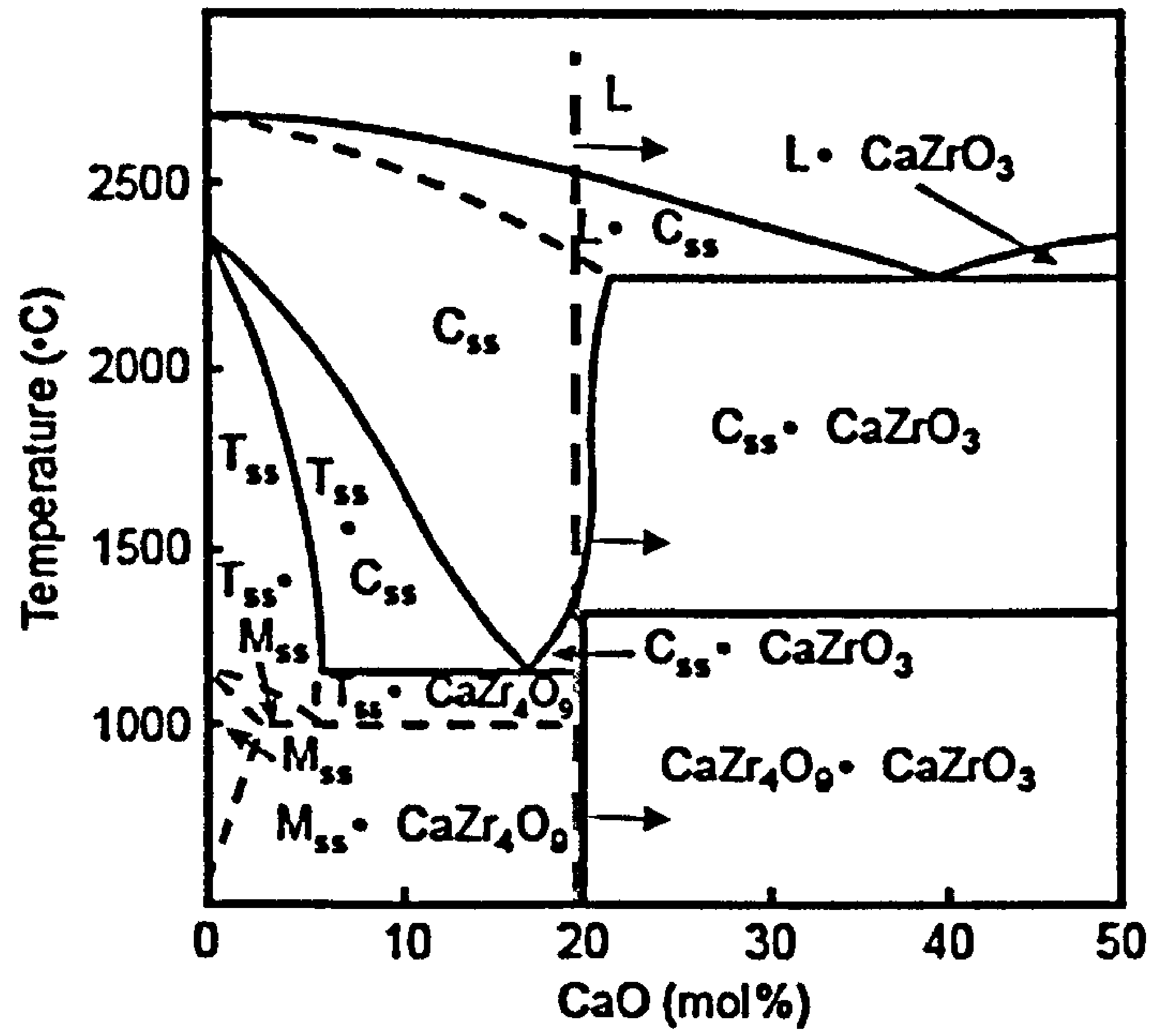

Figure 6-13 CaO – ZrO_2 equilibrium phase diagram (Stubican & Ray 1977). Dashed line and the arrows represent the region valid for sample H-100.

6.3.2.4 Variable Temperature XRD Heat Treatment

The phase stability of selected samples (H-5, H-10, L-50, H-50) was investigated using in-situ variable temperature XRD. Figure 6-14 shows the temperature vs 2θ contour map (2D XRD contour map) of peaks for sample H-5. The coloured lines (representing separate peaks) tilted towards the left hand side with an increase in temperature. This was due to change in lattice parameters accompanying increasing temperature. A dotted line at *ca.* 1100 °C marks the appearance of a new peak, which corresponded to α-TCP (JCPDS pattern 09-348). Scan by scan analysis revealed a similar composition at 1150 °C as well (i.e. HA, CDZ, α-TCP). The high temperature reaction product, $CaZrO_3$, appeared at 1200 °C.

Figure 6-15 shows the 3D variable temperature X-ray diffraction (VT-XRD) powder pattern (intensity vs. 2θ vs. temperature) for sample H-5. The most noticeable features were the appearance and growth of the peaks corresponding to CDZ (above 700 °C) and α-TCP (above 1100 °C), possibly due to further crystallisation and growth of CDZ particles and thermal decomposition of HA due to non-stoichiometry, respectively. Figure 6-16 (a) shows the XRD pattern for sample H-5 collected at room temperature after the room temperature to 1200 °C in-situ XRD heat treatment (showing HA, CDZ, α-TCP and $CaZrO_3$ phases).

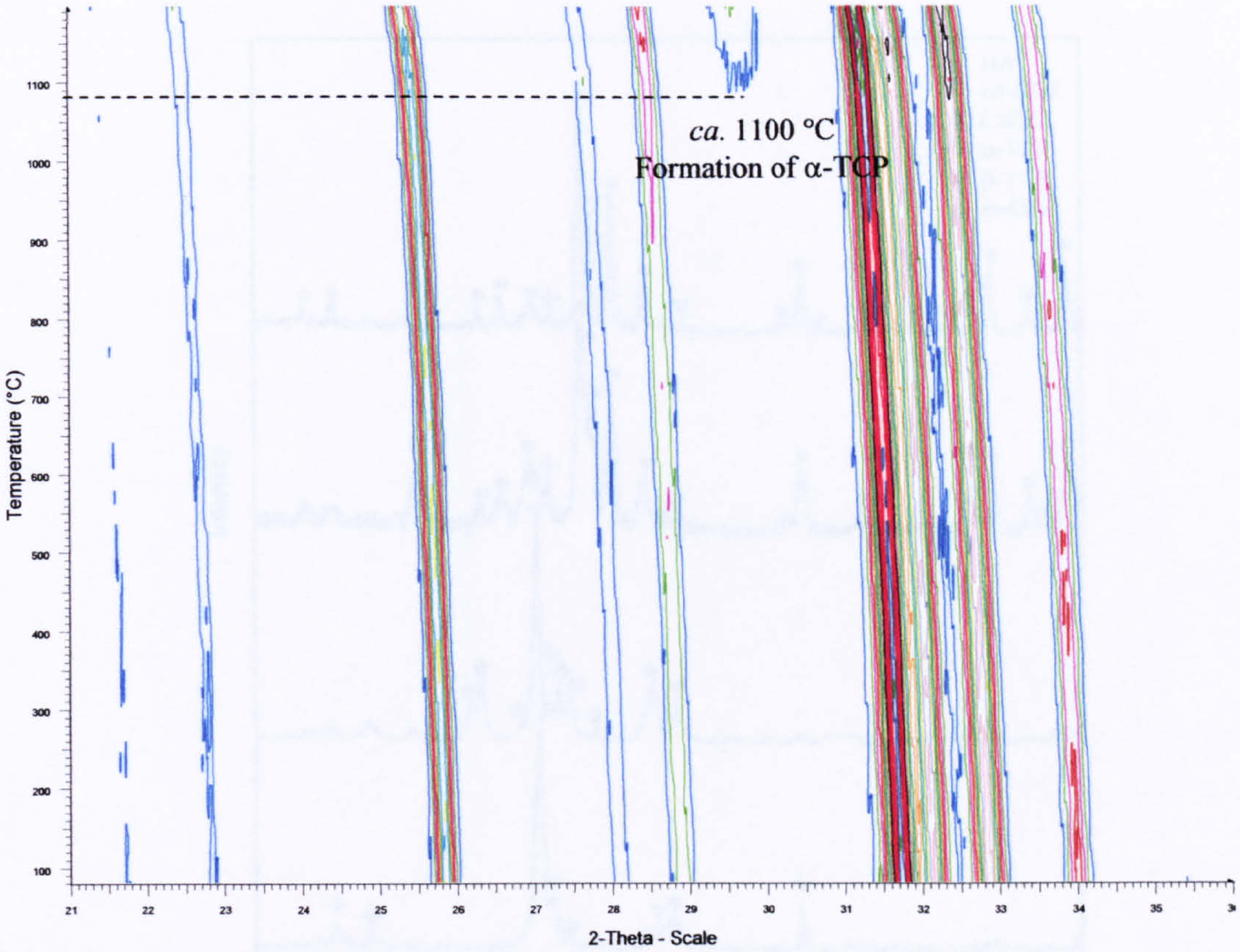

Figure 6-14 2D XRD contour map of sample H-5 (temperature vs. 2θ) showing appearance and disappearance of peaks with increasing temperature.

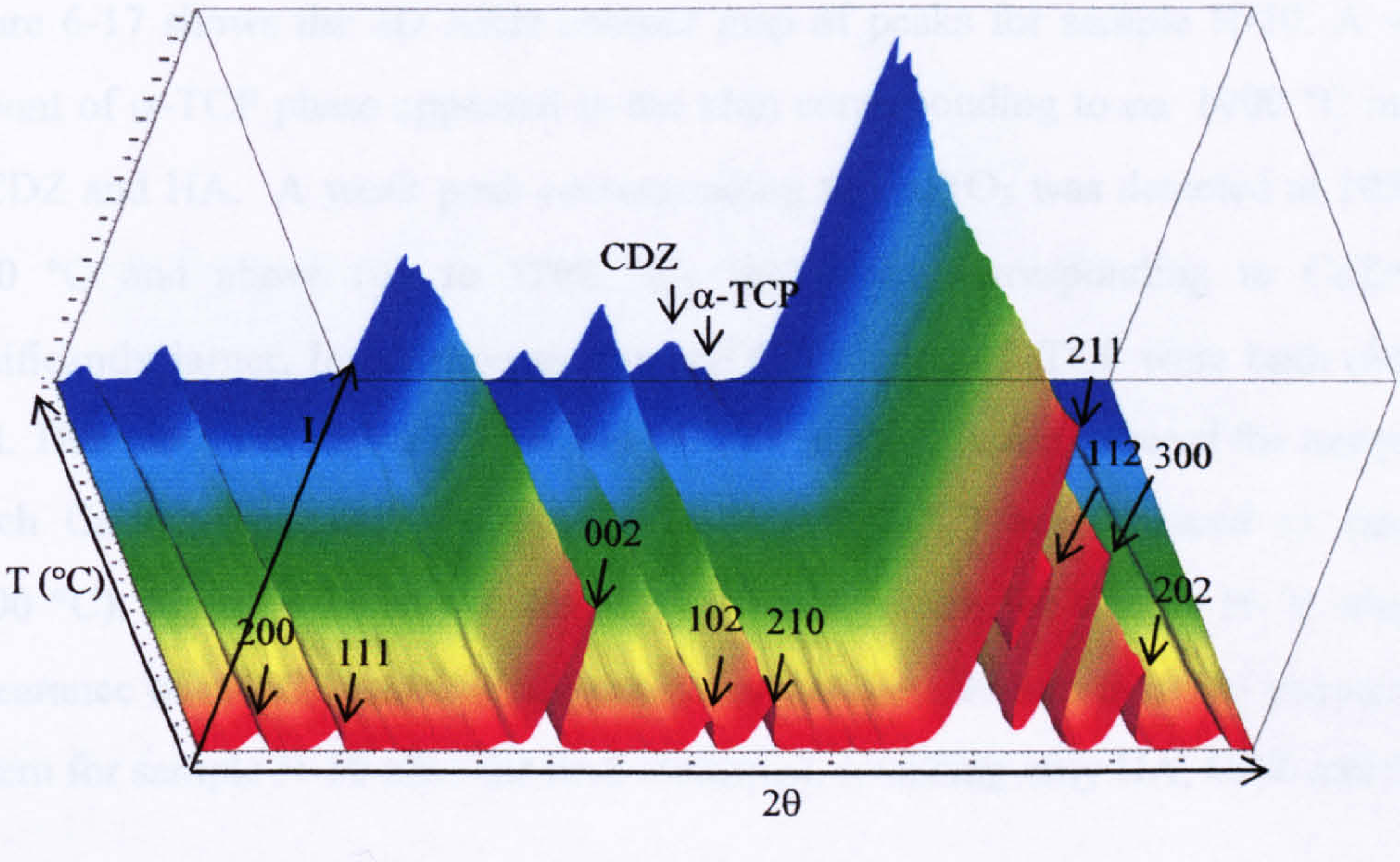

Figure 6-15 3D VT-XRD plot of intensity vs 2θ angle (°) vs temperature (°C) for sample H-5.

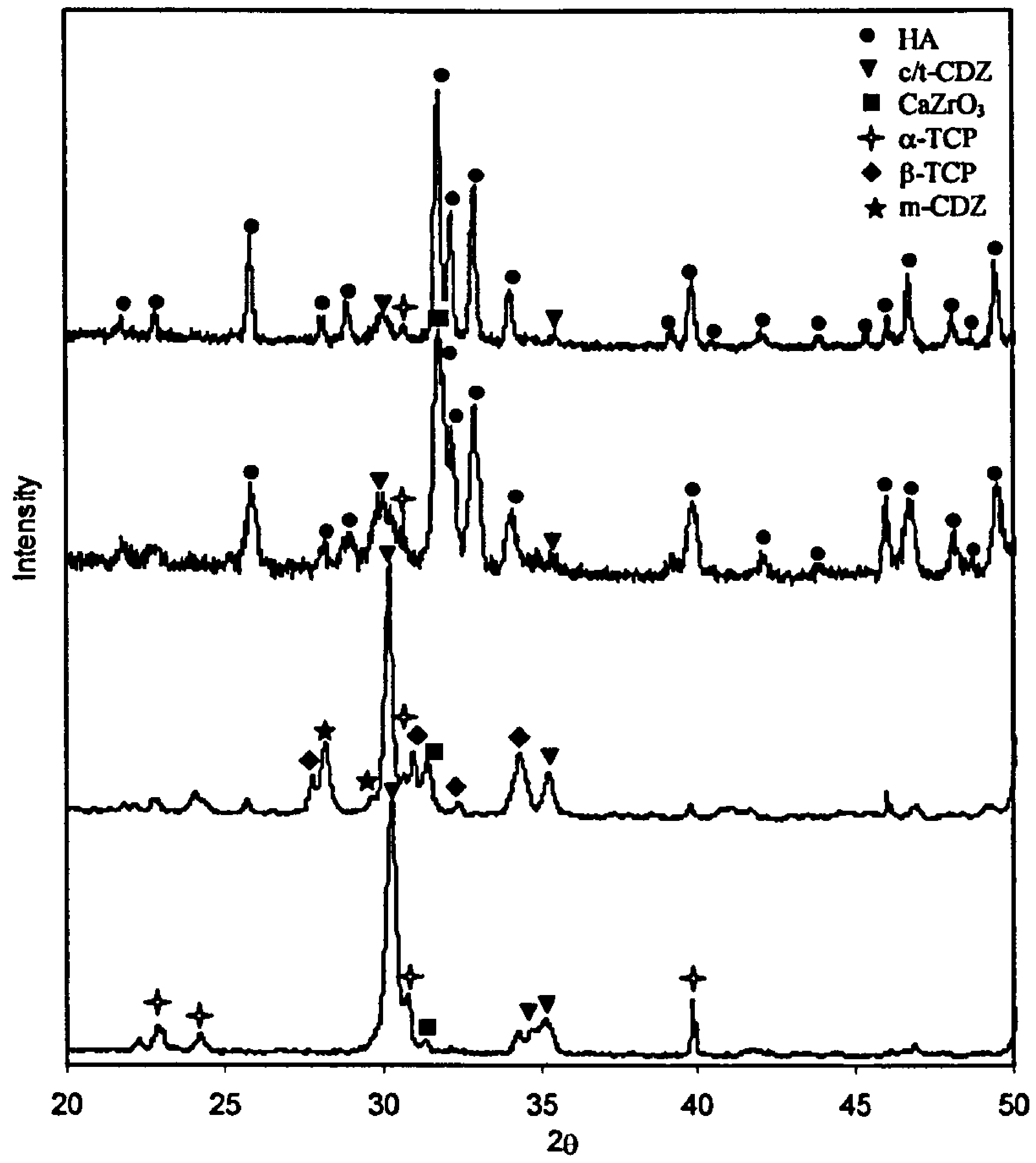

Figure 6-16 X-ray powder diffraction patterns after VT-XRD heat treatment for samples (a) H-5 (b) H-10 (c) L-50 and (d) H-50.

Figure 6-17 shows the 2D XRD contour map of peaks for sample H-10. A very little amount of α-TCP phase appeared in the scan corresponding to *ca.* 1000 °C in addition to CDZ and HA. A weak peak corresponding to $CaZrO_3$ was detected at 1050 °C. At 1100 °C and above (up to 1200 °C), the peaks corresponding to $CaZrO_3$ grew significantly larger. In addition to HA and CDZ, α and β-TCP were both observed as well. Therefore, the higher percentage of CDZ in the mixture lowered the temperature at which $CaZrO_3$ appeared for sample H-10 (1050 °C) as compared to sample H-5 (1200 °C). Figure 6-18 shows the 3D VT-XRD pattern for sample H-10 wherein, the appearance of α-TCP and $CaZrO_3$ peaks can be seen. Figure 6-16 (b) shows the XRD pattern for sample H-10 after the heat-treatment, revealing only HA, CDZ and $CaZrO_3$.

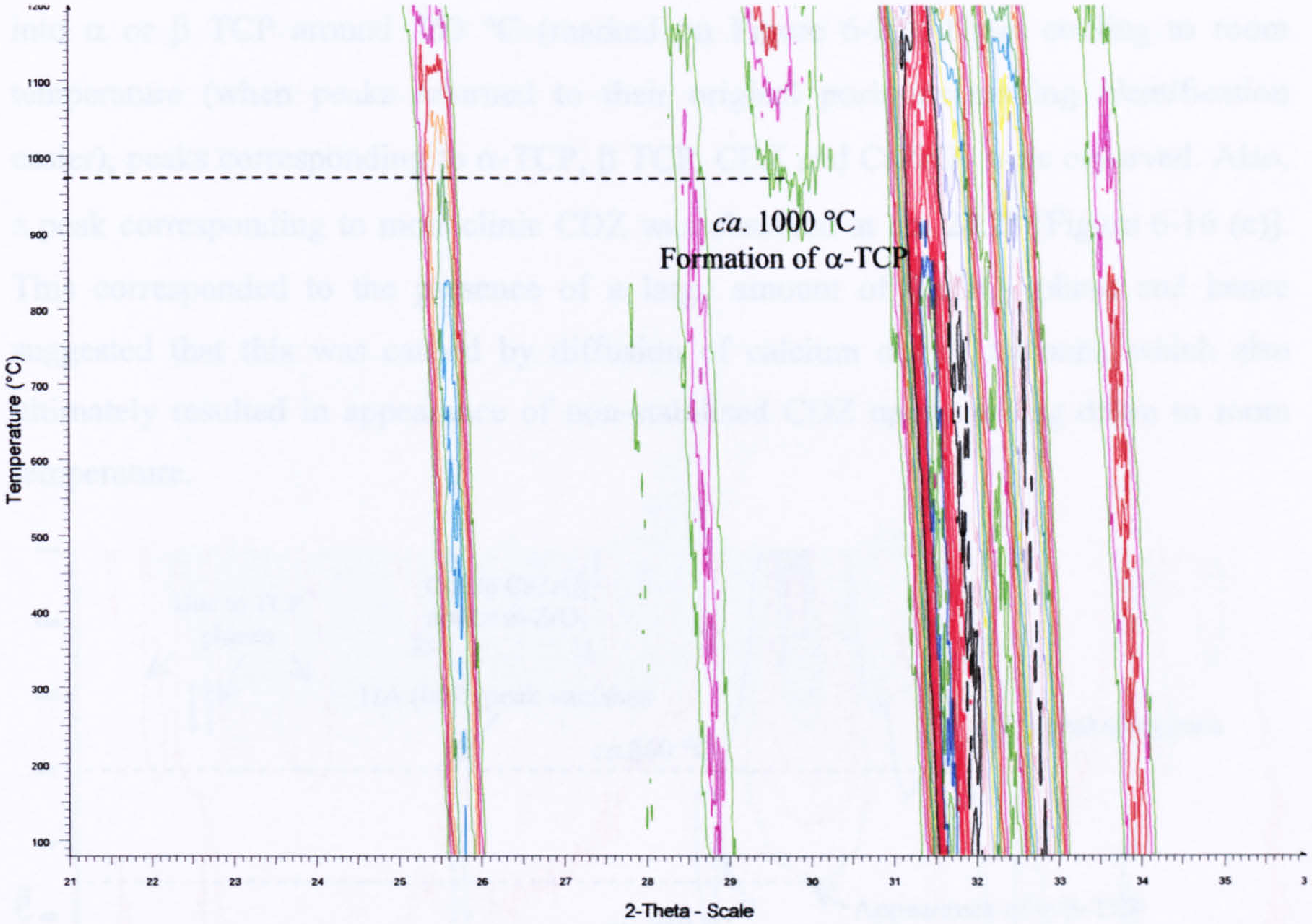

Figure 6-17 2D XRD contour map of sample H-10 (temperature vs. 2θ) showing appearance and disappearance of peaks with increasing temperature.

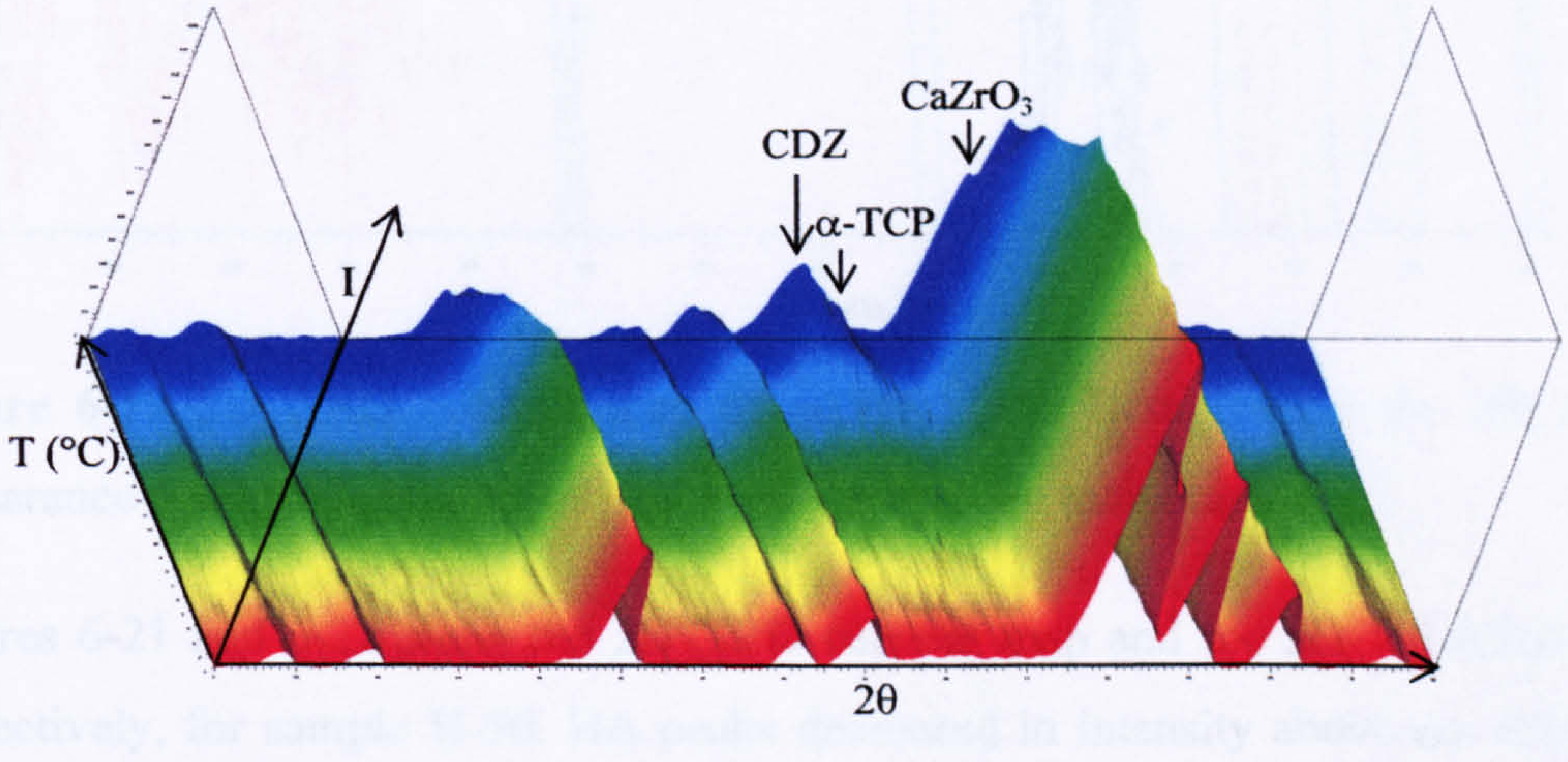

Figure 6-18 3D VT-XRD plot of intensity vs 2θ angle (°) vs temperature (°C) for sample H-10.

Figure 6-19 shows the 2D XRD contour map for sample L-50. HA peaks decreased in intensity above 700 °C (noticeable in the 3D VT-XRD plot shown in Figure 6-20) and were last observed at 860 °C as marked on Figure 6-20. HA also started decomposing into α or β TCP around 750 °C (marked on Figure 6-20). Upon cooling to room temperature (when peaks returned to their original positions making identification easier), peaks corresponding to α-TCP, β TCP, CDZ and $CaZrO_3$ were observed. Also, a peak corresponding to monoclinic CDZ was observed at *ca.* 28.2° [Figure 6-16 (c)]. This corresponded to the presence of a large amount of $CaZrO_3$ phase and hence suggested that this was caused by diffusion of calcium out of zirconia, which also ultimately resulted in appearance of non-stabilised CDZ upon cooling down to room temperature.

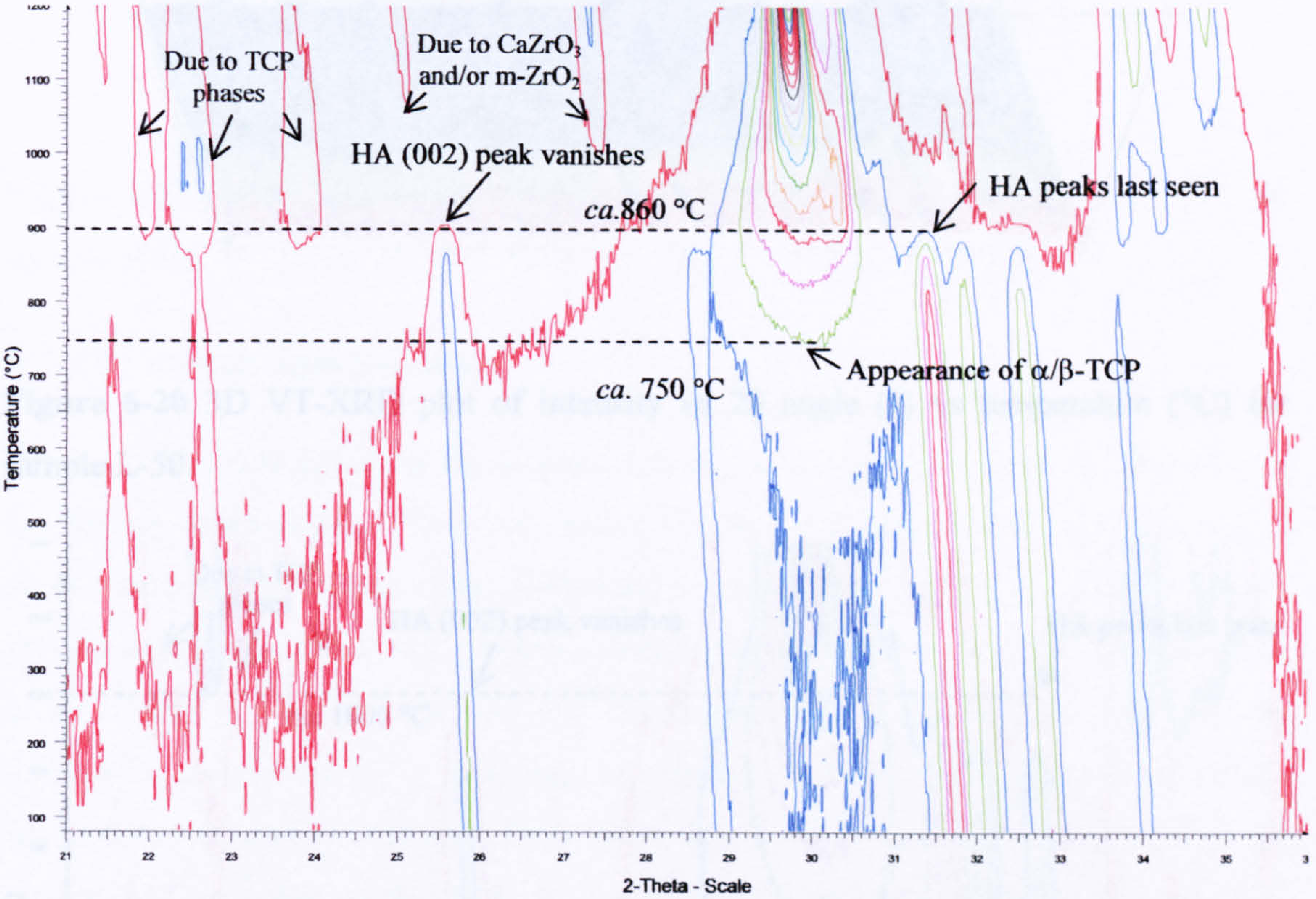

Figure 6-19 2D XRD contour map of sample L-50 (temperature vs. 2θ) showing appearance and disappearance of peaks with increasing temperature.

Figures 6-21 and 6-22 show the 2D XRD contour map and the 3D VT-XRD pattern, respectively, for sample H-50. HA peaks decreased in intensity above *ca.* 650 °C and were last observed at 1000 °C. This suggested that a higher Ca:P molar ratio in solution improved the thermal stability of HA and retarded the solid state reaction that led to $CaZrO_3$. However, in comparison to sample L-50, the TCP phase appeared at a lower temperature (650 °C). This decrease in intensity of main HA peaks corresponded to the appearance of α-TCP peaks. Upon cooling, peaks corresponding to CDZ, α-TCP and $CaZrO_3$ were observed. However, the amount of $CaZrO_3$ formed (using XRD) was significantly lower as compared to that noticed for sample L-50, which suggested that increase in Ca:P molar ratio in solution retarded this high temperature reaction. This possibly also resulted in the absence of the monoclinic zirconia phase (contrary to what was observed for sample L-50).

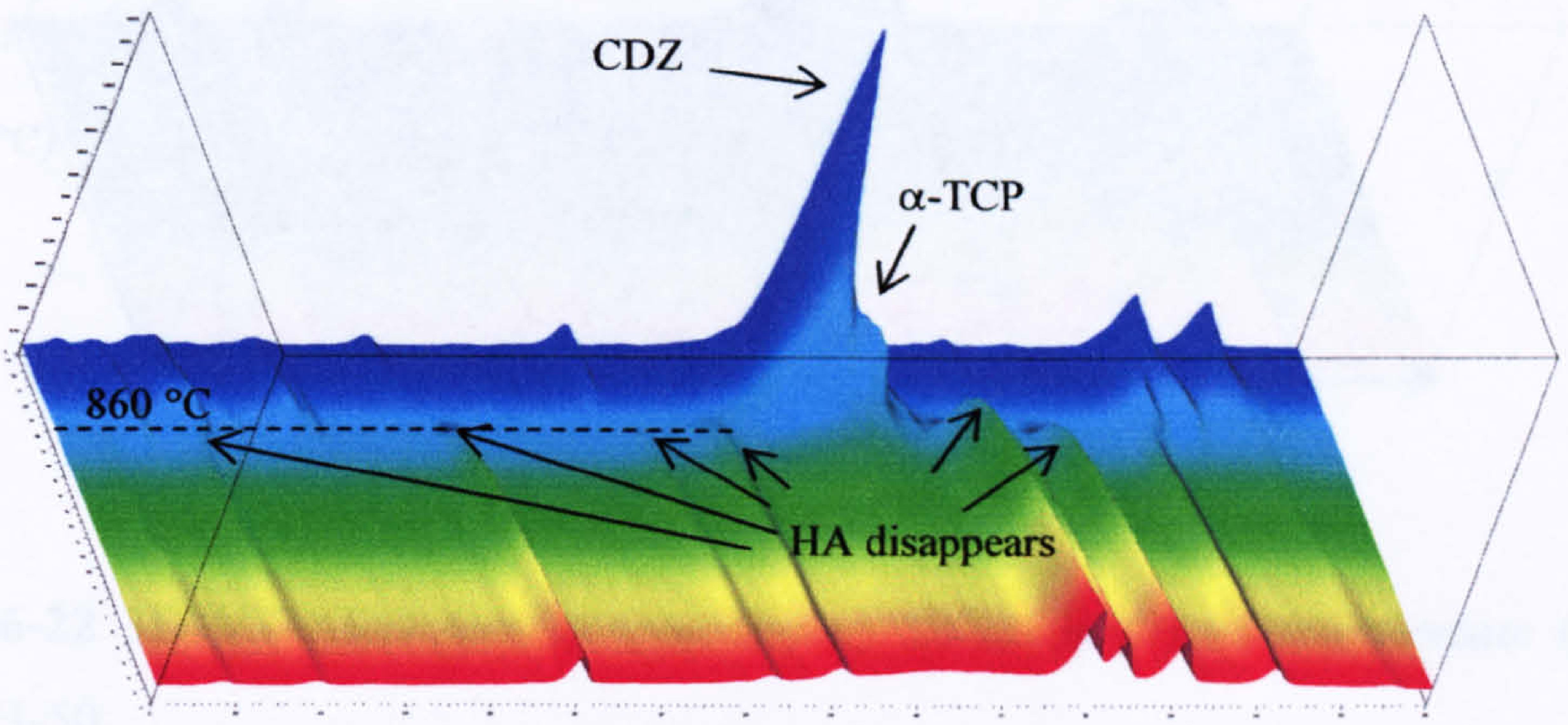

Figure 6-20 3D VT-XRD plot of intensity vs 2θ angle (°) vs temperature (°C) for sample L-50.

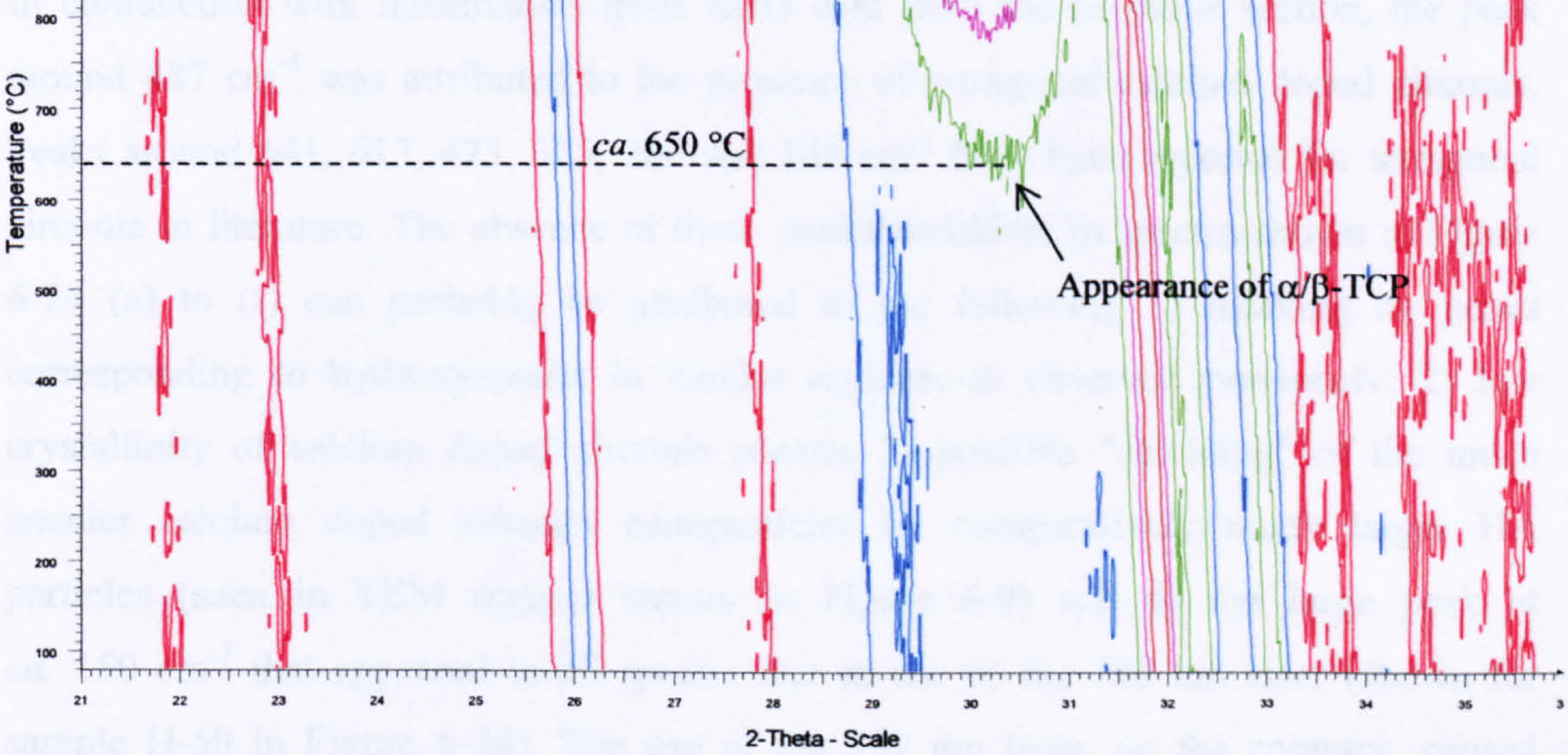

Figure 6-21 2D XRD contour map of sample H-50 (temperature vs. 2θ) showing appearance and disappearance of peaks with increasing temperature.

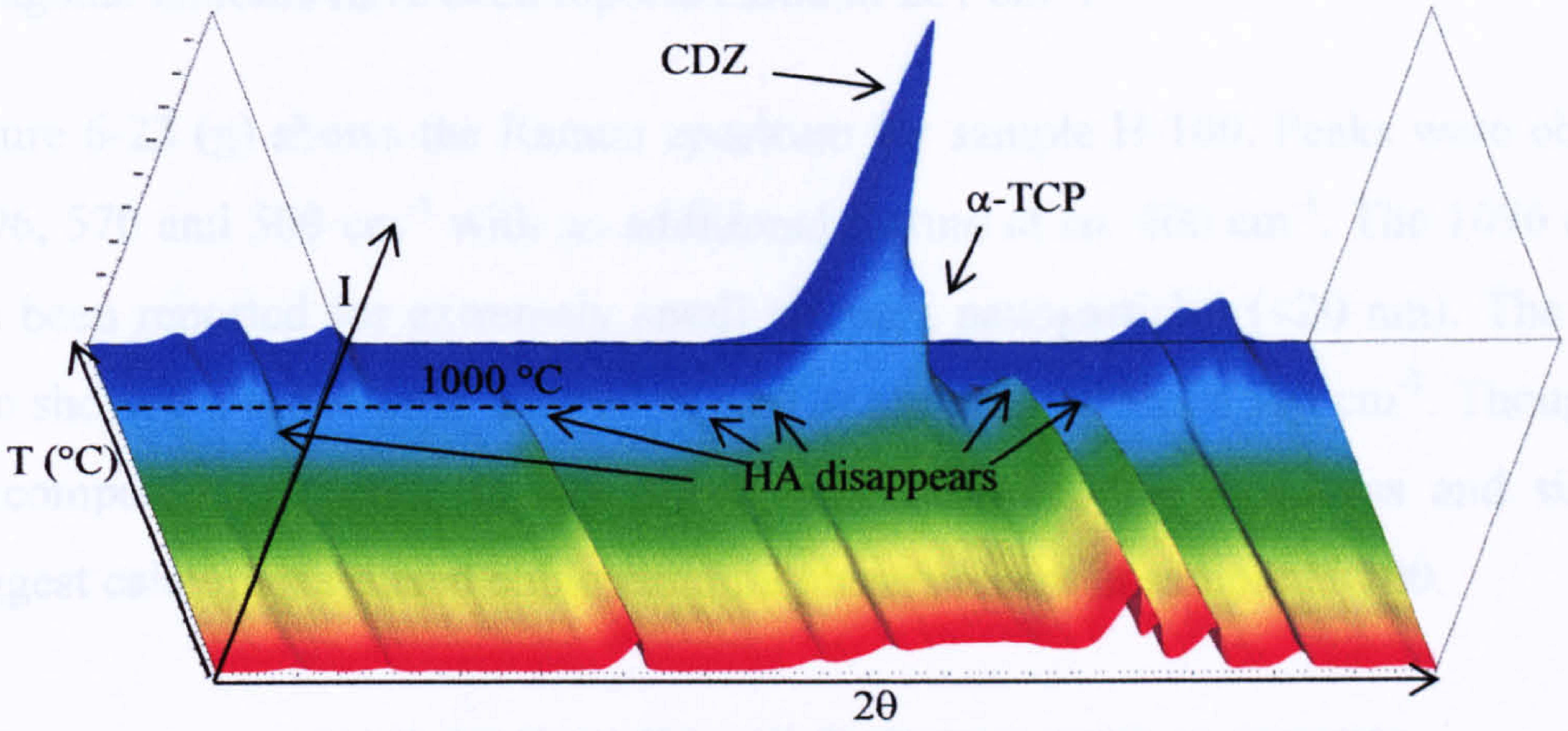

Figure 6-22 3D VT-XRD plot of intensity vs 2θ angle (°) vs temperature (°C) for sample H-50.

6.3.2.5 Raman Spectroscopy

Figures 6-23 (a) to (g) show the Raman spectra for powdered samples. In Figure 6-23 (a) Raman peaks at ca. 1084, 1051 and 1037 cm^{-1}, for sample H-5, corresponded to asymmetric stretching (υ_3) of the P-O bond in phosphate. The peak around 973 cm^{-1}, corresponds to the symmetric stretching mode (υ_1) of the P-O bond of the phosphate group. Peaks at 610, 597 and 581 cm^{-1} corresponded to the υ_4 and peaks at 447 and 431 cm^{-1} corresponded to υ_2 bending, respectively, of the O-P-O linkage in phosphate. In conjunction with information from XRD data from the previous section, the peak around 487 cm^{-1} was attributed to the presence of tetragonal calcium doped zirconia. Peaks around 641, 613, 473, 325, 260 and 146 cm^{-1} have been reported for tetragonal zirconia in literature. The absence of these peaks/shoulders in spectra shown in Figure 6-24 (a) to (f) can probably be attributed to the following 1) masking by peaks corresponding to hydroxyapatite in similar regions, as observed previously; 2) low crystallinity of calcium doped zirconia phases, 3) possible "shielding" of the much smaller calcium doped zirconia nanoparticles by comparatively much larger HA particles (seen in TEM images shown in Figure 6-9) and 4) the large peak at *ca.* 150 cm^{-1} that appeared in all spectra due to use of the 785 nm laser (shown for sample H-50 in Figure 6-24). The use of the 532 nm laser, on the contrary, caused excessive florescence and hence the data collected using the 785 nm laser is presented. However the broadness of the 150 cm^{-1} peak extended to *ca.* 280 cm^{-1}; suggesting presence of peaks which are not totally resolved. Indeed, peaks corresponding to tetragonal zirconia have been reported around 261 cm^{-1}.

Figure 6-23 (g) shows the Raman spectrum for sample H-100. Peaks were observed at 1096, 570 and 500 cm^{-1} with an additional feature at *ca.* 400 cm^{-1}. The 1096 cm^{-1} peak has been reported for extremely small zirconia nanoparticles (<20 nm). The spectrum also showed a broad peak centred at *ca.*570 and a shoulder at 500 cm^{-1}. Though shifted as compared to reports in literature, these features (the broadness and singularity) suggest calcium stabilised cubic zirconia phase present in sample H-100.

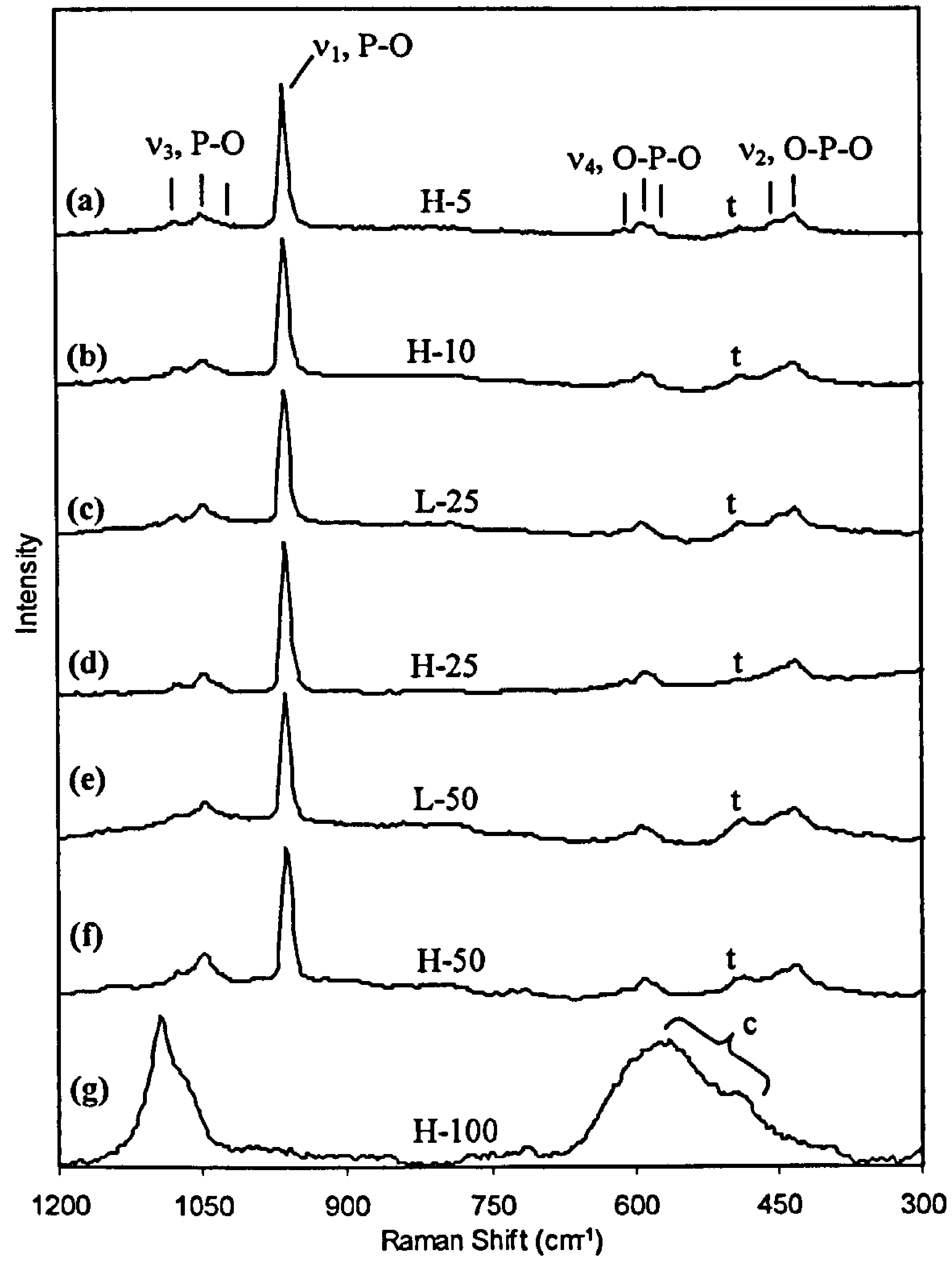

Figure 6-23 Raman spectra in range 1200 – 300 cm^{-1} for samples (a) H-5 (b) H-10 (c) L-25 (d) H-25 (e) L-50 (f) H-50 and (g) H-100. Key: t = tetragonal, c = cubic CDZ.

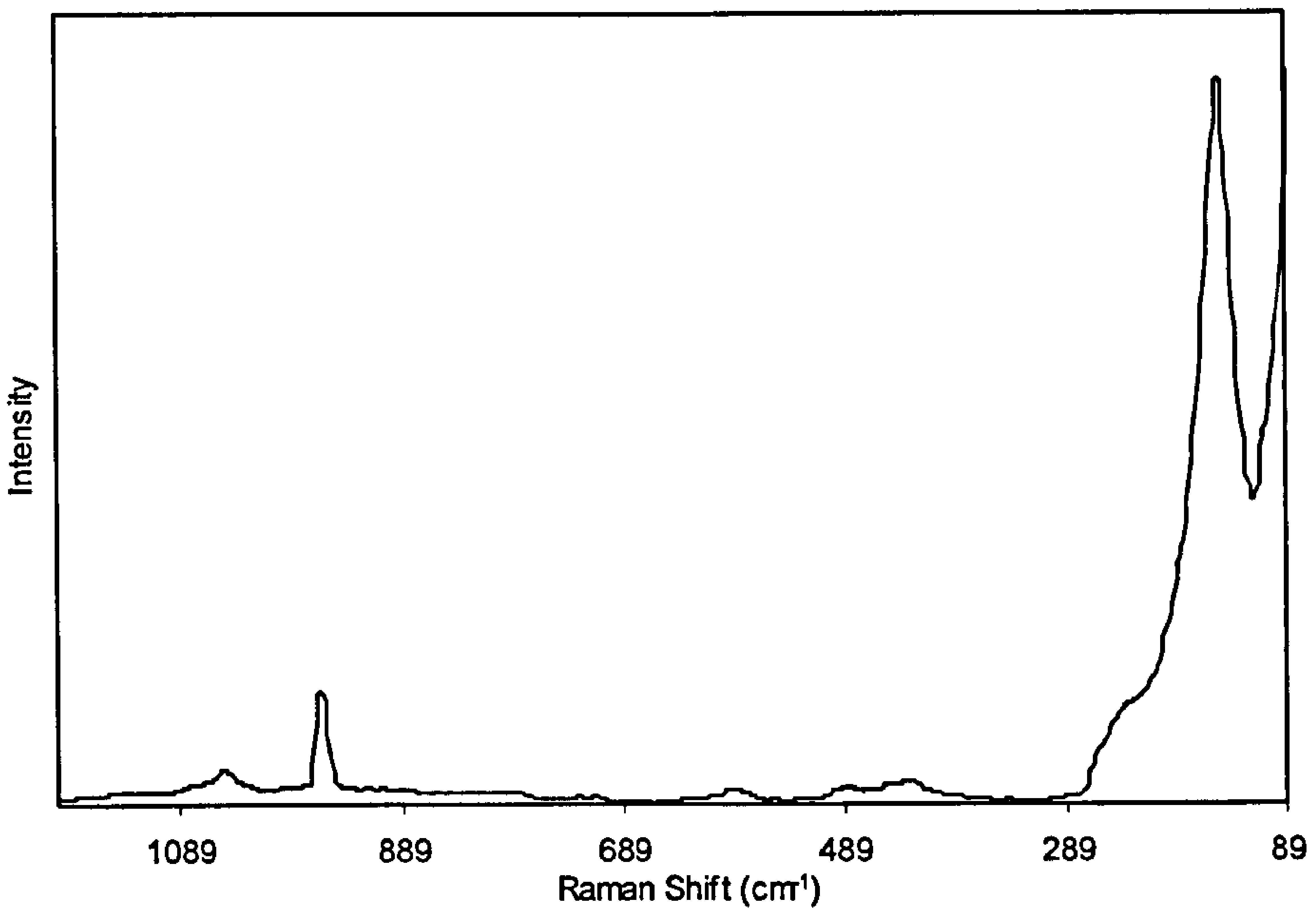

Figure 6-24 Raman spectrum for sample H-50 in the range 89 – 1200 cm^{-1}.

Figures 6-25 (a) to (m) show the Raman spectra for sintered discs. In Figure 6-25 (a), for sample H-5, sintered at 900 °C, the following peaks were observed for HA; at 1086, 1056 and 1036 cm^{-1} due to asymmetric stretching (v_3) and at 972 cm^{-1} due to symmetric stretching (v_1), of the P-O bond in phosphate. Peaks at 631, 601 and 590 cm^{-1} were due to v_4 bending and at 455 and 443 cm^{-1} due to v_2 bending of the O-P-O linkage in phosphate. All sintered discs revealed identical Raman spectra for HA and are hence not discussed individually. Broad and weak features at 496 and 342 cm^{-1} in Figures 6-25 (a) and (b) were possibly due to the presence of tetragonal CDZ in sample H-5. In Figures 6-25 (c) and (d), Raman spectra corresponding to sample H-10 sintered at 900 and 1000 °C, respectively, revealed an additional shoulder at *ca.* 640 cm^{-1}. This was attributed to tetragonal CDZ. Appearance of peaks at 658 and 278 cm^{-1} and a more distinct shoulder at 316 cm^{-1} in the Raman spectrum for sample L-25 sintered at 900 °C [Figure 6-25 (e)] confirm the presence of tetragonal CDZ. This is understandable given that sample L-25 has *ca.* 25 wt% zirconia content, which is much higher than samples H-5 (5 wt%) and H-10 (10 wt%).

Additional features appeared in the 2000 - 1100 cm^{-1} range in Figure 6-25 (e) for sample L-25 sintered at 900 °C. The Raman spectrum in Figure 6-25 (f) for sample L-25 sintered at 1000 °C also revealed similar but more intense peaks in the 2000-1100 cm^{-1} range. Additionally in the same Raman spectrum in Figure 6-25 (f), weak features at 470 cm^{-1} (shoulder) and 332 (weak peak) cm^{-1} corresponding to monoclinic zirconia were also observed. On the contrary, monoclinic zirconia was not observed in the XRD patterns shown in Figure 6-12 (f). This may be attributed to a very low amount of monoclinic zirconia in the sintered sample or the obscuration of monoclinic zirconia peaks due to the broadness of the tetragonal CDZ peak in the corresponding XRD pattern. Similar features (2000 – 1100 cm^{-1} range) were observed for sample H-25 sintered at 900 and 1000 °C in Figures 6-25 (g) and (h), respectively. In the same region, identical peaks but with higher intensities were observed in Figures 6-25 (i) to (l).

Overall, the intensity of the peaks in the 2000-1100 cm^{-1} region increased with zirconia content in the sample and increasing sintering temperature but decreased with increase in in-solution Ca:P molar ratio. Intensities of these peaks were lower for samples H-25 and H-50 as compared to those for samples L-25 and L-50. This corresponded to the inhibiting effect of a higher Ca:P molar ratio on $CaZrO_3$ peaks as seen in Figure 6-12. Therefore, the peaks in the 2000-1100 cm^{-1} range can be attributed to $CaZrO_3$. Also, the variation in intensity of the peak at 278 cm^{-1} matched the variation in intensity of these peaks suggesting that it may too, be attributed to $CaZrO_3$ in addition to tetragonal CDZ. Figure 6-25 (m) shows many peaks in the range 723 – 217 cm^{-1}. Such a large number of peaks and features may suggest presence of all three polymorphs of zirconia; tetragonal, cubic and monoclinic.

6.3.3 Synthesis, Characterisation and SPS of Ion-Substituted Calcium Phosphates

The sinterability and phase stability of ion-substituted calcium phosphates produced using the CHFS system was assessed using Spark Plasma Sintering and subsequent X-ray diffraction analysis. Ion-substituted powder samples $7.5CO_3$-HA$^{\phi}$ (sintered density - 3.28 g cm^{-3}), 5Si-HA (2.62 g cm^{-3}), 0.5Mg-CaP$^{\phi}$ (3.12 g cm^{-3}), 1.5Mg-CaP$^{\phi}$ (2.74 g cm^{-3}), 6Mg-CaP$^{\phi}$ (3.06 g cm^{-3}), and 1.3Zn-CaP$^{\phi}$ (3.16 g cm^{-3}) were spark plasma sintered at 950 °C for 5 minutes 15 seconds under 100 MPa using sintering cycle 8 shown in Figure 6-6 (f), resulting in dense uncracked 20 mm diameter discs. However, a cracked disc was obtained when sample $7.5CO_3$-HA$^{\phi}$ was sintered. Phase-pure hydroxyapatite samples ***ℓ***-HA(450)* (2.92 g cm^{-3}, 93%) and ***m***-HA(450)* (3.16 g cm^{-3}, 100%) were also sintered under identical conditions for comparison purposes.

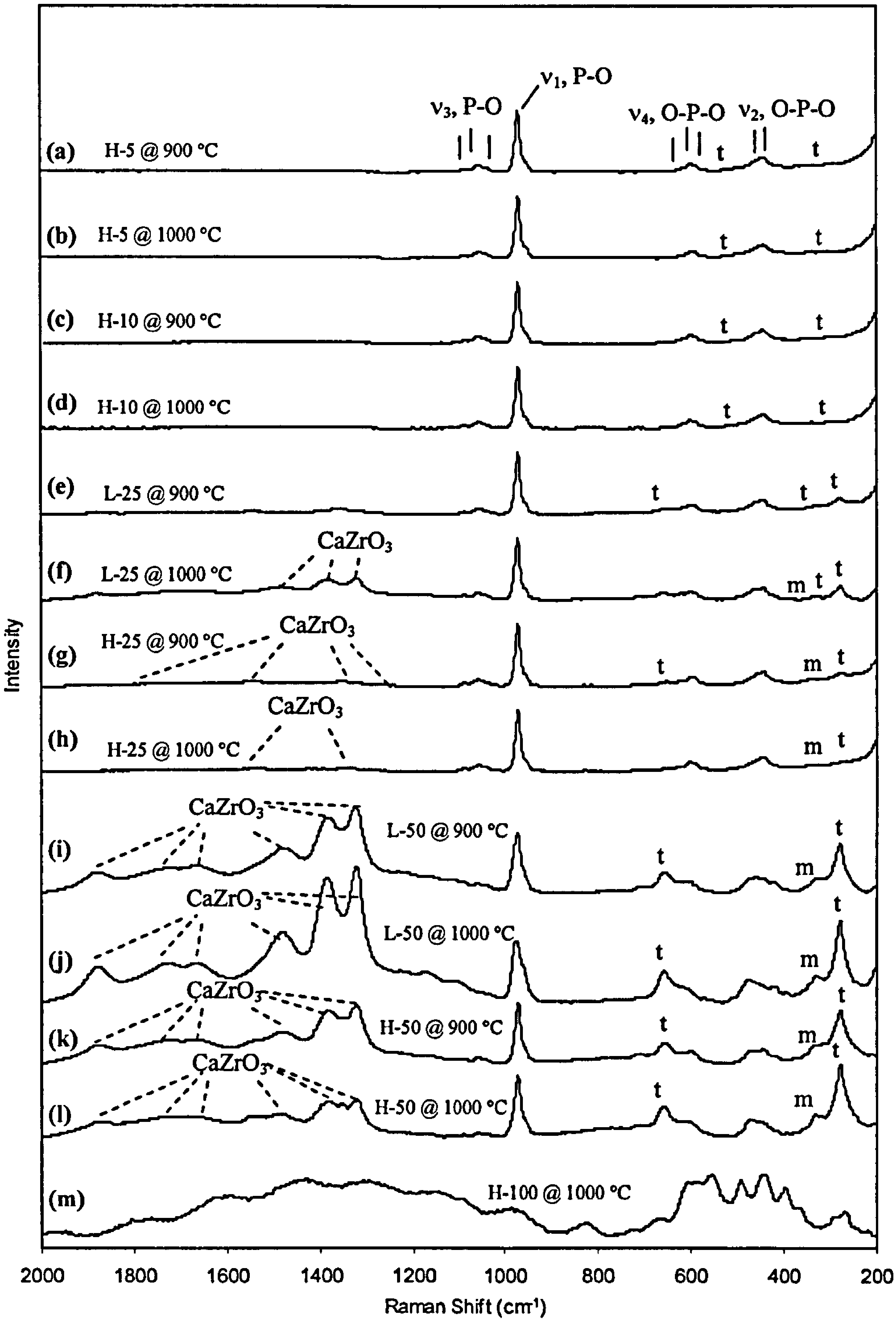

Figure 6-25 Raman spectra in the range 2000 – 200 cm^{-1} for spark plasma sintered samples, H-5 sintered (SPS) at (a) 900 °C and (b) 1000 °C, H-10 sintered (SPS) at (c) 900 °C and (d) 1000 °C, L-25 sintered (SPS) at (e) 900 °C and (f) 1000 °C, H-25 sintered (SPS) at (g) 900 °C and (h) 1000 °C, L-50 sintered (SPS) at (i) 900 °C and (j) 1000 °C, H-50 sintered (SPS) at (k) 900 °C and (l) 1000 °C and (m) H-100 sintered (SPS) at 1000 °C. Key: t = tetragonal, c = cubic, m = monoclinic CDZ.

6.3.3.1 Elemental Analysis

The substitution levels in ion-substituted calcium phosphate samples prior to sintering were measured using an EDS detector attached to a SEM. Sample 5Si-HA$^{\phi}$ contained 1.42 wt% silicon. On the contrary, sample 5Si-HA mentioned in Chapter 4 contained 0.81 wt% silicon. This was possibly due to a higher synthesis temperature (ultimately resulting in higher silicate ion incorporation into HA) for sample 5Si-HA$^{\phi}$ (450°C with mixing point heater at 450 °C as well) as compared to that for sample 5Si-HA (400 °C, no mixing point heater). Samples 0.5Mg-CaP$^{\phi}$, 1.5Mg-CaP$^{\phi}$ and 6Mg-CaP$^{\phi}$ contained 0.58, 1.58 and 6.04 wt% magnesium. Sample 1.3Zn-CaP$^{\phi}$ was found to contain 0.9 wt% zinc.

6.3.3.2 X-ray Diffraction

The XRD patterns of powder samples and spark plasma sintered discs are shown in Figure 6-26 (a) to (l). Figure 6-26 (a) revealed sample 7.5CO$_3$-HA$^{\phi}$ consisted of carbonate substituted HA (compared to JCPDS pattern 09-432 for HA). When this sample was sintered (SPS) at 950 °C, it resulted in a cracked disc with *ca.* 100% theoretical density (possibly due to the CO$_2$ release). Figure 6-26 (b) revealed the disc to consist of HA. A calcite peak (compared to JCPDS pattern 05-586 for calcite) was observed as well, however this was attributed to the plasticine that was used to mount the disc in the sample holder for XRD analysis. The (112) and (002) (c-axis) peaks for HA decreased in intensity and the (300) (a-axis) peak increased in intensity, markedly (Guo et al. 2005). This was possibly due to particle coalescence, growth and subsequent polygonisation. The expected densification behavior of HA rods (particles) is shown in Figure 6-27. The increase in intensity of (300) peak can be explained by the alignment of a few individual HA rods parallel to each other during spark plasma sintering to result in a HA grain in the polycrystalline ceramic.

For powdered samples the most intense peak corresponded to a reflection from the (211) plane. The XRD patterns in Figures 6-26 (c) and (d) for sample 5Si-HA$^{\phi}$ and its corresponding sintered disc were identified as phase-pure HA. The (112) reflection was observed to decrease in intensity upon sintering. The XRD pattern in Figure 6-26 (e) revealed sample 0.5Mg-CaP′ to be reminiscent of phase-pure HA (magnesium substituted HA, Mg-HA). After spark plasma sintering, the discs were found to contain mostly Mg-HA and a small amount of magnesium stabilised Whitlockite, Mg-Whitlockite [compared to JCPDS pattern 042-578 for $Ca_{18}Mg_2H_2(PO_4)_{14}$] as shown in Figure 6-26 (f). In a manner similar to that observed for sintering of sample $7.5CO_3$-HA$^{\phi}$, the (112) and (002) peaks decreased and the (300) peak increased in intensity, respectively, markedly upon sintering. Figure 6-26 (g) shows the XRD pattern for sample 1.5Mg-CaP$^{\phi}$, in which magnesium substituted HA and Mg-stabilised Whitlockite [$Ca_{18}Mg_2H_2(PO_4)_{14}$, minor phase] were observed. Upon sintering, the peaks corresponding to magnesium stabilised Whitlockite increased in intensity, possibly due to thermal decomposition of Mg-HA [Figure 6-26 (h)]. As mentioned in earlier cases in this discussion, the (112) and (200) peaks for Mg-HA decreased and the (300) peak increased in intensity, respectively. Figures 6-26 (i) and (j) show XRD patterns for powdered sample 6Mg-CaP′ and corresponding sintered disc, respectively. Powder 6Mg-CaP′ was identified as phase-pure magnesium stabilised Whitlockite. After spark plasma sintering Mg-Whitlockite was the only phase observed as well.

The XRD pattern in Figure 6-26 (k) for sample 1.3Zn-CaP′ gave good match to phase-pure HA. After sintering [see Figure 6-26 (l)], a biphasic mixture of HA (zinc substituted HA, Zn-HA) (JCPDS pattern 09-432) and β-TCP (zinc stabilised β-TCP, Zn-βTCP) (JCPDS pattern 09-169), was observed. Similar to sintering of other ion-substituted samples, the (112) and (002) peaks decreased and the (300) peak increased in intensity, respectively.

Figures 6-28 (a) and (b) show XRD patterns for samples *ℓ*-HA(450)* and *m*-HA(450)*, revealing near identical HA phases only. Upon sintering sample *ℓ*-HA(450)*, a very small peak corresponding to β-TCP phase appeared [Figure 6-28 (c)], whereas the sample *m*-HA(450)* remained phase-pure [Figure 6-28 (d)]. This was due to a comparatively higher stoichiometry in the latter sample, which was found to improve the thermal behavior of HA as mentioned earlier. After sintering at 950 °C, samples *ℓ*-HA(450)* and *m*-HA(450)* resulted in densities of 93% and 100 % theoretical density (assuming phase-pure HA). The lowered sintered density of *ℓ*-HA(450)*, might be due to formation of β-TCP. In both these spark plasma sintered samples, the (211) peak was the most intense peak. However, in the cases of spark plasma sintering of ion-substituted HA the (300) peak was observed to be the most intense in the HA-phases. This suggested that substitutions in the HA lattice effect grain-growth characteristics of HA during spark plasma sintering, especially in the case of silicon doping where only

83% theoretical density was achieved after spark plasma sintering. Indeed, silicon has been reported to hinder sintering (Putlayev et al. 2006).

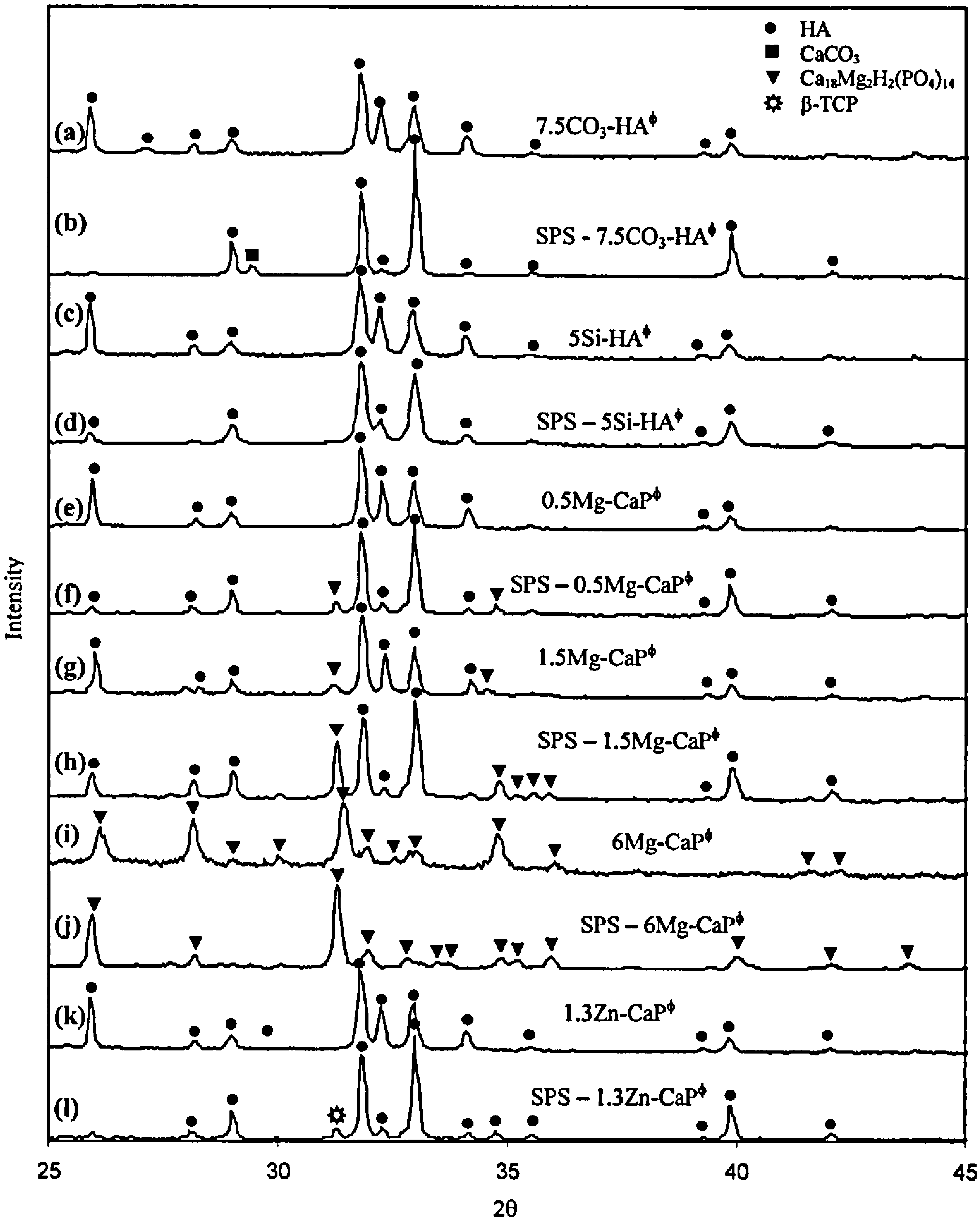

Figure 6-26 XRD patterns for (a) sample 7.5CO$_3$-HA$^{\phi}$ (b) after sintering (SPS) (c) sample 5Si-HA$^{\phi}$ (d) after sintering (SPS) (e) sample 0.5 Mg-CaP$^{\phi}$ (f) after sintering (SPS) (g) 1.5Mg-CaP$^{\phi}$ (h) after sintering (SPS) (i) sample 6Mg-CaP$^{\phi}$ (j) after sintering (SPS) (k) sample 1.3Zn-CaP$^{\phi}$ (l) after sintering (SPS). All samples were sintered at 950 °C for 5 minute 15 seconds under 100 MPa.

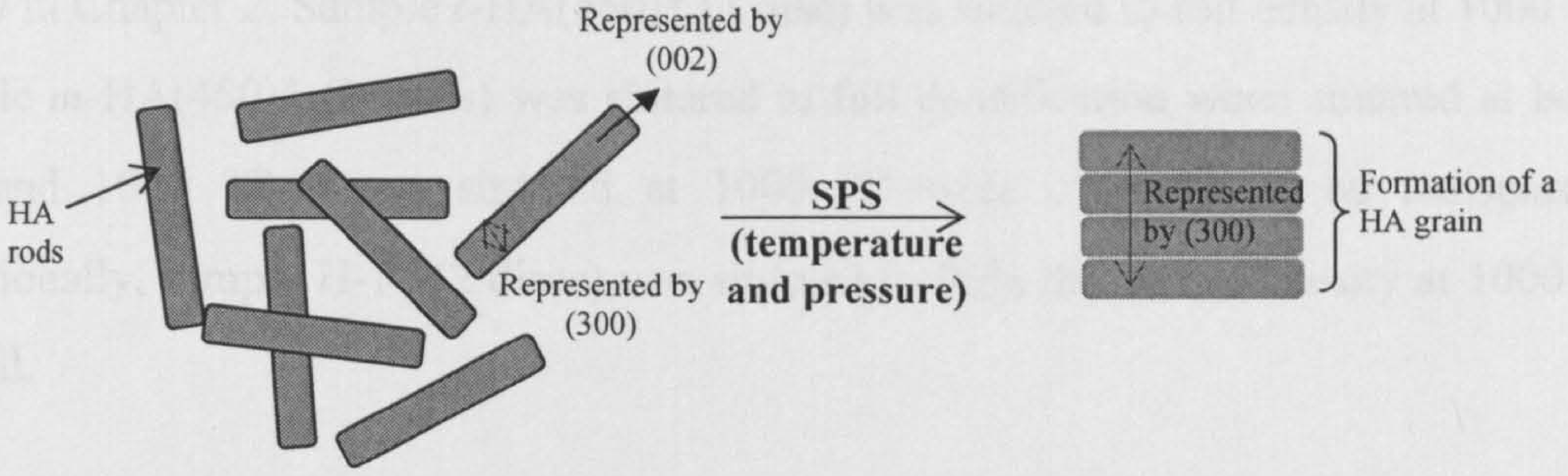

Figure 6-27 Schematic showing the consolidation of HA rods in spark plasma sintering; hence clarifying the reason for increase in (300) peak intensity in XRD patterns

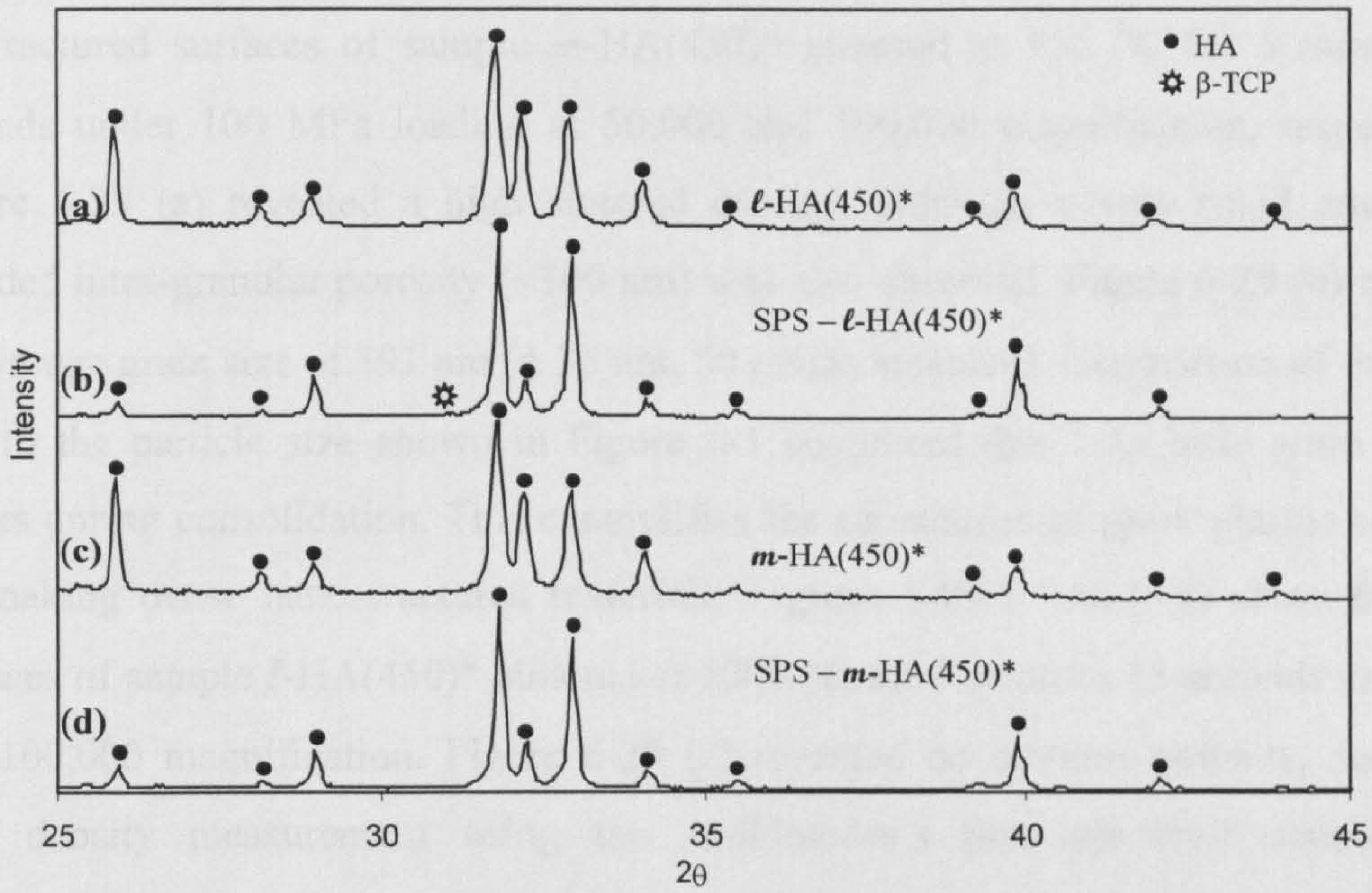

Figure 6-28 XRD patterns for (a) sample *ℓ*-HA(450)* (b) after sintering (SPS) (c) sample *m*-HA(450)* (d) after sintering (SPS). All samples were sintered at 950 °C for 5 minutes 15 seconds under 100 MPa.

6.3.4 Spark Plasma Sintering of HA and 10 wt% CDZ-HA Ceramics for 3-pt Flexural Strength Determination

Spark plasma sintering and characterisation of samples *ℓ*-HA(450)*, *m*-HA(450)* and H-10 has been discussed in detail in the preceding sections. Discs 20 or 30 mm in diameter were spark plasma sintered from their powders as mentioned earlier. In this section selected powder samples were spark plasma sintered for 5 minutes 15 seconds under 100 MPa (125.7 kN) loading [using sintering cycle 8 in Figure 6-6 (f)] to result in larger, 40 mm diameter discs. The larger size facilitated subsequent cutting of multiple rectangular samples for 3-pt flexural strength determination as explained in section

2.3.10 in Chapter 2. Sample *ℓ*-HA(450)* (1 disc) was sintered to full density at 1000 °C. Sample *m*-HA(450)* (2 discs) was sintered to full densification when sintered at both, 950 and 1000 °C. Discs sintered at 1000 °C were observed to be transparent. Additionally, sample H-10 (2 discs) was sintered to 96% theoretical density at 1000 °C as well.

6.3.4.1 Scanning Electron Microscopy

Small pieces of sintered discs were fractured (using a hammer) to observe the microstructure of the fractured surfaces under the SEM. Figures 6-29 (a) and (b) show the fractured surfaces of sample *m*-HA(450)* sintered at 950 °C for 5 minutes 15 seconds under 100 MPa loading at 50,000 and 100,000 magnification, respectively. Figure 6-29 (a) revealed a high sintered density, although a very small amount of rounded inter-granular porosity (<100 nm) was also observed. Figure 6-29 (b) revealed an average grain size of 191 nm (± 35 nm, 50 grains sampled). Comparison of this grain size to the particle size shown in Figure 6-1 suggested that very little grain growth occurs during consolidation. This exemplifies the advantages of spark plasma sintering for making dense nanostructured materials. Figures 6-29 (c) and (d) show fractured surfaces of sample *ℓ*-HA(450)* sintered at 1000 °C for 5 minutes 15 seconds at 50,000 and 100,000 magnification. Figure 6-29 (c) revealed no obvious porosity, consistent with density measurement using the Archimedes's principle (full densification, ~ 100%). Figure 6-29 (d) revealed average grain size of 244 nm (± 81 nm, 50 grains sampled) for sample *ℓ*-HA(450)* sintered at 1000 °C. In comparison to sintering carried out at 950 °C, at 1000 °C a slightly larger average grain size was observed with a slighter larger standard deviation. Figures 6-29 (e) and (f) show the fractured surfaces of sample *m*-HA(450)* sintered at 1000 °C for 5 minutes and 15 seconds under 100 MPa loading. Figures 6-29 (e) and (f) showed sub-micron features with minimal porosity and an average grain size of 212 nm (±60 nm, 50 grains sampled).

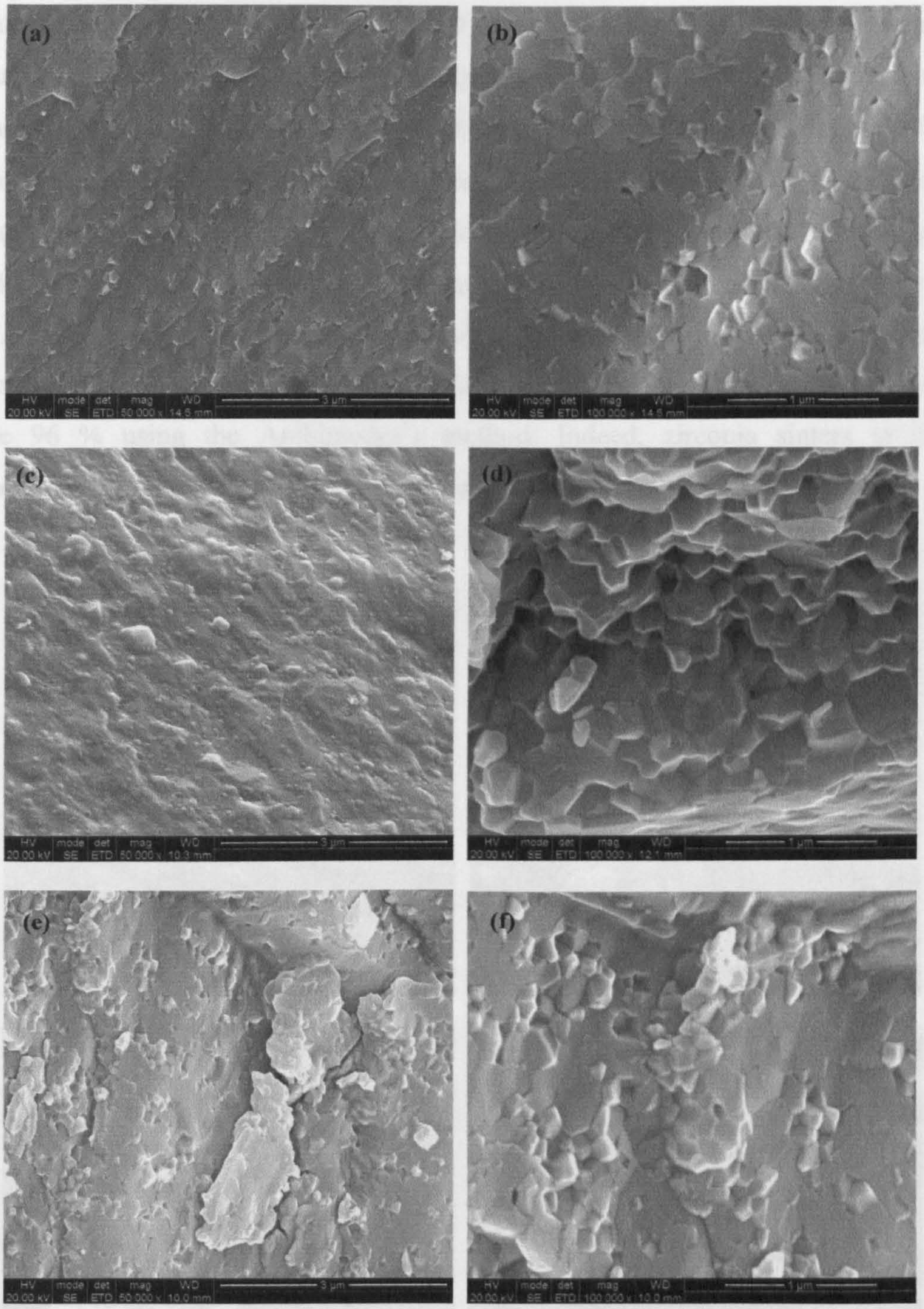

Figure 6-29 SEM images showing the microstructures of, sample ***m***-HA(450)* sintered at 950 °C at magnification (a) x50k [bar = 3 μm] and (b) x100k [bar = 1 μm], sample ***ℓ***-HA(450)* sintered at 1000 °C at magnification (c) x50k [bar = 3 μm] and (d) x100k [bar = 1 μm] and sample ***m***-HA(450)* sintered at 1000 °C at magnification (e) x50k [bar = 3 μm] and (f) x100k [bar = 1 μm].

Figures 6-30 (a) to (e) show SEM images of fractured surfaces of sample H-10 sintered at 1000 °C. Figure 6-30 (a) shows a non-porous region of the sintered disc with sub-micron features at x100k magnification. Figures 6-30 (b) to (d) shows an adjacent, slightly porous region of the sample. In Figure 6-30 (d) two distinct grain sizes in this region of the sintered disc were clearly visible. The larger grains [avg. 210 nm (±40); 50 grains sampled] are likely to be HA whereas the considerably smaller grains [avg. 48 nm, (±12); 50 grains sampled] are likely to be CDZ. In Figure 6-30 (b) a few grains (marked on the figure) were observed to have a rod like particle morphology akin to that of HA prior to sintering. Hence the surface coverage of HA rods by CDZ particles prevents the HA grains from growing and fusing. The density of this disc was measured to be 96 % using the Archimedes's method. Indeed, zirconia sinters at higher temperatures (1100 – 1500 °C), as compared to HA (Chen et al. 2004).

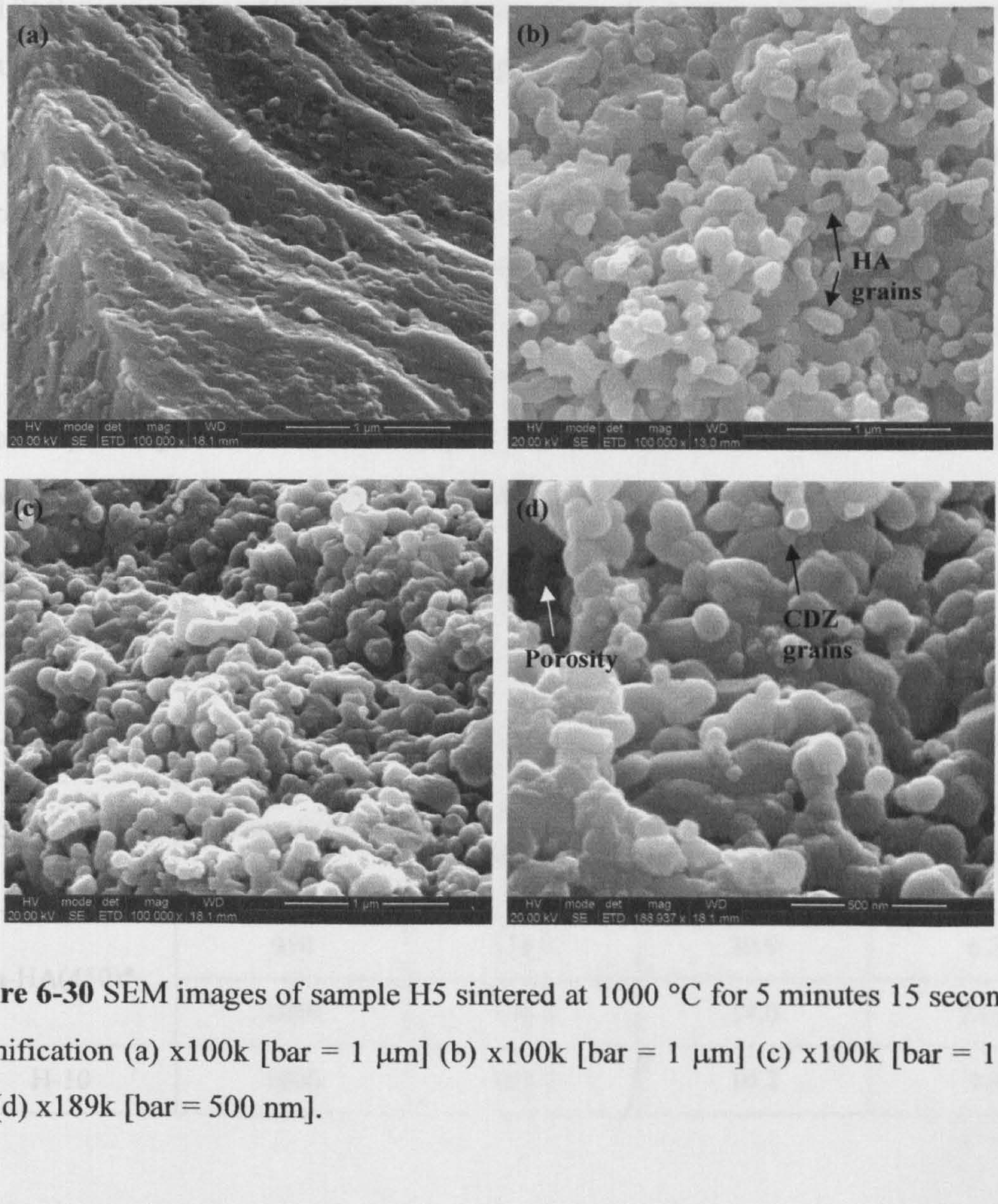

Figure 6-30 SEM images of sample H5 sintered at 1000 °C for 5 minutes 15 seconds at magnification (a) x100k [bar = 1 μm] (b) x100k [bar = 1 μm] (c) x100k [bar = 1 μm] and (d) x189k [bar = 500 nm].

6.3.4.2 Three point (3-pt) Flexural Strength

The details of the flexural strength testing are explained in section 2.3.10 of chapter 2. Sample *m*-HA(450)* spark plasma sintered at 950 °C had a flexural strength of 136.7 MPa (± 20.9). As expected, when sample *m*-HA (450)* was sintered at 1000 °C a higher flexural strength of 158.4 MPa (± 14.0) was measured. Indeed, porosity was not visible as seen previously in SEM images shown in Figures 6-29 (e) and (f). Sample H-10 spark plasma sintered at 1000 °C, however, resulted in a lower flexural strength value of 107.7 MPa (± 10.2). This can be attributed to the presence of porous regions in the sample as observed previously in the SEM images shown in Figure 6-30. This suggested that 1) CDZ nanoparticles hindered the growth and sintering of HA particles and 2) the temperature 1000 °C and sintering time of 5 minutes 15 seconds are probably insufficient for complete sintering to take place.

Sample *m*-HA(450)* sintered at 950 °C had a low Weibull modulus of 6.2. This was attributed to a wide distribution in size and effect of critical defects (which is porosity in this case). The same sample sintered at 1000 °C resulted in a higher Weibull modulus of 11.0. This corresponded to the absence of porosity in the samples when observed under the SEM. Sample H-10 sintered at 1000 °C had a lower Weibull modulus of 9.9 (also due to porosity as observed in Figure 6-30). Hence, in terms of reliability and mechanical performance, sample *m*-HA(450)* sintered at 1000 °C is the best option.

Table 6-6 Details of spark plasma sintered discs, corresponding 3-pt flexural strengths, standard deviations and Weibull moduli.

Sample ID	**SPS Temperature (°C)**	**3-pt Flexural Strength (MPa)**	**Standard Deviation (±)**	**Weibull modulus, m**
m-HA(450)*	950	136.7	20.9	6.2
	1000	158.4	14.0	11.0
H-10	1000	107.7	10.2	9.9

6.4 Conclusions

In this work, HA synthesised at 450 °C and 24 MPa (band heater at 450 °C) with an in-solution Ca:P molar ratio of 1.67 [sample ℓ-HA(450)*] was sintered to full density at 1050 °C within 3 minutes under 100 MPa using spark plasma sintering. Discs sintered at 1000 °C and above, displayed transparency because of their grain sizes being smaller than the wavelength of light. A maximum Vickers hardness of 5.7 GPa was measured for HA sintered at 1050 °C for 3 minutes under 100 MPa. Overall, increase in sintering temperature resulted in an increase in hardness of these samples (due to decrease in porosity). Sintering of sample ℓ-HA(450)* at 950 °C and above resulted in slight decomposition of HA into a β-TCP phase. This was attributed to non-stoichiometry in the powder sample itself and hence the thermal instability of the sample. CHFS of HA with a 2.0 in-solution Ca:P molar ratio [sample *m*-HA(450)*] improved the thermal stability of HA. Sintering at 1000 °C for 5 minutes under 100 MPa resulted in a phase-pure HA phase.

Sintering times and force profiles were found to be important for densification. Increase in sintering time at 950 °C from 3 minutes to 5 minutes 15 seconds increased the sintered density from 95 % to 100 %. The sintering cycle (temperature and force variation with time) was optimised in order to yield un-cracked fully dense sintered discs. Immediate release of force on the die in the spark plasma sintering furnace after completion of sintering time, prior to the cooling ramp, was the key to obtain intact discs.

Mixtures of calcium doped zirconia, CDZ and HA were co-crystallised in a rapid single step using the CHFS system at 450 °C and 24 MPa (band heater at 450 °C). A tetragonal structure was suggested for CDZ in the powder mixtures. HA and CDZ phases in the powder mixtures could be identified based on particle size and morphology under the TEM. After sintering, samples L-25 and L-50 phase-decomposed by HA converting into TCP phases and a high temperature reaction product, $CaZrO_3$. The formation of this latter phase was retarded by using a higher in-solution Ca:P molar ratio of 2.5. Phase evolution and thermal stability of powder mixtures were analysed using in-situ variable temperature XRD. Results indicated samples H-5 and H-10 to be ideal samples in-terms of thermal stability up to 1000 °C. Indeed, samples H-5 and

H-10 were sintered to 96 and 98 % sintered densities, respectively, at 1000 °C resulting in HA and CDZ as the only two phases.

Selected compositions from previous chapters, e.g. ion-substituted calcium phosphates, were re-synthesised at 450 °C and 24 MPa (band heater at 450 °C) using flow rates of 25, 12.5 and 12.5 ml min^{-1} for superheated water, calcium and phosphate source feeds, respectively. In the case of silicate, synthesis at higher temperatures used here, resulted in increased silicate substitution into HA (compared to in chapter 4). With the exception of sample 5Si-HA$^{\phi}$, all ion-substituted samples underwent same phase decomposition/transformation in the conditions used for spark plasma sintering. All samples were sintered at 950 °C for 5 minutes 15 seconds under 100 MPa. Sample 5Si-HA$^{\phi}$ was consolidated by spark plasma sintering to only 83% theoretical density suggesting that presence of silicate in the HA hindered particle coalescence and subsequent densification.

For mechanical testing, 40 mm discs were sintered from samples *m*-HA(450)* at 950 °C (to 100 % density) and 1000 °C (to 100 % density) and H-10 (to 96 % density) at 1000 °C, for 5 minutes 15 seconds under 100 MPa. Sample *m*-HA(450)* sintered at 950 and 1000 °C resulted in 3-pt flexural strengths of *ca.* 137 MPa and *ca.* 158 MPa. These values are higher than those reported in literature. However, sample H-10 sintered at 1000 °C resulted in a lower flexural strength value of *ca.* 108 MPa. This was attributed to the presence of regions of porosity in the sintered disc as seen under the SEM.

Previous chapters and this work, present the Continuous Hydrothermal Flow Synthesis technique as a versatile, rapid, single step method to synthesise phase-pure and ion-substituted calcium phosphates and mixtures with tailorable properties. In this work, the sinterability of a large variety of nano-bio-ceramics was investigated and optimum spark plasma sintering conditions were determined. The novelty and rapidity of this particulate synthesis technology is hence complemented by spark plasma sintering. This work constitutes the first ever detailed report on CHFS of large variety of calcium phosphates and their SPS to high densities including development and understanding of sintering regimes.

6.5 Future Work

In order to sustain the powder consuming sintering studies it would be desirable to upgrade the CHFS systems to synthesise more quantity of the aforementioned bioceramics and mixtures. Higher concentrations of calcium and phosphate source solutions can also help achieve this, while being wary of the susceptibility of the BPR in the CHFS system to fail during production of concentrated suspensions.

It would be interesting to spark plasma sinter CDZ-HA compositions with CDZ contents lower than 10 wt%. SPS of HA synthesised in the CHFS system resulted in a high flexural strength of 158 MPa. It is expected that with a lower CDZ content the sintered density would increase as compared to those attained by using sample H-10 in this chapter. This might ultimately result in flexural strengths much higher than 158 MPa. Further mechanical tests such as fracture toughness determination can given more detailed insight into the benefits of SPS of nano-bioceramics synthesised in CHFS systems. Similar work can also be carried out using TiO_2-HA compositions. Synthesis and subsequent SPS of bioceramics (which sinter at higher temperatures) coated with HA might result in high sintered densities at lower sintering temperatures. Furthermore, SPS of HA to result in porous blocks (scaffolds) is strongly suggested.

Conclusions

A three-pump CHFS system was found suitable for synthesis of hydroxyapatite. Calcium nitrate and diammonium hydrogen phosphate solutions react immediately when exposed to each other. Similarly, this reaction took place inside the T-piece of the CHFS system 1. As hypothesised in the aims of this thesis, the rapid crystallising environment in CHFS system resulted in rapid growth and instant crystallisation of hydroxyapatite particles formed form the amorphous reaction product at the T-piece. Due to the rapidity of the process these particles were named "Instant Hydroxyapatite". Moreover, temperature had a direct affect on the crystallinity of the resulting apatites. The rapidity of the process, however, resulted in non-stoichiometric hydroxyapatite in all reactions. This is encouraging, because biological apatite too, is a poorly crystalline non-stoichiometric carbonated hydroxyapatite. The extent of deviation from stoichiometry of HA synthesised in the CHFS systems was, however, controlled primarily by pH of the solutions and also by Ca:P molar ratios in solution and flow rates. This translated into control over the thermal behavior of these apatites; as highly calcium deficient hydroxyapatite decomposed into β-TCP around *ca.* 750 °C (upon heating). This work formed a large spectrum of hydroxyapatite particles with varying stoichiometry, size and thermal stability controllable by temperature, flow rates and concentrations and pH of solutions used.

Based on these encouraging results the issue of ionic substitutions into HA was then addressed. In the initial work on synthesis of HA in the CHFS system, peaks corresponding to carbonate groups were observed in corresponding FTIR spectroscopic spectra. This was attributed to some dissolved carbonate in the deionised water used for reactions. Leading on from this, urea was used as a carbonate ion source upon dissociation at exposure to hot water inside the mixing point. A maximum of *ca.* 5 wt% carbonate content was achieved in HA as confirmed by spectroscopic and thermal analysis. However, attempts to increase the substitution levels (by adding more urea) resulted in formation of biphasic mixtures of HA and calcium carbonate (calcite). Reports in literature suggest that these biphasic mixtures may be suitable for biomedical usage due to enhanced solubility of calcium carbonate as compared to hydroxyapatite. Difficulty was faced, however, in attaining high silicon incorporation into HA (in the form of silicate ions) due to the difficulty in dissolving silicon acetate. A maximum silicon content of *ca.* 1.4 wt% silicon was achieved. At lower temperatures, for an identical reaction, a silicon content of *ca.* 0.8 wt% was measured. This suggested that increase in the reaction temperature increases incorporation of silicate ions into hydroxyapatite.

In addition to these anionic substitutions, magnesium and zinc ions were also substituted into HA. Maximum contents of 0.7 wt% and 0.9 wt% were attained for magnesium and zinc substitutions into HA, respectively. Further, increase in cationic concentration in solution resulted in formation of biphasic mixtures of HA and other phases. In the case of magnesium substitution, with ever increasing magnesium in solution, initially biphasic mixtures of Mg-Whitlockite and HA were formed. Further increase in magnesium content in solution reduced the amount of HA in the mixtures and eventually phase-pure Mg-Whitlockite was stabilised. This is desirable, as this facilitates synthesis of tailorable biphasic compositions which can allow tailorable dissolution rates. These results demonstrated the ability of the CHFS system to, synthesise ion substituted calcium phosphates and stabilise phases unattainable in a short rapid manner using conventional synthesis methods. As in the case of all ionic substitution reactions, change in concentrations were generally noticed to have a profound effect on the morphology of calcium phosphate particles.

In order to address the issue of poor mechanical properties of HA a two-pronged approach was adopted. Firstly, the ability of the CHFS system to synthesise crystalline, nanosized HA particles was accentuated by spark plasma sintering of these materials. Indeed, *ca.* 100% density was achieved by sintering at 950 °C for 5 minutes 15 seconds under 100 MPa. Good flexural strengths of *ca.* 158 MPa (considerably higher than those achieved by conventional consolidation) were achieved for HA sintered at 1000 °C for 5 minutes 15 seconds under 100 MPa (these discs displayed transparency). With this aim fulfilled, the second approach involved the synthesis of co-precipitates of HA and another phase with superior mechanical properties. Indeed, varying compositions of calcium doped zirconia and hydroxyapatite (CDZ-HA) mixtures were synthesised. VT-XRD studies revealed that formation of the deleterious $CaZrO_3$ phase can be reduced by use of higher Ca:P molar ratios in solution. A composition containing 11.3 wt% CDZ was suggested as the optimum composition. SPS of this composition resulted in a sintered density of *ca.* 96 wt%. Using scanning electron microscopy, it was observed that zirconia grains existed between HA grains suggesting that this hindered full consolidation. Indeed, porosity was observed as well. This ultimately resulted in lower 3-pt flexural strength of *ca.* 108 MPa. However, it is predicted that use of a composition with lower CDZ content may result in higher sintered densities and in turn, better mechanical properties than those achieved for spark plasma sintered HA. Selected ion substituted compositions were also spark plasma sintered to high densities at 950 °C in 5 minutes 15 seconds under 100 MPa. 1.4 wt% silicon containing HA however, was consolidated up to only 83% density suggesting that presence of silicon limited grain growth and sintering. In conclusion, by spark plasma sintering of nano-bioceramics synthesised using CHFS systems, the complimentary nature of these two rapid techniques was demonstrated.

References

Adolfsson, E., Alberius-Henning, P., Hermansson, L., (2000), Phase analysis and thermal stability of hot isostatically pressed zirconia-hydroxyapatite composites, *Journal of the American Ceramic Society*, **83**, 2798-2802.

Adschiri, T., Kanazawa, K., Arai, K., (1992a), Rapid and Continuous Hydrothermal Crystallization of Metal-Oxide Particles in Supercritical Water, *Journal of the American Ceramic Society*, **75**, 1019-1022.

Adschiri, T., Kanazawa, K., Arai, K., (1992b), Rapid and Continuous Hydrothermal Synthesis of Boehmite Particles in Subcritical and Supercritical Water, *Journal of the American Ceramic Society*, **75**, 2615-2618.

Afshar, A., Ghorbani, M., Ehsani, N., Saeri, M. R., Sorrell, C. C., (2003), Some important factors in the wet precipitation process of hydroxyapatite, *Materials & Design*, **24**, 197-202.

Ahn, E. S., Gleason, N. J., Ying, J. Y., (2005), The effect of zirconia reinforcing agents on the microstructure and mechanical properties of hydroxyapatite-based nanocomposites, *Journal of the American Ceramic Society*, **88**, 3374-3379.

Aimable, A., Xin, B., Millot, N., Aymes, D., (2008), Continuous hydrothermal synthesis of nanometric BaZrO3 in supercritical water, *Journal of Solid State Chemistry*, **181**, 183-189.

Akao, M., Aoki, H., Kato, K., (1981), Mechanical-Properties of Sintered Hydroxyapatite for Prosthetic Applications, *Journal of Materials Science*, **16**, 809-812.

Aksakal, B., Hanyaloglu, C., (2008), Bioceramic dip-coating on Ti-6Al-4V and 316L SS implant materials, *Journal of Materials Science-Materials in Medicine*, **19**, 2097-2104.

Albee, F. H., (1920), Triple CaP as a stimulus to osteogenesis, *Annals of Surgery*, **71**, 32-36.

Andres-Verges, M., Fernandez-Gonzalez, C., Martinez-Gallego, M., (1998), Hydrothermal synthesis of calcium deficient hydroxyapatites with controlled size and homogeneous morphology, *Journal of the European Ceramic Society*, **18**, 1245-1250.

Angker, L., Swain, M. V., Kilpatrick, N., (2003), Micro-mechanical characterisation of the properties of primary tooth dentine, *Journal of Dentistry*, **31**, 261-267.

Aoki, H. 1991, *Science and Medical Applications of Hydroxyapatite* Japanese Association of Apatite Sciences (JAAS).

Arce, H., Montero, M. L., Saenz, A., Castano, V. M., (2004b), Effect of pH and temperature on the formation of hydroxyapatite at low temperatures by decomposition of a Ca-EDTA complex, *Polyhedron*, **23**, 1897-1901.

Arce, H., Montero, M. L., Saenz, A., Castano, V. M., (2004a), Effect of pH and temperature on the formation of hydroxyapatite at low temperatures by decomposition of a Ca-EDTA complex, *Polyhedron*, **23**, 1897-1901.

Arifuzzaman, S. M., Rohani, S., (2004), Experimental study of brushite precipitation, *Journal of Crystal Growth*, **267**, 624-634.

Awonusi, A., Morris, M., Tecklenburg, M., (2007), Carbonate Assignment and Calibration in the Raman Spectrum of Apatite, *Calcified Tissue International*, **81**, 46-52.

Balamurugan, A., Balossier, G., Kannan, S., Michel, J., Faure, J., Rajeswari, S., (2007), Electrochemical and structural characterisation of zirconia reinforced hydroxyapatite bioceramic sol-gel coatings on surgical grade 316L SS for biomedical applications, *Ceramics International*, **33**, 605-614.

Balashov, A. B., Golubeva, N. P., Skidan, B. S., (1999), Oxide zinc ceramics for varistors (a review), *Glass and Ceramics*, **56**, 58-60.

Bandyopadhyay, A., Bernard, S., Xue, W. C., Bose, S., (2006), Calcium phosphate-based resorbable ceramics: Influence of MgO, ZnO, and SiO2 dopants, *Journal of the American Ceramic Society*, **89**, 2675-2688.

Barralet, J., Akao, M., Aoki, H., Aoki, H., (2000), Dissolution of dense carbonate apatite subcutaneously implanted in Wistar rats, *Journal of Biomedical Materials Research*, **49**, 176-182.

Barralet, J., Best, S., Bonfield, W., (1998), Carbonate substitution in precipitated hydroxyapatite: An investigation into the effects of reaction temperature and bicarbonate ion concentration, *Journal of Biomedical Materials Research*, **41**, 79-86.

Barralet, J. E., Fleming, G. J. P., Campion, C., Harris, J. J., Wright, A. J., (2003), Formation of translucent hydroxyapatite ceramics by sintering in carbon dioxide atmospheres, *Journal of Materials Science*, **38**, 3979-3993.

Bellissent-Funel, M. C., (2001), Structure of supercritical water, *Journal of Molecular Liquids*, **90**, 313-322.

Ben Abdelkader, S., Ben Cherifa, A., Coulet, M., Khattech, I., Rogez, J., Jemal, M., (2004), Enthalpie de formation de la whitlockite Ca18Mg2H2(PO4)14, *Journal of Thermal Analysis and Calorimetry*, **77**, 863-871.

Bertoni, E., Bigi, A., Cojazzi, G., Gandolfi, M., Panzavolta, S., Roveri, N., (1998), Nanocrystals of magnesium and fluoride substituted hydroxyapatite, *Journal of Inorganic Biochemistry*, **72**, 29-35.

Bianco, A., Cacciotti, I., Lombardi, M., Montanaro, L., Gusmano, G., (2007), Thermal stability and sintering behaviour of hydroxyapatite nanopowders, *Journal of Thermal Analysis and Calorimetry*, **88**, 237-243.

Bigi, A., Boanini, E., Rubini, K., (2004), Hydroxyapatite gels and nanocrystals prepared through a sol-gel process, *Journal of Solid State Chemistry*, **177**, 3092-3098.

Bigi, A., Falini, G., Foresti, E., Gazzano, M., Ripamonti, A., Roveri, N., (1993), Magnesium Influence on Hydroxyapatite Crystallization, *Journal of Inorganic Biochemistry*, **49**, 69-78.

Bigi, A., Falini, G., Foresti, E., Gazzano, M., Ripamonti, A., Roveri, N., (1996), Rietveld structure refinements of calcium hydroxylapatite containing magnesium, *Acta Crystallographica Section B-Structural Science*, **52**, 87-92.

Blood, P. J., Denyer, J. P., Azzopardi, B. J., Poliakoff, M., Lester, E., (2004), A versatile flow visualisation technique for quantifying mixing in a binary system: application to continuous supercritical water hydrothermal synthesis (SWHS), *Chemical Engineering Science*, **59**, 2853-2861.

Blumenthal, N. C., (1989), Mechanisms of Inhibition of Calcification, *Clinical Orthopaedics and Related Research* 279-289.

Boesel, R. W., (1971), Spark Sintering - Unusual Method, *Metal Progress*, **99**, 74-&.

Boldrin, P., Hebb, A. K., Chaudhry, A. A., Otley, L., Thiebaut, B., Bishop, P., Darr, J. A., (2007), Direct synthesis of nanosized $NiCo_2O_4$ spinel and related compounds via continuous hydrothermal synthesis methods, *Industrial & Engineering Chemistry Research*, **46**, 4830-4838.

Boldrin, P. 2008, *Ph.D. Thesis,* Department of Materials, Queen Mary University of London.

Botelho, C. M., Brooks, R. A., Best, S. M., Lopes, M. A., Santos, J. D., Rushton, N., Bonfield, W., (2006), Human osteoblast response to silicon-substituted hydroxyapatite, *Journal of Biomedical Materials Research Part A*, **79A**, 723-730.

Bouler, J. M., LeGeros, R. Z., Daculsi, G., (2000), Biphasic calcium phosphates: Influence of three synthesis parameters on the HA/beta-TCP ratio, *Journal of Biomedical Materials Research*, **51**, 680-684.

Brandaoneto, J., Stefan, V., Mendonca, B. B., Bloise, W., Castro, A. V. B., (1995), The Essential Role of Zinc in Growth, *Nutrition Research*, **15**, 335-358.

Byrappa, K., Adschiri, T., (2007), Hydrothermal technology for nanotechnology, *Progress in Crystal Growth and Characterization of Materials*, **53**, 117-166.

Cabanas, A., Darr, J. A., Lester, E., Poliakoff, M., (2000), A continuous and clean one-step synthesis of nano-particulate Ce1-xZrxO2 solid solutions in near-critical water, *Chemical Communications* 901-902.

Cabanas, A., Darr, J. A., Lester, E., Poliakoff, M., (2001), Continuous hydrothermal synthesis of inorganic materials in a near-critical water flow reactor; the one-step synthesis of nano-particulate Ce1-xZrxO2 (x=0-1) solid solutions, *Journal of Materials Chemistry*, **11**, 561-568.

Cabanas, A., Poliakoff, M., (2001), The continuous hydrothermal synthesis of nano-particulate ferrites in near critical and supercritical water, *Journal of Materials Chemistry*, **11**, 1408-1416.

Cai, S., Wang, Y. W., Hong, L., Peng, Z. Z., Yao, K. D., (2005), Synthesis of carbonated hydroxyapatite nanofibers by mechanochemical methods, *Ceramics International*, **31**, 135-138.

Cai, S., Yu, X. Z., Xiao, Z. Y., Xu, G. H., Lv, H., Yao, K. D., (2007), Synthesis and sintering of nanocrystalline hydroxyapatite powders by gelatin-based precipitation method, *Ceramics International*, **33**, 193-196.

Calvo, C., Gopal, R., (1975), Crystal-Structure of Whitlockite from Palermo Quarry, *American Mineralogist*, **60**, 120-133.

Cansell, F., Aymonier, C., Loppinet-Serani, A., (2003), Review on materials science and supercritical fluids, *Current Opinion in Solid State & Materials Science*, **7**, 331-340.

Cao, J. M., Feng, J., Deng, S. G., Chang, X., Wang, J., Liu, J. S., Lu, P., Lu, H. X., Zheng, M. B., Zhang, F., Tao, J., (2005), Microwave-assisted solid-state synthesis of hydroxyapatite nanorods at room temperature, *Journal of Materials Science*, **40**, 6311-6313.

Cao, L. Y., Zhang, C. B., Huang, J. F., (2005), Influence of temperature, [Ca2+], Ca/P ratio and ultrasonic power on the crystallinity and morphology of hydroxyapatite nanoparticles prepared with a novel ultrasonic precipitation method, *Materials Letters*, **59**, 1902-1906.

Cao, W. P., Hench, L. L., (1996), Bioactive materials, *Ceramics International*, **22**, 493-507.

Caria, P. H. F., Kawachi, E. Y., Bertran, C. A., Camilli, J. A., (2007), Biological assessment of porous-implant hydroxyapatite combined with periosteal grafting in maxillary defects, *Journal of Oral and Maxillofacial Surgery*, **65**, 847-854.

Carlisle, E. M., (1970), Silicon . A Possible Factor in Bone Calcification, *Science*, **167**, 279-&.

Carlisle, E. M., (1982), The Nutritional Essentiality of Silicon, *Nutrition Reviews*, **40**, 193-198.

Chaudhry, A. A., Haque, S., Kellici, S., Boldrin, P., Rehman, I., Fazal, A. K., Darr, J. A., (2006), Instant nano-hydroxyapatite: a continuous and rapid hydrothermal synthesis, *Chemical Communications* 2286-2288.

Chen, B., Zhang, T., Zhang, J., Lin, Q., Jiang, D., (2008), Microstructure and mechanical properties of hydroxyapatite obtained by gel-casting process, *Ceramics International*, **34**, 359-364.

Chen, B. Q., Zhang, Z. Q., Zhang, J. X., Dong, M. J., Jiang, D. L., (2006), Aqueous gel-casting of hydroxyapatite, *Materials Science and Engineering A-Structural Materials Properties Microstructure and Processing*, **435**, 198-203.

Chen, C. W., Oakes, C. S., Byrappa, K., Riman, R. E., Brown, K., TenHuisen, K. S., Janas, V. F., (2004a), Synthesis, characterization, and dispersion properties of hydroxyapatite prepared by mechanochemical-hydrothermal methods, *Journal of Materials Chemistry*, **14**, 2425-2432.

Chen, Q. Z. Z., Thompson, I. D., Boccaccini, A. R., (2006), 45S5 Bioglass (R)-derived glass-ceramic scaffolds for bone tissue engineering, *Biomaterials*, **27**, 2414-2425.

Chen, X., Khor, K. A., Chan, S. H., Yu, L. G., (2004b), Overcoming the effect of contaminant in solid oxide fuel cell (SOFC) electrolyte: spark plasma sintering (SPS) of 0.5 wt.% silica-doped yttria- stabilized zirconia (YSZ), *Materials Science and Engineering A-Structural Materials Properties Microstructure and Processing*, **374**, 64-71.

Chevalier, J., (2006), What future for zirconia as a biomaterial?, *Biomaterials*, **27**, 535-543.

Chihara, Y., Fujimoto, K., Kondo, H., Moriwaka, Y., Sasahira, T., Hirao, Y., Kuniyasu, H., (2007), Anti-tumor effects of liposome-encapsulated titanium dioxide in nude mice, *Pathobiology*, **74**, 353-358.

Chiu, C. Y., Hsu, H. C., Tuan, W. H., (2007), Effect of zirconia addition on the microstructural evolution of porous hydroxyapatite, *Ceramics International*, **33**, 715-718.

Cockcroft, J. K. PROFIL Suite of Data Refinement Programs. [6.21]. 2005.

Coreno, A. J., Coreno, A. O., Cruz, R. J. J., Rodriguez, C. C., (2005), Mechanochemical synthesis of nanocrystalline carbonate-substituted hydroxyapatite, *Optical Materials*, **27**, 1281-1285.

Correia, R. N., Magalhaes, M. C. F., Marques, P. A. A. P., Senos, A. M. R., (1996), Wet synthesis and characterization of modified hydroxyapatite powders, *Journal of Materials Science-Materials in Medicine*, **7**, 501-505.

Corrente, G., Abundo, R., Cardaropoli, G., Martuscelli, G., Trisi, P., (1997), Supracrestal bone regeneration around dental implants using a calcium carbonate and a fibrin-fibronectin sealing system: Clinical and histologic evidence, *International Journal of Periodontics & Restorative Dentistry*, **17**, 171-&.

Cote, L. J., Teja, A. S., Wilkinson, A. P., Zhang, Z. J., (2003), Continuous hydrothermal synthesis of $CoFe_2O_4$ nanoparticles, *Fluid Phase Equilibria*, **210**, 307-317.

Cushing, B. L., Kolesnichenko, V. L., O'Connor, C. J., (2004), Recent advances in the liquid-phase syntheses of inorganic nanoparticles, *Chemical Reviews*, **104**, 3893-3946.

Cuy, J. L., Mann, A. B., Livi, K. J., Teaford, M. F., Weihs, T. P., (2002), Nanoindentation mapping of the mechanical properties of human molar tooth enamel, *Archives of Oral Biology*, **47**, 281-291.

Daculsi, G., Darc, M. B., Corlieu, P., Gersdorff, M., (1992), Macroporous Biphasic Calcium-Phosphate Efficiency in Mastoid Cavity Obliteration - Experimental and Clinical Findings, *Annals of Otology Rhinology and Laryngology*, **101**, 669-674.

Daoud, W. A., Xin, J. H., Pang, G. K. H., (2005), Microstructural evolution of titania nanocrystallites by a hydrothermal treatment: A HRTEM study, *Journal of the American Ceramic Society*, **88**, 443-446.

Darr, J. A., Guo, Z. X., Raman, V., Bououdina, M., Rehman, I. U., (2004), Metal organic chemical vapour deposition (MOCVD) of bone mineral like carbonated hydroxyapatite coatings, *Chemical Communications* 696-697.

Darr, J. A., Poliakoff, M., (1999), New directions in inorganic and metal-organic coordination chemistry in supercritical fluids, *Chemical Reviews*, **99**, 495-541.

deAza, P. N., Santos, C., Pazo, A., deAza, S., Cusco, R., Artus, L., (1997), Vibrational properties of calcium phosphate compounds .1. Raman spectrum of beta-tricalcium phosphate, *Chemistry of Materials*, **9**, 912-915.

Delecrin, J., Takahashi, S., Gouin, F., Passuti, N., (2000), A synthetic porous ceramic as a bone graft substitute in the surgical management of scoliosis - A prospective, randomized study, *Spine*, **25**, 563-569.

Delgado, J. A., Morejon, L., Martinez, S., Ginebra, M. P., Carlsson, N., Fernandez, E., Planell, J. A., Clavaguera-Mora, M. T., Rodriguez-Viejo, J., (1999), Zirconia-toughened hydroxyapatite ceramic obtained by wet sintering, *Journal of Materials Science-Materials in Medicine*, **10**, 715-719.

Diaz, A., Lopez, T., Manjarrez, J., Basaldella, E., Martinez-Blanes, J. M., Odriozola, J. A., (2006), Growth of hydroxyapatite in a biocompatible mesoporous ordered silica, *Acta Biomaterialia*, **2**, 173-179.

Doi, Y., Moriwaki, Y., Aoba, T., Okazaki, M., Takahashi, J., Joshin, K., (1982), Carbonate Apatites from Aqueous and Non-Aqueous Media Studied by Electron-Spin-Resonance, Ir, and X-Ray-Diffraction - Effect of Nh4+ Ions on Crystallographic Parameters, *Journal of Dental Research*, **61**, 429-434.

Donadel, K., Laranjeira, M. C. M., Goncalves, V. L., Favere, V. T., de Lima, J. C., Prates, L. H. M., (2005), Hydroxyapatites produced by wet-chemical methods, *Journal of the American Ceramic Society*, **88**, 2230-2235.

Dorozhkin, S. V., Epple, M., (2002), Biological and medical significance of calcium phosphates, *Angewandte Chemie-International Edition*, **41**, 3130-3146.

Ducheyne, P., Qiu, Q., (1999), Bioactive ceramics: the effect of surface reactivity on bone formation and bone cell function, *Biomaterials*, **20**, 2287-2303.

Eberle, J., Schmidmayer, S., Erben, R. G., Stangassinger, M., Roth, H. P., (1999), Skeletal effects of zinc deficiency in growing rats, *Journal of Trace Elements in Medicine and Biology*, **13**, 21-26.

Ellingsen, J. E., Thomsen, P., Lyngstadaas, S. P., (2006), Advances in dental implant materials and tissue regeneration, *Periodontology 2000*, **41**, 136-156.

Elliott, J. C. 1994, *Structure and chemistry of the apatites and the other calcium orthophosphates* Elsevier Science.

Enderle, R., Gotz-Neunhoeffer, F., Gobbels, M., Muller, F. A., Greil, P., (2005), Influence of magnesium doping on the phase transformation temperature of beta-TCP ceramics examined by Rietveld refinement, *Biomaterials*, **26**, 3379-3384.

Ergun, C., Webster, T. J., Bizios, R., Doremus, R. H., (2002), Hydroxylapatite with substituted magnesium, zinc, cadmium, and yttrium. I. Structure and microstructure, *Journal of Biomedical Materials Research*, **59**, 305-311.

Evis, Z., Doremus, R. H., (2007), Effect of ZrF4 on hot-pressed hydroxyapatite/monoclinic zirconia composites, *Scripta Materialia*, **56**, 53-56.

Evis, Z., Sato, M., Webster, T. J., (2006), Increased osteoblast adhesion on nanograined hydroxyapatite and partially stabilized zirconia composites, *Journal of Biomedical Materials Research Part A*, **78A**, 500-507.

Fadeev, I. V., Shvorneva, L. I., Barinov, S. M., Orlovskii, V. P., (2003), Synthesis and structure of magnesium-substituted hydroxyapatite, *Inorganic Materials*, **39**, 947-950.

Fang, Y., Agrawal, D. K., Roy, D. M., Roy, R., (1995), Fabrication of Transparent Hydroxyapatite Ceramics by Ambient-Pressure Sintering, *Materials Letters*, **23**, 147-151.

Fernandes, B. B., Rodrigues, G., Coelho, G. C., Ramos, A. S., (2005), On iron contamination in mechanically alloyed Cr-Si powders, *Materials Science and Engineering A-Structural Materials Properties Microstructure and Processing*, **405**, 135-139.

Ferreira, A., Oliveira, C., Rocha, F., (2003), The different phases in the precipitation of dicalcium phosphate dihydrate, *Journal of Crystal Growth*, **252**, 599-611.

Ferreira, M. E., Pereira, M. D., Costa, F. G. E., Sousa, J. P., de Carvalho, G. S., (2003), Comparative study of metallic biomaterials toxicity: a histochemical and immunohistochemical demonstration in mouse spleen, *Journal of Trace Elements in Medicine and Biology*, **17**, 45-49.

Fidancevska, E., Ruseska, G., Bossert, J., Lin, Y. M., Boccaccini, A. R., (2007), Fabrication and characterization of porous bioceramic composites based on hydroxyapatite and titania, *Materials Chemistry and Physics*, **103**, 95-100.

Fischer, W., Blass, G., (2006), Residual stress mapping in the zirconia electrolyte layer of a high-temperature solid oxide fuel cell, *Zeitschrift fur Kristallographie* 299-304.

Fratzl, P., Gupta, H. S., Paschalis, E. P., Roschger, P., (2004), Structure and mechanical quality of the collagen-mineral nano-composite in bone, *Journal of Materials Chemistry*, **14**, 2115-2123.

Fujii, E., Ohkubo, M., Tsuru, K., Hayakawa, S., Osaka, A., Kawabata, K., Bonhomme, C., Babonneau, F., (2006), Selective protein adsorption property and characterization of nano-crystalline zinc-containing hydroxyapatite, *Acta Biomaterialia*, **2**, 69-74.

Fukushima, Y., (2000), Application of Supercritical Fluids, *R&D Review of Toyota CRDL*, **35**.

Fukushima, Y. Application of Supercritical Fluids. R&D Review of Toyota CRDL 35[1]. 2006.

Gan, L., Pilliar, R., (2004), Calcium phosphate sol-gel-derived thin films on porous-surfaced implants for enhanced osteoconductivity. Part I: Synthesis and characterization, *Biomaterials*, **25**, 5303-5312.

Getman, E., Loboda, S., Ignatov, A., Demchenko, P., (2004), Carbonate-containing barium hydroxyapatite synthesized by solid state reactions, *Polish Journal of Chemistry*, **78**, 35-43.

Ghosh, A., Suri, A. K., Pandey, M., Thomas, S., Mohan, T. R. R., Rao, B. T., (2006), Nanocrystalline zirconia-yttria system - a Raman study, *Materials Letters*, **60**, 1170-1173.

Gibson, I. R., Best, S. M., Bonfield, W., (1999), Chemical characterization of silicon-substituted hydroxyapatite, *Journal of Biomedical Materials Research*, **44**, 422-428.

Gibson, I. R., Best, S. M., Bonfield, W., (2002), Effect of silicon substitution on the sintering and microstructure of hydroxyapatite, *Journal of the American Ceramic Society*, **85**, 2771-2777.

Gibson, I. R., Bonfield, W., (2002a), Novel synthesis and characterization of an AB-type carbonate-substituted hydroxyapatite, *Journal of Biomedical Materials Research*, **59**, 697-708.

Gibson, I. R., Bonfield, W., (2002b), Preparation and characterization of magnesium/carbonate co-substituted hydroxyapatites, *Journal of Materials Science-Materials in Medicine*, **13**, 685-693.

Gibson, I. R., Rehman, I., Best, S. M., Bonfield, W., (2000), Characterization of the transformation from calcium-deficient apatite to beta-tricalcium phosphate, *Journal of Materials Science-Materials in Medicine*, **11**, 533-539.

Gilson, (2001), SC-type Piston Pump Heads User's Guide.

Ginebra, M. P., Driessens, F. C. M., Planell, J. A., (2004), Effect of the particle size on the micro and nanostructural features of a calcium phosphate cement: a kinectic analysis, *Biomaterials*, **25**, 3453-3462.

Gouin, F., Delecrin, J., Passuti, N., Touchais, S., Poirier, P., Bainvel, J. V., (1995), Biphasic Macroporous Calcium-Phosphate Ceramic Bone Substitute for Filling Bone Defects - A Report of 23 Cases, *Revue de Chirurgie Orthopedique et Reparatrice de l Appareil Moteur*, **81**, 59-65.

Grandjean-Laquerrier, A., Laquerriere, P., Jallot, E., Nedelec, J. M., Guenounou, M., Laurent-Maquin, D., Phillips, T. M., (2006), Influence of the zinc concentration of sol-gel derived zinc substituted hydroxyapatite on cytokine production by human monocytes in vitro, *Biomaterials*, **27**, 3195-3200.

Green, D., Walsh, D., Yang, X. B., Mann, S., Oreffo, R. O. C., (2004), Stimulation of human bone marrow stromal cells using growth factor encapsulated calcium carbonate porous microspheres, *Journal of Materials Chemistry*, **14**, 2206-2212.

Gross, K. A., Walsh, W., Swarts, E., (2004), Analysis of retrieved hydroxyapatite-coated hip prostheses, *Journal of Thermal Spray Technology*, **13**, 190-199.

Gu, Y. W., Loh, N. H., Khor, K. A., Tor, S. B., Cheang, P., (2002), Spark plasma sintering of hydroxyapatite powders, *Biomaterials*, **23**, 37-43.

Gunasekaran, S., Anbalagan, G., Pandi, S., (2006), Raman and infrares spectra of carbonates of calcite structure, *Journal of Raman Spectroscopy*, **37**, 892-899.

Guneri, E., Akkurt, M., (2005), Qualitative Analysis of Stone Samples Taken From Some Patients With the Diseases of Urinary System Using X-ray Powder Diffraction Method, *G.U.Journal of Science*, **18**, 321-327.

Guo, H. B., Khor, K. A., Boey, Y. C., Miao, X. G., (2003), Laminated and functionally graded hydroxyapatite/yttria stabilized tetragonal zirconia composites fabricated by spark plasma sintering, *Biomaterials*, **24**, 667-675.

Guo, L. H., Huang, M., Zhang, X. D., (2003), Effects of sintering temperature on structure of hydroxyapatite studied with Rietveld method, *Journal of Materials Science-Materials in Medicine*, **14**, 817-822.

Guo, X. Y., Xiao, P., (2006), Effects of solvents on properties of nanocrystalline hydroxyapatite produced from hydrothermal process, *Journal of the European Ceramic Society*, **26**, 3383-3391.

Guo, X. Y., Xiao, P., Liu, J., Shen, Z. J., (2005), Fabrication of nanostructured hydroxyapatite via hydrothermal synthesis and spark plasma sintering, *Journal of the American Ceramic Society*, **88**, 1026-1029.

Hakuta, Y., Hayashi, H., Arai, K., (2003), Fine particle formation using supercritical fluids, *Current Opinion in Solid State & Materials Science*, **7**, 341-351.

Hakuta, Y., Ohashi, T., Hayashi, H., Arai, K., (2004), Hydrothermal synthesis of zirconia nanocrystals in supercritical water, *Journal of Materials Research*, **19**, 2230-2234.

Hakuta, Y., Ura, H., Hayashi, H., Arai, K., (2005), Effects of hydrothermal synthetic conditions on the particle size of gamma-AlO(OH) in sub and supercritical water using a flow reaction system, *Materials Chemistry and Physics*, **93**, 466-472.

Han, Y., Xu, K. W., Montay, G., Fu, T., Lu, J., (2002), Evaluation of nanostructured carbonated hydroxyapatite coatings formed by a hybrid process of plasma spraying and hydrothermal synthesis, *Journal of Biomedical Materials Research*, **60**, 511-516.

Hayakawa, S., Ando, K., Tsuru, K., Osaka, A., Fujii, E., Kawabata, K., Bonhomme, C., Babonneau, F., (2007), Structural characterization and protein adsorption property of hydroxyapatite particles modified with zinc ions, *Journal of the American Ceramic Society*, **90**, 565-569.

He, P. F., Lu, T. J., Clegg, W. J., (2000), The cracking of zirconia refractory tubes under hot shock, *Journal of Materials Science*, **35**, 2443-2449.

Heimann, R. B., Vu, T. A., (1997), Effect of CaO on thermal decomposition during sintering of composite hydroxyapatite-zirconia mixtures for monolithic bioceramic implants, *Journal of Materials Science Letters*, **16**, 437-439.

Hench, L. L., (1991), Bioceramics - from Concept to Clinic, *Journal of the American Ceramic Society*, **74**, 1487-1510.

Hench, L. L., (1997), Sol-gel materials for bioceramic applications, *Current Opinion in Solid State & Materials Science*, **2**, 604-610.

Hench, L. L., (1998a), Bioceramics, *Journal of the American Ceramic Society*, **81**, 1705-1728.

Hench, L. L., (1998b), Biomaterials: a forecast for the future, *Biomaterials*, **19**, 1419-1423.

Hench, L. L., (2000), The challenge of orthopaedic materials, *Current Orthopaedics*, **14**, 7-15.

Hench, L. L., West, J. K., (1990), The Sol-Gel Process, *Chemical Reviews*, **90**, 33-72.

Hench, L. L. & Wilson, J. 1993, *An Introduction to Bioceramics* World Scientific Publishing, Singapore.

Herschke, L., Rottstegge, J., Lieberwirth, I., Wegner, G., (2006), Zinc phosphate as versatile material for potential biomedical applications Part 1, *Journal of Materials Science-Materials in Medicine*, **17**, 81-94.

Hetzner, D., (2003), Microindentation Hardness Testing of Materials Using ASTM E384, *Microscopy and Microanalysis*, **9**, 708-709.

Hing, K. A., Revell, P. A., Smith, N., Buckland, T., (2006), Effect of silicon level on rate, quality and progression of bone healing within silicate-substituted porous hydroxyapatite scaffolds, *Biomaterials*, **27**, 5014-5026.

J. Huang and Hing, K., (2002), Standard Test Method for the Biaxial Flexural Testing of Bioceramics and Related Materials, Biomaterials Testing Laboratory, Mechanical Testing Facility, IRC in Biomedical Materials, Queen Mary University of London.

Indarto, A., (2008), Hydrogen production from methane in a dielectric barrier discharge using oxide zinc and chromium as catalyst, *Journal of the Chinese Institute of Chemical Engineers*, **39**, 23-28.

Inuzuka, M., Nakamura, S., Kishi, S., Yoshida, K., Hashimoto, K., Toda, Y., Yamashita, K., (2004), Hydroxyapatite-doped zirconia for preparation of biomedical composites ceramics, *Solid State Ionics*, **172**, 509-513.

Ito, A., Kawamura, H., Otsuka, M., Ikeuchi, M., Ohgushi, H., Ishikawa, K., Onuma, K., Kanzaki, N., Sogo, Y., Ichinose, N., (2002), Zinc-releasing calcium phosphate for stimulating bone formation, *Materials Science & Engineering C-Biomimetic and Supramolecular Systems*, **22**, 21-25.

Ito, A., Maekawa, K., Tsutsumi, S., Ikazaki, F., Tateishi, T., (1997), Solubility product of OH-carbonated hydroxyapatite, *Journal of Biomedical Materials Research*, **36**, 522-528.

Ito, A., Ojima, K., Naito, H., Ichinose, N., Tateishi, T., (2000), Preparation, solubility, and cytocompatibility of zinc-releasing calcium phosphate ceramics, *Journal of Biomedical Materials Research*, **50**, 178-183.

Ito, A., Otsuka, M., Kawamura, H., Ikeuchi, M., Ohgushi, H., Sogo, Y., Ichinose, N., (2005), Zinc-containing tricalcium phosphate and related materials for promoting bone formation, *Current Applied Physics*, **5**, 402-406.

Ivanova, T. I., Frank-Kamenetskaya, O. V., Kol'tsov, A. B., Ugolkov, V. L., (2001), Crystal structure of calcium-deficient carbonated hydroxyapatite. Thermal decomposition, *Journal of Solid State Chemistry*, **160**, 340-349.

Jackson, K. D. O., (1998), A Guide to Identifying Common Inorganic Fillers and Activators Using Vibrational Spectroscopy, *Internet Journal of Vibrational Spectroscopy*, **2**.

Jallot, E., Nedelec, J. M., Grimault, A. S., Chassot, E., Grandjean-Laquerriere, A., Laquerriere, P., Laurent-Maquin, D., (2005), STEM and EDXS characterisation of physico-chemical reactions at the periphery of sol-gel derived Zn-substituted hydroxyapatites during interactions with biological fluids, *Colloids and Surfaces B-Biointerfaces*, **42**, 205-210.

Jarudilokkul, S., Tanthapanichakoon, W., Boonamnuayvittaya, V., (2007), Synthesis of hydroxyapatite nanoparticles using an emulsion liquid membrane system, *Colloids and Surfaces A-Physicochemical and Engineering Aspects*, **296**, 149-153.

Johansen, E., (1964), Microstructure of Enamel and Dentin, *Journal of Dental Research*, **43**, 1007-1020.

Jokanovic, V., Izvonar, D., Dramicanin, M. D., Jokanovic, B., Zivojinovic, V., Markovic, D., Dacic, B., (2006), Hydrothermal synthesis and nanostructure of carbonated calcium hydroxyapatite, *Journal of Materials Science-Materials in Medicine*, **17**, 539-546.

Jones, F. H., (2001), Teeth and bones: applications of surface science to dental materials and related biomaterials, *Surface Science Reports*, **42**, 75-205.

Kalita, S. J., Bhatt, H. A., (2007), Nanocrystalline hydroxyapatite doped with magnesium and zinc: Synthesis and characterization, *Materials Science & Engineering C-Biomimetic and Supramolecular Systems*, **27**, 837-848.

Kani, T., Kani, M., Moriwaki, Y., Doi, Y., (1983), Microbeam X-Ray-Diffraction Analysis of Dental Calculus, *Journal of Dental Research*, **62**, 92-95.

Kannan, S., Ferreira, J. M. F., (2006), Synthesis and thermal stability of hydroxyapatite-beta-tricalcium phosphate composites with cosubstituted sodium, magnesium, and fluorine, *Chemistry of Materials*, **18**, 198-203.

Kannan, S., Lemos, I. A. F., Rocha, J. H. G., Ferreira, J. M. F., (2005), Synthesis and characterization of magnesium substituted biphasic mixtures of controlled hydroxyapatite/beta-tricalcium phosphate ratios, *Journal of Solid State Chemistry*, **178**, 3190-3196.

Kannan, S., Rocha, J. H. G., Ferreira, J. M. F., (2006), Synthesis and thermal stability of sodium, magnesium co-substituted hydroxyapatites, *Journal of Materials Chemistry*, **16**, 286-291.

Kanzaki, N., Onuma, K., Treboux, G., Tsutsumi, S., Ito, A., (2000), Inhibitory effect of magnesium and zinc on crystallization kinetics of hydroxyapatite (0001) face, *Journal of Physical Chemistry B*, **104**, 4189-4194.

Kanzaki, N., Onuma, K., Treboux, G., Tsutsumi, S., Ito, A., (2001), Effect of Impurity on Two-Dimensional Nucleation Kinetics: Case Studies of Magnesium and Zinc on Hydroxyapatite (0001) Face, *Journal of Physical Chemistry B*, **105**, 1991-1994.

Kashchiev, D., (1982), On the Relation Between Nucleation Work, Nucleus Size, and Nucleation Rate, *Journal of Chemical Physics*, **76**, 5098-5102.

Kashchiev, D., van Rosmalen, G. M., (2003), Review: Nucleation in solutions revisited, *Crystal Research and Technology*, **38**, 555-574.

Katsumata, S. I., Matsuzaki, H., Tsuboi, R., Uehara, M., Suzuki, K., (2006), Moderate magnesium-restricted diet affects bone formation and bone resorption in rats, *Magnesium Research*, **19**, 12-18.

Katti, K. S., (2004), Biomaterials in total joint replacement, *Colloids and Surfaces B-Biointerfaces*, **39**, 133-142.

Kawamura, H., Ito, A., Miyakawa, S., Layrolle, P., Ojima, K., Ichinose, N., Tateishi, T., (2000), Stimulatory effect of zinc-releasing calcium phosphate implant on bone formation in rabbit femora, *Journal of Biomedical Materials Research*, **50**, 184-190.

Kaya, C., He, J. Y., Gu, X., Butler, E. G., (2002), Nanostructured ceramic powders by hydrothermal synthesis and their applications, *Microporous and Mesoporous Materials*, **54**, 37-49.

Kellici, S. 2006, *Ph.D. Thesis,* Department of Materials, Queen Mary University of London.

Kelly, J. R., Denry, I., (2008), Stabilized zirconia as a structural ceramic: An overview, *Dental Materials*, **24**, 289-298.

Khalil, K. A., Kim, H. Y., Kim, S. W., Kim, K. W., (2007), Observation of toughness improvement of the hydroxyapatite bioceramics densified using high-frequency induction heat sintering, *International Journal of Applied Ceramic Technology*, **4**, 30-37.

Kim, H. W., Koh, Y. H., Seo, S. B., Kim, H. E., (2003a), Properties of fluoridated hydroxyapatite-alumina biological composites densified with addition of CaF_2, *Materials Science & Engineering C-Biomimetic and Supramolecular Systems*, **23**, 515-521.

Kim, H. W., Koh, Y. H., Yoon, B. H., Kim, H. E., (2002a), Reaction sintering and mechanical properties of hydroxyapatite-zirconia composites with calcium fluoride additions, *Journal of the American Ceramic Society*, **85**, 1634-1636.

Kim, H. W., Kong, Y. M., Koh, Y. H., Kim, H. E., Kim, H. M., Ko, J. S., (2003b), Pressureless sintering and mechanical and biological properties of fluor-hydroxyapatite composites with zirconia, *Journal of the American Ceramic Society*, **86**, 2019-2026.

Kim, H. W., Noh, Y. J., Koh, Y. H., Kim, H. E., Kim, H. M., (2002b), Effect of CaF2 on densification and properties of hydroxyapatite-zirconia composites for biomedical applications, *Biomaterials*, **23**, 4113-4121.

Kim, S., Ryu, H. S., Shin, H., Jung, H. S., Hong, K. S., (2005), In situ observation of hydroxyapatite nanocrystal formation from amorphous calcium phosphate in calcium-rich solutions, *Materials Chemistry and Physics*, **91**, 500-506.

Kim, S. R., Lee, J. H., Kim, Y. T., Riu, D. H., Jung, S. J., Lee, Y. J., Chung, S. C., Kim, Y. H., (2003c), Synthesis of Si, Mg substituted hydroxyapatites and their sintering behaviors, *Biomaterials*, **24**, 1389-1398.

Knowles, J. C., Talal, S., Santos, J. D., (1996), Sintering effects in a glass reinforced hydroxyapatite, *Biomaterials*, **17**, 1437-1442.

Kobayashi, S., Kawai, W., Wakayama, S., (2006), The effect of pressure during sintering on the strength and the fracture toughness of hydroxyapatite ceramics, *Journal of Materials Science-Materials in Medicine*, **17**, 1089-1093.

Kobayashi, T., Shingaki, S., Nakajima, T., Hanada, K., (1993), Chin Augmentation with Porous Hydroxyapatite Blocks, *Journal of Long-Term Effects of Medical Implants*, **3**, 283-294.

Kokubo, T., Ito, S., Sakka, S., Yamamuro, T., (1986), Formation of A High-Strength Bioactive Glass Ceramic in the System Mgo-CaO-SiO_2-P_2O_5, *Journal of Materials Science*, **21**, 536-540.

Kong, Y. M., Bae, C. J., Lee, S. H., Kim, H. W., Kim, H. E., (2005), Improvement in biocompatibility of ZrO_2-Al_2O_3 nano-composite by addition of HA, *Biomaterials*, **26**, 509-517.

Kothapalli, C., Wei, M., Vasiliev, A., Shaw, M. T., (2004), Influence of temperature and concentration on the sintering behavior and mechanical properties of hydroxyapatite, *Acta Materialia*, **52**, 5655-5663.

Kothapalli, C. R., Wei, M., Legeros, R. Z., Shaw, M. T., (2005), Influence of temperature and aging time on HA synthesized by the hydrothermal method, *Journal of Materials Science-Materials in Medicine*, **16**, 441-446.

Koumoulidis, G. C., Katsoulidis, A. P., Ladavos, A. K., Pomonis, P. J., Trapalis, C. C., Sdoukos, A. T., Vaimakis, T. C., (2003), Preparation of hydroxyapatite via microemulsion route, *Journal of Colloid and Interface Science*, **259**, 254-260.

Koutsopoulos, S., (2002), Synthesis and characterization of hydroxyapatite crystals: A review study on the analytical methods, *Journal of Biomedical Materials Research*, **62**, 600-612.

Krajewski, A., Mazzocchi, M., Buldini, P. L., Ravaglioli, A., Tinti, A., Taddei, P., Fagnano, C., (2005), Synthesis of carbonated hydroxyapatites: efficiency of the substitution and critical evaluation of analytical methods, *Journal of Molecular Structure*, **744**, 221-228.

Kuhl, G., Nebergall, W. H., (1963), Hydrogenphosphat- und Carbonatapatite, *Zeitschrift für anorganische und allgemeine Chemie*, **324**, 313-320.

Kumar, R., Cheang, P., Khor, K. A., (2003), Spark plasma sintering and in vitro study of ultra-fine HA and ZrO2-HA powders, *Journal of Materials Processing Technology*, **140**, 420-425.

Kumar, R., Prakash, K. H., Cheang, P., Khor, K. A., (2005), Microstructure and mechanical properties of spark plasma sintered zirconia-hydroxyapatite nano-composite powders, *Acta Materialia*, **53**, 2327-2335.

Kumta, P. N., Sfeir, C., Lee, D. H., Olton, D., Choi, D., (2005), Nanostructured calcium phosphates for biomedical applications: novel synthesis and characterization, *Acta Biomaterialia*, **1**, 65-83.

Kurzweg, H., Heimann, R. B., Troczynski, T., Wayman, M. L., (1998), Development of plasma-sprayed bioceramic coatings with bond coats based on titania and zirconia, *Biomaterials*, **19**, 1507-1511.

Lagier, R., Baud, C. A., (2003), Magnesium whitlockite, a calcium phosphate crystal of special interest in pathology, *Pathology Research and Practice*, **199**, 329-335.

Landi, E., Celotti, G., Logroscino, G., Tampieri, A., (2003), Carbonated hydroxyapatite as bone substitute, *Journal of the European Ceramic Society*, **23**, 2931-2937.

Laquerriere, P., Grandjean-Laquerriere, A., Guenounou, M., Laurent-Maquin, D., Frayssinet, P., Nardin, M., (2003), Correlation between sintering temperature of hydroxyapatite particles and the production of inflammatory cytokines by human monocytes, *Colloids and Surfaces B-Biointerfaces*, **30**, 207-213.

Lazic, S., (1995), Microcrystalline Hydroxyapatite Formation from Alkaline-Solutions, *Journal of Crystal Growth*, **147**, 147-154.

LeGeros, R. Z. 1991, *Calcium Phosphates in Oral Biology and Medicine* Karger AG, Basel, Switzerland.

LeGeros, R. Z., (2001), Formation and Transformation of Calcium Phosphates: Relevance to Vascular Calcification, *Zeitschrift für Kardiologie*, **90**, 116-124.

LeGeros, R. Z., (2002), Properties of osteoconductive biomaterials: Calcium phosphates, *Clinical Orthopaedics and Related Research* 81-98.

LeGeros, R. Z., Bleiwas, C. B., Retino, M., Rohanizadeh, R., LeGeros, J. P., (1999), Zinc effect on the in vitro formation of calcium phosphates: Relevance to clinical inhibition of calculus formation, *American Journal of Dentistry*, **12**, 65-71.

LeGeros, R. Z., Gatti, A. M., Kijkowska, R., Mijares, D. Q., & LeGeros, J. P. 2004, Mg-substituted tricalcium phosphates: Formation and properties, Key Engineering Materials, **254**, 127-130.

Legeros, R.Z., Mijares, D., Gatti, A.M., Legeros, J.P., (2004), Mg-substituted tricalcium phosphates and biphasic calcium phosphates: Formation and properties, Transactions - 7th World Biomaterials Congress, Biomaterials 2004 Congress Managers, Sydney, NSW 2001, Australia 1448.

Lei, M., Li, P. G., Sun, Z. B., Tang, W. H., (2006), Effects of organic additives on the morphology of calcium carbonate particles in the presence of CTAB, *Materials Letters*, **60**, 1261-1264.

Lester, E., Blood, P., Denyer, J., Giddings, D., Azzopardi, B., Poliakoff, M., (2006), Reaction engineering: The supercritical water hydrothermal synthesis of nano-particles, *Journal of Supercritical Fluids*, **37**, 209-214.

Leventouri, T., (2006), Synthetic and biological hydroxyapatites: Crystal structure questions, *Biomaterials*, **27**, 3339-3342.

Leventouri, T., Bunaciu, C. E., Perdikatsis, V., (2003), Neutron powder diffraction studies of silicon-substituted hydroxyapatite, *Biomaterials*, **24**, 4205-4211.

Li, B., Aspden, R. M., (1998), Comparison of the stiffness, density and composition of bone from the calcar femorale and the femoral cortex, *Journal of Materials Science: Materials in Medicine*, **9**, 661-666.

Li, H., Zhu, M. Y., Li, L. H., Zhou, C. R., (2008), Processing of nanocrystalline hydroxyapatite particles via reverse microemulsions, *Journal of Materials Science*, **43**, 384-389.

Li, J., Liao, H., Hermansson, L., (1996), Sintering of partially-stabilized zirconia and partially-stabilized zirconia-hydroxyapatite composites by hot isostatic pressing and pressureless sintering, *Biomaterials*, **17**, 1787-1790.

Li, J. L., Wang, L. J., He, T., Jiang, W., (2007a), Surface graphitization and mechanical properties of hot-pressed bulk carbon nanotubes compacted by spark plasma sintering, *Carbon*, **45**, 2636-2642.

Li, M., Xiao, X., Liu, R., Chen, C., Huang, L., (2007b), Structural characterization of zinc-substituted hydroxyapatite prepared by hydrothermal method, *Journal of Materials Science: Materials in Medicine*.

Liau, L. C. K., Lin, C. C., (2008), Semiconductor characterization of Cr3+-doped titania electrodes with p-n homojunction devices, *Thin Solid Films*, **516**, 1998-2002.

Lim, G. K., Wang, J., Ng, S. C., Chew, C. H., Gan, L. M., (1997), Processing of hydroxyapatite via microemulsion and emulsion routes, *Biomaterials*, **18**, 1433-1439.

Lim, G. K., Wang, J., Ng, S. C., Gan, L. M., (1999), Formation of nanocrystalline hydroxyapatite in nonionic surfactant emulsions, *Langmuir*, **15**, 7472-7477.

Liu, D. M., Troczynski, T., Tseng, W. J., (2001), Water-based sol-gel synthesis of hydroxyapatite: process development, *Biomaterials*, **22**, 1721-1730.

Liu, H. S., Chin, T. S., Lai, L. S., Chiu, S. Y., Chung, K. H., Chang, C. S., Lui, M. T., (1997), Hydroxyapatite synthesized by a simplified hydrothermal method, *Ceramics International*, **23**, 19-25.

Liu, J. B., Ye, X. Y., Wang, H., Zhu, M. K., Wang, B., Yan, H., (2003a), The influence of pH and temperature on the morphology of hydroxyapatite synthesized by hydrothermal method, *Ceramics International*, **29**, 629-633.

Liu, J. B., Ye, X. Y., Wang, H., Zhu, M. K., Wang, B., Yan, H., (2003b), The influence of pH and temperature on the morphology of hydroxyapatite synthesized by hydrothermal method, *Ceramics International*, **29**, 629-633.

Lopez, T., Ortiz, E., Quintana, P., Gonzalez, R. D., (2007), A nanostructured titania bioceramic implantable device capable of drug delivery to the temporal lobe of the brain, *Colloids and Surfaces A-Physicochemical and Engineering Aspects*, **300**, 3-10.

Lopez-Macipe, A., Rodriguez-Clemente, R., Hidalgo-Lopez, A., Arita, I., Garcia-Garduno, M. V., Rivera, E., Castano, V. M., (1998), Wet chemical synthesis of hydroxyapatite particles from nonstoichiometric solutions, *Journal of Materials Synthesis and Processing*, **6**, 21-26.

Manicone, P. F., Iommetti, P. R., Raffaelli, L., (2007), An overview of zirconia ceramics: Basic properties and clinical applications, *Journal of Dentistry*, **35**, 819-826.

Mansur, C., Pope, M., Pascucci, M. R., Shivkumar, S., (1998), Zirconia-calcium phosphate composites for bone replacement, *Ceramics International*, **24**, 77-79.

Marple, B. R., Lima, R. S., Li, H., & Khor, K. A. 2006, *Biomimetic ceramic surfaces produced by thermal spraying nanostructured titania: A coating alternative to hydroxyapatite on orthopedic implants?*

Marti, A., (2000), Inert bioceramics (Al2O3, ZrO2) for medical application, *Injury-International Journal of the Care of the Injured*, **31**, S33-S36.

Martin, R. I., Brown, P. W., (1997), Phase equilibria among acid calcium phosphates, *Journal of the American Ceramic Society*, **80**, 1263-1266.

Mathew, M., Takagi, S., (2001), Structures of biological minerals in dental research, *Journal of Research of the National Institute of Standards and Technology*, **106**, 1035-1044.

Matsumoto, T., Okazaki, M., Inoue, M., Ode, S., Chang-Chien, C., Nakao, H., Hamada, Y., Takahashi, J., (2002), Biodegradation of carbonate apatite/collagen composite membrane and its controlled release of carbonate apatite, *Journal of Biomedical Materials Research*, **60**, 651-656.

Matsuno, T., Morita, M., Watanabe, K., Ono, K., Koishi, M., (2003), Strength of bond to bone and cytotoxicity of sintered bodies of hydroxyapatite/zirconia composite particles, *Journal of Materials Science-Materials in Medicine*, **14**, 547-555.

Matsuno, T., Watanabe, K., Ono, K., Koishi, M., (2000), Microstructure and mechanical properties of sintered body of zirconia coated hydroxyapatite particles, *Journal of Materials Science Letters*, **19**, 573-576.

Mayer, I., Schlam, R., Featherstone, J. D. B., (1997), Magnesium-containing carbonate apatites, *Journal of Inorganic Biochemistry*, **66**, 1-6.

Mcherzynska, B., Matsuura, K., (2008), Spark plasma sintering of W-C binary hard alloys, *Multiscale and Functionally Graded Materials*, **973**, 895-900.

Miao, S. D., Weng, W. J., Cheng, K., Song, C. L., Du, P. Y., Zhao, G. L., Shen, G., Wang, J. X., Han, G. R., (2006), A low temperature co-precipitation preparation of nano-sized zinc containing beta-tricalcium phosphate powders, *Bioceramics 18, Pts 1 and 2*, **309-311**, 565-568.

Miao, X. G., Chen, Y. M., Guo, H. B., Khor, K. A., (2004), Spark plasma sintered hydroxyapatite-yttria stabilized zirconia composites, *Ceramics International*, **30**, 1793-1796.

Millot, N., Xin, B., Pighini, C., Aymes, D., (2005), Hydrothermal synthesis of nanostructured inorganic powders by a continuous process under supercritical conditions, *Journal of the European Ceramic Society*, **25**, 2013-2016.

Miyaji, F., Kono, Y., Suyama, Y., (2005), Formation and structure of zinc-substituted calcium hydroxyapatite, *Materials Research Bulletin*, **40**, 209-220.

Mizutani, Y., Hattori, M., Okuyama, M., Kasuga, T., Nogami, M., (2005), Carbonate-containing hydroxyapatite derived from calcium tripolyphosphate gel with urea, *Journal of Materials Science-Materials in Medicine*, **16**, 709-712.

Morgan, H., Wilson, R. M., Elliott, J. C., Dowker, S. E. P., Anderson, P., (2000), Preparation and characterisation of monoclinic hydroxyapatite and its precipitated carbonate apatite intermediate, *Biomaterials*, **21**, 617-627.

Mostafa, N. Y., (2005), Characterization, thermal stability and sintering of hydroxyapatite powders prepared by different routes, *Materials Chemistry and Physics*, **94**, 333-341.

Munir, Z. A., Anselmi-Tamburini, U., Ohyanagi, M., (2006), The effect of electric field and pressure on the synthesis and consolidation of materials: A review of the spark plasma sintering method, *Journal of Materials Science*, **41**, 763-777.

Murugan, R., Ramakrishna, S., (2006), Production of ultra-fine bioresorbable carbonated hydroxyapatite, *Acta Biomaterialia*, **2**, 201-206.

Nayar, S., Sinha, M. K., Basu, D., Sinha, A., (2006), Synthesis and sintering of biomimetic hydroxyapatite nanoparticles for biomedical applications, *Journal of Materials Science-Materials in Medicine*, **17**, 1063-1068.

Nelson, D. G. A., Featherstone, J. D. B., (1982), Preparation, Analysis, and Characterization of Carbonated Apatites, *Calcified Tissue International*, **34**, S69-S81.

Ng, H. B., Shearwood, C., White, T. J., Yu, L. G., Khor, K. A., (2008), Spark plasma sintering of silver nanopowder, *Biomems and Nanotechnology Iii*, **6799**, U75-U83.

Nicholson, J. W., (1998), Adhesive dental materials--A review, *International Journal of Adhesion and Adhesives*, **18**, 229-236.

Niederberger, M., (2007), Nonaqueous sol-gel routes to metal oxide nanoparticles, *Accounts of Chemical Research*, **40**, 793-800.

Nishino, M., Yamashita, S., Aoba, T., Okazaki, M., Moriwaki, Y., (1981), The laser-Raman spectroscopic studies on human enamel and precipitated carbonate-containing apatites, *Journal of Dental Research*, **60**, 751-755.

Noyori, R., (1999), Supercritical fluids: Introduction, *Chemical Reviews*, **99**, 353-354.

Okada, K., Temuujin, J., Kameshima, Y., MacKenzie, K. J. D., (2003), Simultaneous uptake of ammonium and phosphate ions by composites of gamma-alumina/potassium aluminosilicate gel, *Materials Research Bulletin*, **38**, 749-756.

Oktar, F. N., Meydanoglu, O., Goller, G., Agathopoulos, S., Rocha, G., Ozyegin, S., Eruslu, N., Peker, I., & Kayali, S. 2006, *Sintering effects on mechanical properties of hydroxyapatite-titanium dioxide (HA-TiO2) composites.*

Omori, M., Onoki, T., Hashida, T., Okubo, A., Murakami, Y., (2006), Low temperature synthesis of hydroxyapatite from CaHPO4 center dot 2H(2)O and Ca(OH)(2) based on effect of the spark plasma system (SPS), *Ceramics International*, **32**, 617-621.

Pan, Y., Huang, J. L., Shao, C. Y., (2003), Preparation of beta-TCP with high thermal stability by solid reaction route, *Journal of Materials Science*, **38**, 1049-1056.

Pang, Y. X., Bao, X., (2003), Influence of temperature, ripening time and calcination on the morphology and crystallinity of hydroxyapatite nanoparticles, *Journal of the European Ceramic Society*, **23**, 1697-1704.

Patel, N., Best, S. M., Bonfield, W., Gibson, I. R., Hing, K. A., Damien, E., Revell, P. A., (2002), A comparative study on the in vivo behavior of hydroxyapatite and silicon substituted hydroxyapatite granules, *Journal of Materials Science-Materials in Medicine*, **13**, 1199-1206.

Penel, G., Leroy, G., Rey, C., Bres, E., (1998), MicroRaman spectral study of the PO4 and CO3 vibrational modes in synthetic and biological apatites, *Calcified Tissue International*, **63**, 475-481.

Penel, G., Leroy, G., Rey, C., Sombret, B., Huvenne, J. P., Bres, E., (1997), Infrared and Raman microspectrometry study of fluor-fluor-hydroxy and hydroxy-apatite powders, *Journal of Materials Science-Materials in Medicine*, **8**, 271-276.

Phillips, M. J., Darr, J. A., Luklinska, Z. B., Rehman, I., (2003), Synthesis and characterization of nano-biomaterials with potential osteological applications, *Journal of Materials Science-Materials in Medicine*, **14**, 875-882.

Piekarsk, K., (1973), Analysis of Bone As A Composite-Material, *International Journal of Engineering Science*, **11**, 557.

Porter, A., Patel, N., Brooks, R., Best, S., Rushton, N., Bonfield, W., (2005), Effect of carbonate substitution on the ultrastructural characteristics of hydroxyapatite implants, *Journal of Materials Science-Materials in Medicine*, **16**, 899-907.

Porter, A. E., Best, S. M., Bonfield, W., (2004), Ultrastructural comparison of hydroxyapatite and silicon-substituted hydroxyapatite for biomedical applications, *Journal of Biomedical Materials Research Part A*, **68A**, 133-141.

Porter, A. E., Patel, N., Skepper, J. N., Best, S. M., Bonfield, W., (2003), Comparison of in vivo dissolution processes in hydroxyapatite and silicon-substituted hydroxyapatite bioceramics, *Biomaterials*, **24**, 4609-4620.

Porter, A. E., (2006), Nanoscale characterization of the interface between bone and hydroxyapatite implants and the effect of silicon on bone apposition, *Micron*, **37**, 681-688.

Pramanik, S., Agarwal, A. K., Rai, K. N., Garg, A., (2007), Development of high strength hydroxyapatite by solid-state-sintering process, *Ceramics International*, **33**, 419-426.

Putlayev, V., Veresov, A., Pulkin, M., Soin, A., Kuznetsov, V., (2006), Silicon-substituted hydroxyapatite ceramics (Si-HAp): densification and grain growth through the prism of sintering theories, *Materialwissenschaft und Werkstofftechnik*, **37**, 416-421.

Rajabi, A. H., Behnamghader, A., Kazemadeh, A., Moztarzadeh, F., (2007), Synthesis and characterization of nanocrystalline hydroxyapatite powder via sol-gel method, *3Rd Kuala Lumpur International Conference on Biomedical Engineering 2006*, **15**, 149-151.

Ramay, H. R., Zhang, M. Q., (2003), Preparation of porous hydroxyapatite scaffolds by combination of the gel-casting and polymer sponge methods, *Biomaterials*, **24**, 3293-3302.

Ran, S. L., Gao, L., (2008), Spark plasma sintering of nanocrystalline niobium nitride powders, *Journal of the American Ceramic Society*, **91**, 599-602.

Rao, R. R., Kannan, T. S., (2002), Synthesis and sintering of hydroxyapatite-zirconia composites, *Materials Science & Engineering C-Biomimetic and Supramolecular Systems*, **20**, 187-193.

Rapacz-Kmita, A., Slosarczyk, A., Paszkiewicz, Z., Paluszkiewicz, C., (2004), Phase stability of hydroxyapatite-zirconia (HAp-ZrO2) composites for bone replacement, *Journal of Molecular Structure*, **704**, 333-340.

Ratner, B. D., Hoffman, A. S., Schoen, F. J., & Lemons, J. E. 2004, *Biomaterials Science: An Introduction to Materials in Medicine*, 2nd edn, Elsevier Academic Press.

Redey, S. A., Razzouk, S., Rey, C., Bernache-Assollant, D., Leroy, G., Nardin, M., Cournot, G., (1999), Osteoclast adhesion and activity synthetic hydroxyapatite, carbonated hydroxyapatite, and natural calcium carbonate: Relationship to surface energies, *Journal of Biomedical Materials Research*, **45**, 140-147.

Rehman, I., Bonfield, W., (1997), Characterization of hydroxyapatite and carbonated apatite by photo acoustic FTIR spectroscopy, *Journal of Materials Science-Materials in Medicine*, **8**, 1-4.

Rehman, I., Karsh, M., Hench, L. L., Bonfield, W., (2000), Analysis of apatite layers on glass-ceramic particulate using FTIR and FT-Raman spectroscopy, *Journal of Biomedical Materials Research*, **50**, 97-100.

Reid, J. W., Pietak, A., Sayer, M., Dunfield, D., Smith, T. J. N., (2005), Phase formation and evolution in the silicon substituted tricalcium phosphate/apatite system, *Biomaterials*, **26**, 2887-2897.

Revell, P. A., Damien, E., Zhang, X. S., Evans, P., & Howlett, C. R. 2004, *The effect of magnesium ions on bone bonding to hydroxyapatite coating on titanium alloy implants.*

Rhee, S. H., (2002a), Synthesis of hydroxyapatite via mechanochemical treatment, *Biomaterials*, **23**, 1147-1152.

Rhee, S. H., (2002b), Synthesis of hydroxyapatite via mechanochemical treatment, *Biomaterials*, **23**, 1147-1152.

Rho, J. Y., Kuhn-Spearing, L., Zioupos, P., (1998), Mechanical properties and the hierarchical structure of bone, *Medical Engineering & Physics*, **20**, 92-102.

Riman, R. E., Suchanek, W. L., Byrappa, K., Chen, C. W., Shuk, P., Oakes, C. S., (2002), Solution synthesis of hydroxyapatite designer particulates, *Solid State Ionics*, **151**, 393-402.

Roeder, R. K., Sproul, M. M., Turner, C. H., (2003), Hydroxyapatite whiskers provide improved mechanical properties in reinforced polymer composites, *Journal of Biomedical Materials Research Part A*, **67A**, 801-812.

Rowles, S. L., (1968), The precipitation of Whitlockite from Aqueous Solutions, *Bulletin de la Société Chimique de France* 1797-1802.

Rubin, M. A., Jasiuk, L., Taylor, J., Rubin, J., Ganey, T., Apkarian, R. P., (2003), TEM analysis of the nanostructure of normal and osteoporotic human trabecular bone, *Bone*, **33**, 270-282.

Saeri, M. R., Afshar, A., Ghorbani, M., Ehsani, N., Sorrell, C. C., (2003), The wet precipitation process of hydroxyapatite, *Materials Letters*, **57**, 4064-4069.

Saha, H., Basu, S., Bhattacharyya, P., Basu, P. K., (2007), MEMS based nano crystalline zinc oxide methane gas sensors, *Proceedings of the 2007 International Workshop on the Physics of Semiconductor Devices: Iwpsd-2007* 645-651.

Sarig, S., (2004), Aspartic acid nucleates the apatite crystallites of bone: a hypothesis, *Bone*, **35**, 108-113.

Sato, T., Sue, K., Suzuki, W., Suzuki, M., Matsui, K., Hakuta, Y., Hayashi, H., Arai, K., Kawasaki, S. I., Kawai-Nakamura, A., Hiaki, T., (2008), Rapid and continuous production of ferrite nanoparticles by hydrothermal synthesis at 673 K and 30 MPa, *Industrial & Engineering Chemistry Research*, **47**, 1855-1860.

Schroeder, L. W., Dickens, B., Brown, W. E., (1977), Crystallographic Studies of the Role of Mg as Stabilizing Impurity in beta-Ca3(PO4)2, *Journal of Solid State Chemistry*, **22**, 253-262.

Segal, D., (1997), Chemical synthesis of ceramic materials, *Journal of Materials Chemistry*, **7**, 1297-1305.

Serpone, N., Dondi, D., Albini, A., (2007), Inorganic and organic UV filters: Their role and efficacy in sunscreens and suncare products, *Inorganica Chimica Acta*, **360**, 794-802.

Serre, C. M., Papillard, M., Chavassieux, P., Voegel, J. C., Boivin, G., (1998), Influence of magnesium substitution on a collagen-apatite biomaterial on the production of a calcifying matrix by human osteoblasts, *Journal of Biomedical Materials Research*, **42**, 626-633.

Shen, Z. J., Adolfsson, E., Nygren, M., Gao, L., Kawaoka, H., Niihara, K., (2001), Dense hydroxyapatite-zirconia ceramic composites with high strength for biological applications, *Advanced Materials*, **13**, 214-216.

Shi, S. F., Cao, M. H., Fle, X. Y., Xie, H. M., (2007), Surfactant-assisted hydrothermal growth of single-crystalline ultrahigh-aspect-ratio vanadium oxide nanobelts, *Crystal Growth & Design*, **7**, 1893-1897.

Shi, S. L., Pan, W., Fang, M. H., Fang, Z. Y., (2006), Reinforcement of hydroxyapatite bioceramic by addition of Ti3SiC2, *Journal of the American Ceramic Society*, **89**, 743-745.

Siddharthan, A., Seshadri, S. K., Kumar, T. S. S., (2004), Microwave accelerated synthesis of nanosized calcium deficient hydroxyapatite, *Journal of Materials Science-Materials in Medicine*, **15**, 1279-1284.

Silva, C. C., Pinheiro, A. G., Miranda, M. A. R., Goes, J. C., Sombra, A. S. B., (2003), Structural properties of hydroxyapatite obtained by mechanosynthesis, *Solid State Sciences*, **5**, 553-558.

Silva, V. V., Domingues, R. Z., (1997), Hydroxyapatite-zirconia composites prepared by precipitation method, *Journal of Materials Science-Materials in Medicine*, **8**, 907-910.

Silva, V. V., Lameiras, F. S., (2000), Synthesis and characterization of composite powders of partially stabilized zirconia and hydroxyapatite, *Materials Characterization*, **45**, 51-59.

Silva, V. V., Lameiras, F. S., Domingues, R. Z., (2001a), Microstructural and mechanical study of zirconia-hydroxyapatite (ZH) composite ceramics for biomedical applications, *Composites Science and Technology*, **61**, 301-310.

Silva, V. V., Lameiras, F. S., Domingues, R. Z., (2001b), Synthesis and characterization of calcia partially stabilized zirconia-hydroxyapatite powders prepared by co-precipitation method, *Ceramics International*, **27**, 615-620.

Silva, V. V., Lameiras, F. S., Lobato, Z. I. P., (2002), Biological reactivity of zirconia-hydroxyapatite composites, *Journal of Biomedical Materials Research*, **63**, 583-590.

Siu, G. G., Stokes, M. J., Liu, Y. L., (1999), Variation of fundamental and higher-order Raman spectra of ZrO2 nanograins with annealing temperature, *Physical Review B*, **59**, 3173-3179.

Sivakumar, G. R., Girija, E. K., Kalkura, S. N., Subramanian, C., (1998), Crystallization and characterization of calcium phosphates: Brushite and monetite, *Crystal Research and Technology*, **33**, 197-205.

Slosarczyk, A., Paluszkiewicz, C., Gawlicki, M., Paszkiewicz, Z., (1997), The FTIR spectroscopy and QXRD studies of calcium phosphate based materials produced from the powder precursors with different Ca/P ratios, *Ceramics International*, **23**, 297-304.

Sogo, Y., Ito, A., Fukasawa, K., Sakurai, T., Ichinose, N., (2004), Zinc containing hydroxyapatite ceramics to promote osteoblastic cell activity, *Materials Science and Technology*, **20**, 1079-1083.

Staiger, M. P., Pietak, A. M., Huadmai, J., Dias, G., (2006), Magnesium and its alloys as orthopedic biomaterials: A review, *Biomaterials*, **27**, 1728-1734.

Storck, C., Brockmann, M., Schnellmann, E., Stoeckli, S. J., Schmid, S., (2007), Functional outcome of vocal fold medialization thyroplasty with a hydroxyapatite implant, *Laryngoscope*, **117**, 1118-1122.

Storrie, H., Stupp, S. I., (2005), Cellular response to zinc-containing organoapatite: An in vitro study of proliferation, alkaline phosphatase activity and biomineralization, *Biomaterials*, **26**, 5492-5499.

Stubican, V. S., Ray, S. P., (1977), Phase-Equilibria and Ordering in System Zro2-Cao, *Journal of the American Ceramic Society*, **60**, 534-537.

Suchanek, W. L., Byrappa, K., Shuk, P., Riman, R. E., Janas, V. F., TenHuisen, K. S., (2004a), Mechanochemical-hydrothermal synthesis of calcium phosphate powders with coupled magnesium and carbonate substitution, *Journal of Solid State Chemistry*, **177**, 793-799.

Suchanek, W. L., Byrappa, K., Shuk, P., Riman, R. E., Janas, V. F., TenHuisen, K. S., (2004b), Preparation of magnesium-substituted hydroxyapatite powders by the mechanochemical-hydrothermal method, *Biomaterials*, **25**, 4647-4657.

Sudarsanan, K., Young, R. A., (1982), Significant Precision in Crystal Structural Details: Holly Springs Hydroxyapatite, *Acta Crystallographica B*, **24**, 38.

Sue, K., Kakinuma, N., Adschiri, T., Arai, K., (2004a), Continuous production of nickel fine particles by hydrogen reduction in near-critical water, *Industrial & Engineering Chemistry Research*, **43**, 2073-2078.

Sue, K., Kimura, K., Arai, K., (2004), Hydrothermal synthesis of ZnO nanocrystals using microreactor, *Materials Letters*, **58**, 3229-3231.

Sue, K., Kimura, K., Murata, K., Arai, K., (2004b), Effect of cations and anions on properties of zinc oxide particles synthesized in supercritical water, *Journal of Supercritical Fluids*, **30**, 325-331.

Sue, K. W., Kimura, K., Yamamoto, M., Arai, K., (2004c), Rapid hydrothermal synthesis of ZnO nanorods without organics, *Materials Letters*, **58**, 3350-3352.

Sun, G. B., Cao, M. H., Wang, Y. H., Hu, C. W., Liu, Y. C., Ren, L., Pu, Z. F., (2006), Anionic surfactant-assisted hydrothermal synthesis of high-aspect-ratio ZnO nanowires and their photoluminescence property, *Materials Letters*, **60**, 2777-2782.

Sun, L., Jia, C. C., Lin, C. G., Cao, R. J., (2007a), VC addition prepared ultrarine WC-11Co composites by spark plasma sintering, *Journal of Iron and Steel Research International*, **14**, 85-89.

Sun, L., Lin, C., Jia, C., Jia, X., Xian, M., (2008), Change in relative density of WC-Co cemented carbides in spark plasma sintering process, *Rare Metals*, **27**, 74-77.

Sun, Y. X., Guo, G. S., Tao, D. L., Wang, Z. H., (2007b), Reverse microemulsion-directed synthesis of hydroxyapatite nanoparticles under hydrothermal conditions, *Journal of Physics and Chemistry of Solids*, **68**, 373-377.

Sung, Y. M., Kim, D. H., (2003), Crystallization characteristics of yttria-stabilized zirconia/hydroxyapatite composite nanopowder, *Journal of Crystal Growth*, **254**, 411-417.

Sung, Y. M., Shin, Y. K., Ryu, J. J., (2007), Preparation of hydroxyapatite/zirconia bioceramic nanocomposites for orthopaedic and dental prosthesis applications, *Nanotechnology*, **18**.

Sunkara, B. K., Misra, R. D. K., (2008), Enhanced antibactericidal function of W4+-doped titania-coated nickel ferrite composite nanoparticles: A biomaterial system, *Acta Biomaterialia*, **4**, 273-283.

Suzuki, T., Fujibayashi, S., Nakagawa, Y., Noda, I., Nakamura, T., (2006), Ability of zirconia double coated with titanium and hydroxyapatite to bond to bone under load-bearing conditions, *Biomaterials*, **27**, 996-1002.

Swagelok Company, (2007a), Check Valves.

Swagelok Company, (2007b), Proportinal Relief Valves.

Takami, S., Sato, T., Mousavand, T., Ohara, S., Umetsu, M., Adschiri, T., (2007), Hydrothermal synthesis of surface-modified iron oxide nanoparticles, *Materials Letters*, **61**, 4769-4772.

Takemoto, S., Kusudo, Y., Tsuru, K., Hayakawa, S., Osaka, A., Takashima, S., (2004), Selective protein adsorption and blood compatibility of hydroxy-carbonate apatites, *Journal of Biomedical Materials Research Part A*, **69A**, 544-551.

Tamm, T., Peld, M., (2006), Computational study of cation substitutions in apatites, *Journal of Solid State Chemistry*, **179**, 1581-1587.

Tampieri, A., Celotti, G., Landi, E., (2005), From biomimetic apatites to biologically inspired composites, *Analytical and Bioanalytical Chemistry*, **381**, 568-576.

Tampieri, A., Celotti, G., Landi, E., & Sandri, M. 2004, Magnesium doped hydroxyapatite: Synthesis and characterization, *EURO CERAMICS VIII, Key Engineering Materials*.

Tang, R. K., Hass, M., Wu, W. J., Gulde, S., Nancollas, G. H., (2003), Constant composition dissolution of mixed phases II. Selective dissolution of calcium phosphates, *Journal of Colloid and Interface Science*, **260**, 379-384.

Tang, R. K., Henneman, Z. J., Nancollas, G. H., (2003), Constant composition kinetics study of carbonated apatite dissolution, *Journal of Crystal Growth*, **249**, 614-624.

Tang, R. K., Wu, W. J., Haas, M., Nancollas, G. H., (2001), Kinetics of dissolution of beta-tricalcium phosphate, *Langmuir*, **17**, 3480-3485.

Tang, X. L., Xiao, X. F., Liu, R. F., (2005a), Hydrothermal synthesis and characterization of silicon-substituted hydroxyapatite, *Chinese Journal of Inorganic Chemistry*, **21**, 1500-1504.

Tang, X. L., Xiao, X. F., Liu, R. F., (2005b), Structural characterization of silicon-substituted hydroxyapatite synthesized by a hydrothermal method, *Materials Letters*, **59**, 3841-3846.

Tanner, K. E., McGregor, W. J., That, P. T. T., Ward, I. M., Bonfield, W., (2001), Fatigue of Hapex (TM) - A structural bone replacement material, *Structural Biomaterials for the 21St Century* 229-237.

Tas, A. C., Aldinger, F., (2005), Formation of apatitic calcium phosphates in a Na-K-phosphate solution of pH 7.4, *Journal of Materials Science-Materials in Medicine*, **16**, 167-174.

Terpstra, R. A., Driessens, F. C. M., (1986), Magnesium in Tooth Enamel and Synthetic Apatites, *Calcified Tissue International*, **39**, 348-354.

Thachepan, S., Li, M., Davis, S. A., Mann, S., (2006), Additive-mediated crystallization of complex calcium carbonate superstructures in reverse microemulsions, *Chemistry of Materials*, **18**, 3557-3561.

Thamaraiselvi, T. V., Rajeswari, S., (2004), Biological Evaluation of Bioceramic Materials - A Review, *Trends in Biomaterials and Artificial Organs*, **18**, 9-17.

Thian, E. S., Huang, J., Best, S. M., Barber, Z. H., Bonfield, W., (2005a), A new way of incorporating silicon in hydroxyapatite (Si-HA) as thin films, *Journal of Materials Science-Materials in Medicine*, **16**, 411-415.

Thian, E. S., Huang, J., Best, S. M., Barber, Z. H., Bonfield, W., (2005b), Magnetron co-sputtered silicon-containing hydroxyapatite thin films - an in vitro study, *Biomaterials*, **26**, 2947-2956.

Thian, E. S., Huang, J., Best, S. M., Barber, Z. H., Bonfield, W., (2006a), Novel silicon-doped hydroxyapatite (Si-HA) for biomedical coatings: An in vitro study using acellular simulated body fluid, *Journal of Biomedical Materials Research Part B-Applied Biomaterials*, **76B**, 326-333.

Thian, E. S., Huang, J., Best, S. M., Barber, Z. H., Bonfield, W., (2007), Silicon-substituted hydroxyapatite: The next generation of bioactive coatings, *Materials Science & Engineering C-Biomimetic and Supramolecular Systems*, **27**, 251-256.

Thian, E. S., Huang, J., Best, S. M., Barber, Z. H., Brooks, R. A., Rushton, N., Bonfield, W., (2006b), The response of osteoblasts to nanocrystalline silicon-substituted hydroxyapatite thin films, *Biomaterials*, **27**, 2692-2698.

Thian, E. S., Huang, J., Vickers, M. E., Best, S. M., Barber, Z. H., Bonfield, W., (2006c), Silicon-substituted hydroxyapatite (SiHA): A novel calcium phosphate coating for biomedical applications, *Journal of Materials Science*, **41**, 709-717.

Thompson, I. D., Hench, L. L., (1998), Mechanical properties of bioactive glasses, glass-ceramics and composites, *Proceedings of the Institution of Mechanical Engineers Part H-Journal of Engineering in Medicine*, **212**, 127-136.

Toba, Y., Kajita, Y., Masuyama, R., Takada, Y., Suzuki, K., Aoe, S., (2000), Dietary magnesium supplementation affects bone metabolism and dynamic strength of bone in ovariectomized rats, *Journal of Nutrition*, **130**, 216-220.

Tok, A. I. Y., Du, S. W., Boey, F. Y. C., Chong, W. K., (2007), Hydrothermal synthesis and characterization of rare earth doped ceria nanoparticles, *Materials Science and Engineering A-Structural Materials Properties Microstructure and Processing*, **466**, 223-229.

Towler, M. R., Gibson, I. R., Best, S. M., (2000), Novel processing of hydroxyapatite-zirconia composites using nano-sized particles, *Journal of Materials Science Letters*, **19**, 2209-2211.

Vats, A., Tolley, N. S., Polak, J. M., Gough, J. E., (2003), Scaffolds and biomaterials for tissue engineering: a review of clinical applications, *Clinical Otolaryngology*, **28**, 165-172.

Vazquez, C. G., Barba, C. P., Munguia, N., (2005), Stoichiometric hydroxyapatite obtained by precipitation and sol gel processes, *Revista Mexicana de Fisica*, **51**, 284-293.

Vignoles, M., Bonel, G., Young, R. A., (1987), Occurrence of Nitrogenous Species in Precipitated B-Type Carbonated Hydroxyapatites, *Calcified Tissue International*, **40**, 64-70.

Viswanath, B., Ravishankar, N., (2006), Interfacial reactions in hydroxyapatite/alumina nanocomposites, *Scripta Materialia*, **55**, 863-866.

Vuola, J., Goransson, H., Bohling, T., AskoSeljavaara, S., (1996), Bone marrow induced osteogenesis in hydroxyapatite and calcium carbonate implants, *Biomaterials*, **17**, 1761-1766.

Vuola, J., Taurio, R., Goransson, H., Asko-Seljavaara, S., (1998), Compressive strength of calcium carbonate and hydroxyapatite implants after bone-marrow-induced osteogenesis, *Biomaterials*, **19**, 223-227.

Wang, C., Zhao, J., Zhao, X., Bala, H., Wang, Z., (2006a), Synthesis of nanosized calcium carbonate (aragonite) via a polyacrylamide inducing process, *Powder Technology*, **163**, 134-138.

Wang, Y. J., Zhang, S. H., Wei, K., Zhao, N. R., Chen, J. D., Wang, X. D., (2006b), Hydrothermal synthesis of hydroxyapatite nanopowders using cationic surfactant as a template, *Materials Letters*, **60**, 1484-1487.

Watanabe, Y., Ikoma, T., Monkawa, A., Suetsugu, Y., Yamada, H., Tanaka, J., Moriyoshi, Y., (2005), Fabrication of transparent hydroxyapatite sintered body with high crystal orientation by pulse electric current sintering, *Journal of the American Ceramic Society*, **88**, 243-245.

Webster, T. J., Massa-Schlueter, E. A., Smith, J. L., Slamovich, E. B., (2004), Osteoblast response to hydroxyapatite doped with divalent and trivalent cations, *Biomaterials*, **25**, 2111-2121.

Weiner, S., Traub, W., Wagner, H. D., (1999), Lamellar bone: Structure-function relations, *Journal of Structural Biology*, **126**, 241-255.

White, A. A., Best, S. M., Kinloch, I. A., (2007), Hydroxyapatite-carbon nanotube composites for biomedical applications: A review, *International Journal of Applied Ceramic Technology*, **4**, 1-13.

Whited, B. M., Skrtic, D., Love, B. J., Goldstein, A. S., (2006), Osteoblast response to zirconia-hybridized pyrophosphate-stabilized amorphous calcium phosphate, *Journal of Biomedical Materials Research Part A*, **76A**, 596-604.

Wopenka, B., Pasteris, J. D., (2005), A mineralogical perspective on the apatite in bone, *Materials Science & Engineering C-Biomimetic and Supramolecular Systems*, **25**, 131-143.

Xie, A. J., Shen, Y. H., Li, X. Y., Yuan, Z. W., Qiu, L. G., Zhang, C. Y., Yang, Y. F., (2007), The role of Mg2+ and Mg2+/amino acid in controlling polymorph and morphology of calcium carbonate crystal, *Materials Chemistry and Physics*, **101**, 87-92.

Xu, C. B., Lee, J., Teja, A. S., (2008), Continuous hydrothermal synthesis of lithium iron phosphate particles in subcritical and supercritical water, *Journal of Supercritical Fluids*, **44**, 92-97.

Xu, C. B., Teja, A. S., (2008), Continuous hydrothermal synthesis of iron oxide and PVA-protected iron oxide nanoparticles, *Journal of Supercritical Fluids*, **44**, 85-91.

Xu, J. L., Khor, K. A., (2007), Chemical analysis of silica doped hydroxyapatite biomaterials consolidated by a spark plasma sintering method, *Journal of Inorganic Biochemistry*, **101**, 187-195.

Xu, J. L., Khor, K. A., Gu, Y. W., Kumar, R., Cheang, P., (2005), Radio frequency (rf) plasma spheroidized HA powders: powder characterization and spark plasma sintering behavior, *Biomaterials*, **26**, 2197-2207.

Xu, J. L., Khor, K. A., Kumar, R., (2007), Physicochemical differences after densifying radio frequency plasma sprayed hydroxyapatite powders using spark plasma and conventional sintering techniques, *Materials Science and Engineering A-Structural Materials Properties Microstructure and Processing*, **457**, 24-32.

Yamasaki, Y., Yoshida, Y., Okazaki, M., Shimazu, A., Uchida, T., Kubo, T., Akagawa, Y., Hamada, Y., Takahashi, J., Matsuura, N., (2002), Synthesis of functionally graded MgCO3 apatite accelerating osteoblast adhesion, *Journal of Biomedical Materials Research*, **62**, 99-105.

Yan, L., Li, Y. D., Deng, Z. X., Zhuang, J., Sun, X. M., (2001), Surfactant-assisted hydrothermal synthesis of hydroxyapatite nanorods, *International Journal of Inorganic Materials*, **3**, 633-637.

Yashima, M., Sakai, A., Kamiyama, T., Hoshikawa, A., (2003), Crystal structure analysis of beta-tricalcium phosphate Ca-3(PO4)(2) by neutron powder diffraction, *Journal of Solid State Chemistry*, **175**, 272-277.

Yoshida, K., Kondo, N., Kita, H., Mitamura, M., Hashimoto, K., Toda, Y., (2005), Effect of substitutional monovalent and divalent metal ions on mechanical properties of beta-tricalcium phosphate, *Journal of the American Ceramic Society*, **88**, 2315-2318.

Zaffe, D., (2005), Some considerations on biomaterials and bone, *Micron*, **36**, 583-592.

Zhang, F., Zhou, Z. H., Yang, S. P., Mao, L. H., Chen, H. M., Yu, X. B., (2005), Hydrotherynal synthesis of hydroxyapatite nanorods in the presence of anionic starburst dendrimer, *Materials Letters*, **59**, 1422-1425.

Zhang, G. L., Li, Y. F., Ren, S. X., Zhang, J. M., (2007a), HA active coating on titanium prepared by Spark Plasma Sintering, *Progresses in Fracture and Strength of Materials and Structures, 1-4*, **353-358**, 1679-1682.

Zhang, H. G., Zhu, Q. S., Xie, Z. H., (2005), Mechanochemical-hydrothermal synthesis and characterization of fluoridated hydroxyapatite, *Materials Research Bulletin*, **40**, 1326-1334.

Zhang, H. T., Liu, L. S., Zhai, P. C., Fu, Z. Y., Zhang, Q. J., (2008), Effect of fabrication process on the microstructure and dynamic compressive properties of SiCp/Al composites fabricated by spark plasma sintering, *Materials Letters*, **62**, 443-446.

Zhang, J. X., Iwasa, M., Kotobuki, N., Tanaka, T., Hirose, M., Ohgushi, H., Jiang, D. L., (2006), Fabrication of hydroxyapatite-zirconia composites for orthopedic applications, *Journal of the American Ceramic Society*, **89**, 3348-3355.

Zhang, J. X., Tanaka, H., Ye, F., Jiang, D. L., Iwasa, M., (2007b), Colloidal processing and sintering of hydroxyapatite, *Materials Chemistry and Physics*, **101**, 69-76.

Zhang, Q. Y., Chen, J. Y., Feng, J. M., Cao, Y., Deng, C. L., Zhang, X. D., (2003), Dissolution and mineralization behaviors of HA coatings, *Biomaterials*, **24**, 4741-4748.

Zhao, M., Cai, L., Yu, Q. W., Gong, M. C., Yuan, S. H., Chen, Y. Q., (2007), The application of ceria-zirconia composite oxide in motorcycle catalyst, *Rare Metal Materials and Engineering*, **36**, 277-281.

Zhou, Y., Hirao, K., Yamauchi, Y., Kanzaki, S., (2003), Effects of heating rate and particle size on pulse electric current sintering of alumina, *Scripta Materialia*, **48**, 1631-1636.

Zhou, Y. S., Wei, Q., Ma, H. F., Zhang, Z. L., (2007a), Y/composite titania-silica (CTS) supported catalyst for hydrotreating coker gas oil, *Catalysis Today*, **125**, 211-219.

Zhou, Z. H., Zhou, P. L., Yang, S. P., Yu, X. B., Yang, L. Z., (2007b), Controllable synthesis of hydroxyapatite nanocrystals via a dendrimer-assisted hydrothermal process, *Materials Research Bulletin*, **42**, 1611-1618.

Ziegler, K. J., Doty, R. C., Johnston, K. P., Korgel, B. A., (2001), Synthesis of organic monolayer-stabilized copper nanocrystals in supercritical water, *Journal of the American Chemical Society*, **123**, 7797-7803.

Zioupos, P., Rogers, K. D., (2006), Complementary Physical and Mechanical Techniques to Characterise Tooth: A Bone-like Tissue, *Journal of Bionic Engineering*, **3**, 19-31.

Zou, J. P., Ruan, J. M., Huang, B. Y., Zhou, Z. C., Liu, Y. L., (2005a), Preparation and microstructure of HA-316L stainless steel fibre asymmetrical functionally graded biomaterial, *Journal of Inorganic Materials*, **20**, 1181-1188.

Zou, S., Huang, J., Best, S., Bonfield, W., (2005b), Crystal imperfection studies of pure and silicon substituted hydroxyapatite using Raman and XRD, *Journal of Materials Science-Materials in Medicine*, **16**, 1143-1148.

Zyman, Z., Tkachenko, M., Epple, M., Polyakov, M., Naboka, M., (2006), Magnesium-substituted hydroxyapatite ceramics, *Materialwissenschaft und Werkstofftechnik*, **37**, 474-477.

Appendix A

SOP for Construction of a Counter Current Reactor for Continuous Hydrothermal Flow Synthesis Systems

The counter-current reactor is an important part of the hydrothermal system. It is also referred to as the mixing point. Careful assembly of this part is essential in order to ensure maximum safety under high temperatures and pressures. A schematic (to scale) of the counter-current reactor is shown in Figure A-1. Swagelok parts required for this reactor are listed as follows;

1) 20 cm long piece of 1/8" Swagelok 316L grade pipe
2) 12 cm long piece of 3/8" Swagelok 316L grade pipe
3) 12 cm long piece of 3/8" Swagelok 316L grade pipe
4) Two sets of 1/8" Swagelok 316L grade nuts and ferrules
5) Five sets of 3/8" Swagelok 316L grade nuts and ferrules
6) One 1/8 – 3/8" Swagelok 316L grade reducer
7) 2.5 cm long 3/8" circular Swagelok 316L grade rod

The steps of construction are as follows

1) Make sure that a 20 cm long and perfectly straight piece of 1/8" pipe is available. This piece of pipe should not have any scratches or kinks in it, as this may lead to stress concentration points while at high temperature and pressure, which may result in leakage or worse, an explosion. The ends of the pipe should be filed to a shape resembling Figure A-2. Once this is done, make sure that the scratches on all surfaces around the end of the pipe are smoothed using a fine grade sand paper (500 – 1000 grit). The inner edges of the pipe should also be smoothed using a file.

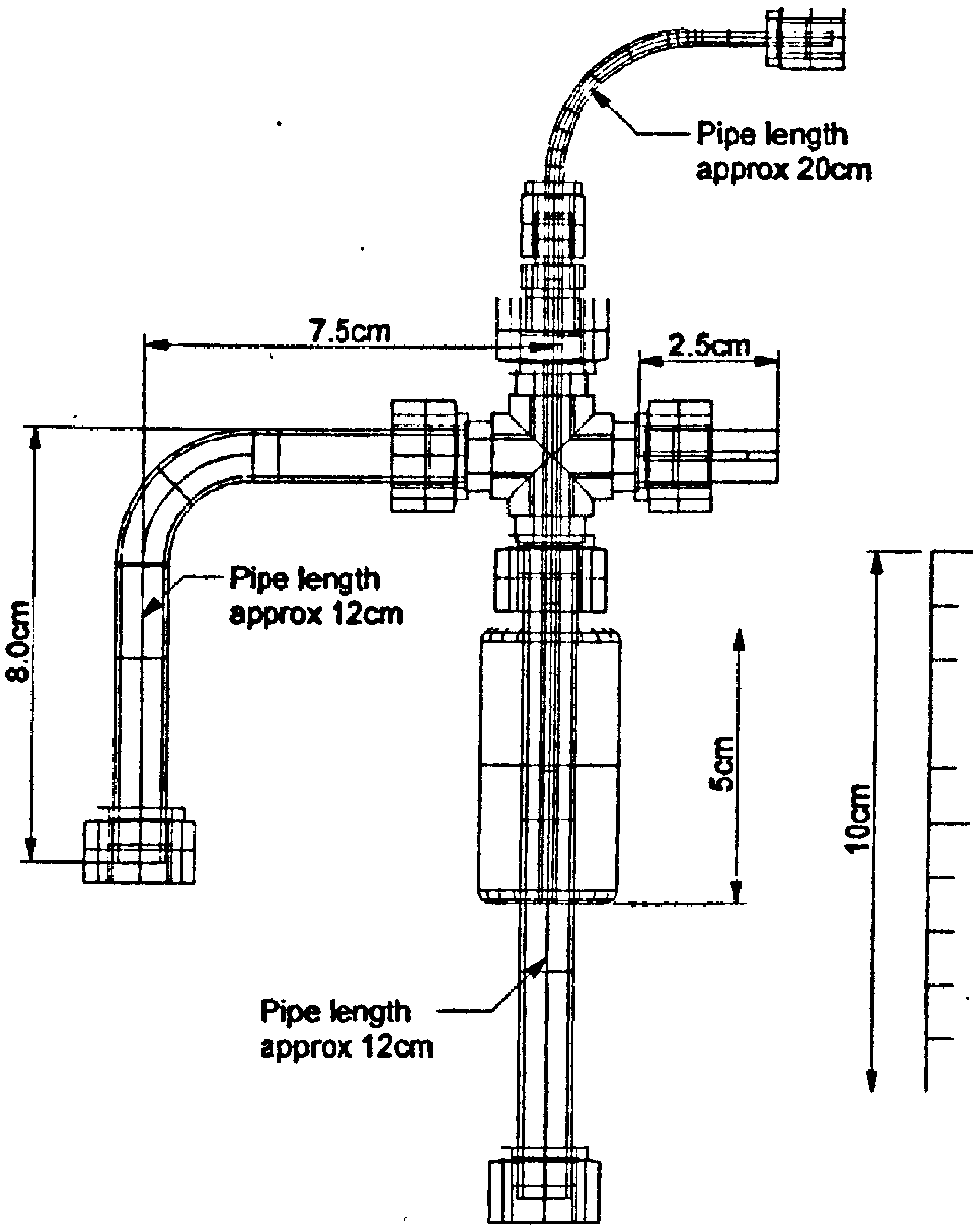

Figure A-1 Schematic of the counter-current reactor showing approximate dimensions (drawing prepared by K. Thompson of CMTG, Department of Chemistry, UCL).

2) Due to its small diameter, the 1/8" pipe is very ductile and can be bent around a suitable circular body to yield a 90-degree bend as shown in Figure A-3.

3) Swage the 1/8" pipe (three quarters turn, ¾) at point A and at point B (see Figure A-3). Point A is the point where the 1/8" pipe goes through a bored-through 1/8 – 3/8" reducer and point B is the connection point to the heater.

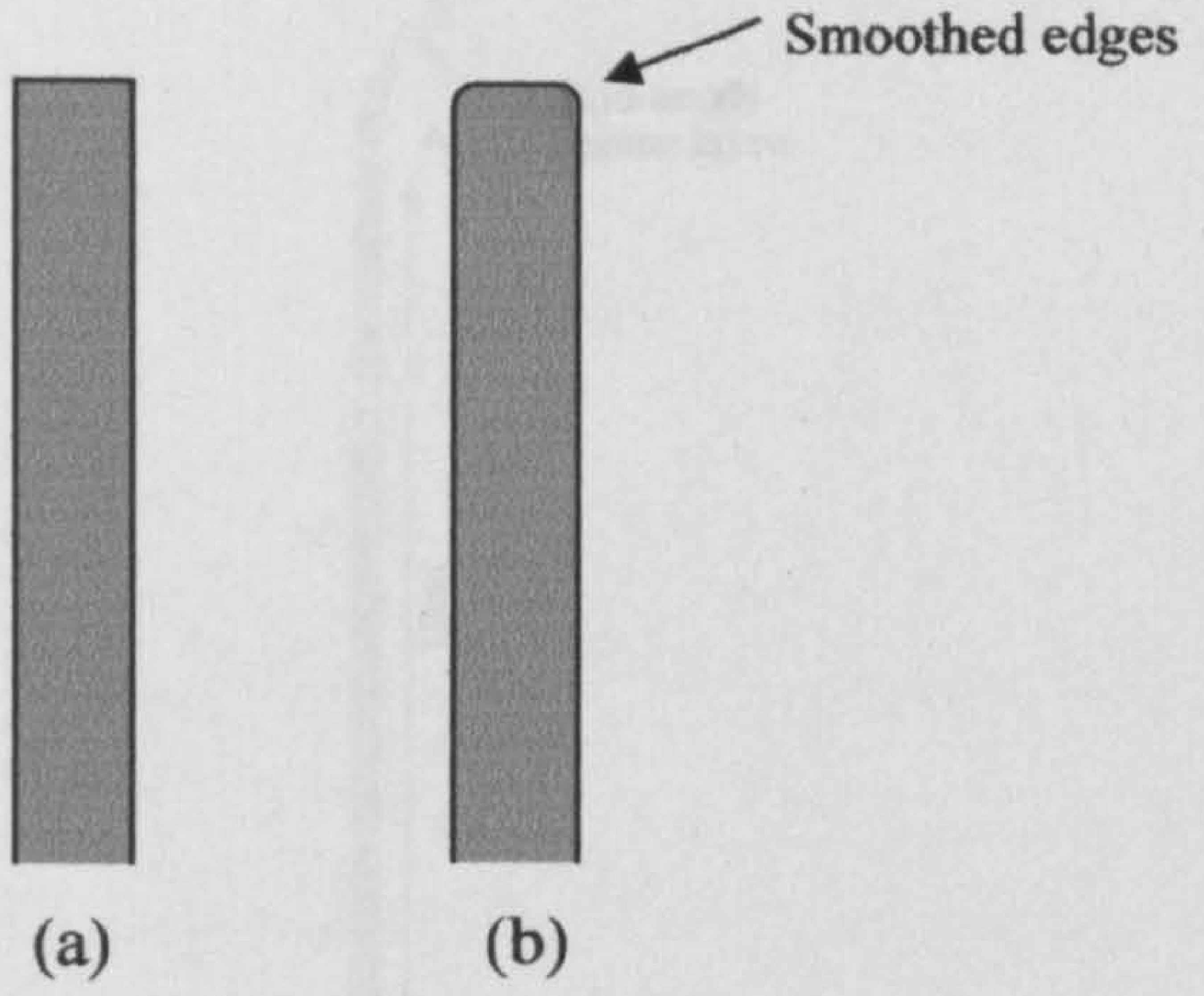

Figure A-2 Schematic representations of cross-sections of (a) original pipe and (b) pipe with smoothed chamfered edges.

4) File the ends of a 12 cm long 3/8" pipe to a shape represented in Figure A-2. Make sure than the scratches on all surfaces around the end of the pipe are smoothed using a fine grade sand paper (500-1000 grit). Swage the inner side of the pipe using a file as well. Swage both ends (one and a quarter turn, 1¼).

5) File the ends of the second piece of 3/8" pipe (12 cm long) as mentioned earlier. Fix the pipe bender in a vice. Arrange the rod in the pipe bender as shown in Figures A-4 (a) and (b) and bend it to a 90 degree angle. Make sure that scratches on all surfaces at the end of the pipe are smoothed using a fine grade sand paper (800-1000 grit). File the inner side of the pipe using a file as well. Once this is done, swage both ends (one and a quarter turn, 1¼).

6) The 2.5 cm long 3/8" circular rod should have a 1/8" diameter and 2 cm deep hole drilled on one of the sides (done on a mounted drill by a technician). This is used to house a k-type thermocouple for temperature measurement at the mixing point. Smooth the edges as before and then swage this bit at one end (one and a quarter turns, 1¼).

7) Connect all the parts together as shown in Figure A-1. Do not over tighten the fittings as this reduces part life.

Note: Replace all the parts mentioned in this SOP after every 15 times it is unscrewed from the system (keep track of the system log book). The parts may be changed earlier if deemed necessary.

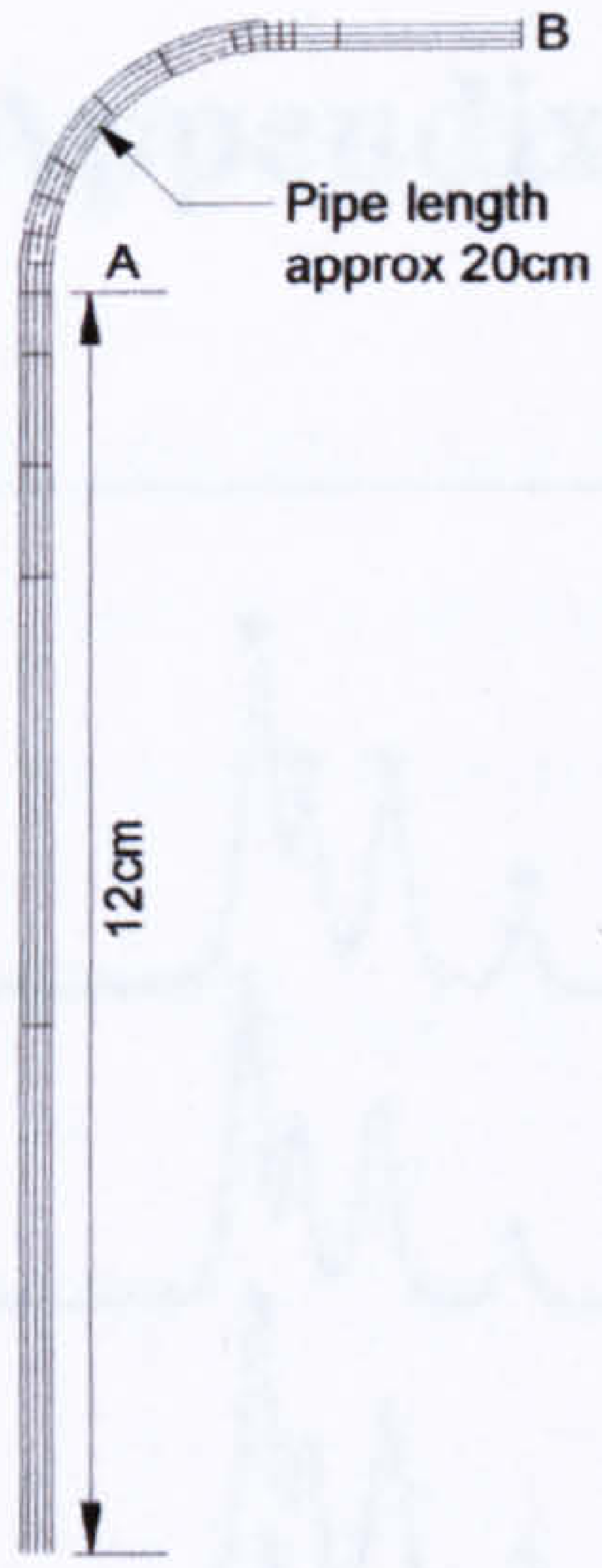

Figure A-3 Mixing point 1/8th inch 316L Swagelok inner pipe (drawing prepared by K. Thompson of CMTG, Department of Chemistry, UCL).

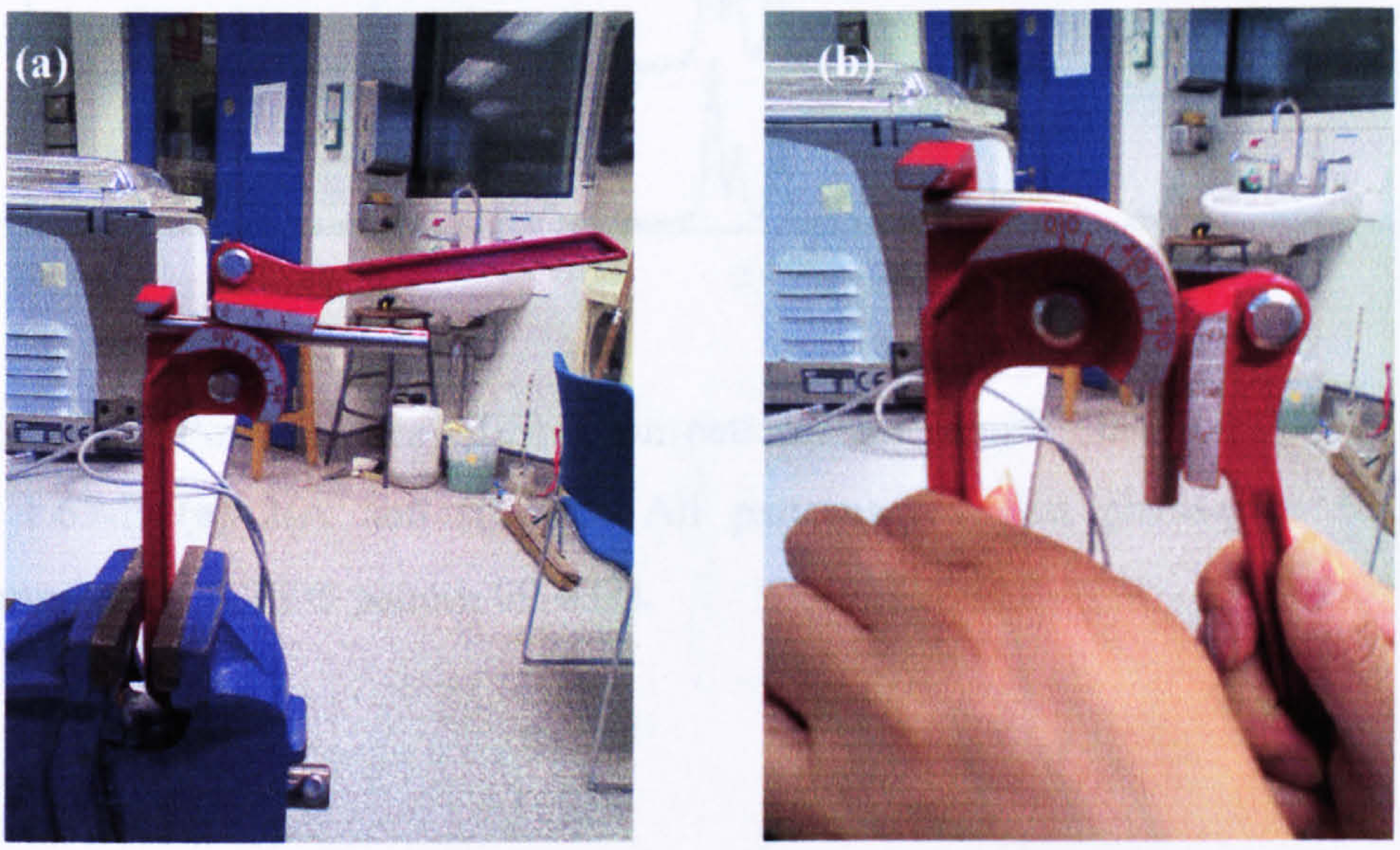

Figure A-4 3/8th inch 316L Swagelok pipe connecting the 3/8th cross-piece to cooler (a) when placed in the pipe bender and (b) bent to give a 90-degree angle.

Appendix B

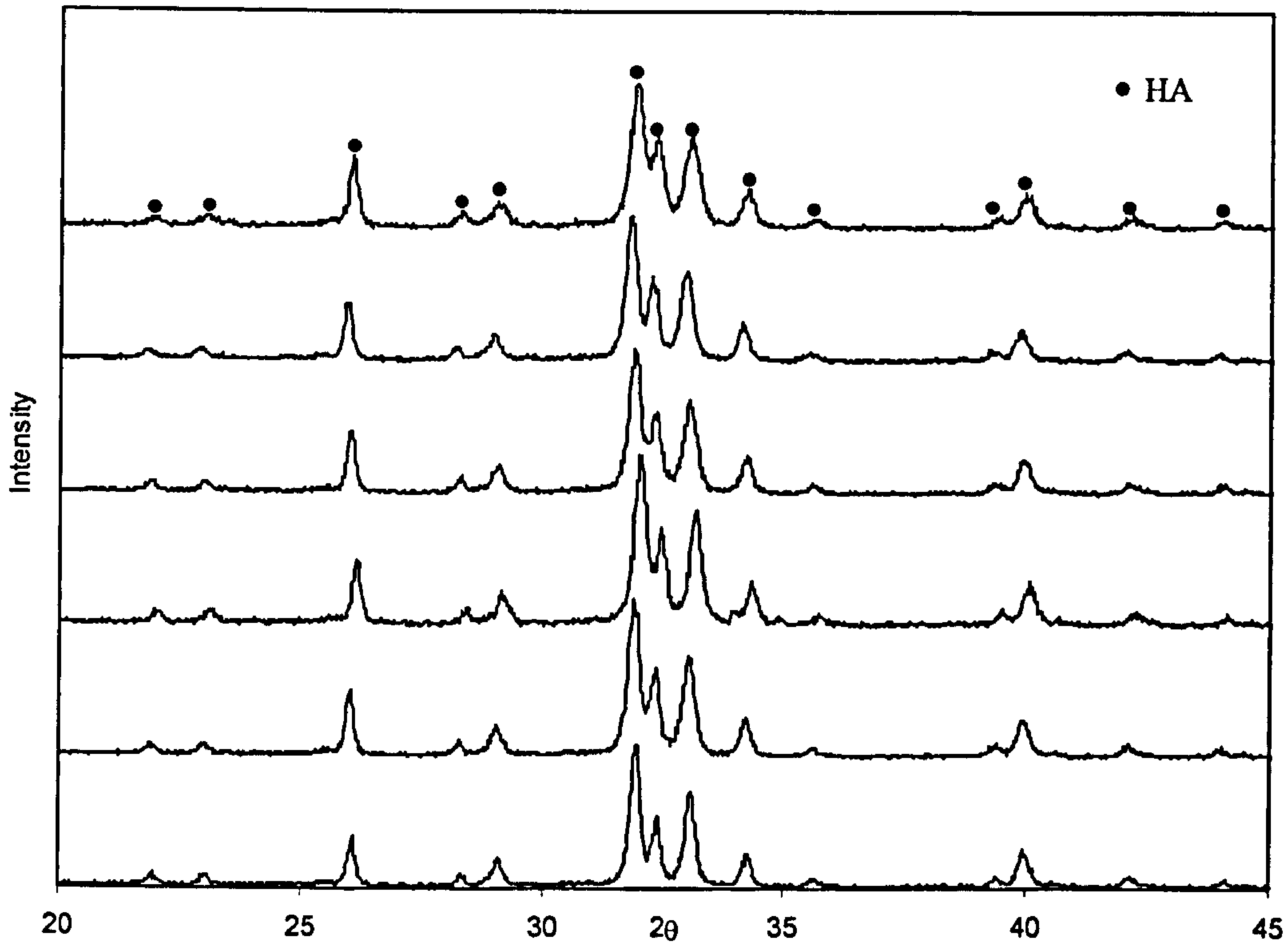

Figure B-1 Powder X-ray diffraction patterns for samples (a) 1-A (b) 1-B (c) 1.67-A (d) 1.67-B (e) 2-A and (f) 2-B. All patterns revealed phase-pure hydroxyapatite (compared to JCPDS pattern 09-432).

Appendix C

Table C-1 Sample IDs, elemental composition (atomic %) determined using EDS as average values of 10 area scans and corresponding Ca:P molar ratios for carbonate substituted samples. SD represents standard deviation.

Sample ID	Atomic %			Ca:P (± SD)
	Ca	P	O	
7.5CO$_3$-HA	69.20	8.47	12.32	1.45 (± 0.04)
11.5CO$_3$-HA	77.65	7.66	14.70	1.92 (± 0.14)
15.7CO$_3$-HA	76.33	8.95	14.72	1.65 (± 0.13)
20CO$_3$-HA	77.33	7.24	15.43	2.13 (± 0.07)
24.6CO$_3$-HA	77.96	6.48	15.56	2.40 (± 0.11)

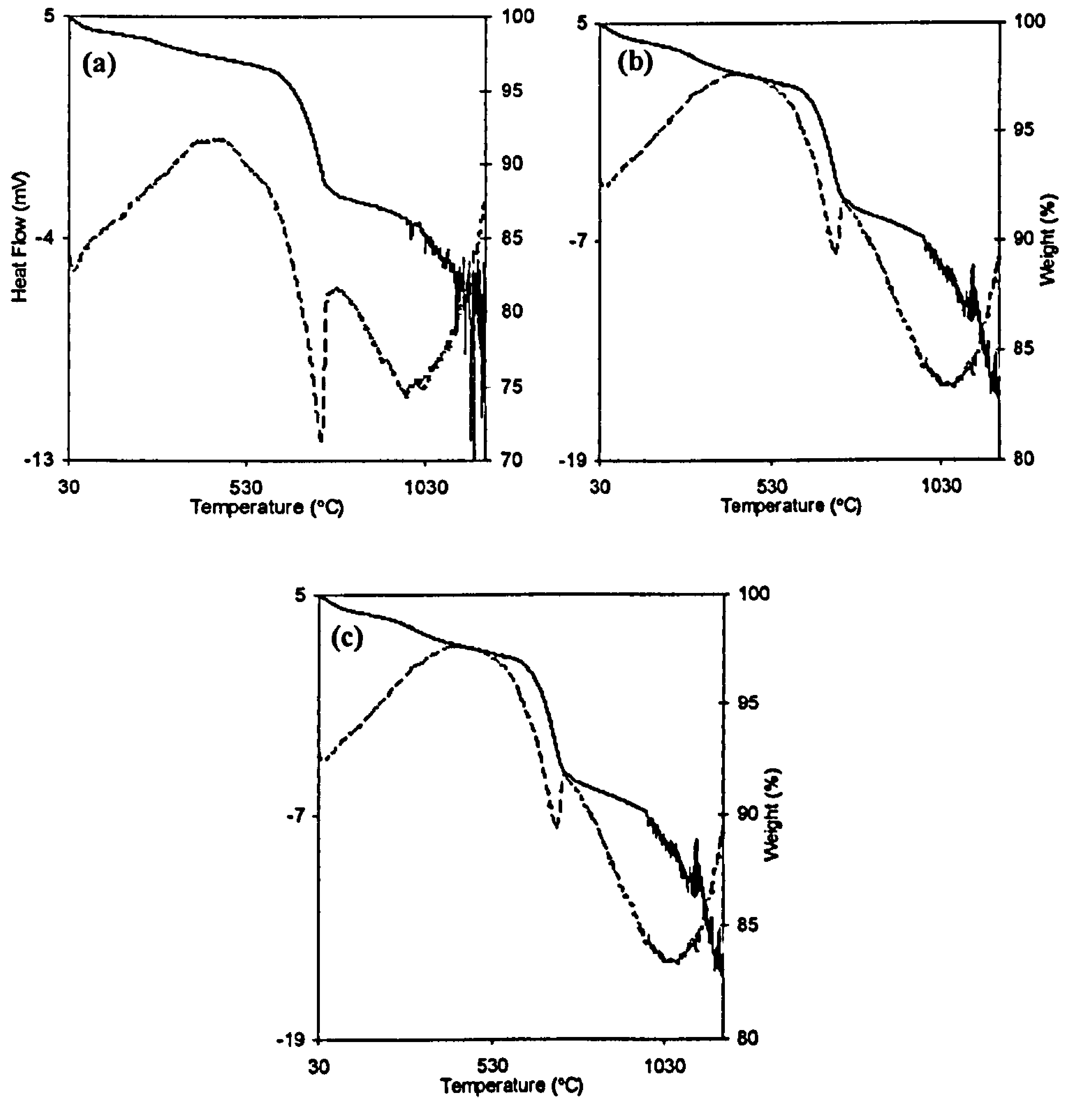

Figure C-1 Simultaneous Thermal Analysis (STA) data showing DSC (dotted line) and TGA (solid line) plots of samples (a) 11.5CO$_3$-HA (b) 15.7CO$_3$-HA and (c) 20CO$_3$-HA.

Table C-2 Sample IDs, elemental composition (atomic %) determined using EDS as average values of 10 area scans and corresponding Ca:P molar ratios for silicate substituted samples. SD represents standard deviation.

Sample ID	**Atomic %**				**Ca:[P+Si] (± SD)**
	O	**Si**	**P**	**Ca**	
1SiHA	73.46	0.20	10.27	16.07	1.53 (± 0.05)
2SiHA	74.89	0.31	9.98	14.83	1.44 (± 0.07)
3SiHA	74.47	0.43	10.00	15.10	1.45 (± 0.10)
4SiHA	74.72	0.39	9.84	15.05	1.47 (± 0.09)
5SiHA	73.58	0.62	9.76	16.04	1.54 (± 0.06)
6SiHA	73.72	0.47	9.97	15.83	1.51 (± 0.06)
8SiHA	75.38	0.71	9.09	14.81	1.51 (± 0.05)
10SiHA	74.56	0.82	9.68	14.95	1.42 (± 0.06)

Appendix D

Synthesis of Calcium Carbonate

This section summarises the attempts to synthesise calcium carbonate in the CHFS system 2. Initially 100.0 mM calcium nitrate was reacted with 100.0 mM urea. A very dilute suspension was collected which yielded a small amount of powder when centrifuged and freeze dried (20 % yield). This sample is labelled as LY-1 (L and Y represent Low Yield). Attempts at increasing the pH of the calcium nitrate solution in a separate reaction, to pH 11 using neat ammonium hydroxide solution (2 mL in 100 mL solution) did not increase the yield significantly (30% yield, sample labelled as LY-2). Use of 300 mM and 800 mM urea solutions in separate reactions, also did not increase the yield and the samples were not retained. After each reaction, the large particle filter in the CHFS system 2 was inspected, and was found to be clean each time (i.e. no particles were "filtered"). The pump rates for both the solutions and superheated water were always 5 mL min^{-1} and 10 mL min^{-1}. The reactions were carried out at 400 °C and 24 MPa. In another experiment, 100.0 mM calcium hydroxide suspension (pH 13.5) was pumped through CHFS system 2 using a Rheodyne 7010 injector in place of one of the pumps in the three pump configuration. Chilled sparkling natural mineral water by Highland Spring company was used as a carbonate source. All the CHFS system reaction parameters were the same as mentioned above. The yield of the product was *ca.* 45% and this sampled is labelled as MY-1 (where MY represents Medium Yield). In order to investigate the effect of magnesium on particle morphology 0.5 mmoles of magnesium nitrate were added to the 9.5 mmoles of calcium nitrate solution in 100 mL deionized water to result in an overall 100.0 mM concentration. This sample is labelled as MY-2. The superheated water was pumped at 10 mL min^{-1}. The carbonate water was pumped at 5 mL min^{-1}. The calcium hydroxide suspension was injected continuously (and manually) to match a 5 mL min^{-1} pumping rate. Suspensions were washed, centrifuged and freeze dried as explained in section 2.2.2.1. All reactions were carried out at 400 °C and 24 MPa in CHFS system 2.

Powder X-ray diffraction patterns in Figures D-1 (a) to (c) revealed samples LY-1, LY-2 and MY-1 all to contain mostly calcite (compared to JCPDS pattern 5-586) and a small amount of vaterite (compared to JCPDS pattern 41-1475) (polymorphs of calcium carbonate). The peaks were observed to very distinct and sharp, representing high crystallinity. Figures D-2 (a) to (d) show the TEM images of samples MY-1 and MY-2.

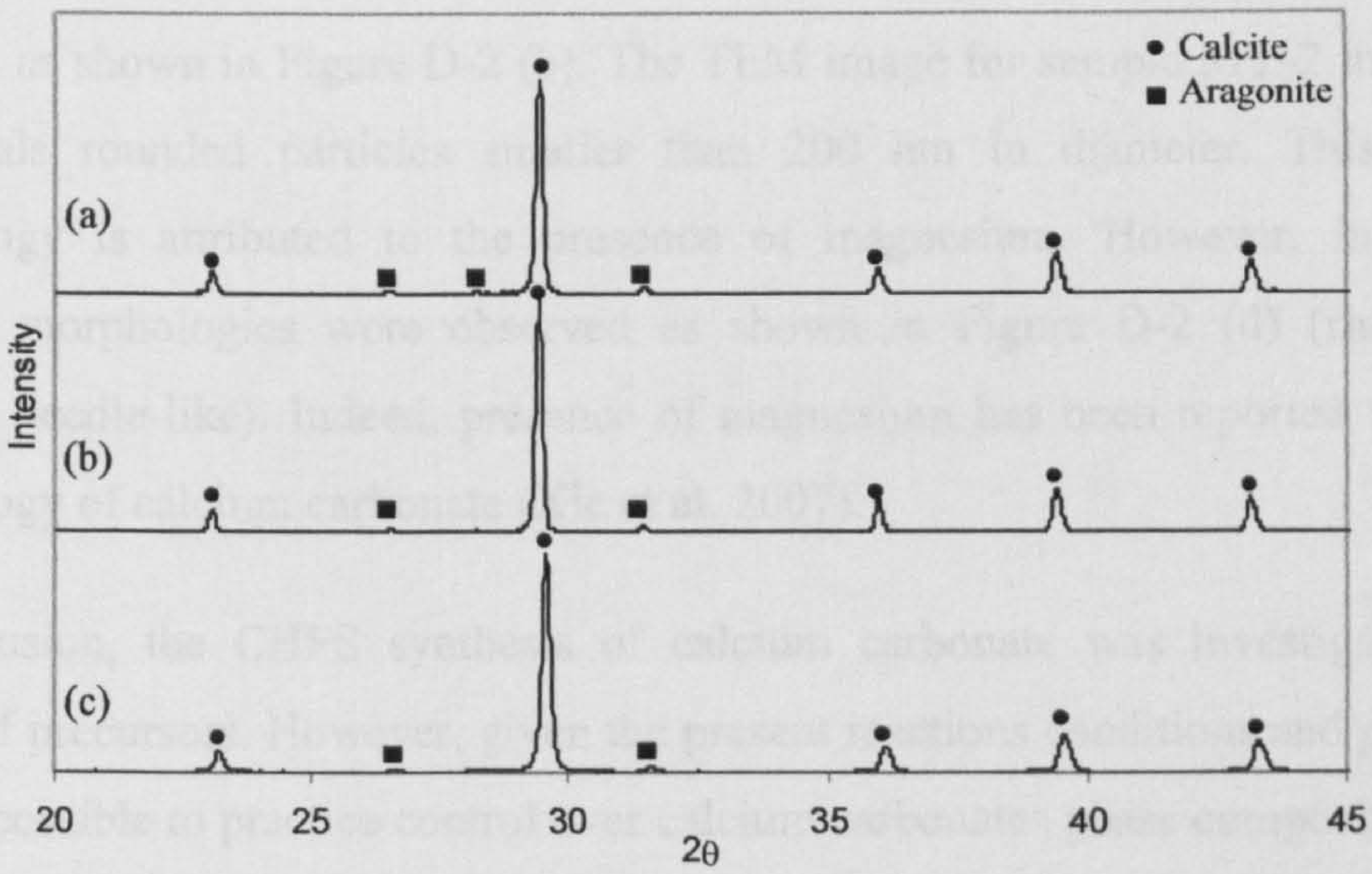

Figure D-1 Powder X-ray diffraction patterns of samples (a) LY-1 (b) LY-2 and (c) MY-1.

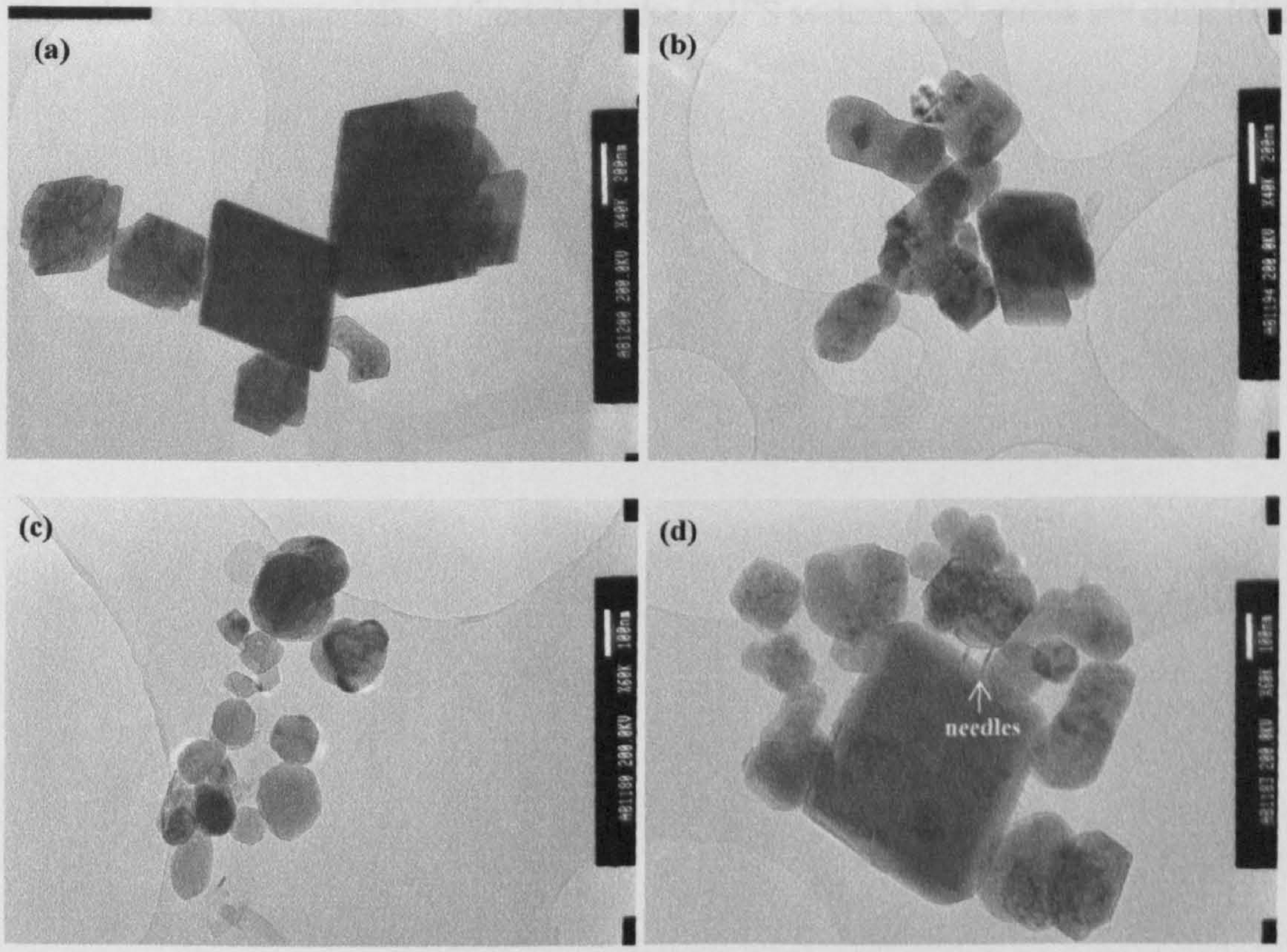

Figure D-2 Transmission electron microscope images, of sample MY-1 at magnification x40K showing (a) rhombohedral calcite particles (b) irregular shaped particles and of sample MY-2 at magnification x60K showing (c) rounded calcite particles and (d) three different morphologies (rounded, rhombohedral and needle-like).

TEM image shown in Figure D-2 (a) reveals the typical rhombohedral morphology of calcite particles in sample MY-1 (Lei et al. 2006). There was a large variation in size but all particles were smaller than 600 nm. Some irregular shaped particles were also observed as shown in Figure D-2 (b). The TEM image for sample MY-2 in Figure D-2 (c) reveals rounded particles smaller than 200 nm in diameter. This change in morphology is attributed to the presence of magnesium. However, in total three different morphologies were observed as shown in Figure D-2 (d) (rhombohedral, rounded, needle-like). Indeed, presence of magnesium has been reported to effect the morphology of calcium carbonate (Xie et al. 2007).

In conclusion, the CHFS synthesis of calcium carbonate was investigated using a variety of precursors. However, given the present reactions conditions and precursors, it was not possible to practice control over calcium carbonates phase composition, particle morphology and size. Use of calcium hydroxide suspension with carbonated water resulted in maximum yields of *ca.* 45%. In comparison to the large variety of calcium phosphate based materials synthesised in the CHFS system, such yields are quite low.

Appendix E

Table E-1 Samples IDs, elemental composition (atomic %) determined using EDS as average values of 10 area scans and corresponding Ca:P molar ratios for magnesium substituted samples. SD represents standard deviation.

Sample ID	**Atomic %**				**(Ca+Mg):P (±SD)**
	O	**P**	**Mg**	**Ca**	
0.5Mg-CaP	74.03	10.56	0.58	14.83	1.46 (± 0.04)
1Mg-CaP	74.21	10.79	0.91	14.09	1.39 (± 0.07)
1.5Mg-CaP	76.06	10.5	1.39	12.05	1.28 (± 0.09)
2Mg-CaP	73.31	11.32	1.83	13.54	1.36 (± 0.06)
4Mg-CaP	70.3	12.83	3.4	13.48	1.31 (± 0.02)
6Mg-CaP	71.71	12.19	5.02	11.08	1.32 (± 0.01)
8Mg-CaP	74.26	10.88	6.65	8.22	1.37 (± 0.02)
10Mg-CaP	75.25	9.68	7.48	7.6	1.56 (± 0.04)
12Mg-CaP	73.74	10.37	9.31	6.58	1.53 (± 0.05)
14Mg-CaP	80.86	11.26	11.69	6.19	1.59 (± 0.07)
Mg-CaP	69.95	12.6	17.45	N/A	N/A

Table E-2 Samples IDs, elemental composition (atomic %) determined using EDS as average values of 10 area scans and corresponding Ca:P molar ratios for zinc substituted samples. SD represents standard deviation.

Sample ID	Atomic %				(Ca+Zn):P (±SD)
	O	P	Ca	Zn	
1.3Zn-CaP	71.91	11.3	16.48	0.31	1.49 (± 0.12)
5.1Zn-CaP	70.57	11.67	15.67	2.1	1.52 (± 0.08)
10Zn-CaP	73.09	11.26	13.06	2.59	1.39 (± 0.06)
14.7Zn-CaP	74.19	11.16	11.09	3.57	1.31 (± 0.06)
19.3Zn-CaP	78.06	9.9	8.19	3.85	1.20 (± 0.11)
23.7Zn-CaP	72.95	11.63	9.16	6.27	1.33 (± 0.07)
28Zn-CaP	71.98	11.98	8.35	7.69	1.34 (± 0.11)
32Zn-CaP	77.97	10.46	6.1	5.47	1.10 (± 0.12)

Appendix F

Three discs of HA were conventionally sintered (pressureless) in a Carbolite box furnace to provide a comparison with spark plasma sintered HA. HA synthesised at 450 °C and 24 MPa in CHFS system 3 using concentrations identical to those used for synthesis of sample HA(400) as reported in Chapter 2. Superheated water was pumped at 25 mL min^{-1} and both the calcium nitrate and diammonium hydrogen phosphate solutions were pumped at 12.5 mL min^{-1} respectively. The schematic diagram of the cross-section of the hardened steel cylindrical die (custom built at Department of Materials, QMUL) is shown in Figure F-1.

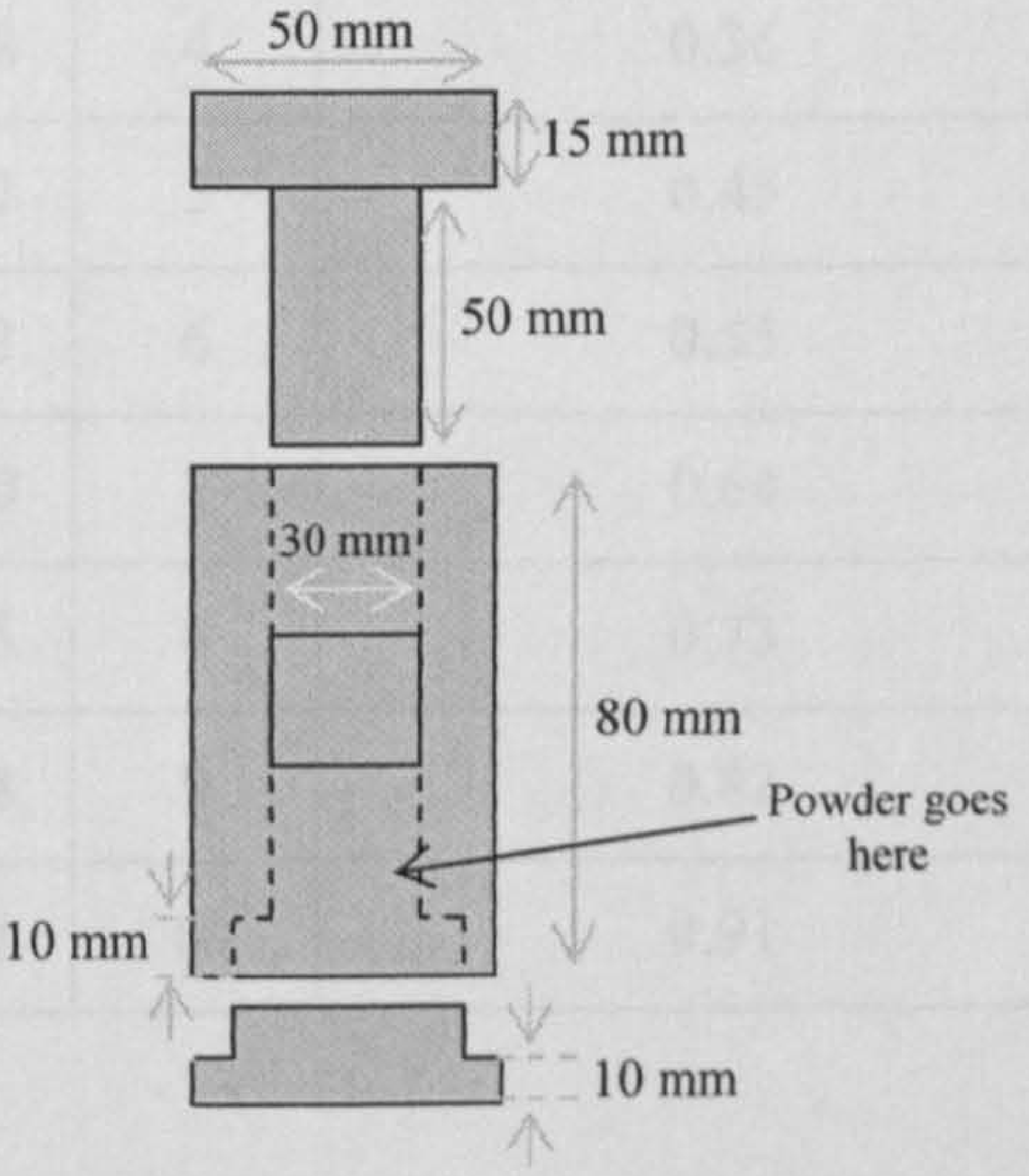

Figure F-1 Schematic diagram of the hardened steel cylindrical die used for conventional sintering.

Three 30 mm diameter discs (disc 1, disc 2 and disc 3) were pressed in a uniaxial Perkin Elmer press under 6 ton load to result in green densities of 46 %, 50 % and 48 % (of theoretical density), respectively. These discs were then sintered at 800 °C, 900 °C and 1000 °C to result in sintered densities of 48%, 51% and 60%, respectively. The densities were determined by measuring the dimensions (3 times per disc). Heating and cooling rates of 2.5 °C min^{-1} were used and all discs were sintered for two hours at the corresponding temperature. As suggested by the sintered densities, no densification took place at 800 °C and 900 °C. Sintering at 1000 °C showed only 12 % increase in densification. These results outlined the difficulty in conventional sintering of HA in the absence of pressure and binders which have been reported to enhance sintering.

Table F-1 3-pt flexural strength values of 10 rectangular specimens cut from 2 discs obtained by spark plasma sintering of sample *m*-HA(450)* at 950°C for 5 minutes 15 seconds and corresponding statistical parameters used to determine the Weibull modulus.

3-pt Flexural Strength σ_f (MPa)	$\ln(\sigma_f)$	Rank, j	Probability of fracture, P_f [j/(n+1)]	ln ln [1/(1-P_f)]
107.30	4.68	1	0.09	-2.35
114.30	4.74	2	0.18	-1.61
118.50	4.77	3	0.27	-1.14
119.70	4.78	4	0.36	-0.79
136.50	4.92	5	0.45	-0.50
138.70	4.93	6	0.55	-0.24
149.00	5.00	7	0.64	0.01
156.50	5.05	8	0.73	0.26
160.60	5.08	9	0.82	0.53
165.60	5.11	10	0.91	0.87

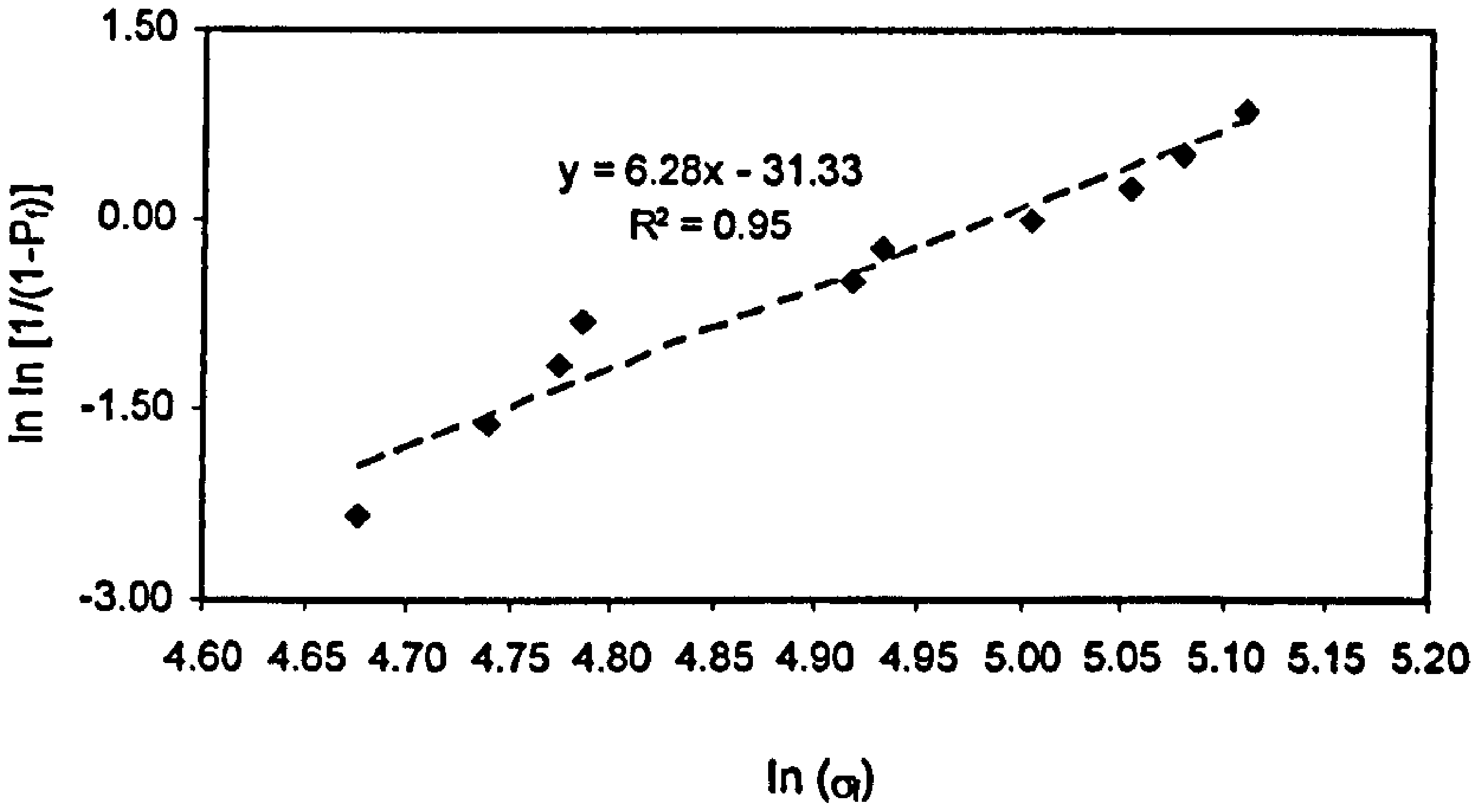

Figure F-2 Plot of ln ln [1/(1-P_f)] vs. ln (σ_f) (corresponding to Table F-1) showing the equation and R^2 value. Weibull modulus, m, is equal to the slope of the fitted trend line.

Table F-2 3-pt flexural strength values of 10 rectangular specimens cut from 2 discs obtained by spark plasma sintering of sample *m*-HA(450)* at 1000 °C for 5 minutes 15 seconds and corresponding statistical parameters used to determine the Weibull modulus.

3-pt Flexural Strength σ_f (MPa)	$\ln(\sigma_f)$	Rank, j	Probability of fracture, P_f [j/(n+1)]	ln ln [1/(1-P_f)]
138.00	4.93	1	0.09	-2.35
140.50	4.95	2	0.18	-1.61
146.30	4.99	3	0.27	-1.14
153.00	5.03	4	0.36	-0.79
154.10	5.04	5	0.45	-0.50
163.00	5.09	6	0.55	-0.24
166.40	5.11	7	0.64	0.01
170.30	5.14	8	0.73	0.26
175.60	5.17	9	0.82	0.53
176.30	5.17	10	0.91	0.87

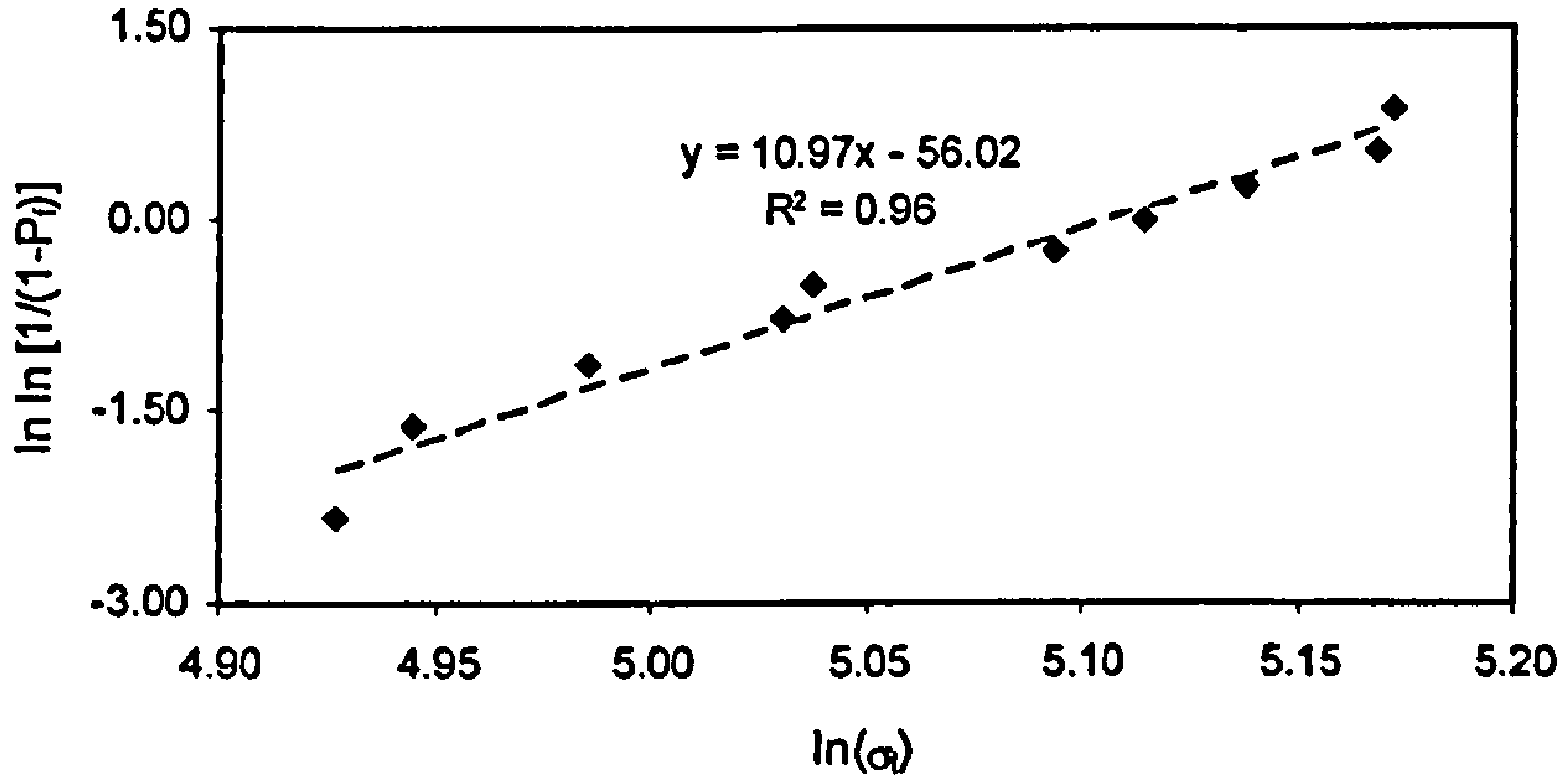

Figure F-3 Plot of ln ln [1/(1-P_f)] vs. ln (σ_f) (corresponding to Table F-2) showing the equation and R^2 value. Weibull modulus, m, is equal to the slope of the fitted trend line.

Table F-3 3-pt flexural strength values of 10 rectangular specimens cut from 2 discs obtained by spark plasma sintering of sample H-10 at 1000 °C for 5 minutes 15 seconds and corresponding statistical parameters used to determine the Weibull modulus.

3-pt Flexural Strength σ_f (MPa)	$\ln(\sigma_f)$	Rank, j	Probability of fracture, P_f [j/(n+1)]	ln ln [1/(1-P_f)]
85.70	4.45	1	0.09	-2.35
99.60	4.60	2	0.18	-1.61
102.40	4.63	3	0.27	-1.14
105.90	4.66	4	0.36	-0.79
107.40	4.68	5	0.45	-0.50
110.80	4.71	6	0.55	-0.24
112.10	4.72	7	0.64	0.01
115.40	4.75	8	0.73	0.26
115.60	4.75	9	0.82	0.53
122.10	4.80	10	0.91	0.87

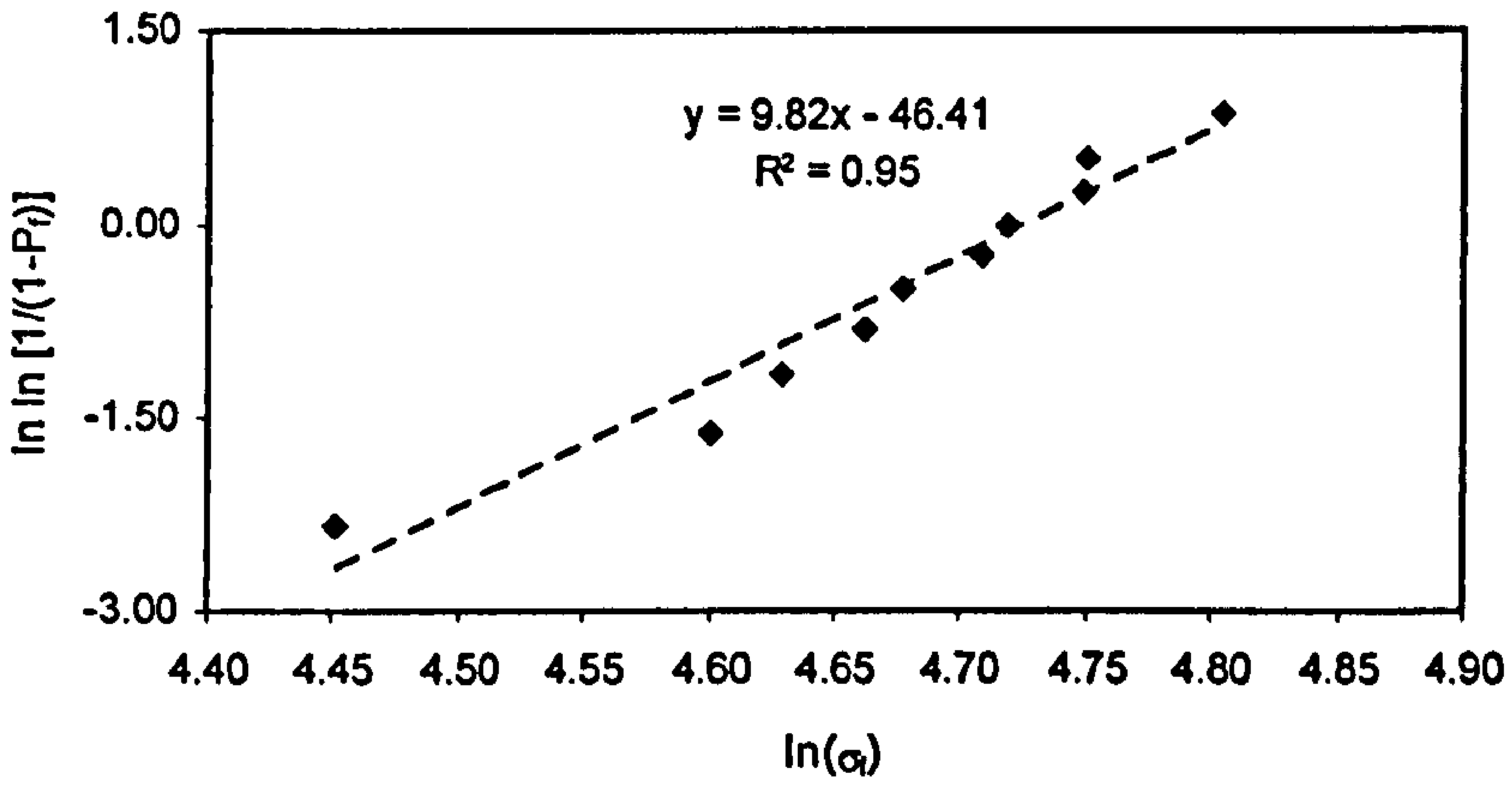

Figure F-4 Plot of ln ln [1/(1-P_f)] vs. ln (σ_f) (corresponding to Table F-3) showing the equation and R^2 value. Weibull modulus, m, is equal to the slope of the fitted trend line.

Appendix G

Synthesis of TiO_2-HA Powders

This section addresses the CHFS of TiO_2-HA co-precipitates. Titanium (IV) bis(ammonium lactato) dihydroxide (TiBALD, 50 wt% in water) (from Sigma-Aldrich (Dorset, UK) was used as a titania precursor. 25 mL of 0.4 M TiBALD were added to 75 mL deionized water. 1.97 g (8.35 mmoles) of calcium nitrate were then added to this solution (final pH 7). 0.66 g (5.00 mmoles) of diammonium hydrogen phosphate were dissolved in 100 mL of deionized water to result in 50.0 mM concentration (pH adjusted to pH 10 using 3 mL neat ammonium hydroxide solution). The amounts of calcium nitrate and diammonium hydrogen phosphate used were such that the Ca:P molar ratio was *ca.* 1.67. The amount of TiBALD solution added was such that, given 100% yields, it would result in 50wt% TiO_2 in HA. CHFS system 3 was used for this reaction. The superheated water was pumped at 25.0 mL min^{-1}. TiBALD containing calcium nitrate solution and diammonium hydrogen phosphate solution were pumped, respectively, at 12.5 mL min^{-1}. The reaction was carried out at 450 °C (band heater at same temperature) and 24 MPa. The collected suspensions were washed, centrifuged and freeze-dried as explained in section 2.2.2.1 (c) in Chapter 2.

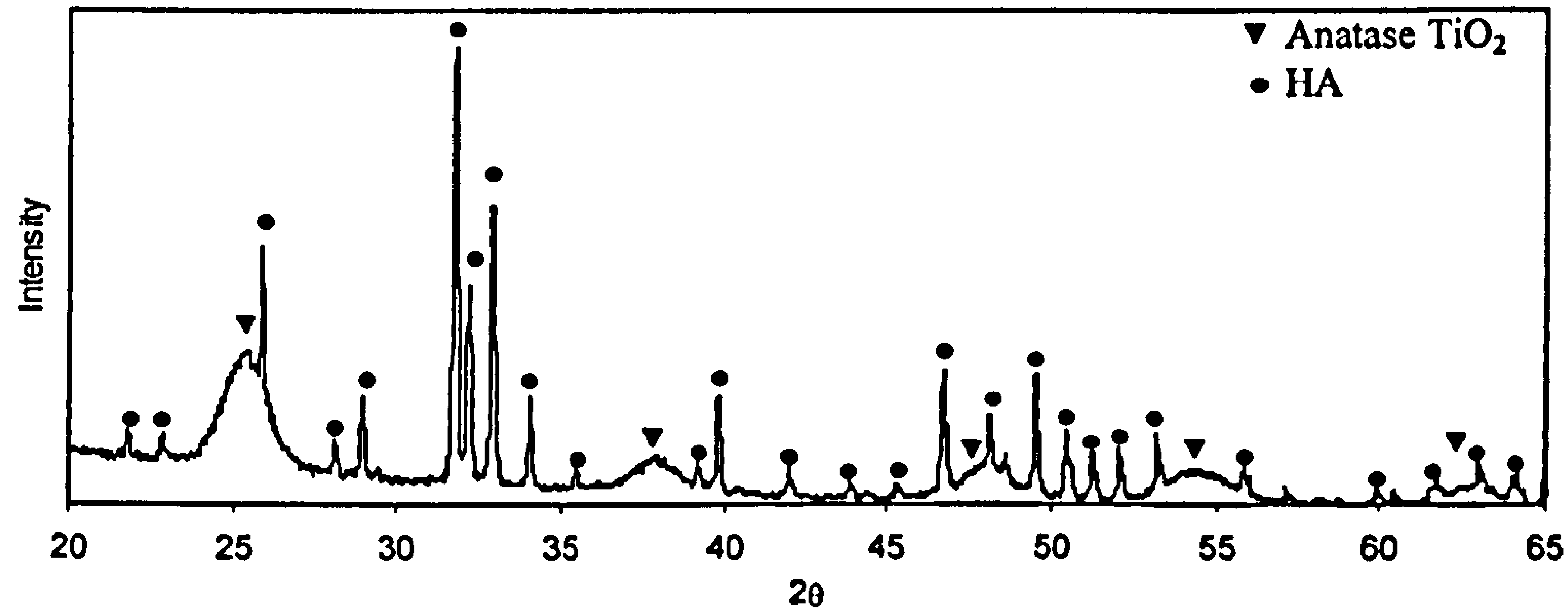

Figure G-1 Powder X-ray diffraction pattern of the TiO_2-HA mixture.

The powder X-ray diffraction pattern in Figure G-1 identifies the sample as a biphasic mixture of anatase titania (compared to JCPDS pattern 21-1272) and HA (compared to JCPDS pattern 09-432). This result shows the CHFS system is a suitable material to develop TiO_2-HA mixtures (with no additional unwanted phases) which can be tested for their photocatalytic activity or spark plasma sintered to enhance the inferior mechanical properties of HA.

List of Publications

Papers

A. A. Chaudhry, S. Haque, S. Kellici, P. Boldrin, I. Rehman, F. A. Khalid, J. A. Darr, **(2006)** Instant Nano-hydroxyapatite: A Continous and Rapid Hydrothermal Synthesis, *Chemical Communications*, 2286-2288

P. Boldrin, A. K. Hebb, A. A. Chaudhry, L. Otley, B. Thiebaut, P. Bishop, J. A. Darr, **(2007)** Direct Synthesis of Nano-size $NiCo_2O_4$ spinel and related compounds via Continuous Hydrothermal Synthesis Methods, *Industrial & Engineering Chemistry Research*, 46, 4830-4838

A. A. Chaudhry, J. Goodall, M. Vickers, J. C. Cockroft, I. Rehman, F. A. Khalid, J. A. Darr, **(2008)** Direct Manufacture of Magnesium Substituted Calcium Phosphate Bioceramics Using Continuous Hydrothermal Flow Synthesis, *Submitted to Journal of Materials Chemistry*

Abstracts

A. A. Chaudhry, H. Yan, M. Reece, J. Corbett, F. McNeil-Watsorf, J. A. Darr, Continuous Hydrothermal Flow Synthesis of Nano-bio-ceramics; Rapid Particle Sizing and Fast Consolidation Via Spark Plasma Sintering, *Nanoparticles 2008, Bradford, UK*, **February 2008,** Poster Presentation

A. A. Chaudhry, P. Boldrin, I. Rehman, J. A. Darr, Continuous Hydrothermal Flow Synthesis of Ion Substituted Calcium Phosphates, *8th International Symposium on Supercritical Fluids, Kyoto, Japan*, **November 2006,** Poster Presentation

A. A. Chaudhry, S. Haque, J. A. Darr, Nano-bioceramics and Surface Coated Bioceramics for Bone Replacement Applications, *Developments in Powder Technology in the Medical Device Industry, Powder Matrix/Meditech Joint Meeting, Nottingham, UK*, **June 2006,** Oral Presentation

A. A. Chaudhry, S. Haque, J. A. Darr, Towards the Goal of Bone Replacement; Nano-bioceramics and Surface Coated Bioceramics, *Developments in Powder Technology in the Medical Device Industry, Powder Matrix/Meditech Joint Meeting, Nottingham, UK*, **June 2006,** Poster Presentation